

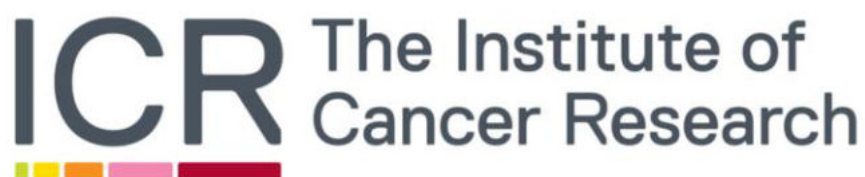
Development of Chemical Tool Compounds Targeting the Non-Catalytic Functions of Tankyrase

Iona Catherine Black

The Institute of Cancer Research
University of London

A thesis submitted in accordance with the requirements for the
degree of Doctor of Philosophy.

January 2023



Declaration of Originality

I confirm that the research presented in this thesis is my own. Where information has been derived from other sources, I confirm that this is indicated in the thesis by references. Work which has been performed by ICR co-workers as part of a collaboration is indicated in the thesis by names of colleagues who performed the work.

Iona C. Black, January 2023

Acknowledgements

I would like to thank my supervisor, Prof. Ian Collins, for his mentorship, support, and wisdom throughout my PhD, and for helping me to learn and develop both as a scientist and personally. I would also like to thank my supervisor, Prof. Sebastian Guettler, for his advice, guidance, and enthusiasm during my PhD, and for his insight into tankyrase biology. I am very grateful to have had such excellent supervisors.

I would like to thank all members of Medicinal Chemistry 2 and the Guettler group for providing their advice and suggestions, for assistance and support in the lab, and for being such great people to have worked with. In particular, I would like to thank John Caldwell, who has helped me daily throughout my PhD: from discussing ideas to guidance in the lab, I cannot thank him enough for his support and encouragement.

I would like to extend my gratitude to everyone who has helped me with various aspects of this project: Stephen Hearnshaw for his efforts with X-ray crystallography; Mirco Meniconi and Andrea Scarpino for performing *in silico* docking studies; Mariola Zaleska, Mark Stubbs, Olivier Pierrat and Ben Broadway for testing PROTAC compounds; and Mark Stubbs again for his help in establishing an FP assay. I owe a huge thank you to Maggie Liu for her training in biophysical NMR assays, which has been fundamental to my PhD.

I have thoroughly enjoyed working within the Division of Cancer Therapeutics and Structural Biology at the ICR, and I am very grateful to the countless colleagues who have helped me in some way, either with their expertise or encouragement, and who have made the ICR such a great place to work. I would like to thank the Masonic Charitable Foundation for providing the funding for my PhD.

Finally, I would like to thank my mum and dad, sisters, friends, the ICR girlies and Tony for their continual support which has kept me going throughout my PhD. Tony: I can't find the words to thank you enough, I really couldn't have finished it without you.

Abstract

Tankyrase (TNKS1 and TNKS2) is a promising target in anti-cancer drug discovery due to its role in regulating cellular processes which are dysregulated in cancer. In addition to catalysing the poly(ADP-ribosyl)ation of substrate proteins, tankyrase is a scaffolding protein which recruits substrate proteins through its ARC domain, and undergoes SAM domain mediated polymerisation. Whilst tankyrase inhibitor development has focused on antagonists of the catalytic PARP domain, the limitations of this approach have been suggested in recent literature highlighting the contribution of catalysis-independent mechanisms to cellular tankyrase functions. The aim of this work is the development of chemical tool compounds targeting the non-catalytic functions of tankyrase.

The development of substrate binding antagonists of the tankyrase ARC domain from a literature-reported fragment hit has been pursued using fragment-based drug discovery. Hit optimisation was undertaken through iterations of *in silico* guided fragment design, synthesis, and testing in biophysical NMR assays against TNKS2 ARC4. Whilst modification of the furan motif did not lead to an increase in binding affinity, quinoxaline substitution led to fragment analogues with improved binding affinity ($K_d = 240 \mu\text{M}$ and $K_d = 120 \mu\text{M}$) which maintain competitive binding in a specific sub-site of the substrate recognition pocket of TNKS2 ARC4. A higher throughput fluorescence polarisation assay was then established and was used to determine the potency of higher affinity compounds based on lead fragments.

Targeted degradation of tankyrase has been pursued by the synthesis of PROTACs from a potent catalytic tankyrase inhibitor in conjunction with a cereblon E3 binding ligand. The synthesis and profiling of heterobifunctional compounds based on the catalytic tankyrase inhibitor XAV939 was undertaken. No evidence of tankyrase degradation in cells was observed, however compounds with a reduced hydrogen-bond donor count showed binding to tankyrase and cereblon in both biochemical and cellular target engagement assays, therefore demonstrating cellular permeability.

Table of Contents

Declaration of Originality	2
Acknowledgements	3
Abstract.....	4
Table of Contents.....	5
List of Figures	13
List of Tables	18
List of Schemes	20
Abbreviations	21
Chapter 1 Introduction.....	26
1.1 Cancer and Targeting Post-translational Modifications.....	26
1.1.1 Hallmarks of Cancer.....	26
1.1.2 Cancer Therapy.....	27
1.1.3 Targeted Therapy in Cancer Treatment	27
1.1.4 Post-translational Modifications in Targeted Therapy.....	29
1.2 ADP-Ribosylation and Poly(ADP-Ribosyl)ation	31
1.2.1 ADP-Ribosyltransferases and Poly(ADP-ribosyl) polymerases.....	31
1.2.2 Catalytic and Regulatory Structural Domains of PARPs	33
1.2.3 PARP Cellular Functions.....	35
1.3 Tankyrase Structural Domains.....	35
1.3.1 Structural Domain Organisation of Tankyrase.....	35
1.3.2 Catalytic PARP Domain of Tankyrase.....	36
1.3.3 Non-catalytic Domains of Tankyrase.....	38
1.3.3.1 Sterile alpha-motif multimerisation (SAM) domain	39
1.3.3.2 Ankyrin repeat cluster (ARC) domain	41
1.4 Cellular Functions of Tankyrase	45

1.4.1	Wnt/ β -Catenin Signalling.....	45
1.4.2	Telomere Maintenance.....	47
1.4.3	Mitotic Spindle Assembly	48
1.4.4	DNA Repair	48
1.4.5	Synthetic Lethality in BRCA-Deficient Tumours	48
1.5	Limitations of Catalytic Tankyrase Inhibitors.....	49
1.5.1	Catalytic Tankyrase Inhibitors	50
1.5.2	Limitations of Catalytic Tankyrase Inhibition	56
1.6	Inhibitors of Tankyrase Non-Catalytic (Scaffolding) Functions.....	58
1.6.1	Peptidomimetic Approaches.....	59
1.6.2	Small Molecule Screening Approaches.....	61
1.6.2.1	Fragment-based screening against the tankyrase ARC domain 61	
1.6.2.2	Virtual high-throughput screening against the tankyrase ARC domain 64	
1.6.2.3	FRET-based high-throughput screening against the tankyrase ARC and SAM domains	65
1.7	Thesis Hypothesis and Aims.....	67
Chapter 2 Initial Structure-Activity Relationship Exploration of a Tankyrase ARC-Binding Fragment Hit.....		
2.1	Introduction to Fragment-Based Drug Discovery	70
2.1.1	Fragment Screening versus High-Throughput Screening	70
2.1.2	Fragment Hit-to-Lead Optimisation	72
2.1.3	Fragment-Based Drug Discovery and Protein-Protein Interactions 75	
2.2	Aim and Strategy for Development of Non-Catalytic Tankyrase Inhibitors using a Fragment-Based Approach.....	75
2.3	<i>In silico</i> binding model of fragment hit against TNKS2 ARC4	77

2.4	First iteration of fragment hit analogues.....	80
2.4.1	Design of analogues guided by <i>in silico</i> modelling	80
2.4.2	Synthesis of initial fragment hit analogues	82
2.5	Establishment of competitive ligand-observed NMR assay	85
2.5.1	Introduction to ligand-observed NMR.....	85
2.5.2	Quality control of TNKS2 ARC4 protein, 3BP2 peptide competitor and fragment stock solutions	88
2.5.3	Testing initial analogues in ligand-observed NMR assay	91
2.6	Second iteration of fragment hit analogues with furan modifications ...	97
2.6.1	Design of second fragment iteration and binding model hypothesis 97	
2.6.2	Synthesis of fragment hit analogues with furan modifications	100
2.6.3	SAR from ligand-observed NMR assay	104
2.7	Establishment of protein-observed NMR assay to determine binding affinities of modified furan analogues	111
2.7.1	Introduction to protein-observed NMR.....	111
2.7.2	Production of ¹⁵ N-labelled TNKS2 ARC4 protein	112
2.7.3	Determining binding affinity of modified furan analogues.....	114
2.7.4	Hypothesised <i>in silico</i> binding model of modified furan analogues 118	
Chapter 3	Identification and Characterisation of a Higher Affinity Fragment against TNKS2 ARC4	121
3.1	Validation of literature-reported ARC-binding compounds.....	121
3.2	Fragment hit analogues investigating quinoxaline replacements and substitutions	125
3.2.1	Design of quinoxaline modifications based on binding model hypothesis.....	125
3.2.2	Synthesis of modified quinoxaline analogues.....	127

3.2.3	Competitive ligand-observed NMR and further SAR analysis	130
3.2.4	Protein-observed NMR with CCT391081 (112).....	135
3.3	Introduction of dimethylamino quinoxaline substitution and identification of a higher affinity fragment CCT393128 (115)	138
3.4	Characterisation of lead fragment CCT393128 (115) binding to the ARC domain	142
3.4.1	Binding site mapping and docking studies from protein-observed NMR	143
3.4.2	Efforts in structural characterisation by X-ray crystallography.....	147
Chapter 4	Further Development and Optimisation of ARC-Binders based on a Lead Fragment	153
4.1	Design of analogues based on hypothesised lead fragment binding mode	153
4.1.1	Design of 3-substituted quinoxaline fragments.....	154
4.1.2	Design of 3-alkylamino quinoxaline peptidomimetics	155
4.2	Synthesis and testing of 3-substituted quinoxaline fragments	159
4.2.1	Synthesis of 3-alkoxy quinoxaline-6-carboxamide fragments....	159
4.2.2	Synthesis of 3-alkylamino quinoxaline-6-carboxamide fragments	161
4.2.3	Synthesis of 3-substituted quinoxalines with matched pair amides	164
4.2.4	Testing of 3-alkoxy and 3-alkylamino quinoxaline fragments in competitive ligand-observed NMR	165
4.2.5	Protein-observed NMR with 3-pyrrolidinyl quinoxaline fragment CCT394001 (144)	172
4.3	Synthesis and testing of 3-alkylamino quinoxaline peptidomimetics ..	176
4.3.1	Synthesis of 3-alkylamino quinoxaline-6-carboxamide peptidomimetics.....	176

4.3.2	Testing of 3-alkylamino quinoxaline peptidomimetics in competitive ligand-observed NMR	182
4.3.3	Testing of 3-pyrrolidinyl quinoxaline peptidomimetics in protein-observed NMR.....	185
4.4	Development of a fluorescence polarisation assay for testing of fragment analogues.....	191
4.4.1	Introduction to fluorescence polarisation and competitive fluorescence polarisation assays	192
4.4.2	Establishment of a competitive fluorescence polarisation assay with a Cy5 probe	194
4.4.2.1	Determination of the optimum Cy5 probe concentration	195
4.4.2.2	Direct binding FP assay of Cy5 probe with TNKS1 ARC4	196
4.4.2.3	Competitive FP assay with unlabelled control peptides	197
4.4.3	Competitive FP assay with unlabelled 3-alkylamino quinoxaline fragment analogues	199
4.4.3.1	Competitive FP assay with unlabelled control compounds ...	200
4.4.3.2	Competitive FP assay with 3-alkylamino quinoxaline fragment analogues.....	202
4.4.3.3	Conclusions	208
Chapter 5	Development of PROTACs for Targeted Tankyrase Degradation	210
5.1	Introduction to Targeted Protein Degradation	210
5.1.1	The Ubiquitin-Proteasome System.....	210
5.1.2	Development of Proteolysis Targeting Chimeras (PROTACs)	211
5.1.3	Targeting Scaffolding Functions with PROTACs	213
5.2	Design and Synthesis of First-generation XAV939-based Tankyrase PROTACs.....	215
5.2.1	Rationale for design of XAV939-based amide-linked PROTACs	215
5.2.2	Synthesis of XAV939-based amide-linked PROTACs.....	218

5.3	Testing of First-generation XAV939-based Tankyrase PROTACs in Target Engagement Assays	219
5.3.1	Assessment of tankyrase engagement using an auto-PARylation assay	219
5.3.2	Testing in biochemical and cellular cereblon target engagement assays	221
5.4	Design and Synthesis of Second-generation XAV939-based Tankyrase PROTACs.....	224
5.4.1	Rationale for design of XAV939-based ether-linked PROTACs ..	224
5.4.2	<i>In Silico</i> Modelling of Ternary Complex Formation	225
5.4.3	Synthesis of XAV939-based ether-linked PROTACs	230
5.5	Testing of Second-generation XAV939-based Tankyrase PROTACs in Target Engagement and Cellular Degradation Assays.....	231
5.5.1	Testing in biochemical and cellular cereblon target engagement assays	231
5.5.2	Assessment of cellular tankyrase engagement using a Wnt/ β -catenin reporter assay	233
5.5.3	Cellular assessment of tankyrase degradation.....	234
Chapter 6	Conclusions and Discussion.....	237
6.1	Substrate Binding Antagonists of the Tankyrase ARC Domain	237
6.1.1	Conclusions.....	237
6.1.2	Discussion and Future Directions.....	239
6.1.2.1	Structural Characterisation of ARC:Fragment Interactions ...	239
6.1.2.2	Lead Fragment Optimisation to Identify Potent Antagonists .	240
6.1.2.3	Identification of Tool Compounds from a Fragment-based Approach	241
6.2	PROTACs for the Targeted Degradation of Tankyrase.....	242
6.2.1	Conclusions.....	242
6.2.2	Discussion and Future Directions.....	243

6.2.2.1	Further Linker Variation to Identify XAV939-based PROTACs	243
6.2.2.2	Development of ARC-binding PROTACs.....	246
6.2.2.3	Identification of Tool Compounds from a PROTAC Approach	247
6.3	Outlook for Non-Catalytic Chemical Tool Compounds of Tankyrase	249
Chapter 7	Experimental Procedures	250
7.1	Synthetic Chemistry	250
7.1.1	General Methods.....	250
7.1.2	Chemical Syntheses from Chapter 2.....	251
7.1.3	Chemical Syntheses from Chapter 3.....	281
7.1.4	Chemical Syntheses from Chapter 4.....	303
7.1.5	Chemical Syntheses from Chapter 5.....	338
7.1.5.1	Synthesis of XAV939-based amide-linked PROTACs	338
7.1.5.2	Synthesis of XAV939-based ether-linked PROTACs.....	343
7.2	Protein Production	348
7.2.1	Expression of Tankyrase ARC4s.....	348
7.2.2	Purification of Tankyrase ARC4s.....	350
7.3	Biophysical and Biochemical Assays	353
7.3.1	Ligand-observed NMR Experiments.....	353
7.3.1.1	Quantitative NMR Assay.....	353
7.3.1.2	Kinetic Solubility NMR Assay.....	354
7.3.1.3	Competitive Ligand-Observed NMR Assay	355
7.3.2	¹ H- ¹⁵ N HSQC Protein-Observed NMR Experiments.....	356
7.3.3	Fluorescence Polarisation Assay	358
7.3.3.1	Cy5 probe titration	359
7.3.3.2	Direct binding FP assay with TNKS1 ARC4.....	359
7.3.3.3	Competitive FP assay with control peptides	360

7.3.3.4	Competitive FP assay with fragment compounds and control peptides	361
7.4	Computational Chemistry	362
7.4.1	MoKa Calculations	362
7.4.2	Minimum Energy Conformations of Fragments	362
7.4.3	Minimum Energy Conformations of Fragments based on CCT170746 (28) bound to TNKS2 ARC4	362
7.4.4	Fragment Docking into TNKS2 ARC4	363
7.4.5	Minimum Energy Conformations of Hybrid Fragment-Peptidomimetics based on CCT393128 (115) and CCT394001 (144) bound to TNKS2 ARC4	364
7.4.6	Minimum Energy Conformations of XAV939-based ether-linked PROTACs	365
Chapter 8	References	366

List of Figures

Figure	Title	Page
Figure 1.1	The hallmarks and enabling characteristics of cancer.	26
Figure 1.2	Small molecule targeted anti-cancer drugs approved from 2001 to 2020.	28
Figure 1.3	Summary of poly(ADP-ribosyl)ation (PARylation).	31
Figure 1.4	Structural domain organisation of the PARP enzymes.	32
Figure 1.5	Interaction of NAD ⁺ with diphtheria toxin.	34
Figure 1.6	TNKS1 and TNKS2 structural domain organisation.	36
Figure 1.7	Catalytic PARP domain of tankyrase.	37
Figure 1.8	TNKS2 SAM-PARP polymerisation characterised by cryo-EM and crystallography.	40
Figure 1.9	Tankyrase ARC domain.	42
Figure 1.10	Interaction of 3BP2 with tankyrase ARC domain.	44
Figure 1.11	Wnt/ β -Catenin signalling.	46
Figure 1.12	An overlay of representative tankyrase inhibitors which illustrate the three classifications of catalytic inhibitors.	49
Figure 1.13	Chemical structures of representative tankyrase inhibitors and key interactions with the catalytic domain.	51
Figure 1.14	Requirement of ARC and SAM domains for Wnt/ β -catenin signalling.	58
Figure 1.15	Chemical structures of two ARC-binding macrocyclised peptidomimetics.	60
Figure 1.16	Identification of small molecule binders of the tankyrase ARC domain from a fragment-based screening approach.	62
Figure 1.17	Hits from virtual screening against the tankyrase ARC domain.	64
Figure 1.18	Hits from FRET-based screening against the tankyrase ARC domain.	65
Figure 2.1	Fragment growing and fragment linking strategies for hit-to-lead optimisation in FBDD.	74
Figure 2.2	<i>In silico</i> model of fragment hit CCT170746 (28) binding to TNKS2 ARC4.	79
Figure 2.3	Chemical structure of fragment hit CCT170746 (28).	81
Figure 2.4	Proposed initial modifications to investigate the SAR of the quinoxaline moiety in CCT170746 (28).	82
Figure 2.5	Proposed initial modifications to the furan moiety of CCT170746 (28) to assess SAR.	82
Figure 2.6	Chemical structure and mechanism of HATU, an amide coupling reagent.	83

Figure 2.7	Spectra from T_2 relaxation-edited (CPMG) and waterLOGSY experiments with fragment CCT373719 (53).	87
Figure 2.8	Analysis of TNKS2 ARC4 following purification by size exclusion chromatography.	89
Figure 2.9	Quality control analysis of 3BP2 16mer competitor peptide.	90
Figure 2.10	Graphical summary of results from testing the first fragment iteration in relaxation-edited (CPMG) ligand-observed NMR.	95
Figure 2.11	Comparison of energy minimised structures of CCT170746 (28) and CCT373722 (54).	97
Figure 2.12	2D representation of CCT170746 (28) interactions with TNKS2 ARC4 residues in binding mode 3.	99
Figure 2.13	Surface representation of TNKS2 ARC4 highlighting hydrophilic and lipophilic residues.	100
Figure 2.14	Summary of the modifications introduced in the second iteration of fragment synthesis.	100
Figure 2.15	Reaction analysis by LCMS, highlighting the major impurities identified in the synthesis of modified furan fragments.	103
Figure 2.16	Graphical summary of results from testing the second fragment iteration in relaxation-edited (CPMG) ligand-observed NMR.	108
Figure 2.17	Energy minimised structures (not docked) of second iteration fragments.	110
Figure 2.18	Summary of ^1H - ^{15}N HSQC protein-observed NMR.	112
Figure 2.19	Analysis of ^{15}N -labelled TNKS2 ARC4 following final purification by size exclusion chromatography.	113
Figure 2.20	Data obtained from protein-observed NMR with control fragment CCT170746 (28).	115
Figure 2.21	Binding site maps produced from protein-observed NMR data for modified furan analogues.	118
Figure 2.22	Predicted fragment binding sites from <i>in silico</i> fragment docking guided by protein-observed NMR data.	120
Figure 3.1	Literature-reported ARC-binding compounds.	122
Figure 3.2	Summary of NMR experiments performed with literature-reported fragment ARC-binding compounds.	125
Figure 3.3	Proposed quinoxaline modifications to further investigate CCT170746 (28) SAR.	126
Figure 3.4	Comparison of calculated logP (MoKa) and measured kinetic solubility for furan and isoxazole matched pairs.	131
Figure 3.5	Energy minimised structures (not docked) of quinoxaline substituted fragments, CCT375550 (98) and CCT390521 (100).	135

Figure 3.6	Binding affinity of CCT391081 (112) determined by protein-observed NMR.	136
Figure 3.7	Protein-observed NMR derived binding-site map of CCT391081 (112).	137
Figure 3.8	Binding equilibria and equilibrium dissociation constants for competitive ligand binding experiments.	141
Figure 3.9	Binding affinity of CCT393128 (115) determined by protein-observed NMR.	142
Figure 3.10	Protein-observed NMR derived binding-site map of CCT393128 (115).	144
Figure 3.11	<i>In silico</i> docking of CCT393128 (115) against TNKS2 ARC4.	145
Figure 3.12	Relaxation-edited ligand-observed NMR for CCT393128 (115).	147
Figure 3.13	Apo and peptide-bound TNKS2 ARC4 crystal structures.	149
Figure 3.14	Production of TNKS1 ARC4 (646-807) for crystallography.	150
Figure 3.15	TNKS1 ARC4 crystals and structure determination.	151
Figure 4.1	Hypothesised binding modes of CCT391081 (112) and CCT393128 (115) from <i>in silico</i> docking to the TNKS2 ARC4:3BP2 crystal structure (PDB: 3TWR).	153
Figure 4.2	Proposed iteration of fragment optimisation based on CCT391081 (112) and CCT393128 (115).	155
Figure 4.3	Overlay of CCT393128 (115) (docked) and 3BP2 bound to TNKS2 ARC4.	156
Figure 4.4	Binding of sequence optimised and MCL1 TBM peptides to TNKS2 ARC4.	157
Figure 4.5	Design of hybrid fragment-peptidomimetic 118 based on CCT393128 (115).	158
Figure 4.6	Example LCMS analysis of Pd-catalysed aminocarbonylation reaction for the synthesis of CCT393088 (129).	161
Figure 4.7	Reaction analysis of Pd-catalysed aminocarbonylation reaction for the synthesis of CCT393936 (141) and CCT393998 (142).	163
Figure 4.8	Structures of ester by-products (155 and 156) from synthesis of CCT395333 (151) and CCT395335 (154).	165
Figure 4.9	Graphical summary of results from testing 3-substituted quinoxaline fragments in relaxation-edited ligand-observed NMR.	169
Figure 4.10	Protein-observed NMR with CCT394001 (144).	174
Figure 4.11	Design and retrosynthetic analysis of hybrid fragment-peptidomimetics.	176
Figure 4.12	Formation of undesired by-products during peptide synthesis.	180

Figure 4.13	<i>In silico</i> modelling of peptidomimetics CCT395505 (118) and CCT395504 (159).	181
Figure 4.14	Graphical summary of results from testing 3-alkylamino quinoxaline peptidomimetic compounds in relaxation-edited ligand-observed NMR.	185
Figure 4.15	Binding affinity determined from protein-observed NMR for 3-pyrrolidinyl quinoxaline compounds.	188
Figure 4.16	Binding site mapping from protein-observed NMR for 3-pyrrolidinyl quinoxaline compounds.	189
Figure 4.17	Principles of a fluorescence polarisation assay.	193
Figure 4.18	Structure of the Cy5-labelled 3BP2 16mer peptide FP probe (Cys-(Cy5)-RSPPDGQS).	194
Figure 4.19	Determination of optimum probe concentration from Cy5-labelled FP probe titration.	195
Figure 4.20	Binding affinity of Cy5-labelled FP probe from direct binding FP assay with TNKS1 ARC4.	196
Figure 4.21	Structures of 3BP2 16mer positive and negative (G6R) control peptides.	198
Figure 4.22	Competitive FP assay with unlabelled control peptides.	199
Figure 4.23	Competitive FP assay with unlabelled control peptides (+ 2% DMSO).	200
Figure 4.24	Competitive FP assay with unlabelled compounds (+ 2% DMSO).	201
Figure 4.25	Competitive FP assay with fanapanel (31).	202
Figure 4.26	Oxidation of 3-methylalkylamino quinoxaline compounds leading to loss of -CH ₂ .	207
Figure 4.27	Oxidation of 3-pyrrolidinyl quinoxaline compounds to corresponding lactams.	207
Figure 5.1	The ubiquitin-proteasome system (UPS).	210
Figure 5.2	Mechanism of PROTAC-mediated degradation.	211
Figure 5.3	Chemical structures of E3 ligase ligands used in current PROTAC design.	212
Figure 5.4	Chemical structures of reported PARP1 PROTACs.	214
Figure 5.5	Identification of a solvent-exposed vector for design of XAV939-based tankyrase PROTACs.	216
Figure 5.6	Chemical structures and retrosynthetic analysis of proposed first-generation tankyrase PROTACs.	217
Figure 5.7	Tankyrase auto-PARylation assay with first-generation XAV939-based PROTACs.	220
Figure 5.8	Biochemical CRBN/DDB1 FP assay with a first-generation XAV939-based PROTAC.	221
Figure 5.9	Cellular CRBN NanoBRET assay with first-generation XAV939-based PROTAC.	223

Figure 5.10	Design strategy for second-generation tankyrase PROTACs.	225
Figure 5.11	<i>In silico</i> protein:protein docking with CRBN and the catalytic domain of TNKS2.	227
Figure 5.12	Rationalisation of linker lengths for second-generation XAV939-based PROTACs based on an <i>in silico</i> model of ternary complex formation.	229
Figure 5.13	Cellular tankyrase Wnt/ β -catenin responsive reporter assay with second-generation XAV939-based PROTACs.	234
Figure 5.14	Western blot analysis of cellular tankyrase levels in HAP1 7TGRR cells.	235
Figure 6.1	Summary diagram of SAR for fragment hit CCT170746 (28).	239
Figure 6.2	Suggested modifications for further SAR exploration of lead fragments.	241
Figure 6.3	Principles of assay technology used to assess PROTAC-mediated ternary complex formation.	244
Figure 6.4	Examples of potential linker variation for the empirical design of tankyrase PROTACs.	246
Figure 6.5	Proposed design strategies for ARC-binding PROTACs.	247
Figure 7.1	The Dock panel in MOE used for ligand-protein docking.	364

List of Tables

Table	Title	Page
Table 1.1	Summary of common post-translational modifications (phosphorylation, methylation, acetylation, ubiquitination and ADP-ribosylation).	30
Table 1.2	Potency and selectivity of catalytic tankyrase inhibitors.	52
Table 1.3	Summary of reported catalytic tankyrase inhibitors.	53
Table 2.1	Fragment screening versus high-throughput screening.	71
Table 2.2	Synthesis of fragments based on 28 <i>via</i> amide coupling, maintaining furan-2-ylmethanamine and varying the quinoxaline-6-carboxylic acid derived left-hand side.	84
Table 2.3	Synthesis of fragments based on 28 <i>via</i> amide coupling, maintaining quinoxaline-6-carboxylic acid and varying the furan-2-ylmethanamine derived right-hand side.	85
Table 2.4	A summary of data obtained from competitive ligand-observed NMR experiments performed with initial fragment CCT170746 (28) analogues.	93
Table 2.5	Synthesis of unsubstituted quinoxaline-6-carboxamide fragments based on 28 <i>via</i> amide coupling, maintaining quinoxaline-6-carboxylic acid and further varying the furan-2-ylmethanamine derived right-hand side.	101
Table 2.6	A summary of data obtained from competitive ligand-observed NMR experiments performed with substituted furan fragment compounds.	104
Table 2.7	A summary of data obtained from competitive ligand-observed NMR experiments performed with furan replacement fragment compounds.	106
Table 2.8	A summary of data for selected fragments determined from ligand-observed (CPMG) and protein-observed NMR assays including dissociation constant (K_d) data determined from ^1H - ^{15}N -HSQC titrations.	117
Table 3.1	A summary of data obtained from competitive ligand-observed NMR experiments performed with literature-reported ARC-binding fragments.	124
Table 3.2	Synthesis of quinazoline-6-carboxamide fragments, maintaining quinazoline-6-carboxylic acid and varying the furan-2-ylmethanamine derived right-hand side.	127
Table 3.3	Synthesis of quinoxaline-6-carboxamide fragments <i>via</i> amide coupling, introducing modifications and substituents to the quinoxaline-6-carboxylic acid component whilst maintaining either the furan-2-yl or isoxazol-5-ylmethanamine.	128
Table 3.4	Synthesis of 2- or 3-methoxy quinoxaline-6-carboxamide fragments <i>via</i> Pd-catalysed aminocarbonylation, whilst	130

	maintaining either the furan-2-yl or isoxazol-5-ylmethanamine.	
Table 3.5	A summary of data obtained from competitive ligand-observed NMR experiments performed with modified quinoxaline analogues.	131
Table 3.6	A summary of data obtained from competitive ligand-observed NMR experiments performed with -NMe ₂ substituted quinoxaline analogues.	140
Table 4.1	Synthesis of 3-alkoxyquinoxaline-6-carboxamide fragments <i>via</i> i) S _N Ar then ii) Pd-catalysed aminocarbonylation.	160
Table 4.2	Synthesis of 3-alkylaminoquinoxaline-6-carboxamide fragments <i>via</i> i) S _N Ar then ii) Pd-catalysed aminocarbonylation.	162
Table 4.3	Synthesis of 3-dimethylaminoquinoxaline-6-carboxamide fragments <i>via</i> i) S _N Ar then ii) Pd-catalysed aminocarbonylation.	164
Table 4.4	A summary of data obtained from competitive ligand-observed NMR experiments performed with 3-substituted quinoxaline fragment compounds.	166
Table 4.5	A summary of data obtained from competitive ligand-observed NMR experiments performed with 3-alkylamino quinoxaline peptidomimetic compounds.	183
Table 4.6	A summary of data for 3-pyrrolidinyl quinoxaline peptidomimetics determined from ligand-observed (CPMG) and protein-observed NMR assays including dissociation constant (K _d) data determined from ¹ H- ¹⁵ N-HSQC titrations	187
Table 4.7	Summary of shifted residues from protein-observed NMR with 3-pyrrolidinyl quinoxaline compounds.	190
Table 4.8	Determination of optimum TNKS1 ARC4 concentration for a competitive FP assay.	197
Table 4.9	Summary of data obtained from competitive FP assay with control peptides and 3-substituted quinoxaline fragment compounds (+2% DMSO).	203
Table 5.1	Summary of data from biochemical and cellular CRBN target engagement assays with second-generation XAV939-based PROTACs and control compounds.	232
Table 7.1	Summary table of all ARC4 constructs produced for ligand-observed and protein-observed NMR, X-ray crystallography studies and competitive FP assays.	348
Table 7.2	Preparation of M9 minimal media used in expression of ¹⁵ N-labelled TNKS2 ARC4.	350
Table 7.3	Buffers used in tankyrase ARC4 purifications.	350
Table 7.4	Molecular weights and molar extinction coefficients of tankyrase ARC4 constructs.	352
Table 7.5	Fragment titration sample preparation for protein-observed NMR experiments.	357

List of Schemes

Scheme	Title	Page
Scheme 3.1	Synthesis of C44 (30).	122
Scheme 3.2	Synthesis of 2,3-dimethoxyquinoxaline-6-carboxylic acid (105) for subsequent amide coupling.	129
Scheme 3.3	Synthesis of 2- or 3-dimethylamino quinoxaline-6-carboxamide fragments <i>via</i> Pd-catalysed aminocarbonylation.	138
Scheme 4.1	Synthesis of <i>N</i> -(isoxazol-5-ylmethyl)-3-(methylamino)quinoxaline-6-carboxamide, CCT394014 (150), <i>via</i> Pd-catalysed aminocarbonylation.	163
Scheme 4.2	Synthesis of <i>N</i> -(furan-2-ylmethyl)-3-methoxy- <i>N</i> -methylquinoxaline-6-carboxamide, CCT395335 (154).	165
Scheme 4.3	Synthesis of 3-dimethylaminoquinoxaline-6-carboxamide peptidomimetic, CCT395505 (118).	178
Scheme 4.4	Synthesis of 3-pyrrolidinylaminoquinoxaline-6-carboxamide peptidomimetic, CCT395504 (159).	179
Scheme 4.5	Synthesis of 3-(dimethylamino)- <i>N</i> -ethylquinoxaline-6-carboxamide, CCT395350 (168).	182
Scheme 4.6	Synthesis of <i>N</i> -(furan-2-ylmethyl)- <i>N</i> -methyl-3-(pyrrolidin-1-yl)quinoxaline-6-carboxamide, CCT395334 (169).	182
Scheme 5.1	Synthesis of XAV939-based amide-linked tankyrase PROTACs.	218
Scheme 5.2	Synthesis of XAV939-based ether-linked tankyrase PROTACs.	231

Abbreviations

1D	One dimensional
2D	Two dimensional
3BP2	SH3 domain-binding protein 2
3D	Three dimensional
Ac	Acetyl
ADP	Adenosine diphosphate
AMDA	α -amino-3-hydroxy-5-methyl-4-isoxazolepropionic acid
APC	Adenomatous polyposis coli
aq.	aqueous
ARC	Ankyrin repeat cluster
ARH	ADP-ribosylhydrolases
ART	ADP-ribosyltransferases
ARTD	Diphtheria toxin-like ADP-ribosyltransferases
ATP	Adenosine triphosphate
AXIN	Axis-inhibition
BCR-ABL	Breakpoint cluster region-Abelson proto-oncogene
BMRB	Biological Magnetic Resonance Data Bank
BRCA	Breast cancer gene
BRET	Bioluminescence resonance energy transfer
CCG	Chemical Computing Group
CcpNMR	Collaborative Computational Project for NMR
CFP	mCerulean fusion protein
CHAPS	3-((3-Cholamidopropyl)dimethylammonio)-1-propanesulfonate
CI	Confidence interval
clAP	Cellular inhibitor of apoptosis proteins
CK1	Casein kinase 1
clogP	Calculated partition coefficient
CPMG	Carr-Purcell-Meiboom-Gill pulse sequence

CRBN	Cereblon
Cryo-EM	Cryogenic electron microscopy
CSP	Chemical shift perturbation
CUL4	Cullin4
Cy5	Cyanine 5
d	Euclidean distance
DC	Destruction complex
DCKA	5,7-Dichlorokynurenic acid
DDB1	Damage-specific DNA binding protein 1
DIPEA	<i>N,N</i> -Diisopropylethylamine
D-loop	Donor loop
DMF	Dimethylformamide
DMSO	Dimethylsulfoxide
DNA	Deoxyribonucleic acid
DNA-PKcs	DNA-dependent protein kinases
DSB	Double-strand breaks
DSF	Differential scanning fluorimetry
DSS	Sodium 3-(trimethylsilyl)propane-1-sulfonate
EH	End-helix
EM	Electron microscopy
equiv.	equivalent
ESI	Electrospray ionisation
F _b	Bound fraction
FBDD	Fragment-based drug discovery
FDA	Food and Drug Administration
FMO	Fragment molecular orbital
FP	Fluorescence polarisation
FPLC	Fast protein liquid chromatography
FRET	Fluorescence resonance energy transfer
GOLD	Genetic Optimisation for Ligand Docking

GSK3	Glycogen synthase kinase 3
GST	Glutathione S-transferase
HATU	<i>O</i> -(7-Azabenzotriazol-1-yl)-1,1,3,3-tetramethyluronium hexafluorophosphate
HBA	Hydrogen bond acceptor
HBD	Hydrogen bond donor
HDAC	Histone deacetylase
HEPES	2-(4-(2-Hydroxyethyl)piperazin-1-yl)ethane-1-sulfonic acid
HOAt	1-Hydroxy-7-azabenzotriazole
HSQC	Heteronuclear single quantum correlation
HTS	High-throughput screening
IC ₅₀	Half maximal inhibitory concentration
ICR	Institute of Cancer Research
ICR CTU	ICR Cancer Therapeutics Unit
IMiD	Immunomodulatory drugs
ITC	Isothermal titration calorimetry
K _d	Dissociation constant
K _i	Inhibition constant
Kin Sol	Kinetic solubility
LCMS	Liquid chromatography-mass spectrometry
MCL1	Myeloid cell leukemia 1
MDB	MOE database
MDC1	Mediator of DNA damage checkpoint protein 1
MDM2	Mouse double minute 2 homolog
ML	Mid-loop
MOE	Molecular Operating Environment
MW	Molecular weight
MWCO	Molecular weight cut-off
NAD ⁺	Nicotinamide adenine dinucleotide
NMDA	N-methyl-D-aspartate receptor

NMPA	National Medical Products Administration
NMR	Nuclear magnetic resonance
NROT	Number of rotatable bonds
NuMA	Nuclear mitotic apparatus protein
PAR	Poly(ADP-ribose)
PARdU	PAR-dependent ubiquitination
PARG	Poly(ADP-ribose) glycohydrolase
PARP	Poly(ADP-ribosyl) polymerase
PBZ	PAR-binding zinc-finger
PDB	Protein Data Bank
PEG	Polyethylene glycol
PPI	Protein-protein interaction
PROTAC	Proteolysis-targeting chimera
PSA	Polar surface area
PTM	Post-translational modification
QToF	Quadrupole time of flight
SAM	Sterile alpha-motif multimerisation
SAR	Structure-activity relationship
SAXS	Small angle X-ray scattering
SBDD	Structure-based drug discovery
SD	Standard deviation
SDF	Structure-data file
SDS-PAGE	Sodium dodecyl sulfate– polyacrylamide gel electrophoresis
SEC	Size exclusion chromatography
SEM	Standard error of the mean
S _N Ar	Nucleophilic aromatic substitution
SPR	Surface plasmon resonance
TARG1	Terminal ADP-ribose glycohydrolase 1
TB	Terrific broth
TBM	Tankyrase-binding motif

TCEP	Tris(2-carboxyethyl)phosphine
TCF/LEF	T-cell factor/lymphoid enhancer factor
TEV	Tobacco etch virus
THF	Tetrahydrofuran
TNKS	Tankyrase
TNKS1	Tankyrase 1
TNKS2	Tankyrase 2
tPSA	Topological polar surface area
t _R	Retention time
TSA	Thermal shift assay
UPS	Ubiquitin-proteasome system
USP25	Ubiquitin-specific protease 25
UV	Ultraviolet
UV-Vis	Ultraviolet-visible
v/v	volume/volume
VHL	von Hippel-Lindau
w/v	weight/volume
waterLOGSY	Water-ligand observed <i>via</i> gradient spectroscopy
XantPhos	4,5-Bis(diphenylphosphino)-9,9-dimethylxanthene
[XantPhos Pd(allyl)]Cl	Allyl[4,5-bis(diphenylphosphino)-9,9-dimethylxanthene] palladium (II) chloride
XantPhos Pd G4	Methanesulfonato(4,5-bis(diphenylphosphino)-9,9-dimethylxanthene)(2'-methylamino-1,1'-biphenyl-2-yl)palladium(II)
YFP	mCitrine fusion protein

Chapter 1 Introduction

1.1 Cancer and Targeting Post-translational Modifications

1.1.1 Hallmarks of Cancer

Cancer is a group of over 200 related diseases which arise from an accumulation of genetic changes, resulting in uncontrolled growth of cells into malignant tumours.¹ The initiation and progression of cancer involves genetic mutations in proto-oncogenes and tumour suppressor genes, leading to the disruption of cellular processes.¹⁻² During the multistep progression of cancer, there are numerous capabilities which are acquired by cells for the evolution of a pre-malignant cancerous lesion, through formation of a local tumour, into metastatic disease (Figure 1.1).³⁻⁴ These functional capabilities were first introduced as the 'hallmarks of cancer' in 2000 and since then, two updates to the original hallmarks have been published to include developments in cancer biology research over the past 20 years.³⁻⁵ In addition, 'enabling characteristics' which allow the functional hallmark traits to be acquired by cancerous cells have been identified.⁴⁻

5

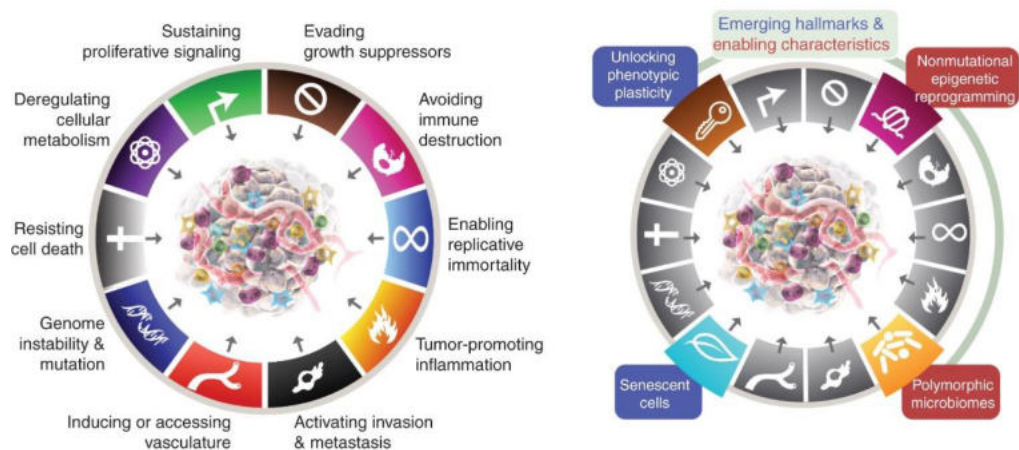


Figure 1.1. The hallmarks and enabling characteristics of cancer. Figure from Hanahan and Weinberg, 2022.⁵

1.1.2 Cancer Therapy

Cancer is a leading cause of death worldwide which was responsible for a total of 10 million deaths in 2020.⁶⁻⁷ It is a major global health concern, with the incidence and mortality rates growing as a result of different epidemiological factors including aging populations and increasing prevalence of risk factors associated with socioeconomic development.⁶ Conventional cancer treatment includes localised therapies such as surgery and radiotherapy targeted at the primary tumour.⁸ However, the spread of cancer throughout the body, or cancer metastasis, is the cause of up to 90% of cancer-related deaths.^{7, 9} Systemic chemotherapy – involving the administration of cytotoxic compounds, typically DNA damaging agents – is another conventional anti-cancer treatment which is used to treat both primary as well as metastatic disease.¹⁰ Chemotherapy resulting in DNA damage inhibits the uncontrolled growth and proliferation of tumours by either initiation of cell cycle arrest or apoptosis.^{8, 10} However, as genotoxic chemotherapy is systemic and non-specific to tumour cells, it leads to side effects and toxicity as a result of targeting rapidly dividing cells throughout the body.⁸ DNA damaging chemotherapy also leads to increased risk of development of secondary cancers as the drugs themselves are carcinogenic.¹⁰ The need for safer and more effective drugs, as well as an increased understanding of the hallmarks and enabling characteristics underlying cancer biology, has led to the emergence and advancement of targeted therapies as novel systemic anti-cancer therapeutics.⁷⁻⁸

1.1.3 Targeted Therapy in Cancer Treatment

Targeted therapy includes biological therapies, hormone therapy, immunotherapy, and small molecule drugs. The development of targeted therapies has resulted from the identification and validation of molecular targets – genes, proteins, hormones and signalling molecules – which are important in oncogenic processes and pathways.¹¹ The first small molecule targeted therapy approved for clinical use by the US Food and Drug Administration (FDA) was imatinib, which was approved in 2001 for the treatment of chronic myeloid leukaemia.^{8, 11} Imatinib is a small molecule inhibitor of BCR-ABL tyrosine kinase,

which is a member of a larger class of proteins known as kinases.¹² Most other small molecule drugs which have been clinically approved in the 20 years since the approval of imatinib are also kinase inhibitors.^{8, 13} Other classes of targeted therapeutics in clinical use include inhibitors of epigenetic regulatory proteins, DNA damage repair enzymes and the proteasome (Figure 1.2).^{8, 13}

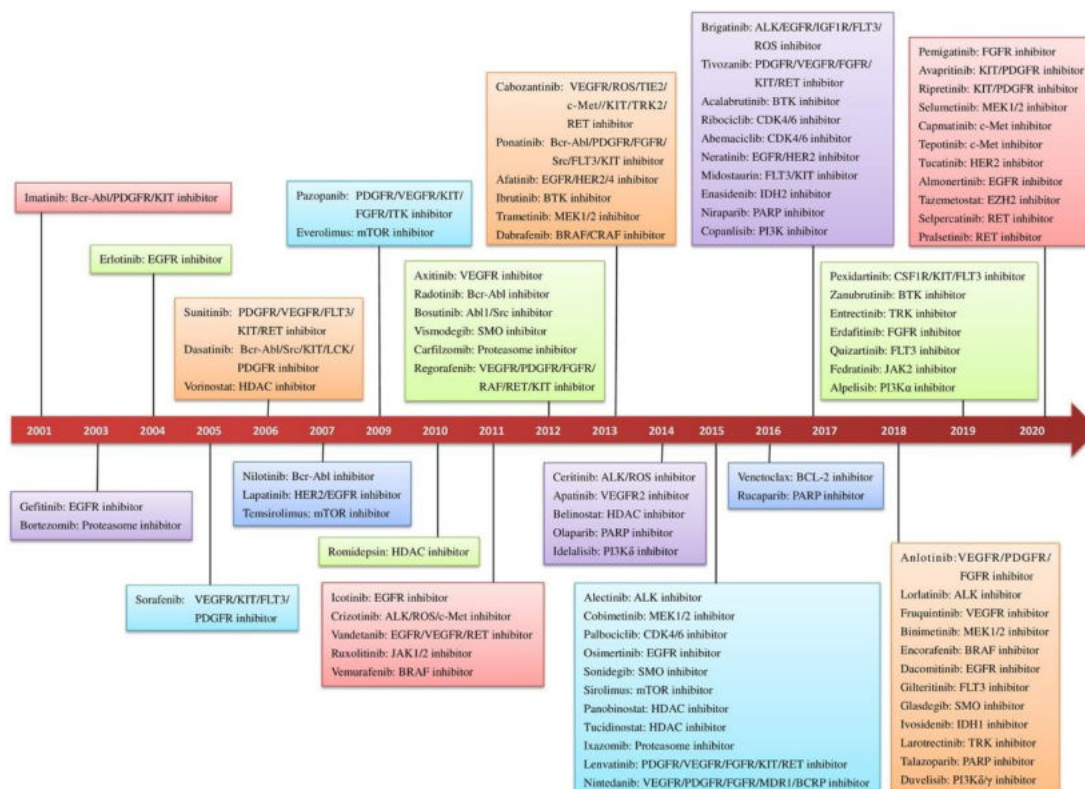


Figure 1.2. Small molecule targeted anti-cancer drugs approved from 2001 to 2020. Timeline for the clinical approval by the US FDA and National Medical Products Administration (NMPA) China. Figure from Zhong, L. *et al*, 2021.⁸

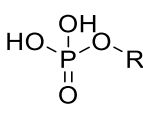
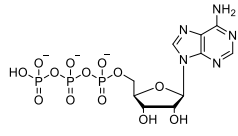
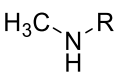
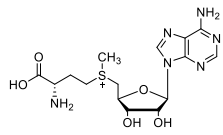
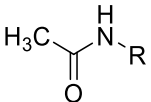
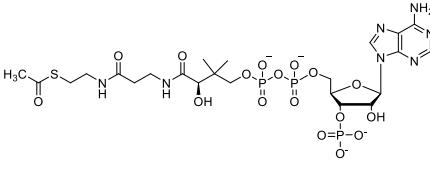
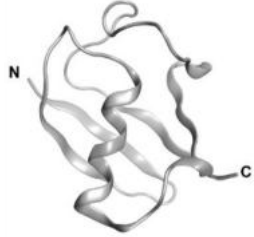
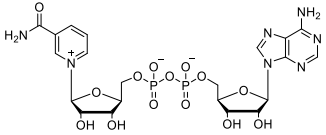
Kinases are a major target in anti-cancer drug development as they catalyse the phosphorylation of proteins, an important example of a post-translational modification (PTM) which is associated with cancer progression. PTM is a reversible control mechanism for the regulation of proteins in cellular processes, by the addition and removal of chemical moieties or modifying proteins to the functional groups of amino acids.¹⁴⁻¹⁶ PTMs can result in the alteration of protein structure or changes in protein-protein interactions, which affect their biological functions and has implications in the development of cancer.¹⁷ Therefore, effector

proteins, such as kinases, which are involved in the regulation of PTMs represent targets for the development of targeted cancer therapeutics.

1.1.4 Post-translational Modifications in Targeted Therapy

There are over 200 examples of PTMs in addition to phosphorylation¹⁷⁻¹⁹, including methylation²⁰⁻²¹, acetylation¹⁵, ubiquitination²²⁻²⁵ and ADP-ribosylation²⁶ (Table 1.1).¹⁵ Phosphorylation is a cellular regulatory mechanism which is integral to cell signalling and the control of cell growth, and over 30 kinase inhibitors have been clinically approved by the US FDA as oncology drugs.^{18-19, 27} Methylation and acetylation of histone proteins are involved in epigenetic regulation of gene expression and transcription, and affect other cellular processes through modification of non-histone proteins such as transcription factor and tumour suppressor p53.^{15, 28} To date, five histone deacetylase (HDAC) regulators are approved for clinical use as cancer therapeutics (Figure 1.2), whilst inhibitors of methyltransferases and demethylases have also entered clinical trials.^{8, 20-21, 29} Further to this, chemical modulators of the ubiquitin-proteasome system, such as immunomodulatory drugs (IMiDs) and heterobifunctional proteolysis-targeting chimeras (PROTACs), are providing novel approaches for targeted protein degradation by E3 ligase-mediated ubiquitination of neosubstrates.^{24, 30} There are currently three IMiDs approved for use in multiple myeloma, and 15 targeted protein degraders have entered clinical trials.³⁰⁻³¹ ADP-ribosylation is another post-translational modification for which inhibition has been validated as an approach in targeted cancer therapy in a clinical setting.³² Olaparib, rucaparib, niraparib and talazoparib are four clinically approved drugs which target ADP-ribosylation through inhibition of poly(ADP-ribosyl) polymerases (PARPs), PARP1 and PARP2 (Figure 1.2).^{8, 33-34}

Table 1.1. Summary of common post-translational modifications (phosphorylation, methylation, acetylation, ubiquitination and ADP-ribosylation). The chemical modification, targeted amino acid residues, and the enzymes and co-substrates involved in the PTM are indicated.

Modification	Residues	Enzymes	Co-substrates
Phosphorylation 	Ser, S Thr, T Tyr, Y	Kinases $\xrightarrow{\hspace{1cm}}$ $\xleftarrow{\hspace{1cm}}$ Phosphatases	 Adenosine-5'-triphosphate (ATP)
Methylation 	Lys, K Arg, R	Methyltransferases $\xrightarrow{\hspace{1cm}}$ $\xleftarrow{\hspace{1cm}}$ Demethylases	 S-Adenosyl-L-methionine (SAM)
Acetylation 	Lys, K	Acetyltransferases $\xrightarrow{\hspace{1cm}}$ $\xleftarrow{\hspace{1cm}}$ Deacetylases	 Acetyl coenzyme A (Acetyl CoA)
Ubiquitination + Ubiquitin protein (8 kDa)	Cys, C Lys, K Ser, S Thr, T	E3 ubiquitin ligases $\xrightarrow{\hspace{1cm}}$ $\xleftarrow{\hspace{1cm}}$ Deubiquitinating enzymes	 Ubiquitin (PDB:3ONS)
ADP-Ribosylation + ADP-ribose	Glu, E Asp, D Ser, S Arg, R Lys, K Cys, C Asn, N	ADP-ribosyl transferases $\xrightarrow{\hspace{1cm}}$ $\xleftarrow{\hspace{1cm}}$ ADP-ribosyl hydrolases	 Nicotinamide adenine dinucleotide (NAD ⁺)

1.2 ADP-Ribosylation and Poly(ADP-Ribosylation)

ADP-ribosylation was first identified in the 1960s when it was observed that diphtheria toxin required nicotinamide adenine dinucleotide (NAD^+) to elicit its pathogenic effect of inhibiting mammalian protein synthesis.³⁵ The post-translational modification of ADP-ribosylation is the reversible covalent transfer of ADP-ribose from the co-substrate NAD^+ to acceptor amino acid residues of target proteins, resulting in the formation of a glycosidic linkage with the release of nicotinamide.^{26, 36-37} Poly(ADP-ribosylation), or PARylation, involves the successive addition of further units of ADP-ribose to substrate proteins resulting in the formation of poly(ADP-ribose) (PAR) chains up to 200 subunits in length (Figure 1.3).³⁶⁻³⁸ Elongation of PAR chains can happen in a linear or branching manner, with branching occurring once every 20 to 50 subunits on average for PARP1/2.³⁸

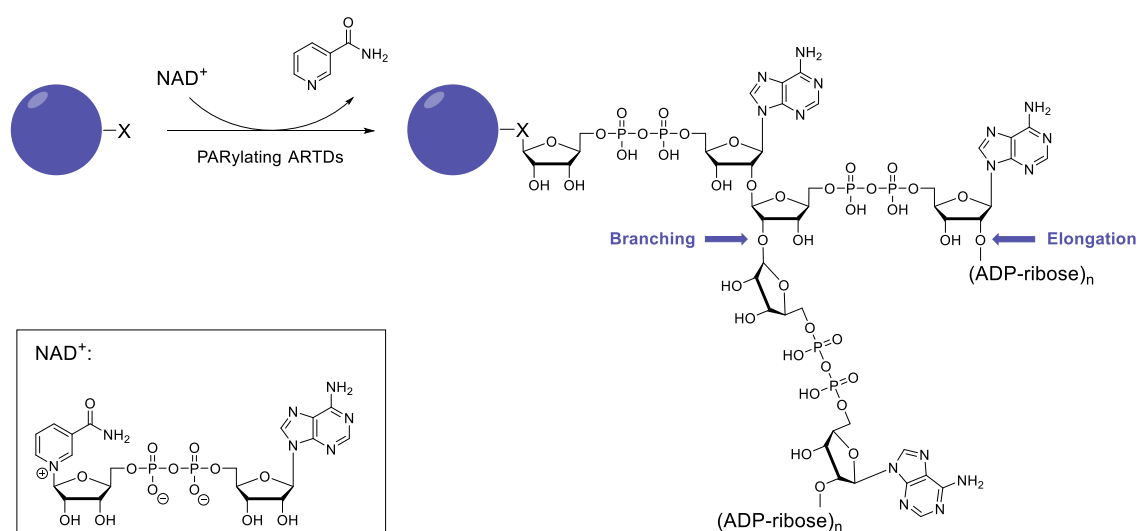


Figure 1.3. Summary of poly(ADP-ribosylation) (PARylation). An acceptor residue (X) of a substrate protein is modified by a unit of ADP-ribose from NAD^+ with the release of nicotinamide. PAR chains are then elongated by the addition of further units of ADP-ribose. Figure adapted from Hottiger *et al*, 2015.³⁹

1.2.1 ADP-Ribosyltransferases and Poly(ADP-ribosyl) polymerases

ADP-ribosylation is catalysed by ADP-ribosyltransferases (ARTs).³⁶ In humans, a subset of the ART family are the 17 poly(ADP-ribosyl) polymerases (PARP1-

16, Figure 1.4).³⁵⁻³⁶ PARPs are alternatively referred to as diphtheria toxin-like ARTs (ARTD1-17), as only four members (PARP1, 2, 5a, and 5b) have been shown to catalyse poly(ADP-ribosyl)ation, whilst the remaining 13 PARPs have been shown to either catalyse mono(ADP-ribosyl)ation or are enzymatically inactive.^{36, 40} Whilst PARPs are the writers of ADP-ribosylation other proteins are also involved in regulating the post-translational modification. Readers of ADP-ribosylation are proteins which contain domains that recognise and bind different regions of ADP-ribosylated substrates; these include macrodomains, PAR-binding zinc-finger (PBZ) and WWE (Trp-Trp-Glu) domains.^{35, 39} ADP-ribosylation modifications including mono- and poly(ADP-ribosyl)ation are removed by erasers of the PTM or ADP-ribosylhydrolases (ARHs), such as poly(ADP-ribose) glycohydrolase (PARG), macroD1, macroD2 and terminal ADP-ribose glycohydrolase 1 (TARG1).^{35, 39}

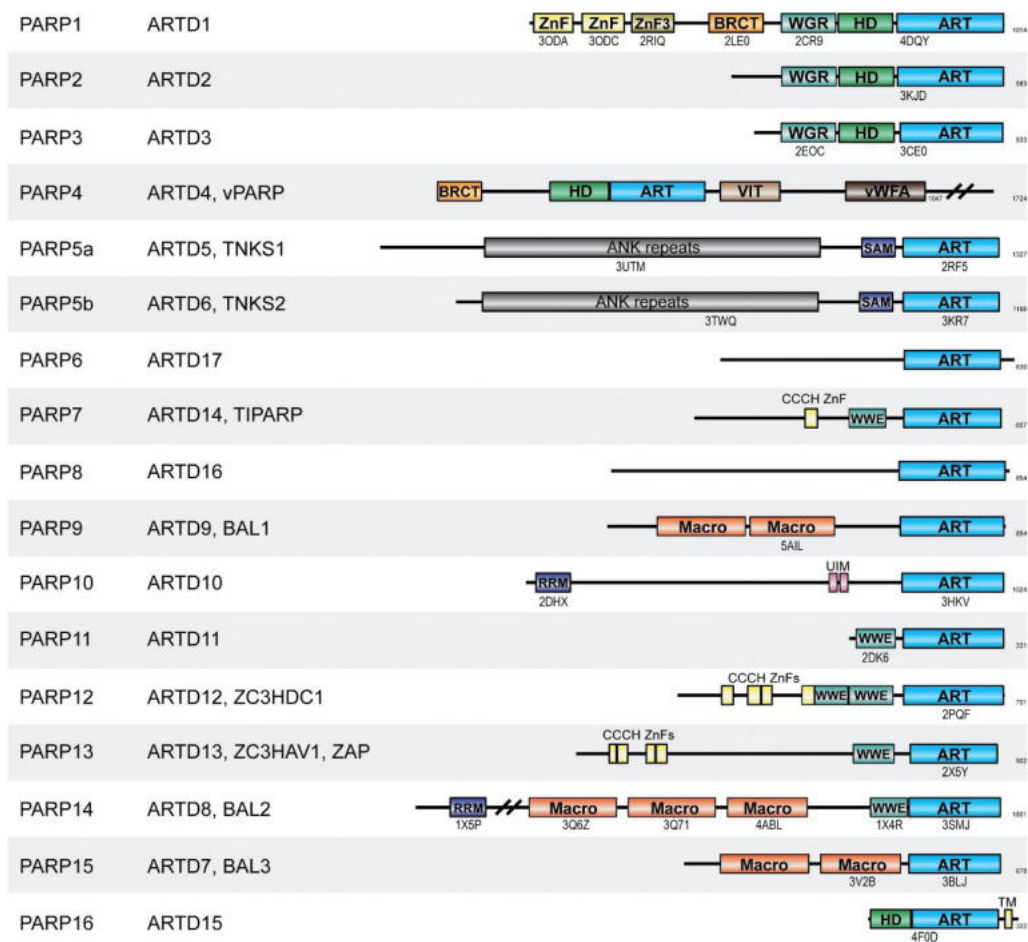


Figure 1.4. Structural domain organisation of the PARP enzymes. The conserved C-terminal catalytic ART domain and variable regulatory domains of PARP1-16 (ARTD1-17). Figure from Barkauskaite *et al*, 2015.³⁵

1.2.2 Catalytic and Regulatory Structural Domains of PARPs

As shown in Figure 1.4, PARP1-16 (ARTD1-17) all possess a highly conserved catalytic ADP-ribosyl transferase (ART) domain, otherwise known as the catalytic PARP domain.³⁵ This domain, which is mostly C-terminal, is required for the binding of NAD⁺ and catalytic transfer of ADP-ribosyl moieties to substrate proteins.⁴¹ Currently, the only crystal structure of an ADP-ribosylating enzyme bound to the fully intact co-substrate NAD⁺ has been solved with diphtheria toxin, from which key features of the ART catalytic domain and binding interactions with NAD⁺ have been determined (Figure 1.5).⁴¹ The domain consists of two binding regions – a ‘donor’ binding site for the binding of co-substrate NAD⁺, and an ‘acceptor’ region which binds either the protein residues for mono(ADP-ribosyl)ation or the distal ADP-ribosyl for poly(ADP-ribosyl)ation. The NAD⁺ or ‘donor’ binding site also consists of two distinct pockets, which bind either the nicotinamide or adenosine regions of NAD⁺ to ensure the correct orientation of the co-substrate for ADP-ribosyl transfer.⁴¹ There is a conserved donor loop (D-loop) within the donor region which varies in length and conformation amongst the PARP family.³⁵ PARPs also possess a triad of residues necessary for determining catalytic PARP activity: PARP1-5b contain the histidine-tyrosine-glutamate (H-Y-E) triad of residues, whereas the remaining PARP6-16 which catalyse either mono(ADP-ribosyl)ation or are enzymatically inactive are characterised by a lack of the glutamate residue in an H-Y-X triad.^{35-37, 41}

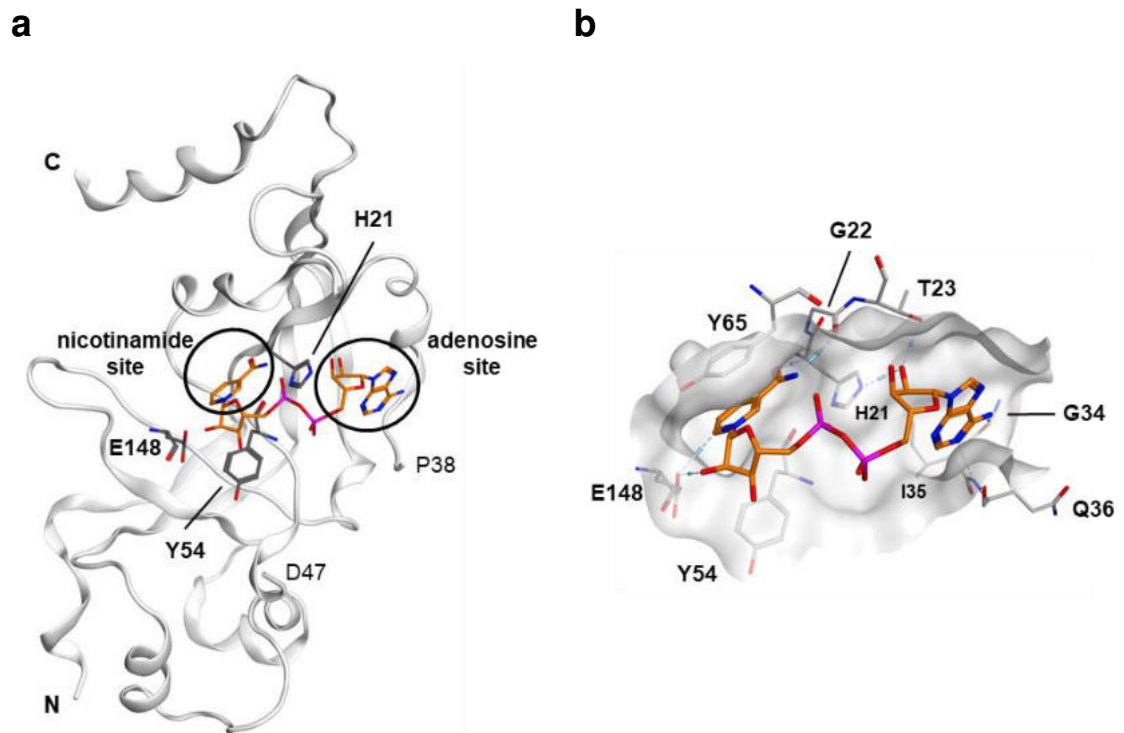


Figure 1.5. Interaction of NAD⁺ with diphtheria toxin. Crystal structure of NAD⁺ (orange) bound to the catalytic domain (1-191) of full-length diphtheria toxin (grey) (PDB: 1TOX). **a**) Nicotinamide and adenosine binding pockets of the ART catalytic domain are circled. The catalytic H-Y-E triad is represented by residues H21, Y54 and E148. Residues between P38 and D47 in the disordered D-loop were not resolved. **b**) Residues involved in key hydrogen bond interactions (H21, G22, T23, G34, I35, Q36, E148) and π -stacking interactions (Y54 and Y65) with NAD⁺ are highlighted.⁴¹

In contrast to the highly conserved C-terminal domain, there is high variability amongst the other less conserved regulatory domains of PARPs (Figure 1.4). These are required for interactions with substrate proteins or nucleic acids, for the recognition of other post-translational modifications or for the regulation of PARP catalytic activity.^{35, 38, 42} PARP1-3 are DNA-dependent PARPs, which require binding of DNA for their full enzymatic activity, whereas PARP7,12-13 have CCCH zinc finger domains which are required for binding viral DNA.^{35, 43} Macrodomains which recognise ADP-ribosylated substrates are present in PARP9,14-15.^{35, 43} PARP5a and PARP5b, otherwise known as tankyrase (TNKS1 and TNKS2 respectively) possess ankyrin repeat cluster (ARC) and sterile alpha-motif multimerisation (SAM) domains for protein-protein

interactions.⁴³ The diverse domain architectures between the different PARP members determines their interactions, localisation and cellular activity.³⁸

1.2.3 PARP Cellular Functions

The involvement of PARPs in many cellular processes has been reported, including DNA damage repair, telomere elongation, gene regulation and immune or stress responses.⁴⁴ PARylation has major regulatory consequences on its substrate proteins due to the addition of large, negatively charged polymeric groups.⁴⁴ These regulatory mechanisms are categorised into: inhibition of protein-protein or protein-nucleic acid interactions; scaffold formation which affects localisation and interactions; and ubiquitination of PARylated substrates.³⁸ Hence, PAR-producing members of the ARTD family – PARP1, PARP2, TNKS1 and TNKS2 – have been the focus of drug discovery efforts for the development of targeted therapeutics.⁴⁴ As discussed in section 1.1.4, the PARP inhibitors which have been approved so far for clinical use in cancer therapy are inhibitors of PARP1 and PARP2. Tankyrase is also an anti-cancer target of interest due to its involvement in key cellular processes which are implicated in cancer.

1.3 Tankyrase Structural Domains

1.3.1 Structural Domain Organisation of Tankyrase

TNKS1 and TNKS2, referred to collectively as tankyrase, are two homologous PARP enzymes in the ARTD family.³⁶ TNKS1 and TNKS2 have a high overall sequence identity of 82% between paralogues, with three common structural domains between them: a catalytic PARP domain, a sterile alpha-motif multimerisation (SAM) domain, and an ankyrin repeat cluster (ARC) domain (Figure 1.6).⁴⁵

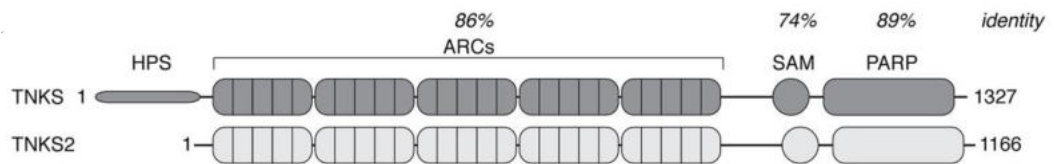


Figure 1.6. TNKS1 and TNKS2 structural domain organisation. Figure adapted from Mariotti *et al*, 2017.⁴⁵

TNKS1 has an additional N-terminal HPS (histidine, proline, and serine) rich region, which is hypothesised to be intrinsically disordered due to its low sequence complexity.⁴⁶⁻⁴⁷ The N-terminal HPS region is absent in TNKS2, however both tankyrase isoforms are largely functionally redundant as determined from studying TNKS1 single knockout and TNKS2 single knockout mice, and the function of the HPS domain remains unknown.⁴⁸

1.3.2 Catalytic PARP Domain of Tankyrase

The C-terminal catalytic PARP, or ART, domain of tankyrase is the site of poly(ADP-ribosyl)ation of substrate proteins and is highly conserved with other PARPs.^{45, 47, 49-51} Both TNKS1 and TNKS2 catalytic domains have been studied by X-ray crystallography and apo crystal structures have provided structural insights (Figure 1.7a/b).^{47, 51-52} There are two anti-parallel β -sheets which are flanked by four α -helices, in an overall structure which is consistent with other ARTD catalytic domains.^{50, 53} Due to this structural homology, key structural features of the catalytic domain have been identified by comparison with the crystal structure of the diphtheria toxin bound to the co-substrate NAD⁺ (**1**).⁴¹ In addition, although there are currently no reported successful attempts in obtaining a crystal structure of NAD⁺ with tankyrase, a crystal structure of the catalytic domain of tankyrase in complex with an NAD⁺ mimic, EB-47 (**2**), has been successfully determined, allowing the nicotinamide and adenosine regions of the donor binding site to be defined in greater detail (Figure 1.7c/d/e).⁵⁴

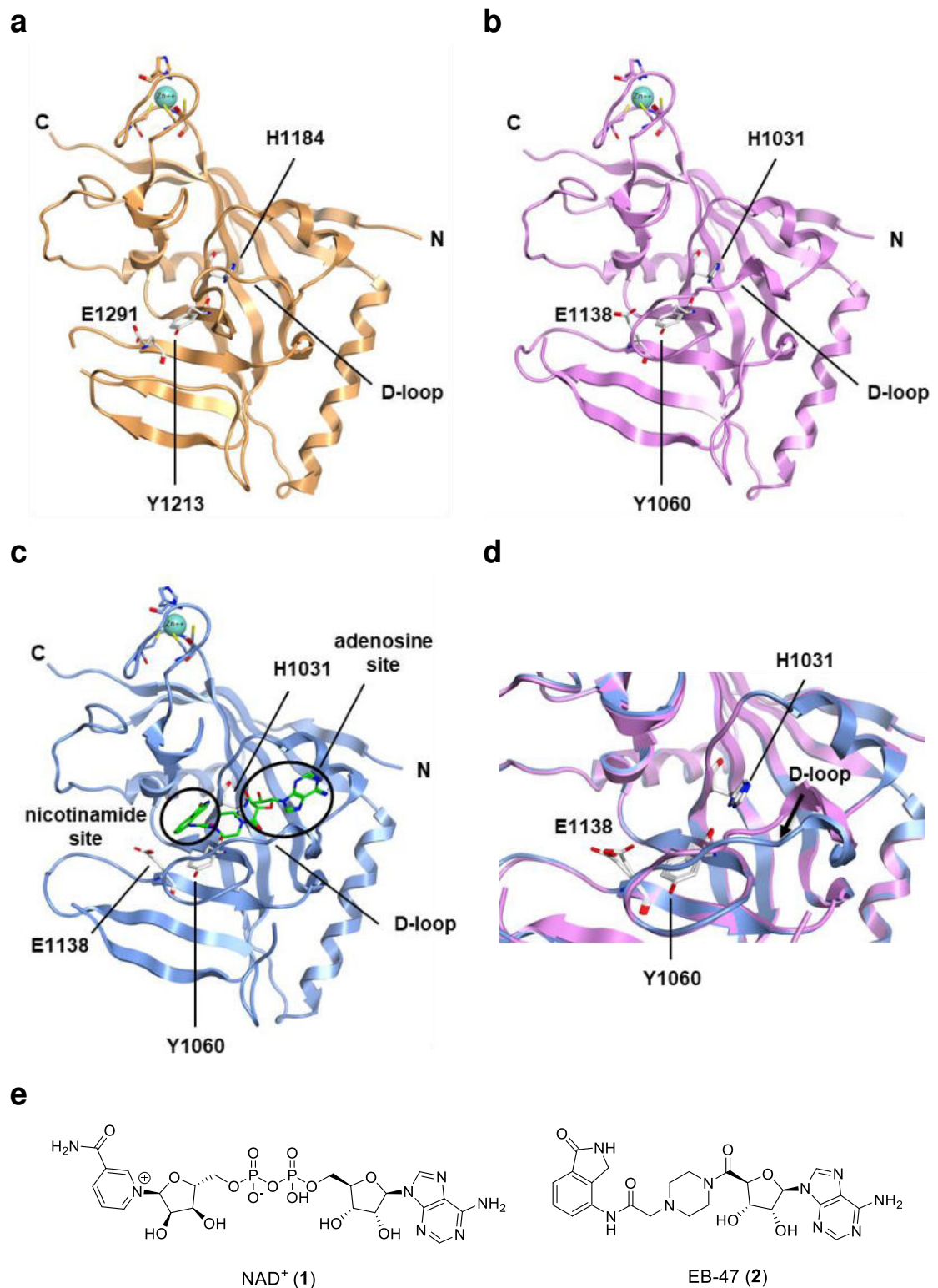


Figure 1.7. Catalytic PARP domain of tankyrase. a) Apo crystal structure of TNKS1 catalytic PARP domain (light orange) (PDB: 2RF5). **b)** Apo crystal structure of TNKS2 catalytic PARP domain (lilac) (PDB: 3KR7). In **a)** and **b)** the D-loop and catalytic H-Y-E triad of residues are highlighted. The zinc-binding CHCC residues are also shown (C1234-H1237-C1242-C1245 in

TNKS1 and C1081-H1084-C1089-C1092 in TNKS2). **c)** Crystal structure of EB-47 (**2**) (green) bound to the TNKS2 catalytic PARP domain (blue) (PDB: 4BJ9), highlighting the nicotinamide and adenosine subsites of the donor region. **d)** Overlay of the apo and EB-47 (**2**) bound crystal structures of TNK2 catalytic PARP domain, highlighting the shift in conformation of the D-loop. **e)** Chemical structures of NAD⁺ (**1**) and NAD⁺ mimic, EB-47 (**2**).

From a comparison of the apo crystal structures of TNKS1 and TNKS2 catalytic domains, it is observed that the D-loop occupies different closed conformations in which the NAD⁺ binding site is partly occupied (Figure 1.7a/b).⁴⁷ Upon binding of the NAD⁺ mimic, EB-47 (**2**), the D-loop of TNKS2 occupies a shifted conformation compared with the apo crystal structure, illustrating the conformation flexibility of this region of the catalytic binding site to allow NAD⁺ binding (Figure 1.7c/d).⁵⁴ The catalytic triad of H-Y-E residues required for PARylation activity is close to the donor NAD⁺ binding site – residues H1184-Y1213-E1291 in TNKS1 (Figure 1.7a) and H1031-Y1060-E1138 in TNKS2 (Figure 1.7b). The glutamic acid residues are required for activation of the ribose 2' hydroxyl of NAD⁺ in the elongation of PAR chains which bind in the acceptor site of tankyrase.⁵³ A unique feature of the catalytic domain of tankyrase in comparison to other ARTD enzymes is a short zinc-binding Cys-His-Cys-Cys (CHCC) motif within a loop region located around 20 Å from the NAD⁺ binding site, in which a zinc ion is tetrahedrally coordinated (Figure 1.7a/b/c).^{51, 55} The biophysical and biochemical characterisation of tankyrase catalytic domain zinc-binding mutants recently revealed that the zinc-binding motif is important for the structural integrity of the acceptor site.⁵⁵

1.3.3 Non-catalytic Domains of Tankyrase

In addition to the C-terminal catalytic domain common to all human ARTDs enzymes, there are two non-catalytic structural domains shared by TNKS1 and TNKS2 which are important in mediating both catalytic and scaffolding functions (Figure 1.6). These are a sterile alpha-motif multimerisation (SAM) domain, and an ankyrin repeat cluster (ARC) domain consisting of five individual ARCs (ARC1-5).⁴⁹

1.3.3.1 Sterile alpha-motif multimerisation (SAM) domain

The SAM domain of tankyrase is situated directly N-terminally to the catalytic PARP domain.^{49, 54} SAM domains are protein-protein interaction modules found in hundreds of human proteins, which typically function in mediating self-association through homo- and hetero-oligomerisation.⁵⁶ The tankyrase SAM domains have been shown to mediate tankyrase polymerisation both *in vitro* and *in vivo* by centrifugation and size exclusion chromatography (SEC) studies.⁵⁶⁻⁵⁷

Structural information regarding SAM-mediated polymerisation of tankyrase has been obtained using crystallography⁵⁷⁻⁵⁸, nuclear magnetic resonance (NMR) spectroscopy⁵⁹, and electron microscopy (EM)^{57, 60}. Initial structural characterisation of tankyrase SAM domain polymerisation by crystallography showed that both TNKS1-SAM and TNKS2-SAM domains form single-stranded, left-handed α -helical filaments.⁵⁷⁻⁵⁸ However, using cryogenic electron microscopy (cryo-EM), Guettler and co-workers recently revealed that a SAM-PARP unit of TNKS2 forms a novel antiparallel double helix of left-handed protofilaments, composed of a central polymeric SAM assembly and protruding PARP domains (Figure 1.8a).⁶⁰ The double-helical polymeric structure was also observed for the isolated SAM domain in negative-stain EM studies and is therefore not dependent on the adjacent PARP domain, suggesting previous single-stranded helical structures of TNKS1 SAM and TNKS2 SAM were selected during crystallisation.^{57-58, 60}

From both crystallographic and cryo-EM structures, adjacent SAM domains within each protofilament form head-to-tail contacts between end-helix (EH) to mid-loop (ML) surfaces, dominated by electrostatic interactions between basic residues of the EH surface and acidic residues of the ML surface with an interface area of 323 Å² (Figure 1.8b).^{57, 60} Site-directed mutagenesis studies showed that V903W^{ML}, Y920A^{EH} and VY903/920WA mutations in TNKS2 SAM domain result in a loss of polymerisation leading to reduced catalytic auto-PARylation activity equal to 50% compared to wild-type TNKS2.^{57, 60}

From the TNKS2 SAM-PARP filament architecture determined by cryo-EM, two novel PARP-PARP domain interfaces were identified (Figure 1.8c), with important functions in regulating both the catalytic and non-catalytic functions of tankyrase.⁶⁰ Whilst combination mutations in the PARP tail-to-tail interface had a minimal effect on tankyrase catalytic PARylation activity, structure-guided mutagenesis of the TNKS2 PARP domain head-to-head interface revealed a combination of five mutations (H1011A, E1046A, H1117A, P1120G and R1143A) that completely abolished tankyrase catalytic auto-PARylation activity.⁶⁰ An allosteric mechanism of tankyrase catalytic activation was proposed in which the head-to-head contacts, which are proximal to the donor site of the catalytic domain, induce an open conformation of the D-loop to allow access to the adenosine region of the NAD⁺ binding site.⁶⁰

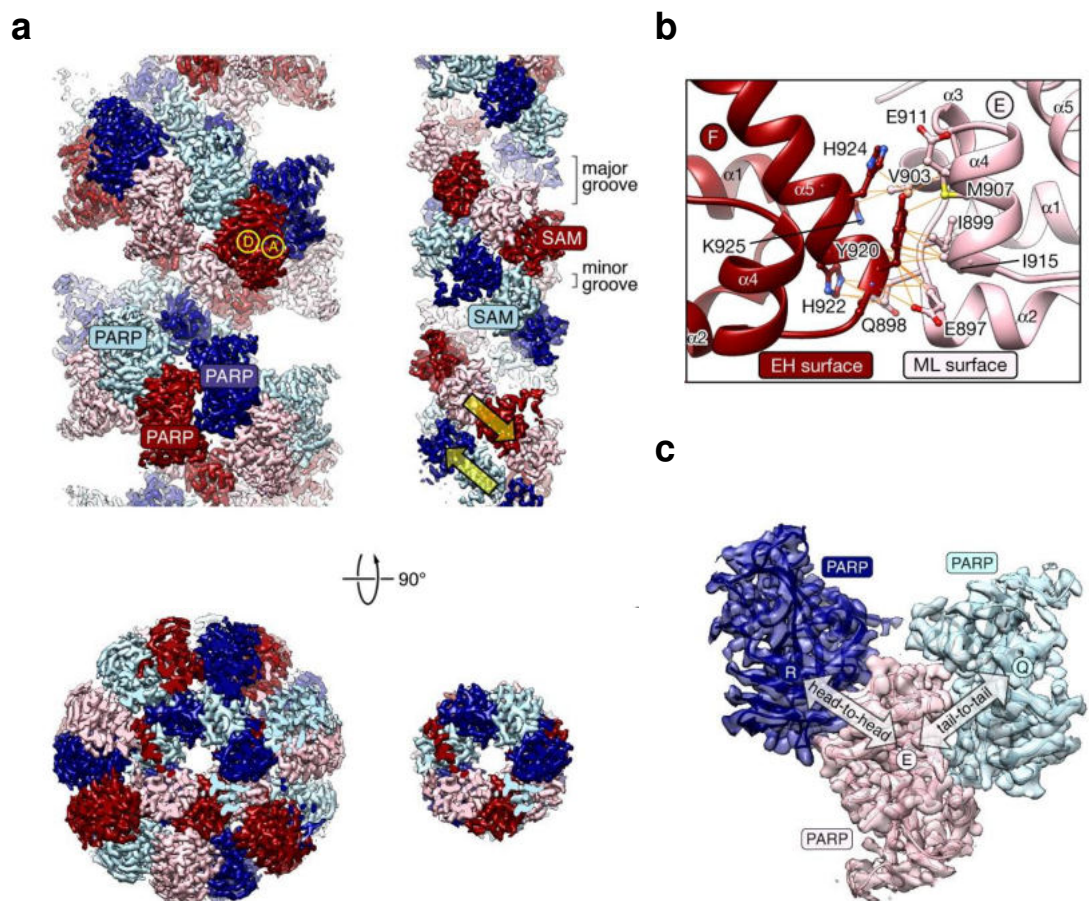


Figure 1.8. TNKS2 SAM-PARP polymerisation characterised by cryo-EM and crystallography. a) Cryo-EM maps (3 Å) of TNKS2 SAM-PARP (left) and after masking out

PARP (right). D and A represent donor and acceptor sites of the PARP domain. **b)** Key interface residues in a TNKS2 SAM dimer pair, with key interactions indicated (orange lines). **c)** Cryo-EM map of three PARP domains with head and tail interfaces indicated by arrows. Figure adapted from Pillay *et al*, 2022.⁶⁰

1.3.3.2 Ankyrin repeat cluster (ARC) domain

The ARC domain of tankyrase is composed of ankyrin repeats, another common structural motif involved exclusively in protein-protein interactions.⁶¹⁻⁶² The ankyrin repeats of tankyrase are organised into five functional regions, named ARCs 1-5, which are separated by linkers containing a highly conserved LLEAAR/K amino acid sequence.^{46, 63-64} Elucidation of the structure of apo TNKS2 ARC4 by X-ray crystallography showed that ARC4 is comprised of five stacked ankyrin repeats (Figure 1.9a).⁶¹⁻⁶² Each of the ankyrin repeats of TNKS2 ARC4 has the canonical loop-helix-loop-helix-loop topology, with the two α -helices arranged antiparallel to one another and the loops extending outwards to form a sheet of β -hairpins.⁶¹⁻⁶² The largest ARC fragment crystal structure currently reported is TNKS1 ARC1-3, in which the structure adopts a U-shape and ARCs 1-2 are linked by a broken helix whilst ARCs 2-3 are linked by a continuous helix (Figure 1.9b).^{46, 65} Small angle X-ray scattering (SAXS) analysis showed that the TNKS1 ARC1-3 construct is conformationally rigid, but that the complete ARC domain of TNKS1 (ARCs 1-5) exhibited high flexibility in solution.^{46, 65} An extended linker between ARCs 3 and 4 was amenable to cleavage upon limited proteolysis and the TNKS1 ARC4-5 construct showed dynamic behaviour in SAXS analysis, suggesting the overall flexibility of the ARC domain originates from these more flexible regions.⁴⁶

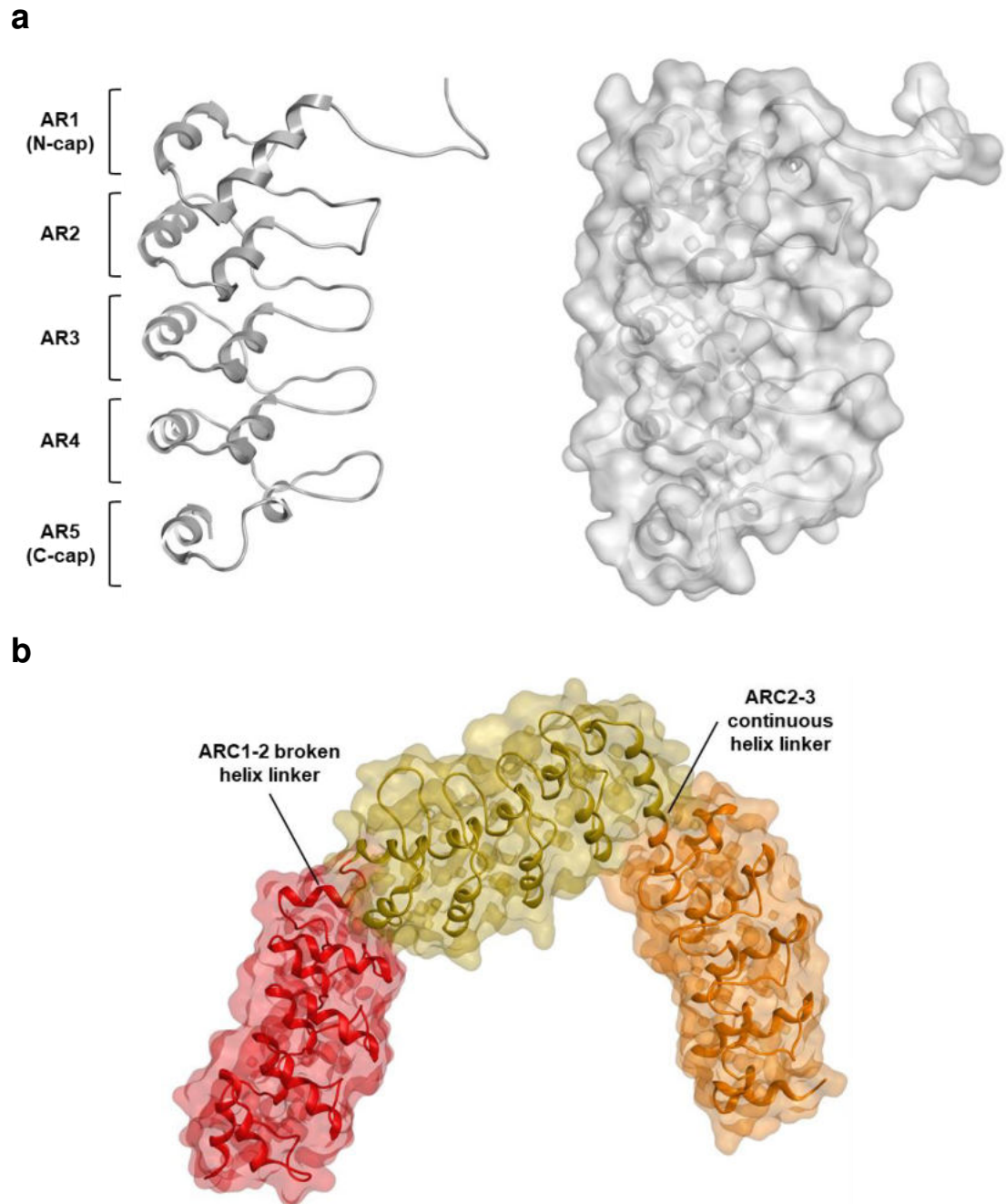


Figure 1.9. Tankyrase ARC domain. a) Apo crystal structure of TNKS2 ARC4 (484-655) (grey) (PDB: 3TWQ). Left: Ribbon representation highlighting the stacked ankyrin repeats (AR) consisting of α -helices and β -hairpin loops. Right: Surface representation. **b)** Crystal structure of TNKS1 ARC1-ARC3 (174-649) (ARC1, red; ARC2, gold; ARC3, orange) bound to IRAP peptides (not shown) (PDB: 3KR7).

The function of the tankyrase ARC domain is the recruitment of substrate proteins.^{61, 63} Specifically, ARCs 1, 2, 4 and 5 are required for the recruitment of

tankyrase-binding proteins whilst ARC3, which has a lower degree of sequence conservation with the other ARCs, is not involved in substrate binding.^{61, 66} Tankyrase substrate proteins bind to the ARC domain through recognition of a tankyrase-binding motif (TBM) peptide sequence.^{46, 61, 67} The TBM was determined as an octameric peptide with a consensus R-X-X-(small hydrophobic/G)-(D/E/I/P)-G-(no P)-(D/E) sequence from the solution-based screening of a peptide library based on SH3 domain-binding protein 2 (3BP2) – a well-characterised tankyrase-binding substrate protein involved in cherubism disease.⁶¹ A TBM peptide library was screened for ARC binding by fluorescence polarisation, and choosing the preferred amino acid at each position (in the context of the parental peptide) gave rise to a REAGDGEE peptide, which bound with a 10-fold higher binding affinity ($K_d = 0.6 \pm 0.04 \mu\text{M}$) compared with the 3BP2 octameric TBM peptide RSPPDGQS ($K_d = 4.9 \pm 0.4 \mu\text{M}$).⁶¹

Crystal structures of TNKS2 ARC4 bound to TBM peptides from different substrate proteins revealed that the peptide-binding pocket is centrally located on the concave face of the ARC domain (Figure 1.10). Furthermore, the interactions observed in the crystal structure of the 3BP2 TBM peptide bound to TNKS2 ARC4 provided an explanation for the consensus TBM sequence and identified hotspots for peptide binding (Figure 1.10).⁶¹ An arginine in position 1 is essential for binding, and forms key interactions in an arginine cradle composed of four residues: W591, F593, E598 and D589. A glycine in position 6, also essential for binding, forms an aromatic sandwich involving two tyrosine residues and a glycine residue in the ARC: Y536, Y569 and G535. Residues in positions 2 to 5 of the TBM peptides are bound in a central patch formed by nine TNKS2 residues (D521, R525, S527, F532, D556, L560, H564, N565 and S568). Finally, C-terminal contacts are formed between residues in position 7 and 8 of the TBM peptide: the main chain carbonyl of the residue in position 7 accepts a hydrogen bond from the imidazole moiety of H571, and a salt bridge is formed to K604 when position 8 is an acidic aspartate or glutamate residue.

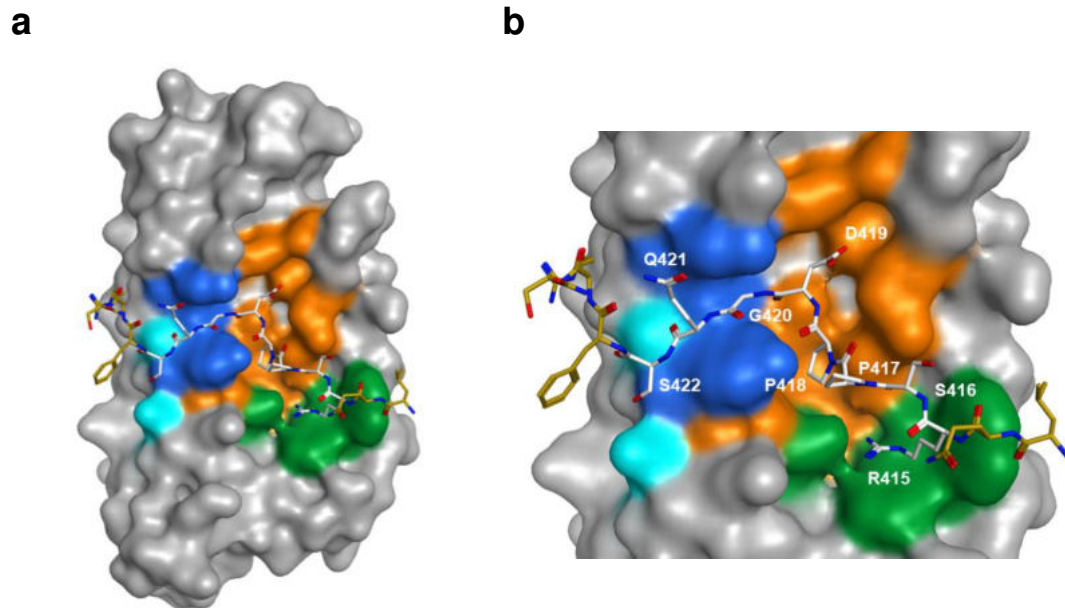


Figure 1.10. Interaction of 3BP2 with tankyrase ARC domain. **a)** Surface representation of TNKS2 ARC4 in complex with 16mer 3BP2 peptide (PDB: 3TWR): TBM residues RSPPDGQS (white) and remaining residues (gold). Key peptide-coordinating residues of TNKS2 ARC4 are coloured: arginine cradle (D589, W591, F593 and E598, green); central patch (D521, R525, S527, F532, D556, L560, H564, N565 and S568, orange); glycine sandwich (Y536, Y569 and G535, blue); C-terminal contacts (H571 and K604, cyan). **b)** Surface representation of TNKS2 ARC4:3BP2 peptide complex as shown in a), with 3BP2 residues labelled RSPPDGQS (purple). Figure adapted from Guettler *et al*, 2011.⁶¹

TBM peptides of tankyrase substrate proteins typically bind with low micromolar affinity to the ARC domain.⁶¹ However, the presence of more than one TBM motif in a tankyrase binder results in an overall increased binding affinity of the substrate for tankyrase through multivalency and avidity effects, as demonstrated with axis-inhibition (AXIN) protein – a tankyrase-binding substrate protein involved in Wnt/ β -catenin signalling.⁴⁶ The flexibility of the ARC domain is hypothesised to allow it to provide an adaptable binding platform for multivalent substrate proteins which can interact with more than one individual ARC.⁴⁶

Many tankyrase binding partners have been identified and validated, with an *in silico* analysis of the human proteome suggesting dozens to hundreds of further potential binders based on TBM motifs found within their sequences.^{53, 61} The binding of substrate proteins to the ARC domain is required for subsequent

tankyrase-mediated PARylation. The addition of negatively charged PAR chains to the substrate proteins can either directly regulate the function of the substrate protein or result in the recruitment of PAR-binding proteins. Often, tankyrase-mediated PARylation results in PAR-dependent ubiquitination (PARdU) and subsequent proteasomal degradation of its substrate proteins by PAR-binding E3 ubiquitin ligases.⁶⁸ In addition, tankyrase also catalyses auto-PARylation, a process in which tankyrase itself is PARylated, allowing for control of its cellular levels by PARdU.⁶⁹ Not all proteins which are recruited to the ARC domain undergo PARylation, suggesting there are additional non-catalytic consequences for tankyrase binders.^{53, 70-71} The diversity of tankyrase binders and substrate proteins which are regulated by recruitment to the ARC domain has implicated tankyrase in a wide range of cellular functions.

1.4 Cellular Functions of Tankyrase

Tankyrase plays a role in Wnt/ β -catenin signalling⁴⁵, telomere maintenance^{49, 63-64, 72-73}, mitotic spindle assembly⁷³⁻⁷⁵, DNA repair⁷⁶⁻⁷⁷, glucose metabolism⁷⁸⁻⁷⁹, Hippo signalling⁸⁰⁻⁸² and bone development^{61, 83}. Embryonic lethality was demonstrated in TNKS1 and TNKS2 double knockout mice, highlighting the essential cellular functions of tankyrase in embryonic development.⁴⁸ Cellular functions of tankyrase-mediated poly(ADP-ribosyl)ation in oncogenic processes have highlighted tankyrase as a potential therapeutic target in cancer.

1.4.1 Wnt/ β -Catenin Signalling

An important function of tankyrase is the regulation of the Wnt/ β -catenin signalling, which culminates in the activation of TCF/LEF transcriptional effectors.^{45, 69} The activity of this pathway is controlled by the level of active β -catenin, which is tightly regulated by the β -catenin destruction complex (DC) (Figure 1.11).^{45, 84} The β -catenin DC contains two scaffolding proteins: adenomatous polyposis coli (APC) and AXIN (AXIN1 or AXIN2).⁸⁵⁻⁸⁶ AXIN is the central scaffold of the DC and, depending on cell type, either AXIN or APC are the concentration-limiting component of the DC.⁴⁵ AXIN itself directly interacts with glycogen synthase kinase 3 (GSK3) and casein kinase 1 (CK1).^{45, 84} Under

basal levels of Wnt/ β -catenin signalling, tankyrase-mediated PARylation of AXIN leads to PAR-dependent ubiquitination and subsequent proteasomal degradation of AXIN, resulting in limited formation of the DC (Figure 1.11a).⁴⁵ Tankyrase thus tunes the receptiveness of cells to incoming Wnt signals. PARylated AXIN and auto-PARylated tankyrase are recognised by the WWE reader domain of ring finger protein RNF146 ubiquitin E3 ligase.⁸⁷ Upon Wnt stimulation, the β -catenin DC is recruited to the cell membrane and remodelled into a Wnt signalosome complex which also induces Wnt, its receptors, and the adaptor protein Dishevelled.⁴⁵ In this context, AXIN is not destabilised by PARylation, but the mechanistic basis for this observation remains unknown. Ultimately, inactivation of the DC by Wnt signalosome formation leads to accumulation of β -catenin and activation of TCF/LEF-dependent transcription (Figure 1.11b).⁴⁵

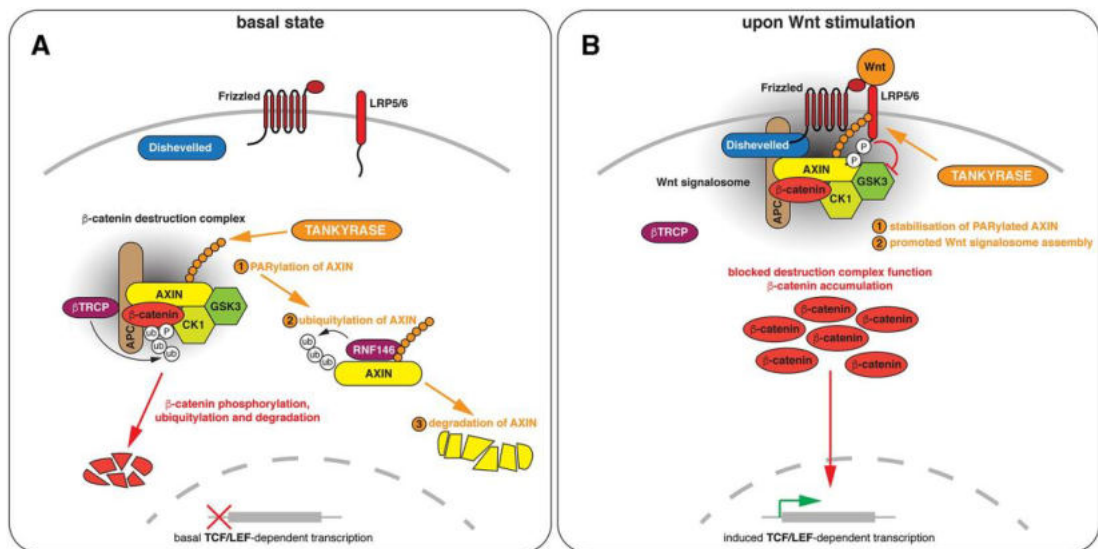


Figure 1.11. Wnt/ β -catenin signalling. Components of the Wnt/ β -catenin signalling pathway in a) a basal state and b) upon Wnt stimulation. Figure adapted from Marriotti *et al*, 2017.⁴⁵

Dysregulation of the Wnt/ β -catenin signalling pathway has been observed in several cancers, and more than 80% of colorectal cancers possess a loss-of-function truncation mutation in the *APC* gene, a suppressor of this pathway.^{84, 88} Inhibition of tankyrase has been shown to increase AXIN levels and subsequently increase formation of β -catenin degradasomes – correlates of the DC observed by light microscopy – in *APC*-mutant cancer cell lines, leading to a reduction in

TCF/LEF dependent transcription.^{69, 89} This highlights a therapeutic opportunity of targeting tankyrase in colorectal cancer.

1.4.2 Telomere Maintenance

Tankyrase has a role in telomere length maintenance through poly(ADP-ribosyl)ation of the telomere-associated protein, TRF1.^{49, 83} TRF1 is a key protein in shelterin, a six-subunit telomeric DNA-binding complex.⁹⁰⁻⁹¹ Telomeric DNA is located at chromosomal ends and consists of TTAGGG base repeats which are not fully replicated during DNA replication, leading to the progressive shortening of telomeres in subsequent cell cycles, which eventually triggers the tumour suppressive mechanism of senescence.⁹⁰⁻⁹¹ Shelterin protects telomeres, which can be regarded as naturally occurring DNA double-strand breaks, from inappropriate DNA repair mechanisms.⁹⁰⁻⁹¹ Shelterin further enables the function of telomerase, a reverse transcriptase, which catalyses the addition of telomeric repeats to chromosomes in stem cells to evade senescence.⁶³ Whilst telomerase is absent or expressed at low levels in normal somatic cells, it is overexpressed in the majority of human cancers.⁹¹

TRF1 functions in both telomere protection and modulation of telomere extension by telomerase, through its interaction with telomeric DNA and assembly into the shelterin complex.⁶³ Tankyrase function is required for normal telomere function in humans.⁷³ PARylation of TRF1 by tankyrase has been proposed to disrupt the interaction of TRF1 with telomeric DNA and potentially shelterin: this remodelling event is hypothesised to enable access of telomerase to telomeric ends for elongation.^{63, 90-91} In this model, tankyrase therefore acts as a positive regulator of telomere extension by removing TRF1-mediated repression of telomerase.⁷³ In tumours, tankyrase PARylation of TRF1 is used as a mechanism to maintain telomere length, thus evading senescence triggered by telomere shortening.⁷³ Hence, tankyrase inhibition is a therapeutic strategy for selectively targeting replicative immortality, an enabling characteristic of cancer.⁷³

1.4.3 Mitotic Spindle Assembly

Tankyrase is also involved in the assembly of mitotic spindles through its interaction with and PARylation of nuclear mitotic apparatus protein (NuMA) which has an important function in the stabilisation of microtubules.^{67, 73-74, 83, 92} Tankyrase has been shown to co-localise with nuclear pore complexes and centrosomes during mitosis.⁷³ The cellular depletion of tankyrase resulted in abnormal microtubules, sister chromatid cohesion and mitotic arrest.⁹² Therefore, the inhibition of tankyrase has the potential to target enhanced mitosis in rapidly dividing cancer cells.^{73-74, 83}

1.4.4 DNA Repair

Tankyrase is involved in the repair of DNA damage, specifically double-strand breaks (DSBs) in which both strands of the DNA helix are broken.^{76, 93} DSBs are repaired by either homologous or non-homologous repair mechanisms.⁹³ Tankyrase is recruited to DSBs through interaction with mediator of DNA damage checkpoint protein 1 (MDC1), which has been shown to promote homologous repair mechanisms to maintain genomic integrity.⁷⁶ In addition, tankyrase also regulates non-homologous repair by PARylation and subsequent stabilisation of DNA-dependent protein kinases (DNA-PKcs).⁹⁴ Inhibition of tankyrase led to a reduction in DNA-PKcs levels which would have an implication in non-homologous repair mechanisms used in cancer to enable genomic instability and mutation.⁹⁴

1.4.5 Synthetic Lethality in BRCA-Deficient Tumours

Inhibitors of DNA-dependent PARPs (PARP1 and PARP2) have been approved for clinical use as targeted therapies in cancers with mutations in either *BRCA1* or *BRCA2* genes.^{8, 33-34} BRCA-deficient cancers have defects in the repair of DSBs by homologous recombination and exhibit synthetic lethality with inhibition of PARP1/2 which are involved in PARylation-dependent DNA repair processes.⁹⁵ Two genes exhibit a synthetic lethal interaction when loss of either gene is tolerated and allows cell survival, but loss of both genes is lethal.⁹⁵ A loss

of cell viability in BRCA-deficient cancers has also been shown with loss of tankyrase.⁹⁶ The synthetic lethal interaction was hypothesised to be a result of excessive chromosome amplification resulting from genomic instability associated with BRCA-deficiency and spindle dysfunction from loss of tankyrase.⁹⁶ Therefore, there is therapeutic opportunity for targeting tankyrase in BRCA-mutated cancers such as breast, ovarian and prostate.

1.5 Limitations of Catalytic Tankyrase Inhibitors

The involvement of tankyrase in the cellular processes highlighted in the previous discussion has resulted in the development of many inhibitors with potential as cancer therapeutics.^{45, 50, 83, 93, 97} Tankyrase inhibitor development efforts have primarily focused on small molecule inhibitors of the conserved catalytic PARP domain, as discussed in recent reviews of tankyrase inhibitors in the patent literature and currently undergoing clinical trials.^{93, 98} All reported catalytic tankyrase inhibitors are antagonists of NAD⁺ binding in the donor site of the PARP domain.^{41, 45} These inhibitors are classified according to the region of the donor site involved in key binding interactions, which has been guided by structural information obtained from inhibitor-bound crystal structures of the tankyrase PARP domains. There are three classifications of catalytic tankyrase inhibitors: nicotinamide mimetics, adenosine binding site inhibitors, and dual binders (Figure 1.12).⁹³

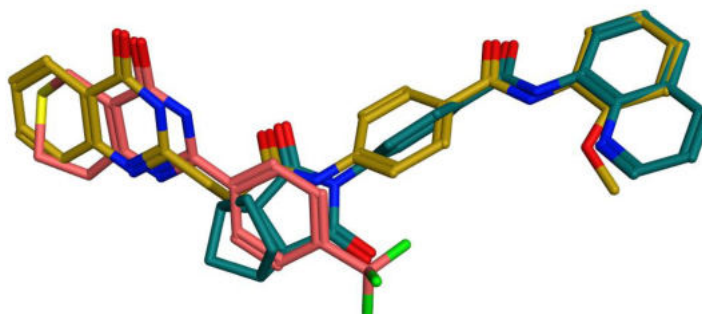


Figure 1.12. An overlay of representative tankyrase inhibitors which illustrate the three classifications of catalytic inhibitors. XAV939 (3) (peach) is a nicotinamide mimetic⁶⁹, whereas

IWR-1 (**4**) (teal) is an example of an adenosine site binder⁸⁸ and quinazolinone **5** (gold) is a dual binding site inhibitor (see Figure 1.13 for chemical structures of inhibitors).⁹⁹

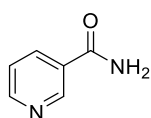
1.5.1 Catalytic Tankyrase Inhibitors

The first reported tankyrase inhibitors, XAV939 (**3**) and IWR-1 (**4**), were identified from high-throughput screening for modulators of Wnt/ β -catenin mediated transcription, using Wnt responsive luciferase reporter assays.^{69, 88} Both compounds (**3** and **4**) were found to inhibit Wnt/ β -catenin signalling through increased levels of AXIN, the central scaffold of the β -catenin destruction complex.^{69, 88} Huang *et al* proposed that stabilisation of AXIN was a consequence of inhibition of the catalytic PARylation activity of tankyrase by XAV939, resulting in reduced PARdU and decreased proteasomal degradation of AXIN.⁶⁹ The stabilisation of AXIN resulted in increased levels of β -catenin degradation which led to reduced Wnt/ β -catenin mediated transcription in an *APC* mutant colorectal cancer (SW480) cell line.⁶⁹ These studies were therefore the first to identify tankyrase as a druggable target in the Wnt pathway which could be modulated by small molecules.

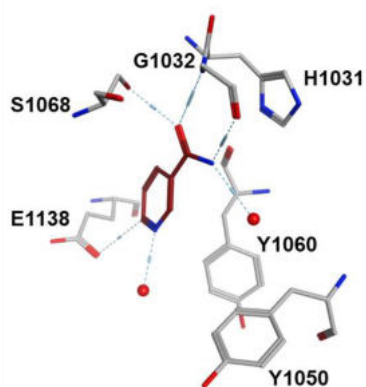
As mentioned previously, the classification of catalytic tankyrase inhibitors was guided by inhibitor co-crystal structures, specifically crystal structures of XAV939 (**3**) and IWR-1 (**4**) bound to the catalytic domain of TNKS2.^{47, 52} The crystal structure of the XAV939 (**3**) complex showed interactions analogous with nicotinamide binding in the catalytic domain, with the lactam moiety forming key hydrogen bonds with S1068 and G1032 (Figure 1.13a/b).⁵² Therefore, XAV939 (**3**) was classified as a nicotinamide mimetic. In contrast, the crystal structure of IWR-1 (**4**) elucidated binding in the proposed adenosine binding site of NAD⁺ within the D-loop region of the catalytic site (Figure 1.13c).^{45, 47, 97} This region is also referred to as the 'induced pocket', as binding of adenosine site inhibitors induces conformational changes in the flexible D-loop. Upon binding of IWR-1 (**4**), distinct conformational changes were induced in three tyrosine residues (Y1050, Y1060 and Y1071) which form interactions with the norbornenyl moiety of IWR-1 (**4**). The first dual-site catalytic tankyrase inhibitor, **5**, was subsequently identified from a substructure search against the Amgen compound library using

the binding motif identified from the IWR-1 (**4**) crystal structure (Figure 1.13d).¹⁰⁰ A crystal structure of dual-site binder **5** bound to the catalytic domain of TNKS1 revealed that two carbonyls from central amide motifs formed hydrogen bonds with Y1213 and D1198 in the adenosine site, whilst the quinazolinone maintained key hydrogen bonds with S1221 and G1185 as the nicotinamide mimetic component (Figure 1.13d).¹⁰⁰

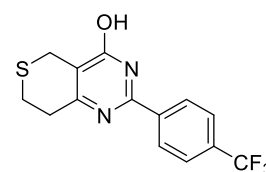
a



nicotinamide

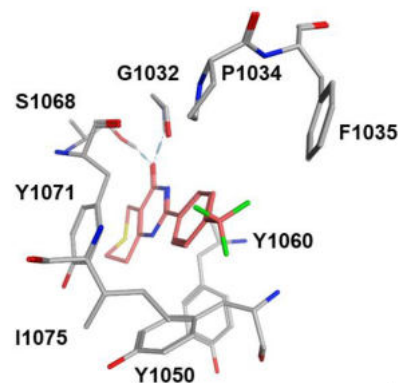


b

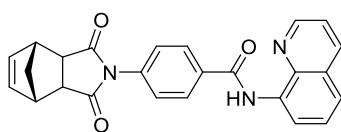


XAV939 (**3**)

nicotinamide site inhibitor

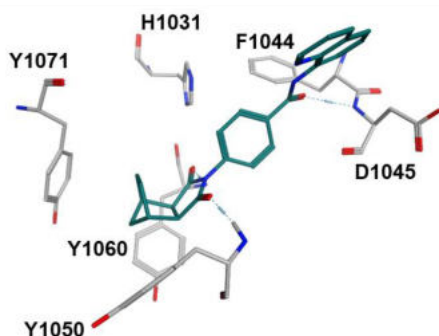


c

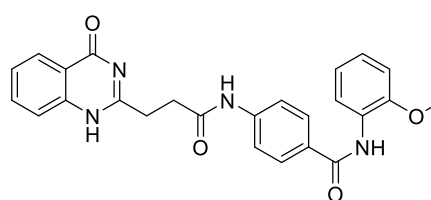


IWR-1 (**4**)

adenosine site inhibitor



d



5

dual-site binder

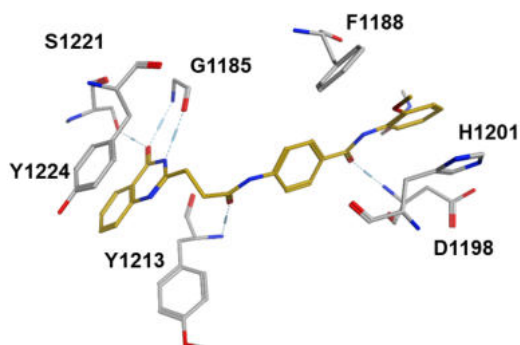


Figure 1.13. Chemical structures of representative tankyrase inhibitors and key interactions with the catalytic domain. **a)** Key interactions of nicotinamide (red) in complex with TNKS2 catalytic domain (PDB: 3U9H): the carboxamide forms three H-bonds with S1068 and G1032, and two H-bonds with water-molecule networks.⁴⁷ **b)** Key interactions of XAV939 (**3**) (pink) in complex with TNKS2 catalytic domain (PDB: 3KR8): two key H-bonds are formed with S1068 and G1032, mimicking nicotinamide binding.⁵² **c)** Key interactions of IWR1 (**4**) (green) in complex with TNKS2 catalytic domain (PDB: 3UA9).⁴⁷ **d)** Key interactions of quinazolinone **5** (gold) in complex with TNKS1 catalytic domain (PDB: 4I9I).¹⁰⁰

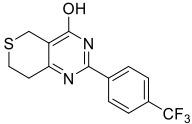
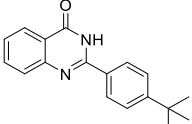
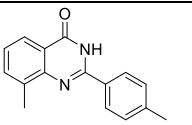
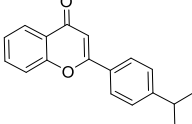
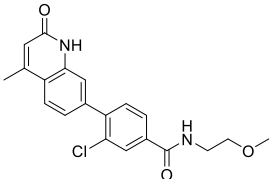
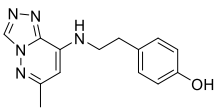
The potency of catalytic tankyrase inhibitors has been determined using different methods including biochemical enzymatic inhibition, fluorescence polarisation (FP) and liquid chromatography-mass spectrometry (LCMS) assays, typically evaluating inhibition of autoPARylation activity of the catalytic PARP domain.¹⁰¹ XAV939 (**3**) and IWR-1 (**4**) were reported as potent and selective binders, with IC₅₀ against TNKS1 and TNKS2 in the range of 10 nM to 150 nM determined from an LCMS based high throughput auto-PARylation assay which monitored the formation of nicotinamide.⁶⁹ However, a recent study demonstrated discrepancies in the initially reported potency of XAV939 (**3**) against PARP1 and PARP2, concluding that it is an unselective tankyrase inhibitor (Table 1.2).¹⁰¹ Adenosine site inhibitors and dual-site binders which form interactions with the induced pocket typically demonstrate more selective tankyrase inhibition as the residues in this region are more variable between ARTD enzymes capable of PARylation, compared to the nicotinamide subsite which is highly conserved.

Table 1.2. Potency and selectivity of catalytic tankyrase inhibitors. Reported potency (half maximal inhibitory concentration, IC₅₀) for catalytic tankyrase inhibitors assessed against TNKS and PARP catalytic domains (Huang *et al*, 2009) or against full length PARPs (Thorsell *et al*, 2017): N.D. = not determined, N.I. = no inhibition.

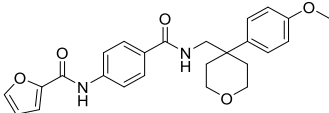
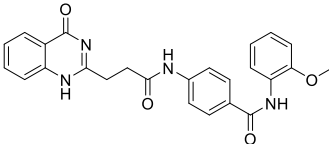
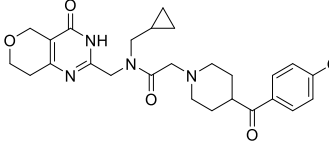
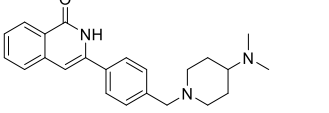
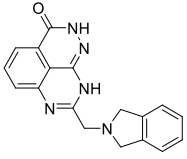
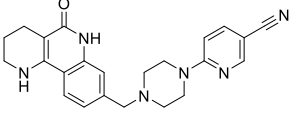
IC ₅₀ (nM)		TNKS1	TNKS2	PARP1	PARP2
XAV939 (3)	Huang <i>et al</i> ⁶⁹	11	5	2194	114
	Thorsell <i>et al</i> ¹⁰¹	95	4	74	27
IWR1 (4)	Huang <i>et al</i> ⁶⁹	131	56	>1875	>1875
	Thorsell <i>et al</i> ¹⁰¹	135	N.D.	N.I.	N.I.
Dual-site binder (5)	Bregman <i>et al</i> ¹⁰⁰	8	2	-	931

Since the discovery of XAV939 (**3**), IWR-1 (**4**) and the first dual-site binder **5**, further efforts have been made to develop more potent tankyrase inhibitors as anti-cancer therapeutics. Between 2013 to 2020, 49 different patents were published from the pharmaceutical industry as well as academic research groups disclosing novel catalytic tankyrase inhibitors as potential anti-cancer therapeutics.⁹⁸ A recent review summarising the literature-reported small molecule tankyrase inhibitors further categorised the nicotinamide mimetics based on their chemotype into cyclic lactams, flavones and nicotinamide bioisosteres, whilst the adenosine binding site inhibitors were divided into the IWR series, 1,2,4-triazoles and JW compounds (Table 1.3).⁹³

Table 1.3. Summary of reported catalytic tankyrase inhibitors. The names, chemical structures, reported IC₅₀ against TNKS1/2 and PARP1/2, PDB codes of crystal structures and references of a selection of catalytic tankyrase inhibitors are indicated.

Name	Structure	IC ₅₀ (μM)	PDB	References
Nicotinamide Mimetics				
XAV939 (3)		TNKS1 IC ₅₀ = 0.011 TNKS2 IC ₅₀ = 0.004 PARP1 IC ₅₀ = 2.194 PARP2 IC ₅₀ = 0.114	3KR8 ⁵² 3UH4 ¹⁰²	Huang <i>et al</i> , 2009 ⁶⁹
2-phenyl-3,4-dihydroquinazolin-4-one (6)		TNKS1 IC ₅₀ = 0.005	4BUD ¹⁰³	Haikarainen <i>et al</i> , 2013 ¹⁰³
2-arylquinazolin-4-one (7)		TNKS1 IC ₅₀ = 0.035 TNKS2 IC ₅₀ = 0.007 PARP1 IC ₅₀ = 0.685	4UFY ¹⁰⁴	Nathubhai <i>et al</i> , 2013 ¹⁰⁵
2-phenyl flavone (8)		TNKS1 IC ₅₀ = 0.006 TNKS2 IC ₅₀ = 0.072 PARP1 IC ₅₀ = 19.1 PARP2 IC ₅₀ = 34.9	4BS4 ¹⁰⁶	Narwal <i>et al</i> , 2013 ¹⁰⁶
4-methyl quinolin-2(1H)-one (9)		TNKS2 IC ₅₀ = 0.009	4J3L ¹⁰⁷	Larsson <i>et al</i> , 2013 ¹⁰⁷
UPF-1854 (10)		TNKS1 IC ₅₀ = 0.012 TNKS2 IC ₅₀ = 0.200 PARP1 IC ₅₀ > 10 PARP2 IC ₅₀ > 10	4M7B ¹⁰⁸	Liscio <i>et al</i> , 2014 ¹⁰⁸

AZ6102 (11)		TNKS1 IC ₅₀ = 0.003 TNKS2 IC ₅₀ = 0.001 PARP1 IC ₅₀ = 2.0 PARP2 IC ₅₀ = 0.5	Johannes <i>et al</i> , 2015 ¹⁰⁹
AZ1366 (12)		TNKS1 IC ₅₀ = 0.003 TNKS2 IC ₅₀ = 0.010 PARP1 IC ₅₀ = 0.559 PARP2 IC ₅₀ = 0.232	Johannes <i>et al</i> , 2015 ¹⁰⁹ Quackenbush <i>et al</i> , 2016 ¹¹⁰
RK-287107 (13)		TNKS1 IC ₅₀ = 0.014 TNKS2 IC ₅₀ = 0.011 PARP1 IC ₅₀ > 100 PARP2 IC ₅₀ = 2.717	5ZQR ¹¹¹ Shirai <i>et al</i> , 2019 ¹¹¹ Mizutani <i>et al</i> , 2018 ¹¹²
RK-582 (14)		TNKS1 IC ₅₀ = 0.036 TNKS2 IC ₅₀ = 0.039 PARP1 IC ₅₀ = 18.19 PARP2 IC ₅₀ = 1.24	6KRO ¹¹³ Shirai <i>et al</i> , 2020 ¹¹³
M2912 (15)		TNKS1 IC ₅₀ = 0.0013 TNKS2 IC ₅₀ = 0.0014 PARP1 IC ₅₀ = 0.14 PARP2 IC ₅₀ = 0.20	7OCV ¹¹⁴ Buchstaller <i>et al</i> , 2021 ¹¹⁴ Menon <i>et al</i> , 2019 ¹¹⁵
Adenosine Site Inhibitors			
IWR-1 (<i>endo</i>) (4)		TNKS1 IC ₅₀ = 0.131 TNKS2 IC ₅₀ = 0.056 PARP1 > 18.7 PARP2 > 18.7	3UA9 ⁴⁷ Chen <i>et al</i> , 2009 ⁸⁸
JW74 (16)		TNKS1 IC ₅₀ = 2.55 TNKS2 IC ₅₀ = 0.65 PARP1 > 19 PARP2 > 19	Waler <i>et al</i> , 2011 ¹¹⁶ Shultz <i>et al</i> , 2012 ¹¹⁷
G007LK (17)		TNKS1 IC ₅₀ = 0.046 TNKS2 IC ₅₀ = 0.025 PARP1 > 20	4HYF ¹¹⁸ Voronkov <i>et al</i> , 2013 ¹¹⁸
WIKI4 (18)		TNKS2 IC ₅₀ = 0.015	4BFP ¹¹⁹ James <i>et al</i> , 2012 ¹²⁰
K-756 (19)		TNKS1 IC ₅₀ = 0.031 TNKS2 IC ₅₀ = 0.036	5ETY ¹²¹ Okada-Iwasaki <i>et al</i> , 2016 ¹²¹

JW55 (20)		TNKS2 IC ₅₀ = 1.9 TNKS2 IC ₅₀ = 0.83 PARP1 IC ₅₀ > 20	5ADQ ¹²²	Waler <i>et al</i> , 2012 ¹²³
Dual Binders				
Quinazolinone (5)		TNKS1 IC ₅₀ = 0.008 TNKS2 IC ₅₀ = 0.002 PARP2 IC ₅₀ = 0.931	4I9I ¹⁰⁰	Bregman <i>et al</i> , 2013 ¹⁰⁰
NVP-TNKS656 (21)		TNKS2 IC ₅₀ = 0.006 PARP1 IC ₅₀ > 19 PARP2 IC ₅₀ = 32		Shultz <i>et al</i> , 2013 ¹²⁴
3-aryl-5-substituted isoquinolin-1-one (21)		TNKS1 IC ₅₀ = 0.013 PARP1 IC ₅₀ = 0.465	4U6A ¹²⁵	Elliott <i>et al</i> , 2015 ¹²⁵
Dual TNKS/PARP Inhibitors				
2X-121 (E7449) (22)		TNKS1 IC ₅₀ = 0.050 TNKS2 IC ₅₀ = 0.050 PARP1 IC ₅₀ = 0.002 PARP2 IC ₅₀ = 0.001 (Yu <i>et al</i> , 2022) ⁹³		McGonigle <i>et al</i> , 2015 ¹²⁶
NOV140201 (JPI-547) (23)		TNKS1 IC ₅₀ = 0.005 TNKS2 IC ₅₀ = 0.001 PARP1 IC ₅₀ = 0.002 (Yu <i>et al</i> , 2022) ⁹³		Lee <i>et al</i> , 2016 ¹²⁷

Currently, only two tankyrase inhibitors have progressed into evaluation in phase I and II clinical trials as cancer therapeutics: 2X-121 (E7449, **22**)^{126, 128} and NOV140201 (JPI-547, **23**)^{129, 98}. Interestingly, both of these compounds are dual inhibitors of TNKS1/TNKS2 and PARP1/PARP2. Most other studies have focussed on the development of inhibitors which are selective for tankyrase over other PARP enzymes, guided by structural information from inhibitor-bound crystal structures. From the number of potent and more selective catalytic tankyrase inhibitors reported, only a limited set of these compounds have shown oral antitumour efficacy in preclinical mouse models: AZ1366 (**12**)¹⁰⁹⁻¹¹⁰, RK-287107 (**13**)¹¹¹⁻¹¹², RK-582 (**14**)¹¹³ and M2912 (**15**)¹¹⁴⁻¹¹⁵ belonging to the nicotinamide mimetics, and JW55 (**20**)¹²³ from the adenosine site binders.¹¹⁴ RK-582 (**14**) and M2912 (**15**) both showed efficacy in colorectal cancer (COLO320) xenograft mouse models, with significant tumour growth inhibition at 20 mg/kg bi-

daily oral dosing, however both compounds showed signs of intestinal toxicity and weight loss at bi-daily doses of 50 mg/kg in tolerability studies, indicating a limited therapeutic window for both compounds.

1.5.2 Limitations of Catalytic Tankyrase Inhibition

Intestinal toxicity is the major adverse effect of tankyrase inhibition which has also been reported in other *in vivo* studies of tankyrase inhibitors in preclinical colorectal cancer models.^{123, 130-131} This is an on-target toxicity associated with inhibition of normal somatic stem cell proliferation in intestinal crypts as a result of modulation of the Wnt/ β -catenin pathway.^{45, 132} The use of tankyrase inhibitors in combination with other drugs targeting other oncogenic dysregulations might provide a strategy for improving the efficacy and safety of tankyrase inhibition.^{45, 115} However, the underlying mechanism of the on-target intestinal toxicity in response to catalytic tankyrase inhibition is not well understood and remains a challenge for the development of anti-cancer therapeutics targeting tankyrase.

Other limitations of targeting the catalytic functions of tankyrase have recently been reported. In addition to inhibiting the tankyrase-mediated PARylation of substrate proteins, tankyrase auto-PARylation is also blocked by catalytic inhibition due to impaired NAD⁺ co-substrate binding.^{45, 69} This consequentially prevents the PAR-dependent ubiquitination of tankyrase by the E3 ubiquitin ligase RNF146, which has a WWE reader domain that recognises PARylated proteins.⁸⁷ Therefore, the proteasomal degradation of tankyrase itself is inhibited and tankyrase is accumulated as a consequence of its catalytic inhibition. This was initially shown with XAV939 (**3**)⁶⁹ and has since been shown with numerous other advanced catalytic tankyrase inhibitors including RK-287107 (**13**)¹¹², RK-582 (**14**)¹¹³ and M2912 (**15**)¹¹⁴. It is hypothesised that the accumulation of tankyrase upon catalytic inhibition might enhance its concentration-dependent scaffolding functions which may also contribute to its cellular roles in oncogenic processes.⁴⁵

The role of tankyrase scaffolding functions in driving tankyrase cellular activity is another potential limitation of catalytic tankyrase inhibition. This has been

primarily studied in the context of the Wnt/ β -catenin signalling, in which it was found that tankyrase was able to promote this signalling pathway independently of its catalytic activity.⁵⁷ The activation of tankyrase-dependent Wnt/ β -catenin signalling was determined in a luciferase reporter assay measuring β -catenin/TCF/LEF-dependent transcription using HEK293T cells transfected with MYC₂-tagged tankyrase constructs.⁵⁷ It was observed that increasing the concentration of the catalytic inhibitor XAV939 (**3**) against both wild-type TNKS2 and catalytically inactive TNKS2 (G1032W) only achieved partial modulation of Wnt/ β -catenin signalling (Figure 1.14a).⁵⁷ Titrations of XAV939 (**3**) to saturating concentrations only reduced TNKS2-dependent Wnt reporter activation to ~ 50%, in agreement with the extent of activation shown for PARylation deficient TNKS2 (G1032W).⁵⁷ Therefore, catalytic inhibition is not sufficient for abolishing cellular Wnt/ β -catenin signalling activity when tankyrase is overexpressed.

Further to this, the effect of regulating the scaffolding functions of tankyrase on Wnt/ β -catenin signalling was determined using the Wnt reporter assay. Deletion of the tankyrase ARC domain (TNKS2 Δ ARC1-5) and mutation of the ARCs capable of substrate binding (TNKS2 xx3xx) both fully abolished Wnt reporter activation (Figure 1.14b).⁵⁷ Auto-PARylation activity was not affected in either of these constructs, suggesting that blocked substrate binding led to the full regulation of Wnt/ β -catenin signalling.⁵⁷ In addition, a full reduction in Wnt reporter activation was observed with deletion of the SAM domain (TNKS2 Δ SAM), and with polymerisation-deficient SAM mutants (V903W^{TNKS2} and Y920A^{TNKS2}; V1056W^{TNKS1} and Y1073A^{TNKS1}), suggesting that tankyrase polymerisation is also essential for Wnt/ β -catenin signalling (Figure 1.14c).⁵⁷ SAM-mediated polymerisation results in formation of PARP-PARP domain interfaces, as discussed in section 1.3.3.1, and the functional consequence of combination mutations in the head-to-head and tail-to-tail interfaces on tankyrase scaffolding was also studied in the context of Wnt/ β -catenin.⁶⁰ Although combination mutations in the head interface only reduced Wnt reporter activation to a level comparable to catalytically inactive G1032W^{TNKS2} (~50%), consistent with an effect on only the catalytic functions of tankyrase, tail combination mutations led to full reduction in Wnt reporter activation suggesting a contribution of the polymerisation-dependent PARP-PARP tail interactions to activation of

non-catalytic tankyrase functions.⁶⁰ Therefore, it is hypothesised that there are both catalytic and non-catalytic functions of tankyrase involved in the activation of Wnt/ β -catenin signalling, which are dependent on both polymerisation and substrate/effector protein recruitment, and that this likely extends to other cellular processes which are regulated by tankyrase.^{45, 57}

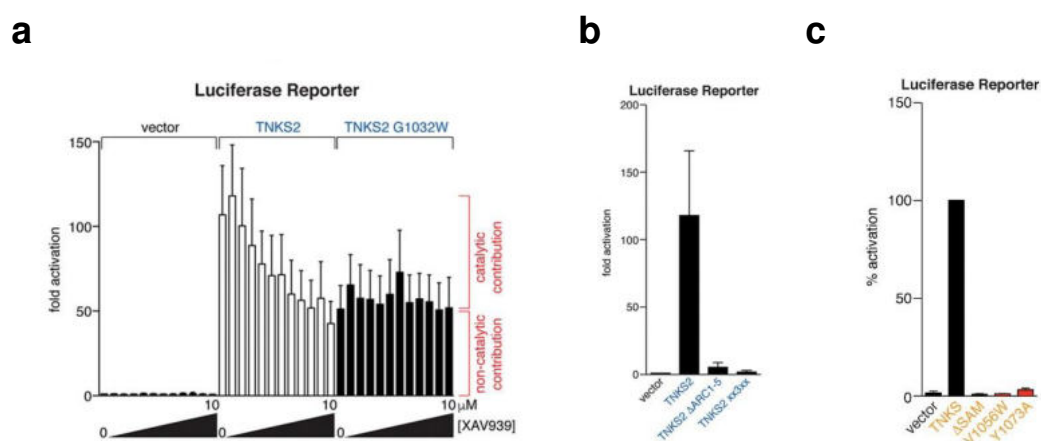


Figure 1.14. Requirement of ARC and SAM domains for Wnt/ β -catenin signalling. Activation of Wnt/ β -catenin signalling was measured by β -catenin/TCF/LEF-dependent transcription in reporter TOPFlash assays in HEK293T cells. **a**) Reduced TOPFlash reporter activation upon catalytic inhibition with XAV939 (**3**) of wild-type and catalytic mutant TNKS2 (G1032W). **b**) TOPFlash reporter activation with wild-type, ARC deleted (Δ ARC1-5) and ARC mutant (xx3xx) TNKS2. **c**) TOPFlash reporter activation with wild-type, SAM deleted (Δ SAM) and SAM mutant (V1056W or Y1073A) TNKS1. Figure adapted from Mariotti *et al*, 2016.⁵⁷

1.6 Inhibitors of Tankyrase Non-Catalytic (Scaffolding) Functions

A recognition of the limitations of the catalytic inhibition of tankyrase has resulted in an interest in targeting the catalysis-independent functions of tankyrase as a novel approach for pharmacological inhibition. Tankyrase non-catalytic functions are regulated by the ARC and SAM domains through protein-protein interactions, which are classically considered a challenging target in drug discovery.¹³³ Different approaches have been taken to develop chemical tool inhibitors of tankyrase scaffolding, including peptidomimetic synthesis and small molecule screening, which are often utilised in the discovery of drugs targeting protein-protein interactions (PPIs).¹³³

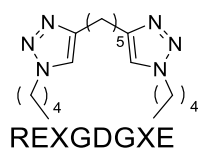
All four studies published so far have mainly focused on the development of antagonists of tankyrase ARC-mediated substrate binding,¹³⁴⁻¹³⁷ with one of these reports also screening for small molecule disruptors of SAM-mediated polymerisation.¹³⁷ As demonstrated in the context of Wnt/ β -catenin signalling, functional studies of ARC and SAM domain deletion and site-directed mutagenesis to remove either substrate-binding or polymerisation functions all resulted in an equivalent and complete reduction of Wnt reporter activation due to regulation of both catalytic and non-catalytic tankyrase functions. Therefore, targeting either the ARC or SAM domain functions could result in an equivalent biological effect from full regulation of tankyrase cellular functions. Both ARC and SAM domains are involved in PPIs with comparable affinities: typical ARC:substrate protein interactions are of low micromolar affinity,⁶¹ whilst SAM:SAM polymerisation-deficient homodimers were determined to bind with high nanomolar affinity (TNKS1 SAM^{V1056W}:SAM^{Y1073A} $K_d = 0.82 \pm 0.16 \mu\text{M}$ and TNKS2 SAM^{V1056W}:SAM^{Y1073A} $K_d = 0.95 \pm 0.17 \mu\text{M}$), although additional domain contacts within the tankyrase filament may account for higher affinities driving self-assembly.^{57, 60} The SAM:SAM head-to-tail interaction can be classified as a flat, electrostatic surface interaction between two globular proteins with no obvious ligandable pockets for small molecule binding.^{57-58, 133} In contrast, the ARC:substrate protein interaction represents a more druggable PPI, in which the globular ARC protein interacts with a peptidic region of the substrate through well-defined interactions in hotspot pockets, which often correlate with ligand binding sites in small molecule screening.^{133, 138-139}

1.6.1 Peptidomimetic Approaches

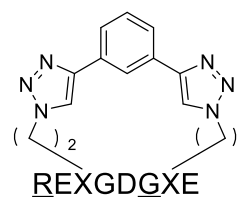
Peptidomimetics are peptide-like compounds which are designed to mimic and disrupt the interaction of a natural peptide with a target protein to which it binds.^{133, 140} Typically, the development of peptidomimetics is motivated by improving the properties of peptides, such as cell permeability and metabolic stability to proteolytic cleavage, to make the compound more drug-like whilst maintaining key binding interactions for the receptor.¹⁴⁰ An improvement in binding affinity and cell permeability can be achieved by amino acid side-chain modifications, or by introduction of non-natural amino acids to allow

macrocyclisation or peptide stapling in the synthesis of conformationally restricted peptidomimetics.¹⁴⁰

In a proof-of-concept study, a series of macrocyclised peptidomimetics with extended non-helical conformations were designed based upon the sequence-optimised octameric TBM peptide, READGDEE, as inhibitors of ARC-mediated substrate binding.¹³⁴ Molecular dynamics simulations were used to investigate optimal linker lengths whilst a computational alanine scan was used to determine amenable positions for incorporation of an unnatural amino acids, and peptidomimetics were next synthesised using a two-component double-click chemistry approach.¹³⁴ Peptidomimetics Cp4n4m5 (**24**) and Cp4n2m3c (**25**) were identified as cell permeable dose-dependent inhibitors of Wnt signalling through disruption of TNKS:AXIN interaction, and the crystal structures of each in complex with TNKS2 ARC4 confirmed that key interactions with the ARC substrate binding domain were maintained (Figure 1.15).¹³⁴



Cp4n4m5 (**24**)



Cp4n2m3 (**25**)

Figure 1.15. Chemical structures of two ARC-binding macrocyclised peptidomimetics. Peptidomimetics Cp4n4m5 (**24**) and Cp4n2m3 (**25**) incorporated unnatural amino acids (X) for macrocyclisation.¹³⁴

A further peptidomimetic approach focused on the replacement of the N-terminal arginine residue from the octameric TBM peptide sequence for the development of drug-like peptidomimetics as antagonists of the ARC:substrate protein interaction.¹³⁵ *In silico* docking was used to identify replacements for the guanidine moiety of *L*-arginine to improve cellular permeability of the peptidomimetics compared with the 3BP2 octameric TBM peptide (*L*-

RSPPDGQS).¹³⁵ In total, five peptidomimetics were synthesised in which the *L*-arginine residue was replaced with non-natural amino acids (*1H*-imidazole-5-pentanoic acid, *1H*-imidazole-1-pentanoic acid, 7-aminoheptanoic acid, *D*-arginine and *L*-citrulline).¹³⁵ However, all five peptidomimetics exhibited lower potency or no competition in a competitive fluorescence polarisation (FP) assay against TNKS1 ARC4 using a Cy5-labelled 3BP2-based TBM peptide probe.¹³⁵ This further demonstrated the previously-reported essentiality of the N-terminal arginine residue in position 1 of the octameric TBM peptide sequence for substrate binding to the tankyrase ARC domain.^{61, 135}

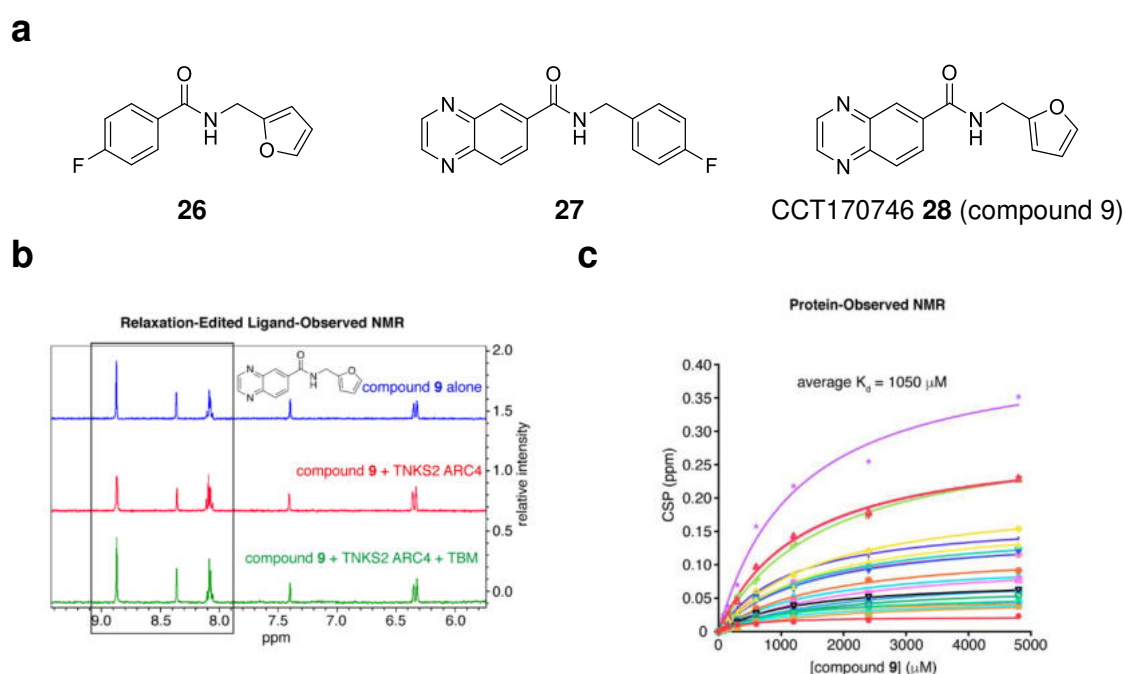
1.6.2 Small Molecule Screening Approaches

In early-phase drug discovery, the identification of small molecule compounds which interact with a validated target protein of interest from screening of compound libraries provides 'hits' or chemical starting points for medicinal chemistry efforts towards novel therapeutics.¹⁴¹ Following the peptidomimetic approaches, different screening methods have been performed to identify hits for the development of small molecule antagonists of tankyrase substrate recruitment and scaffolding.

1.6.2.1 Fragment-based screening against the tankyrase ARC domain

A fragment-based screening approach successfully identified a set of quinoxaline-based fragment molecules which bound to the tankyrase ARC domain.¹³⁵ Fragment-based drug discovery (FBDD) is frequently used for the identification of low molecular weight compounds (< 300 Da) with micromolar to millimolar affinity, using biophysical assay screening techniques such as differential scanning fluorimetry (DSF) and nuclear magnetic resonance (NMR) spectroscopy.¹⁴²⁻¹⁴⁶ A library of ~1,900 fragments was screened against TNKS2 ARC4 and TNKS2 ARC5 domains using DSF and NMR assays.¹³⁵ Using competitive ligand-observed NMR experiments against TNKS2 ARC4, compounds **26**, **27** and CCT170746 (**28**) were identified as fragment hits which were competitive with binding of a 16mer 3BP2 peptide (Figure 1.16a/b).¹³⁵ Protein-observed NMR titration studies against ¹⁵N-labelled TNKS2 ARC4

validated **28** as a fragment hit with good solubility, showing significant chemical shift perturbations (CSPs) of ARC residues which interacted with the hit (Figure 1.16c).¹³⁵ The apparent binding affinity, or dissociation constant (K_d), of CCT170746 (**28**) from protein-observed NMR titration was around 1 mM ($K_d = 1050 \mu\text{M}$) which was confirmed using isothermal titration calorimetry ($K_d = 1200 \pm 380 \mu\text{M}$) (Figure 1.16c/d).¹³⁵ Furthermore, CCT170746 (**28**) exhibited pan-ARC binding to all tankyrase ARC domains in ligand-observed NMR assays, with the exception of TNKS2 ARC1 which was rationalised to result from subtle binding site differences (Figure 1.16e).¹³⁵ The identification of ARC residues and epitope mapping of the fragment binding site was enabled by the full backbone assignment of TNKS2 ARC4 using ^{15}N - ^{13}C labelled protein (Figure 1.16f).^{135, 147} This indicated binding of CCT170746 (**28**) within the aromatic glycine sandwich and central patch residues of the substrate binding domain, which was in agreement with mutagenesis studies.¹³⁵ This ligandability study therefore provided proof-of-concept of targeting the tankyrase ARC domain with small molecule antagonists which, if elaborated to potent binders, could block substrate-binding ARC functions.



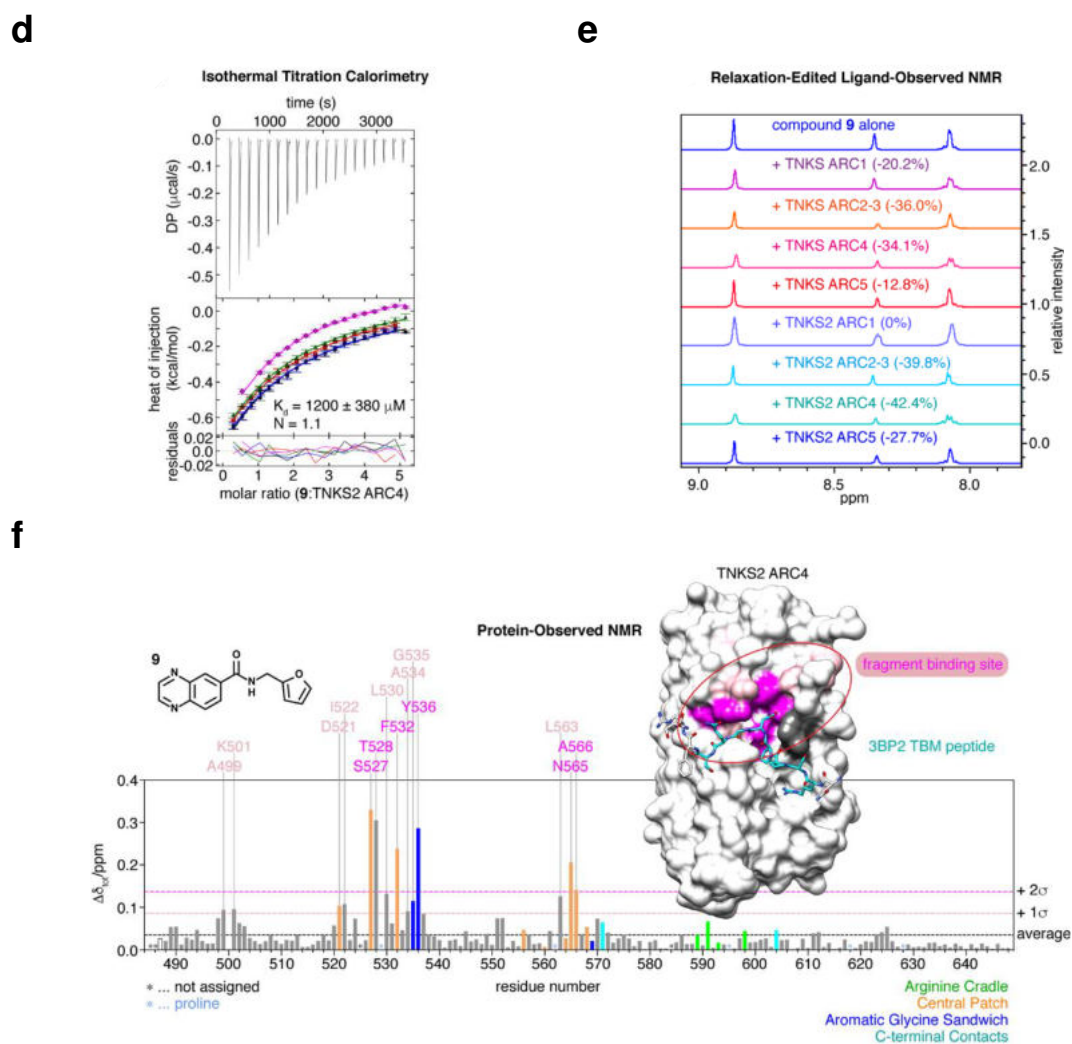


Figure 1.16. Identification of small molecule binders of the tankyrase ARC domain from a fragment-based screening approach. **a)** Chemical structures of fragment hits **26**, **27** and CCT170746 (**28**). **b)** Relaxation-edited ligand-observed NMR spectra for **28** (compound **9**), showing a reduction peak height of ligand signals on addition of TNKS2 ARC4 protein and a recovery of ligand signals with a competitor TBM peptide (Ac-LPHLQRSPPDGQSFRSW-NH₂). **c)** CSPs of peaks which were shifted in a concentration dependent manner plotted against concentration of **28** for determination of K_d from ¹H-¹⁵N HSQC protein-observed NMR titrations. **d)** Determination of K_d from ITC for **28** into TNKS2 ARC4. **e)** Relaxation-edited ligand-observed NMR spectra for **28** against all TNKS1 and TNKS2 ARC domains. **f)** Mapping of the fragment binding site on the surface representation of TNKS2:3BP2 TBM peptide complex. CSPs >2 σ (red) and >1 σ (pink) of average overlap with central patch (orange) and aromatic glycine sandwich (blue) residues, and unassigned residues (dark grey), indicating an overlap of the substrate TBM binding region of the ARC domain. Figure adapted from Pollock *et al*, 2019.¹³⁵

Two further reports identifying compounds binding to the substrate binding domain of tankyrase using alternative screening techniques have since been published.

1.6.2.2 Virtual high-throughput screening against the tankyrase ARC domain

Virtual screening is a computational method used in drug discovery to identify novel compounds from virtual libraries or databases which bind to a target protein of interest.¹⁴⁸ A target-based virtual screen of 200,000 compounds was performed using a docking strategy against the crystal structure of the complex formed by TNKS1 ARC5 and C-terminal residues of ubiquitin-specific protease 25 (USP25) incorporating a TBM peptide sequence (SLSRTPADGR).^{136, 149} USP25 binds to the ARC domain of tankyrase and is a positive regulator of Wnt/ β -catenin signalling through the deubiquitination and stabilisation of tankyrase, which results in increased PARylation, PARdU and proteasomal degradation of AXIN.¹⁴⁹ From the virtual screen, 201 compounds were selected for hit confirmation using a competitive FP assay and isothermal titration calorimetry.¹³⁶ Two hit compounds, C41 (**29**) and C44 (**30**), were identified with reported K_i values between 20-200 μ M against TNKS1 ARC5 (Figure 1.17).¹³⁶ C44 (**30**) was reported to promote the degradation of TNKS1 through disruption of the TNKS1 ARC5:USP25, leading decreased activation of a Wnt luciferase reporter assay by a reduction in β -catenin levels.¹³⁶



Figure 1.17. Hits from virtual screening against the tankyrase ARC domain. Chemical structures of two hit compounds, C41 (**29**) and C44 (**30**), and inhibitory constants (K_i) determined from competitive FP assays against TNKS1 ARC1-5 (178-957) protein.¹³⁶

1.6.2.3 FRET-based high-throughput screening against the tankyrase ARC and SAM domains

In a further study, biochemical assays based on fluorescence resonance energy transfer (FRET) were developed for high-throughput screening of small molecule compounds against the ARC- and SAM-mediated scaffolding functions of tankyrase.¹³⁷ For the identification of novel binders of the ARC domain as potential substrate binding antagonists, a TNKS2 ARC4:TBM FRET pair was developed consisting of a mCerulean (CFP) TNKS2 ARC4 fusion protein and a mCitrine (YFP) tagged sequence-optimised octameric TBM peptide (REAGDGEE).¹³⁷ In addition, a TNKS2 SAM:SAM FRET pair – consisting of TNKS2 SAM^{E897K} and YFP-fused TNKS2 SAM^{Y920A} mutants capable of dimerisation only – was optimised for identifying disruptors of SAM-mediated polymerisation.¹³⁷ A screen of 1,120 compounds against both FRET pairs for validation of the biochemical FRET assays was followed by hit confirmation using a DSF assay.¹³⁷ Whilst no initial hits were confirmed against the SAM domain, two hit compounds were identified against the ARC domain, the AMPA receptor antagonist fanapanel (**31**) and the NDMA receptor antagonist 5,7-dichlorokynurenic acid (DCKA, **32**), with reported K_i values between 20-100 μM (Figure 1.18).^{137, 150-151}



Figure 1.18 Hits from FRET-based screening against the tankyrase ARC domain. Chemical structures of two hit compounds, fanapanel (**31**) and DCKA (**32**), and inhibitory constants (K_i) determined from FRET assays against TNKS2 ARC4.¹³⁷

Overall, the different small molecule screening methods applied so far to target tankyrase substrate recruitment and scaffolding functions have demonstrated the ligandability of the ARC domain, specifically the TBM peptide binding pocket.

Ligands with binding affinities between 20 μM to $\sim 1000 \mu\text{M}$ have been identified as potential chemical start points for the development of potent antagonists of tankyrase substrate-binding functions.¹³⁵⁻¹³⁷ Meanwhile, the ligandability of the SAM domain remains to be determined due to the lack of confirmed hits from only one screening effort reported thus far.¹³⁷ Therefore, targeting tankyrase scaffolding functions through the development of non-catalytic antagonists of substrate binding currently represents a more promising approach compared to development of inhibitors of SAM-mediated polymerisation.

1.7 Thesis Hypothesis and Aims

An understanding of the contribution of tankyrase scaffolding functions to the activation of Wnt/ β -catenin signalling, regulated by SAM-domain-mediated polymerisation and ARC-domain-mediated substrate protein binding, has emerged in recent years. This highlights that cellular functions of tankyrase are not fully regulated by its catalytic inhibition, which is a limitation in the development of catalytic inhibitors to target tankyrase in cancers associated with its aberrant function. In addition, catalytic inhibition can lead to the accumulation of tankyrase which may further accentuate the contribution of its scaffolding functions to cellular processes.

Therefore, it is hypothesised that tankyrase could instead be fully modulated by small molecule chemical inhibitors which block both its catalytic and non-catalytic functions. Further to this, it is hypothesised that inhibition of tankyrase scaffolding would have a different pharmacological effect on cellular functions compared to existing catalytic inhibitors, potentially providing an improved therapeutic strategy for tankyrase inhibition in cancer. Potent and cell-active small molecules which regulate tankyrase scaffolding functions are required to study these hypotheses and to provide starting points for drug discovery efforts. The aim of this thesis was therefore the development of small molecule chemical tool compounds to inhibit the non-catalytic functions of tankyrase using two parallel approaches.

The primary approach of this project was the development of small molecule antagonists of tankyrase substrate binding ARCs using fragment-based drug discovery. A previous fragment screening project had successfully identified a set of fragment molecules from the ICR fragment library which bound to the tankyrase ARC domain.^{135, 152} The aim for this approach was to develop fragment hit CCT170746 (**28**), with good solubility and weak affinity ($K_d \sim 1$ mM) against the TNKS2 ARC4 domain, into a novel series of substrate binding antagonists with sub-micromolar potency. For optimisation of **28** into lead fragments with increased binding affinity for the tankyrase ARC domain, iterations of synthesis of analogues, guided by *in silico* modelling and followed by testing using biophysical NMR assays was pursued.

A parallel approach of this project to regulate tankyrase non-catalytic functions was the development of PROTACs for the targeted degradation of tankyrase by the ubiquitin-proteasome system. The aim was the synthesis of heterobifunctional compounds, by attachment of an existing catalytic tankyrase inhibitor *via* a chemical linker to an E3 ligase recruiting ligand. Subsequent testing of the compounds was pursued to evaluate binary target engagement and tankyrase degradation in a cellular context.

The overall objective, using both approaches, was to develop a set of chemical tools which could be used to differentiate the effects of inhibiting tankyrase non-catalytic functions compared with antagonising its catalytic activity. The fragment-based approach aimed to provide compounds which would disrupt the interaction of tankyrase and its effector proteins. Although not all tankyrase binders are PARylated, binding of substrates to the ARC domain is a prerequisite for their subsequent PARylation. Therefore, non-catalytic inhibitors of ARC:substrate interactions would also inhibit the catalytic PARylation function of tankyrase in this context. Further to this, degradation of tankyrase using the PROTAC approach would remove all its functions, including its catalytic activity and its non-catalytic scaffolding through substrate binding and polymerisation. Potent and efficacious compounds from either method would be suitable to determine whether targeting the non-catalytic functions of tankyrase is an improved approach over catalytic tankyrase inhibition to provide novel anti-cancer therapeutics.

Chapter 2.0, Chapter 3.0, and Chapter 4.0 of this thesis discuss work towards the development of substrate binding antagonists of the tankyrase ARC domain using a fragment-based approach. Chapter 2.0 describes the synthesis of structural analogues of fragment hit CCT170746 (**28**), focusing on modification of the furan motif, and testing of these analogues against TNKS2 ARC4 in biophysical NMR assays to understand the structure-activity relationship of **28** and investigate the proposed *in silico* modelling of **28** bound to TNKS2 ARC4. Chapter 3.0 details the synthesis and biophysical NMR testing of further structural analogues of **28**, with modification to the quinoxaline motif and the identification of a higher affinity lead fragment. Chapter 4.0 then discusses the synthesis of

analogues based on the lead fragment scaffold and the establishment of a competitive fluorescence polarisation assay with increased sensitivity to determine the potency of the higher affinity fragment analogues. Chapter 5.0 of this thesis describes efforts in the development of PROTACs for targeted tankyrase degradation, through the synthesis of heterobifunctional compounds with tankyrase-binding and CRBN-binding ligands, and their profiling in target engagement and degradation assays. Finally, Chapter 6.0 provides a discussion and future outlooks of the fragment and PROTAC approaches for the development of small molecule non-catalytic tankyrase inhibitors.

Chapter 2 Initial Structure-Activity Relationship Exploration of a Tankyrase ARC-Binding Fragment Hit

2.1 Introduction to Fragment-Based Drug Discovery

Fragment-based drug discovery (FBDD) emerged in the early 2000s as a strategy to aid the development of novel small molecule targeted therapeutics.¹⁴⁶ FBDD is a process which starts with screening a fragment library against a target protein, followed by fragment hit validation, then optimisation of validated fragment hits into potent inhibitors.¹⁵³

2.1.1 Fragment Screening versus High-Throughput Screening

Fragment screening, the first step of FBDD, is a complementary approach to high-throughput screening (HTS) of drug-like compounds for the identification of chemical start points in small molecule drug discovery.¹⁵³ There are key differences between the two methodologies (Table 2.1). Typical compounds in HTS libraries are usually selected to be compliant with Lipinski's 'rule of five' guidelines for drug-like physicochemical properties: molecular weight (MW) < 500 Da, calculated partition coefficient (clogP) \leq 5, hydrogen bond donors (HBD) \leq 5, and hydrogen bond acceptors (HBA) \leq 10.¹⁵⁴⁻¹⁵⁵ In contrast, fragments are lower molecular weight compounds which commonly adhere to 'rule of three' guidelines: MW < 300 Da, clogP \leq 3, HBD \leq 3, HBA \leq 3, number of rotatable bonds (NROT) \leq 3 and polar surface area (PSA) \leq 60 Å².¹⁵⁶⁻¹⁵⁷ Fragments are therefore typically composed of less than 20 non-hydrogen atoms and have lower molecular complexity than drug-like compounds, often containing only a limited number of pharmacophoric elements or functional groups.^{146, 158-159} As a result, hits from a fragment screen only have a few interactions with the target protein and bind with weak affinity (μ M to mM) compared with hits from HTS (nM to μ M).¹⁵⁷ However, the use of fragment screening for hit identification allows a more efficient sampling of chemical diversity space, and results in higher hit rates than HTS of drug-like compounds which makes it suitable for more challenging targets such as PPIs.^{146, 153, 155}

Table 2.1. Fragment screening versus high-throughput screening.

	Fragment Screening	High-Throughput Screening
Molecular weight	< 300 Da	< 500 Da
Non-hydrogen atoms	< 20	< 30
Chemical diversity	~10 ¹¹ molecules ¹⁶⁰	> 10 ⁶⁰ molecules ¹⁶¹
Number of compounds in screening library	10 ³ to 10 ⁴ compounds ¹⁶²	10 ⁵ to 10 ⁶ compounds ¹⁶²
Binding affinity (K _d) of hits	μM to mM	nM to μM
Assays used in screening	Biophysical assays	Biochemical or functional assays

Fragment-based drug discovery relies on the use of biophysical assays to detect low affinity (μM to mM) ligand-protein interactions, as the binding affinity is typically out with the upper detection limits of biochemical or functional assays used in HTS.¹⁶³ There are a number of biophysical techniques which are used in fragment screens including DSF (also known as thermal shift assay, TSA), surface plasmon resonance (SPR), isothermal titration calorimetry (ITC), X-ray crystallography and NMR spectroscopy.¹⁶²⁻¹⁶⁴ Some of these are also used as orthogonal methods for fragment hit validation – which requires binding affinity determination and structural information regarding the fragment's binding location – and in hit-to-lead optimisation.¹⁵⁵

A shift in the temperature of thermal unfolding of a protein (melting temperature, T_m) caused by ligand interactions is measured to detect fragment hits in DSF screens, using a fluorescent dye which has an increased quantum yield when bound to hydrophobic patches of unfolded protein.¹⁶⁴⁻¹⁶⁵ DSF is suitable for fragment screening as it is relatively high throughput compared to other biophysical methods, however it is challenging to quantify ligand binding affinity using this method.¹⁶⁶ SPR is also a high throughput biophysical technique which detects a change in the refractive index of light upon fragment binding to immobilised protein on a sensor chip surface, from which the equilibrium dissociation constant, K_d, of ligand-protein binding can be determined.¹⁶⁷ The binding affinity of fragments can also be determined using ITC, as the heat

associated with ligand-protein interactions upon increasing ligand concentrations is measured to calculate the equilibrium association constant (K_a , where $K_a = 1/K_d$).¹⁶⁵ However, ITC is lower throughput compared to DSF and SPR as it uses a larger quantity of protein and subsequently is typically used in fragment hit validation rather than fragment screening.^{165, 168} X-ray crystallography and NMR methods are both applicable to all phases of FBDD (fragment screening, hit validation and hit-to-lead optimisation) and can detect very low affinity binders ($K_d > 1$ mM).¹⁵⁵ FBDD by crystallography requires protein crystallisation, fragment soaking and X-ray diffraction data collection: target proteins which are not amenable to crystallisation cannot be screened and fragments which bind to a non-crystallised conformation are not detected.¹⁶⁹ In contrast to crystallography, NMR experiments to detect fragment binding are solution-based and are applicable to a diversity of targets including flexible proteins and complexes.¹⁷⁰ NMR spectroscopy was the first biophysical method to be applied to fragment-based drug discovery and is a powerful tool to identify and characterise ligand-protein interactions.¹⁷¹⁻¹⁷² There are a number of different NMR experiments used in FBDD which are categorised as either ligand-observed or protein-observed, depending on whether the ligand signals or protein signals are monitored.^{170, 172} Ligand-observed experiments are typically used in fragment screening whilst protein-observed methods – used for structure and binding affinity determination – are more often applied to hit validation and lead optimisation.^{165, 170}

2.1.2 Fragment Hit-to-Lead Optimisation

The overall aim of FBDD is to develop potent inhibitors against a target protein from weakly binding fragment hit compounds identified and validated following a fragment screen.¹⁶⁸ Optimisation of the fragment hits into ligands with sub-micromolar binding affinity is pursued in a fragment hit-to-lead phase.¹⁶² Physicochemical properties of fragment compounds must also be monitored during this phase: fragment-like ‘rule-of-three’ properties should be maintained whilst affinity remains low to ensure compounds with high solubility which can be tested using biophysical methods.¹⁷³⁻¹⁷⁴ As fragment hits progress into potent inhibitors, more sensitive biochemical or functional assays can be used to assess binding, and drug-like physicochemical parameters can be applied.¹⁷⁴

Fragments can be developed into higher affinity compounds using one or more of three main strategies: fragment growing, fragment linking or fragment merging.^{146, 168} In a fragment growing approach, new functional groups and structural modifications are introduced to the hit compound to increase the quantity and quality of its interactions with the target protein, such as in the development of vemurafenib (**35**), an approved drug for the treatment of *BRAF*-mutant cancers (Figure 2.1a).^{162, 175-176} For this strategy, vectors suitable for growing the fragment must be identified and a structure-activity relationship (SAR) of the fragment hit must be established.^{153, 168} In contrast, fragment linking and merging approaches both require two or more fragments which are bound in different regions of the target protein binding pocket but are proximal to one another, such as in the discovery of venetoclax (**40**), a BCL-2 inhibitor which is clinically approved for the treatment of various leukaemias (Figure 2.1b).^{153, 168, 177-178} A linker can be designed to attach the fragments together, or different structural elements of the fragments can be merged to generate larger and more potent inhibitors.^{153, 168}

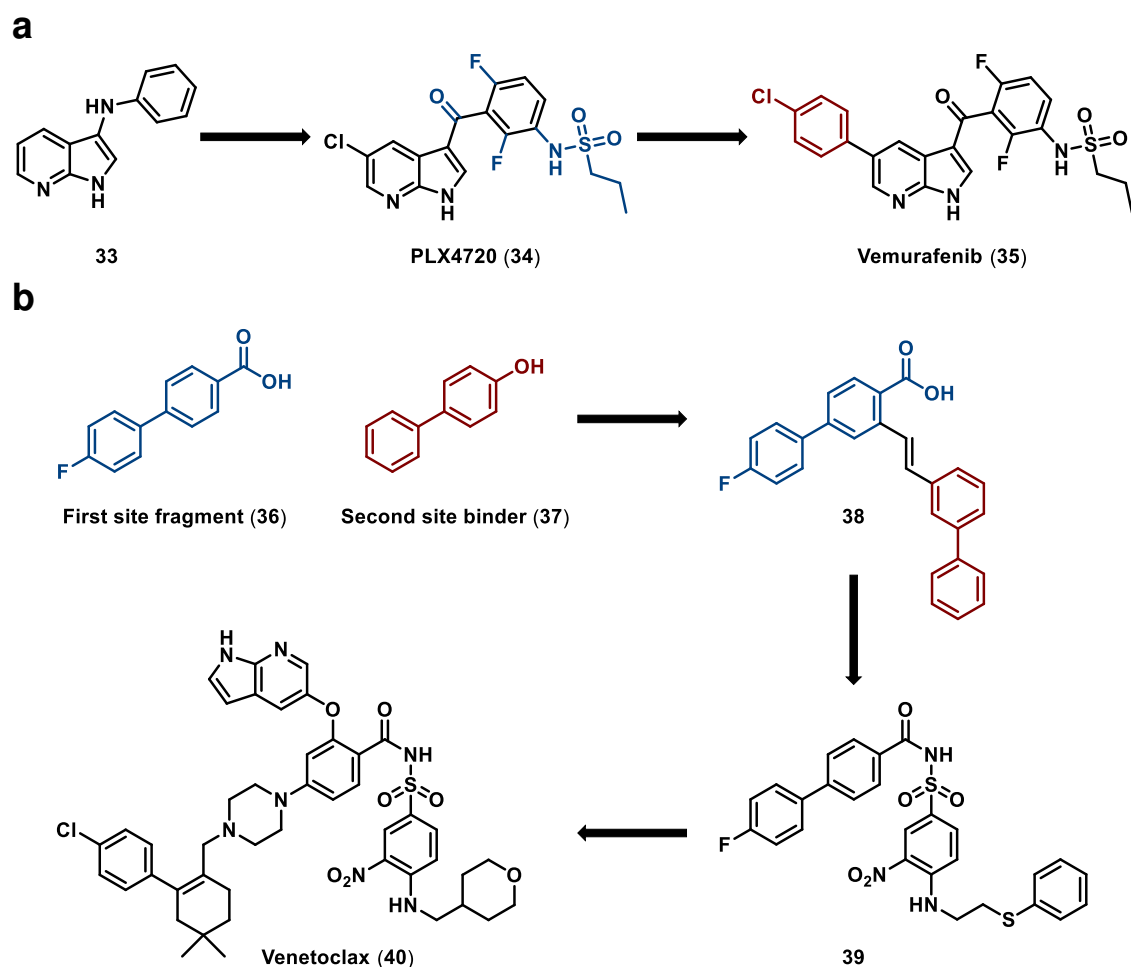


Figure 2.1. Fragment growing and fragment linking strategies for hit-to-lead optimisation in FBDD. a) Development of vemurafenib (**35**) from fragment hit **33** using a fragment growing approach.¹⁷⁵⁻¹⁷⁶ b) Development of venetoclax (**40**) from two proximately-bound fragment hits, **36** and **37**, using a fragment linking approach.¹⁷⁷⁻¹⁷⁸

Structural information on the ligand binding orientation is considered essential for both strategies of fragment hit optimisation – to either identify growth vectors or design optimal linkers – and enables structure-based drug design (SBDD) for the optimisation of fragments into potent inhibitors.^{169, 179} X-ray crystallography is the predominant method used for structural characterisation of fragment-protein complexes in FBDD, however structural information is also obtained from *in silico* docking and different NMR experiments, such as protein-observed ¹H-¹⁵N heteronuclear single quantum correlation (HSQC) spectroscopy.^{169, 180-181} Briefly, protein-observed ¹H-¹⁵N HSQC spectroscopy is used to identify protein residues which interact with a ligand and to identify fragments which are bound in proximal

sites on a protein (refer to section 2.7.1 for further discussion).^{171, 182} It is applied in a method known as 'SAR by NMR', in which fragment hits bound in proximal sites on a protein are identified and structure-guided fragment linking or merging is applied to generate a potent inhibitor, which was fundamental to the development of venetoclax (**40**) and other small molecule therapeutics developed using FBDD.^{170-171, 177-178}

2.1.3 Fragment-Based Drug Discovery and Protein-Protein Interactions

FBDD has successfully resulted in the clinical approval of small molecule inhibitors of PPIs, as exemplified by venetoclax (**40**), which inhibits the interaction of anti-apoptotic BCL-2 with its pro-apoptotic protein binding partners.^{170, 178, 183} Protein-protein interactions are viewed as challenging or even undruggable targets due to their shallow binding pockets and large surface area, however FBDD has led to the discovery of potent inhibitors against these targets in cases when HTS was previously unsuccessful, such as against MMP3 (stromelysin).^{133, 146, 158, 184} In fragment-based screening against PPIs, there is often a correlation between fragment hit binding sites and hotspot regions on the target protein.^{133, 135, 177, 183} Fragments can then be grown to improve interactions within a particular hotspot region or linked from one hotspot to another, in order to generate potent lead inhibitors which can fully disrupt an interaction between two proteins.¹³³

2.2 Aim and Strategy for Development of Non-Catalytic Tankyrase Inhibitors using a Fragment-Based Approach

Fragment-based drug discovery was pursued towards the identification of potent antagonists of the tankyrase ARC domain, capable of disrupting PPIs between tankyrase and its substrate proteins. A quinoxaline-based fragment hit compound CCT170746 (**28**), which had been identified from a fragment screen against TNKS2 ARC4 using ligand-observed NMR, was selected as the chemical start point for this approach.¹³⁵ During hit validation of **28**, its binding affinity against TNKS2 ARC4 was determined as $K_d \sim 1$ mM from ¹H-¹⁵N HSQC protein-observed NMR and ITC experiments.¹³⁵ Further to this, structural information obtained during hit validation – using protein-observed NMR and competitive ligand-

observed NMR experiments – revealed that **28** bound to the glycine sandwich and central patch hotspots in the substrate binding pocket of TNKS2 ARC4.¹³⁵

The overall strategy for this fragment-based project was to develop CCT170746 (**28**) into a potent substrate binding antagonist of the ARC domain using a fragment growing approach for hit-to-lead optimisation. The principal aim was to identify higher affinity, lead fragment analogues of **28** by introducing structural modifications to increase fragment-protein interactions within the glycine sandwich and central patch, and by extending to other hotspot binding regions in the TNKS ARC substrate binding pocket. Therefore, the systematic exploration of SAR around **28** was proposed by the synthesis of fragment analogues, using *in silico* modelling to aid fragment design. A competitive ligand-observed NMR assay using both CPMG and waterLOGSY methods would be used to test all fragment analogues for binding to the substrate recognition pocket of TNKS2 ARC4. Protein-observed NMR (¹H-¹⁵N HSQC) would then be used to determine the binding affinity (K_d) of selected fragment analogues, and for structural characterisation of the fragment binding sites. Biophysical NMR methods were prioritised as there is no requirement for a fluorescent dye, immobilisation of the target protein or protein crystallisation as for other biophysical methods. Ligand-observed and protein-observed NMR would be used to facilitate the identification of lead fragments with increased affinity ($K_d < 300 \mu\text{M}$). The development of lead fragments into chemical inhibitors with submicromolar potency ($K_d < 1 \mu\text{M}$) would then be pursued, using a higher throughput competitive biochemical assay to assess the potency of further compounds.

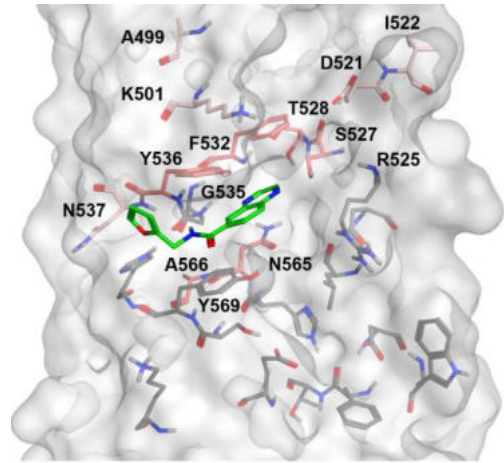
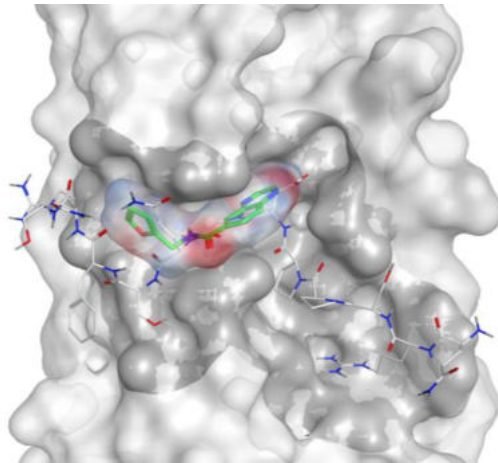
The first aim of the fragment-based approach of the project was to understand the structure-activity relationship (SAR) of fragment hit, CCT170746 (**28**). This chapter describes the synthesis of close structural analogues of **28** and testing of fragments for competitive binding against TNKS2 ARC4 using biophysical ligand-observed NMR methods. Further compounds were then synthesised to explore modification of the furan motif of **28**, and binding affinities of analogues were determined using protein-observed NMR. A second aim was refinement of the *in silico* model of the location and binding mode of fragment hit **28** and its analogues

within the tankyrase ARC domain, based on SAR from ligand- and protein-observed NMR data.

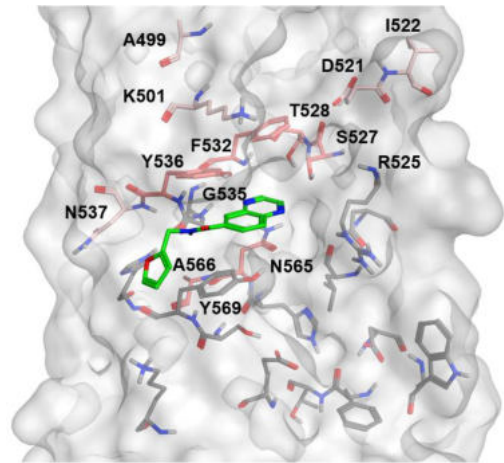
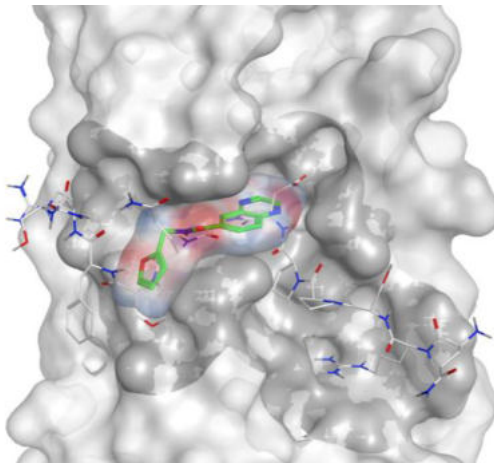
2.3 *In silico* binding model of fragment hit against TNKS2 ARC4

In order to begin fragment hit-to-lead development efforts, an *in silico* docking model of CCT170746 (**28**) bound to TNKS2 ARC4 was established.¹³⁵ This work was undertaken by a co-worker, Mirco Meniconi (ICR Cancer Therapeutics Unit [ICR CTU]), and is reported in Pollock *et al*, 2019.¹³⁵ Fragment docking was performed using Genetic Optimisation for Ligand Docking (GOLD) software which identified eight clusters of fragment binding modes that were consistent with the CSPs observed in protein-observed NMR of TNKS2 ARC4 with **28**.¹³⁵ The binding modes were assessed by quantum mechanical energy calculations which estimated the binding energy of each docking pose using a fragment molecular orbital (FMO) method.^{135, 185-188} The top five ranked binding modes (BM) are shown in Figure 2.2.

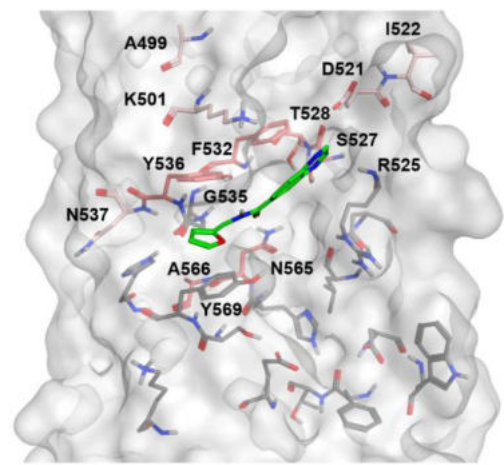
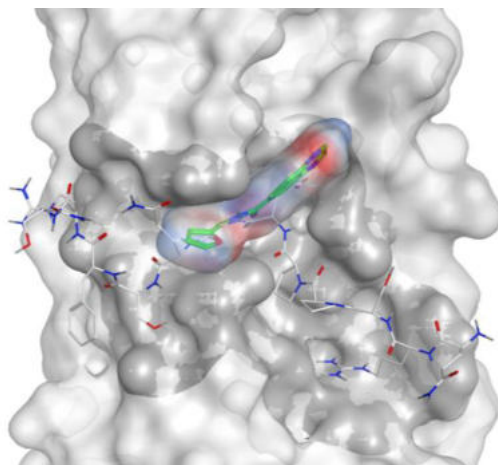
Binding mode 1 (BM1)



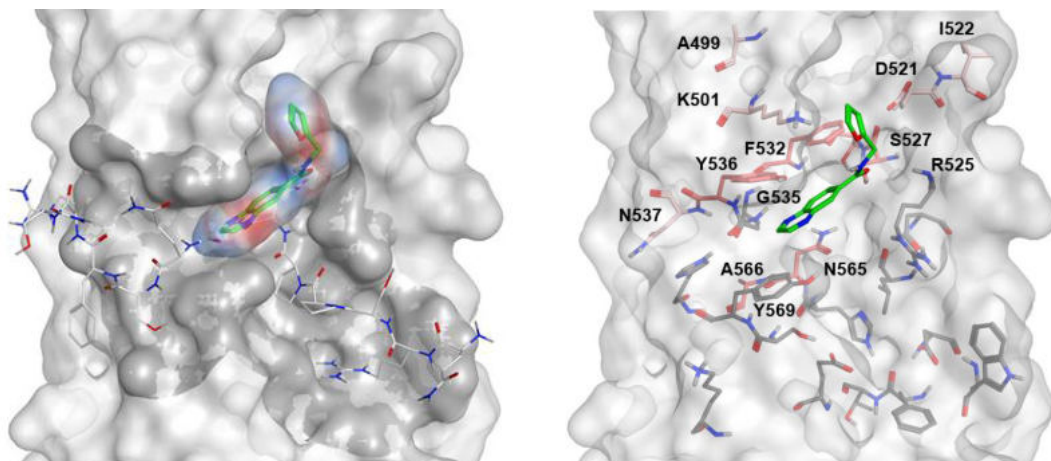
Binding mode 2 (BM2)



Binding mode 3 (BM3)



Binding mode 4 (BM4)



Binding mode 5 (BM5)

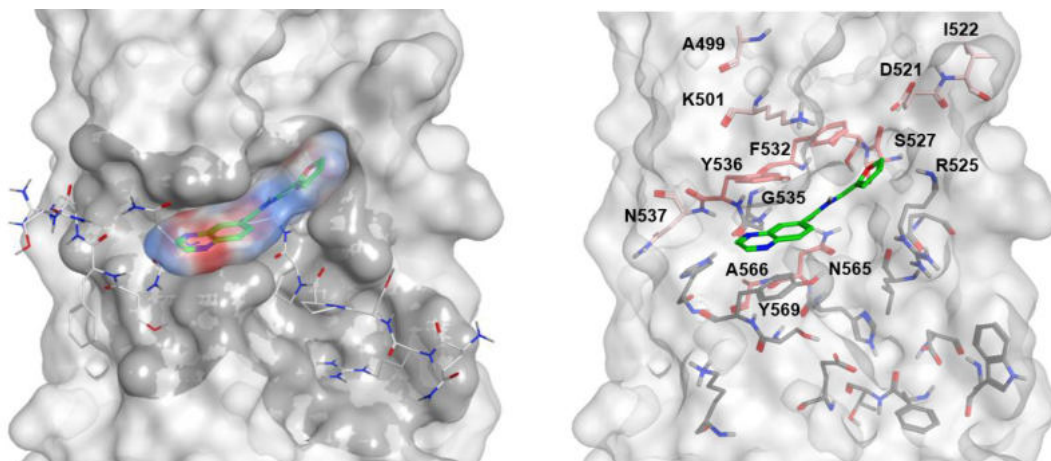


Figure 2.2. *In silico* model of fragment hit CCT170746 (**28**) binding to TNKS2 ARC4. *In silico* docking of CCT170746 (**28**) (green) against a crystal structure of TNKS2 ARC4 bound to 3BP2 TBM peptide (PDB: 3TWR) using GOLD software constrained to a distance of 14 Å from the PDGQS sequence of the 3BP2 TBM peptide identified five binding modes [M. Meniconi, ICR CTU].¹³⁵ Binding modes were ranked by *ab initio* calculation of total interaction energy: BM4 = -75.55 > BM3 = -67.65 > BM5 = -61.95 > BM2 = -58.03 > BM1 = -47.69 [M. Meniconi, ICR CTU].¹³⁵ Left panel: Surface representation of TNKS2 ARC4 (light grey) bound to 3BP2 TBM peptide (white); peptide interaction surface (dark grey) and the electrostatic surface of **28** binding modes are highlighted. Right panel: TNKS2 ARC4 residues which interact with the TBM peptide (grey) and residues which showed strong CSPs (>2σ (dark pink), >1σ (light pink)) in protein-observed NMR with **28** are highlighted.

The hypothesised binding modes of CCT170746 (**28**) can be grouped into two key orientations, in which either the quinoxaline ring is bound in the central patch region (binding modes 1, 2 and 3), or the fragment is flipped with the quinoxaline ring positioned between in the glycine sandwich forming π -stacking interactions (binding modes 4 and 5).¹³⁵ In binding mode 1 and 2, the central amide of **28** sits in the glycine sandwich formed by residues Y536 and Y569 and donates a hydrogen bond to the carbonyl of G535, mimicking the interaction of a TBM residue at position 7.¹³⁵ The quinoxaline motif interacts with central patch residues, whilst the furan moiety extends towards C-terminal contacts.¹³⁵ In binding mode 3, **28** is shifted towards the central patch and the quinoxaline motif is positioned in the sub-pocket formed by TNKS2 ARC4 residues F532, D521, S527 and R525.¹³⁵ The 4-position nitrogen of the quinoxaline ring forms a hydrogen bond with the side-chain hydroxyl of S527, and the central amide carbonyl accepts a hydrogen bond from N565 in the central patch.¹³⁵ The furan motif forms π -stacking interactions with the glycine sandwich tyrosine residues.¹³⁵ In contrast, the orientation of **28** is reversed in binding modes 4 and 5 and the quinoxaline occupies the glycine sandwich formed by Y536 and Y569.¹³⁵ In binding mode 4, the central amide carbonyl forms a hydrogen bond with the hydroxyl of S527, the methylene is positioned towards the central patch sub-pocket, and the furan moiety is directed towards an extended lipophilic region of the central patch.¹³⁵ The central amide accepts a hydrogen bond from N565 and the furan sits in the central patch sub-pocket in binding mode 5.¹³⁵ FMO calculations ranked binding modes 4, 3 and 5 as more energetically favourable than 1 and 2, however synthesis of analogues in a SAR study was necessary to fully test the hypothesised binding modes and identify fragment modifications which could improve binding affinity of the fragment hit (**28**) ($K_d = 1050 \mu\text{M}$).¹³⁵

2.4 First iteration of fragment hit analogues

2.4.1 Design of analogues guided by *in silico* modelling

Fragment hit CCT170746 (**28**) has three distinct chemical motifs which were amenable to modification in a SAR study (Figure 2.3). It was hypothesised that the amide was providing key hydrogen bond interactions in all of the proposed

binding modes from *in silico* docking of **28**.¹³⁵ Due to its ability to provide both a hydrogen bond acceptor from the carbonyl (-C=O) group and hydrogen bond donor from the amine (-N-H) group for hydrogen-bonding interactions with target proteins, the amide bond functionality is encountered frequently in medicinal chemistry.¹⁸⁹ Subsequently, amide coupling is the most common chemical reaction type used in drug discovery and there are many different reagents available to synthesise amides.¹⁹⁰⁻¹⁹¹ Based on the hypothesised interactions of the central amide from *in silico* docking of **28**, and to allow ease of synthesis of compounds by amide coupling reactions, the central amide was maintained in the initial fragment hit analogues. Modification of the quinoxaline and furan motifs was therefore the focus for the first iteration of fragment analogues.

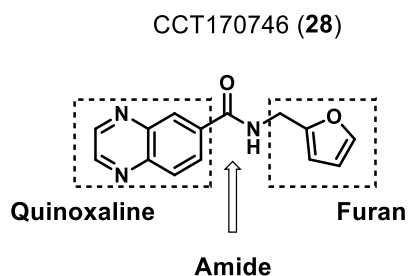


Figure 2.3. Chemical structure of fragment hit CCT170746 (28**).** The three key chemical motifs from which **28** is composed are highlighted.

From *in silico* docking of CCT170746 (**28**), it was hypothesised that in binding modes 4 and 5 the quinoxaline ring forms π -stacking interactions between two electron-rich tyrosine residues (Y536 and Y569), whilst in binding mode 3 the 4-position nitrogen is involved in a hydrogen-bond interaction (S527). Due to the electron withdrawing effect of the two nitrogen heteroatoms in the quinoxaline ring, the aromatic system is more electron-deficient and the nitrogen lone pairs less basic than in corresponding heterocyclic benzopyridines containing only one nitrogen atom – such as quinolines and isoquinolines. The synthesis of fragment hit analogues in which the quinoxaline was replaced with other bicyclic fused 6-6 heterocycles containing nitrogen was proposed (Figure 2.4). From this set of analogues, the aim was to determine both the importance of the position of the nitrogen atoms in the ring and whether fragment binding affinity was affected by electron-deficiency of the ring system.

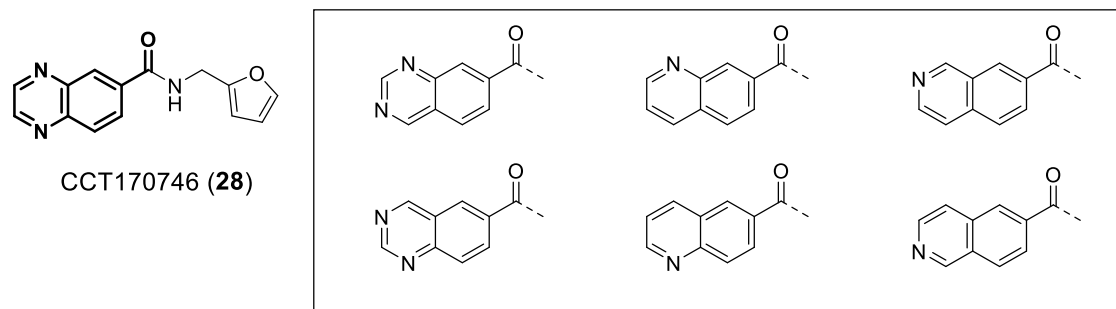


Figure 2.4. Proposed initial modifications to investigate the SAR of the quinoxaline moiety in CCT170746 (28).

Focusing next on the furan moiety, it was hypothesised from *in silico* docking of CCT170746 (28) that the furan was either directed towards the C-terminal contacts (binding modes 1, 2 and 3) or central patch residues (binding modes 4 and 5) of the TBM peptide interaction regions. Introduction of small substituents around the furan ring and at the adjacent methylene position was proposed to assess the potential for fragment growing to increase binding affinity, and to determine any binding pocket restrictions around the furan motif (Figure 2.5). Replacement of the furan with nitrogen-containing 5-membered heterocycles, isoxazole and oxazole, was also proposed to investigate furan ring replacements (Figure 2.5).

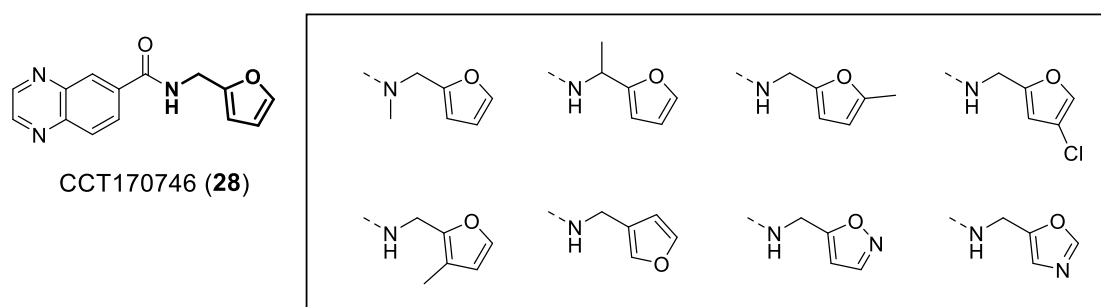


Figure 2.5. Proposed initial modifications to the furan moiety of CCT170746 (28) to assess SAR.

2.4.2 Synthesis of initial fragment hit analogues

Prior to the synthesis of the first iteration of fragment hit analogues, **28** was re-synthesised for use as a control in biophysical NMR assays. CCT170746 (**28**)

was synthesised from quinoxaline-6-carboxylic acid and furan-2-ylmethanamine in a one-step amide coupling reaction to form the central amide bond (Table 2.2). This amide bond was subsequently maintained in all initial fragment hit analogues; therefore, they were synthesised from commercially available acids and amines. A 1-hydroxy-7-azabenzotriazole (HOAt) based amide coupling reagent, *O*-(7-azabenzotriazol-1-yl)-1,1,3,3-tetramethyluronium hexafluorophosphate (HATU), was used to activate the carboxylic acids towards nucleophilic attack of the chosen amine, as outlined in Figure 2.6.¹⁹¹

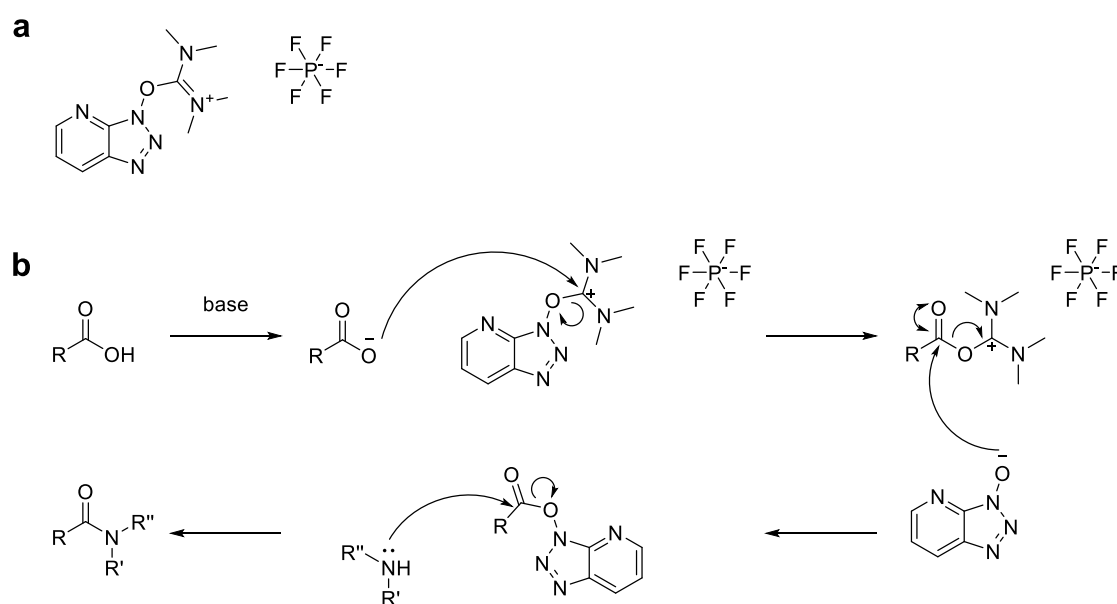


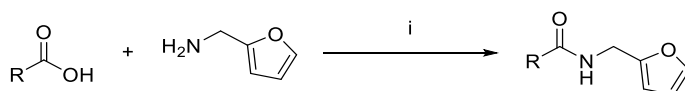
Figure 2.6. Chemical structure and mechanism of HATU, an amide coupling reagent. a) Chemical structure of HATU. **b)** Mechanism of carboxylic acid activation and subsequent amide coupling reaction with amine. Figure adapted from Valeur and Bradley, 2009.¹⁹¹

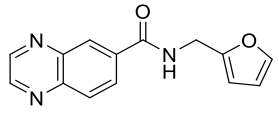
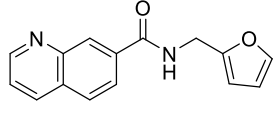
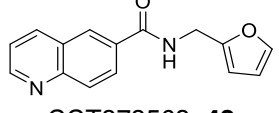
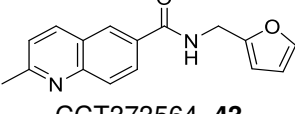
Two sets of fragments were then synthesised in which the quinoxaline carboxylic acid and furfurylamine were varied independently to one another, to allow an understanding of the structural features of **28** required for fragment binding. A set of 7 fragments were synthesised from a variety of structural analogues of quinoxaline carboxylic acid whilst maintaining furan-2-ylmethanamine (Table 2.2, compounds **41** to **47**). A further set of 8 fragments were synthesised by maintaining the quinoxaline-6-carboxylic acid component of **28**, whilst varying the furfurylamine-derived right-hand side (Table 2.3, compounds **48** to **55**). In all cases the reactions went to completion as monitored by LCMS analysis and

fragments were typically isolated in good to moderate yields of between 40-90% with compound purities >95% after one purification. Lower yields were obtained for **46** and **53** due to the co-elution of impurities during initial purification.

Table 2.2. Synthesis of fragments based on 28 via amide coupling, maintaining furan-2-ylmethanamine and varying the quinoxaline-6-carboxylic acid derived left-hand side.

Reagents and conditions: i) HATU, DIPEA, DMF (0.1 M), rt, 17 h to 22 h.



Entry	Yield
 CCT170746, 28	70 mg 64%
 CCT373560, 41	57 mg 56%
 CCT373563, 42	84 mg 78%
 CCT373564, 43	93 mg 88%

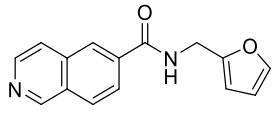
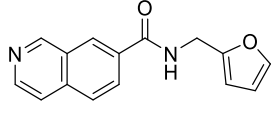
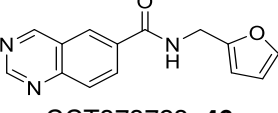
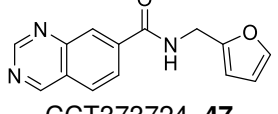
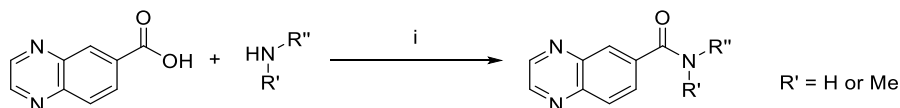
Entry	Yield
 CCT373715, 44	52 mg 48%
 CCT373716, 45	75 mg 69%
 CCT373723, 46	36 mg 33%
 CCT373724, 47	35 mg 47%

Table 2.3. Synthesis of fragments based on 28 via amide coupling, maintaining quinoxaline-6-carboxylic acid and varying the furan-2-ylmethanamine derived right-hand side. Reagents and conditions: i) HATU, DIPEA, DMF (0.1 M), rt, 17 h to 50 h.



Entry	Yield	Entry	Yield
 CCT373538, 48	93 mg 88%	 CCT373718, 52	79 mg 65%
 CCT373568, 49	48 mg 43%	 CCT373719, 53	29 mg 25%
 CCT373569, 50	69 mg 64%	 CCT373722, 54	48 mg 43%
 CCT373717, 51	75 mg 69%	 CCT373725, 55	91 mg 84%

The synthesised fragments were then tested by ligand-observed NMR experiments against TNKS2 ARC4 to assess binding compared with CCT170746 (**28**) and determine whether the structural modifications were tolerated.

2.5 Establishment of competitive ligand-observed NMR assay

2.5.1 Introduction to ligand-observed NMR

In ligand-observed NMR, the experiments used to monitor ligand-protein binding involve observing changes in different NMR parameters of the small molecule – including relaxation, diffusion coefficients, and intermolecular and intramolecular magnetisation transfer.^{143, 192} Ligand-observed NMR methods are preferred in fragment screening as compared with protein-observed NMR, there is no

requirement for isotopic labelling of the protein and less protein is required to detect ligand-protein binding.^{146, 170}

Two ligand-observed NMR methods – transverse T_2 relaxation-edited and waterLOGSY – were used. T_2 relaxation-edited NMR with a Carr-Purcell-Meiboom-Gill (CPMG) filter utilises the slow relaxation of ligands compared with the fast relaxation of proteins to suppress broad protein and protein-bound signals, therefore only signals from unbound ligand are observed.^{143, 192-193} In waterLOGSY (water-ligand observed *via* gradient spectroscopy) NMR experiments, the large bulk water magnetisation is transferred *via* the protein-ligand complex to free ligand, and signals of each appear with opposite NOE signs.¹⁹⁴⁻¹⁹⁵ Both experiments can be used to determine whether ligand binding is competitive as in the presence of a competitive inhibitor, there will be an increase in free ligand and a decrease in protein-bound ligand.¹⁴³ Examples of the spectra obtained in the relaxation-edited and waterLOGSY methods are shown in Figure 2.7, illustrating how each experiment was used to determine fragment binding.

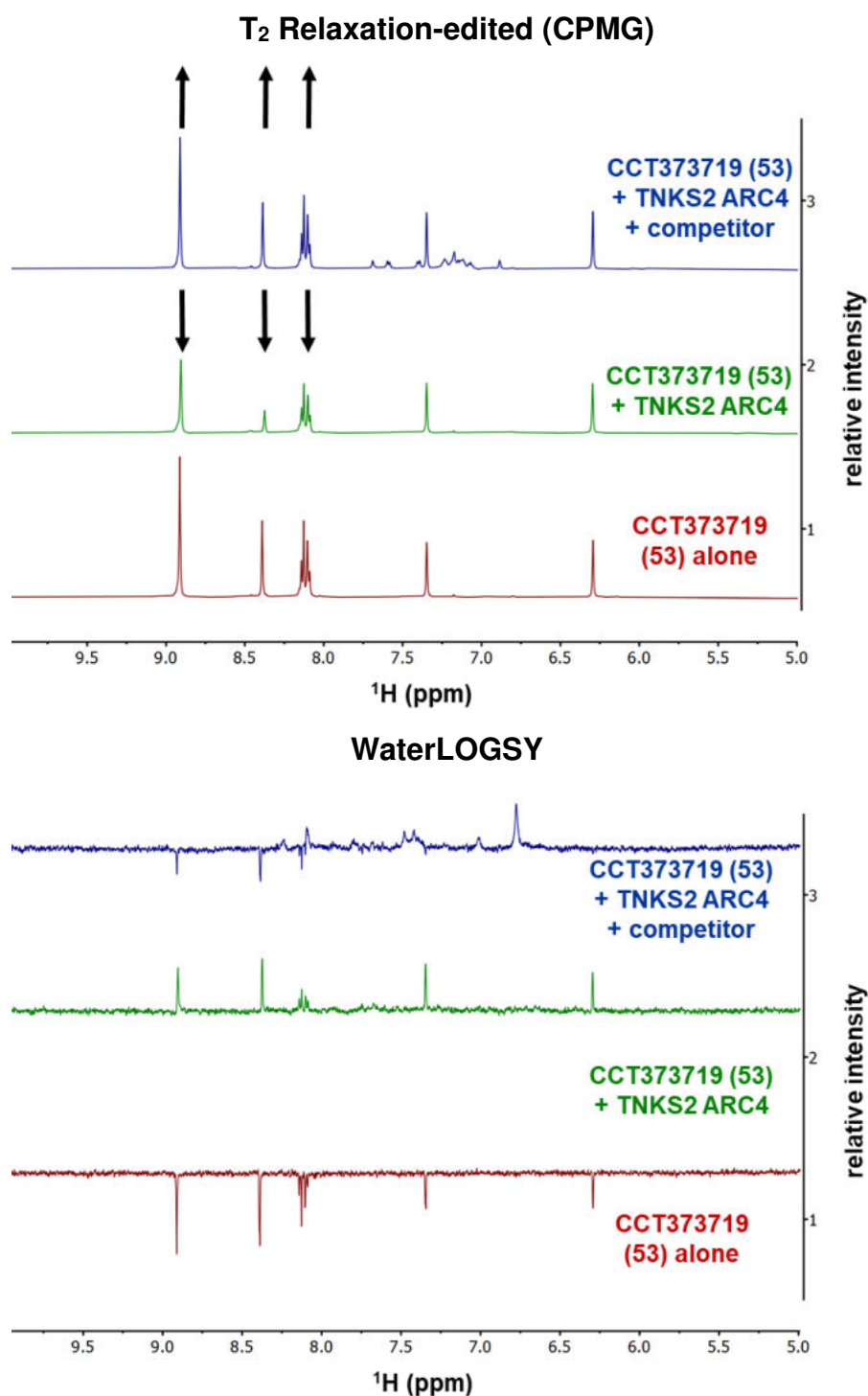


Figure 2.7. Spectra from T₂ relaxation-edited (CPMG) and waterLOGSY experiments with fragment CCT373719 (53). In T₂ relaxation-edited (CPMG) experiments, a decrease in the peak intensity of ligand signals upon addition of protein (TNKS2 ARC4) is observed for binding ligands and the average peak intensity reduction (%) is calculated.¹⁹³ A recovery of ligand signals is observed upon addition of a competitor for fragments which bind in the substrate recognition domain.¹⁴³ In waterLOGSY, signals from free ligand are negatively phased, whereas protein-

bound ligand signals are positively phased. The extent of inversion from the negative to positive phase indicates protein binding, and the recovery of negative signals when a competitor is added indicates competitive binding.^{143, 194}

2.5.2 Quality control of TNKS2 ARC4 protein, 3BP2 peptide competitor and fragment stock solutions

There were three requirements to fulfil in order to establish the competitive ligand-observed NMR assay. Firstly, the production of a large quantity of high purity tankyrase ARC protein was necessary. Secondly, as competitive experiments were performed to assess fragment binding to the substrate binding pocket of tankyrase ARCs, a purified TBM peptide control was purchased and subject to quality control. Lastly, both ligand-observed NMR experiments required a 'compound only' baseline spectra to be acquired; therefore, the preparation and quality control of fragment stock solutions was required.

Fragment hit CCT170746 (**28**) was identified by a ligand-observed NMR screen against TNKS2 ARC4, and in addition showed pan-ARC binding to all the tankyrase substrate-binding ARC domains except for TNKS2 ARC1.¹³⁵ The largest average reduction in signal intensity in the presence of protein from the T_2 relaxation-edited CPMG experiment was observed with TNKS2 ARC4.¹³⁵ Therefore, structural analogues of **28** were also tested against TNKS2 ARC4 in the ligand-observed NMR assay used in this project. TNKS2 ARC4 was produced using an established protocol by expression from *Escherichia coli* and purification by immobilised Ni^{2+} affinity chromatography and size exclusion chromatography (SEC).¹⁹⁶ Following the final purification by size exclusion, TNKS2 ARC4 was obtained in high purity as analysed by SDS-PAGE gel electrophoresis with a yield of 2.7 mg per L of TB expression culture (Figure 2.8a). The protein was also assessed by high resolution native mass spectrometry and the observed molecular weight for the major species was consistent with the expected mass for the construct sequence [Joe Smith, ICR CTU] (Figure 2.8b).

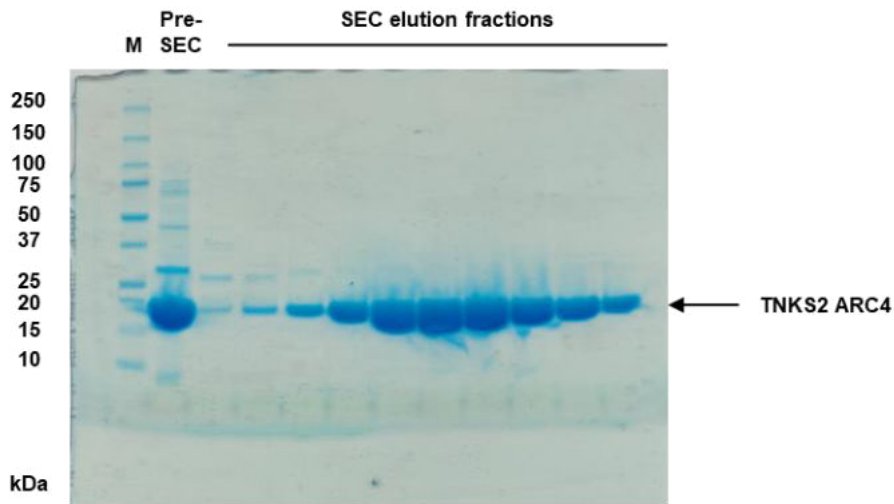
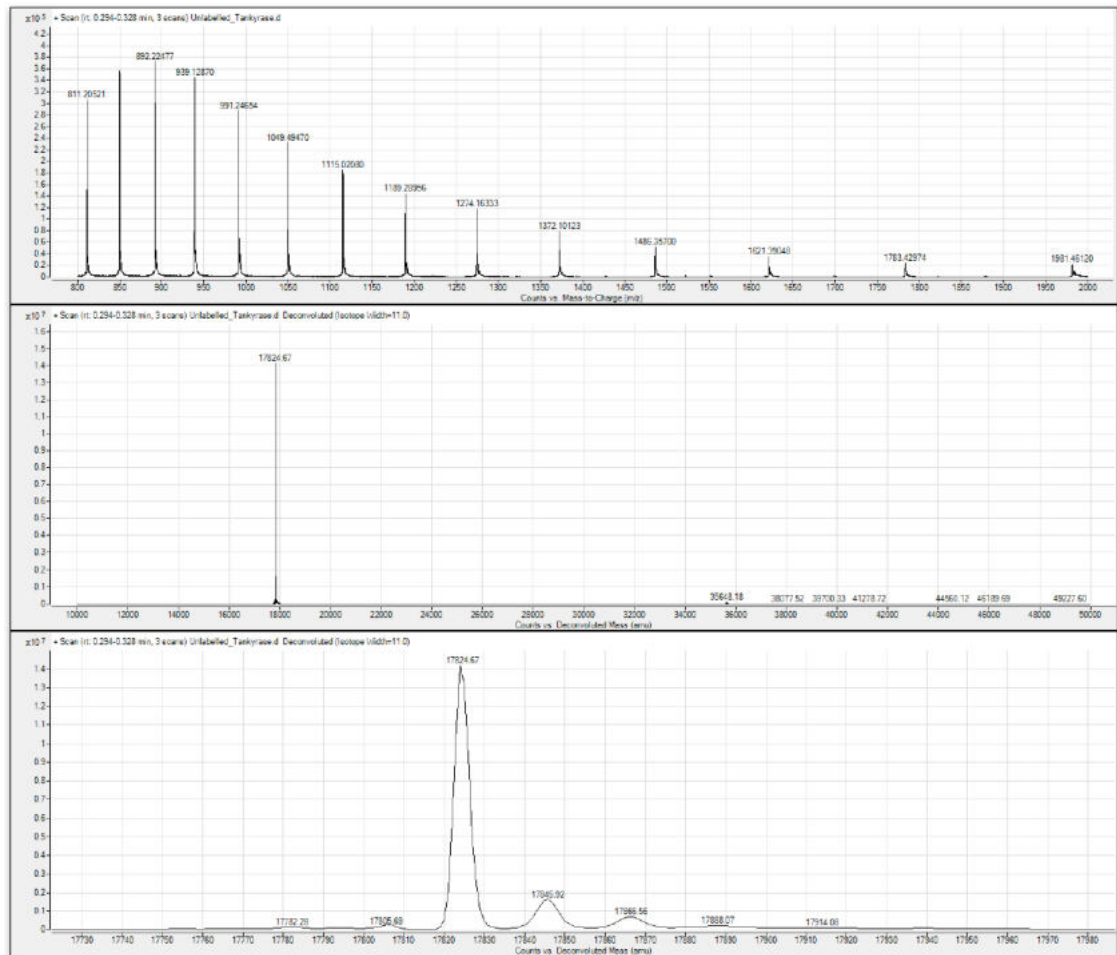
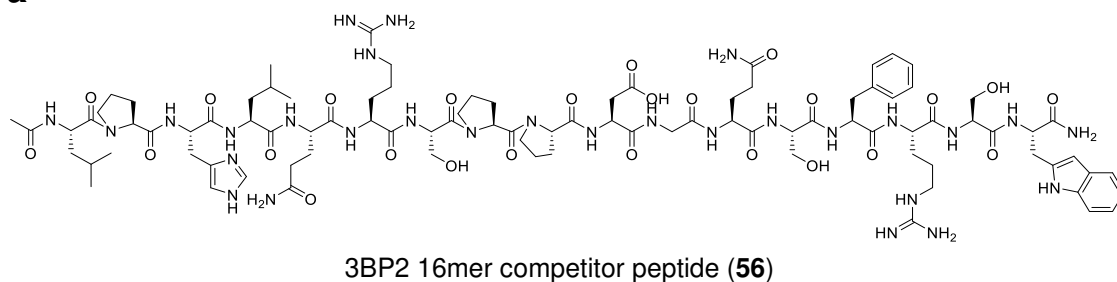
a**b**

Figure 2.8. Analysis of TNKS2 ARC4 following purification by size exclusion chromatography. a) SDS-PAGE analysis of elution fractions, stained with Coomassie (M = marker, SEC = size exclusion chromatography). b) Raw and deconvoluted spectra from analysis of TNKS2 ARC4 by high resolution mass spectrometry (molecular formula: $C_{780}H_{1248}N_{226}O_{242}S_5$;

calculated molecular weight: 17824.16 Da, observed molecular weight: 17825 Da) [Joe Smith, ICR CTU].

The interaction of TNKS2 ARC4 with 3BP2, a substrate of tankyrase, is well studied and its binding has been characterised by crystallography.⁶¹ Therefore a 16mer peptide containing the octameric tankyrase binding motif of 3BP2 (LPHLQRSPPDGQSFRS) was used in competitive experiments. The peptide was purchased from a commercial supplier, with the N- and C- terminus capped as acetyl and primary amides respectively, and an additional tryptophan residue at the C-terminus to enable the concentration of peptide stock solutions to be determined by UV-Vis spectrophotometry (Figure 2.9a). The purchased peptide was subjected to quality control analysis by high resolution LCMS, which showed a purity by UV and mass spectrometry of > 95% [Meirion Richards, ICR CTU] (Figure 2.9b).

a



b



Figure 2.9. Quality control analysis of 3BP2 16mer competitor peptide. a) Structure of the competitor 3BP2 16mer TBM peptide (**56**) (+ tryptophan) (sequence: Ac-LPHLQRSPPDGQSFRSW-CONH₂). b) UV and MS spectra from analysis of 3BP2 16mer peptide by high resolution LCMS molecular formula: C₉₂H₁₃₇N₂₉O₂₅; calculated molecular weight: 2048.03 Da; observed: 1025.5273 [M+2H]²⁺) [Meirion Richards, ICR CTU].

The final requirement for the competitive ligand-observed NMR assay was the accurate preparation of fragment stock solutions at 50 mM in DMSO-d₆. Deuterated DMSO-d₆ was used to avoid signals from the non-deuterated solvent interfering with the detection of ligand signals in the ligand-observed NMR experiments. Firstly, fragment stock solutions were prepared to a calculated concentration of 70 mM in DMSO-d₆. A quantitative proton (¹H) NMR experiment was used to determine the measured concentration of compound stock solutions, by comparison of peak integrals with those of an external calibration standard (10 mM caffeine in DMSO-d₆). Based on the measured concentrations, the dilution volume of DMSO-d₆ required to achieve the desired 50 mM concentration for each fragment stock solution was calculated, ensuring that each fragment stock solution was prepared to the same final concentration. Inspection of the quantitative ¹H NMR spectra for each compound also provided a final quality control check of the synthesised fragments.

2.5.3 Testing initial analogues in ligand-observed NMR assay

Results from testing the first iteration of analogues in ligand-observed NMR experiments are shown in Table 2.4. Firstly, the concentration at which to test each fragment was determined from its measured kinetic solubility. Kinetic solubility was assessed using quantitative ¹H NMR at a fragment concentration of 1000 μM in aqueous HEPES NMR buffer with 2% DMSO-d₆ (Kin. Sol. (μM), Table 2.4). The kinetic solubility was determined from the peak integrals of compound ¹H signals from 5.5 – 9.5 ppm, once again in comparison with an external calibration standard (200 μM caffeine in aqueous HEPES NMR buffer with 2% DMSO-d₆). Fragments which were determined to have solubility greater than 500 μM were tested at this concentration, whilst fragments with lower solubility were either tested at 200 μM or 50 μM. This was done to avoid testing compounds at concentrations higher than their kinetic solubility which could lead

to false positive results due to compound aggregation or precipitation, whilst maximising the signal:noise ratio and the information obtained from the assay for each fragment. For example, waterLOGSY spectra were not processed for fragments tested at 50 μM due to poor signal:noise. The control fragment, CCT170746 (**28**), was tested at all three concentrations to enable a valid comparison of the assay results for fragments tested at different concentrations.

Each fragment was tested using a T_2 relaxation-edited CPMG assay, and binding was quantified by the average peak intensity reduction (%) upon addition of protein (CPMG + protein, Table 2.4). The binding of each fragment was also assessed by a qualitative comparison of waterLOGSY spectra in the absence and presence of protein (waterLOGSY + protein, Table 2.4). Two samples were prepared for all fragments tested – one ‘blank’ sample containing compound only, and one ‘protein’ sample containing compound and TNKS2 ARC4 protein. A low protein concentration of 20 μM was selected for the assay to limit the chemical shift changes in ligand NMR signals which occur in the presence of protein.¹⁹² Relaxation-edited CPMG and waterLOGSY experiments were acquired on both samples, and the spectra were analysed in the region of 5.5 – 9.5 ppm using MestreNova Screen software.¹⁹⁷ For the relaxation-edited experiment, the peak intensity change (I) for each ligand signal between 5.5 – 9.5 ppm was calculated according to equation 2.1 and the average was taken to determine the average peak intensity reduction (%) reported in Table 2.4 (CPMG + protein).

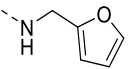
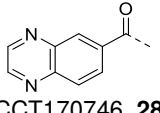
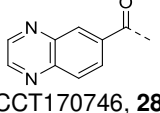
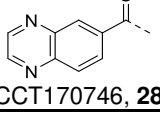
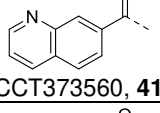
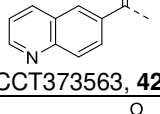
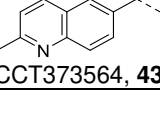
Equation 2.1:
$$I = \frac{(I_{blank} - I_{protein})}{I_{blank}}$$

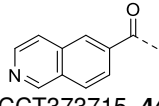
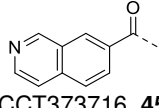
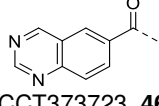
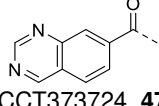
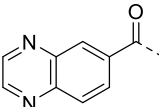
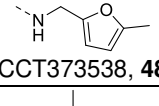
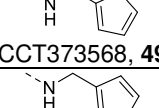
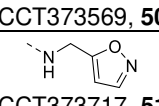
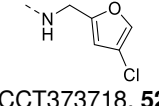
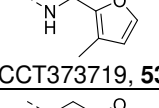
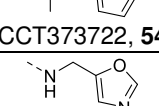
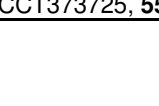
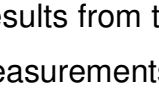
Fragments which showed equivalent or greater binding than CCT170746 (**28**) from relaxation-edited (>20% peak reduction) or waterLOGSY experiments were then tested again, and competitive ligand-observed NMR experiments were also performed with these analogues to determine whether increased binding resulted from binding within the substrate recognition domain of TNKS2 ARC4, from interactions with other potential sites on the ARC, or from non-specific interactions (CPMG and waterLOGSY + competitor, Table 2.4). To this end, a third ‘competitor’ sample was prepared for the competitive experiments which

contained compound, TNKS2 ARC4 and the 3BP2 16mer peptide competitor at a concentration of 200 μM .^{61, 135} Again, spectra were processed in MestreNova Screen software. The peak intensity change (I) for each ligand signal was calculated according to equation 2.2, and averaged to determine the average peak intensity reduction (%) reported in Table 2.4 (CPMG + competitor).

Equation 2.2:
$$I = \frac{(I_{blank} - I_{competitor})}{I_{blank}}$$

Table 2.4. A summary of data obtained from competitive ligand-observed NMR experiments performed with initial fragment CCT170746 (28) analogues. Fragments were tested at either 500 μM , 200 μM or 50 μM depending on aqueous kinetic solubility (Kin. Sol. μM).^a $n = 1$ unless otherwise indicated (arithmetic mean with \pm SD error for $n > 1$); ^b competition with 3BP2 peptide (200 μM), $n = 1$ unless otherwise indicated (arithmetic mean with \pm SD error for $n > 1$); ^c Decrease to baseline and inversion to positive phase indicates binding, minimal decrease to baseline indicates non-binding; ^d signal recovery indicates competitive binding.

Fragment 	Kin. Sol. (μM)	Assay Conc. (μM)	clogP (MoKa)	CPMG	CPMG	WaterLOGSY	WaterLOGSY
				+ protein ^a	+ competitor ^b	+ protein ^c	+ competitor ^d
 CCT170746, 28	898	500	1.0	20% \pm 4% ($n = 9$)	5% \pm 3% ($n = 8$)	Decrease to baseline	Signal recovery
 CCT170746, 28	898	200	1.0	26% \pm 8% ($n = 5$)	8% \pm 4% ($n = 5$)	Decrease to baseline	Signal recovery
 CCT170746, 28	898	50	1.0	29% \pm 7% ($n = 6$)	9% \pm 7% ($n = 6$)	Not observed	Not observed
 CCT373560, 41	979	500	2.0	16%	-	Decrease to baseline	Signal recovery
 CCT373563, 42	314	200	2.0	16%	-	Decrease to baseline	Signal recovery
 CCT373564, 43	179	200	2.4	17%	-	Decrease to baseline	Signal recovery

 CCT373715, 44	593	500	1.9	14%	-	Positive for compound only (aggregation)	-
 CCT373716, 45	988	500	1.9	14%	-	Inversion to positive phase	-
 CCT373723, 46	918	500	1.3	19% ± 0% (n = 2)	10%	Inversion to positive phase	Decrease in positive phase
 CCT373724, 47	865	500	1.3	24% ± 9% (n = 2)	7%	Inversion to positive phase	No decrease in positive phase
Fragment 	Kin. Sol. (μM)	Assay Conc. (μM)	clogP (MoKa)	CPMG + protein^a	CPMG + competitor^b	WaterLOGSY + protein^c	WaterLOGSY + competitor^d
 CCT373538, 48	972	500	1.6	31% ± 7% (n = 2)	3%	Inversion to positive phase	Signal recovery
 CCT373568, 49	1065	500	1.7	25% ± 5% (n = 2)	3%	Inversion to positive phase	Signal recovery
 CCT373569, 50	884	500	0.82	14%	-	Decrease to baseline	Signal recovery
 CCT373717, 51	1008	500	0.13	23% ± 2% (n = 2)	7%	Decrease to baseline	Signal recovery
 CCT373718, 52	217	200	1.9	37% ± 7% (n = 2)	3%	Inversion to positive phase	Signal recovery
 CCT373719, 53	885	500	0.82	24% ± 7% (n = 2)	4%	Inversion to positive phase	Signal recovery
 CCT373722, 54	1012	500	0.91	9%	-	Minimal decrease	-
 CCT373725, 55	1006	500	-0.12	7%	-	Minimal decrease	-

Results from the fragments tested by relaxation-edited NMR in two independent measurements ($n = 2$) showed that the standard deviation (SD, or σ) ranged from ± 0 to 9% (mean $\sigma = \pm 5\%$), demonstrating the intrinsic variability of the NMR assay. Therefore, only fragments which showed a change in peak intensity reduction between 'blank' and 'protein' samples of greater than 2σ compared with

control **28** ($20 \pm 10\%$) were considered to show significantly increased or decreased binding to TNKS2 ARC4, whereas fragments with peak intensity reduction within 2σ of control **28** (10-30%) were classed as showing equivalent binding (Figure 2.10). Fragments with a signal intensity reduction less than 10% in the relaxation-edited experiments from a comparison of 'blank' and 'protein' samples were considered as non-binding. In the competitor relaxation-edited experiments, fragments were considered as competitive if an average signal intensity reduction less than 10% from a comparison of 'blank' and 'competitor' samples was calculated, indicating full recovery of ligand signals (Figure 2.10). For the first iteration of fragment analogues, between 5-40% reduction in signal intensity was observed in the presence of TNKS2 ARC4, and only two analogues (**48** and **52**) showed a significant change in average peak intensity reduction compared with control fragment **28** (Figure 2.10).

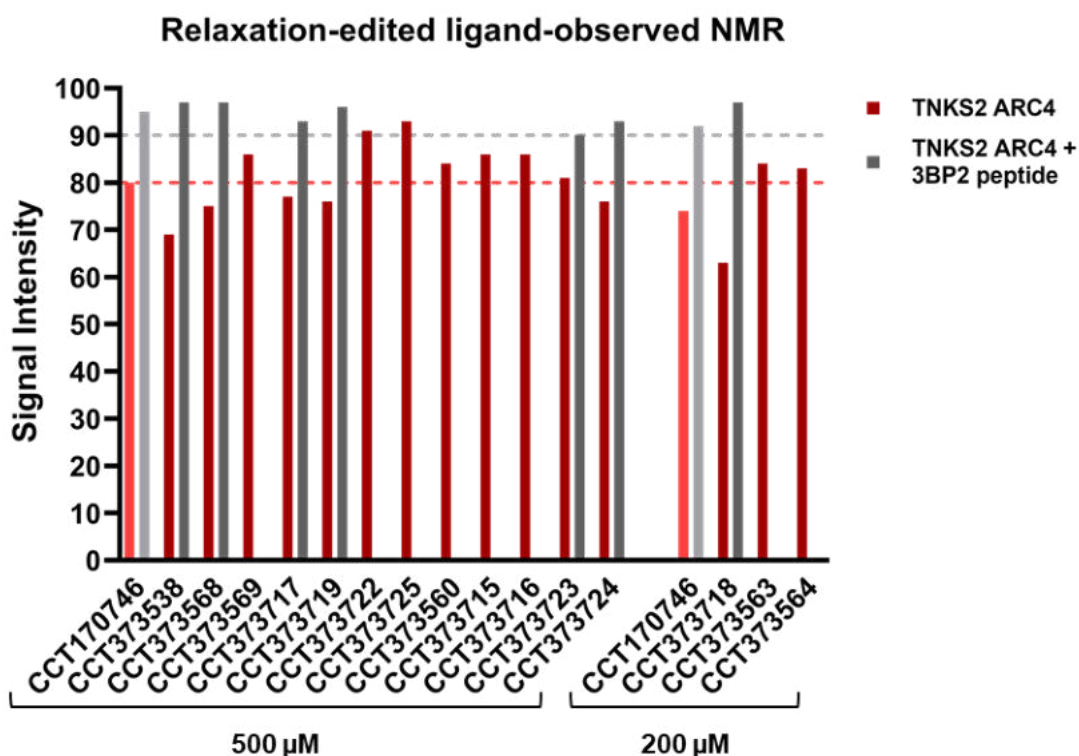


Figure 2.10. Graphical summary of results from testing the first fragment iteration in relaxation-edited (CPMG) ligand-observed NMR. Intensity of fragment ^1H NMR signals in the presence of TNKS2 ARC4 (red bars), and in the presence of TNKS2 ARC4 + 3BP2 peptide competitor (grey bars), as a percentage (%) of ^1H NMR signals in 'compound only' spectra. Y-axis (signal intensity) unit is %. Fragments were tested at either 500 μM or 200 μM depending on

their aqueous kinetic solubility and control fragment CCT170746 (**28**) was tested at both concentrations (pink and light grey bars). The average signal intensity (%) reduction between 'compound only' and 'TNKS2 ARC4' for control fragment CCT170746 (**28**), tested at 500 μ M, was determined as 20% (n=9) (pink dashed threshold). Fragments which showed an average signal intensity (%) reduction of less than 10% between 'compound only' and 'TNKS2 ARC4 + 3BP2 peptide' indicated competitive binding (light grey dashed threshold).

Analysis of ligand-observed NMR results presented in Table 2.4 and Figure 2.10 with the initial set of analogues provided preliminary SAR. Replacement of the quinoxaline moiety with quinolines and isoquinolines did not show a significant effect on the extent of fragment binding to TNKS2 ARC4. Exchanging the quinoxaline for quinazoline isomers also maintained equivalent protein binding to control **28** in relaxation-edited NMR, however both quinazolines **46** and **47** showed stronger binding than **28** from waterLOGSY signals. Interestingly, isoquinoline **44** showed strong positive waterLOGSY signals in the absence of protein, indicating compound aggregation as a concern with this scaffold. Replacement of the furan with an oxazole (**55**) also abolished binding of the fragment to TNKS2 ARC4. However, chlorination at position 4 of the furan ring (**52**) resulted in increased protein binding in relaxation-edited NMR, therefore indicating a preference for lipophilicity at this position of the furan ring. In addition, methylation of the furan ring in the 5 or 3 positions (**48** and **53**) and of the adjacent methylene (**49**) showed equivalent binding to TNKS2 ARC4.

Methylation of the central amide nitrogen (**54**) showed significantly decreased protein binding compared to **28**, supporting the hypothesis that the amide linker was important in fragment binding. It was proposed that the N-H could therefore be required as a hydrogen bond donor, in support of binding modes 1 and 2 from *in silico* docking of **28**. However, it was also hypothesised that N-methylation could influence fragment conformation. The chemical structures of all first iteration fragments were imported into Molecular Operating Environment (MOE) software and energy minimisation was performed using the Energy Minimize function with default parameters.¹⁹⁸ N-methylation induced a substantial change in the energy minimised conformation of **54** compared to **28**. This conformational change would not be tolerated in any of the proposed *in silico* fragment binding

modes (Figure 2.11). All other fragments with quinoxaline or furan modifications maintained an energy minimised conformation consistent with that of **28**.

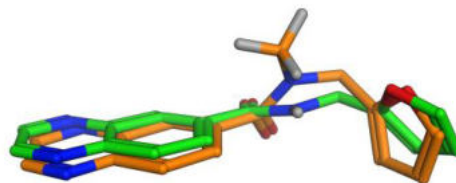


Figure 2.11. Comparison of energy minimised structures of CCT170746 (28) and CCT373722 (54). Energy minimisation of **28** (green) and **54** (orange) was performed using the Energy Minimize function in MOE.¹⁹⁸ A substantial change in energy minimised fragment conformation was observed upon N-methylation of the central amide.

From competitive ligand-observed NMR experiments, quinazolines **46** and **47** showed competitive binding in relaxation-edited experiments but only partially competitive binding in waterLOGSY, whereas **47** showed non-specific binding in competitive waterLOGSY. Therefore, it was hypothesised that the quinoxaline moiety of **28** is required to maintain essential binding interactions in the substrate recognition pocket of TNKS2 ARC4. In contrast, in competitive ligand-observed NMR with **48**, **49**, **52** and **53** it was demonstrated that installing small functional groups around the furan ring maintained competitive binding of the fragments to TNKS2 ARC4 substrate recognition domain. Therefore, further fragment optimisation efforts focused on furan modification was proposed.

2.6 Second iteration of fragment hit analogues with furan modifications

2.6.1 Design of second fragment iteration and binding model hypothesis

The aims of the second iteration of fragment modifications were to further differentiate between the proposed *in silico* binding modes of CCT170746 (**28**)

and to generate higher affinity ligands by introducing substituents from all positions around the furan ring.

Fragment design was aided by *in silico* modelling using Molecular Operating Environment (MOE) software.¹⁹⁸ The initial *in silico* docking of CCT170746 (**28**) – which had been performed using GOLD software – was imported into MOE and prepared using the QuickPrep panel with default parameters. Fragments with furan modifications which had maintained competitive binding against TNKS2 ARC4 were then modelled against each of the five predicted binding modes of **28** using energy minimisation. Furan substituents were added to the chemical structure of **28** using the Builder panel in MOE to generate fragments **48**, **49**, **51**, **52** and **53** in binding modes 1 to 5. The drawn fragments were then energy minimised using the Minimize function in the Builder panel to optimise the coordinates of the molecular data.¹⁹⁸

From this modelling, it was observed that the furan substitutions of fragments **48**, **51**, **52** and **53** were tolerated in all proposed *in silico* binding modes of CCT170746 (**28**) and key hydrogen bond interactions were maintained upon energy minimisation. However, introduction of a methyl group at the furan methylene position in fragment **49** introduced a clash with the protein surface in binding mode 3 and a key hydrogen bond from the fragment amide carbonyl to N565 was not maintained upon *in silico* modelling *via* energy minimisation (Figure 2.12). Since this substitution maintained competitive binding in the ligand-observed NMR assay, this SAR indicated binding mode 3 as less likely and favoured a fragment orientation consistent with either binding modes 1 and 2, or binding modes 4 and 5.

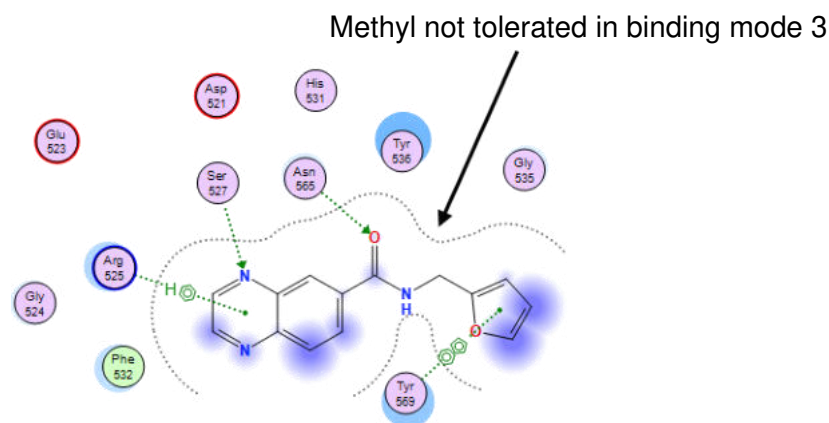


Figure 2.12. 2D representation of CCT170746 (28) interactions with TNKS2 ARC4 residues in binding mode 3. Binding mode 3 from *in silico* docking of **28** was visualised in MOE. Pocket restrictions around the methylene position adjacent to the furan suggest that methyl substitution would not be tolerated in this binding mode.

Therefore, synthesis of a second iteration of fragment optimisation focusing on furan modifications was proposed to further differentiate between *in silico* binding modes 1, 2, 4 and 5. It was hypothesised that introduction of lipophilic substituents could lead to increased binding affinity of the fragments by introduction of van-der-Waals interactions with the lipophilic central patch extension if the fragment was oriented as in binding modes 4 and 5 (Figure 2.13). Conversely, if the fragment was positioned as in binding modes 1 or 2, introduction of more polar heteroaromatic groups could improve binding affinity in the more hydrophilic C-terminal contact region of the substrate recognition pocket of the ARC domain (Figure 2.13). In general, introduction of substitutions larger than the methyl groups introduced previously was proposed to further understand the structural restrictions of the furan binding pocket.

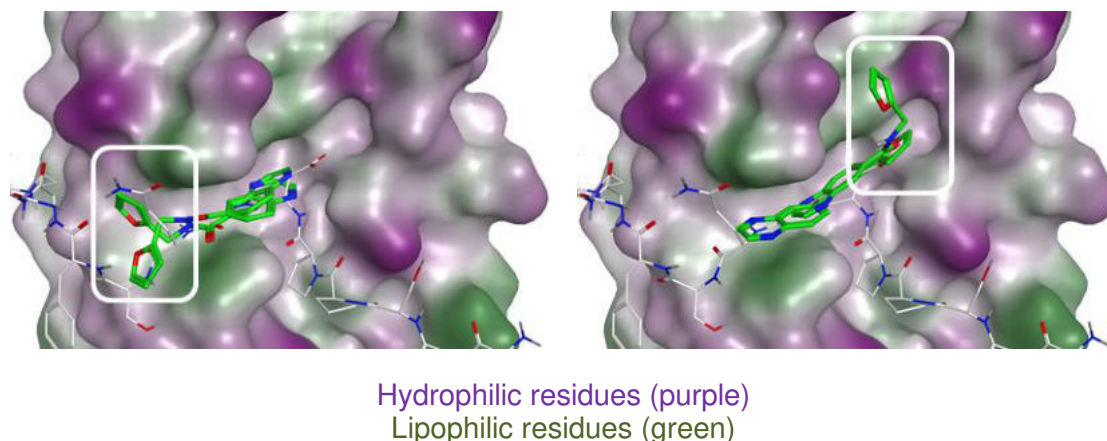


Figure 2.13. Surface representation of TNKS2 ARC4 highlighting hydrophilic and lipophilic residues. Binding modes 1 and 2 (left) versus binding modes 4 and 5 (right) from *in silico* docking of fragment **28** (green) against TNKS2 ARC4 (PDB: 3TWR) are shown.

2.6.2 Synthesis of fragment hit analogues with furan modifications

The compounds synthesised in the second iteration of CCT170746 (**28**) analogues are summarised in Figure 2.14. In addition to furan substitutions, furan replacement with other aromatic and non-aromatic heterocycles was also investigated as the isoxazole retained competitive binding against TNKS2 ARC4.

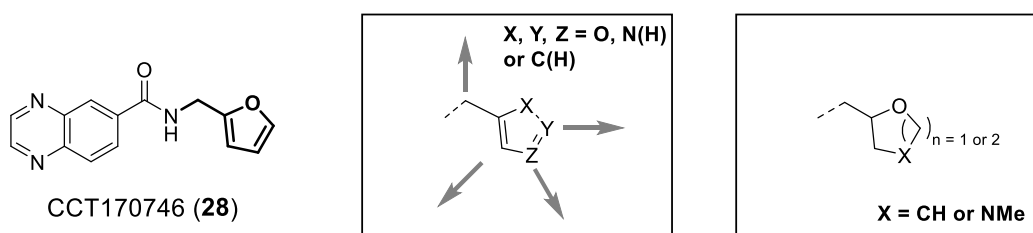
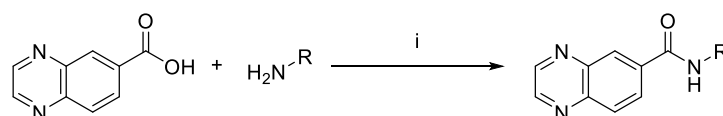


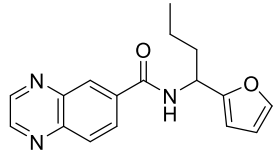
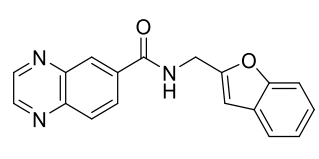
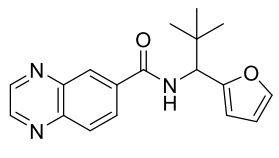
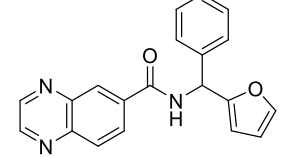
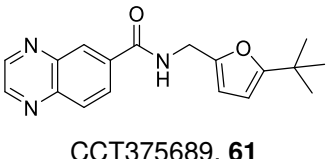
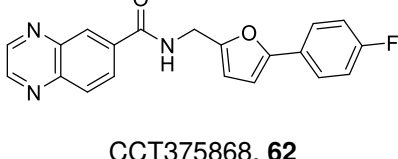
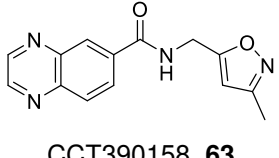
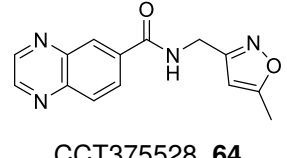
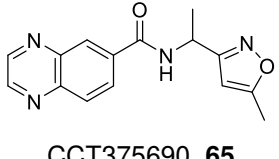
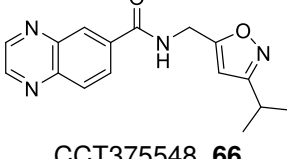
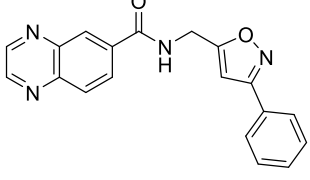
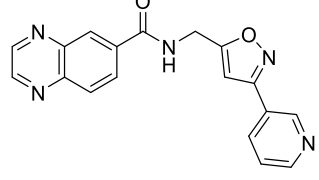
Figure 2.14. Summary of the modifications introduced in the second iteration of fragment synthesis. The second iteration of modifications focused on: 1. Introduction of substituents and furan replacement with alternative 5-membered heterocycles and 2. Introduction of polar substituents and furan replacement with unsaturated heterocycles.

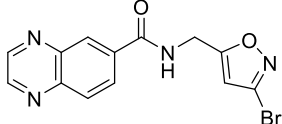
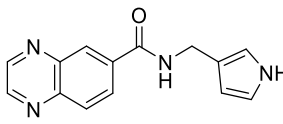
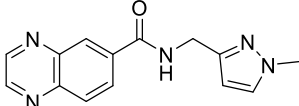
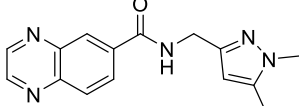
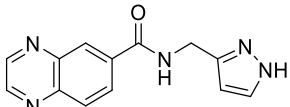
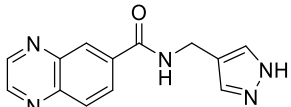
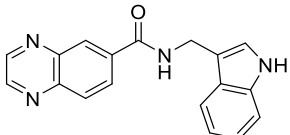
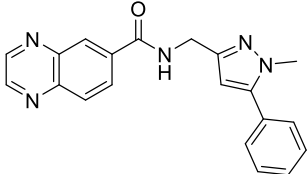
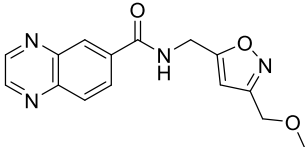
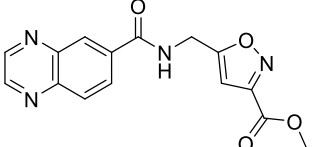
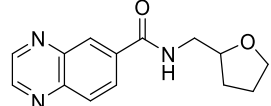
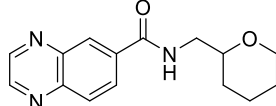
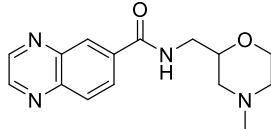
For the synthesis of unsubstituted quinoxaline-6-carboxamide fragments in which the central amide linker was maintained and furan modifications or heterocyclic substitutions were introduced, the desired compounds were efficiently synthesised in a one-step HATU-mediated amide coupling reaction from

quinoxaline-6-carboxylic acid and commercially available amines (Table 2.5). As previously, fragments were isolated in high purity (> 95%) after purification by reverse phase chromatography, with typical yields for this iteration ranging between 35% and 80%.

Table 2.5. Synthesis of unsubstituted quinoxaline-6-carboxamide fragments based on 28 via amide coupling, maintaining quinoxaline-6-carboxylic acid and further varying the furan-2-ylmethanamine derived right-hand side. Reagents and conditions: i) HATU, DIPEA, DMF (0.1 M), rt, 17 h to 26 h.



Entry	Yield	Entry	Yield
 CCT376430, 57	81 mg 60%	 CCT375688, 58	69 mg 53%
 CCT375683, 59	104 mg 77%	 CCT375554, 60	102 mg 72%
 CCT375689, 61	51 mg 38%	 CCT375868, 62	92 mg 61%
 CCT390158, 63	43 mg 36%	 CCT375528, 64	67 mg 58%
 CCT375690, 65	68 mg 56%	 CCT375548, 66	60 mg 43%
 CCT390444, 67	14 mg 10%	 CCT390207, 68	54 mg 37%

 <p>CCT390447, 69</p>	34 mg 23%	 <p>CCT390160, 70</p>	51 mg 46%
 <p>CCT390161, 71</p>	52 mg 43%	 <p>CCT390159, 72</p>	52 mg 41%
 <p>CCT375691, 73</p>	46 mg 41%	 <p>CCT391210, 74</p>	21 mg 19%
 <p>CCT375867, 75</p>	58 mg 47%	 <p>CCT375869, 76</p>	65 mg 45%
 <p>CCT390205, 77</p>	64 mg 50%	 <p>CCT390601, 78</p>	6 mg 6%
 <p>CCT390206, 79</p>	78 mg 70%	 <p>CCT390441, 80</p>	72 mg 62%
 <p>CCT390446, 81</p>	46 mg 37%		

Three fragments – CCT390444 (**67**), CCT391210 (**74**), and CCT390601 (**78**) – proved more challenging to synthesise resulting in yields lower than 20% (Table 2.5). For **67**, unreacted carboxylic acid and impurities were observed by LCMS analysis of the reaction, which was a result of low amine starting material purity (Figure 2.15a). For **74** and **78**, significant by-products formed during the reaction were detected by LCMS (Figure 2.15b and 2.15c) and an additional normal phase purification was required to obtain high purity fragments in both cases.

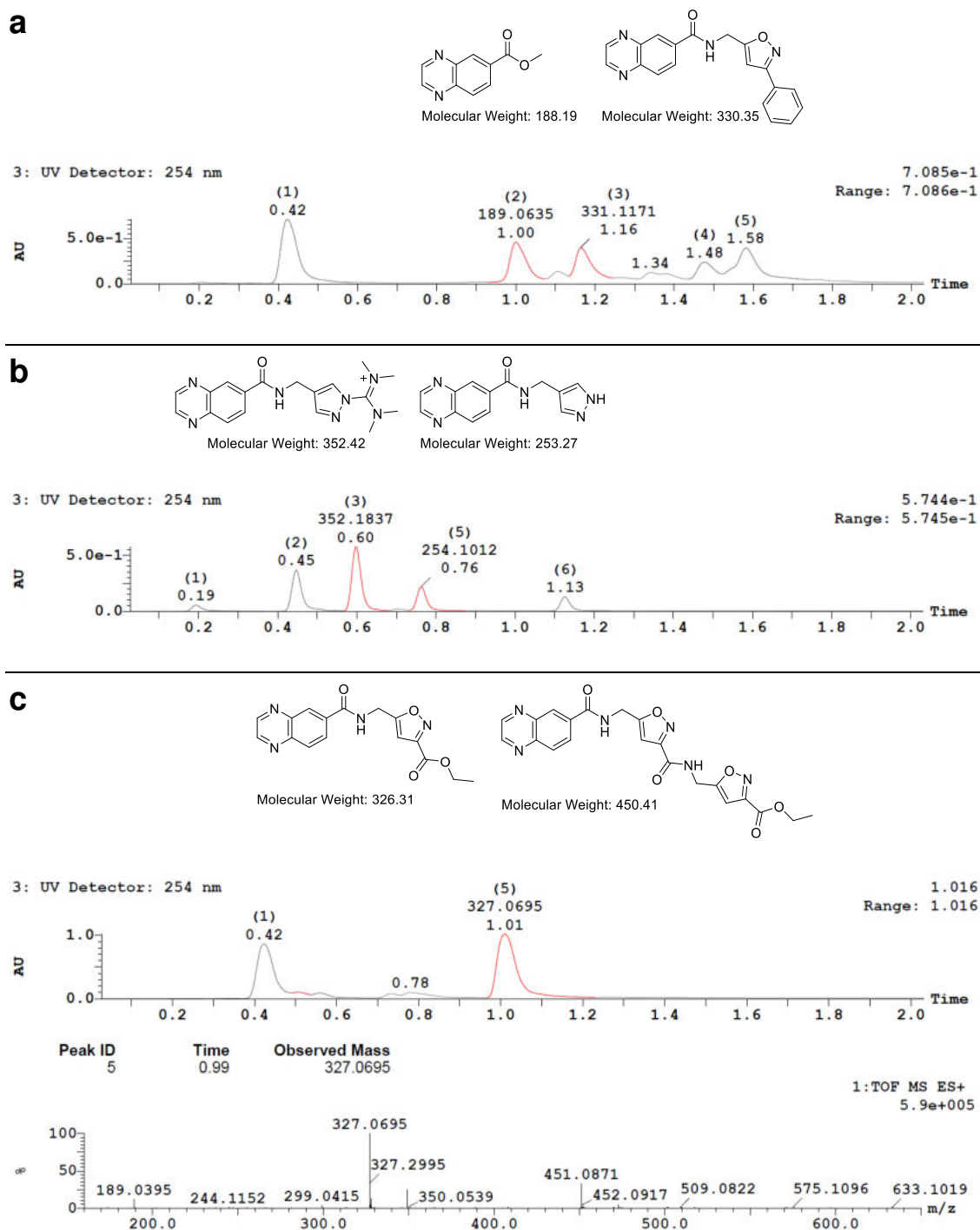


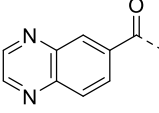
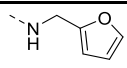
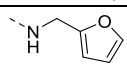
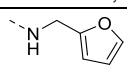
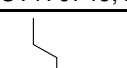
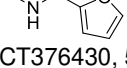
Figure 2.15. Reaction analysis by LCMS, highlighting the major impurities identified in the synthesis of modified furan fragments. a) Synthesis of CCT390444 (**67**): Low purity of the amine starting material resulted in formation of several impurities ($t_R = 1.34, 1.48$ and 1.58 min) and unreacted carboxylic acid which was detected as the methyl ester (m/z 189 $[M+H]^+$, $t_R = 1.00$ min). **b)** Synthesis of CCT391210 (**74**): Major impurity detected was formation of the guanidylated pyrazole by-product (m/z 352 $[M+H]^+$, $t_R = 0.60$ min). **c)** Synthesis of CCT390601

(78): Major impurity detected was formation of the bisamide by-product (m/z 451 $[M+H]^+$, $t_R = 1.01$ min), at the same retention time as the desired product (m/z 327 $[M+H]^+$, $t_R = 1.01$ min).

2.6.3 SAR from ligand-observed NMR assay

For the second iteration of **28** analogues, all fragments were tested in the competitive ligand-observed NMR assay using T_2 relaxation-edited CPMG and waterLOGSY experiments to determine whether the fragments were binding to TNKS2 ARC4 in the substrate recognition pocket. As previously, fragment stock solutions were prepared to a concentration of 50 mM in DMSO- d_6 and the kinetic solubility of the fragments was measured using quantitative 1H NMR at a compound concentration of 1000 μM in aqueous HEPES NMR buffer with 2% DMSO- d_6 (Kin. Sol. (μM), Table 2.6).

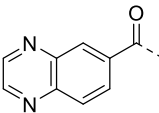
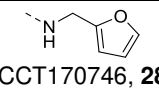
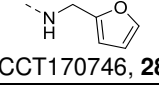
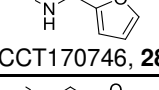
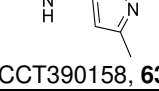
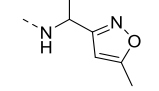
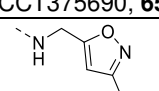
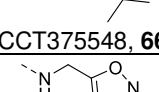
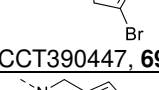
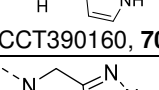
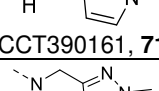
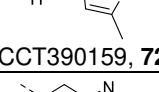
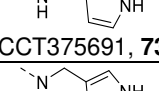
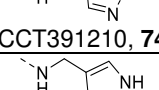
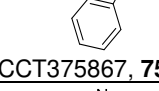
Table 2.6. A summary of data obtained from competitive ligand-observed NMR experiments performed with substituted furan fragment compounds. Fragments were tested at either 500 μM , 200 μM or 50 μM depending on aqueous kinetic solubility (Kin. Sol. μM). ^a $n = 1$ unless otherwise indicated (arithmetic mean with \pm SD error for $n > 1$); ^b competition with 3BP2 peptide (200 μM), $n = 1$ unless otherwise indicated (arithmetic mean with \pm SD error for $n > 1$); ^c Decrease to baseline and inversion to positive phase indicates binding, minimal decrease to baseline indicates non-binding; ^d signal recovery indicates competitive binding.

Fragment 	Kin. Sol. (μM)	Assay Conc. (μM)	clogP (MoKa)	CPMG	CPMG	WaterLOGSY	WaterLOGSY
				+ protein ^a	+ competitor ^b	+ protein ^c	+ competitor ^d
 CCT170746, 28	898	500	1.0	20% \pm 4% ($n = 9$)	5% \pm 3% ($n = 8$)	Decrease to baseline	Signal recovery
 CCT170746, 28	898	200	1.0	26% \pm 8% ($n = 5$)	8% \pm 4% ($n = 5$)	Decrease to baseline	Signal recovery
 CCT170746, 28	898	50	1.0	29% \pm 7% ($n = 6$)	9% \pm 7% ($n = 6$)	Not observed	Not observed
 CCT376430, 57	188	200	2.7	6%	1%	Minimal decrease	-
 CCT375688, 58	150	200	2.4	17%	4%	Inversion to positive phase	Signal recovery

 CCT375554, 60	53	50	3.0	9%	1%	Not observed	Not observed
 CCT375689, 61	51	50	2.8	2%	70% (interference)	Not observed	Not observed
 CCT375868, 62	61	50	3.1	21%	4%	Not observed	Not observed

Considering modifications to the furan ring (Table 2.6), analogues of CCT170746 (**28**) with bulky lipophilic substitutions at the adjacent methylene and 5-position of the furan were tested, with the aim of understanding binding pocket restrictions in these positions. Whilst planar, aromatic substitutions in the 5-position such as 4-fluorophenyl (**62**) and benzofuran (**58**) both maintained competitive binding to TNKS2 ARC4, large *n*-butyl (**57**) and phenyl (**60**) substituents adjacent to the furan were not tolerated. Fragment **59**, with *tert*-butyl substitution at the methylene position, was not tested due to its low kinetic solubility (12 μ M). Overall, introduction of lipophilic furan substitutions had a detrimental effect on aqueous solubility compared with methyl substituted furans, which was associated with a calculated lipophilicity greater than 2.0 (Table 2.4 vs Table 2.6, Kin Sol and clogP). Since replacement of the furan in **28** with an isoxazole (**51**) maintained competitive binding and showed a decrease in clogP from 1.0 to 0.13, furan replacement with other 5-membered heterocycles and introduction of lipophilic substitutions from vectors around the rings to gain binding affinity was investigated (Table 2.7).

Table 2.7. A summary of data obtained from competitive ligand-observed NMR experiments performed with furan replacement fragment compounds. Fragments were tested at either 500 μ M, 200 μ M or 50 μ M depending on aqueous kinetic solubility (Kin. Sol. μ M).
^a $n = 1$ unless otherwise indicated (arithmetic mean with \pm SD error for $n > 1$); ^b competition with 3BP2 peptide (200 μ M), $n = 1$ unless otherwise indicated (arithmetic mean with \pm SD error for $n > 1$); ^c Decrease to baseline and inversion to positive phase indicates binding, minimal decrease to baseline indicates non-binding; ^d signal recovery indicates competitive binding.

Fragment 	Kin. Sol. (μM)	Assay Conc. (μM)	clogP (MoKa)	CPMG	CPMG	WaterLOGSY	WaterLOGSY
				+ protein ^a	+ competitor ^b	+ protein ^c	+ competitor ^d
 CCT170746, 28	898	500	1.0	20% ± 4% (n = 9)	5% ± 3% (n = 8)	Decrease to baseline	Signal recovery
 CCT170746, 28	898	200	1.0	26% ± 8% (n = 5)	8% ± 4% (n = 5)	Decrease to baseline	Signal recovery
 CCT170746, 28	898	50	1.0	29% ± 7% (n = 6)	9% ± 7% (n = 6)	Not observed	Not observed
 CCT390158, 63	1011	500	0.51	16%	6%	Decrease to baseline	Signal recovery
 CCT375690, 65	995	500	1.2	18%	1%	Decrease to baseline	Signal recovery
 CCT375548, 66	1024	500	1.4	36%	5%	Decrease to baseline	Signal recovery
 CCT390447, 69	200	200	0.97	18%	1%	Decrease to baseline	Signal recovery
 CCT390160, 70	866	500	0.56	31%	9%	Inversion to positive phase	Signal recovery
 CCT390161, 71	917	500	-0.21	13%	0%	Minimal decrease	-
 CCT390159, 72	947	500	0.19	13%	3%	Minimal decrease	-
 CCT375691, 73	1043	500	-0.24	14%	5%	Decrease to baseline	Signal recovery
 CCT391210, 74	948	500	0.06	7%	6%	Minimal decrease	-
 CCT375867, 75	564	500	1.8	21%	3%	Inversion to positive phase	Signal recovery
 CCT375869, 76	243	200	1.7	35%	10%	Inversion to positive phase	Signal recovery

 CCT390205, 77	1010	500	-0.05	13%	3%	Inversion to positive phase	Signal recovery
 CCT390601, 78	732	500	0.73	16%	2%	Decrease to baseline	Signal recovery
 CCT390206, 79	950	500	0.78	10%	8%	Minimal decrease	-
 CCT390441, 80	932	500	1.1	11%	0%	Decrease to baseline	Signal recovery
 CCT390446, 81	908	500	-0.08	20%	8%	Decrease to baseline	Signal recovery

Furan replacement with methylated isoxazoles (**63** and **65**) maintained competitive binding and *iso*-propyl substitution at the 5-position (**66**) resulted in substantially increased binding to TNKS2 ARC4 in the relaxation-edited experiment with reduction in peak intensity $>$ control + 2σ . Other 5-substituted isoxazoles with lipophilic phenyl and pyridyl groups (**67** and **68**) had low kinetic solubility (17 μ M and 25 μ M respectively) and therefore were not tested in ligand-observed NMR. Nitrogen-containing pyrazoles also maintained binding comparable to the furan motif, except in the case of 4-pyrazole (**74**), whilst unsubstituted pyrrole (**70**) showed increased binding to TNKS2 ARC4 in both relaxation-edited and waterLOGSY experiments. Further substitution of these heterocycles resulted in the identification of other fragments with increased binding to TNKS2 ARC4 compared to **28** such as indole (**75**) and 5-phenyl pyrazole (**76**), as determined from either relaxation-edited or waterLOGSY methods. It was hypothesised that more polar groups might lead to increased fragment binding affinity if the fragments occupied binding modes 1 or 2, due to interaction with the more hydrophilic C-terminal contact region of the substrate binding pocket. Introduction of ether and ester groups in the 3-position of the isoxazole (**77** and **78**) maintained binding to TNKS2 ARC4. Replacement of the furan with flexible, unsaturated tetrahydrofuran (**79**), tetrahydropyran (**80**) and N-methyl morpholine (**81**) maintained competitive binding but did not lead to any substantial increase in binding as determined by ligand-observed NMR

experiments. A summary of the SAR for the extended furans and furan replacements in the second iteration of fragments is shown in Figure 2.16.

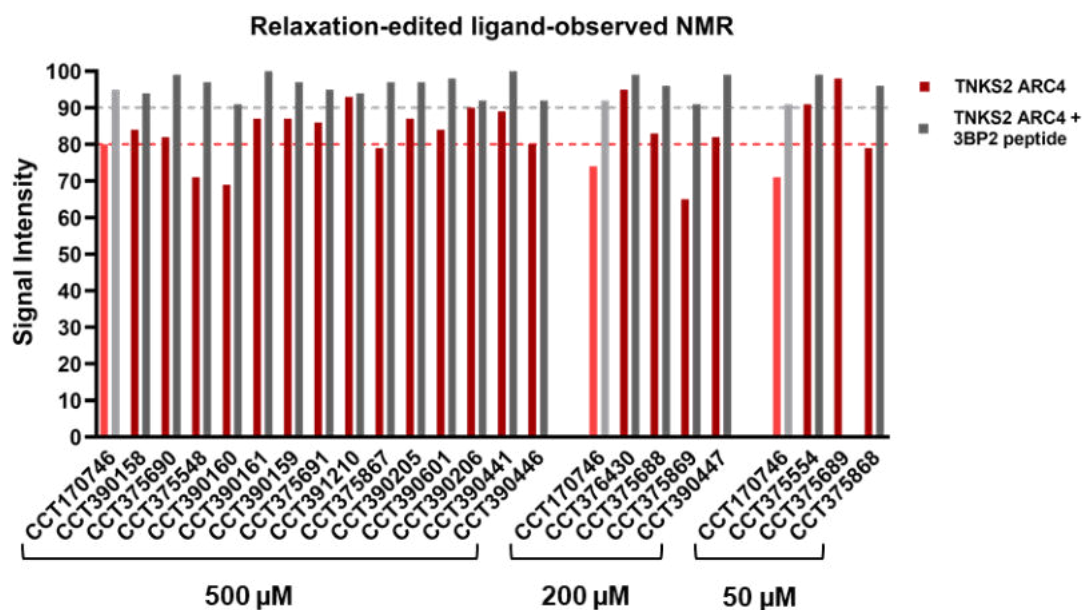
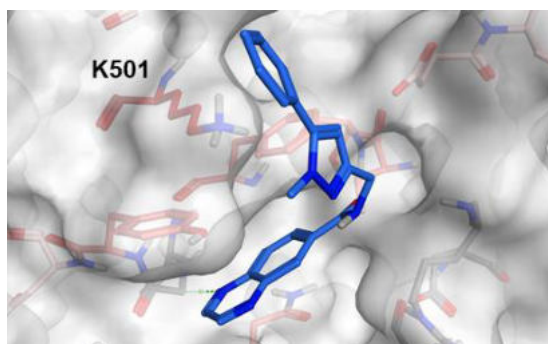
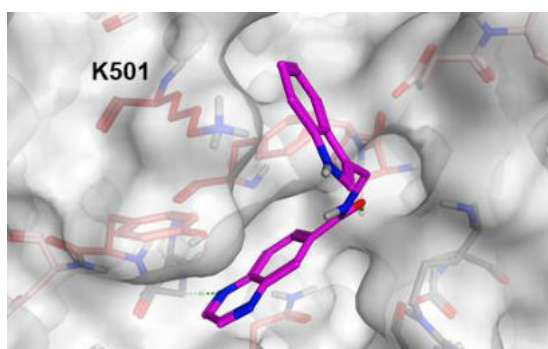
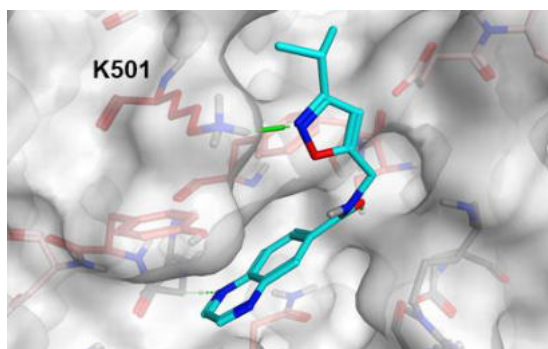


Figure 2.16. Graphical summary of results from testing the second fragment iteration in relaxation-edited (CPMG) ligand-observed NMR. Intensity of fragment ^1H NMR signals in the presence of TNKS2 ARC4 (red bars), and in the presence of TNKS2 ARC4 + 3BP2 peptide competitor (grey bars), as a percentage (%) of ^1H NMR signals in 'compound only' spectra. Y-axis (signal intensity) unit is %. Fragments were tested at either 500 μM , 200 μM or 50 μM depending on their aqueous kinetic solubility and control fragment CCT170746 (**28**) was tested at all three concentrations (pink and light grey bars). The average signal intensity (%) reduction between 'compound only' and 'TNKS2 ARC4' for control fragment CCT170746 (**28**), tested at 500 μM , was determined as 20% ($n=9$) (pink dashed threshold). Fragments which showed an average signal intensity (%) reduction of less than 10% between 'compound only' and 'TNKS2 ARC4 + 3BP2 peptide' indicated competitive binding (light grey dashed threshold).

In silico docking of CCT170746 (**28**) was inspected in MOE to evaluate which of the proposed binding modes would tolerate the second iteration furan modifications that had maintained competitive binding against TNKS2 ARC4. Ablated binding of fragments as a result of butyl and phenyl substituents in the adjacent methylene position supported binding modes 3, 4 or 5 as the more probable since the methylene points towards the protein surface in these poses. Introduction of the pyrrole (**70**), indole (**75**), 5-phenyl pyrazole (**76**) and *iso*-propyl isoxazole (**66**) was tolerated in all binding modes during energy minimisation

studies using the Builder panel in MOE.¹⁹⁸ Key hydrogen bond interactions were maintained except in binding mode 2, in which *iso*-propyl substitution of the isoxazole (**66**) disrupted a hydrogen bond from the central amide N-H to the backbone carbonyl of G535. Interestingly, several new interactions were hypothesised from energy minimisation modelling of the fragments drawn in binding modes 4 and 5. Introduction of indole (**75**) and 5-phenyl pyrazole (**76**) showed potential for a cation- π interaction between phenyl groups and the protonated amine sidechain of K501, whilst a hydrogen bond interaction between this residue and the nitrogen of isoxazole (**66**) was observed in binding mode 4 (Figure 2.17). In binding mode 5, a hydrogen bond of the pyrrole N-H with the sidechain carboxylic acid of D521 for pyrrole (**70**) and indole (**75**) fragments was predicted, and a cation- π interaction with the backbone amide N-H of R525 was predicted for **70**, **75** and pyrazole (**76**) (Figure 2.17).

Binding mode 4



Binding mode 5

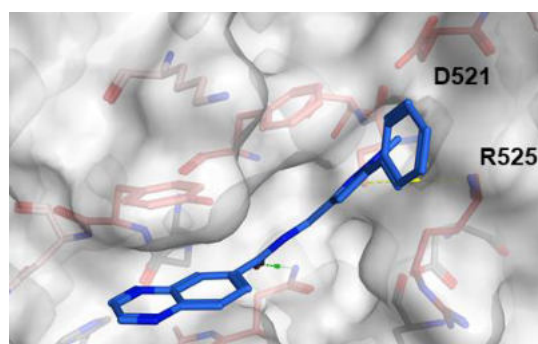
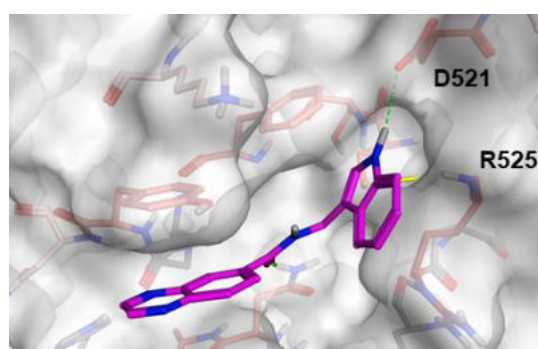
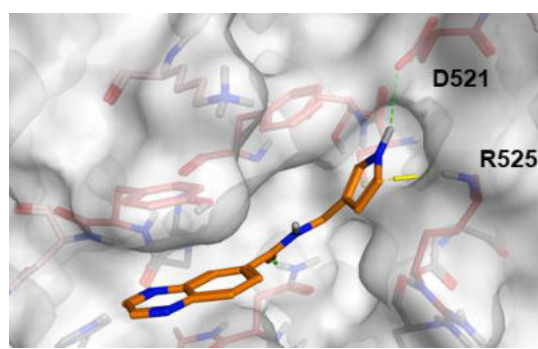


Figure 2.17. Energy minimised structures (not docked) of second iteration fragments. Furan modifications were added to the chemical structure of CCT170746 (**28**) positioned in binding mode 4 (left panel) and binding mode 5 (right panel) against TNKS2 ARC4 (PDB: 3TWR). Energy minimisation was performed using the Minimize function in the Builder panel in MOE (CCT375548, **66**, cyan; CCT390160, **70**, orange; CCT375867, **75**, magenta; CCT375869, **76**, blue).

It was hypothesised that the introduction of these furan modifications would lead to an increase in binding affinity of the fragments if they were occupying either binding modes 4 or 5, as predicted from *in silico* energy minimisations. A protein-observed NMR assay was therefore established to determine whether any

fragment hit analogues (which showed increased binding compared to **28** from ligand-observed NMR methods) had an increased binding affinity compared to CCT170746 (**28**).

2.7 Establishment of protein-observed NMR assay to determine binding affinities of modified furan analogues

2.7.1 Introduction to protein-observed NMR

Establishment of a biophysical assay for determining dissociation constants (K_d) of protein-ligand interactions with expected binding affinities in the μM to mM range was necessary. Several ligand- and protein-observed NMR methods are suitable for determining binding affinity: one of the most commonly used is protein-observed two-dimensional ^1H - ^{15}N HSQC spectroscopy, in which chemical shift perturbations (CSPs) are measured upon increasing ligand concentration.^{182, 199-200} This protein-observed NMR method also provides information on protein residues which are affected by ligand binding, which simultaneously allows the determination of fragment binding affinity and identification of fragment binding sites.¹⁸²

In a ^1H - ^{15}N HSQC spectrum of ^{15}N -labelled protein, a signal is detected for every proton which is directly attached to a nitrogen, such as in the amide bonds composing the protein backbone (Figure 2.18). Each residue of a protein therefore yields at least one NH signal in the HSQC spectrum – with the exception of prolines, which form tertiary amide bonds – providing an assignable ‘fingerprint’ of the protein.²⁰¹ For TNKS2 ARC4, the assignment of signals in the ^{15}N HSQC spectra to its corresponding residue has been previously reported and was accessed from the Biological Magnetic Resonance Data Bank (BMRB) with accession code 27747 (Figure 2.18c).¹⁴⁷ The specific chemical shift (δ) of any signal in a ^{15}N HSQC spectrum is affected by the local chemical environment of the correlating ^1H and ^{15}N nuclei. Therefore, NH signals in proximity to the ligand binding site will experience CSPs ($\Delta\delta$, or Δd) upon titration of an unlabelled ligand.¹⁸² For a system in fast exchange, the dissociation constant is estimated computationally from titration data by applying two-parameter nonlinear least

squares regression curve fitting analysis to CSPs plotted against ligand concentration.¹⁸²

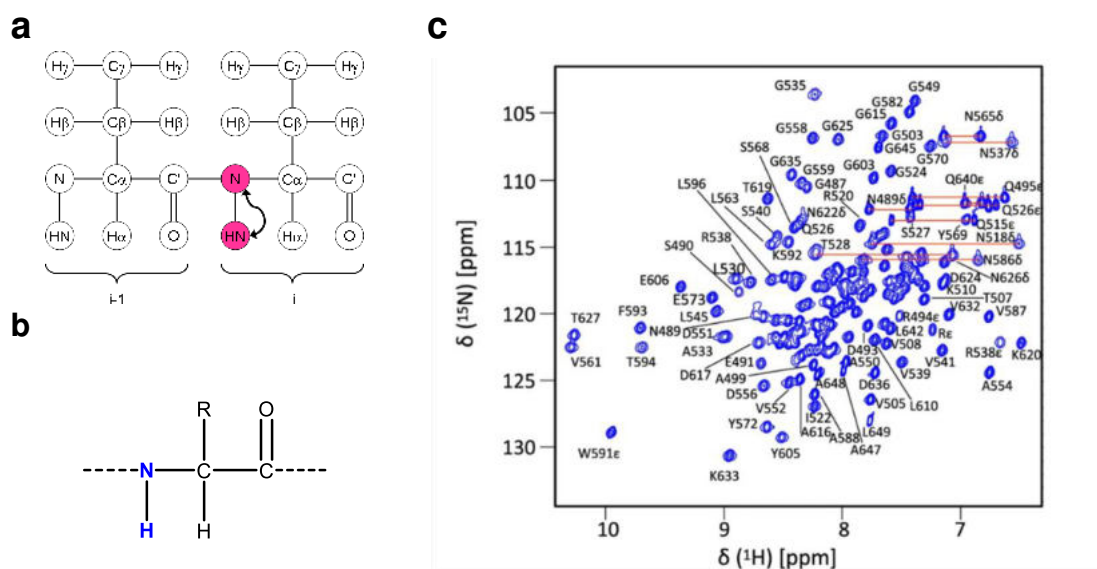
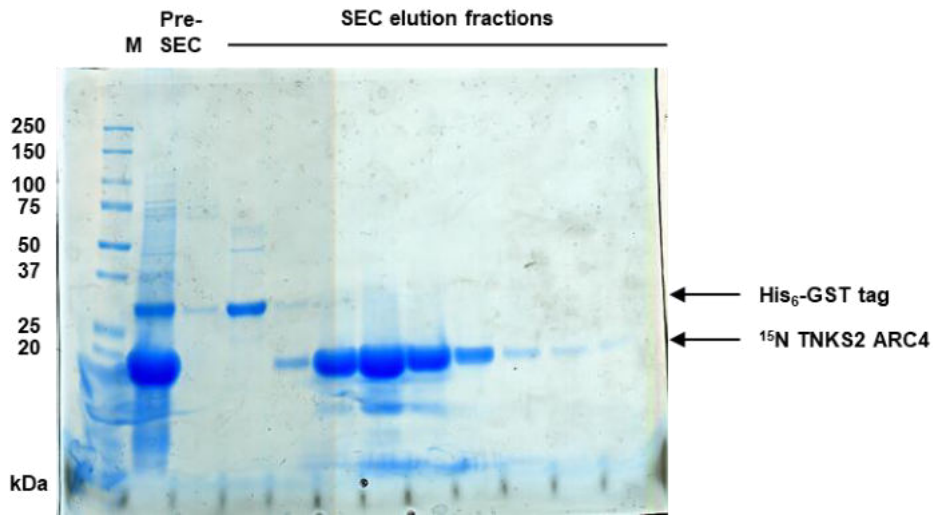


Figure 2.18. Summary of ^1H - ^{15}N HSQC protein-observed NMR. a) During acquisition of a two-dimensional ^1H - ^{15}N HSQC correlation spectrum, magnetisation is transferred from a proton nucleus to an attached nitrogen *via* J-coupling. The chemical shift, δ , is evolved on the nitrogen and magnetisation is transferred back to the proton for detection. Figure adapted from Protein NMR – A Practical Guide.²⁰² b) An N-H amide bond in a protein backbone. c) ^1H - ^{15}N HSQC spectrum of 1 mM uniformly $^{15}\text{N}/^{13}\text{C}$ labelled TNKS2 ARC4 recorded at a temperature of 293 K in a field of 700 MHz, with well resolved peaks labelled with their assignments; pairs of peaks for sidechain NH_2 groups are connected by red lines. Figure adapted from Zaleska *et al*, 2019.¹⁴⁷

2.7.2 Production of ^{15}N -labelled TNKS2 ARC4 protein

The production of ^{15}N -labelled protein was required for the acquisition of ^{15}N HSQC spectra, as ^{15}N is the only spin-active isotope of nitrogen ($I = 1/2$) and has a low natural abundance of 0.4%.²⁰²⁻²⁰³ ^{15}N -labelled TNKS2 ARC4 was produced following a previously established protocol, involving protein expression in *Escherichia coli* grown in minimal media containing ^{15}N - NH_4Cl as the only source of nitrogen, such that ^{15}N was uniformly incorporated as confirmed by mass spectrometry analysis (Figure 2.19).¹³⁵

a



b

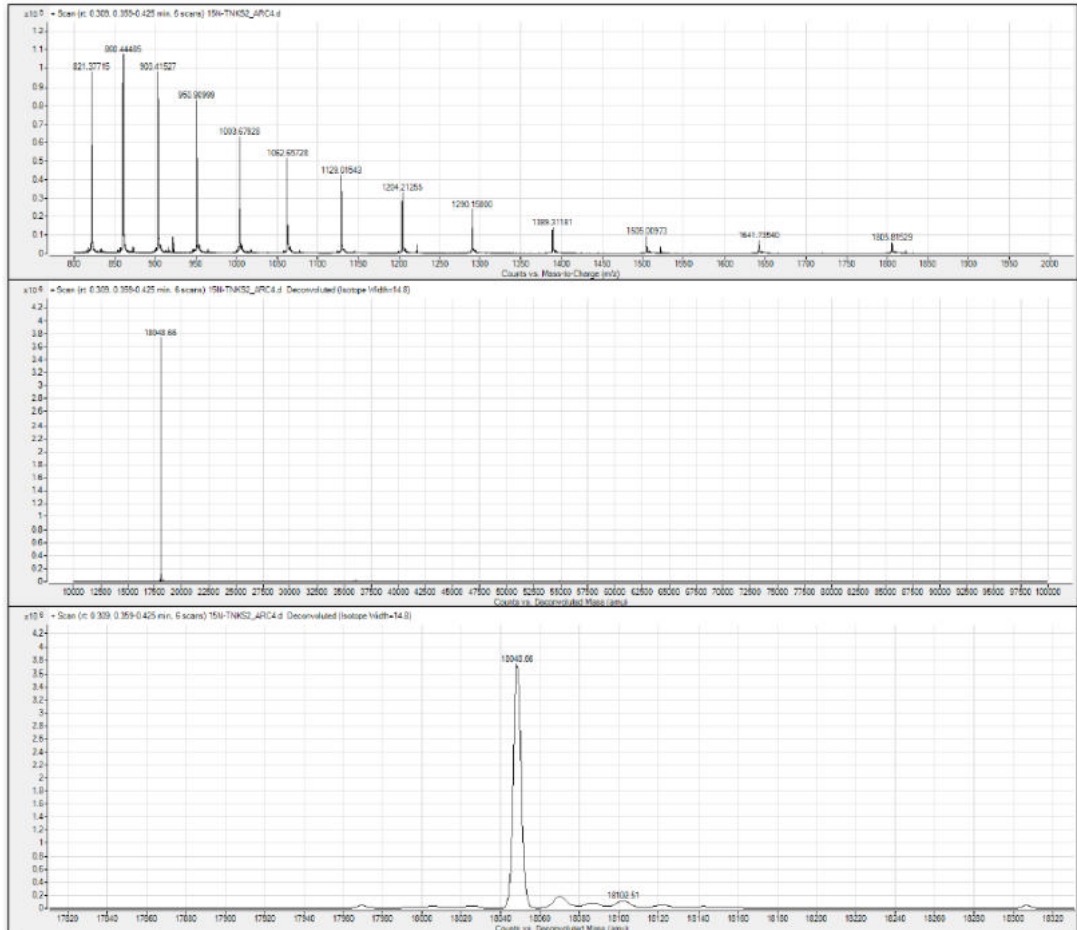


Figure 2.19. Analysis of ¹⁵N-labelled TNKS2 ARC4 following final purification by size exclusion chromatography. a) SDS-PAGE analysis of elution fractions, stained with Coomassie (M = marker, SEC = size exclusion chromatography). b) Raw and deconvoluted spectra from analysis of ¹⁵N TNKS2 ARC4 by high resolution mass spectrometry (molecular formula:

C₇₈₀H₁₂₄₈¹⁵N₂₂₆O₂₄₂S₅; calculated molecular weight: 18048.44 Da; observed molecular weight: 10849 Da).

2.7.3 Determining binding affinity of modified furan analogues

In order to determine the dissociation constants of fragments using ¹H-¹⁵N HSQC protein-observed NMR, a series of ¹H-¹⁵N HSQC correlation spectra of ¹⁵N-labelled TNKS2 ARC4 were acquired with increasing concentrations of each unlabelled ligand in a titration series (Figure 2.20a). A protein concentration of 50 μM was selected due to sensitivity limits of NMR and to allow for a suitable range of ligand concentrations (0-1600 μM) and protein:ligand stoichiometries to be assessed during each titration series, taking into account aqueous fragment solubility as a limiting factor. A constant protein concentration was maintained by preparing each titration point as individual samples, with constant concentrations of DMSO-d₆ (5% v/v) and reference standard DSS (100 μM) in each sample. All spectra were referenced to DSS in both dimensions using TopSpin prior to analysis of CSPs to prevent misinterpretation of changes in chemical shift.²⁰¹ CSPs of backbone NH signals were followed and measured as the average Euclidean distance shifted (d) using CcpNmr AnalysisAssign.²⁰⁴ Signals which had shifted significantly compared with the average calculated CSP over the titration series were identified (Figure 2.20b, $\Delta\delta > \text{average} + 1\sigma$), and for those NH signals which mapped to the peptide binding site, CSPs (d) were plotted against ligand concentration in GraphPad Prism. Dissociation constants (K_d) for each significantly shifted residue were determined by applying two-parameter, nonlinear least squares regression curve fitting analysis to the data (Figure 2.20c). The standard method for determining a 'best' estimate of an overall dissociation constant from protein-observed NMR titrations was then applied, which was to average x different estimates of the dissociation constant from individual fitting of x observed significantly shifted NH signals.^{200, 205} The accuracy and precision of the average K_d value was increased by excluding residues with inadequate curve fits – residues were excluded from calculations if there was an incompletely calculated 95% confidence interval and/or a goodness of fit (R^2) of less than 0.90.¹⁹⁹

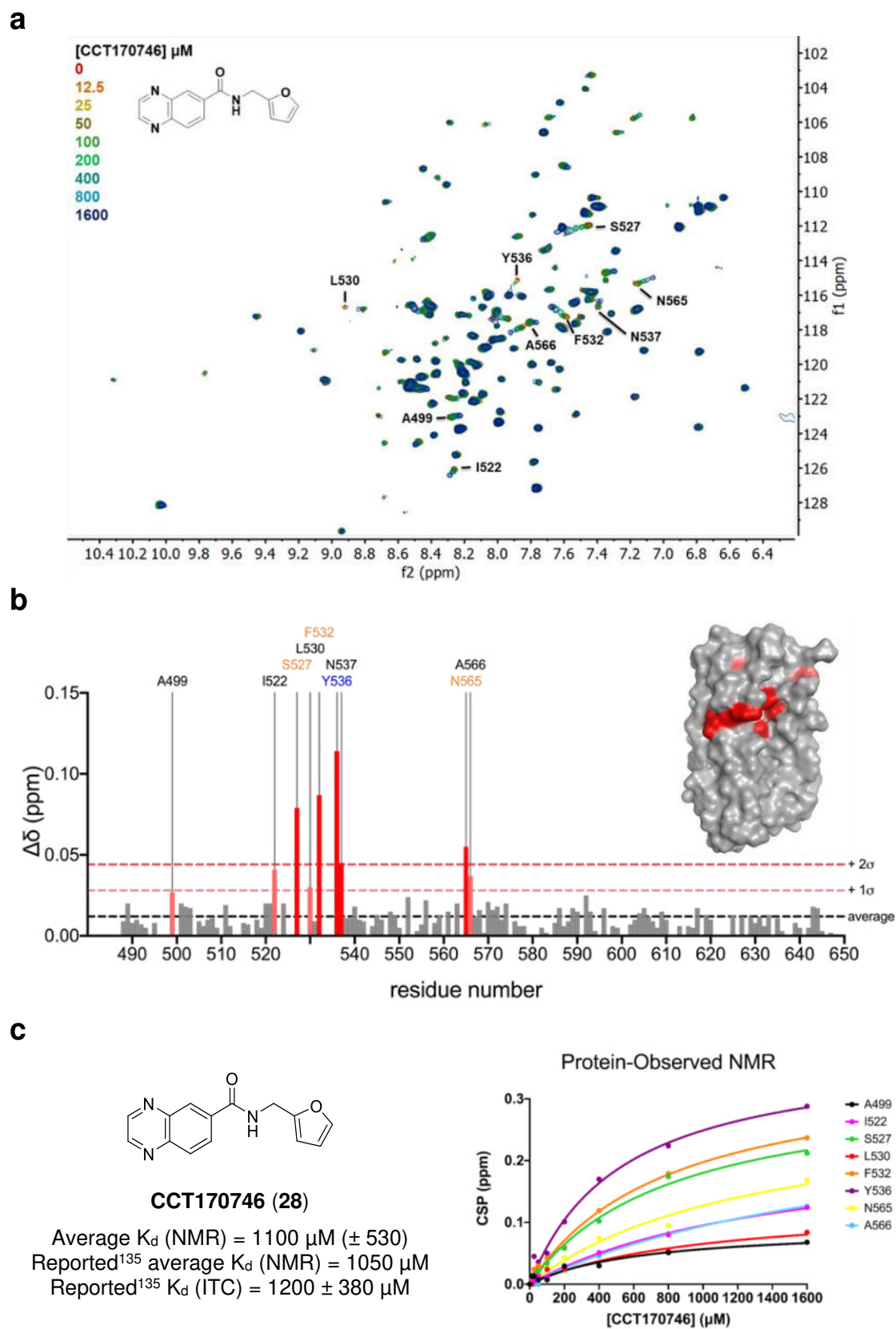
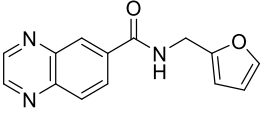
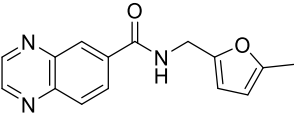
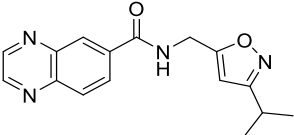
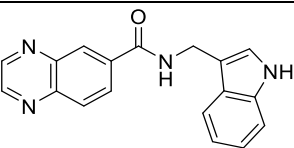
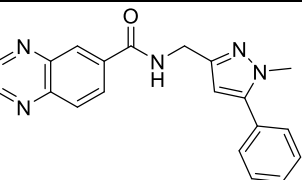
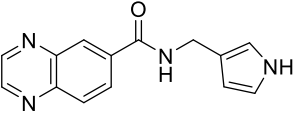
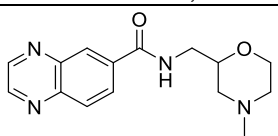


Figure 2.20. Data obtained from protein-observed NMR with control fragment CCT170746 (28). **a**) A series of ^1H - ^{15}N HSQC correlation spectra of ^{15}N -labelled TNKS2 ARC4 (50 μM)

acquired with increasing concentrations (0-1600 μM) of fragment hit CCT170746 (**28**). **b**) Plot of CSPs induced in ^{15}N TNKS2 ARC4 in the presence of **28**, with residues labelled and colour coded to correspond with TBM binding site regions (central patch, orange; glycine sandwich, blue). Residues which showed significant CSPs ($\Delta d > \text{average} + 1\sigma$, pink; $\Delta d > \text{average} + 2\sigma$, red) upon fragment binding are highlighted, and mapped onto the surface representation of TNKS2 ARC4 (PDB: 3TWR). **c**) Structure of CCT170746 (**28**) with K_d by protein-observed NMR, calculated from the average K_d of each residue which showed significant CSPs upon fragment binding ($\Delta d > \text{average} + 1\sigma$). N537 was excluded from average K_d due to an incomplete 95% confidence interval calculation.

To validate the experimental setup and data analysis methods for protein-observed NMR dissociation constant determination, a ^1H - ^{15}N HSQC titration was firstly performed with fragment hit CCT170746 (**28**) (Figure 2.20). An average K_d by NMR for **28** from this experiment was determined as $1100 \pm 530 \mu\text{M}$ (Figure 2.20 and Table 2.8), which was consistent with the previously reported NMR K_d of $1050 \mu\text{M}$ and K_d determined by isothermal titration calorimetry (ITC) of $1200 \pm 380 \mu\text{M}$.¹³⁵ Therefore, ^1H - ^{15}N HSQC titrations for six fragments from the first and second iterations of furan modifications which had shown increased binding compared to **28** from either ligand-observed NMR method were performed. From dissociation constant data for these fragments (Table 2.8), it was determined that none of the modifications assessed so far had resulted in a measured increase in binding affinity to TNKS2 ARC4. All the fragment analogues tested showed between 1-2 mM binding affinities comparable to **28**. Due to the low aqueous solubility of CCT375869 (**76**), complete saturation was not achieved and a value for the dissociation constant was not determined.

Table 2.8. A summary of data for selected fragments determined from ligand-observed (CPMG) and protein-observed NMR assays including dissociation constant (K_d) data determined from ^1H - ^{15}N -HSQC titrations. ^a $n = 1$ unless otherwise stated (arithmetic mean with \pm SD error for $n > 1$).

Fragment	Kin. Sol. (μM)	clogP (MoKa)	CPMG + protein ^a	Average CSP ($+\ 1\sigma$)	Average K_d by NMR (μM) ^b
 CCT170746, 28	898	1.00	20% \pm 4% ($n = 9$)	0.012 (+ 0.016)	1100 (\pm 530)
 CCT373538, 48	972	1.60	31% \pm 7% ($n = 2$)	0.011 (+ 0.013)	2190 (\pm 1080)
 CCT375548, 66	1024	1.40	29% \pm 7% ($n = 2$)	0.009 (+ 0.014)	1480 (\pm 600)
 CCT375867, 75	564	1.80	21%	0.011 (+ 0.012)	910 (\pm 560)
 CCT375869, 76	243	1.70	35%	0.009 (+ 0.009)	Not determined
 CCT390160, 70	866	0.56	31%	0.009 (+ 0.011)	1680 (\pm 630)
 CCT390446, 81	908	-0.08	20%	0.010 (+ 0.012)	1000 (\pm 280)

2.7.4 Hypothesised *in silico* binding model of modified furan analogues

Despite the lack of increased binding affinity from the fragments from the first and second iterations, the availability of the full backbone assignment of ^1H - ^{15}N TNKS2 ARC4 backbone NH amide signals enabled the identification of the fragment binding sites in the ARC domain.¹⁴⁷ Heat-maps, which represent the most probable fragment binding location, were produced by mapping NH signals which showed significant CSPs ($\Delta d > \text{average} + 1\sigma$) upon ligand binding to the corresponding residue in the crystal structure of TNKS2 ARC4 bound to the 3BP2 16mer TBM peptide (PDB: 3TWR) (Figure 2.21). For each fragment tested, shifted NH signals consistently mapped to assigned residues in the substrate-binding groove of TNKS2 ARC4, including glycine sandwich and central patch residues which form interactions with the tankyrase binding motif of 3BP2. This data was consistent with 3BP2-competitive fragment binding observed in ligand-observed NMR experiments and confirmed that structural modifications of CCT170746 (**28**) maintained binding in the substrate-binding region of the ARC domain.

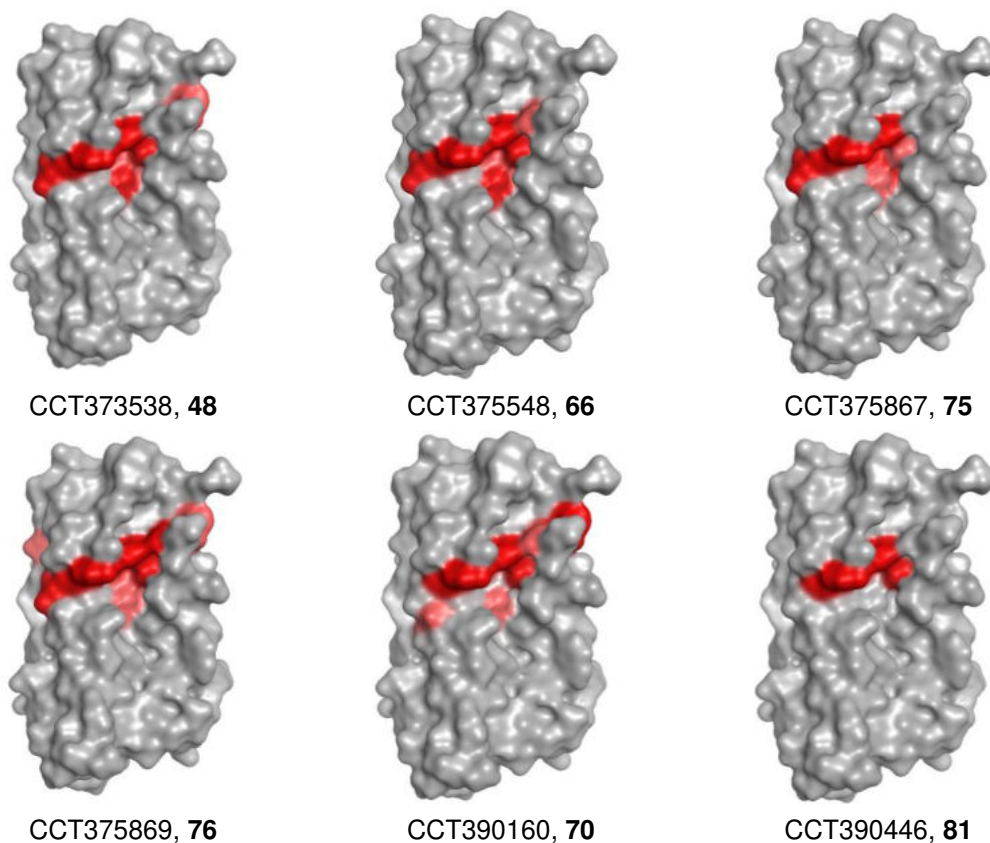


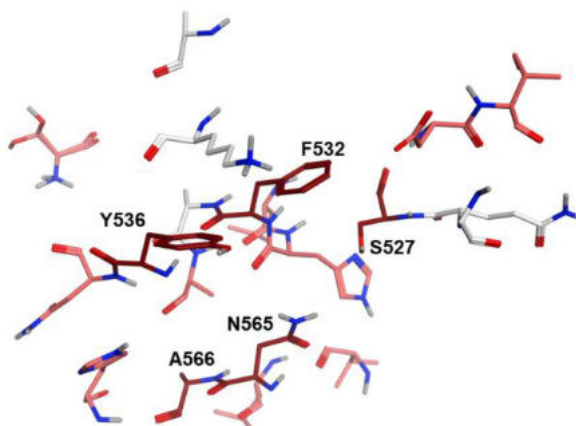
Figure 2.21. Binding site maps produced from protein-observed NMR data for modified furan analogues. Surface heat-maps produced in MOE by mapping residues which showed significant CSPs ($\Delta d > \text{average} + 1\sigma$, pink; $\Delta d > \text{average} + 2\sigma$, red) upon fragment binding onto the surface representation of TNKS2 ARC4 (PDB: 3TWR).

The residues which shifted significantly in response to ligand binding for each fragment tested in protein-observed NMR (**48**, **66**, **75**, **76**, **70** and **81**) were compared. It was determined that all fragments induced shifting of the NH amide signals of S527, F532 and Y536, and all fragments – except for CCT390446 (**81**) – also induced a shift in NH signals for N565 and A566 (Figure 2.22a). The most notable difference between **81** and the other fragments tested was the replacement of furan with a non-aromatic ring, therefore indicating that an aromatic heterocycle was required to induce CSPs from N565 and A566.

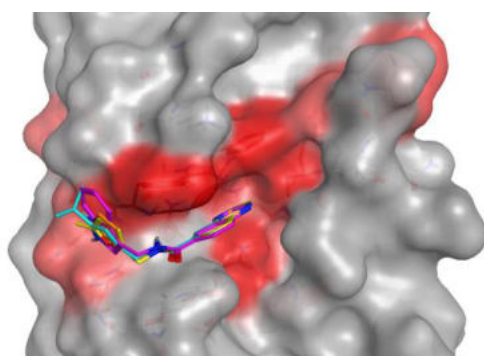
Following this analysis, *in silico* docking of fragments **48**, **66**, **70**, **75**, **76** and **81** was carried out against the crystal structure of TNKS2 ARC4 in complex with the 3BP2 16mer TBM peptide (PDB: 3TWR, chain D).⁶¹ Fragment-protein docking was performed using the dedicated Dock panel in MOE.¹⁹⁸ Within this panel, the TNKS2 ARC4 structure was selected as the receptor and the docking site was selected as the five residues which showed CSPs ($\Delta d > \text{average} + 1\sigma$) upon ligand titration for all fragments tested (S527, F532, Y536, N565 and A566). Therefore, the ligand placement was constrained to within 5 Å of any atom within the selected five residues.¹⁹⁸ The docking was performed using the default methods and scoring functions for Placement and Refinement phases in MOE's Dock algorithm, and the top five ligand-protein docking poses were retained upon refinement for visual inspection.¹⁹⁸ It was observed that fragments CCT373538 **48**, **66**, **70** and **75** all generated docking poses in MOE which were consistent with binding modes 1 or 2 from the reported *in silico* docking of CCT170746 (**28**) against TNKS2 ARC4 (Figure 2.22b/c).¹³⁵ In this binding mode, for **48**, **66**, **70** and **75**, the quinoxaline-6-carboxamide motif – which was maintained in all the tested fragments – was positioned in proximity to the five TNKS2 ARC4 residues which showed consistent CSPs (S527, F532, Y536, N565 and A566). Meanwhile, the furan ring replacements were solvent-exposed in this binding mode, therefore

providing a potential explanation for the lack of increased binding affinity despite toleration of modification and substitution of the furan ring (Figure 2.22b).

a

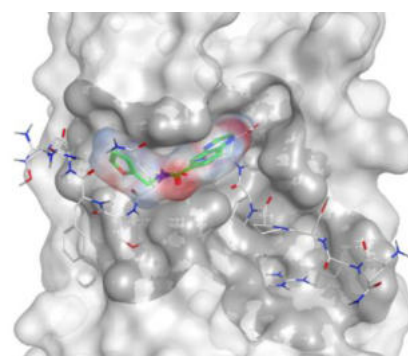


b



Fragment docking against TNKS2 ARC4

c



Binding mode 1

Figure 2.22. Predicted fragment binding sites from *in silico* fragment docking guided by protein-observed NMR data. Ligand-protein docking was performed in MOE against a crystal structure of TNKS2 ARC4 (PDB: 3TWR). **a**) Five key residues which showed consistent CSPs upon fragment titrations (S527, F532 and Y536, N565 and A566), highlighted in red. Other residues which showed CSPs with furan-modified fragments, highlighted in pink. **b**) Surface representation of TNKS2 ARC4, highlighting the location of the five key residues which respond to fragment binding (red surface) and other residues (pink surface). Top scoring docking poses generated from *in silico* docking of fragments in MOE were consistent with binding mode 1 (CCT373538 **48**, yellow; CCT375548 **66**, cyan; CCT390160 **70**, orange; CCT375867 **75**, magenta). **c**) Binding mode 1 from *in silico* docking of **28** (green) against a crystal structure of TNKS2 ARC4 in complex with 3BP2 16mer TBM peptide.

Chapter 3 Identification and Characterisation of a Higher Affinity Fragment against TNKS2 ARC4

In the next phase of the fragment-based approach, the aim was the identification of a higher affinity fragment scaffold based on fragment hit CCT170746 (**28**). This chapter describes firstly the testing of higher affinity literature-reported ARC-binding compounds in ligand- and protein-observed NMR to provide data for more potent compounds in these assays. The synthesis and testing of analogues of **28** with further modifications of the quinoxaline motif is then discussed, followed by identification and characterisation of a higher affinity lead fragment scaffold.

3.1 Validation of literature-reported ARC-binding compounds

Following identification of CCT170746 (**28**) from fragment-based screening as a binder of the tankyrase ARC domain, two further screens were published which identified small molecule ARC-binding compounds (section 1.6.2 and Figure 3.1).¹³⁵⁻¹³⁷ In the earlier of the two reports, C41 (**29**) and C44 (**30**) were identified from a virtual screen against the interaction of USP25 with TNKS1 ARC5, with reported K_i values between 20 and 200 μM as determined from a competitive FP assay.¹³⁶ In the second publication, Lehitö *et al* developed a FRET-based assay which led to the identification of two hit compounds, fanapanel (**31**) and DCKA (**32**), that bound TNKS2 ARC4 with reported K_i values between 20 and 100 μM .¹³⁷

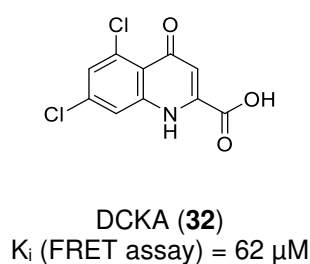
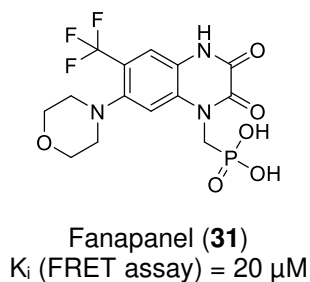
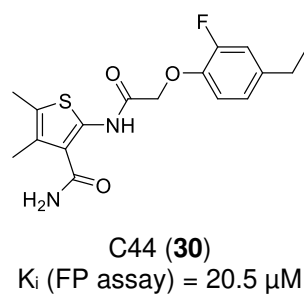
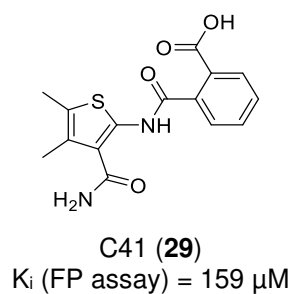
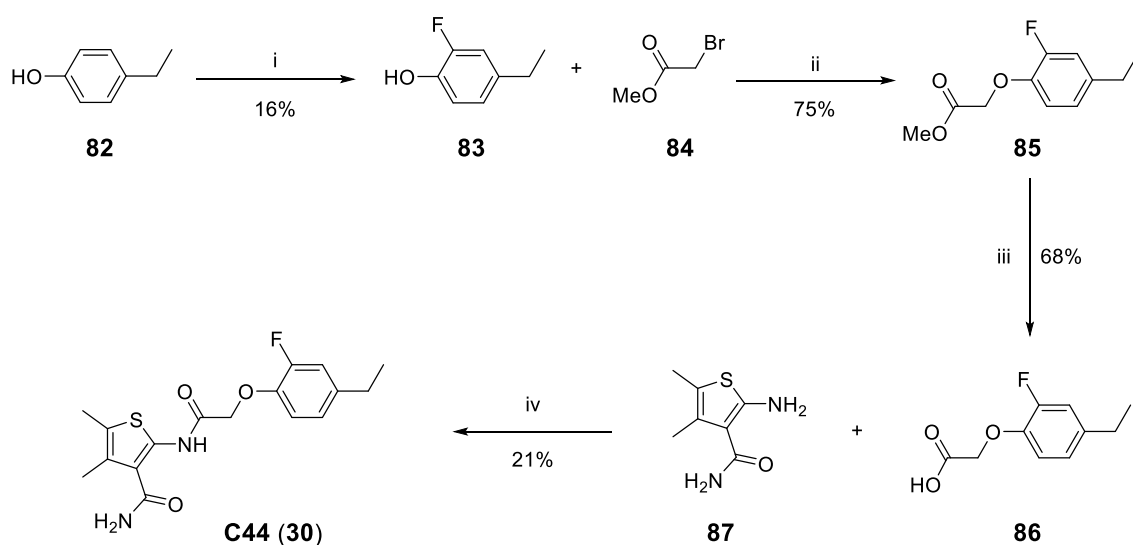


Figure 3.1. Literature-reported ARC-binding compounds. Chemical structures and inhibitory constants (K_i) of four compounds (C41 (**29**), C44 (**30**), fanapanel (**31**) and DCKA (**32**)) which are reported to bind to tankyrase ARC domains.¹³⁶⁻¹³⁷

In order to validate these reports and gain information on potential binding sites of these compounds in the tankyrase ARC domain, the most potent compound from each report was studied by the ligand-observed and protein-observed NMR assays. Fanapanel (**31**) was purchased from a commercial supplier (Apollo Scientific), and C44 (**30**) was synthesised in four steps following the published synthetic route (Scheme 3.1).¹³⁶



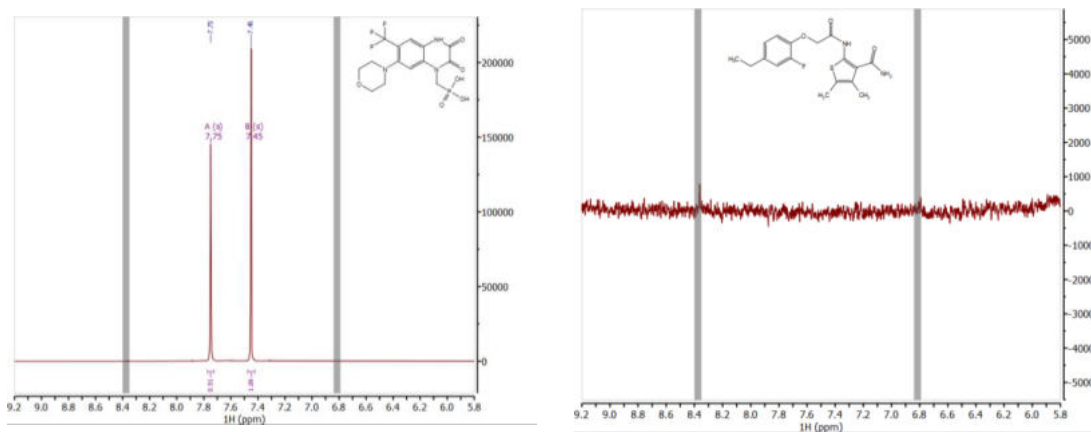
Scheme 3.1. Synthesis of C44 (30). Reagents and conditions: i) SelectFluor, MeOH, 65 °C, 48 h; ii) K₂CO₃, DMF, rt, 22 h; iii) LiOH·H₂O, THF, rt, 3 h; iv) HATU, DIPEA, DMF, rt, 24 h.

Results from testing of C44 (**30**) and fanapanel (**31**) in biophysical NMR assays are shown in Table 3.1 and Figure 3.2. C44 showed no measurable aqueous kinetic solubility and therefore no quantifiable binding in ligand-observed NMR against TNKS2 ARC4, limiting its usefulness as a potential ARC-binding chemical tool compound. However, fanapanel showed a significant 86% reduction in average signal intensity in the relaxation-edited (CPMG) method and was assessed in a ¹H-¹⁵N HSQC titration experiment to confirm the binding affinity and identify the potential binding site (Figure 3.2). The dissociation constant was determined as 100 ± 60 μM, confirming fanapanel as a higher affinity binder of the ARC domain and suggesting that the biophysical NMR method underestimated binding affinity compared with a biochemical FRET assay. Results from testing fanapanel provided supporting evidence that a larger reduction in ligand signal intensity in the presence of protein from relaxation-edited NMR experiments (i.e. closer to 100%) correlated with a higher binding affinity of the ligand. Therefore, a new benchmark for the ligand-observed NMR assay was established, namely that a substantial reduction (> 80%) in average signal intensity could indicate a higher affinity fragment scaffold (K_d ~ 100 μM). As shown in Figure 3.2b/c, titration of fanapanel (**31**) induced significant CSPs in 16 residues which mapped to the central patch and arginine cradle of TNKS2 ARC4, a region of the 3BP2 TBM peptide binding site not targeted by any analogues of CCT170746 (**28**).

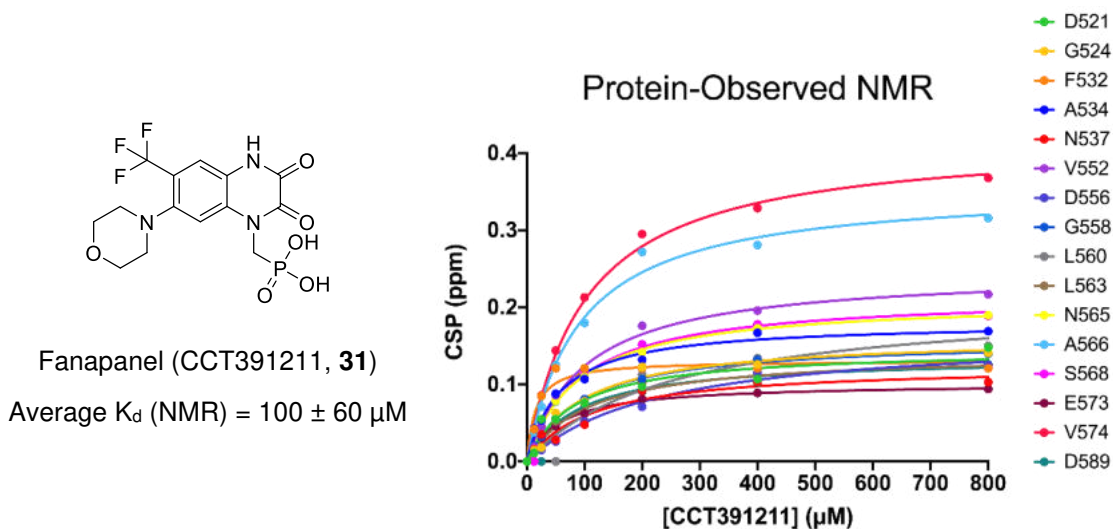
Table 3.1. A summary of data obtained from competitive ligand-observed NMR experiments performed with literature-reported ARC-binding fragments. ^a n = 1; ^b competition with 3BP2 peptide (200 μM), n = 1; ^c Decrease to baseline and inversion to positive phase indicates binding, minimal decrease to baseline indicates non-binding; ^d signal recovery indicates competitive binding.

Fragment	Kin. Sol. (μM)	Assay Conc. (μM)	clogP (MoKa)	CPMG	CPMG	WaterLOGSY	WaterLOGSY
				+ protein ^a	+ competitor ^b	+ protein ^c	+ competitor ^d
CCT391211 (Fanapanel) 31	922	500	-0.24	86%	75%	Decrease to baseline	Partial signal recovery
CCT391271 (C44) 30	0	-	2.3	-	-	-	-

a



b



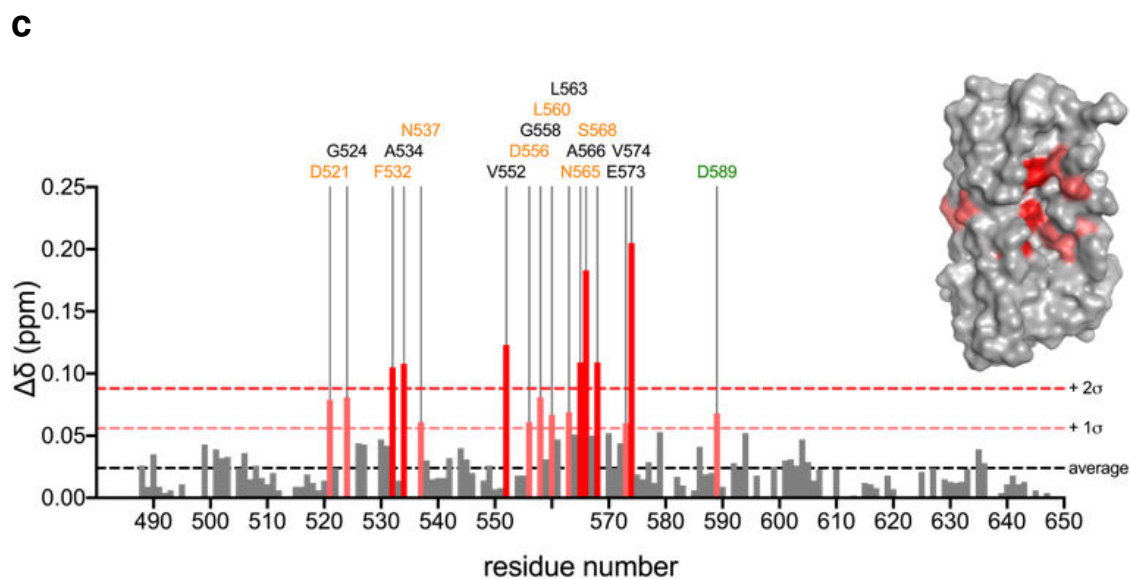


Figure 3.2 Summary of NMR experiments performed with literature-reported fragment ARC-binding compounds. a) Data from aqueous kinetic solubility (^1H NMR) assay for C44 (CCT391271 **30**, 0 μM) and fanapanel (CCT391211 **31**, 922 μM). **b)** Average K_d (NMR) determination for fanapanel calculated from non-linear regression analysis of CSPs against ligand concentration. **c)** Plot of CSPs ($\Delta d > \text{average} + 1\sigma$, pink; $\Delta d > \text{average} + 2\sigma$, red) from fanapanel titration against ^{15}N TNKS2 ARC4 (50 μM) mapped onto the 3BP2 bound crystal structure (PDB: 3TWR), identifying the potential binding site of fanapanel (central patch, orange; arginine cradle, green).

3.2 Fragment hit analogues investigating quinoxaline replacements and substitutions

3.2.1 Design of quinoxaline modifications based on binding model hypothesis

Following thorough exploration of furan substitutions and replacements of CCT170746 (**28**), which did not lead to an increase in fragment binding affinity, the next iteration of fragment **28** SAR focused on modification of the quinoxaline motif for fragment elaboration. As discussed in section 2.5.3, quinoxaline replacement with the quinazoline ring in CCT373723 (**46**) showed increased binding to TNKS2 ARC4 in waterLOGSY but showed an inconclusive result in competitive ligand-observed NMR experiments. Therefore, the next iteration of amide fragment analogues proposed included combinations of quinazoline-6-

carboxylic acid from **46**, with furan modifications from the first iteration which had shown equivalent or ablated binding to TNKS2 ARC4. This was proposed to assess the tractability of SAR between quinoxaline and quinazoline matched pairs and evaluate the indicated requirement of the quinoxaline moiety for competitive fragment binding (Figure 3.3a). Other heterocyclic quinoxaline replacements were also proposed, including incorporation of the 1,4-dihydroquinoxaline-2,3-dione motif from fanapanel (**31**), as well as introduction of small substituents (-Me, -Et, -OMe) around the quinoxaline ring (Figure 3.3b/c).

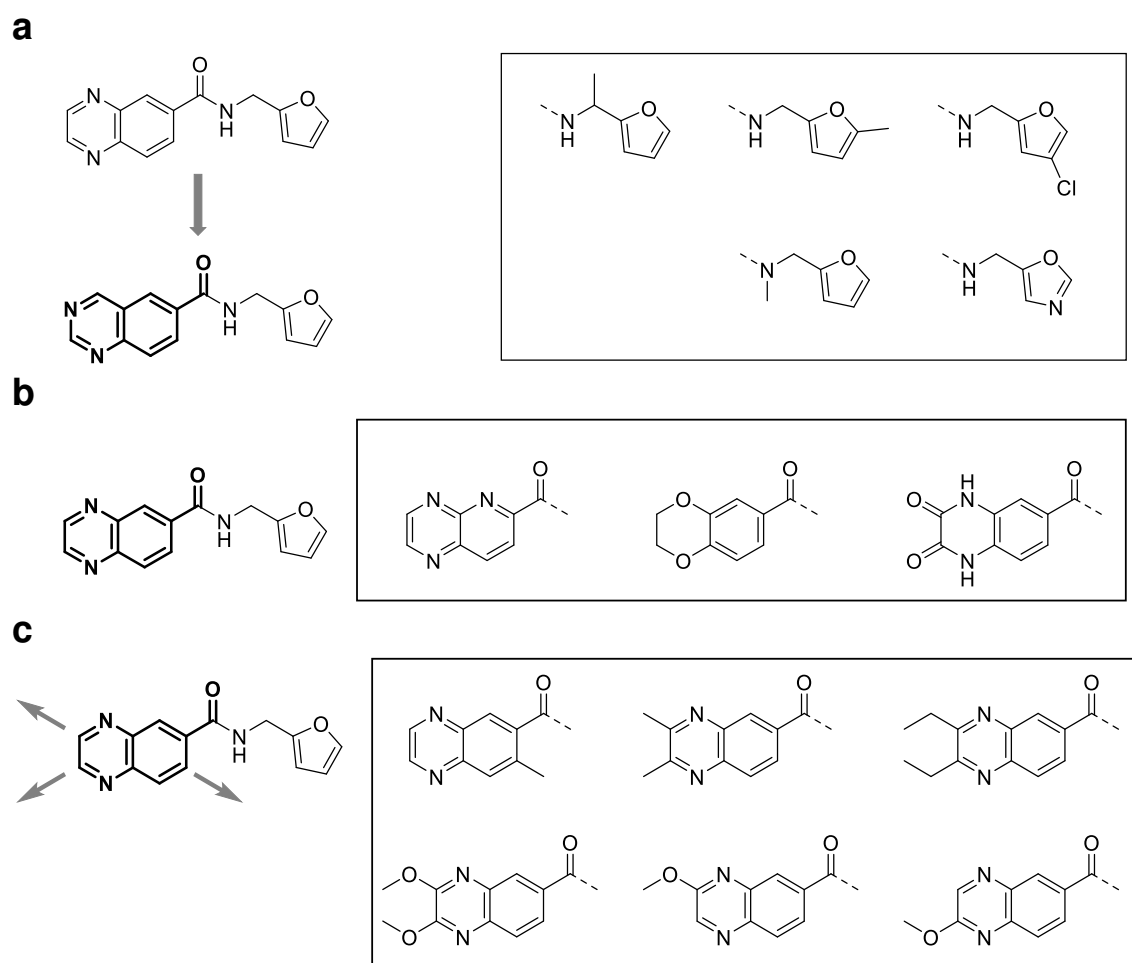


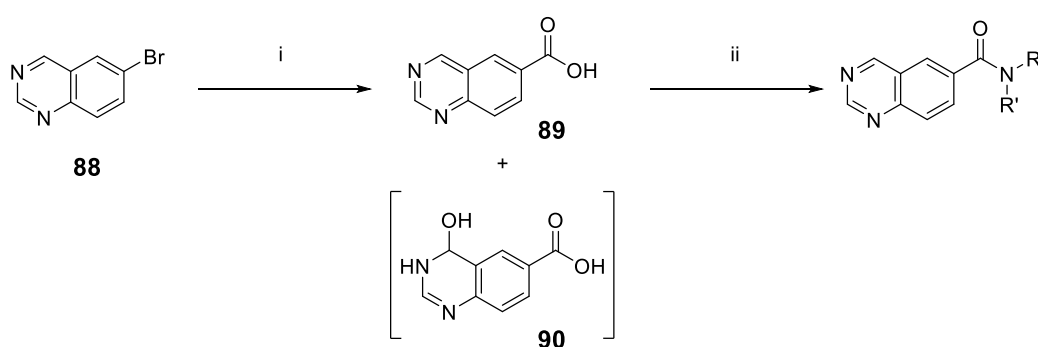
Figure 3.3. Proposed quinoxaline modifications to further investigate CCT170746 (28**) SAR.**
a) Quinazoline matched pairs with different furan modifications. **b)** Quinoxaline replacements. **c)** Introduction of substituents around the quinoxaline ring.

3.2.2 Synthesis of modified quinoxaline analogues

The proposed modified quinoxaline analogues were prepared by one of two short and efficient general synthetic strategies – either *via* the previously described one-step, HATU-mediated amide coupling, or *via* a two-step synthesis involving a palladium-catalysed (Pd-catalysed) carbonylation.

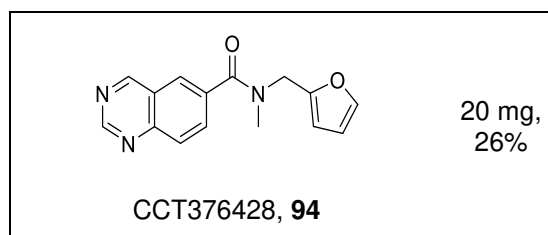
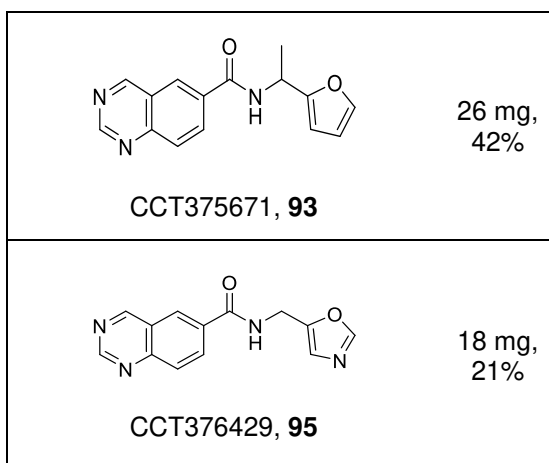
Five quinazoline analogues were synthesised from 6-bromoquinazoline in two steps *via* quinazoline-6-carboxylic acid **89**. Palladium-catalysed carbonylation of **88** using gaseous carbon monoxide in the presence of water provided quinazoline-6-carboxylic acid **89**, which was then reacted with commercially available amines in a HATU-mediated amide coupling reaction to access desired products **91** to **95** (Table 3.2).²⁰⁶ Hydration at the 4-position of the quinazoline motif was observed as an inseparable by-product from the carbonylation reaction, and the corresponding hydrated by-products were also observed following amide coupling. In two cases (**91** and **93**), 10% of this impurity remained following reverse phase purification, observed by ¹H NMR and HRMS.

Table 3.2. Synthesis of quinazoline-6-carboxamide fragments, maintaining quinazoline-6-carboxylic acid and varying the furan-2-ylmethanamine derived right-hand side. Reagents and conditions: i) CO (g), DIPEA, Pd(OAc)₂ and XantPhos (5 mol%), 1,4-dioxane:H₂O (1:1), 60 °C, 22 h; ii) RNHR', HATU, DIPEA, DMF, rt, 5 h to 18 h.



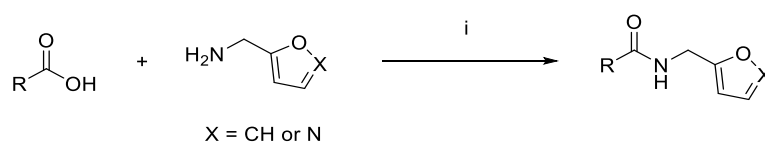
Entry	Yield
 CCT375669, 91	17 mg, 25%

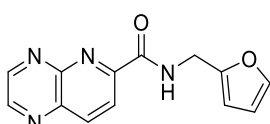
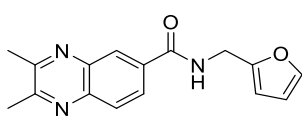
Entry	Yield
 CCT375670, 92	38 mg, 45%

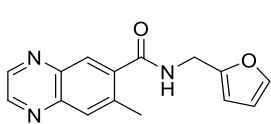
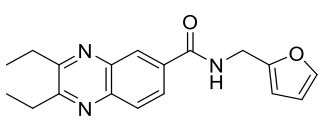


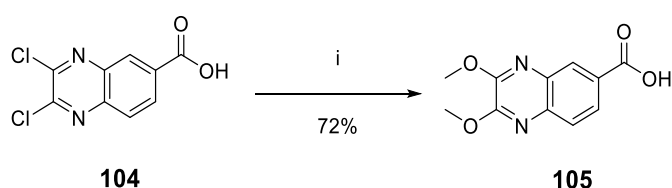
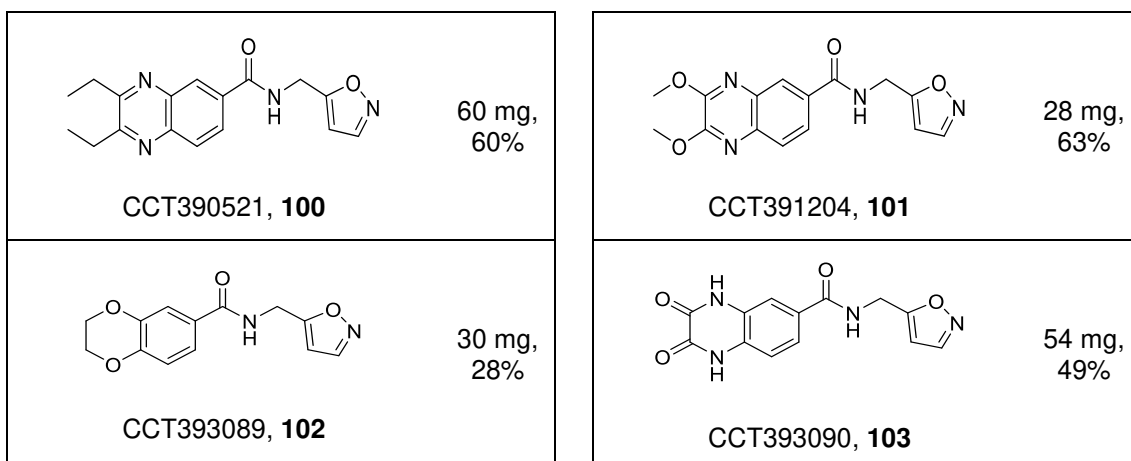
The synthesis of all substituted quinoxaline analogues reported in Table 3.3 was achieved *via* HATU-mediated amide coupling reaction. For the synthesis of CCT391204 (**101**), preparation of 2,3-dimethoxyquinoxaline-6-carboxylic acid (**105**) was required prior to amide coupling. This was achieved by a double-S_NAr reaction from 2,3-dichloroquinoxaline-6-carboxylic acid (**104**) with sodium methoxide in methanol (Scheme 3.2).

Table 3.3. Synthesis of quinoxaline-6-carboxamide fragments *via* amide coupling, introducing modifications and substituents to the quinoxaline-6-carboxylic acid component whilst maintaining either the furan-2-yl or isoxazol-5-ylmethanamine. Reagents and conditions: i) HATU, DIPEA, DMF, rt, 17 h to 46 h.



Entry	Yield
	45 mg, 41%
CCT375994, 96	
	51 mg, 42%
CCT375550, 98	

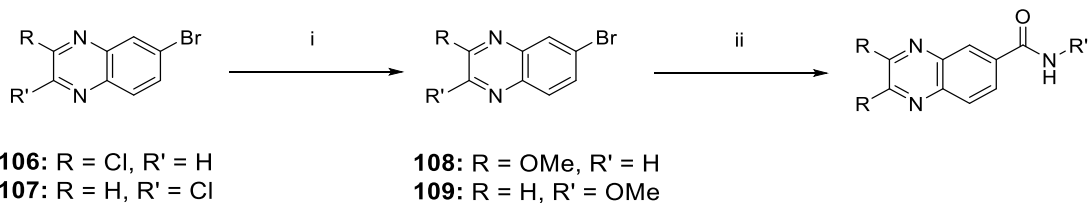
Entry	Yield
	41 mg, 58%
CCT375852, 97	
	66 mg, 65%
CCT390523, 99	



Scheme 3.2. Synthesis of 2,3-dimethoxyquinoxaline-6-carboxylic acid (105) for subsequent amide coupling. Reagents and conditions: i) 0.5 M NaOMe in MeOH, 65 °C, 6 h.

Lastly, 2- and 3- methoxy quinoxaline-6-carboxamide analogues (**110**, **111**, **112**, and **113**) were made in a two-step synthesis from either 2- or 3-chloro 6-bromo quinoxalines (Table 3.4). Following installation of the desired 2- or 3- methoxy substituent by S_NAr reaction, the desired amide products were synthesised *via* Pd-catalysed aminocarbonylation under an atmosphere of CO in the presence of the appropriate amine nucleophile.²⁰⁶

Table 3.4. Synthesis of 2- or 3-methoxy quinoxaline-6-carboxamide fragments via Pd-catalysed aminocarbonylation, whilst maintaining either the furan-2-yl or isoxazol-5-ylmethanamine. Reagents and conditions: i) K_2CO_3 , MeOH, 65 °C, 4 h; ii) $R''NH_2$, CO (g), DIPEA, XantPhos Pd G4 (5 mol%), 1,4-dioxane, 80 °C, 3 h.



Entry	Yield	Entry	Yield
 CCT391082, 110	37 mg, 52%	 CCT391084, 111	38 mg, 51%
 CCT391081, 112	35 mg, 49%	 CCT391083, 113	33 mg, 44%

3.2.3 Competitive ligand-observed NMR and further SAR analysis

Prior to testing in the competitive ligand-observed NMR assay, the aqueous kinetic solubility of all compounds was measured using quantitative 1H NMR at a concentration of 1000 μM in HEPES buffer (Table 3.5, Kin Sol (μM)). As discussed in section 2.6.3, a general decrease in aqueous kinetic solubility corresponding to increasing lipophilicity predicted by calculated logP (MoKa) values was observed (Table 3.5, Kin Sol (μM) and MoKa clogP). For the 2-,3-substituted quinoxaline fragments shown in Figure 3.4, a 5- to 6.5- fold increase in measured kinetic solubility corresponding to reduced clogP of 0.8 to 0.9 units was observed by comparison between isoxazoles and furan matched pairs. Therefore, isoxazoles **100**, **112** and **113** were suitable for testing at 500 μM in the ligand-observed NMR assay, and the less soluble furan matched pairs were not

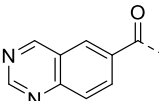
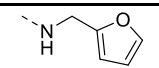
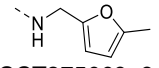
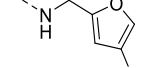
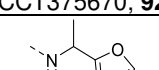
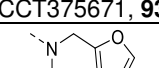
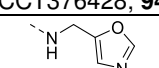
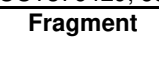
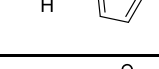
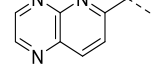
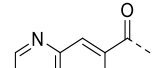
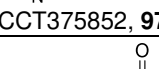
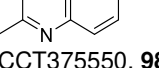
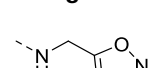
tested. For compounds **101**, **102** and **103**, only the isoxazole amides were synthesised; however, **101** and **103** showed kinetic solubilities < 200 μM despite low predicted lipophilicity ($\text{clogP MoKa} \leq 1.6$) (Table 3.5).

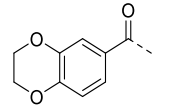
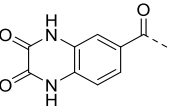
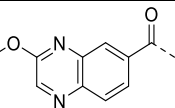
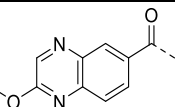
CCT390523, 99 Kin Sol 86 μM $\text{clogP (MoKa)} 2.8$	CCT391082, 110 Kin Sol 160 μM $\text{clogP (MoKa)} 1.8$	CCT391084, 111 Kin Sol 173 μM $\text{clogP (MoKa)} 1.8$	
CCT390521, 100 Kin Sol 559 μM $\text{clogP (MoKa)} 1.9$	CCT391081, 112 Kin Sol 872 μM $\text{clogP (MoKa)} 0.93$	CCT391083, 113 Kin Sol 845 μM $\text{clogP (MoKa)} 0.93$	

Figure 3.4. Comparison of calculated logP (MoKa) and measured kinetic solubility for furan and isoxazole matched pairs.

Table 3.5. A summary of data obtained from competitive ligand-observed NMR experiments performed with modified quinoxaline analogues. Fragments were tested at either 500 μM , 200 μM or 50 μM depending on aqueous kinetic solubility (Kin. Sol. μM). ^a $n = 1$ unless otherwise indicated (arithmetic mean with \pm SD error for $n > 1$); ^b competition with 3BP2 peptide (200 μM), $n = 1$ unless otherwise indicated (arithmetic mean with \pm SD error for $n > 1$); ^c Decrease to baseline and inversion to positive phase indicates binding, minimal decrease to baseline indicates non-binding; ^d signal recovery indicates competitive binding.

Fragment 	Kin. Sol. (μM)	Assay Conc. (μM)	clogP (MoKa)	CPMG	CPMG	WaterLOGSY	WaterLOGSY
				+ protein ^a	+ competitor ^b	+ protein ^c	+ competitor ^d
 CCT170746, 28	898	500	1.0	20% \pm 4% ($n = 9$)	5% \pm 3% ($n = 8$)	Decrease to baseline	Signal recovery
 CCT170746, 28	898	200	1.0	26% \pm 8% ($n = 5$)	8% \pm 4% ($n = 5$)	Decrease to baseline	Signal recovery
 CCT170746, 28	898	50	1.0	29% \pm 7% ($n = 6$)	9% \pm 7% ($n = 6$)	Not observed	Not observed

Fragment 	Kin. Sol. (μM)	Assay Conc. (μM)	clogP (MoKa)	CPMG	CPMG	WaterLOGSY	WaterLOGSY
				+ protein ^a	+ competitor ^b	+ protein ^c	+ competitor ^d
 CCT373723, 46	918	500	1.3	19% ± 0% (n = 2)	10%	Inversion to positive phase	Partial signal recovery
 CCT375669, 91	882	500	1.9	19%	6%	Decrease to baseline	Partial signal recovery
 CCT375670, 92	848	500	2.2	7%	0%	Minimal decrease	-
 CCT375671, 93	924	500	2.0	10%	3%	Minimal decrease	-
 CCT376428, 94	869	500	1.2	34%	11%	Poor S:N ratio	Poor S:N ratio
 CCT376429, 95	1129	500	0.15	1%	0%	Minimal decrease	-
Fragment 	Kin. Sol. (μM)	Assay Conc. (μM)	clogP (MoKa)	CPMG	CPMG	WaterLOGSY	WaterLOGSY
+ protein ^a				+ competitor ^b	+ protein ^c	+ competitor ^d	
 CCT375994, 96	885	500	0.75	22%	5%	Minimal decrease	-
 CCT375852, 97	394	200	1.4	34%	4%	Decrease to baseline	Partial signal recovery
 CCT375550, 98	877	500	2.1	17%	3%	Decrease to baseline	Partial signal recovery
Fragment 	Kin. Sol. (μM)	Assay Conc. (μM)	clogP (MoKa)	CPMG	CPMG	WaterLOGSY	WaterLOGSY
+ protein ^a				+ competitor ^b	+ protein ^c	+ competitor ^d	
 CCT390521, 100	559	500	1.9	0%	0%	Minimal decrease	-
 CCT391204, 101	67	50	1.6	0%	41% (interference)	Not observed	Not observed

 CCT393089, 102	820	500	0.62	38%	28% (13% excluding 6.3-6.5 ppm)	Decrease to baseline	Signal recovery
 CCT393090, 103	178	200	-0.54	23%	19% (3% excluding 6.3-6.5 ppm)	Decrease to baseline	Signal recovery
 CCT391081, 112	872	500	0.93	48% ± 3% (n = 2)	12% ± 3% (n = 2)	Decrease to baseline	Signal recovery
 CCT391083, 113	845	500	0.93	15%	5%	Poor S:N ratio	Poor S:N ratio

Of the quinazoline matched pairs tested, the three methylated compounds (**91**, **93** and **94**) maintained competitive binding comparable to control fragment **28** and the parent quinazoline **46**, whilst introduction of 4-chlorofuran (**92**) and furan replacement with the oxazole (**95**) abolished binding to TNKS2 ARC4. Compared to the quinoxaline matched pairs, three of the quinazoline analogues tested (**92**, **93** and **94**) showed contrasting SAR, suggesting that the two core motifs could occupy distinct binding modes within the TNKS2 ARC4 substrate binding pocket.

Therefore, results from testing substituted quinoxaline analogues in combination with either the furan or isoxazole were assessed to gain further understanding of the quinoxaline series binding mode (Table 3.5). Introduction of an additional nitrogen (**96**) in the ring was tolerated and substituting with a methyl group in the 7-position (**97**) showed increased binding to TNKS2 ARC4, as did replacement of the quinoxaline with benzodioxane (**102**). Replacement of the quinoxaline with the 1,4-dihydroquinoxaline-2,3-dione motif from fanapanel maintained competitive binding but did not result in significantly increased binding for **103**, suggesting different binding modes and interactions are made by these two cores in the different fragment series. Whilst substituting at both the 2- and 3- positions with methyl groups (**98**) maintained competitive binding, larger ethyl groups and 2,3-dimethoxy substitution was not tolerated and abolished fragment binding to TNKS2 ARC4 (**100** and **101**). However, introduction of 2- and 3-methoxy substitutions independently (**112** and **113**) was tolerated, with a preference for

substitution in the 3-position evident from testing CCT391081 (**112**), which showed increased binding to TNKS2 ARC4 compared to CCT170746 (**28**).

Energy minimisation studies of CCT375550 (**98**) and CCT390521 (**100**) were performed in MOE to rationalise the observed SAR for these analogues against the hypothesised binding modes from *in silico* docking of CCT170746 (**28**). The quinoxaline substituents were added to the chemical structure of **28** in binding mode 1 and binding mode 5 using the Builder panel of MOE.¹⁹⁸ This generated the structures of fragments **98** and **100** in binding modes 1 and 5, which were then energy minimised using the Minimize function in the Builder panel.¹⁹⁸ Introduction of the 2,3-dimethyl substitution was tolerated in binding mode 1 and **98** maintained key interactions of **28** with TNKS2 ARC4 upon energy minimisation (Figure 3.5a). However, 2,3-diethylsubstitution of the quinoxaline fragment introduced clashes with the central patch surface and **100** shifted significantly upon energy minimisation, with the central amide no longer stacked within the tyrosine residues of the glycine sandwich region (Figure 3.5b). Upon energy minimisation of **98** and **100** against binding mode 5, in which the quinoxaline orientation is flipped, both 2,3-dimethyl and 2,3-diethyl substitutions were tolerated as the alkyl groups pointed into a solvent exposed region. Therefore, the SAR from introduction of 2,3-disubstitutions provided further support that binding mode 1 was the more probable binding pose occupied by the fragments.

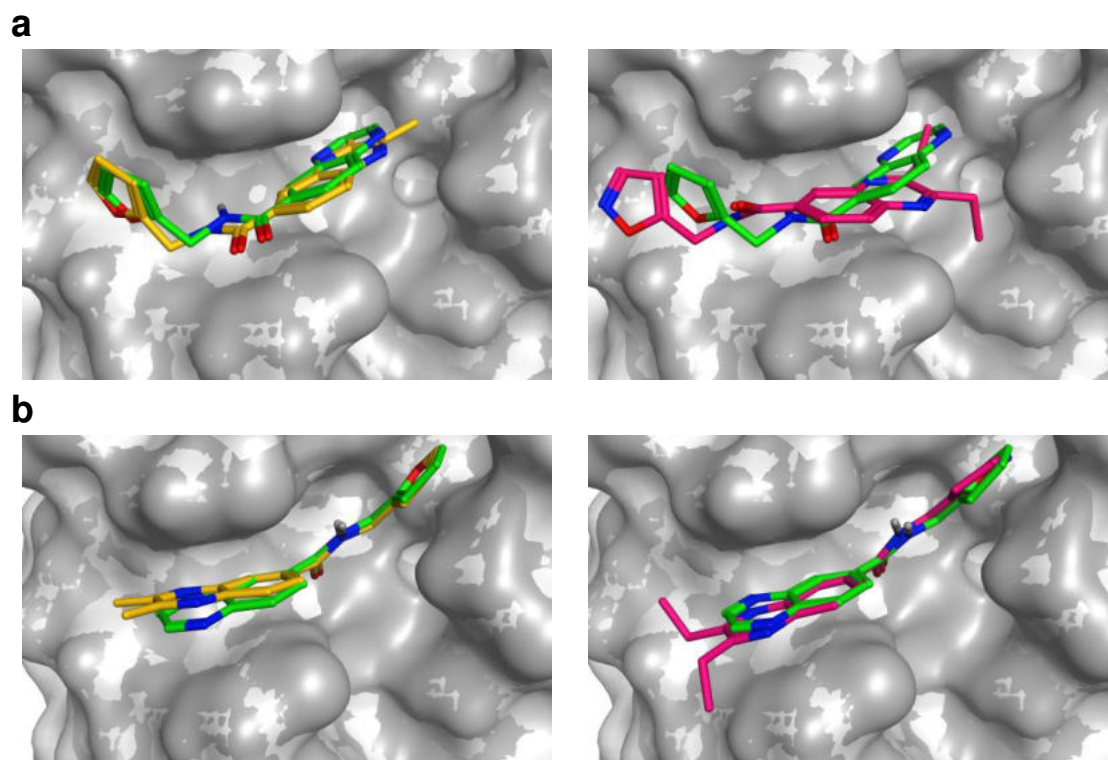
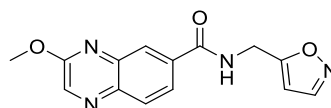
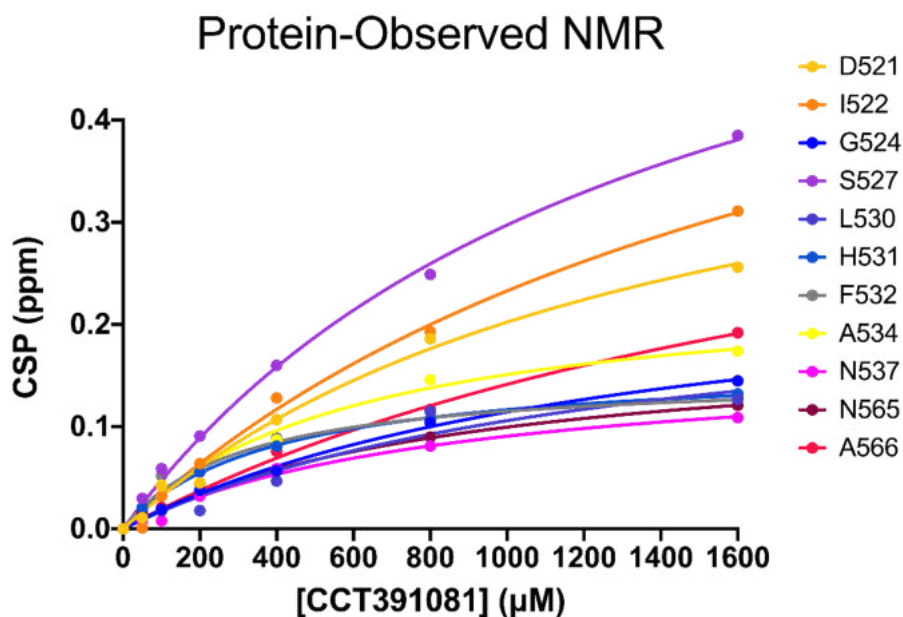


Figure 3.5. Energy minimised structures (not docked) of quinoxaline substituted fragments, CCT375550 (98) and CCT390521 (100). Energy minimised structures of **98** (light orange) and **100** (dark pink) generated using the Minimize function in the Builder panel in MOE against **a**) binding mode 1 and **b**) binding mode 5 from *in silico* docking of CCT170746 (**28**) (green) against TNKS2 ARC4 (PDB: 3WTR).

3.2.4 Protein-observed NMR with CCT391081 (**112**)

Fragment CCT391081 (**112**) was selected for protein-observed NMR to determine whether an increase in average signal intensity reduction in the ligand-observed NMR to ~50% reduction correlated with increased fragment binding affinity. The binding affinity of **112** was determined from a series of ^1H - ^{15}N HSQC spectra of ^{15}N -labelled TNKS2 ARC4 as discussed in section 2.7.3. In total, 16 correlation peaks belonging to backbone amide ^1H - ^{15}N bonds of TNKS2 ARC4 showed significant shifting ($\Delta d > \text{average} + 1\sigma$) in the presence of increasing concentrations of **112**, and K_d values for these individual peaks were determined, ranging from 310 μM to 2260 μM (Figure 3.6). The final average K_d was determined as $1170 \pm 620 \mu\text{M}$ from 11 out of the 16 peaks, as 5 peaks were excluded due to poor curve fits.



CCT391081 (112)

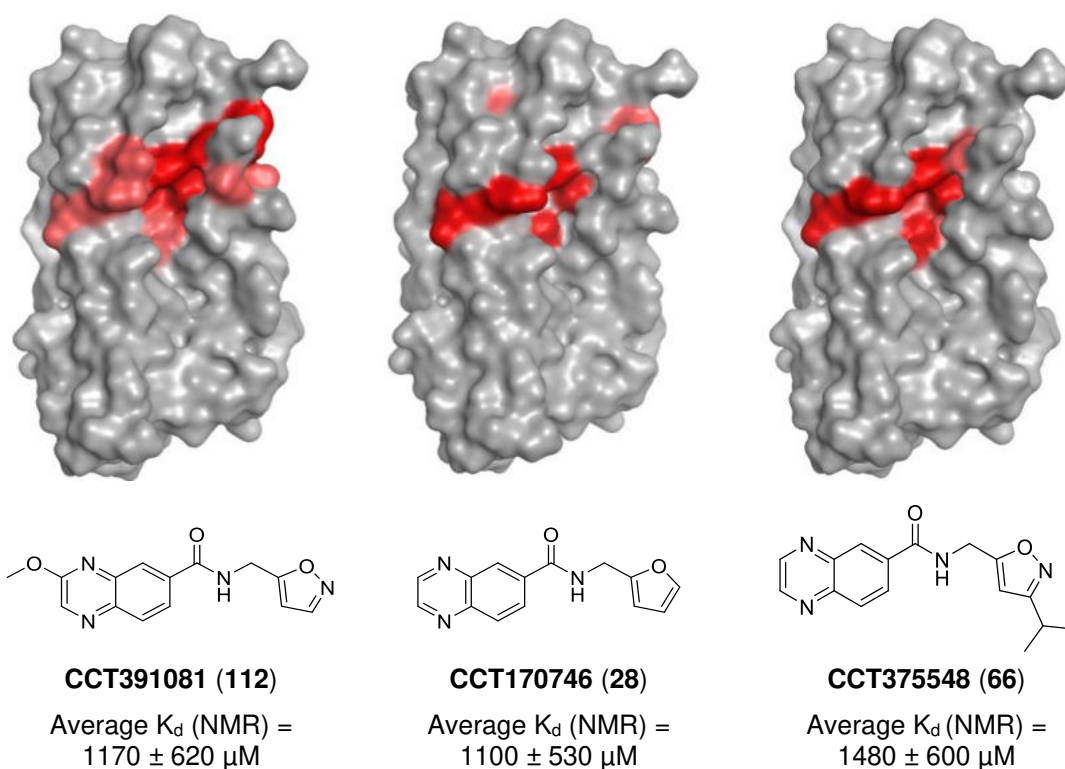
Average K_d (NMR) = $1170 \pm 620 \mu\text{M}$

Figure 3.6. Binding affinity of CCT391081 (112) determined by protein-observed NMR. Structure of CCT391081 (**112**) with K_d determined by protein-observed NMR, calculated from the average K_d of each residue which showed significant CSPs upon fragment binding ($\Delta d > \text{average} + 1\sigma$). 5 residues (K501, Q526, A533, Y526 and C567) were excluded from average K_d determination due to either incomplete 95% CI calculations or curve fits with $R^2 < 0.90$.

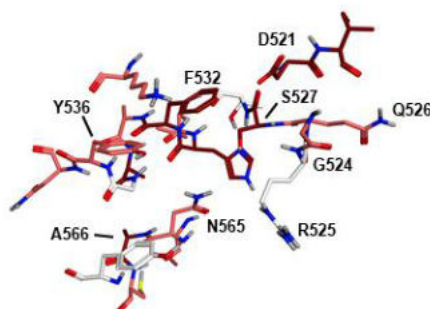
CCT391081 (**112**) therefore showed a comparable K_d to fragment hit CCT170746 (**28**), despite the difference in average signal reduction from the relaxation-edited ligand-observed NMR assay (**28**: 20% ($n = 9$) vs **112**: 48% ($n = 2$)). A binding site heat-map of CSP data from ^1H - ^{15}N HSQC NMR revealed that titration of **112** induced notable shifting of several central patch residues which had not shifted in response to titration of any other fragments, namely G524 and Q526 which together with residues D521, R525 and S527 form a hydrophilic sub-pocket of the central patch (Figure 3.7a/b). Fragment **112** also induced shifting in NH amide signals for the five key residues which shifted in response to the modified furan fragments (S527, F532, Y536, N565 and A566). *In silico* docking of **112** was then performed using the Dock panel in MOE, as described in section 2.7.4.¹⁹⁸ As

previously, the TNKS2 ARC4 structure was selected as the receptor and the docking site was selected as the five residues which showed CSPs ($\Delta d > \text{average} + 1\sigma$) upon ligand titration for all fragments tested thus far (S527, F532, Y536, N565 and A566). The top-scoring docking pose generated for CCT391081 (**112**) showed overlap with binding mode 1 from *in silico* docking of CCT170746 (**28**). It also positioned the 3-methoxy substituent towards the central patch sub-pocket, which was consistent with CSPs from protein-observed NMR (Figure 3.7b).

a



b



c

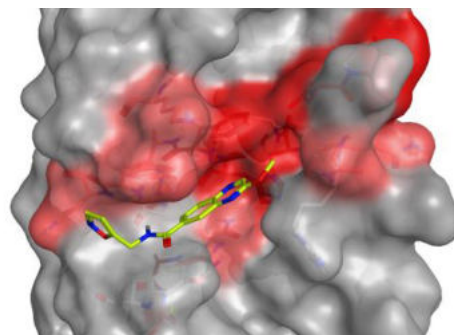
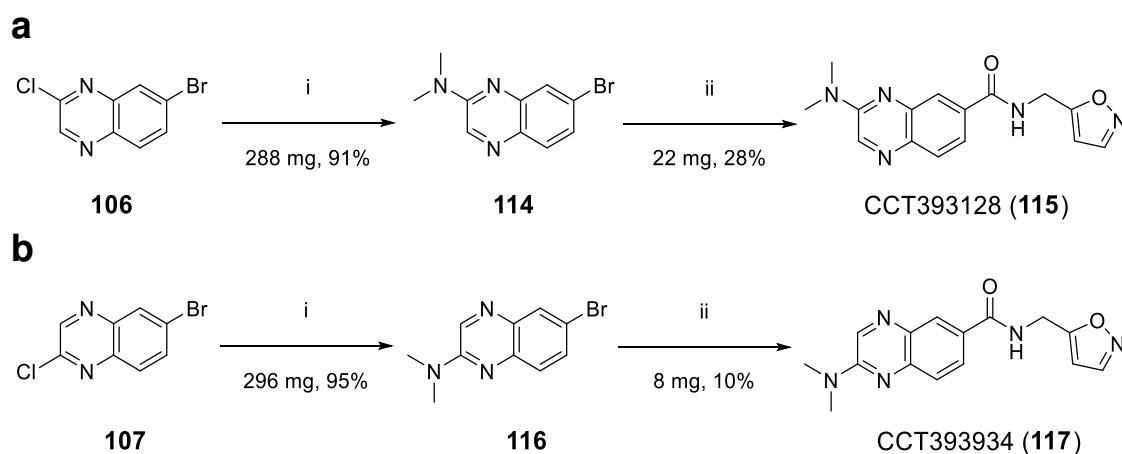


Figure 3.7. Protein-observed NMR derived binding-site map of CCT391081 (112). **a)** Surface heat-maps for fragments CCT391081 (**112**), CCT170746 (**28**) and CCT375548 (**66**) produced in MOE by mapping residues which showed significant CSPs ($\Delta d > \text{average} + 1\sigma$, pink; $\Delta d > \text{average} + 2\sigma$, red) upon fragment binding onto the surface representation of TNKS2 ARC4 (PDB: 3TWR). **b)** Residues from crystal structure of TNKS2 ARC4 (PDB: 3TWR) which showed significant CSPs ($\Delta d > \text{average} + 1\sigma$, pink; $\Delta d > \text{average} + 2\sigma$, red) upon fragment binding. **c)** Top scoring pose from MOE docking of **112** (neon yellow) against TNKS2 ARC4, constrained to residues which show significant CSPs ($> 2\sigma$) upon fragment binding.

3.3 Introduction of dimethylamino quinoxaline substitution and identification of a higher affinity fragment CCT393128 (**115**)

To further investigate the SAR from substitution at the 2- and 3- positions of the quinoxaline ring, two compounds were synthesised with a dimethylamino substituent replacing the methoxy in compounds CCT391081 and CCT391083 (**112** and **113**). Compounds CCT393128 (**115**) and CCT393934 (**117**) were synthesised in two-steps using Pd-catalysed aminocarbonylation to form the central amide bond, in a similar method to the synthesis of 2- and 3-methoxy substituted matched pairs (**112** and **113**) (Scheme 3.3a and 3.3b).

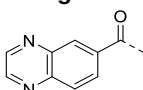
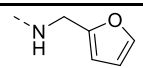
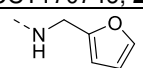
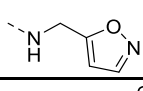
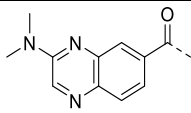
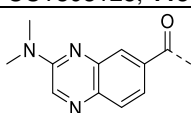
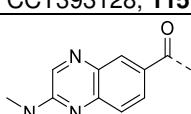


Scheme 3.3. Synthesis of 2- or 3-dimethylamino quinoxaline-6-carboxamide fragments via Pd-catalysed aminocarbonylation. **a)** Synthesis of 3-(dimethylamino)-*N*-(isoxazol-5-ylmethyl)quinoxaline-6-carboxamide, CCT393128 (**115**). Reagents and conditions: i) HNMe₂ (2M in THF), DMF, 80 °C, 4 h; ii) Isoxazol-5-ylmethanamine HCl, CO (g), DIPEA, [XantPhos Pd(allyl)]Cl (5 mol%), 1,4-dioxane, 80 °C, 2.5 h. **b)** Synthesis of 2-(dimethylamino)-*N*-(isoxazol-5-ylmethyl)quinoxaline-6-carboxamide, CCT393934 (**117**). Reagents and conditions: i) HNMe₂

(2M in THF), DMF, 80 °C, 4 h; ii) Isoxazol-5-ylmethanamine HCl, CO (g), DIPEA, XantPhos Pd G4 (5 mol%), 1,4-dioxane, 80 °C, 4 h.

A preference for substitution at the 3- position over the 2- substitution was observed from testing of compounds **115** and **117** in ligand-observed NMR (Table 3.6). Introduction of the 3-dimethylamino substituent showed significantly increased binding of CCT393128 (**115**) to TNKS2 ARC4 compared to CCT170746 (**28**), demonstrated by a reduction in average signal intensity in the relaxation-edited method of 80% and an inversion of ligand signals in the waterLOGSY experiment when tested at 500 μ M. Meanwhile, the same substituent in the 2-position abolished binding of CCT393934 (**117**) to TNKS2 ARC4 and resulted in a compound with lower measured kinetic solubility compared to its regioisomer **115**. CCT393934 (**117**) was therefore tested at 50 μ M in the ligand-observed NMR assay and signals could not be observed in the waterLOGSY experiment. Whilst a valid comparison could still be made between the two compounds tested at different concentrations in the relaxation-edited assay, as shown by control fragment **28** which shows a comparable 20-30% reduction in average signal intensity when tested at both 50 μ M and 500 μ M, CCT393128 (**115**) was also tested at 50 μ M which confirmed the large difference in average signal reduction between regioisomers **115** and **117** (Table 3.6, CPMG + protein).

Table 3.6. A summary of data obtained from competitive ligand-observed NMR experiments performed with -NMe₂ substituted quinoxaline analogues. Fragments were tested at either 500 μ M or 50 μ M depending on aqueous kinetic solubility (Kin. Sol. μ M). ^a n = 1 unless otherwise indicated (arithmetic mean with \pm SD error for n > 1); ^b competition with 3BP2 peptide (200 μ M), n = 1 unless otherwise indicated (arithmetic mean with \pm SD error for n > 1); ^c Decrease to baseline and inversion to positive phase indicates binding, minimal decrease to baseline indicates non-binding; ^d signal recovery indicates competitive binding.

Fragment 	Kin. Sol. (μ M)	Assay Conc. (μ M)	clogP (MoKa)	CPMG	CPMG	WaterLOGSY	WaterLOGSY
				+ protein ^a	+ competitor ^b	+ protein ^c	+ competitor ^d
 CCT170746, 28	898	500	1.0	20% \pm 4% (n = 9)	5% \pm 3% (n = 8)	Decrease to baseline	Signal recovery
 CCT170746, 28	898	50	1.0	29% \pm 7% (n = 6)	9% \pm 7% (n = 6)	Not observed	Not observed
Fragment 	Kin. Sol. (μ M)	Assay Conc. (μ M)	clogP (MoKa)	CPMG	CPMG	WaterLOGSY	WaterLOGSY
				+ protein ^a	+ competitor ^b	+ protein ^c	+ competitor ^d
 CCT393128, 115	861	500	0.95	80% \pm 4% (n = 2)	64% \pm 5% (n = 2)	Inversion to positive phase	Decrease in positive phase
 CCT393128, 115	861	50	0.95	85%	31%	Not observed	Not observed
 CCT393934, X	47	50	0.95	6%	3%	Not observed	Not observed

It was also observed that CCT393128 (**115**) only exhibited partial competition when tested at 500 μ M in a 2.5-fold excess over the 3BP2 peptide competitor at 200 μ M (IC₅₀ = 22 μ M) but showed a greater recovery of free ligand signals when tested at 50 μ M with the competitor in excess (Table 3.6, CPMG + competitor). Therefore, it was hypothesised that **115** does show competitive binding however due to its predicted stronger binding affinity to TNKS2 ARC4 from the ligand-observed NMR assay, an excess of competitor was required for greater displacement of **115** from the protein-ligand complex. This can be rationalised according to the binding equilibria for competitive experiments shown in Figure

3.8.²⁰⁷ For an inhibitor (or competitor) and ligand with comparable binding affinities, K_I and K_D respectively, increasing the concentration of inhibitor with respect to ligand will favour the formation of the protein-inhibitor complex, therefore increasing the concentration of free ligand.

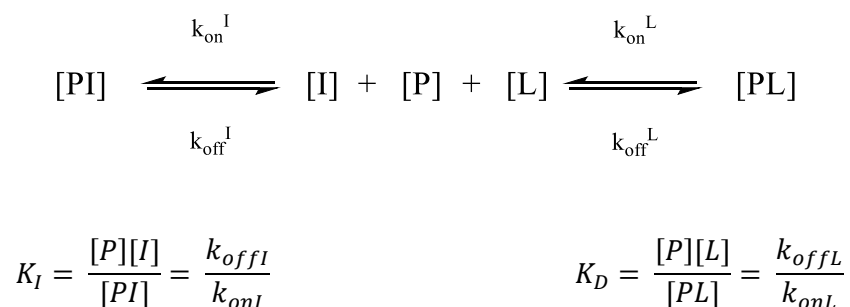
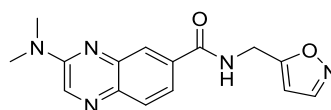
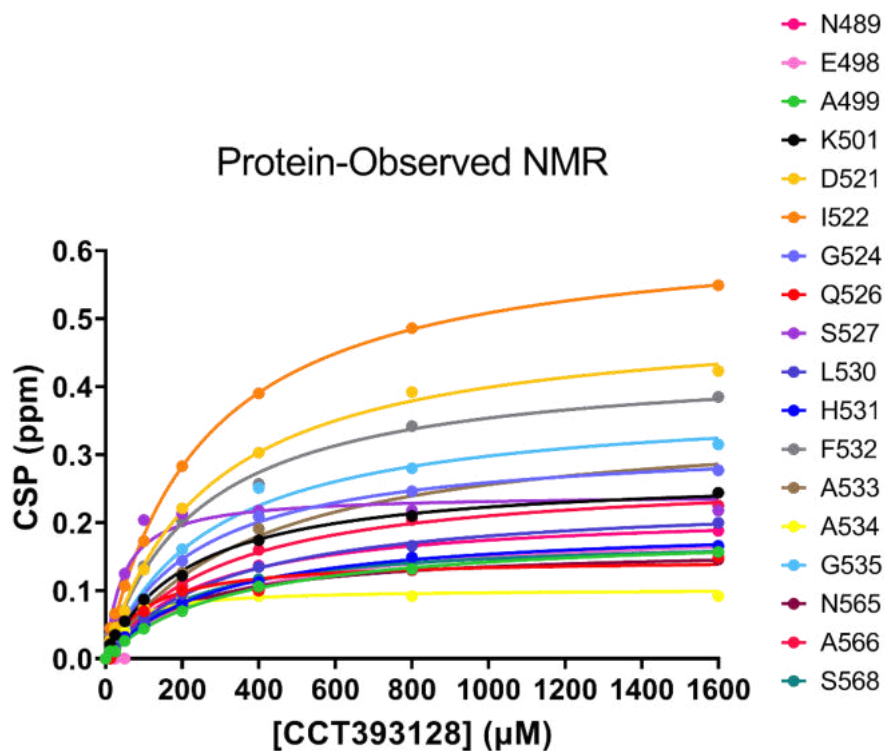


Figure 3.8. Binding equilibria and equilibrium dissociation constants for competitive ligand binding experiments. The competitor inhibitor (I) and ligand (L) compete for the same binding site of a protein (P). Figure adapted from Peng, J. W. *et al*, 2004.²⁰⁷

The reduction in average signal intensity between compound in the absence versus presence of TNKS2 ARC4 from relaxation-edited ligand-observed NMR observed for CCT393128 (**115**) was comparable to the literature-reported ARC-binding fanapanel (CCT391211, **31**) with a K_d of $100 \pm 60 \mu\text{M}$ determined from protein-observed NMR. The binding affinity of **115** was also determined using ^1H - ^{15}N HSQC protein-observed NMR and an average K_d of $240 \pm 90 \mu\text{M}$ was calculated, identifying a 5-fold higher affinity compound and the first sub-millimolar ARC-binder based on CCT170746 (**28**) (Figure 3.9). In total, 18 correlation peaks showed significant CSPs in response to **115** with the K_d values for each peak used in the calculation of the average K_d , ranging from $47 \mu\text{M}$ to $389 \mu\text{M}$. Therefore, as hypothesised, a greater ligand signal reduction ($> 80\%$) observed in the relaxation-edited NMR correlated with identification of a fragment scaffold with a 5-fold higher binding affinity compared with fragment hit **28**.



CCT393128 (115)

Average K_d (NMR) = $240 \pm 90 \mu\text{M}$

Figure 3.9. Binding affinity of CCT393128 (115) determined by protein-observed NMR. Structure of CCT393128 (115) with K_d by protein-observed NMR, calculated from the average K_d of each residue which showed significant CSPs upon fragment binding ($\Delta d > \text{average} + 1\sigma$).

3.4 Characterisation of lead fragment CCT393128 (115) binding to the ARC domain

Different biophysical techniques were then used to characterise the binding site and binding mode of CCT393128 (115), prior to synthesis of further analogues based on the higher affinity 3-alkylaminoquinoxaline scaffold.

3.4.1 Binding site mapping and docking studies from protein-observed NMR

The binding site of CCT393128 (**115**) was elucidated in the first instance by mapping residues which corresponded to ^1H - ^{15}N peaks that had shown significant chemical shift perturbations from titrations with **115** on to a crystal structure surface of TNKS2 ARC4. The resulting binding heat-map revealed interaction of the compound with key central patch residues of the 3BP2 TBM peptide binding site as for previous ligands (Figure 3.10). Fragment **115** also showed CSPs from residues in the upper lipophilic extension of the central patch, and from G535 belonging to the glycine sandwich region of the ARC binding pocket. This provided further evidence that **115** maintained binding in the substrate recognition pocket of the ARC domain. Furthermore, the binding site heat-maps generated from protein-observed NMR with CCT391081 (**112**) and CCT393128 (**115**) showed considerable overlap, with substantial CSPs for 13 common residues from TNKS2 ARC4 observed upon titrations with both compounds. Interestingly, whilst most other fragments tested showed a response from Y536 in the glycine sandwich region, this residue did not respond in the titration with **115** (Figure 3.10).

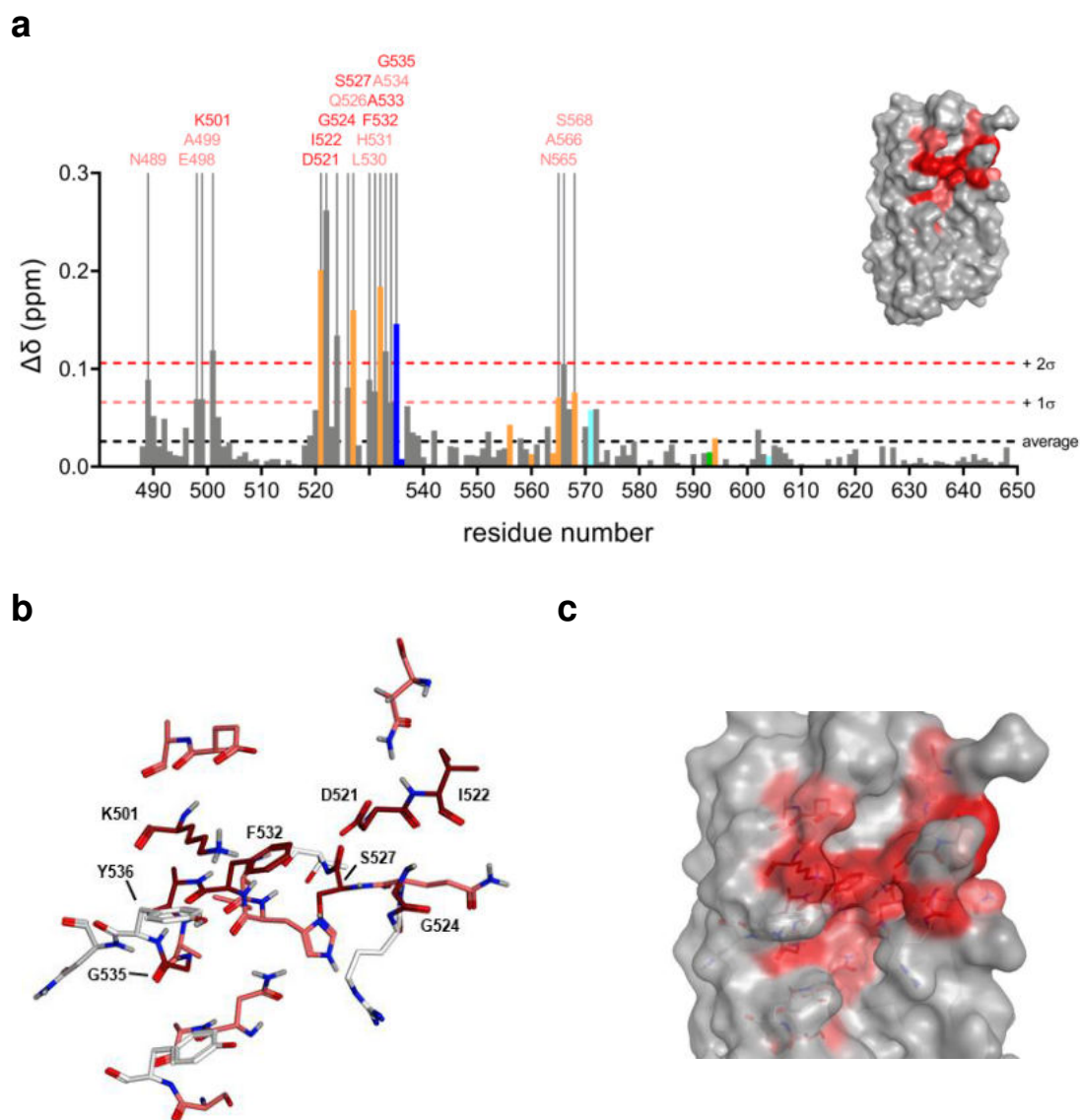
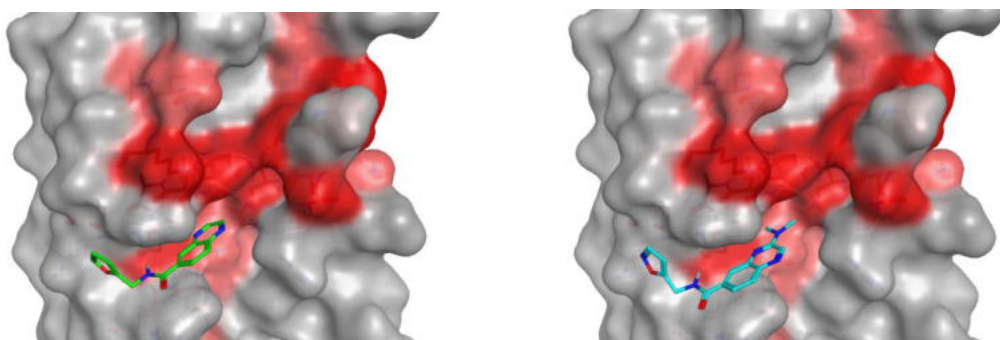


Figure 3.10. Protein-observed NMR derived binding-site map of CCT393128 (115). **a**) Plot of CSPs ($\Delta\delta > \text{average} + 1\sigma$, pink; $\Delta\delta > \text{average} + 2\sigma$, red) from titration of **115** against ^{15}N TNKS2 ARC4 (50 μM) (C-terminal contacts, cyan; glycine sandwich, blue; central patch, orange; arginine cradle, green). **b**) Residues from crystal structure of TNKS2 ARC4 (PDB: 3TWR) which showed significant CSPs ($\Delta\delta > \text{average} + 1\sigma$, pink; $\Delta\delta > \text{average} + 2\sigma$, red) upon binding of **115**. **c**) CSPs ($\Delta\delta > \text{average} + 1\sigma$, pink; $\Delta\delta > \text{average} + 2\sigma$, red) from titration of **115** against ^{15}N TNKS2 ARC4 (50 μM) mapped onto the surface of 3BP2 bound crystal structure (PDB: 3TWR).

For *in silico* docking of CCT393128 (**115**), performed using the Dock panel in MOE, the docking site was selected as all 18 residues which had significant backbone amide CSPs (Figure 3.10a).¹⁹⁸ Out of the five top-scoring ligand-protein docking poses retained following refinement, one pose was consistent

with binding mode 1 from *in silico* docking of CCT170746 (**28**) (Figure 3.11a). A second docking pose was comparable with *in silico* docking of CCT391081 (**112**), in which the 3-dimethylamino substituent was positioned towards the hydrophilic central patch sub-pocket (Figure 3.11b).

a



b

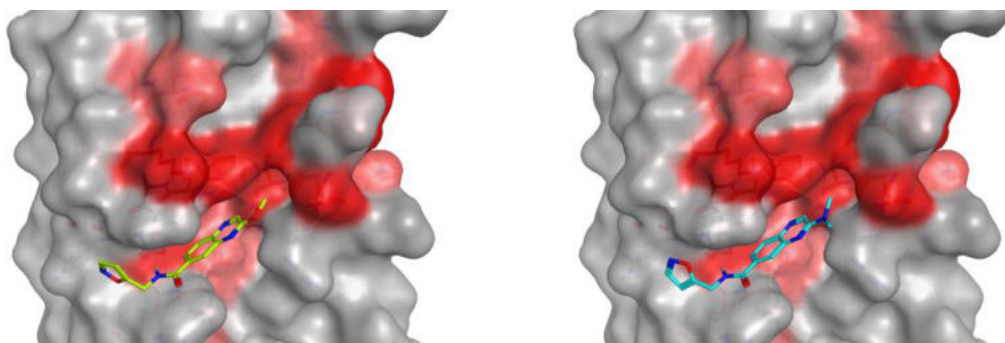
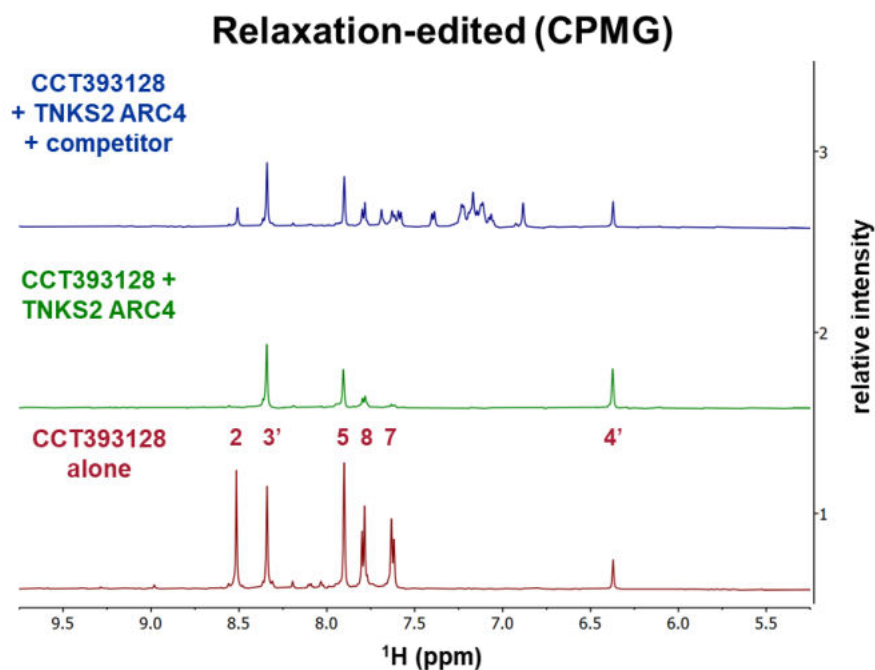


Figure 3.11. *In silico* docking of CCT393128 (115**) against TNKS2 ARC4.** *In silico* docking of **115** was performed in MOE against TNKS2 ARC4 (PDB: 3WTR). All 18 residues which showed significant CSPs ($\Delta d > \text{average} + 1\sigma$ and $\Delta d > \text{average} + 2\sigma$, pink and red) were selected as the receptor site for docking. **a**) Top scoring pose from MOE docking of CCT393128 (**115**) (blue), consistent with binding mode 1 of CCT170746 (**28**) (green). **b**) Second top scoring pose from MOE docking of CCT393128 (**115**) (blue), consistent with top scoring pose of CCT391081 (**112**) (neon yellow).

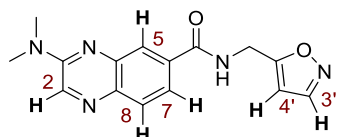
The binding epitope of CCT393128 (**115**) was hypothesised from T_2 relaxation-edited (CPMG) ligand-observed NMR, in order to differentiate between the two proposed *in silico* docking poses of **115**. The spectra obtained from relaxation-edited ligand-observed NMR experiments with **115** were inspected to suggest a binding epitope for **115** (Figure 3.12). In the relaxation-edited CPMG screening

experiments performed with **115**, an average reduction in signal intensity of 80% was calculated upon addition of TNKS2 ARC4 (Table 3.6, CPMG + protein). By comparison of the 'CCT393128 alone' and 'CCT393128 + TNKS2 ARC4' spectra, it was observed that ¹H signals of **115** assigned to aromatic quinoxaline protons 2, 7 and 8 showed a greater reduction in intensity than those assigned to the isoxazole protons 3' and 4' (Figure 3.12). Therefore, it was proposed that the isoxazole ring was less bound to TNKS2 ARC4 compared with the 3-dimethylamino quinoxaline motif. This was consistent with both poses generated from *in silico* docking of **115**, in which the 3-dimethylquinoxaline motif was in closer proximity to the residues which show significant CSPs in protein-observed NMR (Figure 3.11a/b). Additionally, quinoxaline proton 5 showed a 70% reduction in intensity, whilst all other quinoxaline protons showed 100% reduction in intensity (Figure 3.12). This supported the more probable docking pose of **115** to be that shown in Figure 3.11b, in which quinoxaline proton 5 was pointed into solvent-exposed space away from the surface of TNKS2 ARC4.

a



$$I \% = \frac{(I_{blank} - I_{protein})}{I_{blank}} \times 100$$



CCT393128 (**115**)

2-CH	100%	intensity decrease
3'-CH	36%	intensity decrease
5-CH	70%	intensity decrease
8-CH	100%	intensity decrease
7-CH	100%	intensity decrease
4'-CH	0%	intensity decrease

Figure 3.12. Relaxation-edited ligand-observed NMR for CCT393128 (115). The reduction in signal intensity (%) for each ligand ^1H proton of **115** in the presence of TNKS2 ARC4 is shown.

3.4.2 Efforts in structural characterisation by X-ray crystallography

In addition to characterisation of fragment binding by protein- and ligand-observed NMR and *in silico* docking studies, X-ray crystallography was pursued to obtain further structural information on the binding mode of the quinoxaline fragment series, including CCT393128 (**115**), to the tankyrase ARC domain. In X-ray crystallography, X-ray diffraction patterns of ligand-protein crystals are resolved to determine the structure of the complex.¹⁶³ The ligand-protein crystals

are obtained either by growing the crystals in the presence of ligand (co-crystallisation) or addition of ligand solution to protein crystals (soaking).¹⁶³

Crystal structures for tankyrase ARCs have been previously determined in both apo and TBM peptide-bound forms, demonstrating the amenability of the ARC domains for crystallisation.^{46, 61, 66, 149, 208} Co-crystal structures of TNKS2 ARC4 (488-649) with TBM peptides from numerous substrate proteins (3BP2, TERF1, MCL1, LNPEP, NUMA1 and FNBP1) have been determined, and a comparison of the TNKS2 ARC4:3BP2 crystal structure with unbound TNKS2 ARC4 (484-655) showed a fully formed peptide binding site in the apo form and minimal changes in side chain conformation of the protein upon peptide binding (Figure 3.13a/b).⁶¹ These characterised crystals of apo TNKS2 ARC4 (484-655) were previously determined to be unsuitable for soaking experiments with fragment hits identified against the ARC domains, due to crystal contacts in the peptide binding site with N-terminal tail residues from another TNKS2 ARC4 in the asymmetric unit (Figure 3.13b). Previous co-crystallisation efforts with TNKS2 ARC4 (488-649) and TNKS2 ARC4 (484-655) were also unsuccessful.^{135, 152}

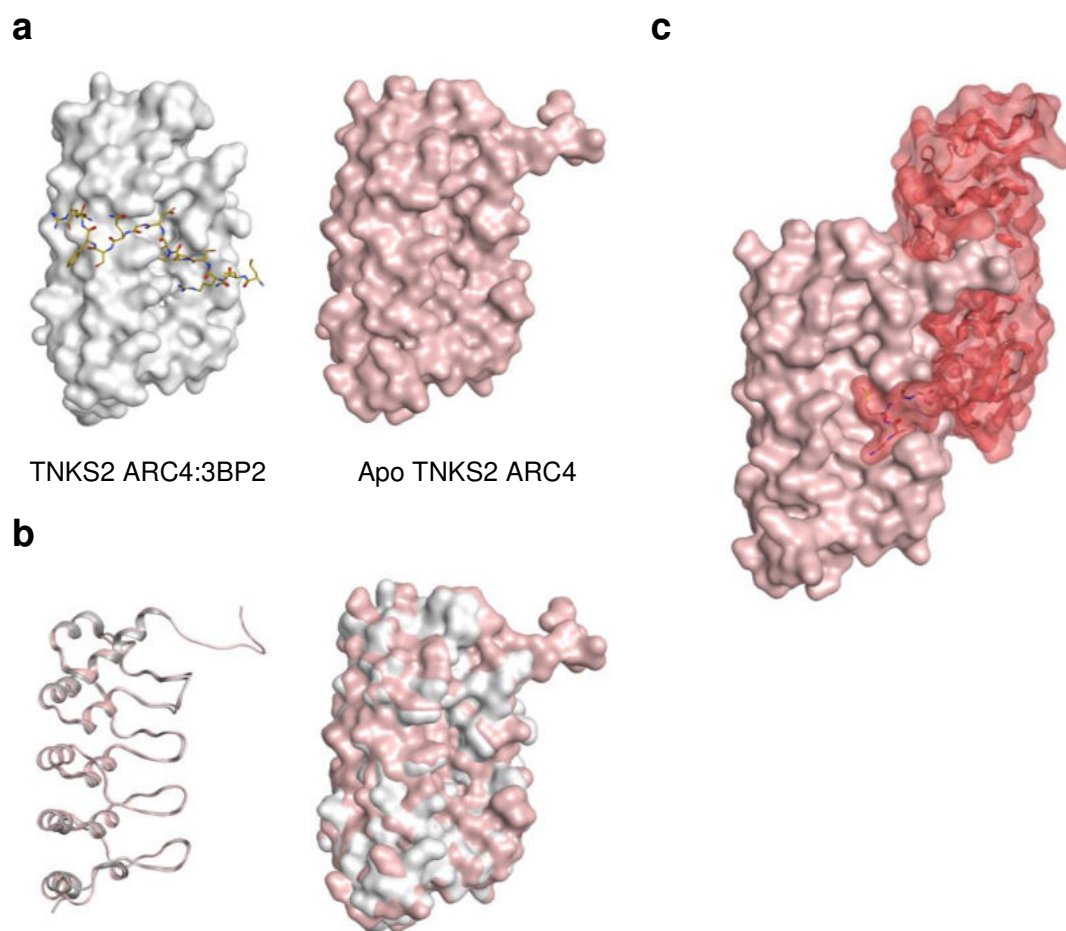


Figure 3.13. Apo and peptide-bound TNKS2 ARC4 crystal structures. a) Comparison of a crystal structure of TNKS2 ARC4 (light grey) bound to 3BP2 TBM peptide (gold) (PDB: 3TWR) with a crystal structure of apo TNKS2 ARC4 (pink) (PDB: 3TWQ). **b)** Ribbon and surface representation of the superimposition of TNKS2 ARC:3BP2 and apo TNKS2 ARC4 crystal structures. **c)** Crystal contacts of the N-terminal tail of one TNKS2 ARC4 (pink) molecule in the peptide binding site of another TNKS2 ARC4 (light pink) molecule in the asymmetric unit.

Therefore, an alternative apo tankyrase ARC domain crystal structure was required for fragment soaking experiments with the quinoxaline fragment analogues. TNKS1 ARC4 was selected for crystallisation due to its closest sequence similarity with TNKS2 ARC4, which had been used in all ligand- and protein-observed NMR fragment binding studies (Figure 3.14a). The TNKS1 ARC4 (646-807) construct required for crystallisation was produced and purified according to an established protocol, which had been used for the production of TNKS2 ARC4 (refer to section 2.5.2).¹⁹⁶ The protein was obtained at high purity

as confirmed by SDS-PAGE gel electrophoresis with a yield of 2 mg per L of TB expression culture (Figure 3.14b).

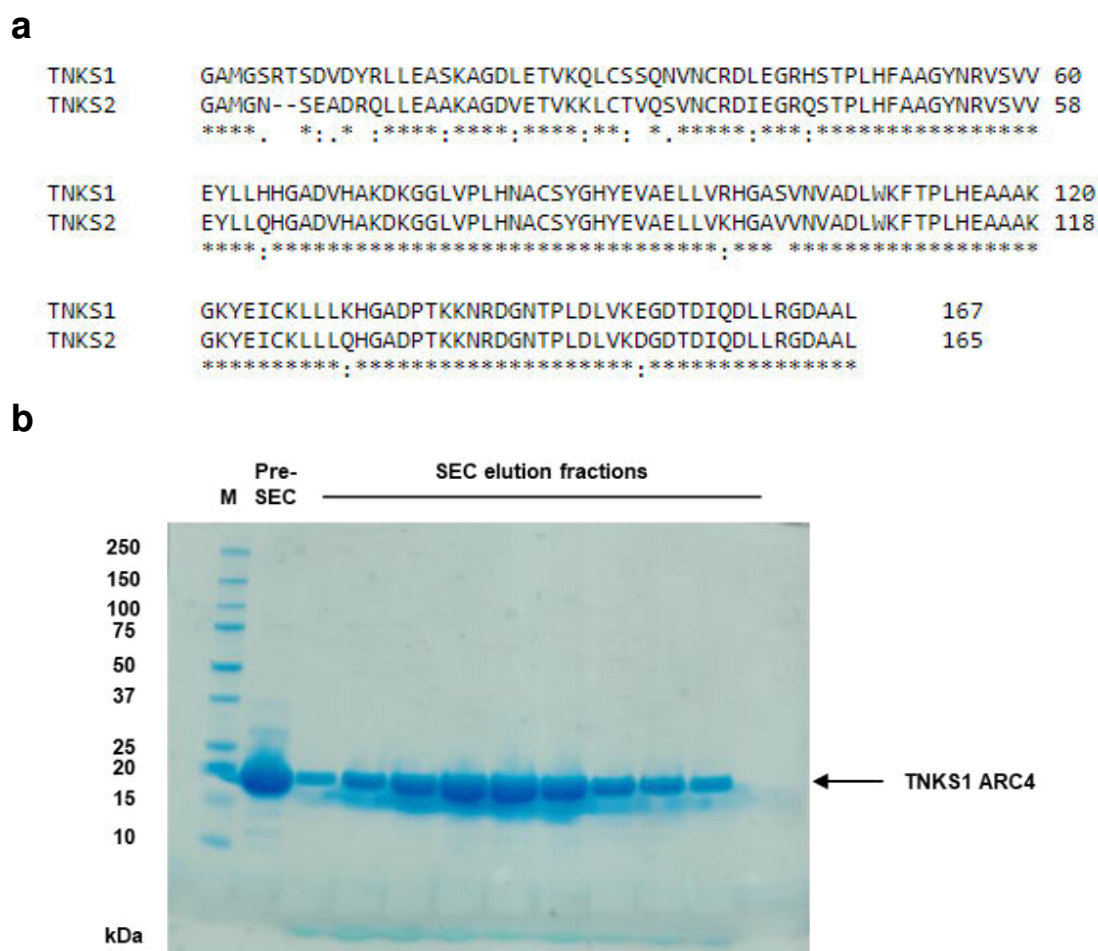


Figure 3.14. Production of TNKS1 ARC4 (646-807) for crystallography. **a)** Sequence alignment of TNKS1 ARC4 (646-807) with TNKS2 ARC4 (488-649) using Clustal Omega (* = identical, : = very similar, . = similar). **b)** SDS-PAGE analysis of elution fractions containing TNKS1 ARC4 (646-807) following purification by size exclusion chromatography, stained with Coomassie (M = marker, SEC = size exclusion chromatography).

Crystallisation studies with TNKS1 ARC4, described in the following discussion, were undertaken by Stephen Hearnshaw (ICR Structural Biology). An initial broad screening of crystallisation buffers in sparse-matrix screens identified conditions which yielded TNKS1 ARC4 crystals within a week (0.1M HEPES pH 7.5, 20% 2-propanol, 20% PEG 4000). These crystallisation conditions were then optimised to improve the quality of TNKS1 ARC4 crystals and to improve crystal

handling by reducing the concentration of 2-propanol (0.1M HEPES pH 7, 0→7% 2-propanol, 8→13% medium molecular weight PEG smear). Sitting drop crystallisation experiments were set up using Swissci 3 lens crystallisation plates. In this format, TNKS1 ARC4 crystals grew within a week and were harvested using ethylene glycol (25% final concentration) as a cryoprotectant (Figure 3.15a). X-ray crystallography was performed with the apo TNKS1 ARC4 crystals which gave datasets that routinely diffracted to resolutions of between 1.2 to 1.5 Å. These crystals constituted a novel crystal form of TNKS1 ARC4 with a solvent-accessible predicted fragment binding site pocket (Figure 3.15b).

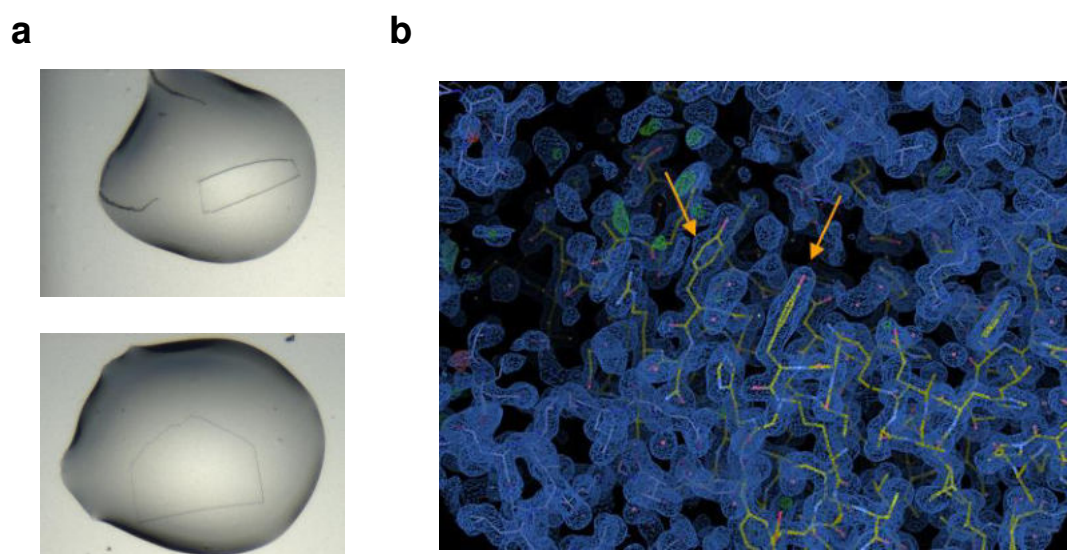


Figure 3.15. TNKS1 ARC4 crystals and structure determination. a) TNK1 ARC4 crystals with planar morphology grown in sitting drop crystallisation experiments [Stephen Hearnshaw, ICR Structural Biology]. **b)** 2Fo-Fc density map from apo TNKS1 ARC4 crystals. Glycine sandwich residues (Y536 and Y569) are highlighted (orange arrows) [Stephen Hearnshaw, ICR Structural Biology].

Fragment soaking experiments were then performed with all compounds which had been characterised in protein-observed NMR experiments: CCT170746 (**28**), CCT375548 (**66**), CCT390160 (**70**), CCT375867 (**75**), CCT391211 (**31**), CCT391081 (**112**) and CCT393128 (**115**) [Stephen Hearnshaw, ICR Structural Biology]. This included the initial fragment hit CCT170746 (**28**) ($K_d = 1100 \mu\text{M}$), as well as higher affinity 3-dimethylamino quinoxaline CCT393128 (**115**) ($K_d =$

240 μM) and CCT391211 (**31**) (fanapanel, $K_d = 100 \mu\text{M}$) fragments. Additionally, fragment soaking was also attempted with CCT390447 (**69**), with 4-bromo substitution of the isoxazole motif. Fragment stock solutions (100 mM in DMSO) were added to drops in crystallisation plates containing TNKS1 ARC4 (20 mM final compound concentration) [Stephen Hearnshaw, ICR Structural Biology]. The fragments were incubated for both short (15 to 30 min) and long (3 to 4 h) soaks prior to the addition of cryoprotectant (25% ethylene glycol) and harvesting [Stephen Hearnshaw, ICR Structural Biology]. X-ray crystallography data were collected at the Diamond Light Source synchrotron (Harwell, UK). However, upon molecular replacement and refinement, none of the maps featured densities that corresponded to the fragments [Stephen Hearnshaw, ICR Structural Biology].

Following unsuccessful attempts at obtaining ligand-bound crystal structures by fragment soaking with TNKS1 ARC4, co-crystallisation was attempted [Stephen Hearnshaw, ICR Structural Biology]. For progression of the quinoxaline fragment series into potent binders of the ARC domain, it was of most interest to obtain a crystal structure of the higher affinity fragment **115**. Therefore, this compound was selected for co-crystallisation experiments. Co-crystallisation was also carried out with fanapanel (**31**), as this would allow fragment merging strategies between the two fragment scaffolds to be explored. However, fanapanel was predicted to bind in proximity to the arginine cradle residues from protein-observed NMR, and there were crystal contacts in this region of the substrate recognition pocket in the novel apo form of TNKS1 ARC4 that would very likely preclude crystal growth in the same crystal form. Compounds **31** and **115** were incubated with TNKS1 ARC4 (10 mg/mL) at 4 °C prior to setting up sitting drop crystallisation plates, but no crystals were obtained from these co-crystallisation studies [Stephen Hearnshaw, ICR Structural Biology]. Therefore, no ARC:fragment crystal structures could be determined using either fragment soaking or co-crystallisation.

Chapter 4 Further Development and Optimisation of ARC-Binders based on a Lead Fragment

The final aim of the fragment-based approach was to develop the higher affinity 3-dimethylamino quinoxaline lead fragment, CCT393128 (**115**), into a series of potent substrate binding antagonists of the ARC domain. This chapter describes the design and synthesis of two different sets of analogues based on the lead fragment and its hypothesised binding mode from *in silico* docking studies. The compounds were tested using ligand- and protein-observed NMR assays. A further aim was to determine whether the compounds were potent enough to be tested in a biochemical assay, which would provide a higher throughput method of ranking the analogues according to their affinity. A competitive fluorescence polarisation assay using a Cy5-labelled tankyrase-binding motif peptide probe was re-established to determine potency of the lead fragment analogues and identify other opportunities for fragment optimisation.

4.1 Design of analogues based on hypothesised lead fragment binding mode

In the absence of a crystal structure of lead fragment CCT393128 (**115**) bound to TNKS2 ARC4, new compounds were designed against the hypothesised binding model generated from protein-observed NMR guided *in silico* docking of **115** and CCT391081 (**112**) (Figure 4.1). The aim was to identify compounds with an improvement in binding affinity compared with **115** ($K_d = 240 \mu\text{M}$) through continued fragment growing efforts.

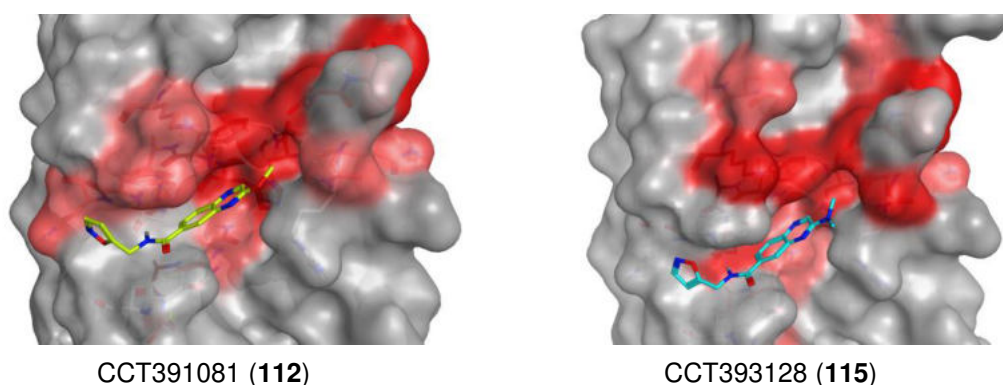


Figure 4.1. Hypothesised binding modes of CCT391081 (112) and CCT393128 (115) from *in silico* docking to the TNKS2 ARC4:3BP2 crystal structure (PDB: 3TWR).

4.1.1 Design of 3-substituted quinoxaline fragments

Further exploration around the 3-position of the quinoxaline substituent was sought and the compounds shown in Figure 4.2 were designed. From the *in silico* binding models of CCT391081 (**112**) and CCT393128 (**115**), the 3-methoxy and 3-dimethylamino substituents were positioned in the hydrophilic central patch sub-pocket of the ARC domain (Figure 4.1). Fragment growing from the 3-dimethylamino substituent of **115** was proposed, by introduction of linear and branched alkyl groups as well as unsaturated nitrogen-containing heterocycles of different sizes, to probe binding pocket restrictions around the 3-position. It was hypothesised that these substituents could access the upper lipophilic extension of the central patch and result in increased ARC binding affinity from lipophilic interactions. Compounds based on CCT391081 (**112**) were also proposed, with larger linear alkoxy substituents installed at the 3-position, despite the lower affinity of **112** compared to **115**. This was proposed to allow a comparison of SAR between O-substituted and N-substituted quinoxaline scaffolds and further rationalise whether **112** and **115** occupied equivalent binding modes as hypothesised from NMR guided *in silico* docking. The *N*-methyl furanyl amides based on **112** and **115** were proposed to study if the SAR for amide *N*-methylation was transferable between 3-substituted and unsubstituted quinoxalines. Finally, two other matched pair compounds were designed, which combined the 3-dimethylamino quinoxaline scaffold with different furan modifications, to assess the tractability of SAR between 3-dimethylamino quinoxaline and unsubstituted quinoxaline matched pair amides.

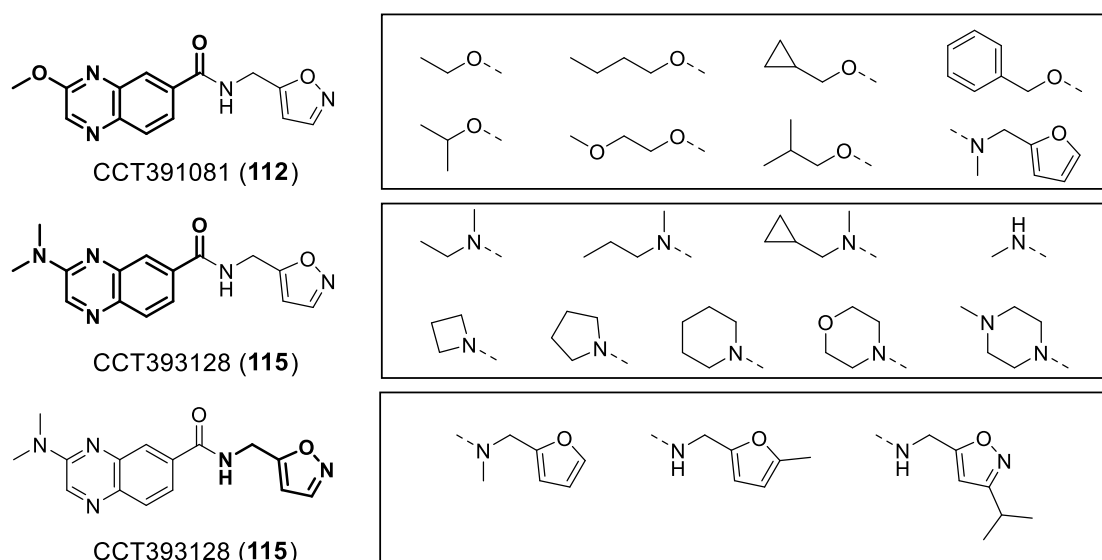


Figure 4.2. Proposed iteration of fragment optimisation based on CCT391081 (112**) and CCT393128 (**115**).** Compounds were designed to explore further substitution from the 3-position of the quinoxaline motif and understand the SAR of amide matched pairs based on **115**.

4.1.2 Design of 3-alkylamino quinoxaline peptidomimetics

In a second strategy to generate more potent compounds from lead fragment CCT393128 (**115**), replacement of the isoxazole ring was pursued. Based on binding affinity data for the fragments tested in protein-observed NMR thus far, it was hypothesised that the 3-dimethylamino quinoxaline motif contributed more binding interactions from **115** to TNKS2 ARC4, compared with the isoxazole motif. From the proposed *in silico* docking model of **115** overlaid with a crystal structure of TNKS2 ARC4 in complex with the 3BP2 16mer, it was observed that the central amide bond of **115** overlaid with the amide bond between residues 6 and 7 of the TBM peptide sequence (Figure 4.3). This highlighted an opportunity to replace the isoxazole ring by hybridisation of the 3-dimethylamino quinoxaline fragment with amino acid residues in position 7 and 8 of the TBM peptides. It was hypothesised that this could improve fragment binding affinity by growing into the C-terminal contacts region of the peptide substrate binding site.

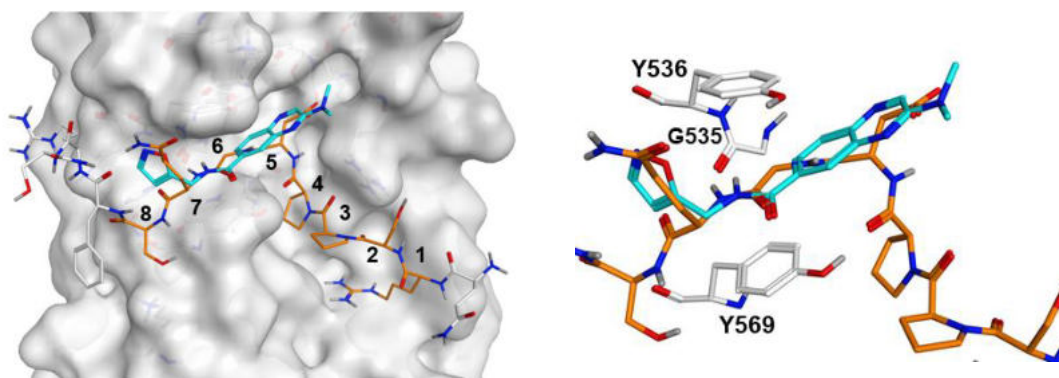


Figure 4.3. Overlay of CCT393128 (115) (docked) and 3BP2 bound to TNKS2 ARC4. The hypothesised binding mode **115** (light blue) from *in silico* docking was overlaid with the crystal structure of TNKS2 ARC4 (white) in complex with the 3BP2 TBM peptide (orange) (PDB: 3TWR).

The optimal position 7 and 8 amino acids from the TBM peptides were desired for merging with the quinoxaline-6-carboxamide. The highest affinity tankyrase binding motif peptide sequence has been previously determined from a peptide library screen of 153 fluorescently-labelled peptides using a FP assay, which originated from exchange of each residue of the 3BP2 8mer TBM peptide (RSPPDGQS) for each of the 20 amino acids in turn.⁶¹ Compared to the 3BP2 TBM peptide sequence which contains a glutamine in position 7 followed by a serine residue in position 8 of the TBM sequence ($K_d = 4.9 \pm 0.4 \mu\text{M}$), the optimised sequence was determined to be REAGD**EE** with two consecutive glutamic acid residues in positions 7 and 8 ($K_d = 0.6 \pm 0.04 \mu\text{M}$) (Figure 4.4a). Whilst all 20 amino acids were tolerated in position 8, the preference for an acidic residue (glutamate or aspartate) was rationalised from a crystal structure of TNKS2 ARC4 in complex with the MCL1 TBM peptide (RPPPIG**AE**, $K_d = 2.4 \pm 0.2 \mu\text{M}$), in which a salt-bridge interaction between the MCL1 TBM glutamate residue and K604 in TNKS2 ARC4 was observed (Figure 4.4b).⁶¹ Additionally, the reported peptide library screen showed that all 20 amino acids apart from proline were tolerated in position 7, whilst an alanine scan across the TBM octapeptide of 3BP2 showed that glutamine to alanine mutation in position 7 had no effect on the peptide binding affinity.⁶¹

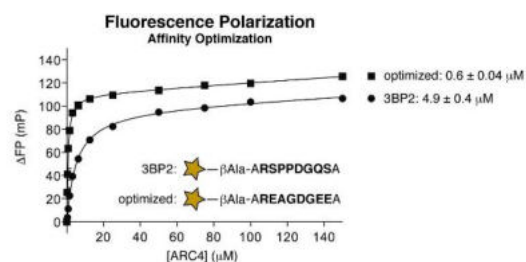
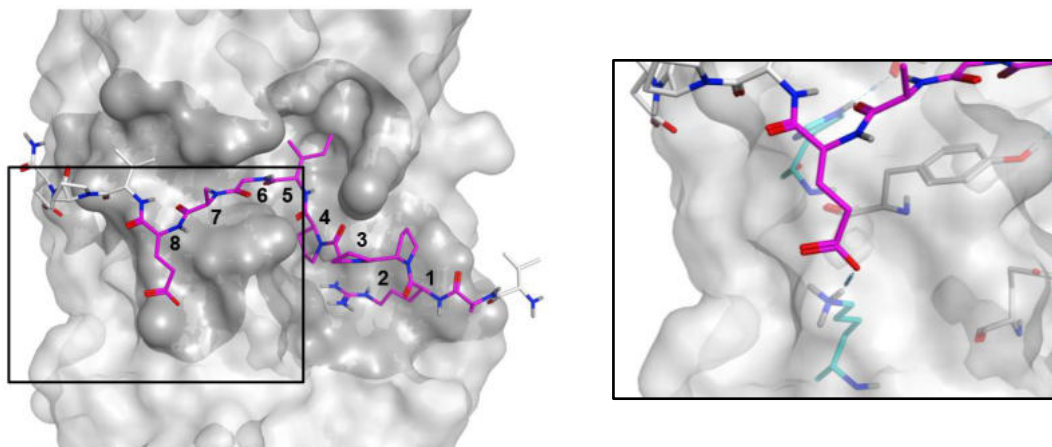
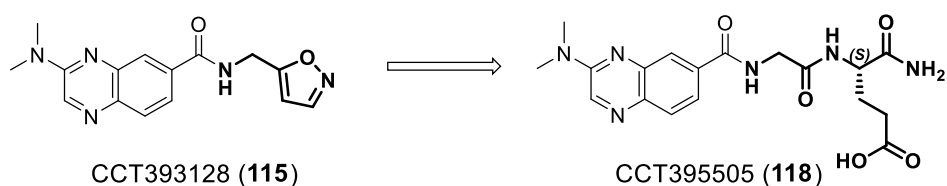
a**b**

Figure 4.4. Binding of sequence optimised and MCL1 TBM peptides to TNKS2 ARC4. **a)** The reported binding affinity (K_d) of fluorescently-labelled 3BP2 and sequence-optimised TBM peptides, determined from an FP binding assay (Figure adapted from Guettler *et al*, 2011).⁶¹ **b)** A crystal structure of TNKS2 ARC4 (white) in complex with a MCL1 TBM peptide (magenta) (PDB: 3WTU), highlighting a salt-bridge interaction between K604^{TNKS2 ARC4} (cyan) and a glutamate in position 8 of the MCL1 TBM peptide.⁶¹

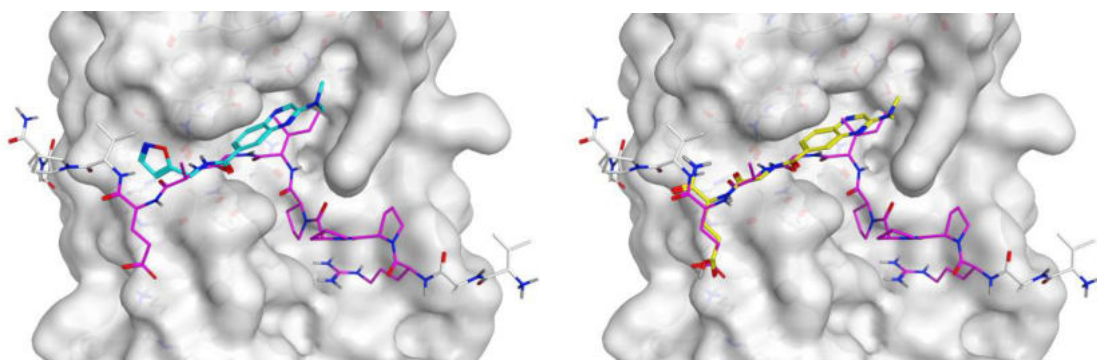
Therefore, a hybrid fragment-peptidomimetic, CCT395505 (**118**), was designed in which the 3-dimethylamino quinoxaline-6-carboxamide motif of **115** was linked to a glutamic acid motif, to potentially mimic the C-terminal salt-bridge interactions observed in the crystal structure of MCL1 in complex with TNKS2 ARC4 (Figure 4.5a). A glycine linker was incorporated between the quinoxaline-6-carboxamide unit and the 'position 8' glutamic acid motif, to mimic the 'position 7' amino acid whilst minimising unnecessary side chain functionality that was not expected to increase fragment binding affinity. *In silico* modelling of **118** against the TNKS2 ARC4:MCL1 crystal structure was performed by energy minimisation using MOE.¹⁹⁸ Firstly, *in silico* docking of **115** bound to TNKS2 ARC4:3BP2 in the

hypothesised binding mode was opened in MOE. The crystal structure of TNKS2 ARC4 in complex with MCL1 peptide was then imported into MOE and prepared using the QuickPrep panel with default parameters. The chemical structure of **115** was modified using the Builder panel in MOE to generate the structure of **118**. Energy minimisation of **118** was performed against the TNKS2 ARC4:MCL1 crystal structure using the Minimize function in MOE.¹⁹⁸ Upon minimisation, the 3-dimethylamino quinoxaline motif of **118** maintained the same position as in the docked structure of **115** bound to TNKS2 ARC4:3BP2. In addition, the glycine and glutamate residues were accommodated and a hydrogen bond between the 'position 8' glutamate and K604^{TNKS2 ARC4} was observed (Figure 4.5b). Therefore, *in silico* modelling by energy minimisation supported that the designed fragment-peptidomimetic could form interactions in the C-terminal contacts region of the ARC domain.

a



b



c

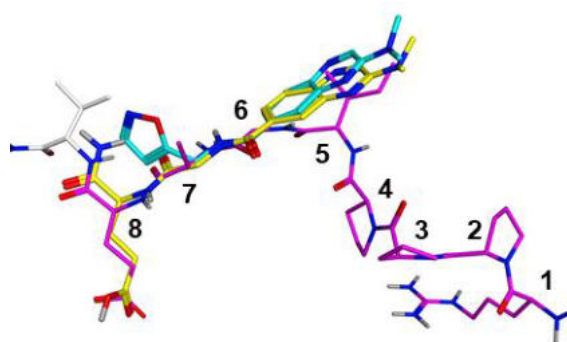


Figure 4.5. Design of hybrid fragment-peptidomimetic 118 based on CCT393128 (115). **a)** Structure of the proposed peptidomimetic compound **118** based on **115**. **b)** Energy minimisation (not docking) of peptidomimetic **118** (yellow) in MOE against the crystal structure of TNKS2 ARC4 bound to MCL1 (purple) maintained an equivalent binding pose to **115** (light blue) from *in silico* docking. **c)** Overlay of the binding poses of **115** (light blue, docking) and peptidomimetic **118** (yellow, energy minimisation) with the TNKS2 ARC4-bound crystal structure of MCL1 TBM peptide (purple).

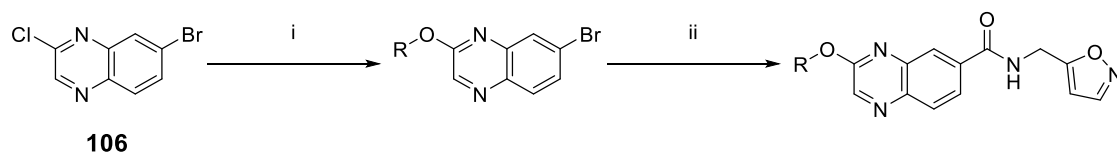
4.2 Synthesis and testing of 3-substituted quinoxaline fragments

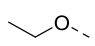
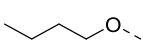
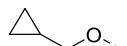
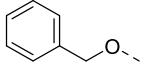
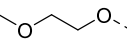
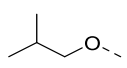
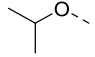
4.2.1 Synthesis of 3-alkoxy quinoxaline-6-carboxamide fragments

A summary of the synthesis of 3-alkoxy quinoxaline-6-carboxamide fragments is shown in Table 4.1. As previously reported for 3-methoxy substituted CCT391081 (**112**), the desired 3-alkoxy substituent was first installed using an S_NAr reaction with 7-bromo-2-chloroquinoxaline (**106**) in the presence of the appropriate alcohol with potassium carbonate as the chosen base. The S_NAr reaction was performed using the simple alcohol as the reaction solvent for ethoxy, *n*-butoxy and *iso*-propoxy analogues (**119**, **120** and **125**). For the remaining four analogues, **121**, **122**, **123** and **124**, the reactions were carried out in DMF with two equivalents of the appropriate alcohol. Following isolation of 3-alkoxy-6-bromoquinoxaline intermediates, a Pd-catalysed aminocarbonylation reaction with isoxazol-5-ylmethanamine was performed to obtain the final desired amide products, **126** to **132**. Full conversion to desired products after a few hours was

observed by LCMS and reaction profiles were clean with no significant formation of by-products (Figure 4.6).

Table 4.1. Synthesis of 3-alkoxyquinoxaline-6-carboxamide fragments via i) S_NAr then ii) Pd-catalysed aminocarbonylation. Reagents and conditions: i) ROH (neat or 0.2 M in DMF), K₂CO₃, 80 °C, 4 h to 78 h; ii) Isoxazol-5-ylmethanamine hydrochloride, CO (g), DIPEA, [Xantphos Pd(allyl)]Cl (5 mol%), 1,4-dioxane (0.5 M), 80 °C, 2 h to 5 h.



Substituent	i) S _N Ar Conditions	Product	Yield	ii) Final Product	Yield
	EtOH (0.2 M)	119	139 mg, 89%	CCT392853, 126	45 mg, 50%
	<i>n</i> -BuOH (0.2 M)	120	108 mg, 62%	CCT392854, 127	38 mg, 39%
	Cyclopropylmethanol (2 equiv), DMF (0.2 M)	121	131 mg, 76%	CCT393087, 128	49 mg, 48%
	BnOH (2 equiv), DMF (0.2 M)	122	155 mg, 78%	CCT393088, 129	62 mg, 55%
	2-methoxyethan-1-ol (2 equiv), DMF (0.2 M)	123	121 mg, 69%	CCT393100, 130	42 mg, 47%
	2-methylpropan-1-ol (2 equiv), DMF (0.2 M)	124	123 mg, 71%	CCT393102, 131	24 mg, 28%
	<i>i</i> -PrOH (0.2 M)	125	138 mg, 84%	CCT393103, 132	28 mg, 33%

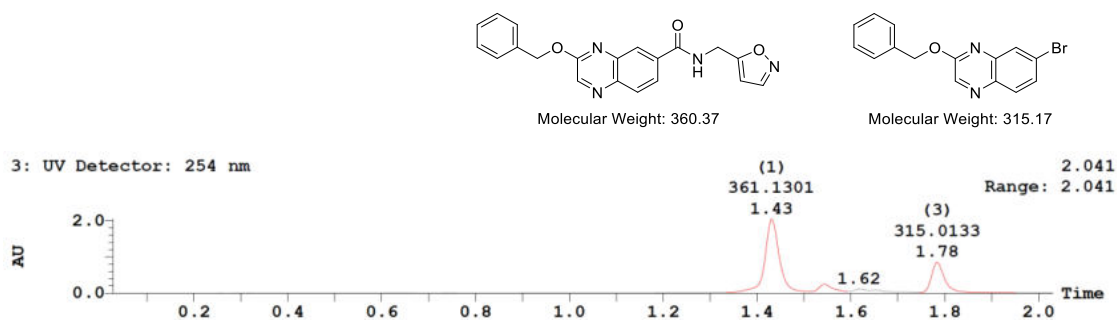
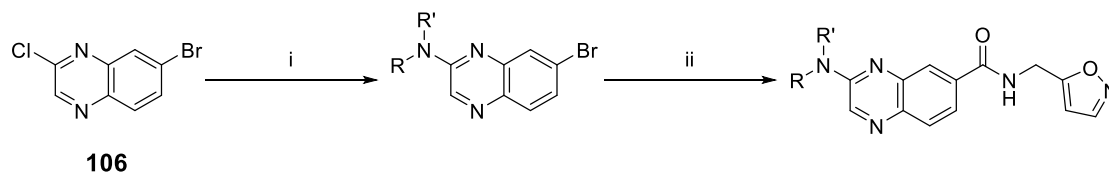


Figure 4.6. Example LCMS analysis of Pd-catalysed aminocarbonylation reaction for the synthesis of CCT393088 (129). LCMS analysis after 3 h showed 69% desired product at $t_R = 1.43$ min and 25% remaining starting material at $t_R = 1.78$ min, quantified by UV detection at 254 nm.

4.2.2 Synthesis of 3-alkylamino quinoxaline-6-carboxamide fragments

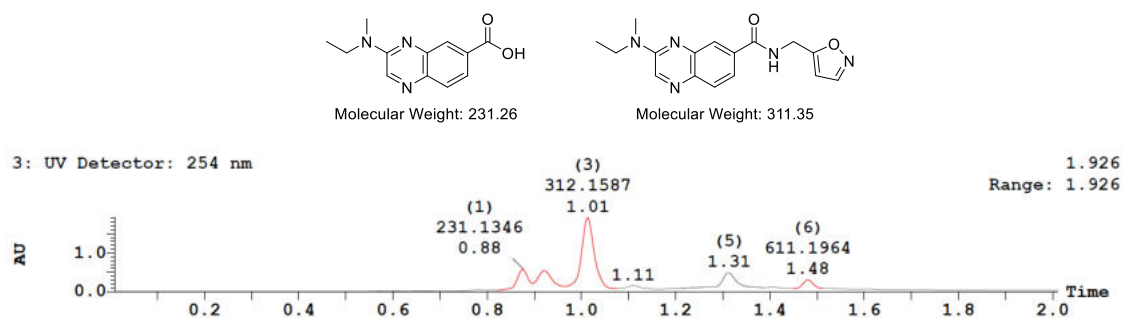
A summary of the synthesis for eight out of the nine planned 3-alkylamino quinoxaline-6-carboxamide fragments is shown in Table 4.2. In these examples, S_NAr reaction of 7-bromo-2-chloroquinoxaline (**106**) was carried out with the appropriate amine to introduce the desired 3-position alkylamino substituents. The amine was added as either a neat solution or as a hydrochloride salt, and no additional base was used for the reactions. The Pd-catalysed aminocarbonylation step with isoxazol-5-ylmethanamine yielded the final desired amide products, **141** to **148**, in all cases, however low yields (< 40%) were obtained for these reactions. This was a result of the formation of corresponding 3-alkylamino quinoxaline-6-carboxylic acid by-products during all aminocarbonylation reactions with aryl bromides **133** to **140**, which was observed by LCMS analysis (Figure 4.7). Except for CCT393936 (**141**) and CCT394006 (**142**), reactions were stopped prior to full conversion of starting material to prevent further formation of the carboxylic acid by-products and allow the desired product to be purified more easily by either reverse or normal phase chromatography.

Table 4.2. Synthesis of 3-alkylaminoquinoxaline-6-carboxamide fragments via i) S_NAr then ii) Pd-catalysed aminocarbonylation. Reagents and conditions: i) HNRR' (neat or hydrochloride salt), DMF (0.5 M), 80 °C, 4 h to 22 h; ii) Isoxazol-5-ylmethanamine hydrochloride, CO (g), DIPEA, Xantphos Pd G4 (5 mol%), 1,4-dioxane (0.5 M), 80 °C, 2 h to 4 h.



Substituent	i) S _N Ar Product	Yield	ii) Aminocarbonylation Product	Yield
	133	159 mg, 96%	CCT393936, 141	13 mg, 16%
	134	167 mg, 95%	CCT393998, 142	39 mg, 45%
	135	127 mg, 78%	CCT394000, 143	33 mg, 40%
	136	146 mg, 85%	CCT394001, 144	34 mg, 39%
	137	165 mg, 92%	CCT394003, 145	26 mg, 29%
	138	172 mg, 95%	CCT394006, 146	41 mg, 46%
	139	121 mg, 67%	CCT394013, 147	36 mg, 40%
	140	150 mg, 79%	CCT394019, 148	8 mg, 9%

a



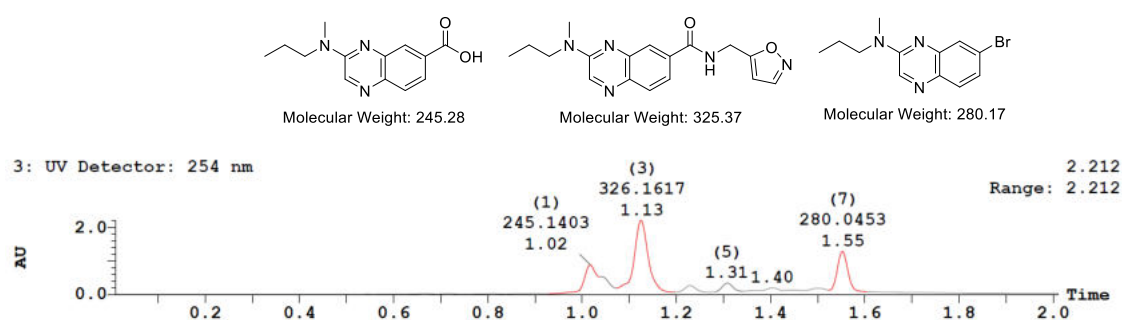
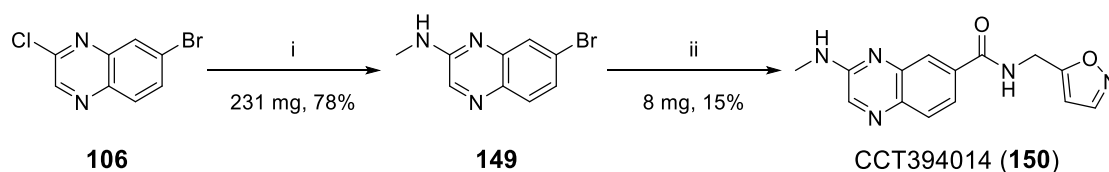
b

Figure 4.7. Reaction analysis of Pd-catalysed aminocarbonylation reaction for the synthesis of CCT393936 (141) and CCT393998 (142). **a** CCT393936 (141): LCMS analysis after 4 h showed 53% desired product at $t_R = 1.01$ min and 13% carboxylic acid by-product at $t_R = 0.88$ min, quantified by UV detection at 254 nm. **b** CCT393998 (142): LCMS analysis after 3.5 h showed 51% desired product at $t_R = 1.13$ min, 17% carboxylic acid by-product at $t_R = 1.02$ min and 19% remaining starting material at $t_R = 1.55$ min, quantified by UV detection at 254 nm.

For the synthesis of the final proposed 3-alkylamino quinoxaline fragment, CCT394014 (**150**), significant carboxylic acid by-product formation was observed during the aminocarbonylation reaction following the conditions used to synthesise parent compound CCT393128 (**115**), and the desired amide compound was not isolated from this reaction. However, swapping the base used in the reaction from DIPEA to potassium carbonate limited the formation of the carboxylate by-product and the desired compound **150** was obtained in a 15% yield following purification by normal phase then reverse phase chromatography (Scheme 4.1).

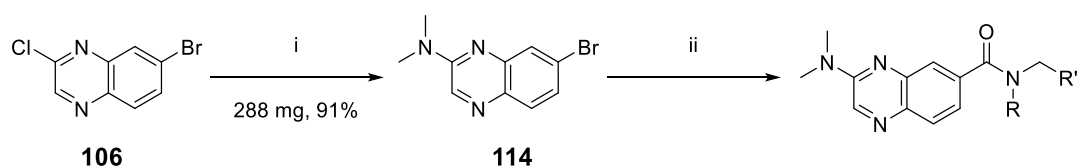


Scheme 4.1. Synthesis of *N*-(isoxazol-5-ylmethyl)-3-(methylamino)quinoxaline-6-carboxamide, CCT394014 (150), via Pd-catalysed aminocarbonylation. Reagents and conditions: i) Methylamine (2 M in THF), DMF (0.5 M), 80 °C, 4 h; ii) Isoxazol-5-ylmethanamine hydrochloride, CO (g), K₂CO₃, Xantphos Pd G4 (5 mol%), 1,4-dioxane (0.5 M), 80 °C, 2 h.

4.2.3 Synthesis of 3-substituted quinoxalines with matched pair amides

The synthesis of a set of three analogues of CCT393128 (**115**) – CCT395333 (**151**) CCT395427 (**152**) and CCT395428 (**153**) – which provided matched pairs to previously discussed unsubstituted quinoxaline analogues (**54**, **48** and **66** respectively), is summarised in Table 4.3. All three compounds (**151**, **152** and **153**) were synthesised from 7-bromo-*N,N*-dimethylquinoxalin-2-amine (**114**), and different amines were used in the final aminocarbonylation step to introduce the desired isoxazole modification.

Table 4.3. Synthesis of 3-dimethylaminoquinoxaline-6-carboxamide fragments via i) S_NAr then ii) Pd-catalysed aminocarbonylation. Reagents and conditions: i) Dimethylamine (2M in THF), DMF (0.5 M), 80 °C, 4 h; ii) RNHCH₂R' (neat or hydrochloride salt), CO (g), DIPEA, Xantphos Pd G4 (5 mol%), 1,4-dioxane (0.5 M), 80 °C, 2 h to 8 h.

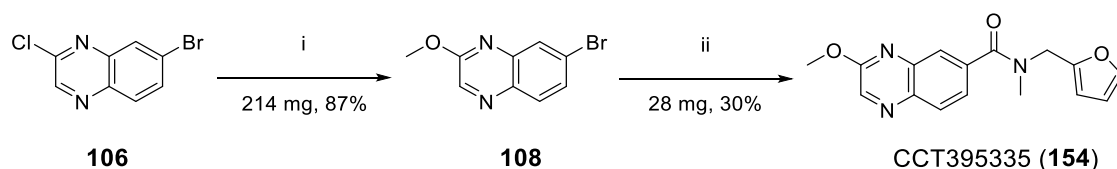


Entry	Yield
 CCT395333, 151	32 mg, 31%
 CCT395428, 153	47 mg, 44%

Entry	Yield
 CCT395427, 152	78 mg, 84%

Lastly, CCT395335 (**154**) was synthesised according to Scheme 4.2. In the synthesis of *N*-methyl furanyl amide matched pair analogues **151** and **154**, the formation of ester by-products **155** and **156** was observed. It was suspected that conversion of *N*-methyl amine **157** to alcohol **158** had occurred upon storage of the amine, which had resulted in the presence of **158** as a competing nucleophile

in the carbonylation reaction and led to the formation of ester by-products **155** and **156** (Figure 4.8). Low yields were therefore obtained in the synthesis of CCT395333 (**151**) and CCT395335 (**154**), however the ester by-products were successfully removed during purification.



Scheme 4.2. Synthesis of *N*-(furan-2-ylmethyl)-3-methoxy-*N*-methylquinoxaline-6-carboxamide, CCT395335 (154**).** Reagents and conditions: i) K_2CO_3 , MeOH (0.21 M), 65 °C, 4 h; ii) 1-(furan-2-yl)-*N*-methylmethanamine, CO (g), DIPEA, Xantphos Pd G4 (5 mol%), 1,4-dioxane (0.5 M), 80 °C, 8 h.

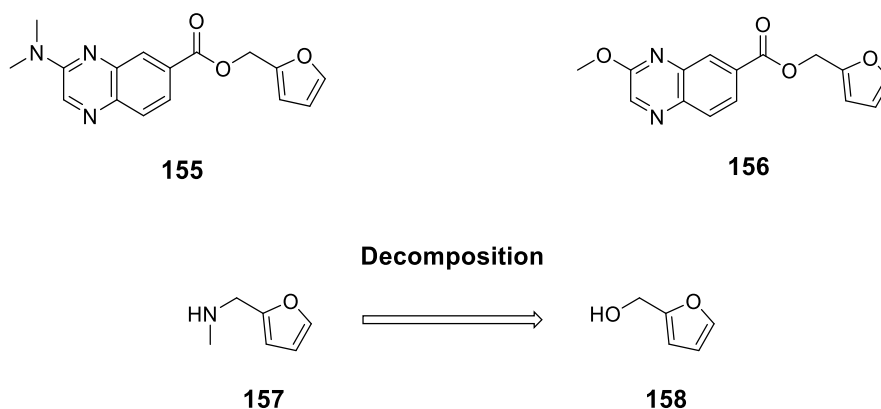


Figure 4.8. Structures of ester by-products (155 and 156) from synthesis of CCT395333 (151) and CCT395335 (154).

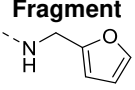
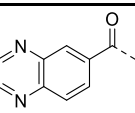
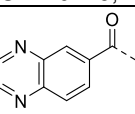
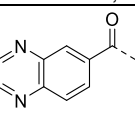
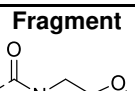
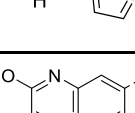
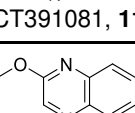
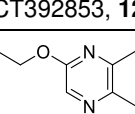
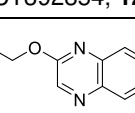
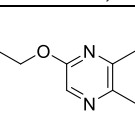
4.2.4 Testing of 3-alkoxy and 3-alkylamino quinoxaline fragments in competitive ligand-observed NMR

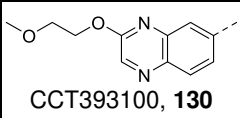
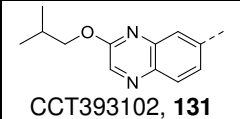
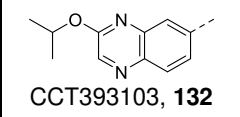
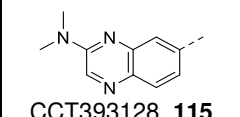
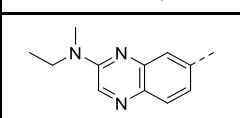
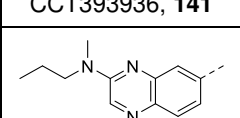
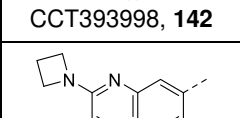
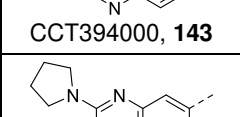
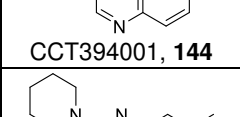
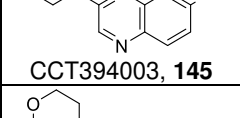
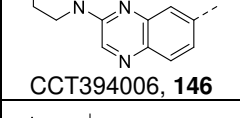
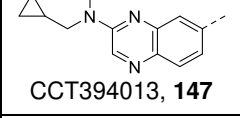
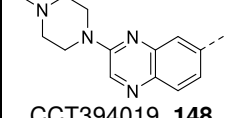
Following successful synthesis and purification of all planned 3-substituted quinoxaline fragments, compound stock solutions were accurately prepared to 50 mM in DMSO- d_6 and aqueous kinetic solubility was measured using quantitative proton ^1H NMR methods, as for compounds discussed in previous chapters (Table 4.4, Kin. Sol. (μM)). All soluble analogues ($> 30 \mu\text{M}$) were then tested for binding against TNKS2 ARC4 using competitive ligand-observed NMR

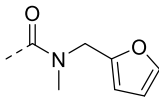
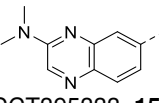
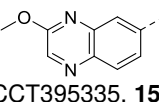
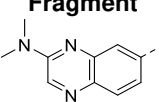
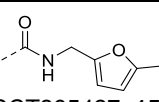
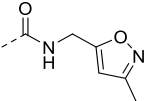
experiments, with exclusion of only 3-benzyloxy analogue CCT393088 (**129**) from testing due to its poor solubility (7 μM) (Table 4.4).

Table 4.4. A summary of data obtained from competitive ligand-observed NMR experiments performed with 3-substituted quinoxaline fragment compounds.

Fragments were tested at either 500 μM , 200 μM or 50 μM depending on aqueous kinetic solubility (Kin. Sol. μM). ^a n = 1 unless otherwise indicated (mean with \pm SD error for n > 1); ^b competition with 3BP2 peptide (200 μM), n = 1 unless otherwise indicated (mean with \pm SD error for n > 1); ^c Decrease to baseline and inversion to positive phase indicates binding, minimal decrease to baseline indicates non-binding; ^d signal recovery indicates competitive binding.

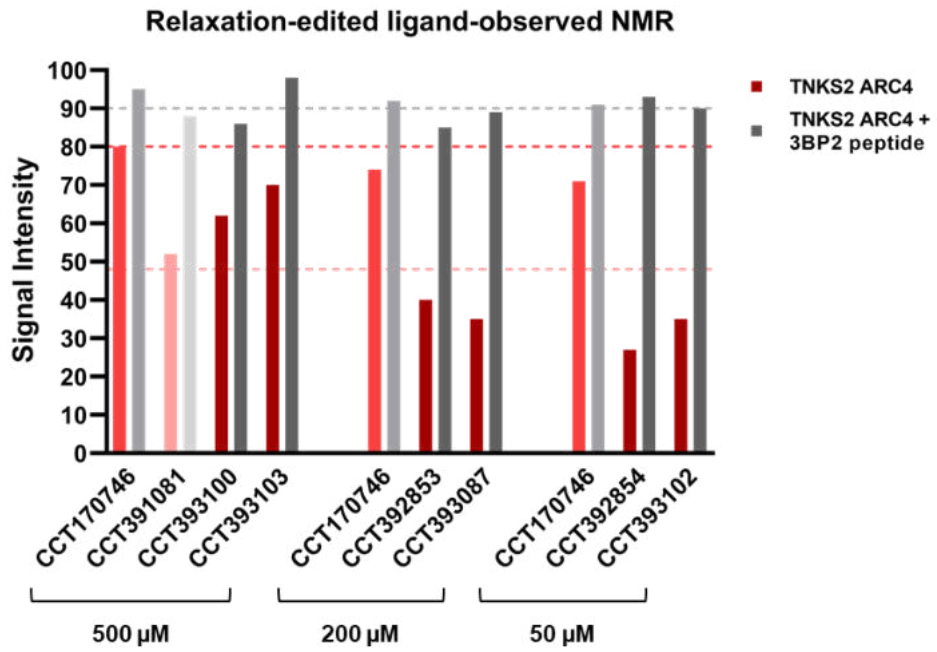
Fragment 	Kin. Sol. (μM)	Assay Conc. (μM)	clogP (MoKa)	CPMG	CPMG	WaterLOGSY	WaterLOGSY
				+ protein ^a	+ competitor ^b	+ protein ^c	+ competitor ^d
 CCT170746, 28	898	500	1.0	20% \pm 4% (n = 9)	5% \pm 3% (n = 8)	Decrease to baseline	Signal recovery
 CCT170746, 28	898	200	1.0	26% \pm 8% (n = 5)	8% \pm 4% (n = 5)	Decrease to baseline	Signal recovery
 CCT170746 28	898	50	1.0	29% \pm 7% (n = 6)	9% \pm 7% (n = 6)	Not observed	Not observed
Fragment 	Kin. Sol. (μM)	Assay Conc. (μM)	clogP (MoKa)	CPMG	CPMG	WaterLOGSY	WaterLOGSY
				+ protein ^a	+ competitor ^b	+ protein ^c	+ competitor ^d
 CCT391081, 112	872	500	0.93	48% \pm 3% (n=2)	12% \pm 3%	Decrease to baseline	Signal recovery
 CCT392853, 126	285	200	1.4	60%	15%	Decrease to baseline	Signal recovery
 CCT392854, 127	49	50	2.4	73%	7%	Not observed	Not observed
 CCT393087, 128	296	200	1.8	65%	11%	Not observed	Not observed
 CCT393088, 129	7	Not tested	2.5	-	-	-	-

 CCT393100, 130	874	500	0.8	38%	14%	Decrease to baseline	Signal recovery
 CCT393102, 131	34	50	2.2	65%	10%	Not observed	Not observed
 CCT393103, 132	759	500	1.7	30%	2%	Inversion to positive phase	Signal recovery
 CCT393128, 115	861	500	0.95	80% ± 4% (n = 2)	64% ± 5% (n = 2)	Inversion to positive phase	Decrease in positive phase
 CCT393936, 141	858	500	1.5	68%	39%	Decrease to baseline, inversion at 7.9 ppm	Signal recovery
 CCT393998, 142	922	500	1.9	77%	50%	Inversion to positive phase	Decrease in positive phase
 CCT394000, 143	1056	500	1.1	80%	62%	Inversion to positive phase	Decrease in positive phase
 CCT394001, 144	928	500	1.5	93%	79%	Inversion to positive phase	Decrease in positive phase
 CCT394003, 145	93	50	1.9	86%	24%	Not observed	Not observed
 CCT394006, 146	929	500	0.54	85%	54%	Inversion to positive phase	Decrease in positive phase
 CCT394013, 147	391	200	1.8	85%	39%	Inversion to positive phase	Decrease in positive phase
 CCT394019, 148	839	500	0.66 clogD (MoKa) -0.26	71%	57%	Inversion to positive phase	Decrease in positive phase
 CCT394014, 150	942	500	0.78	93%	77%	Inversion to positive phase	Decrease in positive phase

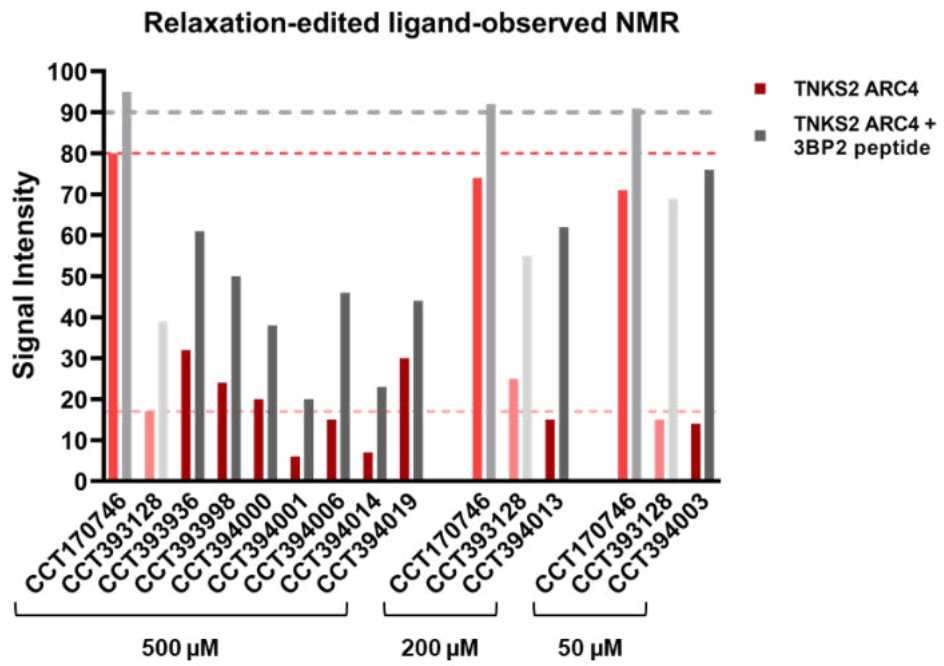
Fragment 	Kin. Sol. (μM)	Assay Conc. (μM)	clogP (MoKa)	CPMG	CPMG	WaterLOGSY	WaterLOGSY
				+ protein ^a	+ competitor ^b	+ protein ^c	+ competitor ^d
 CCT395333, 151	881	500	1.7	19%	6%	Minimal decrease	-
 CCT395335, 154	845	500	1.7	6%	1%	Minimal decrease	-
Fragment 	Kin. Sol. (μM)	Assay Conc. (μM)	clogP (MoKa)	CPMG	CPMG	WaterLOGSY	WaterLOGSY
				+ protein ^a	+ competitor ^b	+ protein ^c	+ competitor ^d
 CCT395427, 152	78	50	2.4	78%	44%	Not observed	Not observed
 CCT395428, 153	557	500	2.2	94%	56%	Inversion to positive phase	Decrease in positive phase

Compounds 3-methoxy CCT391081 (**112**) and 3-dimethylamino CCT393128 (**115**) were re-tested as additional controls, to allow a comparison of results from the O-substituted and N-substituted quinoxalines against their respective parent compounds. The data for control fragment CCT170746 (**28**) is also shown again in Table 4.4. In the relaxation-edited experiment, the intrinsic variability of the relaxation-edited CPMG experiment had been previously demonstrated from the mean standard deviation (σ) of fragments tested in two individual replicates (mean $\sigma = \pm 5\%$) (section 2.5.3). Only fragments which showed a change in peak intensity reduction between 'blank' and 'protein' samples of greater than 2σ compared with control compounds ($2\sigma = 10\%$) were considered to show significantly increased or decreased binding to TNKS2 ARC4. For O-substituted analogues and N-substituted quinoxalines, compounds with peak intensity reduction within 2σ of parent control compounds CCT391081 (**112**) and CCT393128 (**115**) ($48\% \pm 10\%$ and $83\% \pm 10\%$ respectively) were classed as showing equivalent binding to the controls (Figure 4.9).

a



b



C

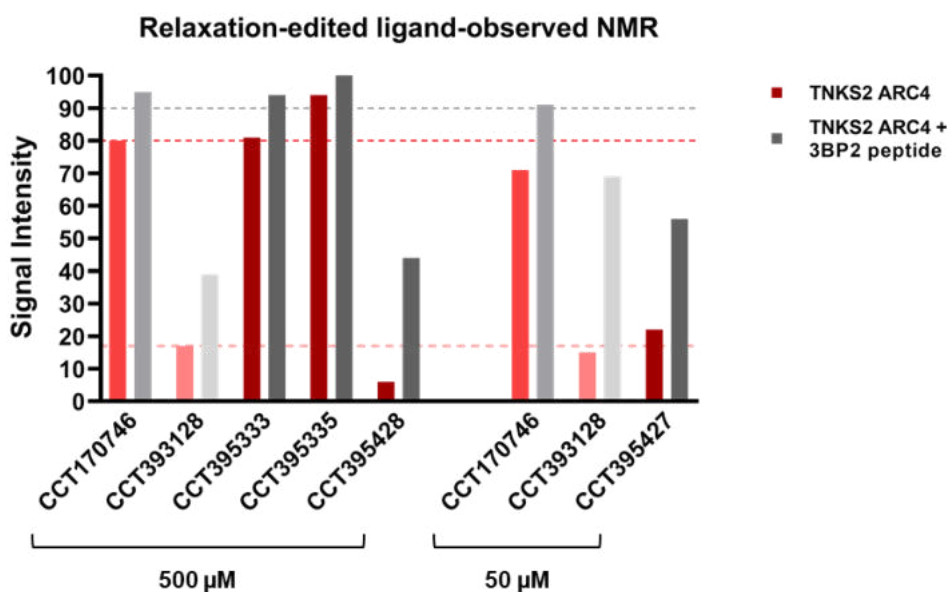


Figure 4.9. Graphical summary of results from testing 3-substituted quinoxaline fragments in relaxation-edited ligand-observed NMR. Intensity of fragment ^1H NMR signals in the presence of TNKS2 ARC4 (red bars), and in the presence of TNKS2 ARC4 + 3BP2 peptide competitor (grey bars), as a percentage (%) of ^1H NMR signals in ‘compound only’ spectra. Y-axis (signal intensity) unit is %. Fragments were tested at either 500 μM , 200 μM or 50 μM depending on their aqueous kinetic solubility. Average reduction in signal intensity (%) for CCT170746 (**28**) (500 μM) in the presence of TNKS2 ARC4 is represented by dashed pink threshold, and recovery in signal intensity with 3BP2 16mer peptide competitor is represented by grey dashed threshold. **a) 3-alkoxy substituted quinoxaline analogues** (Table 4.4, entries **126** to **132**): Average reduction in signal intensity (%) for CCT391081 (**112**) (500 μM) in the presence of TNKS2 ARC4 is represented by dashed light pink threshold. **b) 3-alkylamino substituted quinoxaline analogues** (Table 4.4, entries **141** to **150**): Average reduction in signal intensity (%) for CCT393128 (**115**) (500 μM) in the presence of TNKS2 ARC4 is represented by dashed light pink threshold. **c) 3-substituted quinoxalines with matched pair amides** (Table 4.4: entries **151**, **154**, **152** and **153**): Average reduction in signal intensity (%) for CCT393128 (**115**) (500 μM) in the presence of TNKS2 ARC4 is represented by dashed light pink threshold.

From the results shown in Table 4.4 and Figure 4.9, it can be concluded that out of the 20 compounds tested in this iteration, 18 compounds maintained binding to TNKS2 ARC4 in the relaxation-edited CPMG experiment. The two exceptions were *N*-methyl furanyl amide compounds, **151** and **154** (Figure 4.9c). This SAR provided experimental evidence that 3-substituted quinoxaline fragments occupy a binding mode consistent with the unsubstituted quinoxaline fragment series, in

which *N*-methylation of the central amide (**54**) was also not tolerated (section 2.5.3). It was consistent with protein-observed NMR guided *in silico* docking of CCT391081 (**112**) and CCT393128 (**115**), which positioned the fragments in a pose comparable to binding mode 1. In this binding mode, methylation of the central amide N-H would result in a loss of binding affinity by disrupting a hydrogen-bond interaction with the backbone carbonyl of G535 (Figure 4.1, section 4.1). Further support of the 3-alkoxy and 3-alkylamino quinoxalines occupying a comparable binding mode was obtained by the introduction of larger alkyl groups. Introduction of linear ethyl (**126** and **141**), propyl (**142**), cyclopropyl methyl (**128** and **147**) butyl (**127**) and 2-methoxyethoxy (**130**) groups to either the O- or N-substituted quinoxaline scaffolds was tolerated (Figure 4.9a/b).

In the 3-alkoxy quinoxaline series, introduction of the branched *iso*-propyl group (**132**) decreased binding to TNKS2 ARC4 whilst extending the branching out by one carbon with the introduction of the 2-*iso*-butyl (**131**) substituent showed slightly increased binding to TNKS2 ARC4 compared with parent compound CCT391081 (**112**) (Figure 4.9a). For the 3-alkylamino quinoxaline scaffold, introduction of 4-, 5- and 6-membered heterocyclic substituents (**143**, **144**, **145**, **146** and **148**) was tolerated (Figure 4.9b). Fragment **150** with 3-methylamine substitution also showed strong binding to TNKS2 ARC4 (Figure 4.9b), as did **152** and **153** which were matched pairs to previous unsubstituted quinoxaline analogues (Figure 4.9c). All 3-alkylamino quinoxaline compounds maintained binding comparable to CCT393128 (**115**) in the CPMG (71% to 93% average reduction in signal intensity) and waterLOGSY (signal inversion) assays in the presence of TNKS2 ARC4 (Table 4.4, entries **141** to **150**). Therefore, it was hypothesised that these compounds would have equivalent or increased binding affinity against TNKS2 ARC4 compared to **115**, and increased binding affinity compared to fragment hit CCT170746 (**28**). However, the compounds could not be ranked according to the average reduction in signal intensity (%) in the presence of TNKS2 ARC4 as the upper limit of detection in relaxation-edited experiment (CPMG + protein) had been reached.

In the competitive ligand-observed NMR experiments in the presence of both TNKS2 ARC4 and 3BP2 16mer peptide (20 μ M and 200 μ M respectively), all the

3-alkoxy quinoxaline fragments were considered competitive binders. In the presence of TNKS2 ARC4 and 3BP2 competitor, these compounds showed average reduction in signal intensity less than 15% in the relaxation-edited experiments and signal recovery in the waterLOGSY experiment, comparable to parent compound CCT391081 (**112**) (Table 4.4, CPMG and waterLOGSY + competitor). However, the 3-alkylamino quinoxaline analogues showed average reduction in signal intensity between 24% to 79% in the presence of competitor, therefore full recovery of ligand signals was not observed. These compounds were all tested at 500 μM , apart from **145** and **147** which were tested at 50 μM and 200 μM respectively. As the compounds were hypothesised to have a TNKS2 ARC4 binding affinity comparable to CCT393128 (**115**), an excess of competitor was likely to be required to achieve displacement of these compounds from the protein-ligand complex (as discussed in section 3.3). Therefore, competitiveness of the 3-alkylamino quinoxaline analogues also could not be determined according to the average reduction in signal intensity (%) in the presence of TNKS2 ARC4 and 3BP2 16mer peptide competitor.

Testing of all 3-alkylamino quinoxaline analogues of **115** in protein-observed NMR experiments was considered, in order to rank the compounds according to their binding affinity. This would also determine whether the compounds bound to the substrate recognition pocket of TNKS2 ARC4 from binding site mapping. However, as testing of more than 10 analogues was required, data analysis was expected to be time consuming, and a large quantity of ^{15}N -labelled protein would be required. Therefore, the development of a higher throughput biochemical assay suitable for measuring the affinity of compounds with expected $K_d < 300 \mu\text{M}$ was proposed. As competition of the 3-alkylamino substituted quinoxaline analogues could not be determined from ligand-observed NMR, a competitive biochemical assay format was also required.

4.2.5 Protein-observed NMR with 3-pyrrolidinyl quinoxaline fragment CCT394001 (**144**)

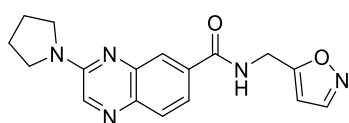
Prior to establishing a biochemical assay to assess the affinity of 3-alkylamino quinoxaline analogues, a representative compound from this series was selected

for testing in protein-observed NMR experiments. CCT394001 (**144**) was chosen, to determine how its binding affinity and predicted binding site compared to CCT393128 (**115**). A titration series of **144** (0 to 1600 μM) in the presence of ^{15}N -labelled TNKS2 ARC4 was prepared and ^1H - ^{15}N spectra were acquired and analysed. The binding affinity of **144** was determined as $120 \pm 30 \mu\text{M}$ from an average of K_d values for 15 correlation peaks which showed significant shifting, ranging from 85 μM to 180 μM (Figure 4.10a). Therefore, **144** and **115** ($K_d = 240 \mu\text{M}$) bound to TNKS2 ARC4 with similar affinity. In total, 16 backbone amide NH peaks showed significant shifting ($\Delta d > \text{average} + 1\sigma$), however a K_d value could not be determined for the peak assigned to S527 as it showed a slow-exchange regime rather than concentration-dependent, fast-exchange kinetics (Figure 4.10b). The shifted residues were mapped on to the surface of the TNKS2 ARC4:3BP2 crystal structure to provide a binding site heat-map, which revealed substantial binding site overlap between **144** and its parent fragment, **115** (Figure 4.10c/d). As observed with **115**, the residues which shifted in response to titration of **144** primarily mapped to the central patch with G535 from the glycine sandwich region also showing significant shifting (Figure 4.10e), which suggested an equivalent binding mode was likely occupied by both analogues. Energy minimisation of **144** was performed in MOE to determine whether the 3-pyrrolidinyl substituent would be tolerated in the hypothesised binding mode of **115** from NMR-guided *in silico* docking. The 3-pyrrolidinyl substituent was added to the docked structure of **115** to obtain **144**, and energy minimisation of **144** was performed against the TNKS2 ARC4:3BP2 crystal structure using the Builder panel in MOE.¹⁹⁸ This *in silico* modelling by energy minimisation suggested that 3-pyrrolidinyl quinoxaline substitution was tolerated in this binding mode (Figure 4.10f).

In silico docking of CCT394001 (**144**) was next performed against TNKS2 ARC4 using the Dock panel in MOE.¹⁹⁸ The docking site was selected as all 16 residues which showed backbone amide CSPs ($\Delta d > \text{average} + 1\sigma$) upon titration of **144**. However, none of the *in silico* docking poses generated were consistent with the *in silico* docking of CCT393128 (**115**), despite the overlap of their binding site maps and the residues selected as the docking site. The top-scoring docking poses, retained upon refinement, were instead consistent with binding modes 4

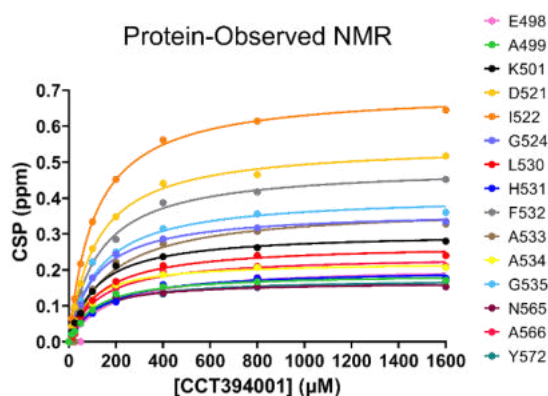
and 5 from *in silico* docking of CCT170746 (**28**) performed in GOLD. Previous SAR from 2,3-disubstituted quinoxaline analogues had ruled out these binding modes (Figure 3.5, section 3.2.3). These docking poses were also less consistent with protein-observed NMR data as the 3-pyrrolidinyl substituent, which had led to increased binding affinity, was not in proximity to residues which had experienced CSPs in response to titration of **144**.

a

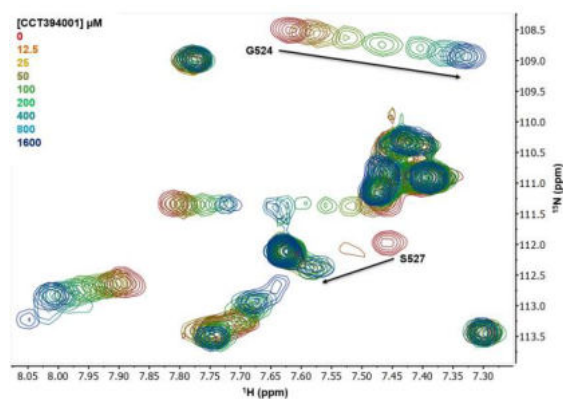


CCT394001 (144)

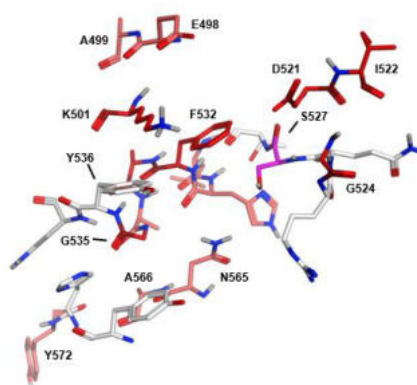
Average K_d (NMR) = 120 (\pm 30) μ M



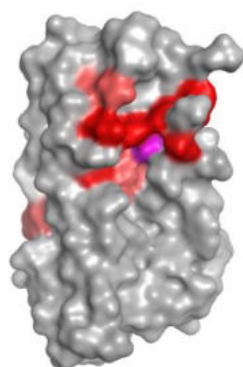
b



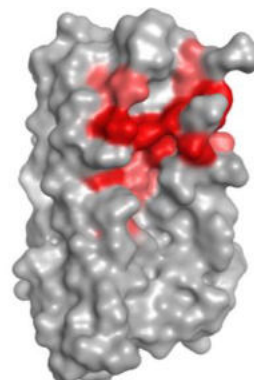
c



d



CCT394001 (144)



CCT393128 (115)

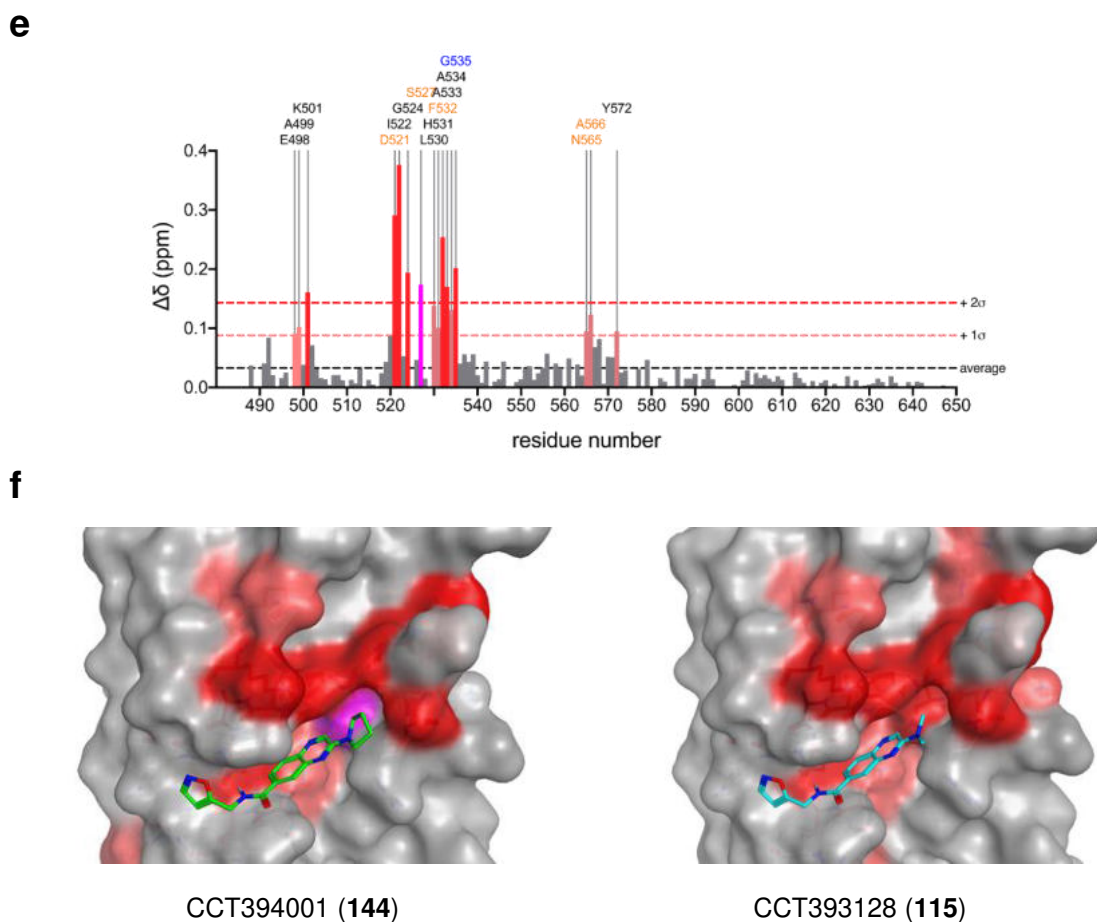
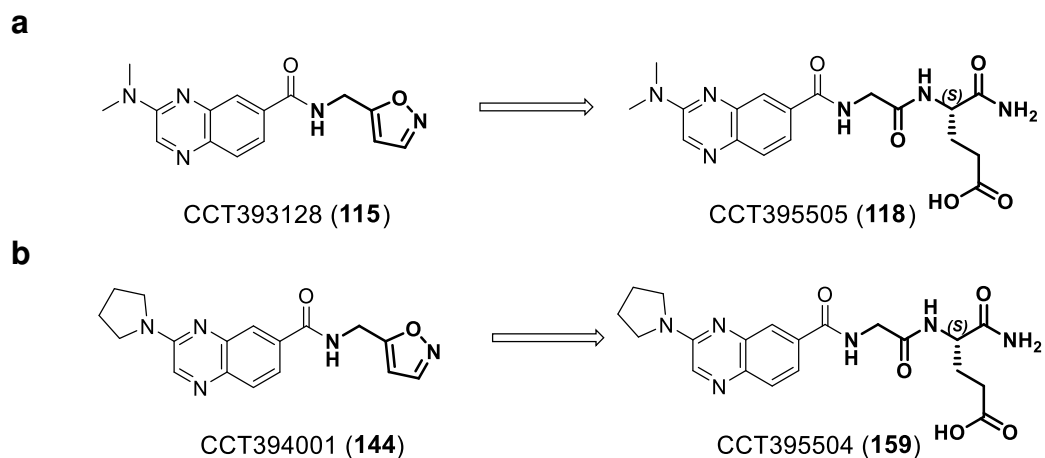


Figure 4.10. Protein-observed NMR with CCT394001 (144). **a)** Average K_d (NMR) determination for **144** calculated from non-linear regression analysis of CSPs against ligand concentration. **b)** Slow-exchange kinetics were observed for S527 from ^1H - ^{15}N HSQC correlation spectra of ^{15}N -labelled TNKS2 ARC4 with increasing concentrations of **144**. **c)** Residues from crystal structure of TNKS2 ARC4 (PDB: 3TWR) which showed significant CSPs ($\Delta d > \text{average} + 1\sigma$, pink; $\Delta d > \text{average} + 2\sigma$, red; slow-exchange S527, magenta) upon CCT394001 **X** binding. **d)** CSPs from **144** and **115** mapped onto the 3BP2 bound crystal structure (PDB: 3TWR). **e)** Plot of CSPs from **144** titration against ^{15}N TNKS2 ARC4 (50 μM) (central patch, orange; glycine sandwich, blue). **f)** Energy minimisation (not docking) of **144** (green) in MOE against TNKS2 ARC4: 3BP2 crystal structure (PDB: 3TWR) maintained an equivalent binding pose to **115** (light blue) from *in silico* docking.

4.3 Synthesis and testing of 3-alkylamino quinoxaline peptidomimetics

4.3.1 Synthesis of 3-alkylamino quinoxaline-6-carboxamide peptidomimetics

Replacement of the isoxazole moiety of CCT393128 (**115**) was next explored through the synthesis of hybrid fragment-peptidomimetics. The desired compound CCT395505 (**118**) in which the 3-dimethylaminoquinoxaline scaffold was merged with a Gly-Glu dipeptide is shown in Figure 4.11a. From protein-observed NMR, 3-pyrrolidinylquinoxaline fragment CCT394001 (**144**) was also determined to be a higher affinity fragment compared to fragment hit CCT170746 (**28**) ($K_d = 120 \mu\text{M}$ vs $K_d = 1100 \mu\text{M}$) and hypothesised to occupy a similar binding mode to **115** from binding heat-maps. Therefore, the synthesis of peptidomimetic CCT395504 (**159**) based on the 3-pyrrolidinylquinoxaline scaffold was also proposed (Figure 4.11b). Retrosynthetic analysis of desired peptidomimetic compounds **118** and **159** was performed (Figure 4.11c). Key bonds were identified which could be formed using reactions that had been successful in the synthesis of other fragment targets (Figure 4.11c).



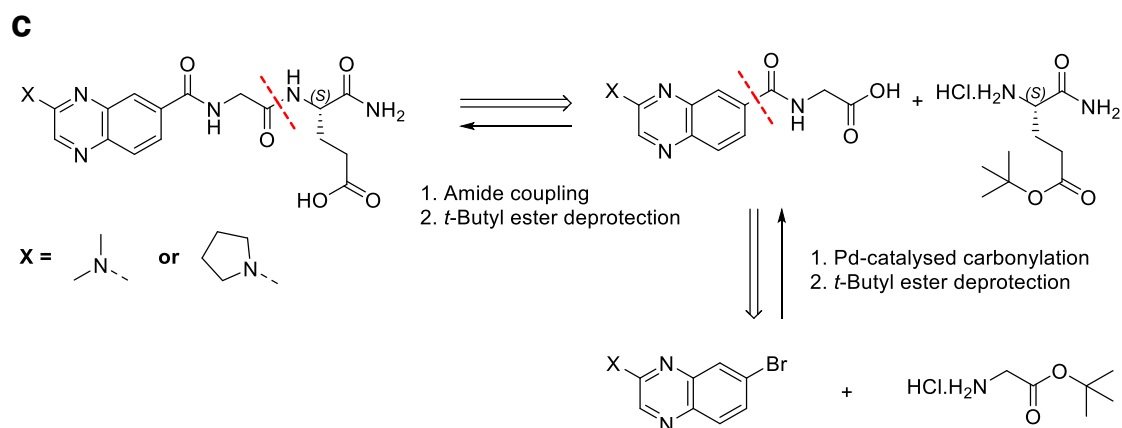
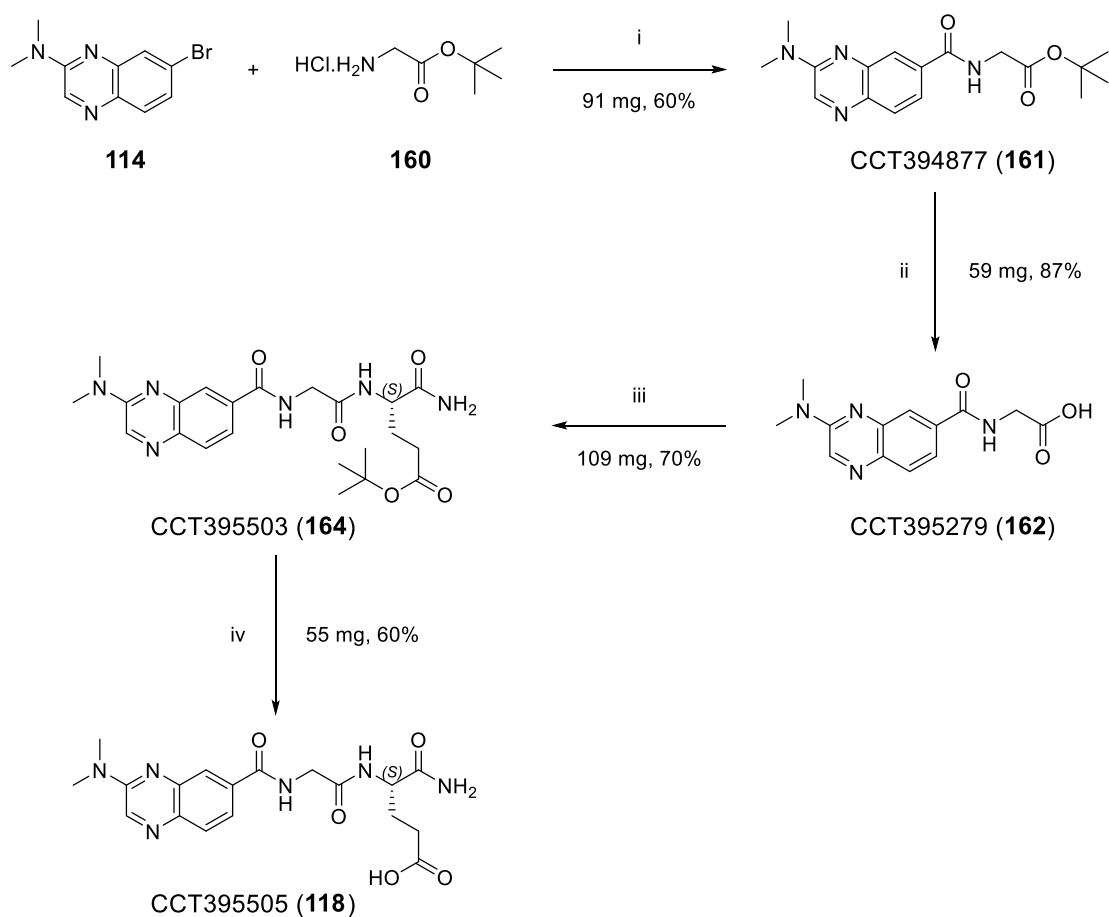
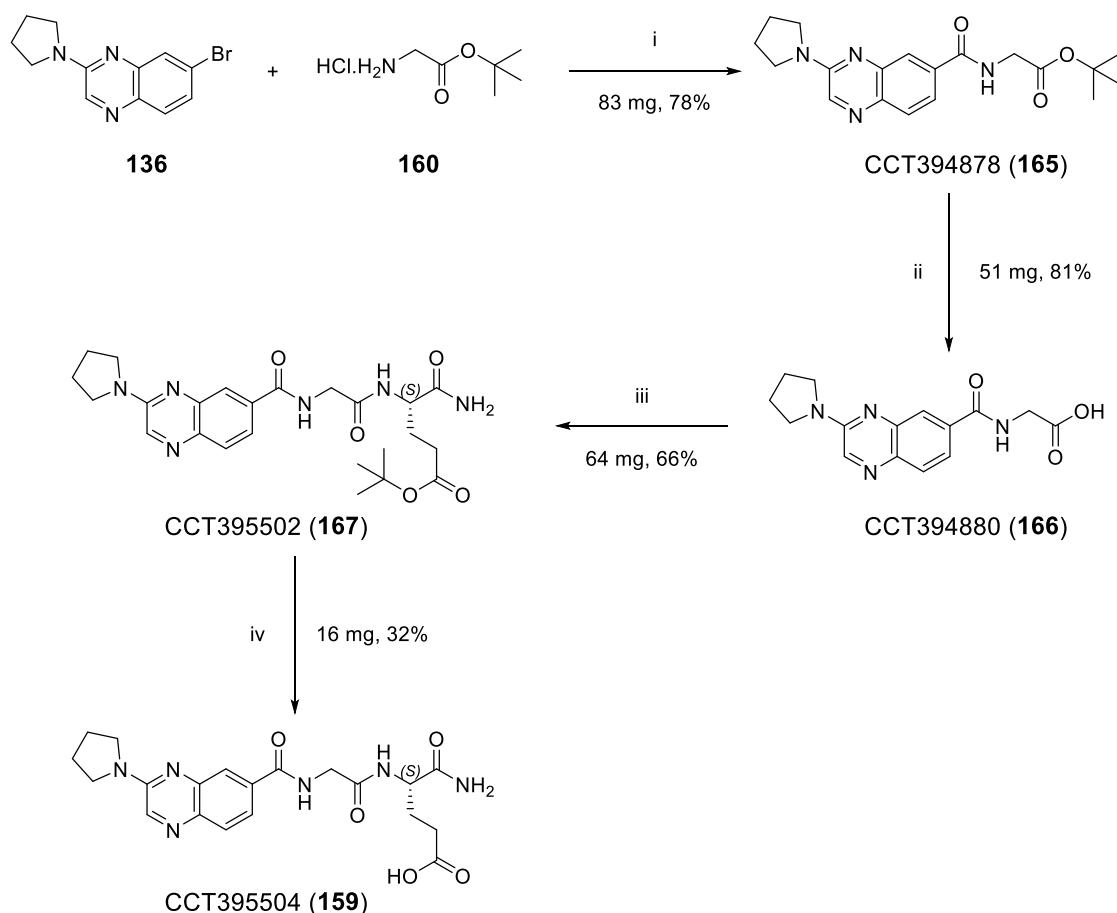


Figure 4.11. Design and retrosynthetic analysis of hybrid fragment-peptidomimetics. a) Structure of the proposed peptidomimetic compound CCT395505 (**118**) based on CCT393128 (**115**). **b)** Structure of the proposed peptidomimetic compound CCT395504 (**159**) based on CCT394001 (**144**). **c)** Retrosynthetic analysis of the desired peptidomimetic compounds **118** and **159** and the proposed forward synthesis.

A four-step route was designed for synthesis of CCT395505 (**118**) and CCT395504 (**159**) (Scheme 4.3 and Scheme 4.4 respectively), starting from the 3-alkylamino substituted quinoxaline bromides **114** and **136** which were previously accessed by S_NAr reaction of 7-bromo-2-chloroquinoxaline **106** with the appropriate amines (refer to section 3.3 and section 4.2.2). Palladium-catalysed aminocarbonylation reaction of the quinoxaline bromides (**114** and **136**) with *tert*-butyl ester glycine **160** yielded CCT394877 (**161**) and CCT394878 (**165**). These intermediates were subjected to *tert*-butyl ester deprotection under acidic conditions to provide carboxylic acids CCT395279 (**162**) and CCT394880 (**166**). Amide coupling reactions of **162** and **166** with *tert*-butyl ester protected glutamic acid **163**, using HATU as the coupling reagent, yielded CCT395503 (**164**) and CCT395502 (**167**). A final *tert*-butyl ester deprotection of the glutamic acid sidechain was performed under acidic conditions to yield the final desired peptidomimetics CCT395505 (**118**) and CCT395504 (**159**).



Scheme 4.3. Synthesis of 3-dimethylaminoquinoxaline-6-carboxamide peptidomimetic, CCT395505 (118). Reagents and conditions: i) CO (g), DIPEA, Xantphos Pd G4 (5 mol%), 1,4-dioxane (0.5 M), 80 °C, 12 h; ii) Formic acid, CH₂Cl₂ (0.2 M), 40 °C, 48 h; iii) H-Glu(O^tBu)-NH₂.HCl (163), HATU, DIPEA, DMF (0.1 M), rt, 3 h; iv) CF₃CO₂H:CH₂Cl₂ (1:1), 0 °C, 2 h.



Scheme 4.4. Synthesis of 3-pyrrolidinylaminoquinoxaline-6-carboxamide peptidomimetic, CCT395504 (159). Reagents and conditions: i) CO (g), DIPEA, Xantphos Pd G4 (5 mol%), 1,4-dioxane (0.5 M), 80 °C, 3.5 h; ii) Formic acid, CH₂Cl₂ (0.2 M), 40 °C, 96 h; iii) H-Glu(O^tBu)-NH₂.HCl (**163**), HATU, DIPEA, DMF (0.1 M), rt, 26 h; iv) CF₃CO₂H:CH₂Cl₂ (1:1), 0 °C, 1 h.

There were two considerations made in choosing the *tert*-butyl ester protecting group for the glutamic acid sidechain during the synthesis of **118** and **159**. To maintain the desired (*S*) stereochemistry upon deprotection the glutamic acid building block (**163**) was purchased with an acid-labile *tert*-butyl ester protecting group rather than with a base-labile methyl ester protecting group, as epimerisation of amino acids can occur readily under basic conditions during peptide synthesis (Figure 4.12a).²⁰⁹ Secondly, the potential formation a six-membered cyclic imide rings during the synthesis of peptides containing glutamic acid residues was a concern in the final step of the synthesis of peptidomimetics **118** and **159** (Figure 4.12b).²⁰⁹ Use of the sterically hindered *tert*-butyl ester protecting group minimised this risk and formation of the cyclic imide by-product

was not observed in reaction analysis by LCMS during the final acidic deprotection step.

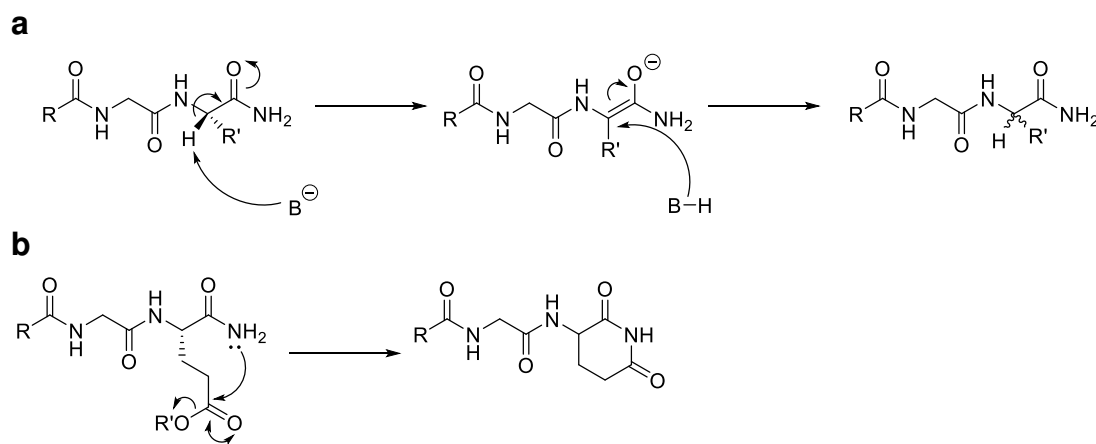


Figure 4.12. Formation of undesired by-products during peptide synthesis. a) Base-mediated (B⁻) epimerisation during peptide synthesis *via* an enolate mechanism. **b)** Mechanism of cyclic imide ring formation during synthesis of peptides containing a glutamic acid. Figure adapted from Jones, 1992.²⁰⁹

The linear synthetic route towards desired peptidomimetics allowed each intermediate (**161**, **162**, **164**, **165**, **166** and **167**) to be tested in ligand-observed NMR, in addition to final compounds CCT395505 (**118**) and CCT395504 (**159**). The *tert*-butyl ester protected glutamate compounds CCT395502 (**164**) and CCT395503 (**167**) were tested as control compounds which would be unable to form the hypothesised salt-bridge interaction with K604 and would have lower affinity compared with final peptidomimetics **118** and **159**. Unprotected and *tert*-butyl ester protected glycine intermediates – CCT394877 (**161**) and CCT394878 (**165**), CCT395279 (**162**) and CCT394880 (**166**) – were tested to assess the effect of replacing the isoxazole with either a carboxylic acid or ester functionality on fragment binding affinity. *In silico* modelling of **159** against the TNKS2 ARC4:MCL1 crystal structure was performed by energy minimisation using MOE, as described for **118** in section 4.1.2. In addition to the hypothesised salt-bridge interaction between the glutamate residue with K604^{TNKS2 ARC4}, a hydrogen bond interaction of the glycine carbonyl to the imidazole sidechain NH of H571^{TNKS2 ARC4} was predicted. Therefore, 3-dimethylamino substituted **161** and **162**, and 3-pyrrolidinyl substituted quinoxalines **165** and **166**, could also have increased

affinity compared with parent compounds CCT393128 (**115**) and CCT394001 (**144**) respectively (Figure 4.13).

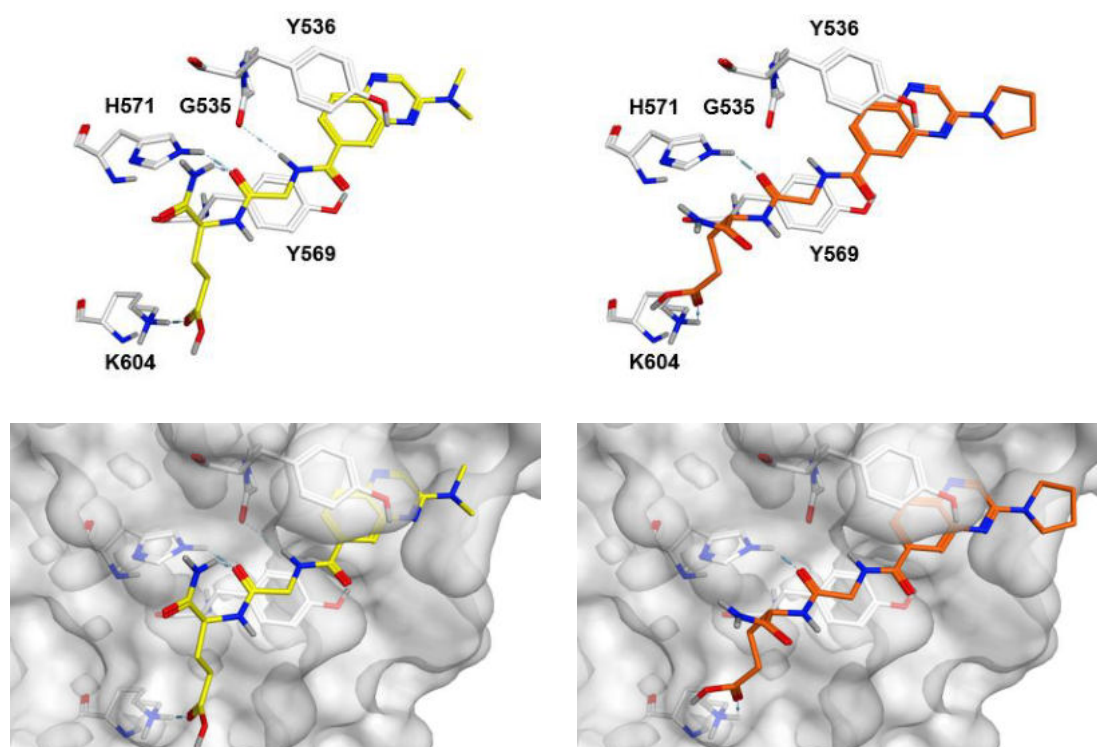
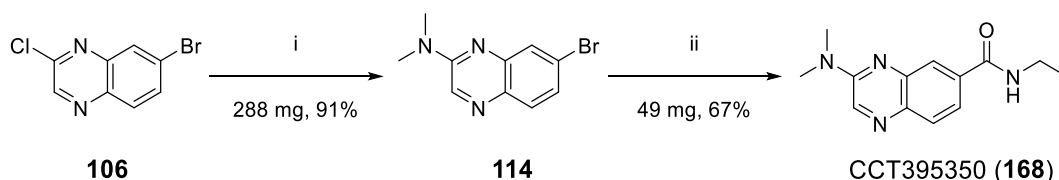
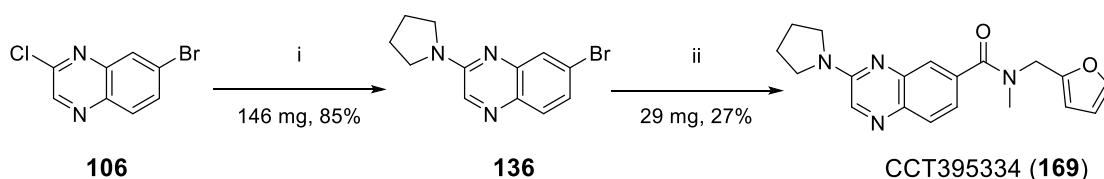


Figure 4.13. *In silico* modelling of peptidomimetics CCT395505 (**118**) and CCT395504 (**159**). Energy minimisation (not docking) of **118** (yellow) and **159** (dark orange) in MOE against TNKS2 ARC4:MCL1 crystal structure (white) revealed potential hydrogen bonds with K604 and H571.

A final two compounds were synthesised to fill gaps identified in the SAR for the 3-dimethylamino and 3-pyrrolidinyl quinoxaline scaffolds. Ethyl amide CCT395350 (**168**) was synthesised to determine whether removal of the isoxazole motif was detrimental to the binding affinity of CCT393128 (**115**). Meanwhile, CCT395334 (**169**) was synthesised to determine whether *N*-methylation of the central amide was tolerated in the 3-pyrrolidinyl quinoxaline scaffold. Both compounds were synthesised from 3-alkylamino substituted quinoxaline bromides, **114** and **136**, in Pd-catalysed aminocarbonylation reactions with the necessary amine to form the desired amides (Scheme 4.5 and Scheme 4.6).



Scheme 4.5. Synthesis of 3-(dimethylamino)-*N*-ethylquinoxaline-6-carboxamide, CCT395350 (168). Reagents and conditions: i) Dimethylamine (2M in THF), DMF (0.5 M), 80 °C, 4 h; ii) Ethanamine hydrochloride, CO (g), DIPEA, Xantphos Pd G4 (5 mol%), 1,4-dioxane (0.5 M), 80 °C, 2 h to 8 h.



Scheme 4.6. Synthesis of *N*-(furan-2-ylmethyl)-*N*-methyl-3-(pyrrolidin-1-yl)quinoxaline-6-carboxamide, CCT395334 (169). Reagents and conditions: i) pyrrolidine, DMF (0.2 M), 80 °C, 22 h; ii) 1-(furan-2-yl)-*N*-methylmethanamine, CO (g), DIPEA, Xantphos Pd G4 (5 mol%), 1,4-dioxane (0.5 M), 80 °C, 8 h.

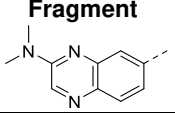
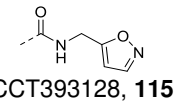
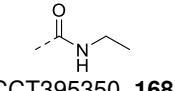
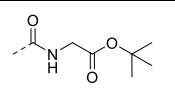
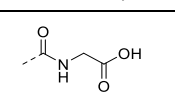
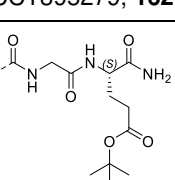
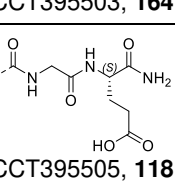
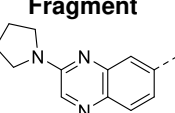
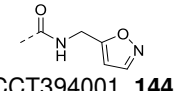
4.3.2 Testing of 3-alkylamino quinoxaline peptidomimetics in competitive ligand-observed NMR

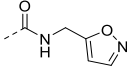
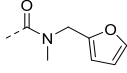
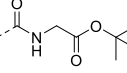
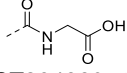
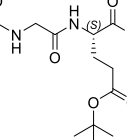
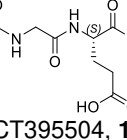
From the peptidomimetic synthesis, there were eight novel compounds to test in the competitive ligand-observed NMR, in addition to the two compounds CCT395350 (**168**) and CCT395334 (**169**). The results from testing of these ten compounds, and control compounds CCT393128 (**115**) and CCT394001 (**144**), in kinetic solubility, relaxation-edited and waterLOGSY assays are shown in Table 4.5. All compounds had good solubility ($K_{in} Sol > 500 \mu M$) and were therefore tested at the top concentration in the ligand-observed NMR assays, except for 3-pyrrolidinyl quinoxaline compound CCT394878 (**165**) which was tested at 50 μM due to its low aqueous kinetic solubility (48 μM). Therefore, 3-pyrrolidinyl parent fragment **144** was also tested at 50 μM for comparison (Table 4.5). As previously discussed, compounds with peak intensity reduction within 2σ (10%) of parent compounds CCT393128 (**115**) and CCT394001 (**144**) ($83\% \pm$

10% and 94% ± 10% respectively) were classed as showing equivalent binding to the controls (Figure 4.14).

Table 4.5. A summary of data obtained from competitive ligand-observed NMR experiments performed with 3-alkylamino quinoxaline peptidomimetic compounds.

Compounds were tested at either 500 μM, 200 μM or 50 μM depending on aqueous kinetic solubility (Kin. Sol. μM). ^a n = 1 unless otherwise indicated (mean with ± SD error for n > 1); ^b competition with 3BP2 peptide (200 μM), n = 1 unless otherwise indicated (mean with ± SD error for n > 1); ^c Decrease to baseline and inversion to positive phase indicates binding, minimal decrease to baseline indicates non-binding; ^d signal recovery indicates competitive binding.

Fragment 	Kin. Sol. (μM)	Assay Conc. (μM)	clogP (MoKa)	CPMG	CPMG	WaterLOGSY	WaterLOGSY
				+ protein ^a	+ competitor ^b	+ protein ^c	+ competitor ^d
 CCT393128, 115	861	500	0.95	83% ± 5% (n = 3)	61% ± 5% (n = 3)	Inversion to positive phase	Decrease in positive phase
 CCT395350, 168	901	500	1.7	92%	36%	Inversion to positive phase	Signal recovery
 CCT394877, 161	802	500	2.1	68%	7%	Decrease to baseline	Signal recovery
 CCT395279, 162	890	500	0.88 clogD (MoKa) -2.3	94%	38%	Inversion to positive phase	Signal recovery
 CCT395503, 164	836	500	1.0	72%	15%	Decrease to baseline	Signal recovery
 CCT395505, 118	851	500	-0.74 clogD (MoKa) -3.9	54%	7%	Decrease to baseline	Signal recovery
Fragment 	Kin. Sol. (μM)	Assay Conc. (μM)	clogP (MoKa)	CPMG	CPMG	WaterLOGSY	WaterLOGSY
				+ protein ^a	+ competitor ^b	+ protein ^c	+ competitor ^d
 CCT394001, 144	928	500	1.5	94% ± 1% (n = 2)	80% ± 1% (n = 2)	Inversion to positive phase	Decrease in positive phase

 CCT394001, 144	928	50	1.5	85%	45%	Not observed	Not observed
 CCT395334, 169	564	500	2.3	18%	7%	Positive for compound only (aggregation)	-
 CCT394878, 165	48	50	2.6	87%	21%	Not observed	Not observed
 CCT394880, 166	839	500	1.4 clogD (MoKa) -1.7	99%	89%	Inversion to positive phase (7.9 ppm)	Signal recovery (7.9 ppm)
 CCT395502, 167	765	500	1.6	95%	36%	Inversion to positive phase	Signal recovery
 CCT395504, 159	733	500	-0.18 clogD (MoKa) -3.3	86%	31%	Decrease to baseline (Inversion at 7.9 ppm)	Signal recovery

A substantial reduction in binding to TNKS2 ARC4 was observed for peptidomimetic **118**, compared with parent fragment **115**, in both relaxation-edited and waterLOGSY experiments (Table 4.5, CPMG and waterLOGSY + protein). This result indicated that **118** would have decreased binding affinity compared to **115**, which suggested that the 3-dimethylamino quinoxaline peptidomimetic was unable to form the C-terminal interactions predicted from *in silico* modelling (Figure 4.13). **161** and **164** with *tert*-butyl esters also showed reduced binding to TNKS2 ARC4 in ligand-observed NMR compared with **115**. However, unprotected glycine carboxylic acid **162** and *N*-ethylamide **168** both maintained binding to TNKS2 ARC4, which indicated that replacement of the isoxazole in this scaffold was tolerated.

For the 3-pyrrolidinyl quinoxaline compounds tested, *N*-methyl furanyl **169** showed strong positive waterLOGSY signals in the compound-only spectra, which indicated compound aggregation. Meanwhile, all the peptidomimetic compounds derived from the 3-pyrrolidinyl quinoxaline scaffold (**165**, **166**, **167**,

and **159**) showed a similar level of binding to TNKS2 ARC4 as parent compound **144** in the ligand-observed NMR assay (Table 4.5, CPMG and waterLOGSY + protein). In relaxation-edited (CPMG) experiments, the average reduction in signal intensity for these four compounds ranged from 86% to 99% in the presence of TNKS2 ARC4. Therefore, these compounds could not be ranked or differentiated from one another as they all achieved signal reduction in the upper detection limit of the CPMG assay (Figure 4.14).

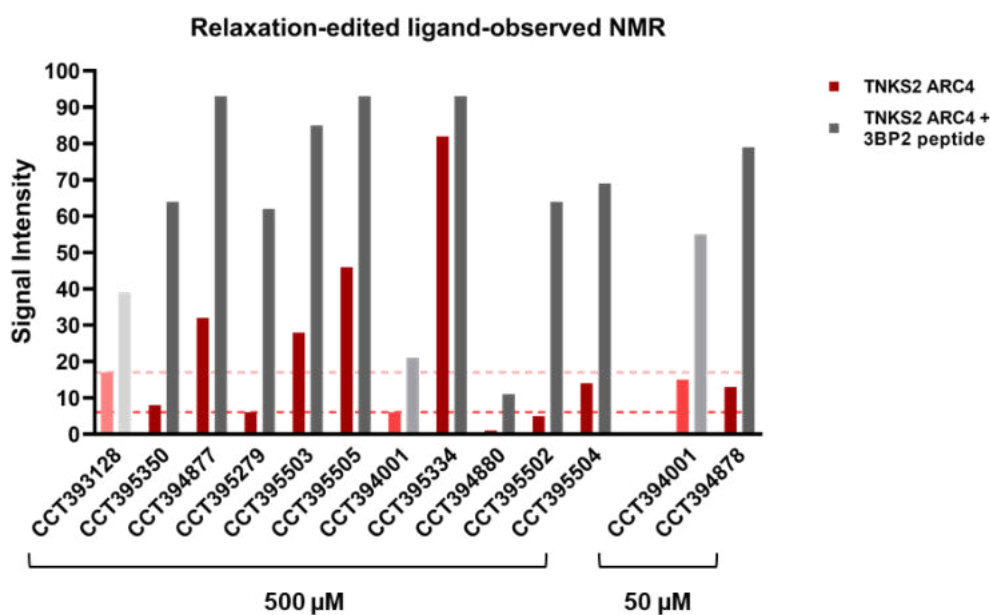


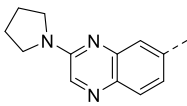
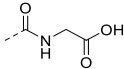
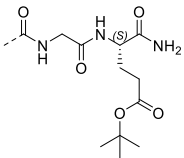
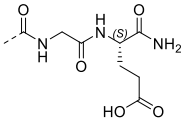
Figure 4.14. Graphical summary of results from testing 3-alkylamino quinoxaline peptidomimetic compounds in relaxation-edited ligand-observed NMR. Intensity of fragment ^1H NMR signals in the presence of TNKS2 ARC4 (red bars), and in the presence of TNKS2 ARC4 + 3BP2 peptide competitor (grey bars), as a percentage (%) of ^1H NMR signals in 'compound only' spectra. Y-axis (signal intensity) unit is %. Fragments were tested at either 500 μM or 50 μM depending on their aqueous kinetic solubility. Average reduction in signal intensity (%) for CCT393128 (**115**) (500 μM) in the presence of TNKS2 ARC4 is represented by dashed light pink threshold, whilst average reduction in signal intensity (%) for CCT394001 (**144**) (500 μM) in the presence of TNKS2 ARC4 is represented by dashed dark pink threshold.

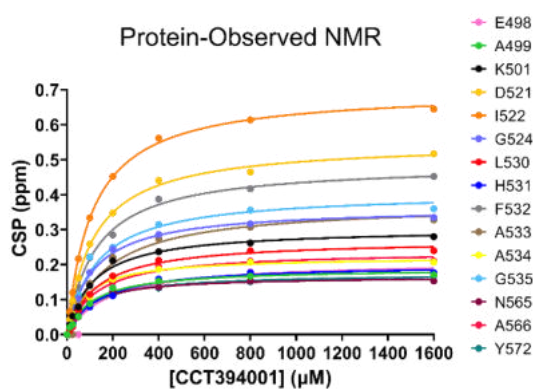
4.3.3 Testing of 3-pyrrolidinyl quinoxaline peptidomimetics in protein-observed NMR

The 3-pyrrolidinyl quinoxaline compounds were tested in protein-observed NMR experiments to rank the compounds and assess whether final peptidomimetic

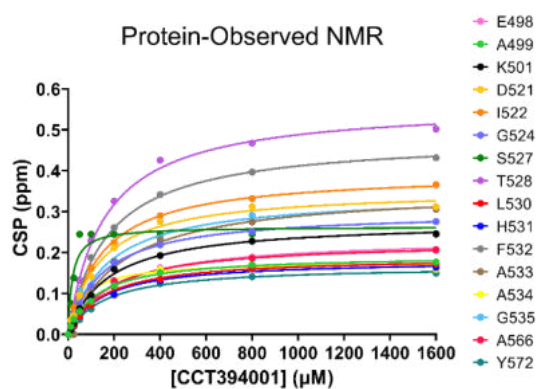
CCT395504 (**159**) had improved binding affinity compared with parent compound CCT394001 (**144**). Due to its low aqueous solubility, CCT394878 (**165**) was not tested in protein-observed NMR. A concentration of ^{15}N TNKS2 ARC4 used was $50\ \mu\text{M}$ and a sufficient ligand excess to obtain a saturation curve would not be achieved with **165**. The dissociation constants determined from ^1H - ^{15}N HSQC titration experiments for **166**, **167**, and **159** are shown in Table 4.6 and Figure 4.15. Compound **166**, with a final average K_d of $150 \pm 50\ \mu\text{M}$, showed an equivalent binding affinity to parent compound **144** ($K_d = 120\ \mu\text{M}$), therefore replacement of the isoxazole with a carboxylic acid motif maintained binding to TNKS2 ARC4. However, a loss of binding affinity was observed upon introduction of the glutamic acid residue, with a final average K_d of $520 \pm 120\ \mu\text{M}$ determined for CCT395502 (**167**) and $590 \pm 110\ \mu\text{M}$ determined for the full peptidomimetic CCT395504 (**159**).

Table 4.6. A summary of data for 3-pyrrolidinyl quinoxaline peptidomimetics determined from ligand-observed (CPMG) and protein-observed NMR assays including dissociation constant (K_d) data determined from ^1H - ^{15}N -HSQC titrations. ^a $n = 1$ unless otherwise indicated (mean with \pm SD error for $n > 1$).

Fragment	Kin. Sol. (μM)	clogP (MoKa)	CPMG + protein ^a	Average CSP (+ 1σ)	Average K_d by NMR (μM)
 CCT394001, 144	928	1.5	94% \pm 1% ($n = 2$)	0.033 (+ 0.055)	120 (\pm 30)
 CCT394880, 166	839	1.4 clogD (MoKa) -1.7	99%	0.029 (+ 0.046)	150 (\pm 50)
 CCT395502, 167	765	1.6	95%	0.020 (+ 0.031)	520 (\pm 120)
 CCT395504, 159	733	-0.18 clogD (MoKa) -3.3	86%	0.016 (+ 0.025)	590 (\pm 110)



CCT394001 (144)
Average K_d (NMR) = 120 (\pm 30) μM



CCT394880 (166)
Average K_d (NMR) = 150 (\pm 50) μM

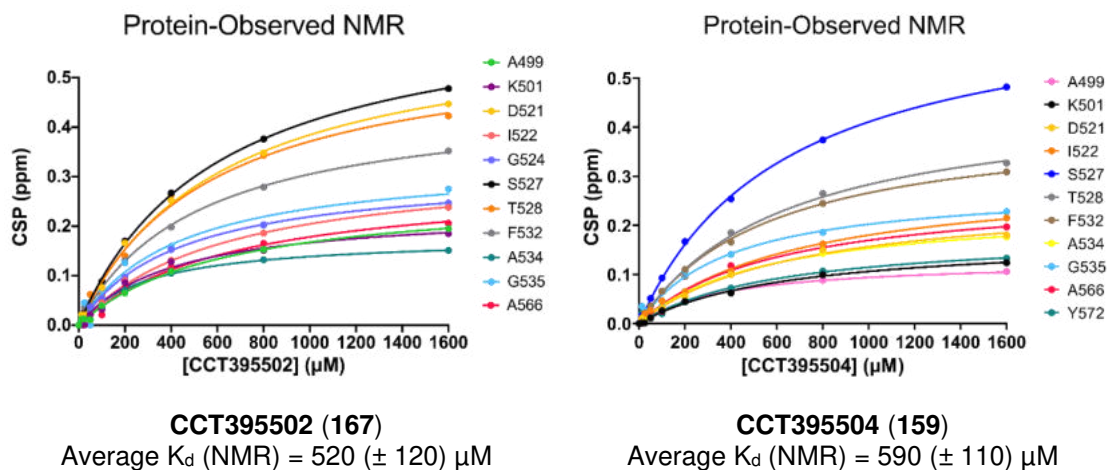


Figure 4.15. Binding affinity determined from protein-observed NMR for 3-pyrrolidinyl quinoxaline compounds. Average K_d (NMR) determination for **144**, **166**, **167** and **159**, calculated from non-linear regression analysis of significant CSPs ($\Delta d > \text{average} + 1\sigma$) against ligand concentration.

Therefore, introduction of the bulky glutamic acid residue was not tolerated, and the C-terminal interactions hypothesised from *in silico* modelling of peptidomimetic CCT395504 (**159**) were not achieved (Figure 4.13). The decreased binding affinity of **159** was consistent with the weaker binding observed in ligand-observed NMR experiments for the 3-dimethylamino quinoxaline peptidomimetic CCT395505 (**118**). This further supports the hypothesis that CCT393128 (**115**) and CCT394001 (**144**) bind to TNKS2 ARC4 in an equivalent binding mode, but it is possibly different to the binding mode suggested from NMR-guided *in silico* docking of **115** (Figure 4.1, section 4.1).

To gain insight into the binding site of the 3-pyrrolidinyl quinoxaline peptidomimetics, backbone amide ^1H - ^{15}N correlation signals which shifted ($\Delta d > \text{average} + 1\sigma$) in response to titrations with **166**, **167** and **159** were mapped on to the surface of TNKS2 ARC4 (Figure 4.16). For CCT394001 (**144**) and CCT394880 (**166**), the average CSP and standard deviation across all the TNKS2 ARC4 residues was calculated as 0.033 (+ 0.055) and 0.029 (+ 0.046) respectively (Table 4.6, Average CSP (+ 1σ)). Both the average CSP and standard deviation were around two-fold higher than for lower affinity compounds CCT395502 (**167**) and CCT395504 (**159**), showing a correlation between

dissociation constants (K_d) and the average Euclidean distance (d) shifted for backbone amide NH signals.

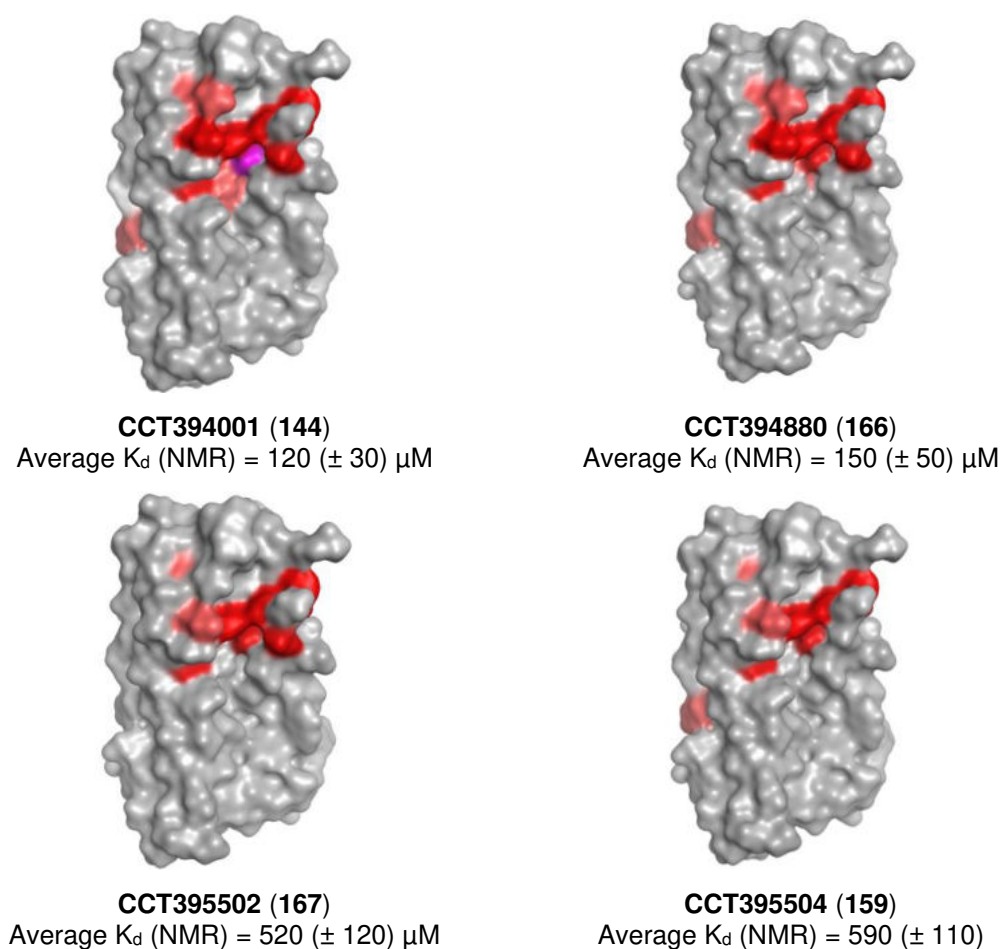
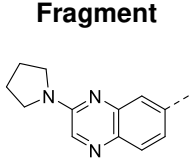
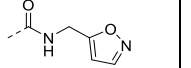
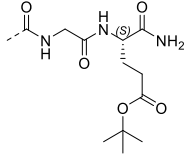
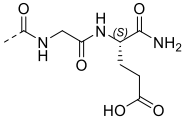


Figure 4.16. Binding site mapping from protein-observed NMR for 3-pyrrolidinyl quinoxaline compounds. Residues with significant CSPs ($\Delta d >$ average + 1σ , pink; $\Delta d >$ average + 2σ , red) from ^1H - ^{15}N HSQC titrations with **144**, **166**, **167** and **159** mapped onto the TNKS2 ARC4:3BP2 crystal structure (PDB: 3TWR).

From the binding heat-maps generated, it was observed that replacement of the isoxazole with peptide residues produced no new areas of interaction with the surface of TNKS2 ARC4 (Figure 4.16). In particular, there were no significant CSPs detected from the backbone NH of C-terminal contact residues, providing further evidence that the hypothesised interactions from *in silico* modelling with H571^{TNKS2 ARC4} and K604^{TNKS2 ARC4} were not achieved. Instead, all the 3-pyrrolidinyl compounds tested induced CSPs from nine common backbone NH of residues, which mapped primarily to the central patch region of TNKS2 ARC4

(Table 4.7). This suggested that the 3-pyrrolidin-1-yl quinoxaline-6-carboxamide motif is positioned in proximity to these nine residues which show consistent CSPs, as this motif was maintained across **144**, **166**, **167** and **159**. Higher affinity compounds **144** and **166** ($K_d \sim 100 \mu\text{M}$) both showed significant CSPs from a total of 16 residues each, and the binding site maps were identical except for two residues (T528 and N565). Therefore, the carboxylic acid of **166** was able to maintain any interactions of the isoxazole motif of **144** with TNKS2 ARC4.

Table 4.7. Summary of shifted residues from protein-observed NMR with 3-pyrrolidinyl quinoxaline compounds. Shifted residues of ^{15}N -labelled TNKS2 ARC4 with significant CSPs ($\Delta\delta > \text{average} + 1\sigma$) upon titration of each compound are represented by ticks.

Fragment					
		CCT394001 (144)	CCT394880, (166)	CCT395502 (167)	CCT395504 (159)
TNKS2 ARC4 residues significantly shifted upon fragment binding ($> \text{average} + 1\sigma$)	E498	✓	✓		
	A499	✓	✓	✓	✓
	K501	✓	✓	✓	✓
	D521	✓	✓	✓	✓
	I522	✓	✓	✓	✓
	G524	✓	✓		✓
	S527	✓	✓	✓	✓
	T528		✓	✓	✓
	L530	✓	✓		
	H531	✓	✓		
	F532	✓	✓	✓	✓
	A533	✓	✓		
	A534	✓	✓	✓	✓
	G535	✓	✓	✓	✓
	N565	✓			
	A566	✓	✓	✓	✓
Y572	✓	✓	✓		

In conclusion, synthesis and testing of hybrid fragment-peptidomimetic compounds CCT395505 (**118**) and CCT395504 (**159**) did not lead to compounds with improved binding affinity compared to parent compounds CCT393128 (**115**)

and CCT394001 (**144**). Introduction of the glutamic acid moiety to the 3-pyrrolidinyl quinoxaline scaffold was not tolerated and led to a five-fold decrease in binding affinity for CCT395502 (**167**) and **159** compared to **144**, despite all 3-pyrrolidinyl compounds showing between 86% to 99% average reduction in signal intensity in the presence of TNKS2 ARC4 from the relaxation-edited ligand-observed NMR experiment. Therefore, the relaxation-edited experiment was unable to differentiate compounds with K_d of 100 μM from those with K_d of 500 μM based on the 3-pyrrolidinyl quinoxaline scaffold. This provided further reason to replace the ligand-observed NMR assay with a more sensitive biochemical assay for testing and ranking higher affinity fragments. Furthermore, it was predicted from binding site heat-maps that the 3-alkylamino substituted quinoxaline-6-carboxamide motif bound within the central patch of the ARC domain. *In silico* docking of **115** to TNKS2 ARC4:3BP2 using MOE identified a fragment binding pose that was consistent with: CSPs from protein-observed NMR, SAR from previous fragment optimisation iterations, and binding mode 1 from *in silico* docking of CCT170746 (**28**) using GOLD. However, the design of hybrid fragment-peptidomimetics guided by the *in silico* docked structure of **115** resulted in compounds with no increase in binding affinity, which were therefore hypothesised not to form the predicted C-terminal interactions. To guide the design of further compounds or peptidomimetics based on **115**, a fragment-bound crystal structure of TNKS2 ARC4 is desired for greater confidence in the binding model.

4.4 Development of a fluorescence polarisation assay for testing of fragment analogues

The development of the fragment hit CCT170746 (**28**) ($K_d = 1100 \mu\text{M}$) into higher affinity lead fragments CCT393128 (**115**) ($K_d = 240 \mu\text{M}$) and CCT394001 (**144**) ($K_d = 120 \mu\text{M}$) had progressed the project to a stage of lead fragment optimisation. The aim of this phase was to progress lead fragments into potent substrate binding antagonists of the tankyrase ARC domain. The ligand-observed NMR assay was no longer useful for ranking fragment analogues with higher affinity, and competitiveness of the compounds with the TBM peptide could not

be reliably determined. It would not be efficient to test all synthesised analogues based on the lead fragments in protein-observed NMR to determine their binding affinities and binding sites, due to the low throughput of this technique. Therefore, to aid the development of the lead fragments into higher affinity analogues, a higher throughput biochemical assay was desired which would allow the potency of all synthesised analogues to be determined. A biochemical assay would also be more sensitive than biophysical NMR techniques and would allow determination of affinity for compounds spanning from $K_d < 1 \mu\text{M}$ to $100 \mu\text{M}$. A competitive biochemical assay was also desired to assess whether compounds bound to the substrate binding pocket of TNKS2 ARC4.

A competitive fluorescence polarisation (FP) assay was selected as the biochemical assay of choice to determine potency (IC_{50}) of higher affinity fragment analogues. This assay technique had previously been used to assess the binding of TBM peptides to the tankyrase ARC domain, and to determine potency of peptide mimetics based on TBM peptides fragment analogues.^{61, 135, 196} Therefore, there was literature precedent for the use of this biochemical assay to assess binders of the tankyrase ARC domains.

4.4.1 Introduction to fluorescence polarisation and competitive fluorescence polarisation assays

A fluorescence polarisation assay is a type of fluorescence-based biochemical assay which has been used since the 1990s in research and drug discovery to study the binding of a fluorescent probe to a biological target.²¹⁰⁻²¹³ The fluorescent probe is often a small molecule ligand or peptide labelled with a fluorophore tag, which binds to the target protein of interest.²¹⁴ A key principle of fluorescence polarisation assays is that the excitation of a fluorophore which is freely rotating in solution with linearly plane polarised light results in the emission of depolarised light.^{213, 215} The polarisation of the fluorescence emission is calculated from the difference in intensity of emitted light detected by polarisers which are oriented parallel (||) and perpendicular (⊥) to the plane of polarisation of the excitation light (equation 4.1).^{211, 216} Fluorescence anisotropy is also

calculated from these terms and is therefore related to fluorescence polarisation (equation 4.2).²¹⁶⁻²¹⁷

Equation 4.1:
$$FP = \frac{I_{\parallel} - I_{\perp}}{I_{\parallel} + I_{\perp}}$$

Equation 4.2:
$$FA = \frac{I_{\parallel} - I_{\perp}}{I_{\parallel} + 2I_{\perp}}$$

The polarisation of a fluorophore is inversely related to its molecular rotation.^{213, 215} Therefore, when a fluorescent probe which is freely rotating in solution is excited with plane-polarised light, the emitted light is depolarised (Figure 4.17a).²¹⁸ In the presence of its binding partner, the fluorescent probe is bound in a larger molecular complex which has slower rotation due to increased molecular volume.²¹⁹ Therefore, the emitted light retains a high degree of polarisation in the same plane as the excitation source (Figure 4.17b).²¹⁸ In a competitive FP assay, displacement of the fluorescent probe from its binding partner with unlabelled small molecule ligands leads to an increase of free probe in solution and the emission of depolarised fluorescence.^{214, 218} Therefore, titration of an unlabelled ligand results in a concentration-dependent decrease in FP which can be used to determine the potency or IC_{50} (concentration at 50% inhibition) of the small molecule ligand.^{210, 214}

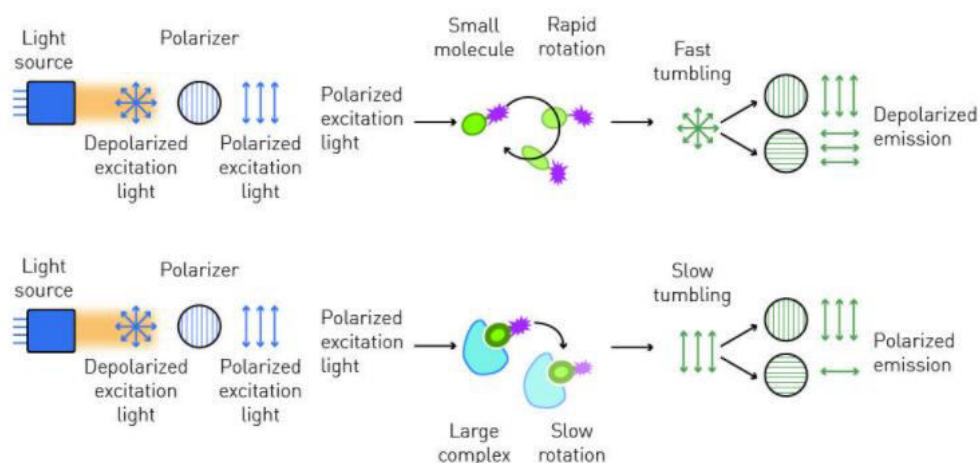
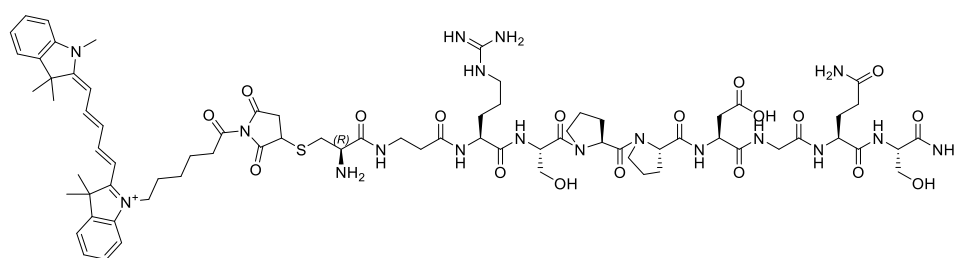


Figure 4.17. Principles of a fluorescence polarisation assay. Rapid rotation of an unbound fluorophore-labelled small molecule probe results in the emission of depolarised light upon excitation with polarised light. A fluorophore-labelled probe which is bound to protein has slow rotation and emitted light retains polarisation. Figure from BMG Labtech – Fluorescence Polarization.²²⁰

4.4.2 Establishment of a competitive fluorescence polarisation assay with a Cy5 probe

A competitive fluorescence polarisation assay had previously been established to determine the potency of peptide mimetics based on TBM peptides against the TNKS1 ARC4 domain.^{135, 152} In this assay, the FP probe used was an octameric peptide based on the TBM of the 3BP2 substrate protein, labelled with a far-red Cy5 fluorophore ($\lambda_{\text{ex}} = 640 \text{ nm}$, $\lambda_{\text{em}} = 675 \text{ nm}$).¹³⁵ The fluorophore was coupled through a cysteine maleimide at the N-terminus to minimise steric interference of the fluorophore with the peptide-ARC interaction (Cys-(Cy5)-RSPPDGQS (**170**), Figure 4.18).^{135, 152, 196} The Cy5 competitive FP assay was previously used to determine potency for peptide mimetics with IC_{50} values in the range of $22 \mu\text{M}$ to $522 \mu\text{M}$, therefore it was predicted that it would be suitable for testing 3-alkylamino quinoxaline fragments based on CCT393128 (**115**) ($K_{\text{d}} = 240 \mu\text{M}$).¹³⁵



Cy5-labelled 3BP2 8mer peptide (**170**)

Figure 4.18. Structure of the Cy5-labelled 3BP2 16mer peptide FP probe (Cys-(Cy5)-RSPPDGQS).

There were three essential steps to complete to re-establish the competitive Cy5 FP assay so that it could be used to measure the potency of 3-alkylamino quinoxaline fragment analogues.^{135, 152, 196}

4.4.2.1 Determination of the optimum Cy5 probe concentration

Firstly, a Cy5 probe titration was performed against an excess of TNKS1 ARC4 to determine the optimum concentration of probe to use in the FP assay. The Cy5-labelled 3BP2 8mer peptide probe (Cys-(Cy5)-RSPPDGQS) was purchased from a commercial supplier (JPT peptides), and TNKS1 ARC4 was produced according to established protocols as discussed in section 3.4.2. The probe was titrated from 0.06 nM to 25 nM in a ten-point two-fold titration series in the presence (10 μ M) and absence (0 μ M) of TNKS1 ARC4 (Figure 4.19). A consistent signal window of 70 to 80 mP units was achieved between protein-bound and free probe at Cy5 probe concentrations ranging from 0.88 nM and 7 nM. In this range, the polarisation readings in both conditions (with and without TNKS1 ARC4) were independent of probe concentration. A final probe concentration of 5 nM was selected for the FP assay, which was consistent with the previously used conditions.¹⁵²

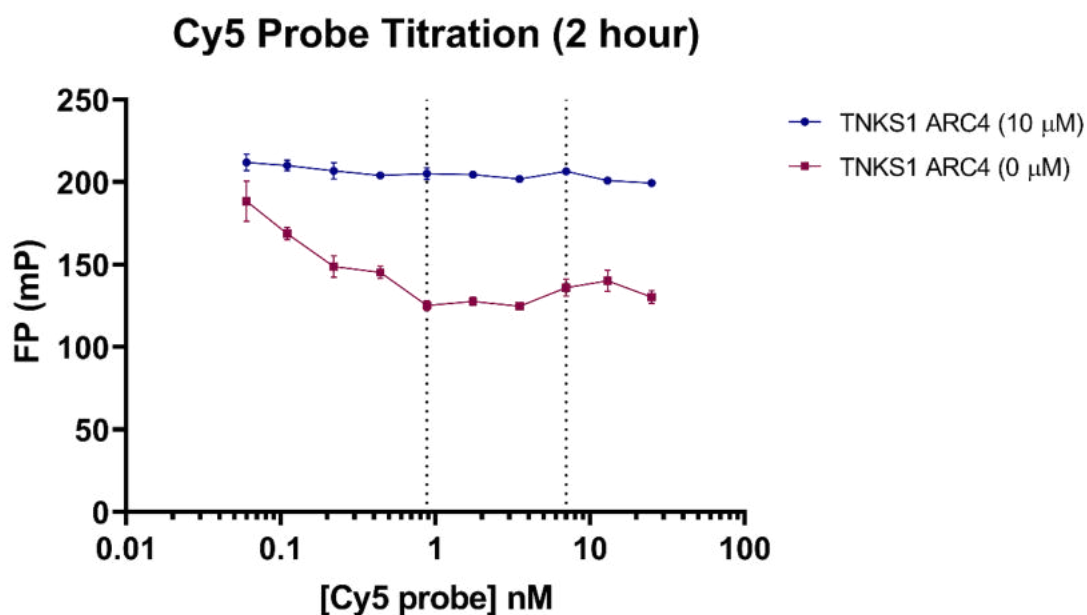


Figure 4.19. Determination of optimum probe concentration from Cy5-labelled FP probe titration. Data shown is from one independent experiment; mean of technical triplicate ($n = 3$) readings with \pm SEM error bars.

4.4.2.2 Direct binding FP assay of Cy5 probe with TNKS1 ARC4

The next step was to perform a titration of TNKS1 ARC4 against a constant concentration of Cy5 probe (**170**) in a direct binding FP experiment, to determine the optimum concentration of protein to use in the competitive FP assay. TNKS1 ARC4 was titrated from 0 μM to 25 μM in an eleven-point two-fold titration series, in the presence of 5 nM Cy5 probe. A plate reading was taken after 2 h of incubation in the dark at room temperature. The mean FP values from technical triplicate readings at each TNKS1 ARC4 concentration were baseline corrected by subtraction of the free Cy5 probe FP reading (5 nM Cy5 probe at 0 μM TNKS1 ARC4) to give corrected mean FP values (ΔFP mP). The ΔFP values were plotted against TNKS1 ARC4 concentration, and a non-linear regression analysis using a one-site total binding model was performed to yield a K_d value of 3.9 μM for the Cy5-labelled 3BP2 8mer peptide probe (Figure 4.20).^{135, 152, 196} This value was consistent with the low micromolar affinities for 3BP2 TBM peptides against the tankyrase ARC domains previously reported in the literature.^{61, 152, 196} Additional plate readings were taken after 3 h, 4 h, 5 h, and 24 h incubation times and equivalent K_d values were obtained (4.2 μM , 6.2 μM , 4.8 μM and 4.8 μM respectively), therefore binding equilibrium was reached at the initial time-point of 2 h and an incubation time of 2 h was used in the competitive FP assay.

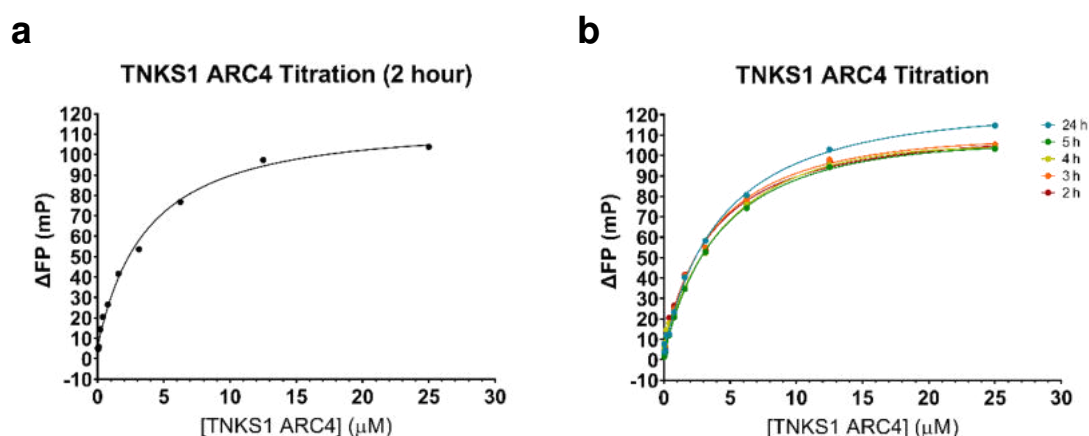


Figure 4.20. Binding affinity of Cy5-labelled FP probe from direct binding FP assay with TNKS1 ARC4. Data shown is from one independent experiment; mean FP values were calculated from technical triplicate ($n = 3$) readings. **a)** Binding affinity of Cy5 probe at 2 h. **b)** Overlay of Cy5 probe binding affinity at 2 h, 3 h, 4 h, 5 h, and 24 h.

From the direct binding experiment and Cy5 probe K_d determination, the optimum concentration of protein for the competitive FP assay was calculated. For competitive FP experiments, a protein concentration giving a bound fraction between 0.5 and 0.8 is typically selected ($0.5 < F_b < 0.8$).²¹⁴ Using the calculated probe K_d , the concentration of protein at different bound fractions (F_b) can be determined from equation 4.3. A bound fraction ranging from 0.5 to 0.8 corresponded to TNKS1 ARC4 concentrations ranging from 3.9 to 15.6 μM . A median bound fraction between 0.5 and 0.8 was chosen for the competitive FP assay ($F_b = 0.65$), corresponding to a TNKS1 ARC4 concentration of 7.25 μM (Table 4.8).

Equation 4.3:
$$[TNKS1\ ARC4] = \left(\frac{K_d \times F_b}{1 - F_b} \right) + F_b \times [probe]$$

Table 4.8. Determination of optimum TNKS1 ARC4 concentration for a competitive FP assay. Calculations of TNKS1 ARC4 concentration at different bound fractions (F_b) were determined using a Cy5 probe K_d of 3.9 μM .

Bound Fraction (F_b)	Calculation	TNKS1 ARC4 (μM)
$F_b = 0.5$	$\left(\frac{3.9 \times 0.5}{1 - 0.5} \right) + (0.5 \times 0.005)$	3.91 μM
$F_b = 0.8$	$\left(\frac{3.9 \times 0.8}{1 - 0.8} \right) + (0.8 \times 0.005)$	15.64 μM
$F_b = 0.65$	$\left(\frac{3.9 \times 0.65}{1 - 0.65} \right) + (0.65 \times 0.005)$	7.25 μM

4.4.2.3 Competitive FP assay with unlabelled control peptides

The final step in re-establishment of the Cy5 competitive FP assay was to test unlabelled 3BP2 peptides as controls. The positive control peptide chosen was the 3BP2 16mer peptide containing the octameric TBM within the sequence (Ac-LPHLQRSPPDGQSF~~RSW~~-NH₂, **56**), which had previously been used as the competitor in ligand-observed NMR experiments. A negative control peptide based on the 3BP2 16mer peptide was also tested, with a glycine to arginine mutation at position 6 (G6R) of the octameric TBM sequence (Ac-LPHLQRSPPDRQSF~~RSW~~-NH₂, **171**). The positive and negative controls were

purchased from a commercial supplier (JPT peptides) with the N- and C- terminus capped as acetyl and primary amides respectively, and an additional tryptophan residue at the C-terminus to enable the concentration of peptide stock solutions to be determined spectrophotometrically (Figure 4.21). Stock solutions were prepared to a concentration of 10 mM in HEPES buffer (25 mM HEPES pH 7.5, 100 mM NaCl, 1 mM TCEP).

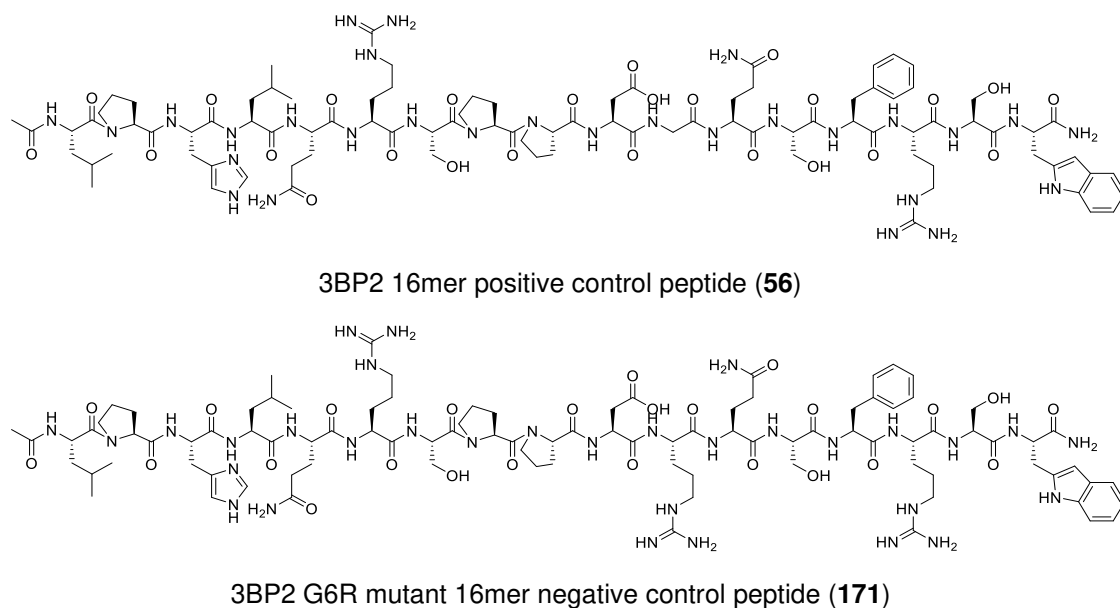


Figure 4.21. Structures of 3BP2 16mer positive and negative (G6R) control peptides.

The competition assay with the control peptides was performed with Cy5-labelled probe (5 nM) and TNKS1 ARC4 (7.25 μ M) in FP assay buffer containing CHAPS detergent (0.01% w/v) to minimise non-specific binding in wells. The unlabelled control peptides were titrated in technical duplicate from 3 nM to 935 μ M in a twelve-point three-fold titration series against Cy5 probe and TNKS1 ARC4 and the fluorescence polarisation readings were taken after 2 h of plate incubation (Figure 4.22). The FP values at each concentration were normalised to 100% (maximum signal) using the mean FP value for high control wells (Cy5 probe and TNKS1 ARC4) and to 0% (minimum signal) using the mean FP value for low control wells (Cy5 probe only) (Figure 4.22). Non-linear regression curve fit analysis was performed in GraphPad Prism (v 9.3.1) using a log(inhibitor) vs. response – variable slope (four parameters model) to calculate IC₅₀ values.

As shown in the titration curves in Figure 4.22, the IC₅₀ of the 3BP2 16mer positive control peptide (**56**) was calculated as 32 μM, which was within two-fold of the IC₅₀ (22 μM) determined from the Cy5 competitive FP assay used to test peptide mimetics.¹⁵² The 3BP2 G6R mutant 16mer peptide (**171**) showed decreased competitive binding to TNKS1 ARC4 with the Cy5 probe, with an IC₅₀ > 1000 μM (80% normalised FP response at 1000 μM), indicating that it was suitable for use as a negative control in the assay.

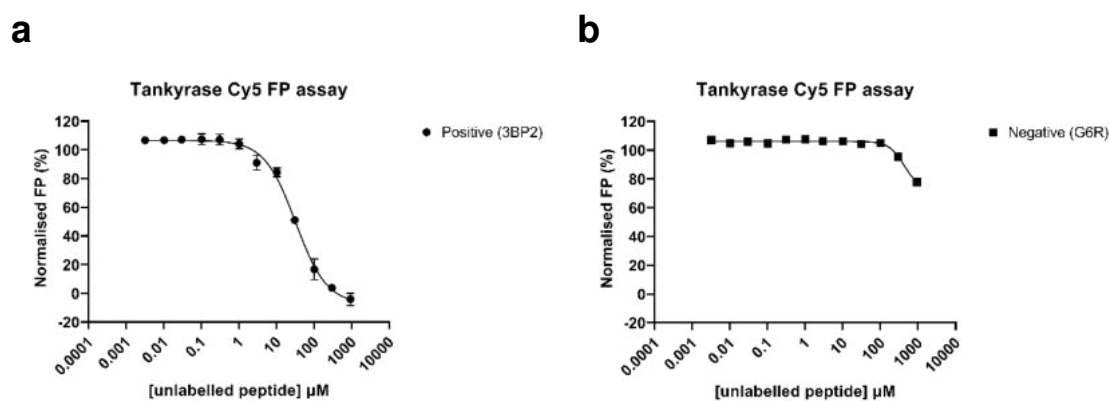


Figure 4.22. Competitive FP assay with unlabelled control peptides. Data shown is from one independent experiment; mean of technical duplicate ($n = 2$) readings with \pm SEM error bars. **a**) 3BP2 16mer positive control peptide (**56**) titration, with a calculated IC₅₀ = 32 μM. **b**) 3BP2 G6R mutant 16mer negative control peptide (**171**) titration, with a calculated IC₅₀ > 1000 μM.

In conclusion, optimum probe and protein concentrations were selected and competitive binding with positive and negative control peptides was assessed, yielding an IC₅₀ for the positive control which was consistent with its previously reported potency.

4.4.3 Competitive FP assay with unlabelled 3-alkylamino quinoxaline fragment analogues

The Cy5 competitive FP assay was successfully re-established and was next used to assess the potency of 3-alkylamino quinoxaline fragment analogues which could not be ranked using the biophysical ligand-observed NMR assay.

4.4.3.1 Competitive FP assay with unlabelled control compounds

In the competitive FP assay, unlabelled fragment analogues were titrated from 50 mM DMSO- d_6 stock solutions, therefore each well contained a final DMSO- d_6 concentration of 2% (v/v). The 3BP2 positive (**56**) and G6R negative (**171**) peptide control titrations along with high and low control wells were backfilled with 2% DMSO (v/v), so that buffer conditions were identical to fragment titrations. An equivalent IC_{50} of 29 μ M for the 3BP2 positive control peptide was determined with the addition of 2% DMSO to the FP assay buffer, from the mean of two independent experiments (Figure 4.23).

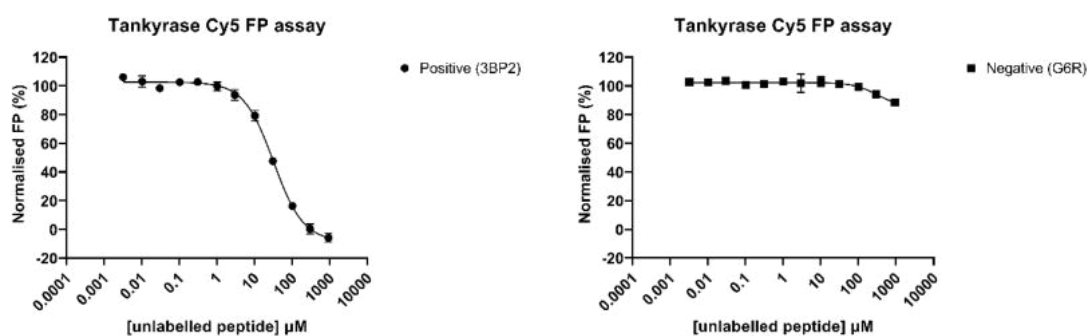


Figure 4.23. Competitive FP assay with unlabelled control peptides (+ 2% DMSO). Data shown is from one independent experiment; mean of technical duplicate ($n = 2$) readings with \pm SEM error bars. **a)** 3BP2 16mer positive control peptide (**56**) titration, with a calculated $IC_{50} = 32 \mu$ M. $IC_{50} (\pm SD) = 29 \pm 5 \mu$ M determined from mean of $n = 2$ independent experiments. **b)** 3BP2 G6R mutant 16mer negative control peptide (**171**) titration.

Initially, unsubstituted quinoxaline fragment hit CCT170746 (**28**) ($K_d = 1100 \mu$ M) and lead fragment 3-dimethylsubstituted quinoxaline fragment CCT393128 (**115**) ($K_d = 240 \mu$ M) were tested as small molecule controls for the competitive FP assay (Figure 4.24). The unlabelled fragment controls were titrated 3 nM to 1000 μ M in a twelve-point three-fold titration series against Cy5 probe (5 nM) and TNKS1 ARC4 (7.25 μ M). No binding was detected for **28**, which was expected due to its weak affinity against TNK2 ARC4 as determined by protein-observed NMR. A full sigmoidal competition curve was achieved with **115** and a mean IC_{50} of 103 μ M was calculated from unconstrained curve fit analysis from two

independent experiments. This potency was within two-fold of the binding affinity determined for **115** against TNKS2 ARC4 from protein-observed NMR ($K_d = 240 \mu\text{M}$). Therefore, the potency range of the competitive FP assay was sufficient for testing the 3-alkylamino substituted quinoxaline fragment analogues based on **115**.

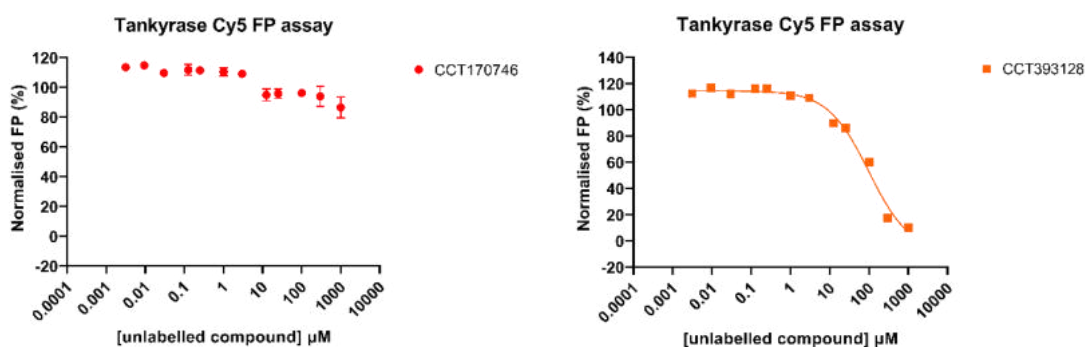
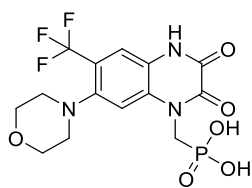


Figure 4.24. Competitive FP assay with unlabelled compounds (+ 2% DMSO). Data shown is from one independent experiment; mean of technical duplicate ($n = 2$) readings with \pm SEM error bars. **a)** CCT170746 (**28**) titration, no competitive binding. **b)** CCT393128 (**115**) titration, with a calculated $IC_{50} = 99 \mu\text{M}$. $IC_{50} (\pm \text{SD}) = 103 \pm 6 \mu\text{M}$ determined from mean of $n = 2$ independent experiments.

Fanapanel (CCT391211, **31**) was also tested as a potential control compound originating from a different fragment series, however **31** did not show competitive binding with the Cy5-labelled 3BP2 TBM peptide against TNKS1 ARC4 (Figure 4.25). This result was surprising as this compound had a K_d of $100 \pm 60 \mu\text{M}$ against TNKS2 ARC4 and was determined to bind in the arginine cradle and central patch regions from protein-observed NMR. This compound was originally identified as an ARC-binder from a biochemical competitive FRET screening assay against TNKS2 ARC4, using a labelled probe based on the optimised TBM octameric peptide sequence (REAGDGEE).¹³⁷ Therefore, **31** either did not bind to TNKS1 ARC4, or was not competitive with a TBM peptide based on the 3BP2 substrate. This highlighted a requirement to test potent compounds for multi-ARC binding and for competition with a range of TBM peptides based on different substrate proteins, in order to develop a universal substrate binding antagonist for different disease implications.



Fanapanel (CCT391211, **31**)

Average K_d (NMR) = $100 \pm 60 \mu\text{M}$
 No competitive binding (FP assay)

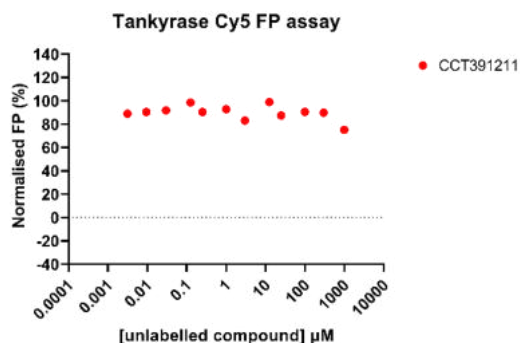


Figure 4.25. Competitive FP assay with fanapanel (31). Data is from one independent experiment.

4.4.3.2 Competitive FP assay with 3-alkylamino quinoxaline fragment analogues

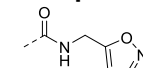
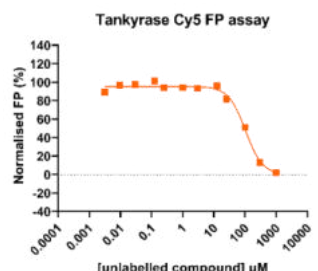
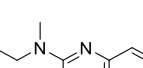
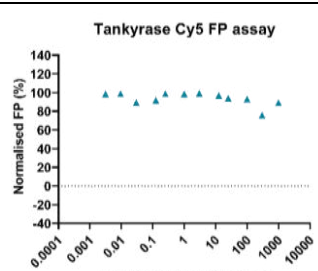
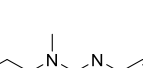
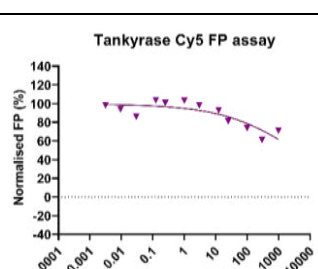

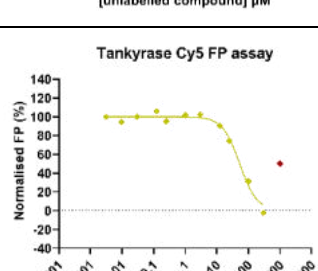

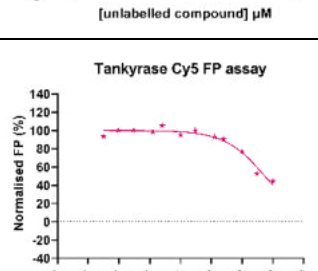
A total of 13 analogues with 3-alkylamino quinoxaline substitutions and isoxazole replacements were tested in the Cy5 competitive FP assay (Figure 4.23 and Table 4.9). However, no analogues were identified which were more potent than lead fragment CCT393128 (**115**). Only 5 out the 13 compounds tested produced FP data which was analysed to determine IC_{50} values (**141**, **142**, **143**, **146** and **148**). To obtain curve fits for these compounds from which to determine approximate IC_{50} values, the bottom plateau of the curve was constrained to 0% for all compounds which showed competitive binding (**142**, **143**, **146** and **148**). For positive controls, 3BP2 16mer peptide (**56**) and CCT393128 (**115**), constraint of the curves to a bottom plateau = 0% yielded equivalent IC_{50} values to the unconstrained curves (Table 4.9).

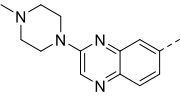
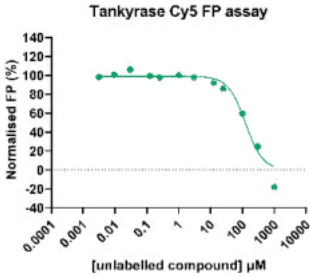
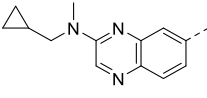
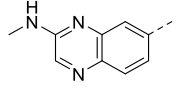
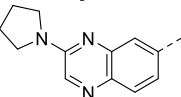
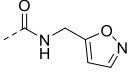
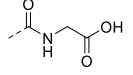
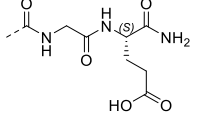
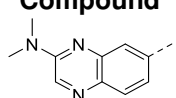
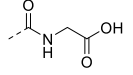
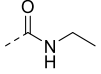
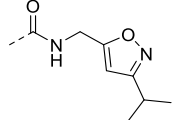
Compound CCT393936 (**141**) did not show competitive binding, despite its structural similarity to CCT393128 (**115**). An IC_{50} was not calculated for CCT393998 (**142**) as the constrained curve reached a minimum of 61% normalised FP response ($\text{IC}_{50} > 1000 \mu\text{M}$). Therefore, extending from the 3-dimethylamino substituent of lead fragment **115** with linear ethyl and propyl groups was detrimental to ARC affinity. For compounds with different sized heterocycles introduced in the quinoxaline 3-position, potencies comparable to **115** were determined. Insolubility at the top fragment concentration ($\text{IC}_{50} > 1000 \mu\text{M}$) was suspected for 3-azetidyl substituted CCT394000 (**143**). Exclusion of

this data point as an outlier gave a full curve with a good fit and an IC_{50} of 53 μM for this compound, which was within two-fold of **115**. An IC_{50} of 541 μM was calculated from the constrained curve for 3-morpholinoquinoxaline CCT394006 (**146**), which showed 44% normalised FP response at 1000 μM . For CCT394019 (**148**), a constrained curve fit with a bottom plateau of 0% was applied as the normalised FP value at the top fragment concentration was below a mathematically reasonable value (-20%). An IC_{50} of 124 μM was determined for CCT394019 (**148**) from this constrained curve fit, which was equipotent with **115**. Therefore, cyclic 3-alkylamino substitution of the quinoxaline motif was tolerated but did not lead to any compounds with significant improvement in potency compared with **115**.

Table 4.9. Summary of data obtained from competitive FP assay with control peptides and 3-substituted quinoxaline fragment compounds (+2% DMSO). ^a Data shown is from one independent experiment; mean of technical duplicate (n = 2) readings with \pm SEM error bars for control peptides; constrained curve fits to a minimum normalised FP (bottom plateau) of 0%. ^b N.T. = not tested. ^c N.Id. = None identified.

Compound	Cy5 competitive FP curve ^a	IC_{50} Hill slope R^2	LCMS (% Parent Compound) ^b	LCMS (% Major Impurity) ^c
3BP2 16mer peptide, 56 (positive control)		$IC_{50} = 23 \mu M$ Hill slope = -1.32 $R^2 = 0.98$	N.T.	N.T.
3BP2 G6R 16mer peptide, 171 (negative control)		No competitive binding	N.T.	N.T.

Compound	Cy5 competitive FP curve	IC ₅₀ Hill slope R ²	LCMS (% Parent Compound)	LCMS (% Major Impurity)
 CCT393128, 115		IC ₅₀ = 103 μM Hill slope = -1.59 R ² = 0.99	81%	14%: loss of 14 amu
 CCT393936, 141		No competitive binding	91%	N.Id.
 CCT393998, 142		IC ₅₀ > 1000 μM	95%	N.Id.
 CCT394000, 143		IC ₅₀ = 53 μM Hill slope = -1.60 R ² = 0.98	68%	N.Id.
 CCT394006, 146		IC ₅₀ = 541 μM Hill slope = -0.67 R ² = 0.96	89%	N.Id.

 CCT394019, 148		$IC_{50} = 124 \mu M$ $Hill\ slope = -1.60$ $R^2 = 0.96$	73%	N.Id.
 CCT394013, 147	Assay interference	N.D.	62%	23%: loss of 14 amu
 CCT394014, 150	Assay interference	N.D.	22%	44%: loss of 14 amu
Compound 	Cy5 competitive FP curve	IC_{50} Hill slope R^2	LCMS (% Parent Compound)	LCMS (% Major Impurity)
 CCT394001, 144	Low purity	N.D.	0%	67%: gain of 14 amu
 CCT394880, 166	Low purity	N.D.	35%	59%: gain of 14 amu
 CCT395504, 159	Assay interference	N.D.	0%	67%: gain of 14 amu
Compound 	Cy5 competitive FP curve	IC_{50} Hill slope R^2	LCMS (% Parent Compound)	LCMS (% Major Impurity)
 CCT395279, 162	Assay interference	N.D.	65%	27%: loss of 14 amu
 CCT395350, 168	Assay interference	N.D.	26%	56%: loss of 14 amu
 CCT395428, 153	Assay interference	N.D.	37%	46%: loss of 14 amu

For all compounds tested in the Cy5 competitive FP assay, the 50 mM DMSO- d_6 stock solutions used in compound titrations had been stored for between 4 to 8 months in nitrogen storage pods. LCMS analysis of the stock solutions was performed after the compounds had been tested in the FP assay for retrospective quality control. The purity was generally lower than desired; however, it was considered reasonable to report the IC_{50} values determined for compounds with purity > 65%. For the 5 analogues (**141**, **142**, **143**, **146** and **148**), for which FP data was discussed in the previous section, reasonable purities between 68% to 95% remaining parent compound were determined from retrospective LCMS analysis and no major impurities were identified (Table 4.9). The purity of control compound CCT393128 (**115**) was also acceptable at 81% parent compound. The major impurity identified for **115** was hypothesised to have formed from oxidation at the *N*-methyl followed by loss of formaldehyde, resulting in an impurity with a mass loss of 14 amu ($-CH_2$) compared to the parent compound. This was consistent with the major impurities identified for fragments containing the 3-methylamino quinoxaline substituent (**147**, **150**, **162**, **168** and **153**), as illustrated by the general structure shown in Figure 4.26. Meanwhile, LCMS analysis for compounds containing the 3-pyrrolidinyl heterocyclic substitution (**144**, **166** and **159**) revealed that minimal parent compound was remaining for these compounds after long-term storage in nitrogen pods (8 months for **144**, 4 months for **166** and **159**). The compound instability was suspected to be a result of oxidation at the carbon adjacent to the nitrogen on the 3-pyrrolidinyl substituents, resulting in formation of the stable lactams for which the mass was observed in LCMS analysis (Figure 4.27). Due to the low purity of CCT394001 (**144**) and CCT394880 (**166**) (Table 4.9, LCMS (% Parent Compound)), FP data obtained for these compounds was not analysed.

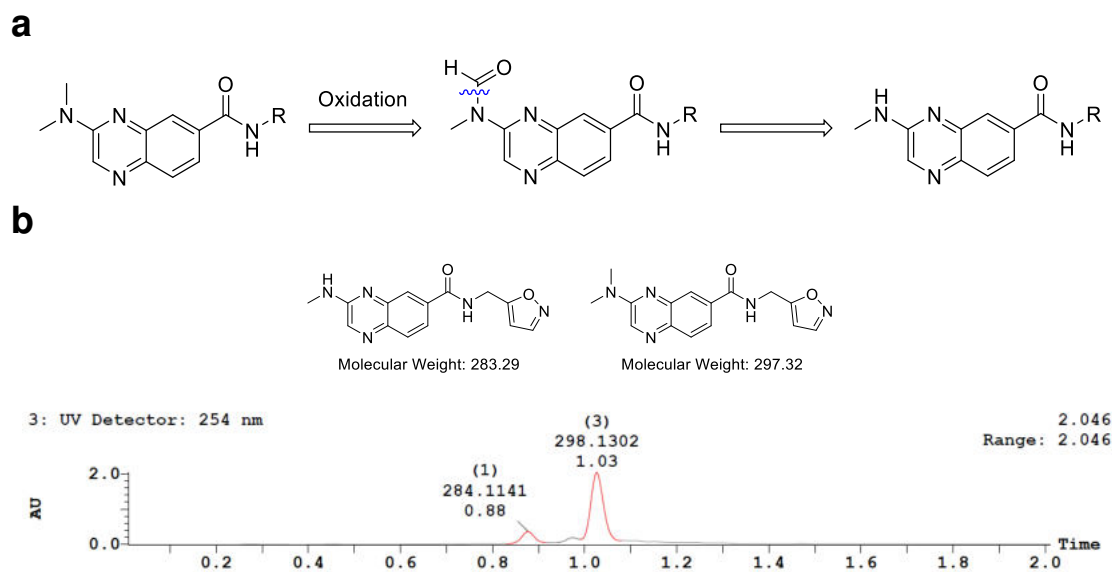


Figure 4.26. Oxidation of 3-methylalkylamino quinoxaline compounds leading to loss of -CH₂. **a)** General structure of the hypothesised products formed by oxidation of the 3-methylalkylamino quinoxaline compounds upon long-term storage of 50 mM DMSO-d₆ stock solutions. **b)** LCMS analysis of CCT393128 (**115**) 50 mM DMSO-d₆ stock solutions used in FP assay after 8 months storage in nitrogen pods: 81% parent compound ($t_R = 1.03$ min, $m/z = 298$ [M+H]⁺); 14% major impurity ($t_R = 0.88$, $m/z = 284$ [M+H]⁺) corresponding to loss of -CH₂; quantified by UV detection at 254 nm.

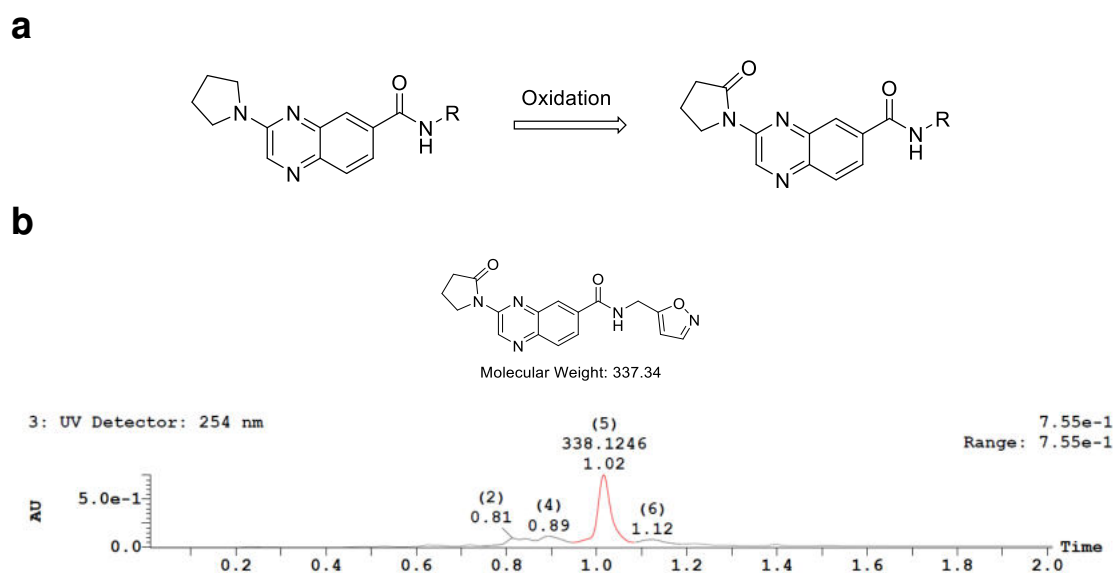


Figure 4.27. Oxidation of 3-pyrrolidinyl quinoxaline compounds to corresponding lactams. **a)** General structure of the hypothesised products formed by oxidation of the 3-pyrrolidinyl

quinoxaline compounds upon long-term storage of 50 mM DMSO-d₆ stock solutions. **b)** LCMS analysis of CCT394001 (**144**) 50 mM DMSO-d₆ stock solutions used in FP assay after 8 months storage in nitrogen pods: No remaining parent compound ($m/z = 324$ [M+H]⁺); major impurity detected corresponded to oxidised compound ($t_R = 1.02$, $m/z = 338$ [M+H]⁺).

Further to the compound instability revealed from LCMS analysis, 6 out of the total 14 analogues tested (**147**, **150**, **159**, **162**, **168** and **153**) showed assay interference in the Cy5 competitive FP assay (Table 4.9). The fluorescence intensity detectors were saturated at high compound concentrations of these compounds, therefore normalised FP values could not be determined and IC₅₀ values could not be calculated. A visual assessment of the fragment stock solutions revealed that the compounds showing assay interference were strongly red in colour, whereas stock solutions for compounds which did not interfere were typically light yellow in colour. This suggested the presence of a highly conjugated compound in the stock solutions of compounds which interfered. Although compounds **147**, **150**, **159**, **162**, **168** and **153** generally showed lower stock solution purity from LCMS (< 70% parent compound), the major impurities formed by oxidative degradation of the parent compound were likely not the source of the red colour and should not be more conjugated than the parent compounds. Therefore, it was hypothesised that a highly conjugated polymeric impurity might have formed upon long-term storage of the stock solutions, or that stock solutions of the interfering compounds might have contained leftover palladium catalyst which was not sufficiently removed by purification after aminocarbonylation reactions used in fragment synthesis.

4.4.3.3 Conclusions

In conclusion, a competitive FP assay was re-established to assess the affinity of 3-alkylamino quinoxaline analogues against TNKS1 ARC4. The binding affinity of the Cy5-labelled probe ($K_d = 3.9$ μ M) and potency determined for the 3BP2 16mer TBM positive control (IC₅₀ = 32 μ M) were both consistent with the literature-reported values determined from this assay previously, therefore the assay was next used to assess the potency of fragment analogues.^{135, 152} Whilst fragment hit CCT170746 (**28**) ($K_d = 1100$ μ M) showed no competitive binding in the FP assay, titration of lead fragment CCT393128 (**115**) ($K_d = 240$ μ M) fully

displaced the Cy5-labelled peptide and an IC_{50} of 103 μ M was determined from the mean of two independent experiments. However, no 3-alkylamino quinoxaline fragments were identified which were more substantially more potent than **115**. FP assay data could not be interpreted for 2 out of the 13 compounds tested (**144** and **166**), due to low purity of compound stock solutions. Overall, LCMS analysis of the 3-alkylamino quinoxaline fragments revealed susceptibility of the compound series to oxidative decomposition and compound instability upon long-term storage as 50 mM DMSO- d_6 stock solutions. Future repeats of the assay would need to be performed with 50 mM DMSO- d_6 stock solutions prepared immediately prior to testing. Stock solutions and solid compound stocks should also be monitored by frequent LC-MS analysis to determine the rate of compound oxidation. Furthermore, 6 out of the 13 compounds tested (**147**, **150**, **159**, **162**, **168** and **153**) showed interference in the FP assay, which correlated with a strong red colour in the stock solutions. This was hypothesised to result from a coloured impurity: either palladium catalyst or ligand left over from compound synthesis, or a polymeric impurity formed upon long-term storage of DMSO stock solutions. Prior to future assays to determine the potency of the 6 compounds, solid stocks should be subject to further purification to remove any palladium catalyst or ligand present, and new 50 mM DMSO- d_6 stock solutions should be prepared. Future repeats of the Cy5 competitive FP assays will then be used to assess all 3-alkylamino quinoxaline analogues synthesised so far, in order to identify any compounds which are more potent than CCT393128 (**115**). This will direct the future development of potent substrate binding antagonists of the ARC domain.

Chapter 5 Development of PROTACs for Targeted Tankyrase Degradation

5.1 Introduction to Targeted Protein Degradation

Protein degradation is an emerging strategy for the development of new therapeutics in targeted drug discovery which has achieved clinical proof-of-concept in recent years.³⁰ A fundamental approach in this strategy is the development of small molecules which can hijack the cellular ubiquitin-proteasome system (UPS) for the degradation of target proteins of interest.²³⁻²⁴

5.1.1 The Ubiquitin-Proteasome System

The ubiquitin-proteasome system is required for the maintenance of normal protein homeostasis. Ubiquitin-mediated protein degradation occurs through an enzymatic cascade, involving the activation of the small protein ubiquitin, transfer of ubiquitin to a substrate protein lysine residue and subsequent polyubiquitination of the protein which is recognised and degraded by the 26S proteasome (Figure 5.1).^{24, 221} Ubiquitin transfer to target proteins is achieved by E1 ubiquitin-activating enzymes (two examples), E2 ubiquitin-conjugating enzymes (~40 examples), and E3 ubiquitin ligase family members (~600 examples) which consist of four different classes: HECT-domains, U-box, monomeric RING and multisubunit RING E3 ligases.^{24, 221} The E3 ligases function in the recruitment of substrate proteins for proteasomal degradation by the recognition of peptidic motifs known as degrons.²²²

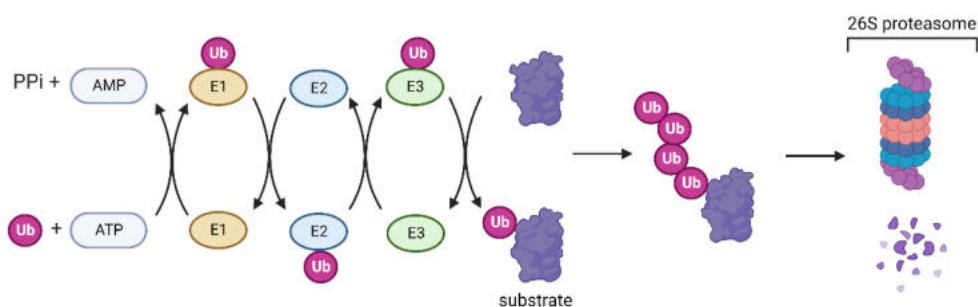


Figure 5.1. The ubiquitin-proteasome system (UPS). Ubiquitin-mediated protein degradation requires the activation of ubiquitin by E1 enzymes then transfer of ubiquitin from E2 enzymes to substrate proteins which are recognised by E3 ligases. Polyubiquitination of the substrate protein results in recognition and degradation by the 26S proteasome. Figure adapted “Ubiquitination”, by BioRender.com, 2022.

5.1.2 Development of Proteolysis Targeting Chimeras (PROTACs)

Targeting the UPS for the chemically induced degradation of selected substrate proteins has been successfully achieved with proteolysis targeting chimeras (PROTACs).²³⁻²⁴ PROTACs are heterobifunctional molecules composed of an E3 ligase recruiting ligand and a ligand for binding a target protein of interest, attached by a chemical linker.²²³⁻²²⁴ The formation of a ternary complex, driven by the PROTAC, results in proximity-mediated ubiquitination of the target protein by the recruited E3 ligase, followed by 26S proteasomal degradation of the protein of interest (Figure 5.2).²²⁵⁻²²⁶

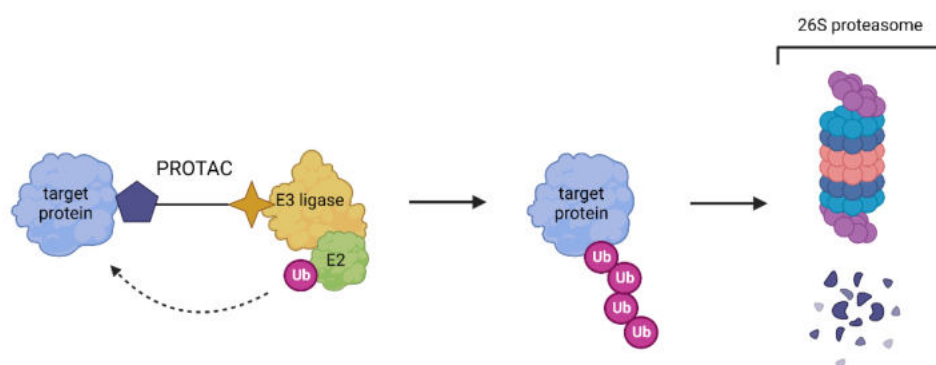
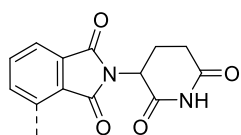


Figure 5.2. Mechanism of PROTAC-mediated degradation. The heterobifunctional PROTAC has a ligand which binds to the target protein attached through a chemical linker to a ligand which recruits an E3 ligase complex, resulting in the serial transfer of ubiquitin and thereby polyubiquitination of the protein of interest, which is then recognised for 26S proteasomal degradation. Figure created with BioRender.com, 2022.

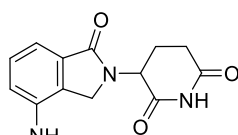
In the development of PROTACs towards a selected target protein, there are important considerations with regards to the chosen E3 ligase, the target protein and its selected ligand, and the linker.²²⁷ Although there are over 600 known E3 ligases, only four of these are typically employed in the PROTAC methodology

due to existing, well-characterised chemical ligands for these E3 ligases: cereblon (CRBN), von Hippel-Lindau (VHL), cellular inhibitor of apoptosis proteins (cIAP) and mouse double minute 2 homolog (MDM2) (Figure 5.3).^{222, 228-229} However, E3 ligases are differentially expressed across cellular compartments and tissue types, therefore the E3 ligase targeted by a specific PROTAC can influence whether degradation of the target protein is achieved.²³⁰⁻²³¹ Efforts to expand the selection of E3 ligases for use in targeted protein degradation have focused on the identification of improved ligands for previously untargeted E3 ligases.^{229, 232-234}

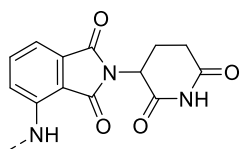
CRBN recruiting ligands:



Thalidomide (172)

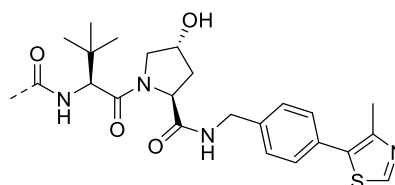


Lenalidomide (173)



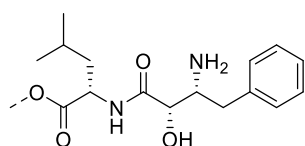
Pomalidomide (174)

VHL recruiting ligands:



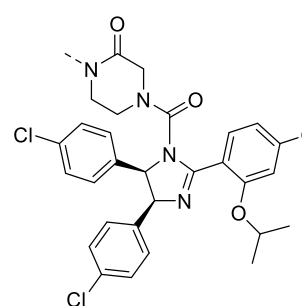
VH032 (175)

cIAP recruiting ligands:



MetBS (176)

MDM2 recruiting ligands:



Nutlin (177)

Figure 5.3. Chemical structures of E3 ligase ligands used in current PROTAC design. Linker attachment points are highlighted with a dashed bond.²²⁹

Research has also been performed to understand the significance of the linker and its influence on protein degradation.²³⁵⁻²³⁶ Importantly, the length and

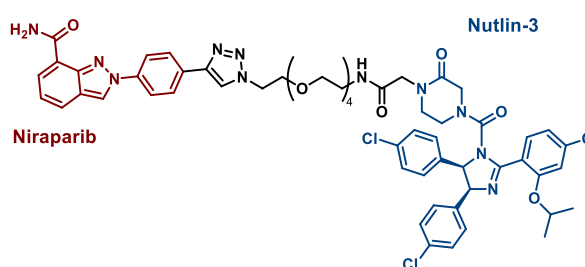
flexibility of the linker affects whether an essential ternary complex is formed between the target protein, E3 ligase and the PROTAC, and whether the complex is stabilised cooperatively, through novel protein-protein interactions and protein-linker interactions.²³⁷⁻²³⁸ In addition, the chemical structure of the linker can be modified to improve the physiochemical properties of the heterobifunctional molecules.²³⁹⁻²⁴⁰

With regards to the selection of a ligand for the target protein, existing catalytic inhibitors of protein function are often chosen. However, any ligand which binds to an E3 ligase-accessible site on the target protein with reasonable affinity ($\geq 1-500$ nM) is potentially sufficient.³⁰ The ligand does not need to be highly potent as the degradation potency of PROTACs is driven by productive ternary complexes and a catalytic mechanism of action, compared to potency of inhibitors which is dependent on binding site occupancy and a stoichiometric mechanism of action.^{223, 226} The lack of requirement for a highly potent binder of the target protein ligand extends the PROTAC methodology to proteins which are considered 'undruggable' with classical small molecule inhibitors. Highly selective inhibitors are not necessarily required as target protein ligands either, as the formation of a successful ternary complex and subsequent transfer of ubiquitin to the target protein is required for degradation, and therefore the selectivity of PROTACs can often be improved compared to a non-selective parent inhibitor.^{223, 241-242}

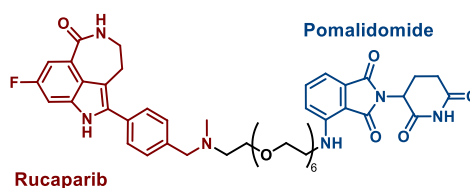
5.1.3 Targeting Scaffolding Functions with PROTACs

PROTACs have gained attention as pharmacological tools for regulating the non-catalytic, or scaffolding, functions of proteins which are often not affected by small molecule inhibitors of catalytic functions.²⁴³⁻²⁴⁴ As PROTACs result in the degradation of the entire target protein, the catalytic and non-catalytic functions of the target protein are removed, and the cellular effects of these functions are modulated.²⁴³⁻²⁴⁴ Therefore, scaffolding proteins are a highly applicable target for PROTAC technology.³⁰

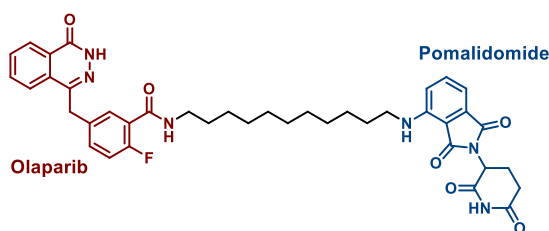
The inhibition of non-catalytic functions with PROTAC-mediated degradation has so far only been studied in the context of kinases, epigenetic targets, and tumour metabolic targets as discussed in a recent review.²⁴³ One further target protein with scaffolding functions which has been targeted using a PROTAC approach is PARP1, a DNA-dependent member of the poly(ADP-ribosyl) polymerase family of enzymes.²⁴⁴⁻²⁴⁹ Clinically approved inhibitors niraparib, rucaparib and olaparib, which bind to the catalytic NAD⁺ co-substrate binding site in the catalytic domain, were selected as the target protein binding ligands in the design of successful PROTAC degraders of PARP1 (Figure 5.4).²⁴⁵⁻²⁴⁸



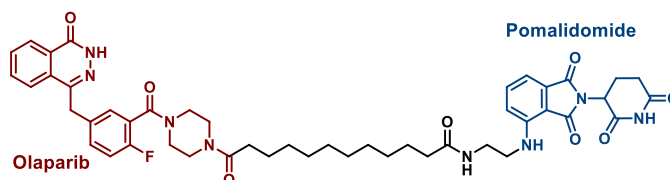
178 (Zhao *et al*, 2019)²⁴⁵



179, iRucaparib-AP6 (Wang *et al*, 2019)²⁴⁶



180, SK-575 (Cao *et al*, 2020)²⁴⁷



181 (Zhang *et al*, 2020)²⁴⁸

Figure 5.4. Chemical structures of reported PARP1 PROTACs.

Catalytic inhibitors of PARP1 have been shown to effectively kill tumour cells through inhibition of PARylation in the early stages of the DNA damage response (DDR).²⁴⁶ However, they also inhibit auto-PARylation of PARP1 which causes 'PARP1 trapping' in DNA-PARP1 scaffolds at DNA lesions, leading to further cytotoxicity through interference with DNA replication and cellular stress responses.^{244, 246} In 2019, Wang *et al* published a rucaparib-based PROTAC, iRucaparib-AP6 (**179**), which was able to block both catalytic ADP-ribosylation function and 'PARP1 trapping' scaffolding functions through chemically-induced degradation of PARP1.²⁴⁶ In contrast to rucaparib, iRucaparib-AP6 (**179**) did not result in DNA damage mediated by PARP1 trapping and prevented cytotoxic growth suppression in muscle cells and primary cardiomyocytes, therefore suggesting that PARP1 degradation could offer different therapeutic effects compared to PARP1 inhibition.^{244, 246, 249}

Therefore, the suitability of the PROTAC strategy towards members of the PARP family has been successfully demonstrated, and provides proof-of-concept for targeting the poly(ADP-ribosyl)ation functions and scaffolding functions of tankyrase using a heterobifunctional chemically-induced degradation approach.

5.2 Design and Synthesis of First-generation XAV939-based Tankyrase PROTACs

5.2.1 Rationale for design of XAV939-based amide-linked PROTACs

In the development of tankyrase degraders, the synthesis of PROTACs incorporating existing potent catalytic inhibitors of tankyrase attached *via* a suitable linker to an E3 ligase targeting moiety was proposed.^{237, 250-251} For all heterobifunctional compounds synthesised in this study to target tankyrase, the well-characterised catalytic inhibitor XAV939 (**3**) was selected as the tankyrase binding ligand.⁶⁹ XAV939 (**3**) was previously used as a chemical tool compound by Guettler and co-workers to study the catalytic and non-catalytic contributions of tankyrase in activation of Wnt/ β -catenin signalling.⁵⁷ The crystal structure of

XAV939 (**3**) bound to the catalytic PARP domain of TNKS2 was analysed to identify a suitable solvent-exposed position for attachment of a linker.⁵² From this analysis, the *para*-trifluoromethyl (-CF₃) substituent at the 4-position of the phenyl was identified as the most suitable position for attachment of a linker and conjugation of XAV939 (**3**) into a PROTAC (Figure 5.5).⁵² In addition, previous SAR studies of XAV939 (**3**) and other nicotinamide mimetics demonstrated that a range of *para*-phenyl substitutions are tolerated, including other electron-withdrawing groups and hydrophobic or polar substituents, due to minimal interaction of substituents at this position with tankyrase.^{93, 124}

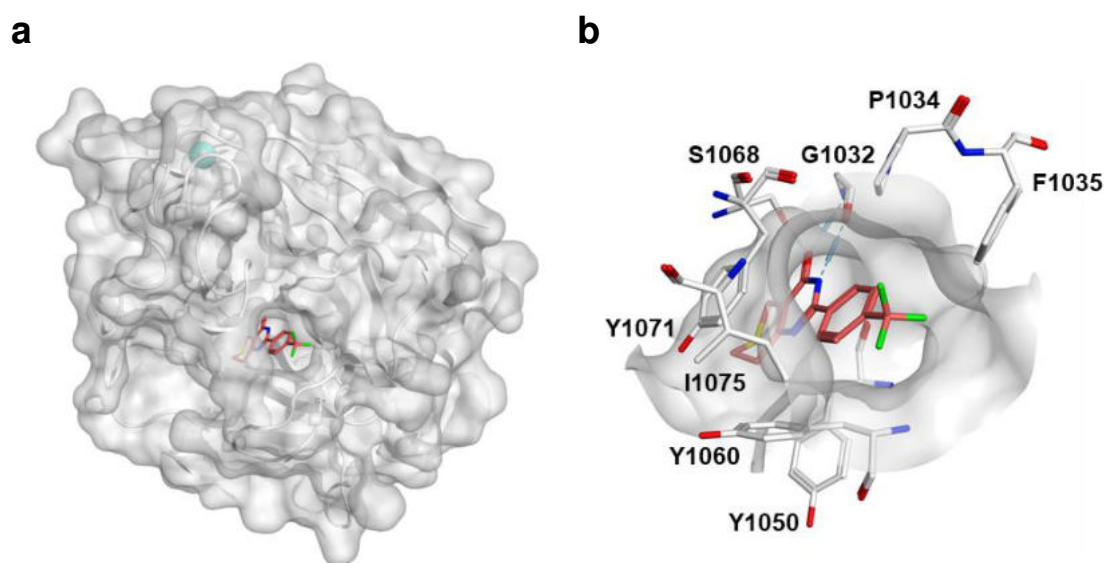


Figure 5.5. Identification of a solvent-exposed vector for design of XAV939-based tankyrase PROTACs. Crystal structure of XAV939 (**3**) (pink) bound to the catalytic domain of TNKS2 (grey) (PDB: 3KR8).⁵² **a)** Protein surface and ribbon representation highlighting the solvent-exposed -CF₃ group of XAV939 (**3**). **b)** Key interactions and interaction surface of XAV939 (**3**) with TNKS2.

The cullin4 E3 ligase complex containing cereblon as its substrate receptor (CUL4^{CRBN}) was selected as the E3 ligase targeted in the development of tankyrase degraders.^{24, 250} Therefore, thalidomide (**172**) was incorporated into the heterobifunctional compounds as a CRBN recruiting ligand and was linked to XAV939 through substitution of the phthalimide ring at the 4-position (Figure 5.6).²⁵²⁻²⁵³ The ligands for tankyrase and CRBN were connected by linkers

comprised of polyethylene glycol (PEG) units, which is a typical choice in heterobifunctional compound design due to its flexibility and amphiphilicity which can modulate the physicochemical properties of larger molecules.^{235-236, 254} Compounds with varying PEG linker lengths were proposed to allow evaluation of the effect of linker length on ternary complex formation and degradation of tankyrase (Figure 5.6). From analysis of the TNKS2 catalytic domain crystal structure in complex with XAV939 (**3**), a minimum linker length of 11 atoms containing a central 1-PEG unit was hypothesised to be sufficient for the linker to extend into solvent-exposed space and allow CRBN recruitment through the thalidomide motif.

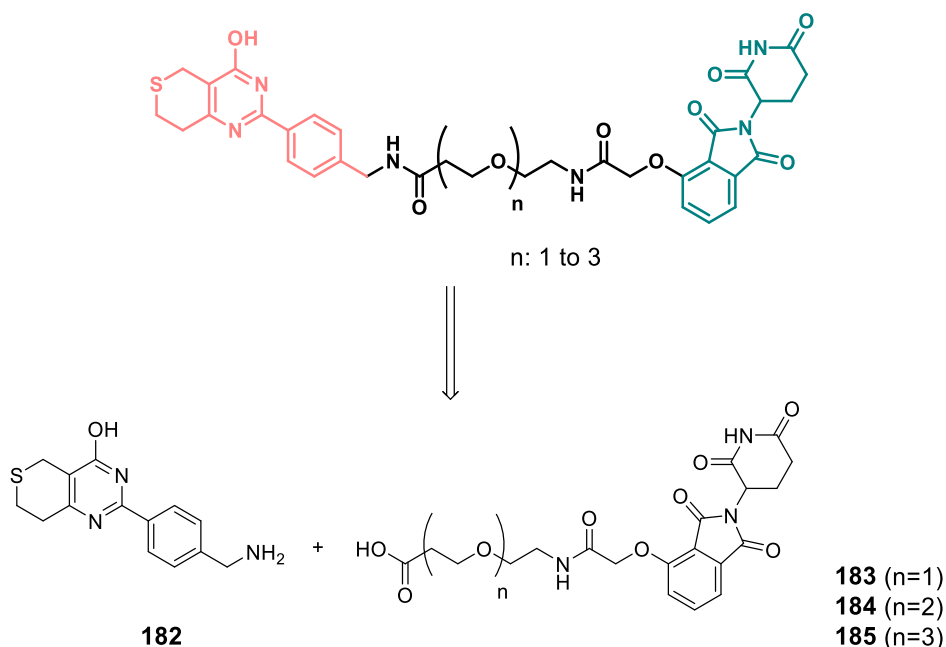


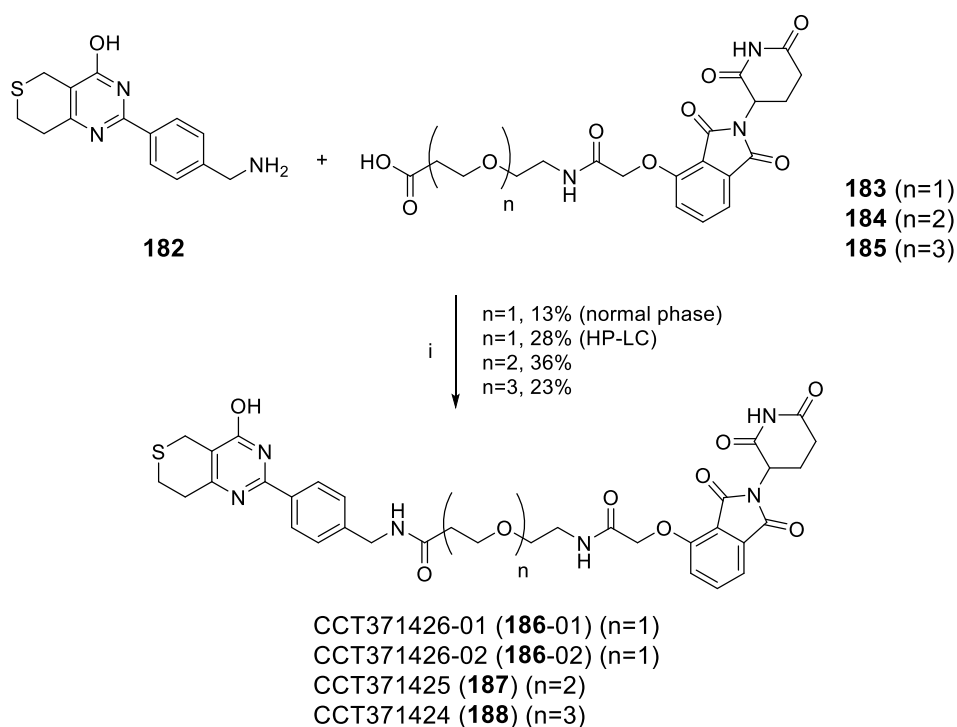
Figure 5.6. Chemical structures and retrosynthetic analysis of proposed first-generation tankyrase PROTACs. The XAV939-based tankyrase binding ligand is highlighted in pink, the PEG linker is coloured black, and the CUL4^{CRBN} E3 ligase recruiting motif based on thalidomide is highlighted in teal.

To aid the synthesis of heterobifunctional compounds based on XAV939 (**3**), the -CF₃ group was modified with a benzylic amine handle to allow the final PROTACs to be synthesised by amide bond formation. The desired benzylic amine, **182**, was synthesised by a co-worker following a two-step, literature-reported synthesis [John Caldwell, ICR CTU].⁶⁹ The E3 ligase recruiting components **183**, **184** and **185** (Figure 5.6), composed of thalidomide conjugated

to 1-, 2-, and 3-PEG linkers respectively, were also synthesised following a four-step synthetic route from 4-hydroxythalidomide by a co-worker [John Caldwell, ICR CTU].²³⁹

5.2.2 Synthesis of XAV939-based amide-linked PROTACs

The synthesis of the desired PROTACs – CCT371426-01 (**186-01**), CCT371425 (**187**) and CCT371424 (**188**) – was successfully achieved *via* a HATU-mediated amide coupling reaction of benzylic amine **182** with the E3 ligase recruiting components **183**, **184** and **185** (Scheme 5.1). The final PROTACs **186-01**, **187** and **188** were isolated in reasonable yields after a single purification by normal phase chromatography to purities > 85%, acceptable for proof-of-concept biological testing. However, optimisation of the purification strategy was required to provide these compounds in higher purity (> 95%) for further assays. To evaluate alternative purification methods, CCT371426-02 (**186-02**) was re-synthesised using a HATU-mediated amide coupling reaction and purification was instead performed by preparative HP-LC. This successfully provided CCT371426-02 (**186-02**) with a final purity of 95%.



Scheme 5.1. Synthesis of XAV939-based amide-linked tankyrase PROTACs. Reagents and conditions: i) **183**, **184**, or **185**, HATU, DIPEA, DMF (0.1 M), rt, 16 h to 22 h.

5.3 Testing of First-generation XAV939-based Tankyrase PROTACs in Target Engagement Assays

5.3.1 Assessment of tankyrase engagement using an auto-PARylation assay

The three initial PROTACs synthesised based on XAV939 (**3**) were assessed for tankyrase binding in the Division of Structural Biology in collaboration with Guettler and co-workers as indicated. CCT371426-01 (**186-01**), CCT371425 (**187**) and CCT371424 (**188**) were tested for inhibition of catalytic tankyrase activity as an indirect readout of target protein engagement. This was assessed in an *in vitro* auto-PARylation assay using recombinantly expressed full length wild-type TNKS2 [Mariola Zaleska, ICR Structural Biology]. Auto-PARylation was detected by western blotting using an anti-pan-ADP-ribose binding reagent (Figure 5.7). All three compounds showed inhibition of TNKS2 auto-PARylation activity comparable to the parent inhibitor XAV939 (**3**). This indicated successful binding of the heterobifunctional compounds to the catalytic domain of tankyrase, and showed that -CF₃ to benzylic amide substitution as well as addition of PEG linkers were both tolerated.

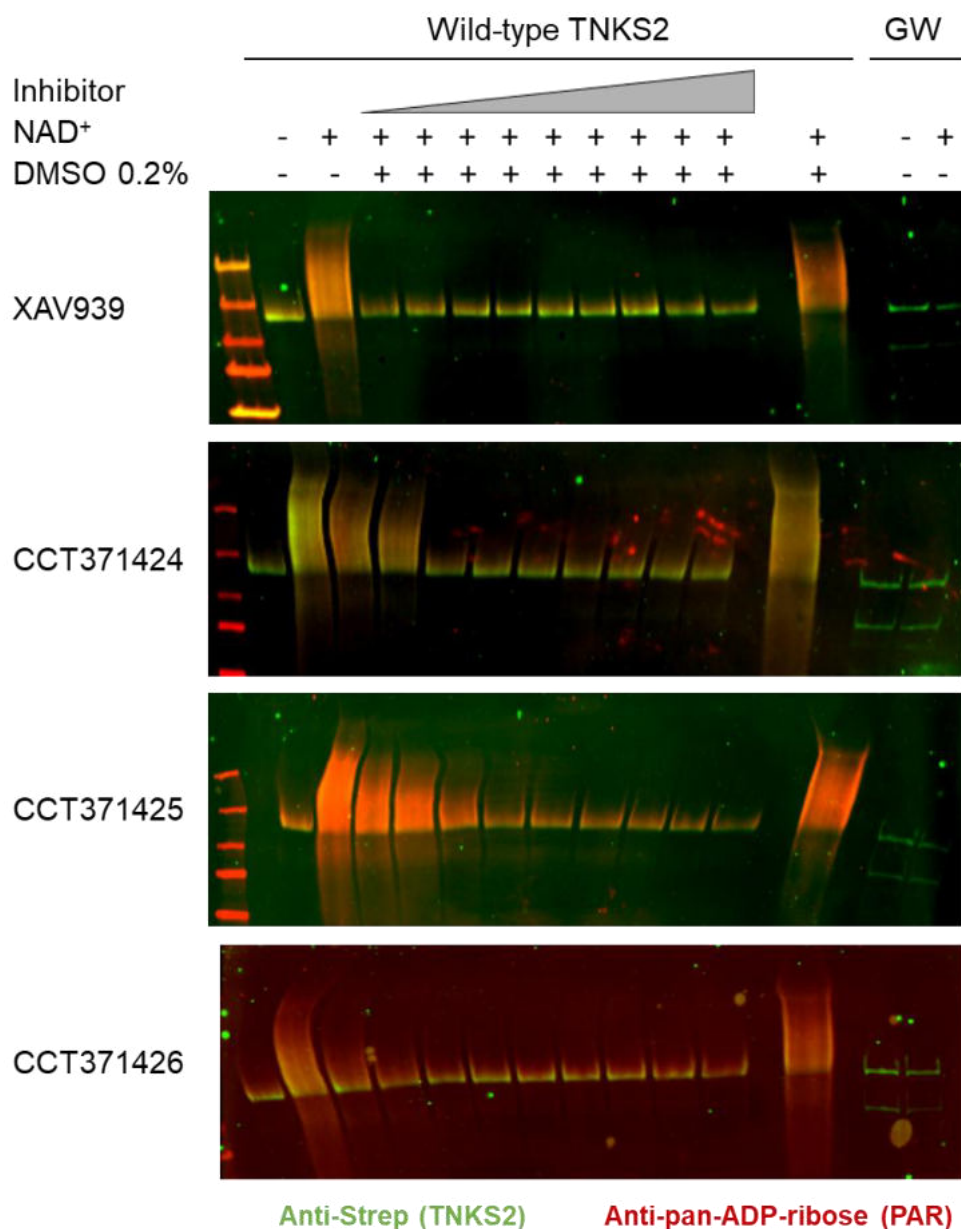


Figure 5.7. Tankyrase auto-PARylation assay with first-generation XAV939-based PROTACs. *In vitro* auto-PARylation of full-length, wild-type TNKS2 with NAD⁺ at increasing concentrations (0.039, 0.078, 0.156, 0.312, 0.625, 1.25, 2.5, 5 and 10 μ M) of inhibitors, XAV939 (**3**) and XAV939-based PROTACs: CCT371424 (**188**), CCT371425 (**187**) and CCT371426 (**186**), analysed by western blotting with anti-Strep (TNKS2) and anti-pan-ADP-ribose (PAR) primary antibodies, and fluorophore-conjugated secondary antibodies. GW represents a catalytically inactive G1032W^{TNKS2} mutant with no auto-PARylation function.⁵⁷

5.3.2 Testing in biochemical and cellular cereblon target engagement assays

The amide-linked PROTACs were next tested to evaluate binding to cereblon, using established biochemical and cellular assays within the Division of Cancer Therapeutics [ICR CTU], which were run by co-workers as indicated. CCT371426-02 (**186-02**) was tested as a representative compound for the series due to its higher final purity of 95%.

A biochemical competitive fluorescence polarisation assay using a Sulfo-Cy5 fluorophore-labelled thalidomide-based probe was used to determine the potency of **186-02** against the CRBN-DDB1 complex [Mark Stubbs, ICR CTU] (Figure 5.8). The development of this assay has been previously described in the literature.^{239, 255} The biochemical potency of **186-02** against CRBN-DDB1 was determined as $IC_{50} = 0.96 \mu M$, which was comparable to the potency of thalidomide determined as $IC_{50} = 1.34 \pm 0.37 \mu M$ ($n = 70$) in this assay (Figure 5.8). Therefore, the introduction of a linker conjugated to XAV939 (**3**) was tolerated with regards to binding of the thalidomide component of **186-02** to CRBN-DDB1.

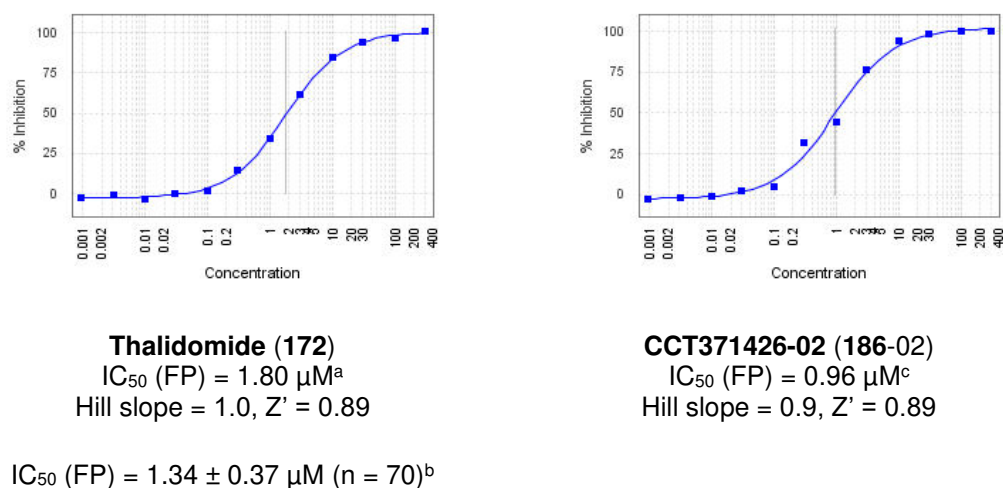


Figure 5.8. Biochemical CRBN/DDB1 FP assay with a first-generation XAV939-based PROTAC. a) Thalidomide (**172**) positive control titration. ^a IC_{50} determined from data shown, one independent experiment ($Z' = 0.89$). ^b IC_{50} determined from geometric mean of $n = 70$ independent

experiments. **b)** CCT371426-02 (**186-02**) titration. ^cIC₅₀ determined from data shown, one independent experiment (Z' = 0.89). X-axis (concentration) unit is μM.

Following this, the affinity of CCT371426-02 (**186-02**) for CRBN in a cellular context was determined using a NanoBRET target engagement assay [Olivier Pierrat, ICR CTU]. Briefly, this assay relies on the loss of bioluminescence resonance energy transfer (BRET) signal between a NanoLuc luciferase-CRBN fusion protein, expressed in live HEK293T cells, and a cell permeable fluorescent NanoBRET CRBN-binding tracer upon competitive displacement of the tracer by test compounds (Figure 5.9a).²⁵⁶⁻²⁵⁷ The cellular potency of compounds against CRBN is determined, as well as an indication of the cellular permeability of test compounds. CC-885 (**189**), a CRBN ligand with a biochemical potency determined as IC₅₀ = 0.149 ± 0.07 μM (n = 9) in the competitive FP assay, was used as a positive control in the NanoBRET target engagement assay (Figure 5.9b/c).²⁵⁸ The cellular potency of **189** was determined from this assay as IC₅₀ = 0.0066 μM. In contrast, **186-02** showed no measurable displacement of the NanoBRET tracer (IC₅₀ > 30 μM) despite its reasonable biochemical potency (IC₅₀ = 0.96 μM) (Figure 5.9d). Therefore, it was suspected that **186-02** had poor cellular permeability which resulted in limited cellular CRBN target engagement.

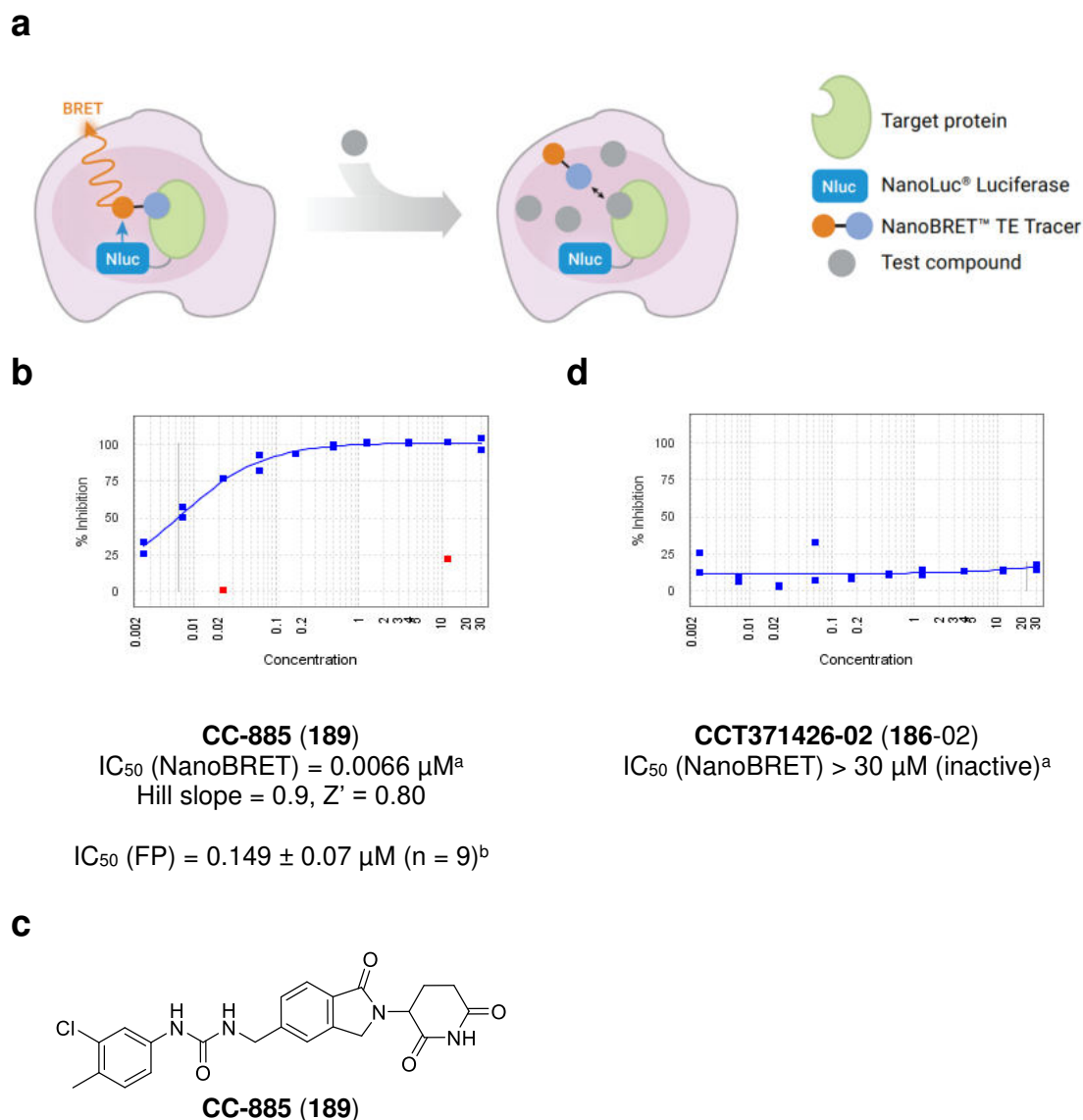


Figure 5.9. Cellular CRBN NanoBRET assay with first-generation XAV939-based PROTAC.

a) Principle of the NanoBRET target engagement assay. Figure from Promega – NanoBRET™ TE Intracellular E3 Ligase Assays.²⁵⁷ **b)** CC-885 (189) titration. **c)** Chemical structure of CC-885 (189).²⁵⁸ **d)** CCT371426-02 (186-02) titration. ^a IC_{50} determined from data shown, one independent experiment performed in technical duplicate ($Z' = 0.80$). ^b IC_{50} determined from biochemical competitive FP assay, from geometric mean of n = 9 independent experiments. X-axis (concentration) unit is μM .

From data published by Promega, two PROTAC degraders of BRD4, dBET1²⁵² and dBET6²⁵⁹, showed cellular potencies of $IC_{50} = 0.22 \mu M$ and $IC_{50} = 1.9 \mu M$, respectively, in the NanoBRET CRBN target engagement in live HEK293T cells.²⁵⁷ Prior to testing of any XAV939-based PROTACs in tankyrase

degradation assays, cellular target engagement at levels comparable to these well-characterised BRD4 degraders was desired to allow clear interpretation of any positive or negative results observed. It was hypothesised that efforts to improve the cellular permeability of the XAV939-based heterobifunctional compounds would result in measurable cellular potency against CRBN in the NanoBRET target engagement assay.

5.4 Design and Synthesis of Second-generation XAV939-based Tankyrase PROTACs

5.4.1 Rationale for design of XAV939-based ether-linked PROTACs

Heterobifunctional compounds often have high molecular weights (> 500 Da) and exist in the chemical space beyond Lipinski's 'rule of five' guidelines.^{154, 260} It is therefore more challenging to design heterobifunctional compounds with good physicochemical properties such as permeability.^{240, 261} Membrane permeability of compounds is limited by a high total number of hydrogen bond donor (HBD) groups and a high topological polar surface area (tPSA, Å²).²⁶²⁻²⁶³

In the first-generation XAV939-based tankyrase PROTACs, the two amides in the linker contributed two out of a total of four HBDs to the heterobifunctional compounds (Figure 5.10). The other two HBDs originated from the structures of the ligands XAV939 and thalidomide, which provide essential interactions with tankyrase and CRBN target proteins, respectively.^{52, 255} Therefore, in the design of second-generation XAV939-based PROTACs, the HBD count was reduced to three by removing the amide bond connected to the thalidomide motif from the linker (Figure 5.10). In the proposed compounds, the thalidomide motif would instead be incorporated into the heterobifunctional compounds through an ether bond. This structural change resulted in a 20 Å² reduction in calculated tPSA (MoKa) for each equivalent PEG linker length in addition to a reduction in total HBD count, which was also hypothesised to benefit the cellular permeability of the compounds.

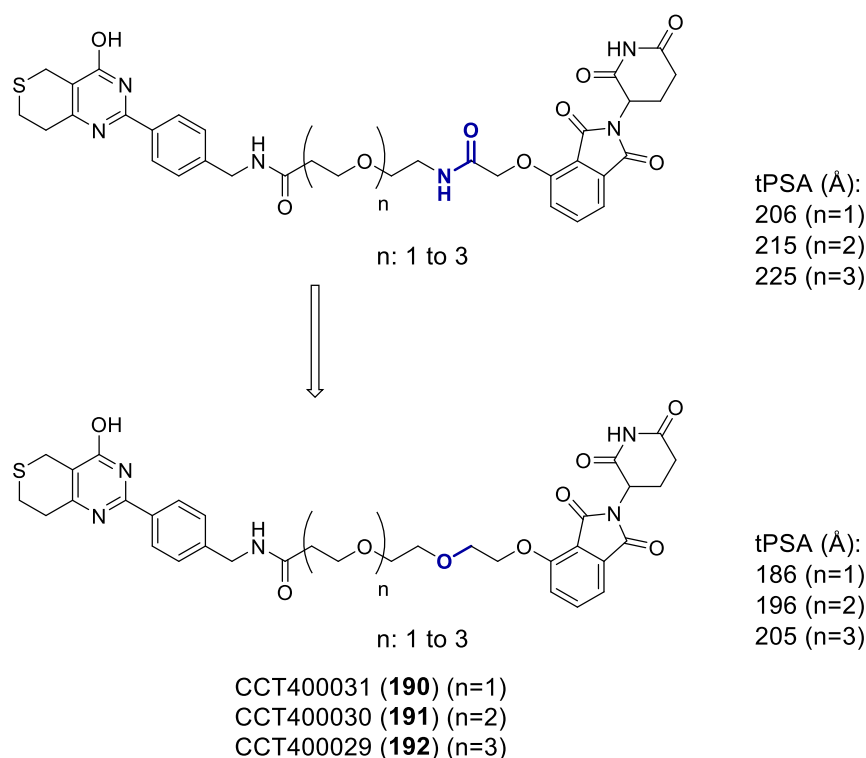


Figure 5.10. Design strategy for second-generation tankyrase PROTACs. A HBD was removed from the linker between the tankyrase binding ligand (XAV939) and the CUL4^{CRBN} E3 ligase recruiting motif (thalidomide) by switching an amide for an ether as highlighted in dark blue.

5.4.2 *In Silico* Modelling of Ternary Complex Formation

To rationalise the choice of linker lengths for the ether-linked XAV939-based PROTACs, *in silico* modelling of ternary complex formation was pursued. The development of efficacious PROTACs requires the formation of productive ternary complexes between the target protein, E3 ligase and the heterobifunctional compound, in which the length of the linker component is particularly important in bringing together the target protein and E3 ligase for proximity-mediated transfer of ubiquitin.^{235, 237} The characterisation of ternary complex formation has been pursued by obtaining X-ray crystal structures and analysis of these has shown that interactions between the linker and both proteins can be important in ternary complex formation.^{241, 264-267} However, obtaining crystal structures of ternary complexes for structure-based PROTAC design is challenging and time-consuming to pursue.²⁶⁸

In silico methods for structure prediction and modelling of PROTAC-mediated ternary complex poses have therefore been developed to aid the rational design of PROTACs. These published methods include those based on protein-protein docking, developed using MOE or Rosetta software, and those based on molecular dynamics simulations.²⁶⁸⁻²⁷² In the development of *in silico* methods using MOE software, validation was firstly performed by evaluating the ability of the method to reproduce ternary complexes from previously elucidated X-ray crystal structures.²⁶⁹⁻²⁷⁰ The methods were then applied in retrospective case studies and were used to successfully rationalise the experimentally determined degradation efficacy of PROTACs for which the ternary complex structure was unknown, illustrating the ability to use *in silico* methods to generate computationally modelled starting points for iterative PROTAC design.²⁶⁹⁻²⁷⁰

For the design of second-generation XAV939-based PROTACs, protein-protein docking between the catalytic domain of tankyrase and CRBN from the CUL4^{CRBN} E3 ligase complex was performed in MOE to model how these proteins might form a cooperative ternary complex in the presence of heterobifunctional compounds. The docking was performed by a co-worker from *In Silico* Chemistry within the Division of Cancer Therapeutics [Andrea Scarpino, ICR CTU]. The structures of the catalytic domain of TNKS2 catalytic domain in complex with XAV939 (**3**) (PDB: 3KR8)⁵² and an in-house structure of CRBN in complex with pomalidomide (**174**) were prepared using the QuickPrep panel of MOE with default parameters. Protein-protein docking was performed within the dedicated panel in MOE using the prepared CRBN:pomalidomide complex as the receptor and the prepared TNKS2:XAV939 complex as the ligand. Refinement of the protein-protein docking poses was carried out using MOE's rigid body scheme, and the 100 lowest energy conformations after refinement were further processed by calculating the distance between the centroids of the respective small molecules. It was rationalised that a heterobifunctional compound would bring the proteins together in a conformation in which the two ligand binding sites were in reasonable proximity. Therefore, six docking poses with an intermolecular distance shorter than 30 Å were visually inspected as potential models for cooperative ternary complex formation (Figure 5.11).

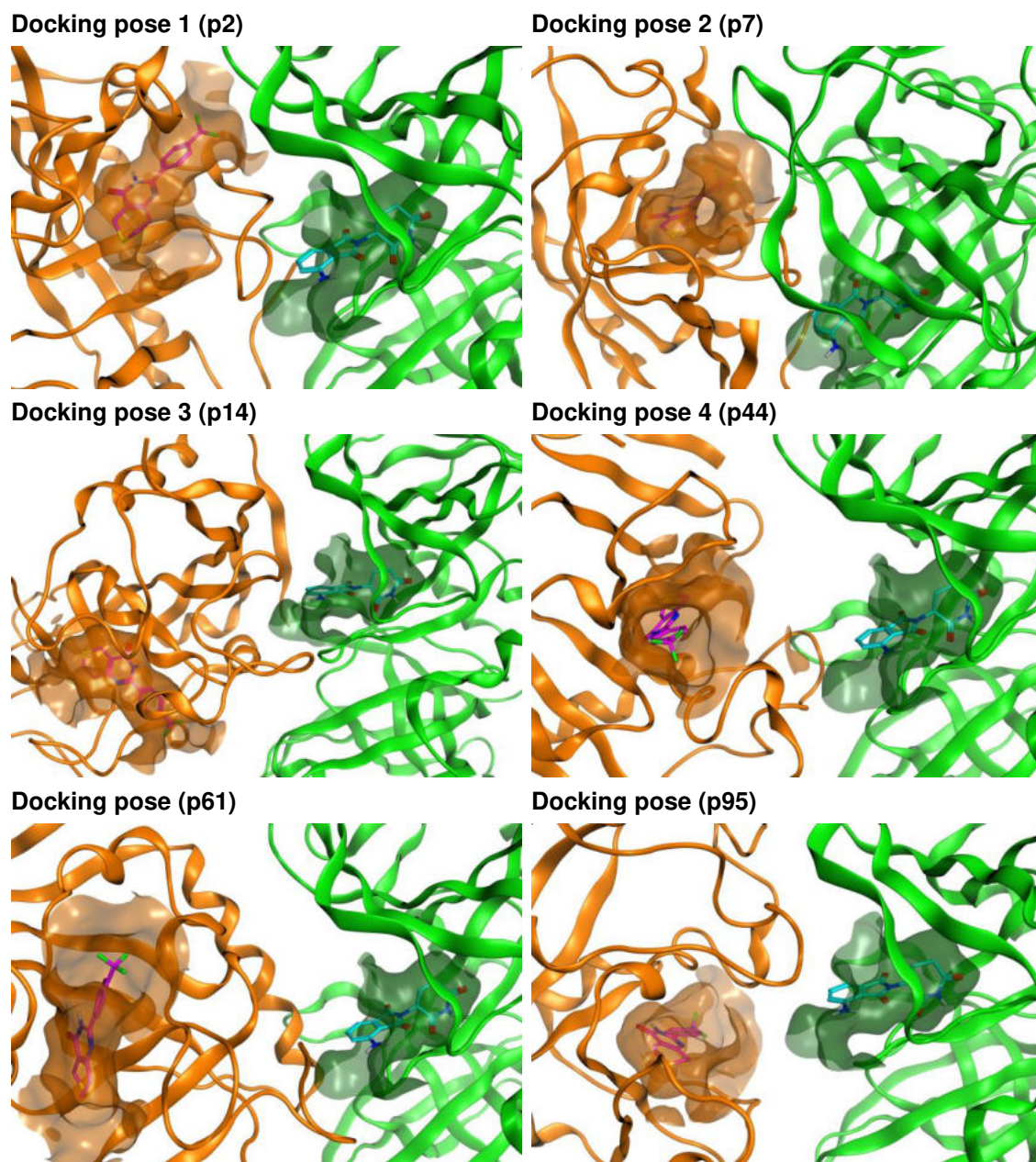


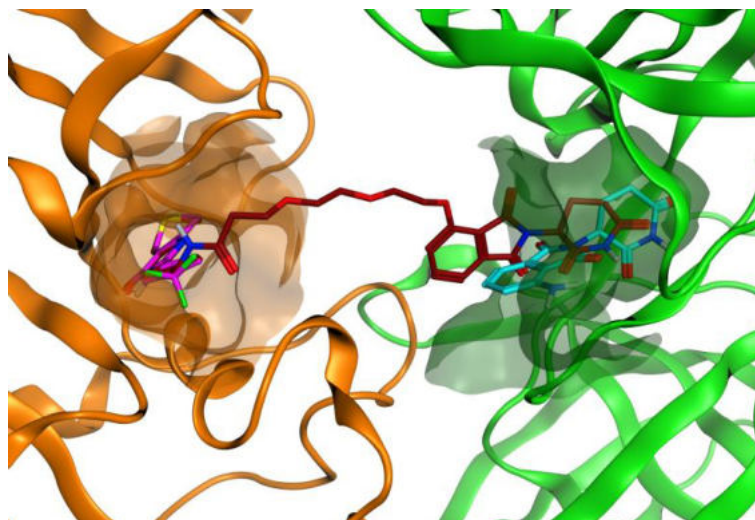
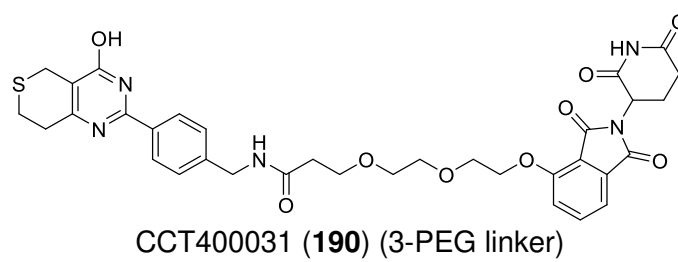
Figure 5.11. *In silico* protein:protein docking with CRBN and the catalytic domain of TNKS2. Six protein:protein interaction poses with an intermolecular distance shorter than 30 Å between the centroids of XAV939 (**3**) and pomalidomide (**174**), generated from *in silico* docking of a TNKS2:XAV939 (orange/purple) complex (PDB: 3KR8) against a CRBN:pomalidomide (green/cyan) complex.

Out of the six CRBN:TNKS2 catalytic domain complex poses, docking pose 4 (p44) showed an ideal geometry and distance between the attachment points of

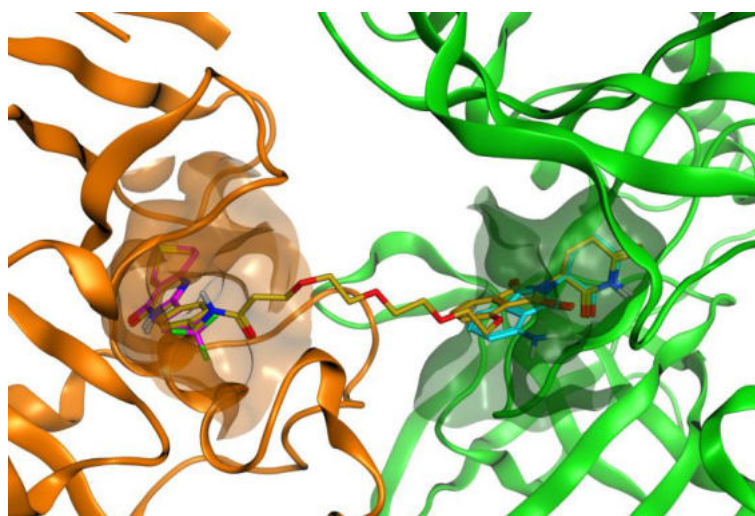
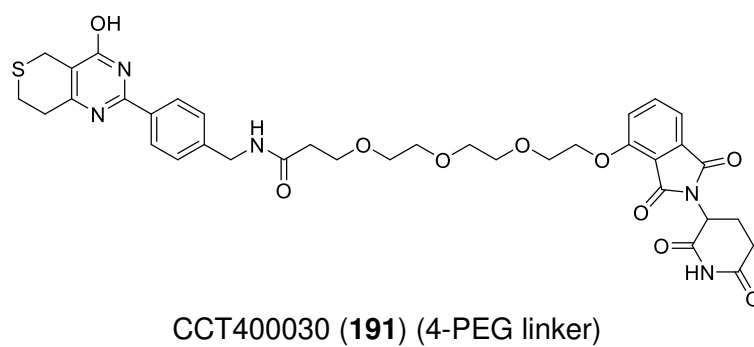
the ligands. This pose was selected for *in silico* modelling to rationalise the choice of linker lengths in the design of second-generation XAV939-based tankyrase PROTACs. The -CF₃ group of XAV939 (**3**) was modified to a benzylic amide and the 4-NH₂ group of pomalidomide (**174**) was modified to a 4-OH group using the Builder panel in MOE. The modified structures retained the conformation of their respective parent compounds XAV939 and pomalidomide upon energy minimisation within the ligand binding sites. The attachment points of the modified structures were then connected by linkers of 3-PEG to 5-PEG units using the Builder panel in MOE, and energy minimisation of the resulting compounds – CCT400031 (**190**), CCT400030 (**191**) and CCT400029 (**192**) – was performed in the presence of CRBN and the TNKS2 catalytic domain proteins (Figure 5.12).

It was observed that linker lengths of 4- and 5-PEG units of **191** and **192** were tolerated and allowed both ligands to maintain key interactions in their respective binding sites upon energy minimisation in the model (Figure 5.12a/b). However, a 3-PEG linker (**190**) would not be of a sufficient length for the XAV939-based ether-linked PROTACs if this *in silico* model was representative of ternary complex formation, as the thalidomide motif was removed from the CRBN binding pocket upon energy minimisation (Figure 5.12c). Therefore, in the design of second-generation XAV939-based ether-linked tankyrase PROTACs, linker lengths of 3-PEG, 4-PEG and 5-PEG units were chosen to test the hypothesised *in silico* ternary complex modelling.

a



b



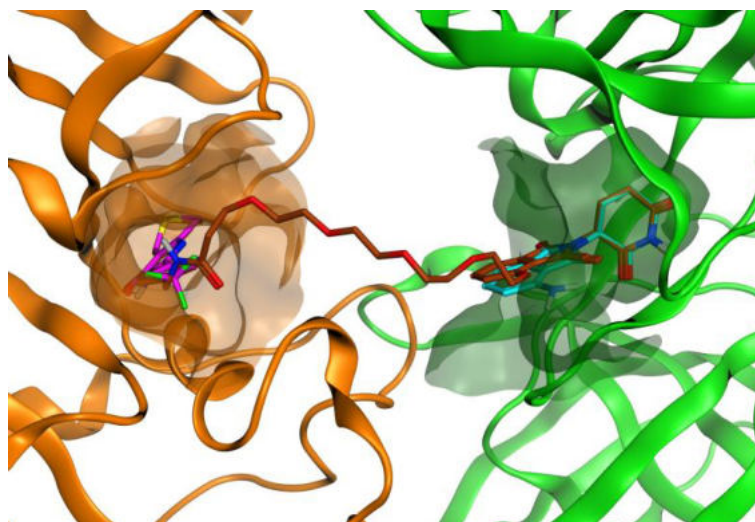
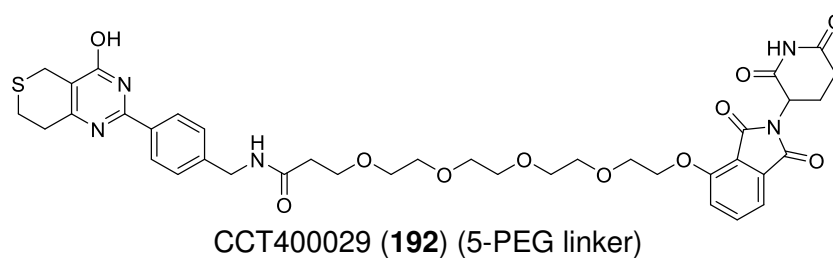
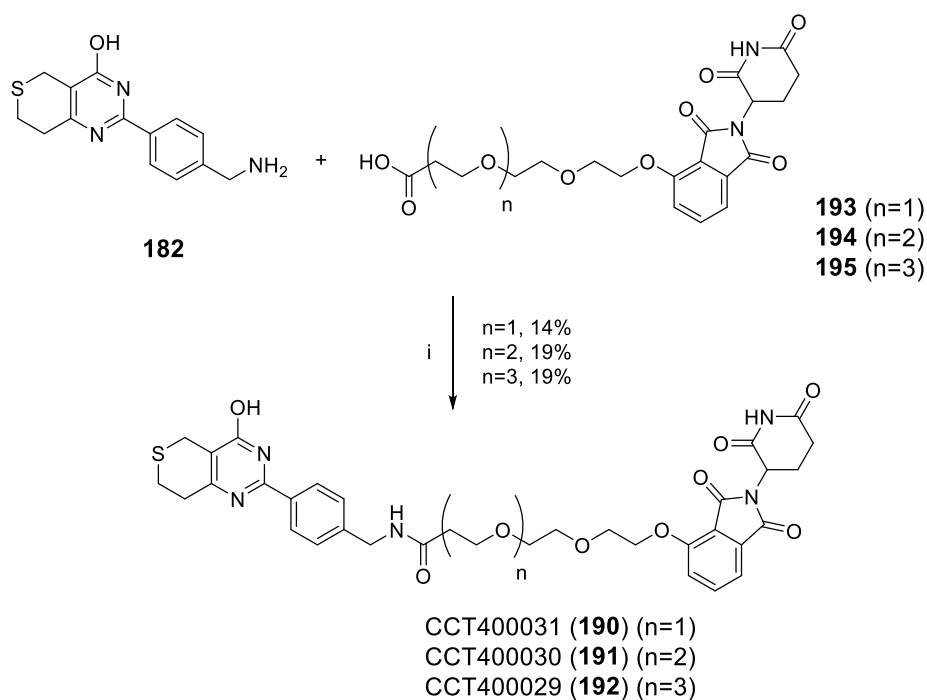
c

Figure 5.12. Rationalisation of linker lengths for second-generation XAV939-based PROTACs based on an *in silico* model of ternary complex formation. Energy minimisation (not docking) of PROTACs **a**) CCT400031 (**190**) (dark orange), **b**) CCT400030 (**191**) (gold) and **c**) CCT400029 (**192**) (dark red) in MOE against docking pose 4 (p44) from protein:protein docking of TNKS2:XAV939 (orange/purple) complex (PDB: 3KR8) against a CRBN:pomalidomide (green/cyan) complex.

5.4.3 Synthesis of XAV939-based ether-linked PROTACs

For the synthesis of the desired ether-linked PROTACs – CCT400031 (**190**), CCT400030 (**191**) and CCT400029 (**192**) – the E3 ligase recruiting components (**193**, **194** and **195**) consisting of thalidomide conjugated through an ether linkage to 3-, 4-, and 5-PEG linkers, were purchased from a commercial supplier (Tenova Pharma). Amide coupling of benzylic amine **182** with carboxylic acids **193**, **194** or **195** was performed under HATU-mediated conditions, resulting in isolation of PROTACs **190**, **191** and **192** following purification by preparative HP-LC with final purities > 92% (Scheme 5.2).



Scheme 5.2. Synthesis of XAV939-based ether-linked tankyrase PROTACs. Reagents and conditions: i) **193**, **194**, or **195**, HATU, DIPEA, DMF (0.1 M), rt, 20 h to 24 h.

5.5 Testing of Second-generation XAV939-based Tankyrase PROTACs in Target Engagement and Cellular Degradation Assays

5.5.1 Testing in biochemical and cellular cereblon target engagement assays

The ether-linked PROTACs were first tested in cereblon target engagement assays to determine whether the reduced HBD count in the linker had resulted in improved cellular target engagement and permeability of the heterobifunctional compounds. As previously, these assays were run by co-workers in the Division of Cancer Therapeutics [ICR CTU] as indicated. As shown in Table 5.1, CCT400031 (**190**), CCT400030 (**191**) and CCT400029 (**192**) showed comparable biochemical potencies ($IC_{50} \sim 0.6 \mu\text{M}$ to $1 \mu\text{M}$, $n = 2$) to thalidomide **172** ($IC_{50} = 1.34 \pm 0.37 \mu\text{M}$, $n = 70$) in the competitive FP assay against CRBN-DDB1 [Mark Stubbs, ICR CTU]. The potency of the ether-linked compounds was therefore also consistent with the previously tested amide-linked CCT371426-02 (**186-02**) ($IC_{50} = 0.96 \mu\text{M}$), demonstrating that the change to the linker was

tolerated and maintained affinity of the thalidomide component against the E3 ligase.

In the cellular CRBN NanoBRET target engagement assay (Table 5.1), the second-generation compounds (**190**, **191** and **192**) showed detectable binding to CRBN with low micromolar cellular potencies ($IC_{50} \sim 1 \mu\text{M}$ to $5 \mu\text{M}$, $n = 1$) [Olivier Pierrat, ICR CTU]. Therefore, ether-linked compounds showed improved CRBN engagement in a cellular context compared to the amide-linked compound **186-02** as hypothesised, which was attributed to improved cellular permeability due to a reduction of the HBD count in the linker and subsequent reduction in tPSA. With cellular potencies comparable to the well-characterised BRD4 degraders dBET1 and dBET6 ($IC_{50} = 0.22 \mu\text{M}$ and $IC_{50} = 1.9 \mu\text{M}$),²⁵⁷ the second-generation ether-linked XAV939-based PROTACs were progressed and submitted for further profiling in tankyrase target engagement and degradation assays.

Table 5.1. Summary of data from biochemical and cellular CRBN target engagement assays with second-generation XAV939-based PROTACs and control compounds. IC_{50} values are calculated from a dose-response curve using a log[inhibitor] vs response – variable slope (four parameter) model. ^a IC_{50} (\pm SD) determined from mean of $n = 2$ independent experiments, except where otherwise indicated. ^b IC_{50} determined from one independent experiment performed in technical duplicate. ^c IC_{50} (\pm SD) determined from mean of $n = 2$ independent experiments performed in technical duplicate.

Compound	CRBN FP assay ^a (Biochemical IC_{50})	CRBN NanoBRET assay ^b (Cellular IC_{50} , HEK293T cells)
CCT400031 (190)	$IC_{50} = 1.02 \pm 0.52 \mu\text{M}$	$IC_{50} = 1.04 \mu\text{M}$
CCT400030 (191)	$IC_{50} = 0.61 \pm 0.06 \mu\text{M}$	$IC_{50} = 3.44 \mu\text{M}$
CCT400029 (192)	$IC_{50} = 0.77 \pm 0.24 \mu\text{M}$	$IC_{50} = 5.37 \mu\text{M}$
Thalidomide (172)	$IC_{50} = 1.36 \pm 0.28 \mu\text{M}$	—
CC-885 (189)	$IC_{50} = 0.149 \pm 0.07 \mu\text{M}$ ($n = 9$)	$IC_{50} = 0.011 \pm 0.005 \mu\text{M}^c$

5.5.2 Assessment of cellular tankyrase engagement using a Wnt/ β -catenin reporter assay

The assay discussed in the following section was performed by a co-worker in the Guettler lab within the Division of Structural Biology [Ben Broadway, ICR Structural Biology]. The second-generation XAV939-based PROTACs – CCT400031 (**190**), CCT400030 (**191**) and CCT400029 (**192**) – were tested in a Wnt/ β -catenin responsive reporter assay in haploid HAP1 7TGGRR human cells [Ben Broadway, ICR Structural Biology]. Upon increasing concentrations of XAV939 (**3**), reporter activation decreased in line with catalytic inhibition of tankyrase resulting in decreased levels of active β -catenin. The assay therefore provided an indirect readout of tankyrase target engagement in a cellular context. XAV939-based compounds CCT400031 (**190**) and CCT400030 (**191**) showed decreased Wnt/ β -catenin reporter activation upon increasing concentrations of compound in a manner consistent with XAV939 (**3**) as a positive control (Figure 5.13), as did CCT400029 (**192**) (data not shown, n = 1 independent experiment). Therefore, the heterobifunctional compounds based on XAV939 (**3**) maintained inhibitory cellular potency against tankyrase at a level comparable to the parent compound. Interestingly, in HAP1 7TGGRR cells with low endogenous tankyrase expression, Wnt signalling activation was reduced to ~10% upon treatment with XAV939 (**3**) (10 μ M). This contrasted to the ~50% reduction with XAV939 (**3**) treatment (10 μ M) observed in previous luciferase reporter assays using HEK293T cells transiently transfected with, and therefore overexpressing, MYC₂-tagged tankyrase constructs (Figure 1.14a), as discussed in section 1.5.2. The difference in the extent of modulation of Wnt/ β -catenin signalling activation upon catalytic inhibition in these two contexts was therefore hypothesised to be a result of the different level of tankyrase expression in these cell lines. It was hypothesised that catalytic inhibition of tankyrase would have a greater effect on modulating the activation of Wnt signalling when tankyrase levels are low, as the concentration-dependent scaffolding functions of tankyrase which are able to promote Wnt/ β -catenin signalling independently of catalytic activity would be reduced, compared to when tankyrase is overexpressed.

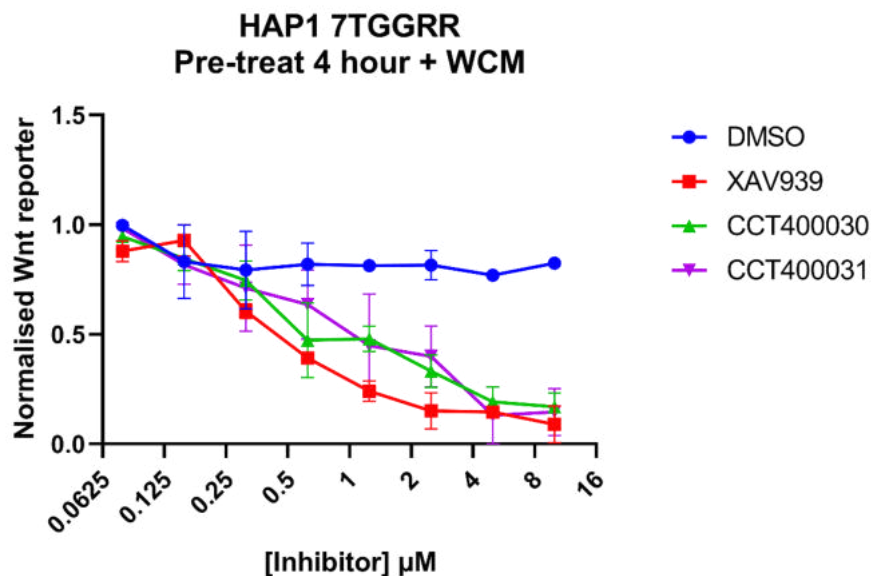


Figure 5.13. Cellular tankyrase Wnt/ β -catenin responsive reporter assay with second-generation XAV939-based PROTACs. Activation of Wnt/ β -catenin-dependent transcription by endogenous tankyrase in haploid HAP1 7TGRR human cells at increasing concentrations (0.078, 0.156, 0.312, 0.625, 1.25, 2.5, 5 and 10 μM) of inhibitors, XAV939 (**3**) and XAV939-based PROTACs: CCT400031 (**190**) and CCT400030 (**191**). HAP1 7TGRR cells were pre-treated with inhibitors for 4 h then media was exchanged for Wnt conditioned media (50%), and cells were incubated with inhibitors for 24 h prior to measurement of luciferase signal. Wnt luminescence and reference luminescence was normalised to DMSO. Data shown is mean of two independent biological replicates ($n = 2$) with \pm SEM error bars.

5.5.3 Cellular assessment of tankyrase degradation

Following confirmation of both cereblon and tankyrase binary target engagement in cells with the second-generation XAV939-based PROTACs, the compounds were progressed to an assessment of tankyrase (TNKS1 and TNKS2) degradation in a cellular context [Ben Broadway, ICR Structural Biology]. This work was also performed in the Division Structural Biology in collaboration with Guettler and co-workers as indicated. Haploid HAP1 7TGRR cells were treated with CCT400031 (**190**) and CCT400030 (**191**) at a concentration range consistent with that used in the Wnt/ β -catenin reporter assay (Figure 5.14). After 24 h incubation, tankyrase protein levels in HAP1 7TGRR cells were assessed by western blotting using a commercial TNKS1/TNKS2 antibody (E10) (Santa Cruz Biotechnology).

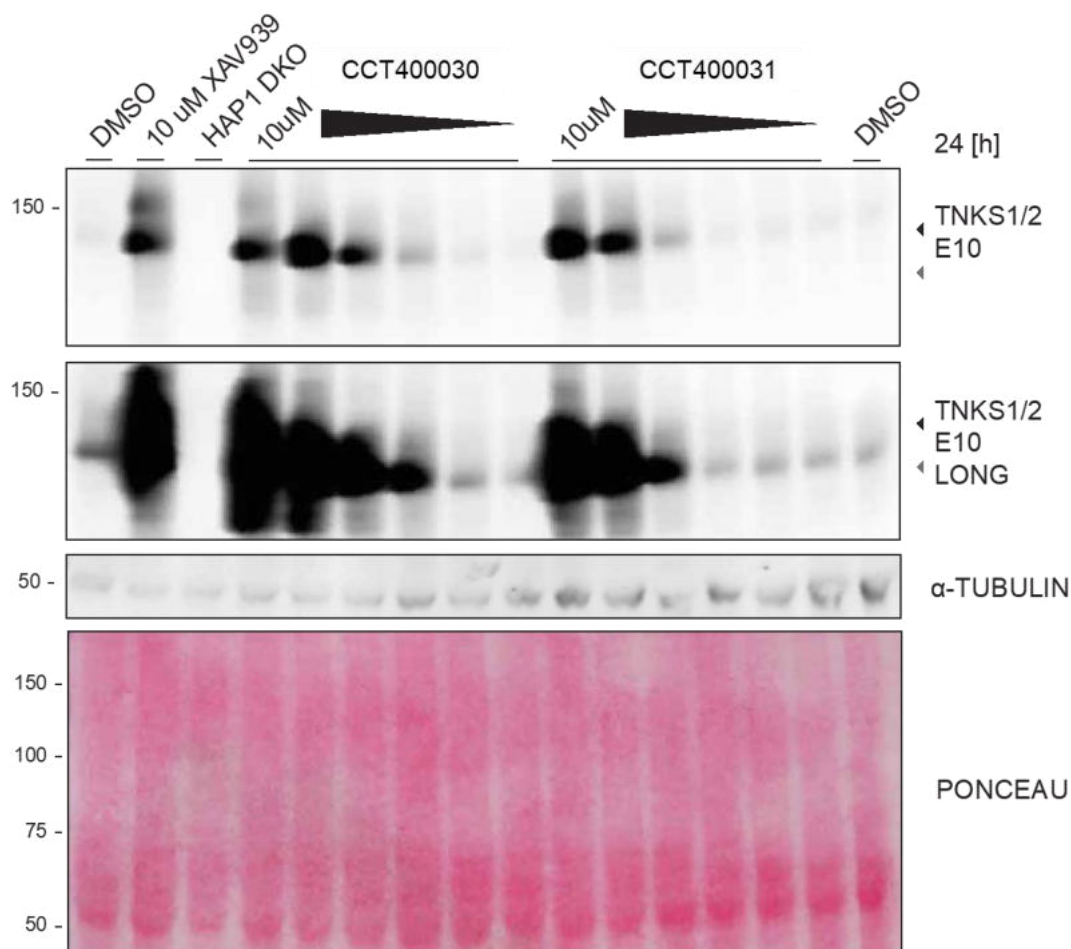


Figure 5.14. Western blot analysis of cellular tankyrase levels in HAP1 7TGRR cells. HAP1 7TGRR cells were incubated at increasing concentrations (0.041, 0.13, 0.37, 1.11, 3.33, and 10 μM) of inhibitors, XAV939 (**3**) and XAV939-based PROTACS, CCT400031 (**190**) and CCT400030 (**191**), for 24 h prior to western blot analysis. HAP1 DKO refers to a double TNKS1 and TNKS2 knockout HAP1 7TGRR cell line. Images with different integration times (exposures) are shown: Top image is a short exposure and second-top image is a long exposure.

As shown in Figure 5.14, degradation was not observed with either of the heterobifunctional compounds tested. Instead, stabilisation of tankyrase protein levels was detected upon increasing concentrations of CCT400031 (**190**) and CCT400030 (**191**) up to 10 μM. This observation was consistent with typical behaviour of catalytic tankyrase inhibitors, such as XAV939 (10 μM XAV939, Figure 5.14), which cause tankyrase accumulation as a result of auto-PARylation inhibition, and subsequent inhibition of ubiquitination and degradation through a PAR-dependent pathway mediated by the RNF146 E3 ligase complex (refer to discussion in section 1.5.2).⁵⁷

Several explanations for the lack of successful tankyrase degradation with the second-generation XAV939-based PROTACs were hypothesised. In the first instance, the heterobifunctional compounds might be unable to form a stable ternary complex with the target protein (tankyrase) and the recruited E3 ligase (CRBN) due to insufficient linker lengths in the two ether-linked PROTACs tested. Whilst *in silico* modelling suggested that CCT400030 (**191**), but not CCT400031 (**190**), would be able to bring together the catalytic domain of tankyrase with CRBN in a cooperative ternary complex, it is possible that this pose was not able to be adopted in the cellular context.

Alternatively, a ternary complex may have formed in which there was no proximal lysine available on the target protein for ubiquitin transfer by the E3 ligase complex. Therefore, unsuccessful poly-ubiquitination of tankyrase may have precluded CUL4^{CRBN}-mediated proteasomal degradation of tankyrase. From analysis of the TNKS2 catalytic domain crystal structure in complex with XAV939 (**3**), it was observed that all 10 lysine residues in the tankyrase catalytic domain are proximal to the protein surface and 2 of the total lysine residues were on the same face of the protein as the XAV939 (**3**) binding site. However, access of the E3 ligase machinery to any of the 10 surface lysine residues for ubiquitination might have been limited depending on the ternary complex conformation.

Finally, the use of a catalytic inhibitor, such as XAV939 (**3**), as the tankyrase-binding ligand may not be ideal in the design of PROTACs for targeted tankyrase degradation. A net depletion in intracellular levels of a target protein is necessary for a PROTAC to be a successful degrader: a requirement of this is that the degradation rate is faster than the rate of resynthesis of the target protein.²⁷³ For the XAV939-based tankyrase PROTACs, stabilisation of tankyrase through inhibition of its catalytic functions is a further degradation-competitive mechanism which affects the intracellular levels of tankyrase. Therefore, further work is required on the PROTAC approach for targeted tankyrase degradation to identify successful heterobifunctional degraders of tankyrase and elucidate whether tankyrase is a target compatible with this methodology.

Chapter 6 Conclusions and Discussion

6.1 Substrate Binding Antagonists of the Tankyrase ARC Domain

6.1.1 Conclusions

A well-characterised fragment hit, CCT170746 (**28**), was selected as the chemical start point for fragment-based drug discovery towards potent inhibitors of tankyrase ARC-mediated substrate binding using a fragment growing strategy. Initial work focused on the design of close structural analogues of **28**, guided by *in silico* docking of the fragment against TNKS2 ARC4.¹³⁵ The fragment analogues were efficiently synthesised using one-step HATU-mediated amide coupling reactions. A ligand-observed NMR assay using both CPMG and waterLOGSY methods was established to screen all fragment analogues (with kinetic solubility > 50 μ M) against unlabelled TNKS2 ARC4, and competition with a 16mer 3BP2 TBM peptide was assessed to confirm binding to the substrate recognition pocket. From testing of the initial analogues in ligand-observed NMR, replacement of the quinoxaline ring did not show any improvements in fragment binding to TNKS2 ARC4. Introducing substituents in positions 3-, 4-, and 5-around the furan ring and replacement of the furan with nitrogen-containing, substituted heterocycles identified several analogues (**48**, **66**, **75**, **76**, **70** and **81**) which showed potentially increased binding to TNKS2 ARC4 from ligand-observed NMR. A protein-observed NMR assay – which evaluated chemical shift perturbations in the ¹H-¹⁵N HSQC spectra of ¹⁵N-labelled TNKS2 ARC4 upon increasing fragment concentrations – was then established to determine fragment binding affinities and revealed that no furan modifications had led to an improvement in affinity against TNKS2 ARC4. However, binding site mapping of the fragments aided in refinement of the *in silico* binding model and suggested that the analogues occupied either binding mode 1 or 2 from reported *in silico* docking of **28** against TNKS2 ARC4.

Validation studies with a literature-reported ARC-binding compound, fanapanel (**31**)¹³⁷, showed that a significant reduction (>80%) in average signal intensity in relaxation-edited (CPMG) ligand-observed NMR was indicative of a 10-fold

higher affinity binder (**31**, $K_d \sim 100 \mu\text{M}$) against TNKS2 ARC4. Further fragment analogues based on CCT170746 (**28**) were synthesised using Pd-catalysed aminocarbonylation reactions – focused on the introduction of minor substitutions to the quinoxaline ring to identify different vectors for fragment growing efforts – and tested through the established ligand-observed and protein-observed assay cascade. The introduction of a 3-dimethylamino substitution to the quinoxaline motif resulted in the identification of CCT393128 (**115**) ($K_d = 240 \mu\text{M}$), a 5-fold higher affinity fragment compared to fragment hit **28**. Structural characterisation of **115** was performed using competitive ligand-observed NMR, protein-observed NMR and NMR-guided *in silico* docking. Together, these experiments provided evidence that the compound maintained competitive binding to the substrate binding pocket of TNKS2 ARC4 in a manner consistent with binding mode 1 from *in silico* docking of **28**. Attempts at obtaining further structural information from a ligand-bound X-ray crystal structure of TNKS2 ARC4 were unsuccessful.

SAR exploration around the higher affinity lead fragment CCT393128 (**115**) was then pursued towards the development of potent inhibitors of tankyrase:substrate interactions. Based on the hypothesised binding mode of **115** from *in silico* docking studies, two sets of analogues were designed. The first set explored the introduction of lipophilic substituents extending from the 3-dimethylamino quinoxaline scaffold in combination with the isoxazolylmethyl amide. The introduction of 3-pyrrolidinyl substitution resulted in CCT394001 (**144**) ($K_d = 120 \mu\text{M}$), with 10-fold higher affinity compared to CCT170746 (**28**). The second set of analogues then explored replacement of the isoxazole through merging the 3-dimethylamino or 3-pyrrolidinyl quinoxaline scaffolds with amino acid residues to extend into the C-terminal contacts region of the substrate peptide binding site. However, the final peptidomimetic based on the 3-pyrrolidinyl quinoxaline motif, CCT395504 (**159**) ($K_d = 590 \mu\text{M}$), showed a 5-fold decrease in binding affinity compared to its parent fragment **144**. Many fragment analogues from both series of lead fragment optimisation bound at the upper limit of detection for the relaxation-edited (CPMG) ligand-observed NMR assay (>70% reduction in average signal intensity). A competitive biochemical FP assay was established and the potency of **115** ($\text{IC}_{50} = 103 \mu\text{M}$) was successfully determined against TNKS1 ARC4. Therefore, this higher throughput and more sensitive biochemical

assay can be used to test the binding of further analogues based on **115**, in future efforts to develop potent substrate binding antagonists of the tankyrase ARC domain. Overall, testing of fragment analogues using biophysical ligand-observed and protein-observed NMR methods and the competitive biochemical FP assay successfully allowed determination of the SAR of fragment hit CCT170746 (**28**) binding to TNKS2 ARC4, as summarised in Figure 6.1, and identification of higher affinity lead fragments through hit optimisation.

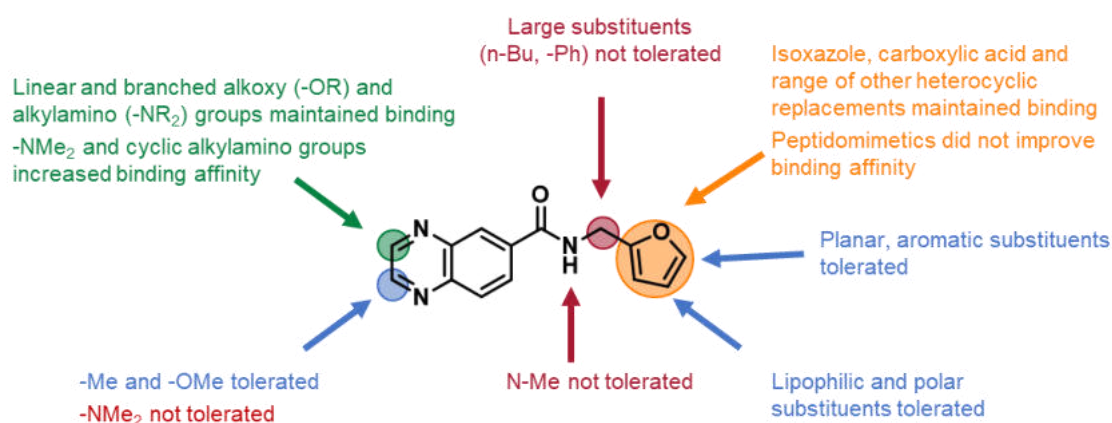


Figure 6.1. Summary diagram of SAR for fragment hit CCT170746 (28**).** Structure of CCT170746 (**28**), with regions of the fragment hit highlighted in which modifications which were either tolerated (blue), not tolerated (red), maintained competitive binding (orange) or increased binding (green) to TNKS2 ARC4.

6.1.2 Discussion and Future Directions

6.1.2.1 Structural Characterisation of ARC:Fragment Interactions

X-ray crystallography will be highly desired to gain direct structural insights into the binding mode of highest affinity ARC-binding fragments identified so far: CCT393128 (**115**) ($K_d = 240 \mu\text{M}$) and CCT394001 (**144**) ($K_d = 120 \mu\text{M}$). Extensive screening of TNKS1 ARC4:fragment co-crystallisation conditions will be required, as only limited co-crystallisation trials were attempted thus far. In addition, further fragment soaking conditions could be investigated against TNKS1 ARC4 or other crystallisable tankyrase ARC domains.^{46, 66, 149} Fragment:ARC co-crystal structures would enable rational, structure-based fragment growing to generate more potent substrate binding antagonists, by introduction of functional groups

for specific interactions with the tankyrase ARC domain. Further co-crystallisation experiments with fanapanel (**31**), which is predicted to bind in the central patch and arginine cradle region from protein-observed NMR, could also be attempted to identify opportunities for fragment merging with **115** or **144**.

In the absence of a fragment-bound ARC crystal structure, intermolecular NOE experiments (¹⁵N-¹³C NOESY-HSQC) could be performed to determine distance restraints between protein residues and ligand signals, for constrained *in silico* docking of fragments to TNKS2 ARC4.²⁷⁴ Uniformly double-labelled ¹⁵N-¹³C TNKS2 ARC4 would be required for this, which has previously been successfully produced in a good yield according to a published protocol.¹⁴⁷

6.1.2.2 Lead Fragment Optimisation to Identify Potent Antagonists

Prior to future rounds of fragment optimisation based on the quinoxaline scaffold, the source of assay interference observed with compounds CCT394001 (**144**) and CCT394880 (**166**) should be identified and removed, and compound stock solutions should be prepared immediately prior to the FP assay to prevent oxidative degradation observed with compounds **147**, **150**, **159**, **162**, **168** and **153**. Further SAR exploration of lead fragments **115** and **144** could be undertaken to identify more potent inhibitors of ARC:substrate protein interactions. For example, additional 3-alkylamino substitution of the quinoxaline ring would enable an increased understanding of binding pocket restrictions in this region (Figure 6.2a). Saturated N-heterocyclic substituents containing four to six atoms are tolerated in this position, therefore fragment growing around these rings may lead to higher affinity compounds. Another region of the compounds which is suitable for further optimisation is the isoxazole motif (Figure 6.2b). From previous SAR exploration, isoxazole replacement with a carboxylic acid (**162** and **166**) maintained binding affinity for TNKS2 ARC4 as determined by protein-observed NMR. Removal of the isoxazole (**168**) was also tolerated based on ligand-observed NMR, suggesting it forms minimal ligand-protein interactions and occupies a solvent-exposed region. The isoxazole motif could be removed in further analogues to allow for other ligand-protein interactions to be optimised whilst maintaining fragment-like 'rule of three' compliant properties.¹⁵⁶⁻¹⁵⁷ Finally,

a region of fragment hit CCT170746 (**28**) which has not yet been extensively modified is the central amide motif (Figure 6.2c). Based on the SAR from N-methylation, it was determined to be important to fragment conformation and/or act as an essential hydrogen bond donor. The central amide motif could be replaced with amide bioisosteres in future efforts to identify potent substrate binding antagonists of tankyrase.¹⁸⁹

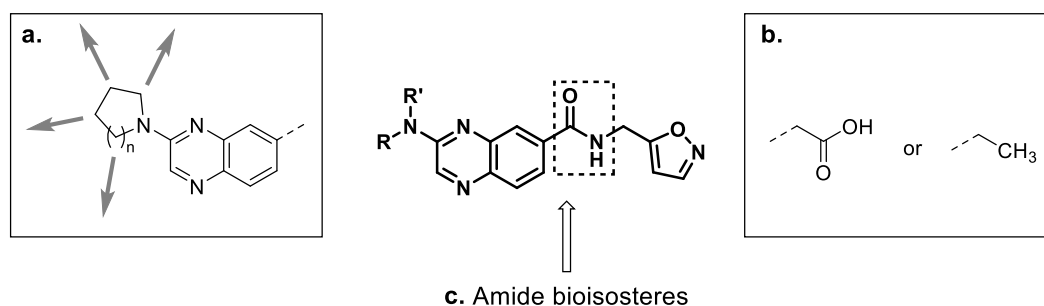


Figure 6.2. Suggested modifications for further SAR exploration of lead fragments. a) Fragment growing from the quinoxaline 3-position by substitution with N-heterocycles. **b)** Replacement of the isoxazole ring. **c)** Substitution of the central amide with bioisosteres.

6.1.2.3 Identification of Tool Compounds from a Fragment-based Approach

The possibility of inhibiting tankyrase function by disruption of ARC:substrate interactions has been demonstrated by literature-reported, cell-permeable stapled peptidomimetics, and by the identification of small molecules which bind to ARC domains with moderate to weak affinity (K_d or $K_i = 20 \mu\text{M}$ to $1100 \mu\text{M}$).¹³⁴⁻¹³⁷ The work reported in this thesis is currently the only study which has extensively explored the SAR of a hit identified from small molecule screening efforts against tankyrase ARCs, and has pursued structural characterisation of hit analogues. Although fragment optimisation has proven to be challenging, it was demonstrated that structural modifications can be introduced to increase the binding affinity of quinoxaline-based compounds against ARC4 whilst maintaining a robust binding location in the central patch and glycine sandwich regions. The work has highlighted that continued optimisation and refinement of the quinoxaline fragments is feasible through the approaches discussed in this thesis, with the aim to develop ARC:substrate PPI inhibitors with submicromolar affinity. Furthermore, the biophysical NMR experiments used in this study can be

applied as an orthogonal method for hit confirmation for future screening campaigns performed in the field. It was demonstrated that a hit identified from a literature-reported virtual screen, C44 (**30**),¹³⁶ showed unmeasurable solubility in the NMR solubility assay and was unsuitable for characterisation using ligand- and protein-observed NMR assays (section 3.1). This raises questions around whether this compound binds to the ARC domain in a specific manner and whether it is suitable as a tool compound. In addition, the previously unknown binding site of fanapanel (**31**)¹³⁷ was refined to the arginine cradle and central patch regions of TNKS2 ARC4 using the protein-observed NMR assay. Interestingly, whilst fanapanel (**31**) was confirmed to bind TNKS2 ARC4 with moderate affinity ($K_d = 100 \mu\text{M}$) in protein-observed NMR titration, no displacement of a Cy5-labelled 3BP2 TBM peptide probe was observed upon titration of **31** in a competitive FP assay against TNKS1 ARC4. This suggests that multiple binding hotspots on the ARC may need to be targeted simultaneously to achieve competition. Furthermore, it is hypothesised that substrate binding antagonists will be required to bind all ARCs capable of substrate recruitment due to the functional redundancy between ARCs and tankyrase paralogues.^{48, 135} This has highlighted the importance of assessing multi-ARC binding for potent compounds against ARCs 1, 2, 4 and 5 from both TNKS1 and TNKS2, which could be achieved using competitive FP assays with a variety of fluorophore labelled TBM peptides based on different substrates.^{61, 135, 196} Following the identification of potent and cell permeable substrate binding antagonists capable of multi-ARC binding, these tool compounds will be used to study tankyrase:substrate/effector protein interactions, which could support the development of substrate binding antagonists as novel tankyrase-targeted therapeutics.

6.2 PROTACs for the Targeted Degradation of Tankyrase

6.2.1 Conclusions

The targeted degradation of tankyrase using PROTACs has been pursued as a second approach for the development of chemical tool compounds to study tankyrase cellular functions, whether achieved by catalytic or scaffolding

activities. An initial set of three PROTACs with different linker lengths were synthesised based on a toolbox catalytic tankyrase inhibitor, XAV939 (**3**). An amide coupling conjugation strategy was used to link XAV939 (**3**) to a thalidomide motif for targeting the CUL4^{CRBN} E3 ligase complex, resulting in compounds with two amide bonds in the linker and a total of four hydrogen bond donors. A representative compound, CCT371426-02 (**186-02**), from this series showed no cellular target engagement of CRBN ($IC_{50} > 30 \mu M$), suggesting poor cellular permeability for the first-generation amide-linked compounds. Therefore, a further set of XAV939-based PROTACs were synthesised in which an ether bond replaced one of the linker amides to improve the physicochemical properties of the compounds, with linker lengths chosen based on *in silico* modelling of ternary complex formation. All three compounds – CCT400031 (**190**), CCT400030 (**191**) and CCT400029 (**192**) – demonstrated binary CRBN target engagement in biochemical and cellular assays, indicating that cellular permeability was achieved, and demonstrated cellular tankyrase target engagement in a Wnt/ β -catenin responsive transcription reporter assay. However, stabilisation rather than degradation of tankyrase was observed upon treatment of human HAP1 reporter cells with **190** or **191**, replicating XAV939-mediated catalytic inhibition of tankyrase rather than demonstrating degradation *via* a PROTAC mechanism.

6.2.2 Discussion and Future Directions

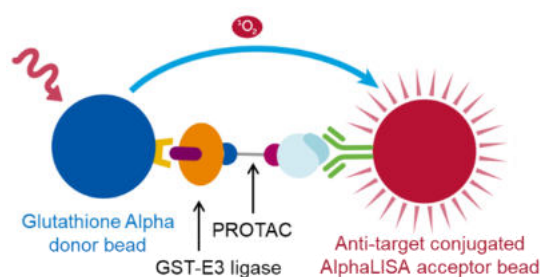
Further efforts are therefore required to identify PROTACs for the successful targeted degradation of tankyrase. Suggestions for future work on this approach are discussed here, based on the hypothesised explanations for the lack of tankyrase degradation observed with the ether-linked XAV939-based PROTACs.

6.2.2.1 Further Linker Variation to Identify XAV939-based PROTACs

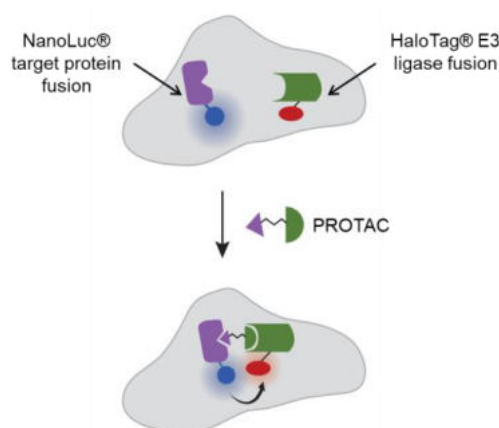
Linker design is a crucial element of generating successful PROTAC degraders, as the linker can influence ternary complex formation, degradation potency (DC_{50}) and isoform selectivity, as well as compound properties such as rigidity, lipophilicity, solubility and permeability.^{235-236, 253} One potential explanation for the lack of tankyrase degradation observed with the two ether-linked, XAV939-based

compounds tested thus far (**190** and **191**) is limited formation of a stable ternary complex due to unsuitable linker lengths. Ternary complex formation can be characterised using cell-free proximity assays which detect protein-protein interactions, such as AlphaLISA and HTRF assays (PerkinElmer)²⁷⁵, or using a cell-based technology such as NanoBRET (Promega)²⁷⁶ (Figure 6.3). Therefore, CCT400031 (**190**) and CCT400030 (**191**) could be tested in such assays to determine if the lack of tankyrase degradation results from limited ternary complex formation with tankyrase and CRBN. A solution to overcome this would involve the synthesis of third-generation XAV939-based heterobifunctional compounds, with systematic variation in length and composition of the linker, and evaluation of ternary complex formation prior to western blot evaluation of tankyrase degradation.

AlphaLISA (Linked Immunosorbent assay)



Cellular NanoBRET assay



HTRF (Homogenous Time-Resolved FRET)

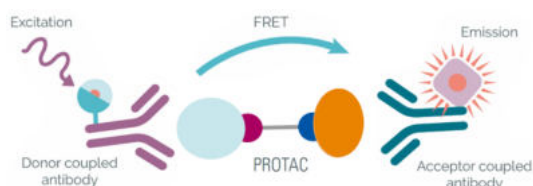


Figure 6.3. Principles of assay technology used to assess PROTAC-mediated ternary complex formation. AlphaLISA (Linked Immunosorbent assay): Figure adapted from PerkinElmer – Targeted Protein Degradation Assays and Reagents.²⁷⁵ HTRF (Homogenous Time-Resolved FRET): Figure adapted from PerkinElmer – HTRF® technology Basics.²⁷⁷ Cellular NanoBRET assay: Figure adapted from Promega – Targeted Protein Degradation.²⁷⁶

A variety of functionalised linkers connected to thalidomide *via* the 4- or 5-position can be accessed through well-established synthetic routes or from commercial suppliers, which could facilitate wider and more empirical linker exploration for XAV939-based PROTACs (Figure 6.4).^{253, 278-279} Alternatively, linkers connected to ligands for targeting CRL2^{VHL}, such as VH032 (**175**), could also be explored in further XAV939-based heterobifunctional compound design if no successful CRBN-targeted PROTACs are identified.^{253, 280} The number and diversity of heterobifunctional compounds required to develop a successful PROTAC degrader using empirical iterations of design, synthesis and western blot screening has been demonstrated by Ciulli *et al* in a recent literature report of LRRK2 (leucine-rich repeat kinase 2) degraders.²⁸¹ An initial set of 12 compounds were synthesised, incorporating ligands for VHL, CRBN and cIAP E3 ligases, which provided three weakly potent VHL-targeted LRRK2 degraders.²⁸¹ A further 18 second-generation compounds were synthesised, which focused on optimisation of the first-generation PROTAC degraders, and linker modification resulted in the identification of a potent, selective and orally bioavailable PROTAC degrader of LRRK2, XL01126.²⁸¹ Therefore, a diversity-led synthesis and western blot screening of a larger set of XAV939-based PROTACs could be required to identify a successful tankyrase degrader hit.

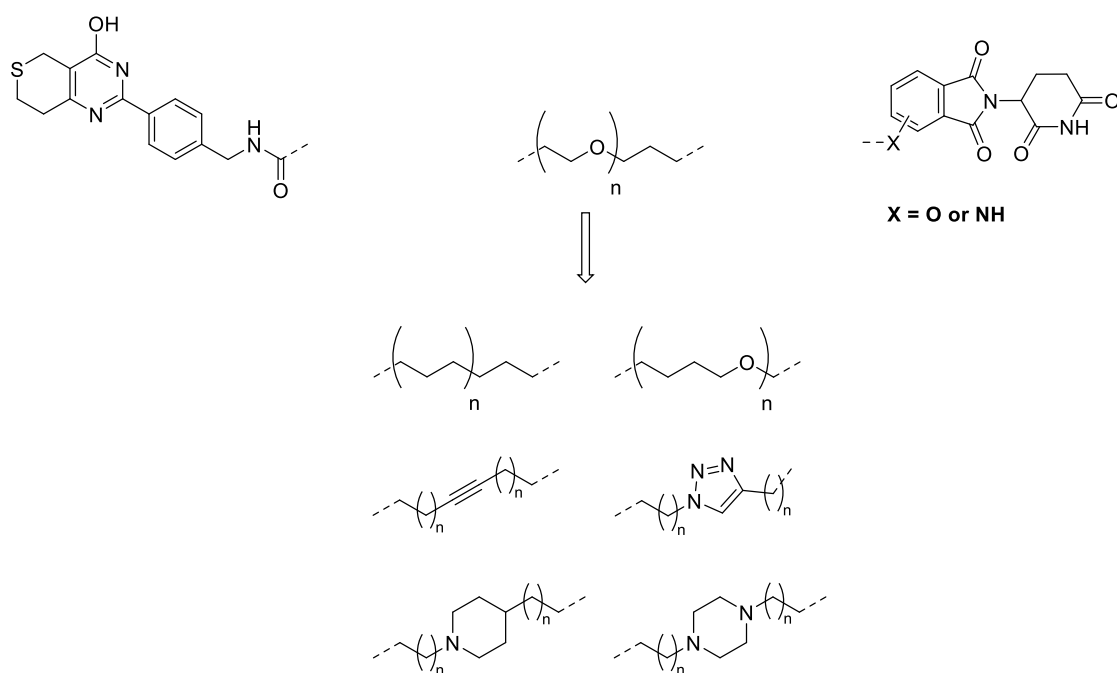


Figure 6.4. Examples of potential linker variation for the empirical design of tankyrase PROTACs. XAV939-based heterobifunctional compounds which could be investigated for linker optimisation, based on literature for cereblon-directed PROTACs.^{236, 278}

6.2.2.2 Development of ARC-binding PROTACs

Another hypothesis for the lack of tankyrase degradation observed with CCT400031 (**190**) and CCT400030 (**191**) is a competing mechanism of tankyrase stabilisation upon blocking its catalytic activity with XAV939-based heterobifunctional compounds. The stabilisation of tankyrase upon its catalytic inhibition adds further complexity to the interpretation of intracellular tankyrase levels detected in western blotting upon increasing concentrations of XAV939-based PROTACs. Therefore, the use of a catalytic tankyrase inhibitor as the target ligand may be unsuitable in the design of PROTACs for targeted tankyrase degradation.

In contrast, tankyrase-targeted PROTACs based on non-catalytic inhibitors, such as the ARC-binding fragments discovered in this thesis, should not result in tankyrase accumulation. Future studies could therefore investigate the development of heterobifunctional compounds which bind to tankyrase through its ARC domain, rather than its catalytic domain. Since the tankyrase ARC

domain is unique within the PARP family, it is predicted that PROTACs based on substrate binding antagonists would not suffer with PARP selectivity issues.^{36, 53} In contrast, XAV939 has limited selectivity for tankyrase over PARP1 and PARP2, and therefore these family members may also be destabilised by XAV939-based PROTACs.¹⁰¹

Substrate binding antagonists with low micromolar affinity ($K_d < 10 \mu\text{M}$), developed from further optimisation of lead fragments detailed in this thesis – CCT393128 (**115**) and CCT394001 (**144**) – would be suitable to be incorporated into ARC-binding PROTACs. The development of PROTACs based on weak affinity ligands has been successfully demonstrated for other protein targets as the PROTAC strategy requires only a ligandable protein site.^{223, 225, 282} Based on the SAR of the lead fragments discussed in this thesis, it was demonstrated that the isoxazole moiety can be replaced by a carboxylic acid functionality (section 6.1.2.2), suitable for linker attachment to a ligand for targeting either the CRBN or VHL E3 ligases (Figure 6.5). The assay cascade demonstrated in this thesis for the XAV939-based PROTACs would be adaptable for characterising ARC-binding PROTACs, using the established competitive FP assay to determine binary target engagement with tankyrase through its ARC domain (section 4.4).

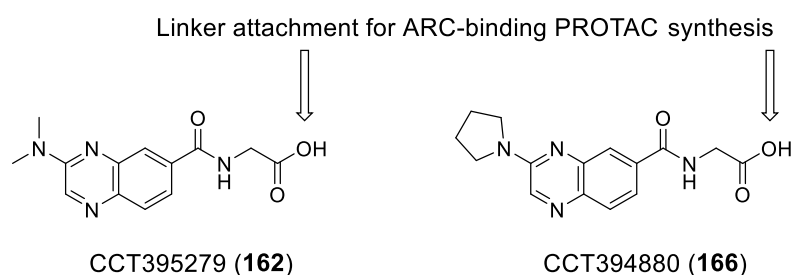


Figure 6.5. Proposed design strategies for ARC-binding PROTACs. Linker attachment from the carboxylic acid motif using amide coupling chemistry with higher affinity analogues of CCT395279 (**162**) and CCT394880 (**166**) could be suitable for the generation of ARC-binding tankyrase PROTACs.

6.2.2.3 Identification of Tool Compounds from a PROTAC Approach

The development of PROTACs for targeted protein degradation is an emerging therapeutic modality in small molecule drug discovery, which is particularly

applicable to proteins with scaffolding functions.^{30, 244} The work discussed in this thesis represents the first reported efforts to apply this technology towards the tankyrases. An assay cascade was established to evaluate cellular binary target engagement against tankyrase and CRBN, which was then used to successfully guide linker modifications and identification of cell permeable heterobifunctional compounds. Evaluation of cellular target engagement and confirmation of dose-dependent ternary complex formation are both required to confirm a ubiquitin-proteasome-dependent mechanism of action for successful PROTAC degraders.²⁴ Therefore, the assays demonstrated and applied in the thesis, supplemented by ternary complex formation assays suggested in section 6.2.2.1, could be applied to guide the future identification and characterisation of XAV939-based tankyrase-targeted PROTACs. Furthermore, this work has shown that the use of catalytic inhibitors, which result in tankyrase stabilisation, as the tankyrase-recruiting motif may be incompatible in PROTAC development due to tankyrase stabilisation. The synthesis of ARC-binding PROTACs from the lead fragments detailed in this thesis could overcome this potential limitation of the XAV939-based PROTACs. If competent heterobifunctional degraders of tankyrase can be identified using either catalytic site binders or ARC-binding motifs, then the selectivity of the compounds for tankyrase degradation could be assessed by global proteomics studies to determine any off-target degradation, such as IMiD targets of thalidomide for CRBN-targeted PROTACs, or destabilisation of other PARP family members.^{24, 223} The development of potent heterobifunctional degraders which selectively induce the degradation of tankyrase *via* the ubiquitin-proteasome system could then be used as chemical tool compounds to further study the consequence of tankyrase scaffolding.

6.3 Outlook for Non-Catalytic Chemical Tool Compounds of Tankyrase

The long-term aim of the project reported in this thesis is the identification of potent inhibitors of tankyrase which could regulate both its catalytic and non-catalytic functions and provide a novel targeted therapeutic approach for cancers associated with aberrant tankyrase function. Tankyrase is a particular target of interest in colorectal cancer cases with constitutive activation of the Wnt/ β -catenin signalling (~90%), which is driven by mutation of the tumour suppressor *APC* and consequent impaired β -catenin degradation.^{114, 283-284} Wnt/ β -catenin reporter assays will be used to determine whether complete suppression of Wnt activation, as observed with loss-of-function mutations in the non-catalytic SAM and ARC domains,⁵⁷ can be achieved with potent and cell-active small molecule chemical tool inhibitors of non-catalytic tankyrase functions. Non-catalytic chemical tool compounds will then be used to depict the contribution of scaffolding functions to other tankyrase-dependent cellular processes. In conclusion, a fragment-based approach has resulted in the identification of quinoxaline-based compounds with improved affinity against the tankyrase ARC domain compared with the fragment hit, which could be further improved towards potent substrate binding antagonists. In parallel, the synthesis of heterobifunctional PROTACs for targeted tankyrase degradation has been pursued, and profiling of these compounds has highlighted future efforts required to identify successful tankyrase degraders. Both approaches could be combined to identify ARC-directed tankyrase PROTACs as molecular probes to investigate both catalytic and non-catalytic functions of tankyrase.

Chapter 7 Experimental Procedures

7.1 Synthetic Chemistry

7.1.1 General Methods

All reagents were purchased from commercial suppliers and used as received without further purification. All reactions were performed using anhydrous solvents. Automated silica column chromatography was performed using a Biotage Isolera system. Biotage SNAP KP-Sil and Biotage SNAP Ultra C18 prepacked silica gel cartridges were used for normal phase and reverse phase chromatography respectively. Ion-exchange chromatography was performed using ISOLUTE Flash SCX-2 (acidic) cartridges or ISOLUTE Flash-NH₂ (basic) cartridges.

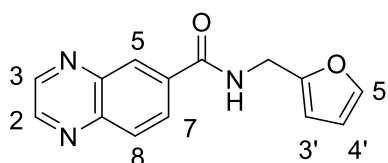
NMR spectra were recorded on Bruker AMX500 or AV-NEO 600 spectrometers using internal deuterium locks. All NMR were acquired at 298 K and processed using Bruker Topspin 4.0. Chemical shifts (δ) are reported in parts per million (ppm) relative to tetramethylsilane ($\delta = 0$ using the following residual solvent signals: CDCl₃ (δ_{H} 7.26, δ_{C} 77.2), CD₃OD (δ_{H} 3.32, δ_{C} 49.0), DMSO-d₆ (δ_{H} 2.50, δ_{C} 39.5). ¹H NMR data is reported in the following format: chemical shift, multiplicity, *J* coupling integration and assignment. ¹³C data is reported in the following format: chemical shift and assignment. LCMS and HRMS were recorded using either an Agilent 1260 Infinity II series UPLC and diode array detector coupled to a 6530 Quadrupole time of flight (QToF) mass spectrometer (Phenomenex Kinetex C18 column, 30 x 2.1 mm, 2.6 μ , 100A) or a Waters Acquity UPLC detector with Waters Xevo G2QToF mass spectrometer (Phenomenex Kinetex C18 column, 30 x 2.1 mm², 2.6 μ m), with ionisation by positive-ion electrospray (ESI⁺). Analytical separation was carried out at 40 °C with UV detection at 254, 280 and 214 nm. The mobile phase was a mixture of MeOH (solvent A) and water (solvent B), each modified with 0.1% formic acid. Gradient elution was carried out from 10:90 (A:B) to 90:10 (A:B) over 2 min or 4 min with flow rate of 0.6 mL/min or 0.4 mL/min (Agilent) and 0.5 mL/min or 0.3 mL/min

(Xevo) respectively. Compound purity was assessed by UV absorbance at 254 nm.

7.1.2 Chemical Syntheses from Chapter 2

General Procedure A: HATU (249 mg, 0.65 mmol, 1.5 equiv) was added to a solution of quinoxaline-6-carboxylic acid (75 mg, 0.43 mmol, 1 equiv), amine (0.43 mmol, 1 equiv) and DIPEA (0.23 mL, 1.29 mmol, 3 equiv) in DMF (4.3 mL, 0.10 M). The reaction was stirred at rt, and then concentrated *in vacuo* using a Biotage V-10 instrument to afford crude residue, which was purified by flash column chromatography to afford desired product.

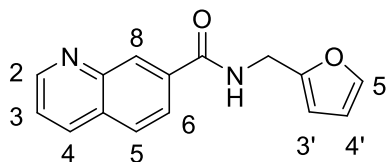
***N*-(Furan-2-ylmethyl)quinoxaline-6-carboxamide (28)**



HATU (152 mg, 0.65 mmol) was added to a solution of quinoxaline-6-carboxylic acid (75 mg, 0.43 mmol), furan-2-ylmethanamine (38 μ L, 0.43 mmol) and DIPEA (0.23 mL, 1.29 mmol) in DMF (4.3 mL, 0.10 M) and the reaction was stirred at rt for 17 h. The reaction was concentrated *in vacuo* using a Biotage V-10 instrument and the crude residue was purified by reverse phase silica chromatography eluting 0-90% MeOH in water (+0.1% formic acid). The fractions containing product were collected and evaporated *in vacuo* to afford *N*-(furan-2-ylmethyl)quinoxaline-6-carboxamide (**28**) (70 mg, 64%) as a pale brown solid. ^1H NMR (600 MHz, $\text{DMSO-}d_6$) δ 9.39 (t, $J = 5.7$ Hz, 1H, -NH), 9.06 – 9.00 (m, 2H, 2-CH and 3-CH), 8.64 (d, $J = 2.0$ Hz, 1H, 5-CH), 8.30 (dd, $J = 8.7, 2.0$ Hz, 1H, 7-CH), 8.18 (d, $J = 8.7$ Hz, 1H, 8-CH), 7.60 (dd, $J = 1.9, 0.9$ Hz, 1H, 5'-CH), 6.42 (dd, $J = 3.2, 1.8$ Hz, 1H, 4'-CH), 6.35 – 6.33 (m, 1H, 3'-CH), 4.55 (d, $J = 5.6$ Hz, 2H, -CH₂). ^{13}C NMR (151 MHz, $\text{DMSO-}d_6$) δ 165.1 (-C=O), 152.1 (2'-qC), 147.0 (2-CH or 3-CH), 146.7 (2-CH or 3-CH), 143.4 (8a-qC), 142.2 (5'-CH), 141.6 (4a-qC), 135.2 (6-qC), 129.4 (8-CH), 128.6 (7-CH), 128.4 (5-CH), 110.5 (4'-CH),

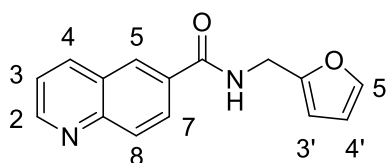
107.1 (3'-CH), 36.3 (-CH₂). LCMS (ESI⁺) *m/z* 254 [M+H]⁺, t_R = 1.00 min. HRMS (ESI⁺) [M+H]⁺ calcd. for C₁₄H₁₁N₃O₂: 254.0929; found: 254.0930, purity 98.9%.

***N*-(Furan-2-ylmethyl)quinoline-7-carboxamide (41)**



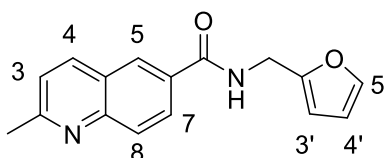
HATU (143 mg, 0.60 mmol) was added to a solution of quinoline-7-carboxylic acid (70 mg, 0.40 mmol), furan-2-ylmethanamine (36 μ L, 0.40 mmol) and DIPEA (0.21 mL, 1.21 mmol) in DMF (4.0 mL, 0.10 M) and the reaction was stirred at rt for 18 h. The reaction was concentrated *in vacuo* using a Biotage V-10 instrument and the crude residue was purified by reverse phase silica chromatography eluting 0-90% MeOH in water (+0.1% formic acid). The fractions containing product were collected and evaporated *in vacuo* to afford *N*-(furan-2-ylmethyl)quinoline-7-carboxamide (**41**) (57 mg, 56%) as an off-white solid. ¹H NMR (600 MHz, DMSO-*d*₆) δ 9.30 (t, *J* = 5.7 Hz, 1H, -NH), 8.99 (dd, *J* = 4.2, 1.7 Hz, 1H, 2-CH), 8.58 – 8.55 (m, 1H, 8-CH), 8.44 – 8.41 (m, 1H, 4-CH), 8.09 – 8.03 (m, 2H, 5-CH and 6-CH), 7.62 (dd, *J* = 8.3, 4.2 Hz, 1H, 3-CH), 7.60 (dd, *J* = 1.8, 0.9 Hz, 1H, 5'-CH), 6.41 (dd, *J* = 3.2, 1.8 Hz, 1H, 4'-CH), 6.32 (dd, *J* = 3.3, 1.1 Hz, 1H, 3'-CH), 4.53 (d, *J* = 5.7 Hz, 2H, -CH₂). ¹³C NMR (151 MHz, DMSO-*d*₆) δ 165.7 (-C=O), 152.3 (2'-qC), 151.5 (2-CH), 147.1 (8a-qC), 142.1 (5'-CH), 135.9 (4-CH), 134.8 (7- qC), 129.3 (4a-qC), 128.3 (5-CH or 6-CH), 128.2 (8-CH), 124.9 (5-CH or 6-CH), 122.7 (3-CH), 110.5 (4'-CH), 107.0 (3'-CH), 36.2 (-CH₂). LCMS (ESI⁺) *m/z* 253 [M+H]⁺, t_R = 1.03 min. HRMS (ESI⁺) [M+H]⁺ calcd. for C₁₅H₁₃N₂O₂: 253.0972; found: 253.0979, purity 100%.

***N*-(Furan-2-ylmethyl)quinoline-6-carboxamide (42)**



HATU (150 mg, 0.64 mmol) was added to a solution of quinoline-6-carboxylic acid (74 mg, 0.43 mmol), furan-2-ylmethanamine (38 μ L, 0.43 mmol) and DIPEA (0.22 mL, 1.28 mmol) in DMF (4.3 mL, 0.10 M) and the reaction was stirred at rt for 22 h. The reaction was concentrated *in vacuo* using a Biotage V-10 instrument and the crude residue was purified by reverse phase silica chromatography eluting 0-90% MeOH in water (+0.1% formic acid). The fractions containing product were collected and evaporated *in vacuo* to afford *N*-(furan-2-ylmethyl)quinoline-6-carboxamide (**42**) (84 mg, 78%) as an off-white solid. ^1H NMR (600 MHz, DMSO- d_6) δ 9.21 (t, J = 5.7 Hz, 1H, -NH), 8.98 (dd, J = 4.3, 1.7 Hz, 1H, 2-CH), 8.54 (d, J = 2.0 Hz, 1H, 5-CH), 8.47 (dd, J = 8.4, 2.0 Hz, 1H, 4-CH), 8.19 (dd, J = 8.8, 2.0 Hz, 1H, 7-CH), 8.08 (d, J = 8.8 Hz, 1H, 8-CH), 7.61 (dd, J = 8.3, 4.1 Hz, 1H, 3-CH), 7.60 – 7.59 (m, 1H, 5'-CH), 6.42 (dd, J = 3.2, 1.8 Hz, 1H, 4'-CH), 6.33 (d, J = 3.2 Hz, 1H, 3'-CH), 4.54 (d, J = 5.7 Hz, 2H, -CH $_2$). ^{13}C NMR (151 MHz, DMSO- d_6) δ 165.7 (-C=O), 152.3 (2'-qC), 152.1 (2-CH), 148.7 (8a-qC), 142.1 (5'-CH), 137.1 (4-CH), 131.9 (6-qC), 129.0 (8-CH), 128.1 (5-CH), 127.7 (7-CH), 127.1 (4a-qC), 122.2 (3-CH), 110.5 (4'-CH), 107.0 (3'-CH), 36.2 (-CH $_2$). LCMS (ESI $^+$) m/z 253 [M+H] $^+$, t_R = 0.93 min. HRMS (ESI $^+$) [M+H] $^+$ calcd. for C $_{15}$ H $_{13}$ N $_2$ O $_2$: 253.0972; found: 253.0976, purity 100%.

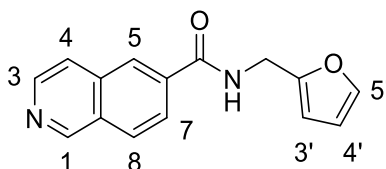
***N*-(Furan-2-ylmethyl)-2-methylquinoline-6-carboxamide (43)**



HATU (146 mg, 0.62 mmol) was added to a solution of 2-methylquinoline-6-carboxylic acid (74 mg, 0.40 mmol), furan-2-ylmethanamine (35 μ L, 0.40 mmol) and DIPEA (0.21 mL, 1.19 mmol) in DMF (4.0 mL, 0.10 M) and the reaction was stirred at rt for 22 h. The reaction was concentrated *in vacuo* using a Biotage V-10 instrument and the crude residue was purified by reverse phase silica chromatography eluting 0-90% MeOH in water (+0.1% formic acid). The fractions containing product were collected and evaporated *in vacuo* to afford *N*-(furan-2-ylmethyl)-2-methylquinoline-6-carboxamide (**43**) (93 mg, 88%) as a pale brown solid. ^1H NMR (600 MHz, DMSO- d_6) δ 9.16 (t, J = 5.7 Hz, 1H, -NH), 8.47 (d, J =

2.0 Hz, 1H, 5-CH), 8.33 (d, $J = 8.4$ Hz, 1H, 4-CH), 8.14 (dd, $J = 8.8, 2.0$ Hz, 1H, 7-CH), 7.96 (d, $J = 8.8$ Hz, 1H, 8-CH), 7.59 (d, $J = 1.8$ Hz, 1H, 5'-CH), 7.49 (d, $J = 8.4$ Hz, 1H, 3-CH), 6.41 (dd, $J = 3.2, 1.8$ Hz, 1H, 4'-CH), 6.32 (d, $J = 3.2$ Hz, 1H, 3'-CH), 4.52 (d, $J = 5.6$ Hz, 2H, -CH₂), 2.68 (s, 3H, -CH₃). ¹³C NMR (151 MHz, DMSO-*d*₆) δ 165.7 (-C=O), 160.6 (2-qC), 152.3 (2'-qC), 148.4 (8a-qC), 142.1 (5'-CH), 137.1 (4-CH), 131.1 (6-qC), 128.2 (8-CH), 127.8 (5-CH), 127.7 (7-CH), 125.3 (4a-qC), 122.9 (3-CH), 110.5 (4'-CH), 107.0 (3'-CH), 36.2 (-CH₂), 25.0 (-CH₃). LCMS (ESI⁺) m/z 267 [M+H]⁺, $t_R = 0.86$ min. HRMS (ESI⁺) [M+H]⁺ calcd. for C₁₆H₁₅N₂O₂: 267.1128; found: 267.1133, purity 100%.

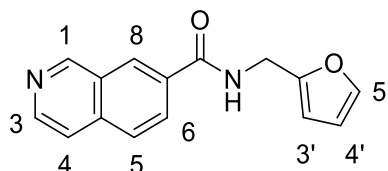
***N*-(Furan-2-ylmethyl)isoquinoline-6-carboxamide (44)**



HATU (153 mg, 0.65 mmol) was added to a solution of isoquinoline-6-carboxylic acid (75 mg, 0.43 mmol), furan-2-ylmethanamine (38 μ L, 0.43 mmol) and DIPEA (0.23 mL, 1.30 mmol) in DMF (4.3 mL, 0.10 M) and the reaction was stirred at rt for 17 h. The reaction was concentrated *in vacuo* using a Biotage V-10 instrument and the crude residue was purified by reverse phase silica chromatography eluting 0-90% MeOH in water (+0.1% formic acid). The fractions containing product were collected and evaporated *in vacuo* to afford *N*-(furan-2-ylmethyl)isoquinoline-6-carboxamide (**44**) (58 mg, 42%) as a brown solid. ¹H NMR (600 MHz, DMSO-*d*₆) δ 9.39 (s, 1H, 1-CH), 9.27 (t, $J = 5.7$ Hz, 1H, -NH), 8.58 (d, $J = 5.8$ Hz, 1H, 3-CH), 8.49 (d, $J = 1.7$ Hz, 1H, 5-CH), 8.21 (d, $J = 8.5$ Hz, 1H, 8-CH), 8.09 (dd, $J = 8.5, 1.7$ Hz, 1H, 7-CH), 7.93 (d, $J = 5.7$ Hz, 1H, 4-CH), 7.60 (d, $J = 1.8$ Hz, 1H, 5'-CH), 6.42 (dd, $J = 3.3, 1.8$ Hz, 1H, 4'-CH), 6.34 (d, $J = 3.2$ Hz, 1H, 3'-CH), 4.53 (d, $J = 5.6$ Hz, 2H, -CH₂). ¹³C NMR (151 MHz, DMSO-*d*₆) δ 165.7 (-C=O), 152.3 (1-CH), 152.1 (2'-qC), 143.6 (3-CH), 142.2 (5'-CH), 135.7 (6-qC), 134.6 (4a-qC), 128.9 (8a-qC), 127.9 (8-CH), 126.1 (5-CH), 125.7 (7-CH), 121.1 (4-CH), 110.5 (4'-CH), 107.1 (3'-CH), 36.2 (-CH₂). LCMS

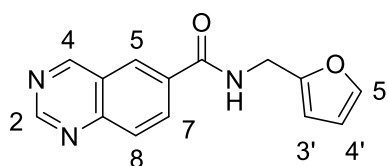
(ESI⁺) *m/z* 253 [M+H]⁺, *t_R* = 0.76 min. HRMS (ESI⁺) [M+H]⁺ calcd. for C₁₅H₁₃N₂O₂: 253.0977; found: 253.0981, purity 100%.

***N*-(Furan-2-ylmethyl)isoquinoline-7-carboxamide (45)**



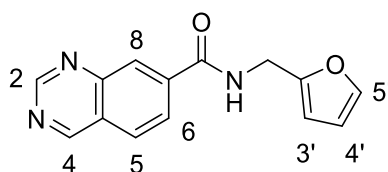
HATU (153 mg, 0.65 mmol) was added to a solution of isoquinoline-7-carboxylic acid (75 mg, 0.43 mmol), furan-2-ylmethanamine (38 μ L, 0.43 mmol) and DIPEA (0.23 mL, 1.30 mmol) in DMF (4.3 mL, 0.10 M) and the reaction was stirred at rt for 22 h. The reaction was concentrated *in vacuo* using a Biotage V-10 instrument and the crude residue was purified by reverse phase silica chromatography eluting 0-90% MeOH in water (+0.1% formic acid). The fractions containing product were collected and evaporated *in vacuo* to afford *N*-(furan-2-ylmethyl)isoquinoline-7-carboxamide (**45**) (75 mg, 69%) as an orange solid. ¹H NMR (600 MHz, DMSO-*d*₆) δ 9.41 (s, 1H, 1-CH), 9.25 (t, *J* = 5.7 Hz, 1H, -NH), 8.67 (d, *J* = 1.7 Hz, 1H, 8-CH), 8.59 (d, *J* = 5.7 Hz, 1H, 3-CH), 8.21 (dd, *J* = 8.6, 1.8 Hz, 1H, 6-CH), 8.05 (d, *J* = 8.6 Hz, 1H, 5-CH), 7.89 (d, *J* = 5.7 Hz, 1H, 4-CH), 7.60 (d, *J* = 1.8 Hz, 1H, 5'-CH), 6.42 (dd, *J* = 3.2, 1.8 Hz, 1H, 4'-CH), 6.34 (d, *J* = 3.2 Hz, 1H, 3'-CH), 4.54 (d, *J* = 5.6 Hz, 2H, -CH₂). ¹³C NMR (151 MHz, DMSO-*d*₆) δ 165.5 (-C=O), 153.4 (1-CH), 152.2 (2'-qC), 144.3 (3-CH), 142.1 (5'-CH), 136.4 (4a-qC), 132.9 (8a-qC), 128.7 (6-CH), 127.5 (7-qC and 8-CH), 126.7 (5-CH), 120.2 (4-CH), 110.5 (4'-CH), 107.1 (3'-CH), 36.2 (-CH₂). LCMS (ESI⁺) *m/z* 253 [M+H]⁺, *t_R* = 0.76 min. HRMS (ESI⁺) [M+H]⁺ calcd. for C₁₅H₁₃N₂O₂: 253.0972; found: 253.0978, purity 100%.

***N*-(Furan-2-ylmethyl)quinazoline-6-carboxamide (46)**



HATU (150 mg, 0.64 mmol) was added to a solution of quinazoline-6-carboxylic acid (74 mg, 0.42 mmol), furan-2-ylmethanamine (37 μ L, 0.42 mmol) and DIPEA (0.23 mL, 1.30 mmol) in DMF (4.2 mL, 0.10 M) and the reaction was stirred at rt for 19 h. The reaction was concentrated *in vacuo* using a Biotage V-10 instrument and the crude residue was purified by reverse phase silica chromatography eluting 0-90% MeOH in water (+0.1% formic acid). The fractions containing product were collected and evaporated *in vacuo* to afford *N*-(furan-2-ylmethyl)quinazoline-6-carboxamide (**46**) (36 mg, 33%) as a pale brown solid. ^1H NMR (600 MHz, DMSO- d_6) δ 9.72 (s, 1H, 4-CH), 9.38 (s, 1H, 2-CH), 9.33 (t, J = 5.7 Hz, 1H, -NH), 8.70 (d, J = 2.0 Hz, 1H, 5-CH), 8.44 (dd, J = 8.8, 2.0 Hz, 1H, 7-CH), 8.09 (d, J = 8.7 Hz, 1H, 8-CH), 7.60 (d, J = 1.8 Hz, 1H, 5'-CH), 6.42 (dd, J = 3.2, 1.8 Hz, 1H, 4'-CH), 6.35 (d, J = 3.2 Hz, 1H, 3'-CH), 4.54 (d, J = 5.6 Hz, 2H, -CH $_2$). ^{13}C NMR (151 MHz, DMSO- d_6) δ 165.0 (-C=O), 161.8 (4-CH), 156.3 (2-CH), 152.0 (2'-qC), 150.3 (8a-qC), 142.2 (5'-CH), 133.3 (6-qC), 132.7 (7-CH), 127.9 (8-CH), 127.8 (5-CH), 124.0 (4a-qC), 110.5 (4'-CH), 107.2 (3'-CH), 36.3 (-CH $_2$). LCMS (ESI $^+$) m/z 254 [M+H] $^+$, t_R = 0.82 min. HRMS (ESI $^+$) [M+H] $^+$ calcd. for C $_{14}$ H $_{12}$ N $_3$ O $_2$: 254.0929; found: 254.0925, purity 97.7%.

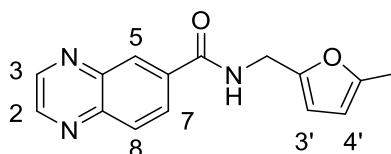
***N*-(Furan-2-ylmethyl)quinazoline-7-carboxamide (47)**



HATU (100 mg, 0.43 mmol) was added to a solution of quinazoline-7-carboxylic acid (50 mg, 0.29 mmol), furan-2-ylmethanamine (25 μ L, 0.29 mmol) and DIPEA (0.15 mL, 0.86 mmol) in DMF (2.9 mL, 0.10 M) and the reaction was stirred at rt for 19 h. The reaction was concentrated *in vacuo* using a Biotage V-10 instrument and the crude residue was purified by reverse phase silica chromatography eluting 0-90% MeOH in water (+0.1% formic acid). The fractions containing product were collected and evaporated *in vacuo* to afford *N*-(furan-2-ylmethyl)quinazoline-7-carboxamide (**47**) (35 mg, 47%) as an orange solid. ^1H NMR (600 MHz, DMSO- d_6) δ 9.70 (s, 1H, 4-CH), 9.43 (t, J = 5.7 Hz, 1H, -NH),

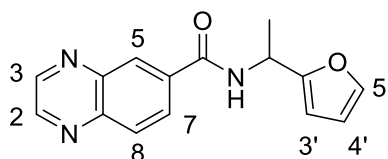
9.39 (s, 1H, 2-CH), 8.51 (d, $J = 1.6$ Hz, 1H, 8-CH), 8.26 (d, $J = 8.5$ Hz, 1H, 5-CH), 8.18 (dd, $J = 8.5, 1.6$ Hz, 1H, 6-CH), 7.60 (d, $J = 1.8$ Hz, 1H, 5'-CH), 6.42 (dd, $J = 3.2, 1.8$ Hz, 1H, 4'-CH), 6.34 (d, $J = 3.2$ Hz, 1H, 3'-CH), 4.54 (d, $J = 5.6$ Hz, 2H, -CH₂). ¹³C NMR (151 MHz, DMSO-*d*₆) δ 165.1 (-C=O), 160.9 (4-CH), 155.8 (2-CH), 152.0 (2'-qC), 149.0 (8a-qC), 142.2 (5'-CH), 139.2 (7-qC), 128.2 (5-CH), 126.7 (8-CH), 126.5 (6-CH), 125.7 (4a-qC), 110.5 (4'-CH), 107.2 (3'-CH), 36.3 (-CH₂). LCMS (ESI⁺) m/z 254 [M+H]⁺, $t_R = 0.85$ min. HRMS (ESI⁺) [M+H]⁺ calcd. for C₁₄H₁₂N₃O₂: 254.0929; found: 254.0921, purity 98.5%.

***N*-((5-Methylfuran-2-yl)methyl)quinoxaline-6-carboxamide (48)**



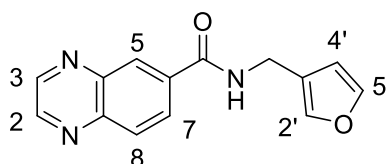
HATU (144 mg, 0.61 mmol) was added to a solution of quinoxaline-6-carboxylic acid (71 mg, 0.41 mmol), (5-methylfuran-2-yl)methanamine (44 μ L, 0.41 mmol) and DIPEA (0.21 mL, 1.22 mmol) in DMF (4.1 mL, 0.10 M) and the reaction was stirred at rt for 17 h. The reaction was concentrated *in vacuo* using a Biotage V-10 instrument and the crude residue was purified by reverse phase chromatography eluting 0-90% MeOH in water (+0.1% formic acid). The fractions containing product were collected and evaporated *in vacuo* to afford *N*-((5-methylfuran-2-yl)methyl)quinoxaline-6-carboxamide (**48**) (92 mg, 84%) as a pale brown solid. ¹H NMR (600 MHz, DMSO-*d*₆) δ 9.35 (t, $J = 5.7$ Hz, 1H, -NH), 9.06 – 9.00 (m, 2H, 2-CH and 3-CH), 8.64 (d, $J = 1.9$ Hz, 1H, 5-CH), 8.30 (dd, $J = 8.7, 2.0$ Hz, 1H, 7-CH), 8.18 (d, $J = 8.7$ Hz, 1H, 8-CH), 6.20 (d, $J = 3.0$ Hz, 1H, 4'-CH), 6.02 – 5.99 (m, 1H, 3'-CH), 4.48 (d, $J = 5.6$ Hz, 2H, -CH₂), 2.24 (d, $J = 1.1$ Hz, 3H, -CH₃). ¹³C NMR (151 MHz, DMSO-*d*₆) δ 165.0 (-C=O), 150.7 (5'-qC), 150.3 (2'-qC), 147.0 (2-CH or 3-CH), 146.7 (2-CH or 3-CH), 143.4 (8a-qC), 141.6 (4a-qC), 135.23 (6-qC), 129.3 (8-CH), 128.6 (7-CH), 128.4 (5-CH), 107.9 (4'-CH), 106.4 (3'-CH), 36.3 (-CH₂), 13.3 (-CH₃). LCMS (ESI⁺) m/z 268 [M+H]⁺, $t_R = 1.24$ min. HRMS (ESI⁺) [M+H]⁺ calcd. for C₁₅H₁₄N₃O₂: 268.1081; found: 268.1075, purity 100%.

***N*-(1-(Furan-2-yl)ethyl)quinoxaline-6-carboxamide (49)**



HATU (153 mg, 0.65 mmol) was added to a solution of quinoxaline-6-carboxylic acid (75 mg, 0.43 mmol), 1-(furan-2-yl)ethan-1-amine (48 μ L, 0.43 mmol) and DIPEA (0.23 mL, 1.30 mmol) in DMF (4.3 mL, 0.10 M) and the reaction was stirred at rt for 20 h. The reaction was concentrated *in vacuo* using a Biotage V-10 instrument and the crude residue was purified by reverse phase silica chromatography eluting 0-90% MeOH in water (+0.1% formic acid). The fractions containing product were collected and evaporated *in vacuo* to afford *N*-(1-(furan-2-yl)ethyl)quinoxaline-6-carboxamide (**49**) (48 mg, 43%) as a brown solid. ^1H NMR (600 MHz, DMSO- d_6) δ 9.21 (d, J = 8.2 Hz, 1H, -NH), 9.05 – 9.02 (m, 2H, 2-CH and 3-CH), 8.66 (d, J = 1.9 Hz, 1H, 5-CH), 8.30 (dd, J = 8.7, 2.0 Hz, 1H, 7-CH), 8.18 (d, J = 8.7 Hz, 1H, 8-CH), 7.60 (d, J = 1.8 Hz, 1H, 5'-CH), 6.42 (dd, J = 3.3, 1.8 Hz, 1H, 4'-CH), 6.33 (d, J = 3.2 Hz, 1H, 3'-CH), 5.38 – 5.30 (m, 1H, -CH), 1.54 (d, J = 7.0 Hz, 3H, -CH $_3$). ^{13}C NMR (151 MHz, DMSO- d_6) δ 164.5 (-C=O), 156.0 (2'-qC), 147.0 (2-CH or 3-CH), 146.7 (2-CH or 3-CH), 143.4 (8a-qC), 141.9 (5'-CH), 141.6 (4a-qC), 135.4 (6-qC), 129.3 (8-CH), 128.8 (7-CH), 128.5 (5-CH), 110.3 (4'-CH), 105.5 (3'-CH), 42.7 (-CH), 19.0 (-CH $_3$). LCMS (ESI $^+$) m/z 268 [M+H] $^+$, t_{R} = 1.13 min. HRMS (ESI $^+$) [M+H] $^+$ calcd. for C $_{15}$ H $_{14}$ N $_3$ O $_2$: 268.1086; found: 268.1084, purity 100%.

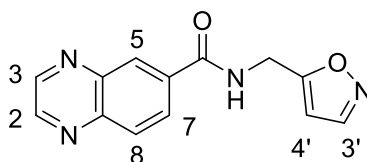
***N*-(Furan-3-ylmethyl)quinoxaline-6-carboxamide (50)**



HATU (151 mg, 0.64 mmol) was added to a solution of quinoxaline-6-carboxylic acid (75 mg, 0.43 mmol), furan-3-ylmethanamine (40 μ L, 0.43 mmol) and DIPEA

(0.22 mL, 1.30 mmol) in DMF (4.3 mL, 0.10 M) and the reaction was stirred at rt for 20 h. The reaction was concentrated *in vacuo* using a Biotage V-10 instrument and the crude residue was purified by reverse phase silica chromatography eluting 0-90% MeOH in water (+0.1% formic acid). The fractions containing product were collected and evaporated *in vacuo* to afford *N*-(furan-3-ylmethyl)quinoxaline-6-carboxamide (**50**) (69 mg, 64%) as a pale brown solid. ¹H NMR (600 MHz, DMSO-*d*₆) δ 9.27 (t, *J* = 5.8 Hz, 1H, -NH), 9.05 – 9.01 (m, 2H, 2-CH and 3-CH), 8.62 (d, *J* = 2.0 Hz, 1H, 5-CH), 8.29 (dd, *J* = 8.7, 2.0 Hz, 1H, 7-CH), 8.18 (d, *J* = 8.7 Hz, 1H, 8-CH), 7.66 – 7.64 (m, 1H, 2'-CH), 7.62 – 7.60 (m, 1H, 5'-CH), 6.52 (dd, *J* = 1.7, 0.9 Hz, 1H, 4'-CH), 4.39 (d, *J* = 6.0 Hz, 2H, -CH₂). ¹³C NMR (151 MHz, DMSO-*d*₆) δ 165.1 (-C=O), 147.0 (2-CH or 3-CH), 146.7 (2-CH or 3-CH), 143.3 (8a-qC and 5'-CH), 141.6 (4a-qC), 140.0 (2'-CH), 135.5 (6-qC), 129.3 (8-CH), 128.6 (7-CH), 128.3 (5-CH), 123.1 (3'-qC), 110.7 (4'-CH), 34.2 (-CH₂). LCMS (ESI⁺) *m/z* 254 [M+H]⁺, *t*_R = 1.21 min. HRMS (ESI⁺) [M+H]⁺ calcd. for C₁₄H₁₂N₃O₂: 254.0929; found: 254.0926, purity 100%.

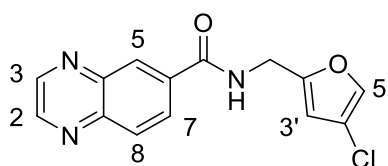
***N*-(isoxazol-5-ylmethyl)quinoxaline-6-carboxamide (51)**



HATU (151 mg, 0.64 mmol) was added to a solution of quinoxaline-6-carboxylic acid (75 mg, 0.43 mmol), isoxazol-5-ylmethanamine hydrochloride (58 mg, 0.43 mmol) and DIPEA (0.30 mL, 1.70 mmol) in DMF (4.3 mL, 0.10 M) and the reaction was stirred at rt for 20 h. The reaction was concentrated *in vacuo* using a Biotage V-10 instrument and the crude residue was purified by reverse phase silica chromatography eluting 0-90% MeOH in water (+0.1% formic acid). The fractions containing product were collected and evaporated *in vacuo* to afford *N*-(isoxazol-5-ylmethyl)quinoxaline-6-carboxamide (**51**) (75 mg, 69%) as a brown solid. ¹H NMR (600 MHz, DMSO-*d*₆) δ 9.59 (t, *J* = 5.8 Hz, 1H, -NH), 9.07 – 9.02 (m, 2H, 2-CH and 3-CH), 8.66 (d, *J* = 2.0 Hz, 1H, 5-CH), 8.51 (d, *J* = 1.8 Hz, 1H, 3'-CH), 8.30 (dd, *J* = 8.7, 2.0 Hz, 1H, 7-CH), 8.20 (d, *J* = 8.7 Hz, 1H, 8-CH), 6.44 (d, *J* =

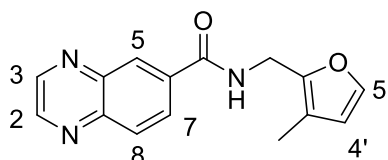
1.8 Hz, 1H, 4'-CH), 4.72 (d, $J = 5.7$ Hz, 2H, -CH₂). ¹³C NMR (151 MHz, DMSO-*d*₆) δ 169.2 (5'-qC), 165.4 (-C=O), 150.9 (3'-CH), 147.2 (2-CH or 3-CH), 146.8 (2-CH or 3-CH), 143.5 (8a-qC), 141.6 (4a-qC), 134.8 (6-qC), 129.5 (8-CH), 128.5 (7-CH), 128.5 (5-CH), 101.5 (4'-CH), 35.3 (-CH₂). LCMS (ESI⁺) m/z 255 [M+H]⁺, $t_R = 0.84$ min. HRMS (ESI⁺) [M+H]⁺ calcd. for C₁₃H₁₁N₄O₂: 255.0882; found: 255.0884, purity 100%.

***N*-((4-Chlorofuran-2-yl)methyl)quinoxaline-6-carboxamide (52)**



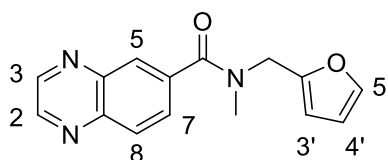
HATU (150 mg, 0.64 mmol) was added to a solution of quinoxaline-6-carboxylic acid (74 mg, 0.42 mmol), (4-chlorofuran-2-yl)methanamine hydrochloride (71 mg, 0.43 mmol) and DIPEA (0.30 mL, 1.70 mmol) in DMF (4.2 mL, 0.10 M) and the reaction was stirred at rt for 19 h. The reaction was concentrated *in vacuo* using a Biotage V-10 instrument and the crude residue was purified by reverse phase silica chromatography eluting 0-90% MeOH in water (+0.1% formic acid). The fractions containing product were collected and evaporated *in vacuo* to afford *N*-((4-chlorofuran-2-yl)methyl)quinoxaline-6-carboxamide (**52**) (80 mg, 65%) as a yellow solid. ¹H NMR (600 MHz, DMSO-*d*₆) δ 9.42 (t, $J = 5.7$ Hz, 1H, -NH), 9.06 – 9.02 (m, 2H, 2-CH and 3-CH), 8.64 (d, $J = 1.9$ Hz, 1H, 5-CH), 8.29 (dd, $J = 8.7$, 2.0 Hz, 1H, 7-CH), 8.19 (d, $J = 8.7$ Hz, 1H, 8-CH), 7.87 (d, $J = 1.0$ Hz, 1H, 5'-CH), 6.53 (d, $J = 1.1$ Hz, 1H, 3'-CH), 4.52 (d, $J = 5.6$ Hz, 2H, -CH₂). ¹³C NMR (151 MHz, DMSO-*d*₆) δ 165.2 (-C=O), 153.3 (2'-qC), 147.1 (2-CH or 3-CH), 146.7 (2-CH or 3-CH), 143.4 (8a-qC), 141.6 (4a-qC), 138.6 (5'-CH), 135.0 (6-qC), 129.4 (8-CH), 128.6 (7-CH), 128.5 (5-CH), 114.9 (4'-qC), 108.6 (3'-CH), 36.4 (-CH₂). LCMS (ESI⁺) m/z 288 [M+H]⁺, $t_R = 1.19$ min. HRMS (ESI⁺) [M+H]⁺ calcd. for C₁₄H₁₁N₃O₂Cl: 288.0540; found: 288.0537, purity 100%.

***N*-((3-Methylfuran-2-yl)methyl)quinoxaline-6-carboxamide (53)**



HATU (152 mg, 0.65 mmol) was added to a solution of quinoxaline-6-carboxylic acid (75 mg, 0.43 mmol), (3-methylfuran-2-yl)methanamine (48 μ L, 0.43 mmol) and DIPEA (0.23 mL, 1.29 mmol) in DMF (4.3 mL, 0.10 M) and the reaction was stirred at rt for 19 h. The reaction was concentrated *in vacuo* using a Biotage V-10 instrument and the crude residue was purified by reverse phase silica chromatography eluting 0-90% MeOH in water (+0.1% formic acid). The fractions containing product were collected and evaporated *in vacuo* to afford *N*-((3-methylfuran-2-yl)methyl)quinoxaline-6-carboxamide (**53**) (29 mg, 25%) as a brown solid. ^1H NMR (600 MHz, DMSO- d_6) δ 9.32 (t, J = 5.6 Hz, 1H, -NH), 9.04 – 9.01 (m, 2H, 2-CH and 3-CH), 8.62 (d, J = 1.9 Hz, 1H, 5-CH), 8.29 (dd, J = 8.7, 2.0 Hz, 1H, 7-CH), 8.17 (d, J = 8.7 Hz, 1H, 8-CH), 7.50 (d, J = 1.8 Hz, 1H, 5'-CH), 6.30 (d, J = 1.8 Hz, 1H, 4'-CH), 4.50 (d, J = 5.6 Hz, 2H, -CH $_2$), 2.06 (s, 3H, -CH $_3$). ^{13}C NMR (151 MHz, DMSO- d_6) δ 164.9 (-C=O), 147.2 (2'-qC), 147.0 (2-CH or 3-CH), 146.7 (2-CH or 3-CH), 143.3 (8a-qC), 141.6 (4a-qC), 141.2 (5'-CH), 135.2 (6-qC), 129.3 (8-CH), 128.6 (7-CH), 128.4 (5-CH), 116.3 (3'-qC), 113.1 (4'-CH), 34.3 (-CH $_2$), 9.6 (-CH $_3$). LCMS (ESI $^+$) m/z 268 [M+H] $^+$, t_R = 1.13 min. HRMS (ESI $^+$) [M+H] $^+$ calcd. for C $_{15}$ H $_{14}$ N $_3$ O $_2$: 268.1081; found: 268.1080, purity 98.9%.

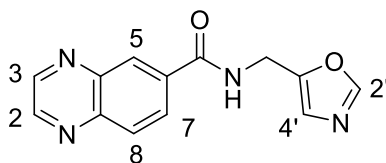
***N*-(Furan-2-ylmethyl)-*N*-methylquinoxaline-6-carboxamide (54)**



HATU (146 mg, 0.62 mmol) was added to a solution of quinoxaline-6-carboxylic acid (72 mg, 0.41 mmol), 1-(furan-2-yl)-*N*-methylmethanamine (47 μ L, 0.41 mmol) and DIPEA (0.22 mL, 1.24 mmol) in DMF (4.1 mL, 0.10 M) and the reaction was stirred at rt for 17 h. The reaction was concentrated *in vacuo* using a Biotage V-10 instrument and the crude residue was purified by reverse phase silica

chromatography eluting 0-90% MeOH in water (+0.1% formic acid). The fractions containing product were collected and evaporated *in vacuo* to afford *N*-(furan-2-ylmethyl)-*N*-methylquinoxaline-6-carboxamide (**54**) (48 mg, 43%) as a yellow solid. ^1H NMR (600 MHz, DMSO- d_6) δ 9.03 – 9.00 (m, 2H, 2-CH and 3-CH), 8.21 – 8.08 (m, 2H, 5-CH and 8-CH), 7.93 – 7.85 (m, 1H, 7-CH), 7.68 – 7.66 (m, 1H, 5'-CH), 6.51 – 6.34 (m, 2H, 3'-CH and 4'-CH), 4.80 – 4.42 (m, 2H, -CH $_2$), 3.02 – 2.90 (m, 3H, -NCH $_3$). ^{13}C NMR (151 MHz, DMSO- d_6) δ 146.7 (2-CH or 3-CH), 146.6 (2-CH or 3-CH), 143.3 – 142.8 (m, 8a-qC), 142.3 (5'-CH), 141.6 (4a-qC), 137.6 (6-qC), 129.7 (8-CH), 128.7 (7-CH), 127.2 (5-CH), 110.6 (4'-CH), 108.7 (3'-CH), 47.6+43.1 (-CH $_2$), 36.8+32.5 (-CONCH $_3$) (2 x qC missing, rotational isomers observed). LCMS (ESI $^+$) m/z 268 [M+H] $^+$, t_{R} = 1.20 min. HRMS (ESI $^+$) [M+H] $^+$ calcd. for C $_{15}$ H $_{14}$ N $_3$ O $_2$: 268.1081; found: 268.1083, purity 100%.

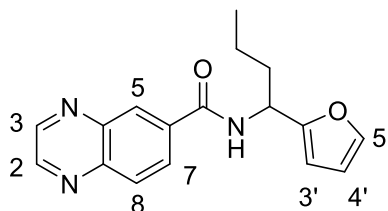
***N*-(Oxazol-5-ylmethyl)quinoxaline-6-carboxamide (55)**



HATU (150 mg, 0.64 mmol) was added to a solution of quinoxaline-6-carboxylic acid (74 mg, 0.42 mmol), oxazol-5-ylmethanamine hydrochloride (57 mg, 0.42 mmol) and DIPEA (0.30 mL, 1.70 mmol) in DMF (4.2 mL, 0.10 M) and the reaction was stirred at rt for 50 h. The reaction was concentrated *in vacuo* using a Biotage V-10 instrument and the crude residue was purified by reverse phase silica chromatography eluting 0-90% MeOH in water (+0.1% formic acid). The fractions containing product were collected and evaporated *in vacuo* to afford *N*-(oxazol-5-ylmethyl)quinoxaline-6-carboxamide (**55**) (91 mg, 82%) as a brown solid ^1H NMR (600 MHz, DMSO- d_6) δ 9.44 (t, J = 5.6 Hz, 1H, -NH), 9.06 – 9.01 (m, 2H, 2-CH and 3-CH), 8.63 (d, J = 1.9 Hz, 1H, 5-CH), 8.31 (s, 1H, 2'-CH), 8.29 (dd, J = 8.7, 2.0 Hz, 1H, 7-CH), 8.19 (d, J = 8.7 Hz, 1H, 8-CH), 7.12 (s, 1H, 4'-CH), 4.62 (d, J = 5.5 Hz, 2H, -CH $_2$). ^{13}C NMR (151 MHz, DMSO- d_6) δ 165.3 (-C=O), 151.7 (2'-CH), 149.2 (5'-qC), 147.1 (2-CH or 3-CH), 146.8 (2-CH or 3-CH), 143.4 (8a-qC), 141.6 (4a-qC), 135.0 (6-qC), 129.4 (8-CH), 128.6 (7-CH), 128.5 (5-CH),

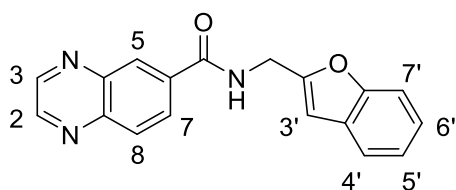
123.6 (4'-CH), 34.1 (-CH₂). LCMS (ESI⁺) *m/z* 255 [M+H]⁺, t_R = 0.82 min. HRMS (ESI⁺) [M+H]⁺ calcd. for C₁₃H₁₁N₄O₂: 255.0882; found: 255.0880, purity 97.9%.

***N*-(1-(Furan-2-yl)butyl)quinoxaline-6-carboxamide (57)**



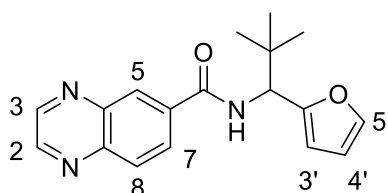
The reaction was carried out with 1-(furan-2-yl)butan-1-amine (61 mg, 0.43 mmol, 1 equiv) for 17 h according to general procedure A. The crude residue was purified by reverse phase silica chromatography eluting 5-95% MeOH in water (+0.1% formic acid), and fractions containing product were collected and evaporated *in vacuo* to afford *N*-(1-(furan-2-yl)butyl)quinoxaline-6-carboxamide (**57**) (81 mg, 60%) as a brown solid. ¹H NMR (500 MHz, DMSO-*d*₆) δ 9.13 (d, *J* = 8.4 Hz, 1H, -NH), 9.06 – 9.00 (m, 2H, 2-CH and 3-CH), 8.66 (d, *J* = 1.9 Hz, 1H, 5-CH), 8.29 (dd, *J* = 8.7, 2.0 Hz, 1H, 7-CH), 8.18 (d, *J* = 8.6 Hz, 1H, 8-CH), 7.59 (dd, *J* = 1.8, 0.8 Hz, 1H, 5'-CH), 6.41 (dd, *J* = 3.2, 1.8 Hz, 1H, 4'-CH), 6.32 (dd, *J* = 3.2, 0.8 Hz, 1H, 3'-CH), 5.28 – 5.19 (m, 1H, -CH), 1.94 – 1.88 (m, 2H, -CHCH₂), 1.48 – 1.27 (m, 2H, -CH₂CH₃), 0.93 (t, *J* = 7.4 Hz, 3H, -CH₃). ¹³C NMR (126 MHz, DMSO-*d*₆) δ 164.9 (-C=O), 155.5 (2'-qC), 147.0 (2-CH or 3-CH), 146.7 (2-CH or 3-CH), 143.4 (8a-qC), 141.8 (5'-CH), 141.6 (4a-qC), 135.4 (6-qC), 129.3 (8-CH), 128.8 (7-CH), 128.4 (5-CH), 110.3 (4'-CH), 105.7 (3'-CH), 46.7 (-CH), 34.9 (-CHCH₂), 19.0 (-CH₂CH₃), 13.6 (-CH₃). LCMS (ESI⁺) *m/z* 296 [M+H]⁺, t_R = 1.39 min. HRMS (ESI⁺) [M+H]⁺ calcd. for C₁₇H₁₈N₃O₂: 296.1393; found: 296.1399, error = 1.9 ppm, purity 95.3%.

***N*-(Benzofuran-2-ylmethyl)quinoxaline-6-carboxamide (58)**



The reaction was carried out with benzofuran-2-ylmethanamine hydrochloride (79 mg, 0.43 mmol, 1 equiv) for 17 h according to general procedure A. The crude residue was purified by reverse phase silica chromatography eluting 5-95% MeOH in water (+0.1% formic acid), and fractions containing product were collected and evaporated *in vacuo* to afford *N*-(benzofuran-2-ylmethyl)quinoxaline-6-carboxamide (**58**) (69 mg, 53%) as an orange solid. ¹H NMR (600 MHz, DMSO-*d*₆) δ 9.55 (t, *J* = 5.6 Hz, 1H, -NH), 9.06 – 9.02 (m, 2H, 2-CH and 3-CH), 8.68 (d, *J* = 1.9 Hz, 1H, 5-CH), 8.33 (dd, *J* = 8.7, 2.0 Hz, 1H, 7-CH), 8.20 (d, *J* = 8.7 Hz, 1H, 8-CH), 7.62 – 7.57 (m, 1H, 4'-CH), 7.55 (dd, *J* = 8.1, 1.1 Hz, 1H, 7'-CH), 7.27 (ddd, *J* = 8.3, 7.2, 1.4 Hz, 1H, 6'-CH), 7.22 (*app td*, *J* = 7.4, 1.1 Hz, 1H, 5'-CH), 6.83 (d, *J* = 1.0 Hz, 1H, 3'-CH), 4.75 – 4.71 (m, 2H, -CH₂). ¹³C NMR (151 MHz, DMSO-*d*₆) δ 165.3 (-C=O), 155.4 (2'-qC), 154.2 (7'a-qC), 147.1 (2-CH or 3-CH), 146.7 (2-CH or 3-CH), 143.4 (8a-qC), 141.6 (4a-qC), 135.0 (6-qC), 129.4 (8-CH), 128.6 (7-CH), 128.5 (5-CH), 128.1 (3'a-qC), 123.9 (6'-CH), 122.8 (5'-CH), 120.9 (4'-CH), 111.0 (7'-CH), 103.7 (3'-CH), 36.9 (-CH₂). LCMS (ESI⁺) *m/z* 304 [M+H]⁺, *t*_R = 1.27 min. HRMS (ESI⁺) [M+H]⁺ calcd. for C₁₈H₁₄N₃O₂: 304.1086; found: 304.1089, error = 1.0 ppm, purity 100 %.

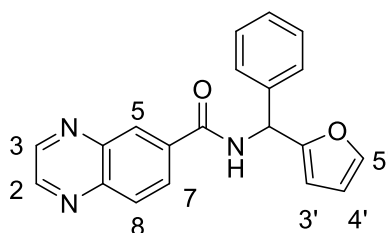
***N*-(1-(Furan-2-yl)-2,2-dimethylpropyl)quinoxaline-6-carboxamide (59)**



The reaction was carried out with 1-(furan-2-yl)-2,2-dimethylpropan-1-amine (66 mg, 0.43 mmol, 1 equiv) for 17 h according to general procedure A. The crude residue was purified by reverse phase silica chromatography eluting 5-95% MeOH in water (+0.1% formic acid), and fractions containing product were collected and evaporated *in vacuo* to afford *N*-(1-(furan-2-yl)-2,2-dimethylpropyl)quinoxaline-6-carboxamide (**59**) (104 mg, 77%) as an off-white solid. ¹H NMR (600 MHz, DMSO-*d*₆) δ 9.07 – 9.02 (m, 2H, 2-CH and 3-CH), 8.95 (d, *J* = 9.6 Hz, 1H, -NH), 8.62 (d, *J* = 1.9 Hz, 1H, 5-CH), 8.23 (dd, *J* = 8.7, 2.0 Hz, 1H, 7-CH), 8.17 (d, *J* = 8.7 Hz, 1H, 8-CH), 7.60 (dd, *J* = 1.8, 0.9 Hz, 1H, 5'-CH),

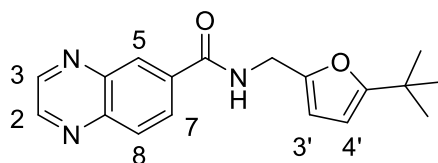
6.49 – 6.45 (m, 1H, 3'-CH), 6.43 (dd, $J = 3.3, 1.8$ Hz, 1H, 4'-CH), 5.19 (d, $J = 9.6$ Hz, 1H, -CH), 1.00 (s, 9H, 3 × -CH₃). ¹³C NMR (151 MHz, DMSO-*d*₆) δ 165.7 (-C=O), 154.1 (2'-qC), 147.0 (2-CH or 3-CH), 146.6 (2-CH or 3-CH), 143.3 (8a-qC), 141.5 (2C, 4a-qC and 5'-CH), 135.8 (6-qC), 129.2 (8-CH), 129.1 (7-CH), 128.6 (5-CH), 110.3 (4'-CH), 107.2 (3'-CH), 55.8 (-CH), 35.5 (-qC(CH₃)₃), 26.6 (3C, 3 × -CH₃). LCMS (ESI⁺) m/z 310 [M+H]⁺, $t_R = 1.33$ min. HRMS (ESI⁺) [M+H]⁺ calcd. for C₁₈H₂₀N₃O₂: 310.1555; found: 310.1555, error = 0.0 ppm, purity 98.9%.

***N*-(Furan-2-yl(phenyl)methyl)quinoxaline-6-carboxamide (60)**



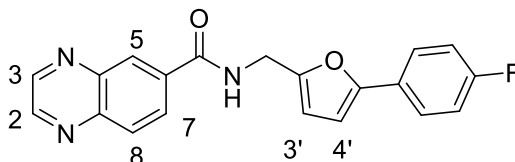
The reaction was carried out with furan-2-yl(phenyl)methanamine (90 mg, 0.43 mmol, 1 equiv) for 17 h according to general procedure A. The crude residue was purified by reverse phase silica chromatography eluting 5-95% MeOH in water (+0.1% formic acid), and fractions containing product were collected and evaporated *in vacuo* to afford *N*-(furan-2-yl(phenyl)methyl)quinoxaline-6-carboxamide (**60**) (102 mg, 72%) as a pale orange solid. ¹H NMR (600 MHz, DMSO-*d*₆) δ 9.82 (d, $J = 8.4$ Hz, 1H, -NH), 9.06 – 9.01 (m, 2H, 2-CH and 3-CH), 8.73 (d, $J = 2.0$ Hz, 1H, 5-CH), 8.32 (dd, $J = 8.7, 2.0$ Hz, 1H, 7-CH), 8.18 (d, $J = 8.8$ Hz, 1H, 8-CH), 7.66 (dd, $J = 1.9, 0.9$ Hz, 1H, 5'-CH), 7.51 – 7.46 (m, 2H, 2 × Ar-CH), 7.43 – 7.37 (m, 2H, 2 × Ar-CH), 7.35 – 7.30 (m, 1H, Ar-CH), 6.48 (d, $J = 8.4$ Hz, 1H, -CH), 6.44 (dd, $J = 3.3, 1.8$ Hz, 1H, 4'-CH), 6.19 (dd, $J = 3.3, 1.0$ Hz, 1H, 3'-CH). ¹³C NMR (151 MHz, DMSO-*d*₆) δ 164.9 (-C=O), 154.2 (2'-qC), 147.1 (2-CH or 3-CH), 146.7 (2-CH or 3-CH), 143.4 (8a-qC), 142.7 (5'-CH), 141.6 (4a-qC), 139.9 (Ar-qC), 135.1 (6-qC), 129.3 (8-CH), 128.9 (7-CH), 128.8 (5-CH), 128.4 (2C, 2 × Ar-CH), 127.6 (Ar-CH), 127.5 (2C, 2 × Ar-CH), 110.5 (4'-CH), 107.8 (3'-CH), 51.1 (-CH). LCMS (ESI⁺) m/z 352 [M+Na]⁺, $t_R = 1.28$ min. HRMS (ESI⁺) [M+H]⁺ calcd. for C₂₀H₁₆N₃O₂: 330.1242; found: 330.1239, error = -0.9 ppm, purity 100%.

***N*-((5-(*Tert*-butyl)furan-2-yl)methyl)quinoxaline-6-carboxamide (61)**



The reaction was carried out with (5-(*tert*-butyl)furan-2-yl)methanamine (65 mg, 0.43 mmol, 1 equiv) for 17 h according to general procedure A. The crude residue was purified by reverse phase silica chromatography eluting 5-95% MeOH in water (+0.1% formic acid), and fractions containing product were collected and evaporated *in vacuo* to afford *N*-((5-(*tert*-butyl)furan-2-yl)methyl)quinoxaline-6-carboxamide (**61**) (51 mg, 38%) as a red brown oil. ¹H NMR (600 MHz, DMSO-*d*₆) δ 9.35 (t, *J* = 5.7 Hz, 1H, -NH), 9.05 – 9.01 (m, 2H, 2-CH and 3-CH), 8.63 (d, *J* = 2.0 Hz, 1H, 5-CH), 8.29 (dd, *J* = 8.7, 2.0 Hz, 1H, 7-CH), 8.18 (d, *J* = 8.7 Hz, 1H, 8-CH), 6.17 (d, *J* = 3.1 Hz, 1H, 4'-CH), 5.98 (d, *J* = 3.1 Hz, 1H, 3'-CH), 4.50 (d, *J* = 5.6 Hz, 2H, -CH₂), 1.23 (s, 9H, 3 × -CH₃). ¹³C NMR (151 MHz, DMSO-*d*₆) δ 165.2 (-C=O), 162.5 (5'-qC), 150.1 (2'-qC), 147.0 (2-CH or 3-CH), 146.7 (2-CH or 3-CH), 143.4 (8a-qC), 141.6 (4a-qC), 135.4 (6-qC), 129.4 (8-CH), 128.6 (7-CH), 128.4 (5-CH), 107.2 (4'-CH), 102.9 (3'-CH), 36.5 (-CH₂), 32.2 (5'-qC), 28.9 (-CH₃). LCMS (ESI⁺) *m/z* 310 [M+H]⁺, *t*_R = 1.40 min. HRMS (ESI⁺) [M+Na]⁺ calcd. for C₁₈H₁₉N₃O₂Na: 332.1375; found: 332.1367, error = -2.4 ppm, purity 98.3%.

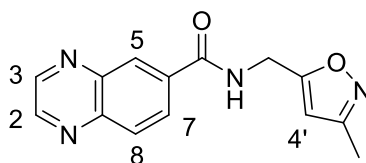
***N*-((5-(4-Fluorophenyl)furan-2-yl)methyl)quinoxaline-6-carboxamide (62)**



The reaction was carried out with (5-(4-fluorophenyl)furan-2-yl)methanamine (97 mg, 0.43 mmol, 1 equiv) for 17 h according to general procedure A. The crude residue was purified by reverse phase silica chromatography eluting 5-95% MeOH in water (+0.1% formic acid), and fractions containing product were collected and evaporated *in vacuo* to afford *N*-((5-(4-fluorophenyl)furan-2-

yl)methyl)quinoxaline-6-carboxamide (**62**) (92 mg, 61%) as a yellow orange solid. ^1H NMR (600 MHz, $\text{DMSO-}d_6$) δ 9.45 (t, $J = 5.6$ Hz, 1H, -NH), 9.06 – 9.02 (m, 2H, 2-CH and 3-CH), 8.66 (d, $J = 2.0$ Hz, 1H, 5-CH), 8.32 (dd, $J = 8.7, 2.0$ Hz, 1H, 7-CH), 8.19 (d, $J = 8.7$ Hz, 1H, 8-CH), 7.75 – 7.69 (m, 2H, 2 \times Ar-CH), 7.28 – 7.23 (m, 2H, 2 \times Ar-CH), 6.88 (d, $J = 3.3$ Hz, 1H, 4'-CH), 6.46 (d, $J = 3.3$ Hz, 1H, 3'-CH), 4.61 (d, $J = 5.6$ Hz, 2H, -CH₂). ^{13}C NMR (151 MHz, $\text{DMSO-}d_6$) δ 165.2 (-C=O), 161.3 (d, $J = 244.6$ Hz, -CF), 152.1 (2'-CH), 151.3 (5'-CH), 147.1 (2-CH or 3-CH), 146.7 (2-CH or 3-CH), 143.4 (8a-qC), 141.6 (4a-qC), 135.2 (6-qC), 129.4 (8-CH), 128.6 (7-CH), 128.4 (5-CH), 127.0 (d, $J = 3.2$ Hz, Ar-qC), 125.3 (d, $J = 8.2$ Hz, 2C, 2 \times Ar-CH), 115.9 (d, $J = 21.8$ Hz, 2C, 2 \times Ar-CH), 109.5 (3'-CH), 106.5 (4'-CH), 36.5 (-CH₂). LCMS (ESI⁺) m/z 370 [M+Na]⁺, $t_R = 1.38$ min. HRMS (ESI⁺) [M+H]⁺ calcd. for C₂₀H₁₅N₃O₂F: 348.1148; found: 348.1148, error = -1.4 ppm, purity 97.4%.

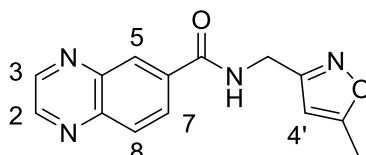
***N*-((3-Methylisoxazol-5-yl)methyl)quinoxaline-6-carboxamide (**63**)**



The reaction was carried out with (3-methylisoxazol-5-yl)methanamine (48 mg, 0.43 mmol, 1 equiv) for 18 h according to general procedure A. The crude residue was purified by reverse phase silica chromatography eluting 5-80% MeOH in water (+0.1% formic acid), fractions containing product were collected and concentrated *in vacuo*. The residue was further purified by reverse phase silica chromatography eluting 5-80% MeOH in water (+0.1% formic acid). Fractions containing product were collected and evaporated *in vacuo* to afford *N*-((3-methylisoxazol-5-yl)methyl)quinoxaline-6-carboxamide (**63**) (43 mg, 36%) as an off-white solid. ^1H NMR (600 MHz, $\text{DMSO-}d_6$) δ 9.56 (t, $J = 5.8$ Hz, 1H, -NH), 9.07 – 9.02 (m, 2H, 2-CH and 3-CH), 8.65 (d, $J = 1.9$ Hz, 1H, 5-CH), 8.30 (dd, $J = 8.7, 2.0$ Hz, 1H, 7-CH), 8.20 (d, $J = 8.7$ Hz, 1H, 8-CH), 6.29 (s, 1H, 4'-CH), 4.66 – 4.61 (m, 2H, -CH₂), 2.21 (s, 3H, -CH₃). ^{13}C NMR (151 MHz, $\text{DMSO-}d_6$) δ 169.6 (5'-qC), 165.4 (-C=O), 159.6 (3'-qC), 147.1 (2-CH or 3-CH), 146.8 (2-CH or 3-

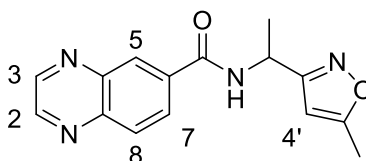
CH), 143.5 (8a-qC), 141.6 (4a-qC), 134.8 (6-qC), 129.5 (8-CH), 128.5 (7-CH), 128.5 (5-CH), 102.8 (4'-CH), 35.3 (-CH₂), 10.9 (-CH₃). LCMS (ESI⁺) *m/z* 269 [M+H]⁺, *t_R* = 0.88 min. HRMS (ESI⁺) [M+H]⁺ calcd. for C₁₄H₁₃N₄O₂: 269.1033; found: 269.1032, error = -0.4 ppm, purity 96.9%.

***N*-((5-Methylisoxazol-3-yl)methyl)quinoxaline-6-carboxamide (64)**



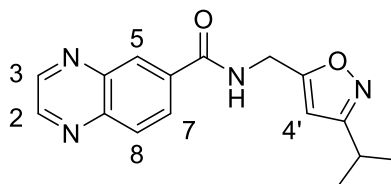
The reaction was carried out with (5-methylisoxazol-3-yl)methanamine (48 mg, 0.43 mmol, 1 equiv) for 18 h according to general procedure A. The crude residue was purified by reverse phase silica chromatography eluting 5-80% MeOH in water (+0.1% formic acid), and fractions containing product were collected and evaporated *in vacuo* to afford *N*-((1-methyl-5-phenyl-1*H*-pyrazol-3-yl)methyl)quinoxaline-6-carboxamide (**64**) (67 mg, 58%) as a brown solid. ¹H NMR (600 MHz, DMSO-*d*₆) δ 9.49 (t, *J* = 5.9 Hz, 1H, -NH), 9.08 – 9.01 (m, 2H, 2-CH and 3-CH), 8.64 (d, *J* = 2.0 Hz, 1H, 5-CH), 8.29 (dd, *J* = 8.7, 2.0 Hz, 1H, 7-CH), 8.19 (d, *J* = 8.7 Hz, 1H, 8-CH), 6.25 – 6.20 (m, 1H, 4'-CH), 4.54 (d, *J* = 5.9 Hz, 2H, -CH₂), 2.38 (d, *J* = 0.9 Hz, 3H, -CH₃). ¹³C NMR (151 MHz, DMSO-*d*₆) δ 169.6 (5'-qC), 165.4 (-C=O), 162.0 (3'-qC), 147.1 (2-CH or 3-CH), 146.7 (2-CH or 3-CH), 143.4 (8a-qC), 141.6 (4a-qC), 135.0 (6-qC), 129.4 (8-CH), 128.5 (7-CH), 128.4 (5-CH), 101.3 (4'-CH), 35.1 (-CH₂), 11.8 (-CH₃). LCMS (ESI⁺) *m/z* 269 [M+H]⁺, *t_R* = 1.03 min. HRMS (ESI⁺) [M+H]⁺ calcd. for C₁₄H₁₃N₄O₂: 269.1039; found: 269.1027, error = -4.5 ppm, purity 99.1%.

***N*-1-(5-Methylisoxazol-3-yl)ethyl)quinoxaline-6-carboxamide (65)**



The reaction was carried out with 1-(5-methylisoxazol-3-yl)ethan-1-amine (54 mg, 0.43 mmol, 1 equiv) for 17 h according to general procedure A. The crude residue was purified by reverse phase silica chromatography eluting 5-80% MeOH in water (+0.1% formic acid), and fractions containing product were collected and evaporated *in vacuo* to afford *N*-(1-(5-methylisoxazol-3-yl)ethyl)quinoxaline-6-carboxamide (**65**) (68 mg, 56%) as an off-white solid. ¹H NMR (600 MHz, DMSO-*d*₆) δ 9.27 (d, *J* = 8.1 Hz, 1H, -NH), 9.06 – 9.02 (m, 2H, 2-CH and 3-CH), 8.66 (d, *J* = 2.0 Hz, 1H, 5-CH), 8.29 (dd, *J* = 8.7, 2.0 Hz, 1H, 7-CH), 8.19 (d, *J* = 8.7 Hz, 1H, 8-CH), 6.26 (d, *J* = 1.1 Hz, 1H, 4'-CH), 5.36 – 5.28 (m, 1H, -CH), 2.38 (d, *J* = 0.9 Hz, 3H, -CH₃), 1.55 (d, *J* = 7.1 Hz, 3H, 5'-CCH₃). ¹³C NMR (151 MHz, DMSO-*d*₆) δ 169.4 (3'-qC), 166.0 (5'-qC), 164.8 (-C=O), 147.1 (2-CH or 3-CH), 146.7 (2-CH or 3-CH), 143.4 (8a-qC), 141.6 (4a-qC), 135.2 (6-qC), 129.3 (8-CH), 128.7 (7-CH), 128.5 (5-CH), 100.5 (4'-CH), 42.2 (-CH), 19.6 (5'-CCH₃), 11.8 (-CH₃). LCMS (ESI⁺) *m/z* 283 [M+H]⁺, *t*_R = 0.99 min. HRMS (ESI⁺) [M+H]⁺ calcd. for C₁₅H₁₅N₄O₂: 283.1195; found: 283.1197, error = 0.7 ppm, purity 97.9%.

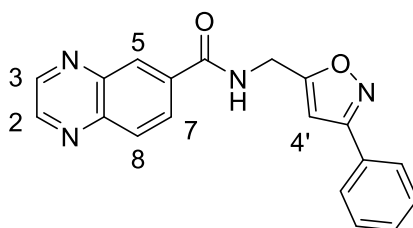
***N*-((3-Isopropylisoxazol-5-yl)methyl)quinoxaline-6-carboxamide (66)**



The reaction was carried out with (3-isopropylisoxazol-5-yl)methanamine (69 mg, 0.43 mmol, 1 equiv) for 17 h according to general procedure A. The crude residue was purified by reverse phase silica chromatography eluting 5-80% MeOH in water (+0.1% formic acid), and fractions containing product were collected and evaporated *in vacuo* to afford *N*-((3-isopropylisoxazol-5-yl)methyl)quinoxaline-6-carboxamide (**66**) (68 mg, 56%) as a brown solid. ¹H NMR (600 MHz, DMSO-*d*₆) δ 9.55 (t, *J* = 5.8 Hz, 1H, -NH), 9.07 – 9.01 (m, 2H, 2-CH and 3-CH), 8.67 (d, *J* = 2.0 Hz, 1H, 5-CH), 8.31 (dd, *J* = 8.7, 2.0 Hz, 1H, 7-CH), 8.20 (d, *J* = 8.7 Hz, 1H, 8-CH), 6.39 (s, 1H, 4'-CH), 4.65 (d, *J* = 5.7 Hz, 2H, -CH₂), 2.97 (hept, *J* = 6.9 Hz, 1H, -CH), 1.20 (d, *J* = 6.9 Hz, 6H, 2 × -CH₃). ¹³C NMR (151 MHz, DMSO-*d*₆) δ

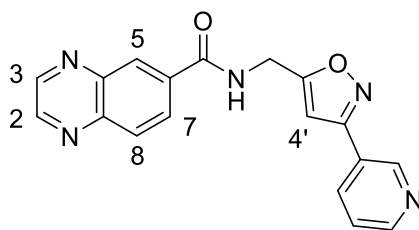
169.5 (3'-qC), 168.9 (5'-qC), 165.4 (-C=O), 147.1 (2-CH or 3-CH), 146.8 (2-CH or 3-CH), 143.5 (8a-qC), 141.6 (4a-qC), 134.8 (6-qC), 129.4 (8-CH), 128.6 (7-CH), 128.6 (5-CH), 100.3 (4'-CH), 35.4 (-CH₂), 25.9 (-CH), 21.5 (2C, 2 × -CH₃). LCMS (ESI⁺) *m/z* 297 [M+H]⁺, *t_R* = 1.20 min. HRMS (ESI⁺) [M+H]⁺ calcd. for C₁₆H₁₇N₄O₂: 297.1351; found: 297.1361, error = 3.4 ppm, purity 100%.

***N*-((3-Phenylisoxazol-5-yl)methyl)quinoxaline-6-carboxamide (67)**



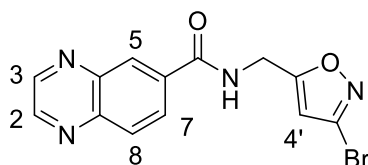
The reaction was carried out with (3-phenylisoxazol-5-yl)methanamine (75 mg, 0.43 mmol, 1 equiv) for 17 h according to general procedure A. The crude residue was dissolved in CH₂Cl₂ (25 mL) and water (50 mL) was added. The aqueous phase was extracted with CH₂Cl₂ (3 × 25 mL), then organic phases were combined and washed with sat. aq. NaHCO₃ solution (50 mL), and concentrated *in vacuo*. The crude residue was purified by reverse phase silica chromatography eluting 5-95% MeOH in water (+0.1% formic acid), and fractions containing product were collected and evaporated *in vacuo* to afford *N*-((3-phenylisoxazol-5-yl)methyl)quinoxaline-6-carboxamide (**67**) (14 mg, 10%) as a white solid. ¹H NMR (600 MHz, DMSO-*d*₆) δ 9.65 (t, *J* = 5.7 Hz, 1H -NH), 9.08 – 9.03 (m, 2H, 2-CH and 3-CH), 8.70 (d, *J* = 1.9 Hz, 1H, 5-CH), 8.33 (dd, *J* = 8.7, 2.0 Hz, 1H, 7-CH), 8.22 (d, *J* = 8.7 Hz, 1H, 8-CH), 7.92 – 7.85 (m, 2H, 2 × Ar-CH), 7.53 – 7.46 (m, 3H, 3 × Ar-CH), 7.02 (d, *J* = 0.9 Hz, 1H, 4'-CH), 4.75 (dd, *J* = 5.7, 0.8 Hz, 2H, -CH₂). ¹³C NMR (151 MHz, DMSO-*d*₆) δ 170.9 (5'-qC), 165.5 (-C=O), 161.9 (3'-qC), 147.2 (2-CH or 3-CH), 146.8 (2-CH or 3-CH), 143.5 (8a-qC), 141.6 (4a-qC), 134.8 (6-qC), 130.2 (Ar-CH), 129.5 (8-CH), 129.1 (2C, 2 × Ar-CH), 128.6 (2C, 5-CH and 7-CH), 128.5 (Ar-qC), 126.6 (2C, 2 × Ar-CH), 100.3 (4'-CH), 35.6 (-CH₂). LCMS (ESI⁺) *m/z* 331 [M+H]⁺, *t_R* = 1.17 min. HRMS (ESI⁺) [M+H]⁺ calcd. for C₁₉H₁₅N₄O₂: 331.1190; mass found: 331.1205, error = 4.6, purity 98.0%.

***N*-((3-(Pyridin-3-yl)isoxazol-5-yl)methyl)quinoxaline-6-carboxamide (68)**



The reaction was carried out with (3-(pyridin-3-yl)isoxazol-5-yl)methanamine dihydrochloride (107 mg, 0.43 mmol, 1 equiv) for 17 h according to general procedure A. The crude residue was purified by trituration with CH₂Cl₂ (10 mL) and solid was collected by filtration under vacuum to afford *N*-((3-(3-pyridyl)isoxazol-5-yl)methyl)quinoxaline-6-carboxamide (**68**) (54 mg, 37%) as a pale brown solid. ¹H NMR (600 MHz, DMSO-*d*₆) δ 9.67 (t, *J* = 5.8 Hz, 1H, -NH), 9.09 (dd, *J* = 2.3, 0.9 Hz, 1H, Ar-CH), 9.07 – 9.03 (m, 2H, 2-CH and 3-CH), 8.70 (d, *J* = 2.0 Hz, 1H, 5-CH), 8.68 (dd, *J* = 4.8, 1.6 Hz, 1H, Ar-CH), 8.33 (dd, *J* = 8.7, 2.0 Hz, 1H, 7-CH), 8.28 (*app* dt, *J* = 8.0, 1.9 Hz, 1H, Ar-CH), 8.22 (d, *J* = 8.7 Hz, 1H, 8-CH), 7.54 (ddd, *J* = 8.0, 4.8, 0.9 Hz, 1H, Ar-CH), 7.15 (d, *J* = 1.0 Hz, 1H, 4'-CH), 4.79 – 4.75 (m, 2H, -CH₂). ¹³C NMR (151 MHz, DMSO-*d*₆) δ 171.4 (5'-qC), 165.5 (-C=O), 159.8 (3'-qC), 151.1 (Ar-CH), 147.5 (Ar-CH), 147.2 (2-CH or 3-CH), 146.8 (2-CH or 3-CH), 143.5 (8a-qC), 141.6 (4a-qC), 134.8 (6-qC), 134.0 (Ar-CH), 129.5 (8-CH), 128.6 (5-CH or 7-CH), 128.6 (5-CH or 7-CH), 124.6 (Ar-qC), 124.2 (Ar-CH), 100.3 (4'-CH), 35.6 (-CH₂). LCMS (ESI⁺) *m/z* 332 [M+H]⁺, *t*_R = 0.92 min. HRMS (ESI⁺) [M+H]⁺ calcd. for C₁₈H₁₄N₅O₂: 332.1142; found: 332.1148, error = 1.8 ppm, purity 98.8%.

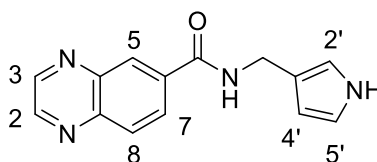
***N*-((3-Bromoisoxazol-5-yl)methyl)quinoxaline-6-carboxamide (69)**



The reaction was carried out with (3-bromoisoxazol-5-yl)methanamine (76 mg, 0.43 mmol, 1 equiv) for 18 h according to general procedure A. The crude residue was purified by reverse phase silica chromatography eluting 5-80% MeOH in water (+0.1% formic acid), and fractions containing product were collected and

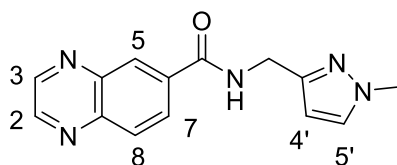
evaporated *in vacuo* to afford *N*-((3-bromoisoxazol-5-yl)methyl)quinoxaline-6-carboxamide (**69**) (34 mg, 23%) as an orange solid. ¹H NMR (600 MHz, DMSO-*d*₆) δ 9.60 (t, *J* = 5.7 Hz, 1H, -NH), 9.07 – 9.02 (m, 2H, 2-CH and 3-CH), 8.66 (d, *J* = 1.9 Hz, 1H, 5-CH), 8.29 (dd, *J* = 8.7, 2.0 Hz, 1H, 7-CH), 8.20 (d, *J* = 8.7 Hz, 1H, 8-CH), 6.82 – 6.79 (m, 1H, 4'-CH), 4.73 – 4.68 (m, 2H, -CH₂). ¹³C NMR (151 MHz, DMSO-*d*₆) δ 172.5 (5'-qC), 165.6 (-C=O), 147.2 (2-CH or 3-CH), 146.8 (2-CH or 3-CH), 143.5 (8a-qC), 141.6 (4a-qC), 140.6 (3'-qC), 134.6 (6-qC), 129.5 (8-CH), 128.6 (7-CH), 128.5 (5-CH), 105.7 (4'-CH), 35.5 (-CH₂). LCMS (ESI⁺) *m/z* 332/334 [M+H]⁺, t_R = 1.00 min. HRMS (ESI⁺) [M+H]⁺ calcd. for C₁₃H₁₀N₄O₂Br: 334.9962; found: 334.9974, error = 3.61 ppm, purity 96.9%.

N-((1*H*-Pyrrol-3-yl)methyl)quinoxaline-6-carboxamide (**70**)



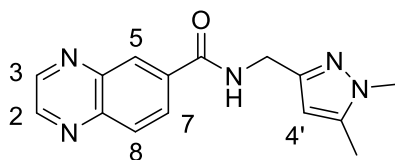
The reaction was carried out with (1*H*-pyrrol-3-yl)methanamine (41 mg, 0.43 mmol, 1 equiv) for 18 h according to general procedure A. The crude residue was purified by reverse phase silica chromatography eluting 5-80% MeOH in water (+0.1% formic acid), and fractions containing product were collected and evaporated *in vacuo* to afford *N*-((1*H*-pyrrol-3-yl)methyl)quinoxaline-6-carboxamide (**70**) (51 mg, 46%) as a brown solid. ¹H NMR (600 MHz, DMSO-*d*₆) δ 10.59 (br s, 1H, -NH), 9.11 (t, *J* = 5.7 Hz, 1H, -NH), 9.05 – 9.00 (m, 2H, 2-CH and 3-CH), 8.61 (d, *J* = 1.9 Hz, 1H, 5-CH), 8.29 (dd, *J* = 8.7, 2.0 Hz, 1H, 7-CH), 8.16 (d, *J* = 8.7 Hz, 1H, 8-CH), 6.73 (*app* q, *J* = 2.1 Hz, 1H, 2'-CH), 6.67 (*app* q, *J* = 2.5 Hz, 1H, 5'-CH), 6.06 (*app* q, *J* = 2.2 Hz, 1H, 4'-CH), 4.39 (d, *J* = 5.6 Hz, 2H, -CH₂). ¹³C NMR (151 MHz, DMSO-*d*₆) δ 164.7 (-C=O), 146.8 (2-CH or 3-CH), 146.6 (2-CH or 3-CH), 143.2 (8a-qC), 141.6 (4a-qC), 135.9 (6-qC), 129.2 (8-CH), 128.7 (7-CH), 128.2 (5-CH), 120.2 (3'-qC), 117.6 (5'-CH), 115.9 (2'-CH), 107.5 (4'-CH), 36.4 (-CH₂). LCMS (ESI⁺) *m/z* 275 [M+Na]⁺, t_R = 0.84 min. HRMS (ESI⁺) [M+H]⁺ calcd. for C₁₄H₁₃N₄O: 253.1084; found: 253.1087, error = 1.27 ppm, purity 99.4%.

***N*-((1-Methyl-1*H*-pyrazol-3-yl)methyl)quinoxaline-6-carboxamide (71)**



The reaction was carried out with (1-methyl-1*H*-pyrazol-3-yl)methanamine (48 mg, 0.43 mmol, 1 equiv) for 22 h according to general procedure A. The crude residue was purified by reverse phase silica chromatography eluting 5-80% MeOH in water (+0.1% formic acid), and fractions containing product were collected and evaporated *in vacuo* to afford *N*-((1-methyl-1*H*-pyrazol-3-yl)methyl)quinoxaline-6-carboxamide (**71**) (52 mg, 43%) as a pale brown solid. ¹H NMR (600 MHz, DMSO-*d*₆) δ 9.31 (t, *J* = 5.8 Hz, 1H, -NH), 9.06 – 9.01 (m, 2H, 2-CH and 3-CH), 8.63 (d, *J* = 1.9 Hz, 1H, 5-CH), 8.30 (dd, *J* = 8.7, 2.0 Hz, 1H, 7-CH), 8.17 (d, *J* = 8.7 Hz, 1H, 8-CH), 7.59 (d, *J* = 2.2 Hz, 1H, 5'-CH), 6.18 (d, *J* = 2.2 Hz, 1H, 4'-CH), 4.48 (d, *J* = 5.8 Hz, 2H, -CH₂), 3.79 (s, 3H, -CH₃). ¹³C NMR (151 MHz, DMSO-*d*₆) δ 165.0 (-C=O), 149.3 (3'-qC), 146.9 (2-CH or 3-CH), 146.6 (2-CH or 3-CH), 143.3 (8a-qC), 141.6 (4a-qC), 135.5 (6-qC), 131.4 (5'-CH), 129.3 (8-CH), 128.6 (7-CH), 128.3 (5-CH), 104.0 (4'-CH), 38.3 (-CH₂), 37.1 (-CH₃). LCMS (ESI⁺) *m/z* 268 [M+H]⁺, *t*_R = 0.84 min. HRMS (ESI⁺) [M+H]⁺ calcd. for C₁₄H₁₄N₅O: 268.1193; found: 268.1198, error = 1.74 ppm, purity 95.0%.

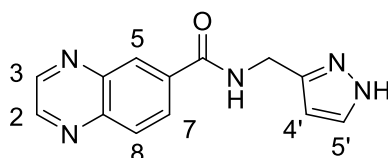
***N*-((1,5-Dimethyl-1*H*-pyrazol-3-yl)methyl)quinoxaline-6-carboxamide (72)**



The reaction was carried out with (1,5-dimethyl-1*H*-pyrazol-3-yl)methanamine (54 mg, 0.43 mmol, 1 equiv) for 18 h according to general procedure A. The crude residue was purified by reverse phase silica chromatography eluting 5-80% MeOH in water (+0.1% formic acid), and fractions containing product were collected and evaporated *in vacuo* to afford *N*-((1,5-dimethyl-1*H*-pyrazol-3-

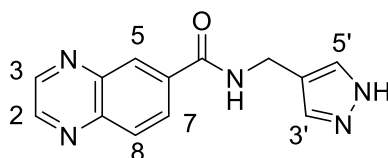
yl)methyl)quinoxaline-6-carboxamide (**72**) (52 mg, 41%) as a pale brown solid. ^1H NMR (600 MHz, $\text{DMSO-}d_6$) δ 9.27 (t, $J = 5.8$ Hz, 1H, -NH), 9.04 – 9.01 (m, 2H, 2-CH and 3-CH), 8.62 (d, $J = 1.9$ Hz, 1H, 5-CH), 8.29 (dd, $J = 8.7, 2.0$ Hz, 1H, 7-CH), 8.17 (d, $J = 8.7$ Hz, 1H, 8-CH), 6.00 – 5.97 (m, 1H, 4'-CH), 4.41 (d, $J = 5.8$ Hz, 2H, -CH₂), 3.66 (s, 3H, -NCH₃), 2.20 (d, $J = 0.7$ Hz, 3H, -CH₃). ^{13}C NMR (151 MHz, $\text{DMSO-}d_6$) δ 164.9 (-C=O), 147.8 (3'-qC), 146.9 (2-CH or 3-CH), 146.6 (2-CH or 3-CH), 143.3 (8a-qC), 141.6 (4a-qC), 139.0 (5'-qC), 135.5 (6-qC), 129.3 (8-CH), 128.6 (7-CH), 128.3 (5-CH), 103.7 (4'-CH), 37.1 (-CH₂), 35.6 (-NCH₃), 10.7 (-CH₃). LCMS (ESI⁺) m/z 282 [M+H]⁺, $t_R = 0.92$ min. HRMS (ESI⁺) [M+H]⁺ calcd. for C₁₅H₁₆N₅O: 282.1349; found: 282.1353, error = 1.25 ppm, purity 95.6%

***N*-((1*H*-Pyrazol-3-yl)methyl)quinoxaline-6-carboxamide (**73**)**



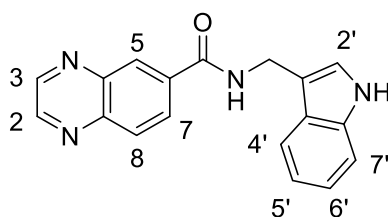
The reaction was carried out with (1*H*-pyrazol-3-yl)methanamine (43 mg, 0.43 mmol, 1 equiv) for 17 h according to general procedure A. The crude residue was purified by reverse phase silica chromatography eluting 5-95% MeOH in water (+0.1% formic acid), and fractions containing product were collected and evaporated *in vacuo* to afford *N*-((1*H*-pyrazol-3-yl)methyl)quinoxaline-6-carboxamide (**73**) (46 mg, 41%) as an off-white solid. ^1H NMR (600 MHz, $\text{DMSO-}d_6$) δ 12.87 – 12.50 (m, 1H, -NH), 9.33 (br s, 1H, -NH), 9.07 – 9.00 (m, 2H, 2-CH and 3-CH), 8.64 (d, $J = 2.0$ Hz, 1H, 5-CH), 8.30 (dd, $J = 8.7, 2.0$ Hz, 1H, 7-CH), 8.18 (d, $J = 8.7$ Hz, 1H, 8-CH), 7.75 – 7.25 (m, 1H, 5'-CH), 6.22 (d, $J = 2.1$ Hz, 1H, 4'-CH), 4.55 (d, $J = 5.8$ Hz, 2H, -CH₂). ^{13}C NMR (151 MHz, $\text{DMSO-}d_6$) δ 165.1 (-C=O), 147.0 (2-CH or 3-CH), 146.7 (2-CH or 3-CH), 143.3 (8a-qC), 141.6 (4a-qC), 135.5 (6-qC), 129.3 (8-CH), 128.7 (7-CH), 128.4 (5-CH), 103.2 (4'-CH), 37.1 (-CH₂), (2 × C missing). LCMS (ESI⁺) m/z 254 [M+H]⁺, $t_R = 0.83$ min. HRMS (ESI⁺) [M+H]⁺ calcd. for C₁₃H₁₂N₅O: 254.1042; found: 254.1041, error = -0.4 ppm, purity 95.1%.

***N*-((1*H*-Pyrazol-4-yl)methyl)quinoxaline-6-carboxamide (**74**)**



The reaction was carried out with (1*H*-pyrazol-4-yl)methanamine dihydrochloride (73 mg, 0.43 mmol, 1 equiv) for 26 h according to general procedure A. The crude residue was purified by reverse phase silica chromatography eluting 5-95% MeOH in water (+0.1% formic acid), fractions containing product were collected and concentrated *in vacuo*. The residue was further purified by normal phase silica chromatography eluting 0-20% MeOH in CH₂Cl₂. The fractions containing product were collected and evaporated *in vacuo* to afford *N*-((1*H*-pyrazol-4-yl)methyl)quinoxaline-6-carboxamide (**74**) (21 mg, 19%) as a white solid. ¹H NMR (600 MHz, DMSO) δ 12.67 (br s, 1H), 9.22 (t, *J* = 5.7 Hz, 1H), 9.05 – 8.99 (m, 2H), 8.61 (d, *J* = 2.0 Hz, 1H), 8.29 (dd, *J* = 8.7, 2.0 Hz, 1H), 8.17 (d, *J* = 8.7 Hz, 1H), 7.69 (br s, 1H), 7.49 (br s, 1H), 4.42 (d, *J* = 5.6 Hz, 2H). ¹³C NMR (151 MHz, DMSO) δ 164.9 (-C=O), 146.9 (2-CH or 3-CH), 146.6 (2-CH or 3-CH), 143.3 (8a-qC), 141.6 (4a-qC), 135.6 (6-qC), 129.3 (8-CH), 128.7 (7-CH), 128.2 (5-CH), 117.8 (3'-CH or 5'-CH), 33.8 (-CH₂), (2 × C missing). LCMS (ESI⁺) *m/z* 254 [M+H]⁺, *t_R* = 0.76 min. HRMS (ESI⁺) [M+H]⁺ calcd. for C₁₃H₁₂N₅O: 254.1036; found: 254.1042, error = 2.06 ppm, purity 97.5%.

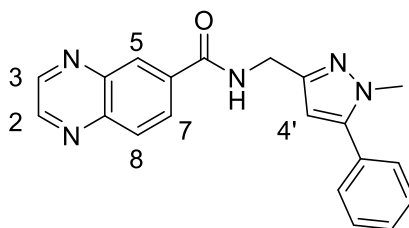
***N*-((1*H*-Indol-3-yl)methyl)quinoxaline-6-carboxamide (75)**



The reaction was carried out with (1*H*-indol-3-yl)methanamine (60 mg, 0.43 mmol, 1 equiv) for 17 h according to general procedure A. The crude residue was purified by reverse phase silica chromatography eluting 5-90% MeOH in water (+0.1% formic acid), and fractions containing product were collected and evaporated *in vacuo* to afford *N*-((1*H*-indol-3-yl)methyl)quinoxaline-6-

carboxamide (**75**) (58 mg, 47%) as a brown solid. ^1H NMR (600 MHz, $\text{DMSO-}d_6$) δ 10.95 – 10.93 (m, 1H, -NH), 9.24 (t, $J = 5.6$ Hz, 1H, -NH), 9.03 – 8.98 (m, 2H, 2-CH and 3-CH), 8.61 (d, $J = 1.9$ Hz, 1H, 5-CH), 8.31 (dd, $J = 8.7, 2.0$ Hz, 1H, 7-CH), 8.16 (d, $J = 8.7$ Hz, 1H, 8-CH), 7.69 (dd, $J = 7.9, 1.2$ Hz, 1H, 4'-CH), 7.36 (dd, $J = 8.1, 1.0$ Hz, 1H, 7'-CH), 7.34 (d, $J = 2.5$ Hz, 1H, 2'-CH), 7.08 (ddd, $J = 8.1, 7.0, 1.2$ Hz, 1H, 6'-CH), 6.99 (ddd, $J = 8.0, 7.0, 1.0$ Hz, 1H, 5'-CH), 4.70 (d, $J = 5.5$ Hz, 2H, -CH₂). ^{13}C NMR (151 MHz, $\text{DMSO-}d_6$) δ 164.9 (-C=O), 146.9 (2-CH or 3-CH), 146.6 (2-CH or 3-CH), 143.3 (8a-qC), 141.6 (4a-qC), 136.3 (6-qC), 135.8 (7'a-qC), 129.2 (8-CH), 128.7 (7-CH), 128.2 (5-CH), 126.5 (3'a-qC), 124.1 (2'-CH), 121.1 (6'-CH), 118.7 (4'-CH), 118.5 (5'-CH), 112.2 (2'a-qC), 111.4 (7'-CH), 34.9 (-CH₂). LCMS (ESI⁺) m/z 303 [M+H]⁺, $t_R = 1.21$ min. HRMS (ESI⁺) [M+H]⁺ calcd. for C₁₈H₁₅N₄O: 303.1246; found: 303.1243, error = -1.0 ppm, purity 100%.

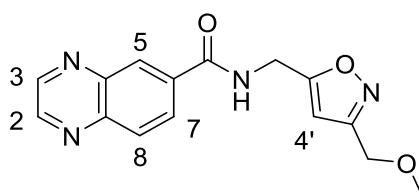
***N*-((1-Methyl-5-phenyl-1*H*-pyrazol-3-yl)methyl)quinoxaline-6-carboxamide (76)**



The reaction was carried out with (1-methyl-5-phenyl-1*H*-pyrazol-3-yl)methanamine (80 mg, 0.43 mmol, 1 equiv) for 17 h according to general procedure A. The crude residue was purified by reverse phase silica chromatography eluting 5-95% MeOH in water (+0.1% formic acid), and fractions containing product were collected and evaporated *in vacuo* to afford *N*-((1-methyl-5-phenyl-1*H*-pyrazol-3-yl)methyl)quinoxaline-6-carboxamide (**76**) (65 mg, 45%) as a brown oil. ^1H NMR (600 MHz, $\text{DMSO-}d_6$) δ 9.37 (t, $J = 5.8$ Hz, 1H, -NH), 9.05 – 9.01 (m, 2H, 2-CH and 3-CH), 8.66 (d, $J = 2.0$ Hz, 1H, 5-CH), 8.32 (dd, $J = 8.7, 2.0$ Hz, 1H, 7-CH), 8.18 (d, $J = 8.7$ Hz, 1H, 8-CH), 7.54 – 7.46 (m, 4H, 4 × Ar-CH), 7.45 – 7.40 (m, 1H, Ar-CH), 6.37 (s, 1H, 4'-CH), 4.52 (d, $J = 5.8$ Hz, 2H, -CH₂), 3.82 (s, 3H, -CH₃). ^{13}C NMR (151 MHz, $\text{DMSO-}d_6$) δ 165.1 (-C=O),

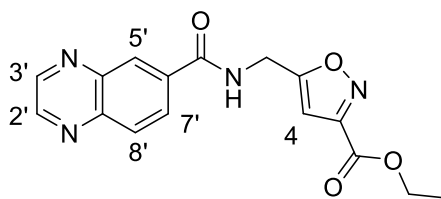
148.6 (3'-qC), 147.0 (2-CH or 3-CH), 146.7 (2-CH or 3-CH), 143.6 (5'-qC), 143.3 (8a-qC), 141.6 (4a-qC), 135.5 (6-qC), 130.2 (Ar-qC), 129.3 (8-CH), 128.8 (2C, 2 × Ar-CH), 128.7 (7-CH), 128.4 (5-CH), 128.3 (3C, 3 × Ar-CH), 104.5 (4'-CH), 37.4 (-CH₂), 37.1 (-CH₃). LCMS (ESI⁺) *m/z* 344 [M+H]⁺, *t_R* = 1.24 min. HRMS (ESI⁺) [M+H]⁺ calcd. for C₂₀H₁₈N₅O: 344.1511; found: 344.1506, error = -1.5 ppm, purity 100%.

***N*-((3-(Methoxymethyl)isoxazol-5-yl)methyl)quinoxaline-6-carboxamide (77)**



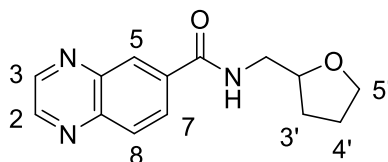
The reaction was carried out with (3-(methoxymethyl)isoxazol-5-yl)methanamine (77 mg, 0.43 mmol, 1 equiv) for 18 h according to general procedure A. The crude residue was purified by reverse phase silica chromatography eluting 5-80% MeOH in water (+0.1% formic acid), and fractions containing product were collected and evaporated *in vacuo* to afford *N*-((3-methoxymethyl)isoxazol-5-yl)methyl)quinoxaline-6-carboxamide (**77**) (64 mg, 50%) as an off-white solid. ¹H NMR (600 MHz, DMSO-*d*₆) δ 9.58 (t, *J* = 5.8 Hz, 1H, -NH), 9.07 – 9.02 (m, 2H, 2-CH and 3-CH), 8.66 (d, *J* = 1.9 Hz, 1H, 5-CH), 8.30 (dd, *J* = 8.7, 2.0 Hz, 1H, 7-CH), 8.20 (d, *J* = 8.7 Hz, 1H, 8-CH), 6.44 (d, *J* = 0.8 Hz, 1H, 4'-CH), 4.69 (dd, *J* = 5.7, 0.9 Hz, 2H, -CH₂), 4.45 (s, 2H, -OCH₂), 3.29 (s, 3H, -OCH₃). ¹³C NMR (151 MHz, DMSO-*d*₆) δ 170.3 (5'-qC), 165.4 (-C=O), 161.2 (3'-qC), 147.2 (2-CH or 3-CH), 146.8 (2-CH or 3-CH), 143.5 (8a-qC), 141.6 (4a-qC), 134.8 (6-qC), 129.5 (8-CH), 128.6 (2C, 5-CH and 7-CH), 101.6 (4'-CH), 64.8 (-OCH₂), 57.9 (-OCH₃), 35.4 (-CH₂). LCMS (ESI⁺) *m/z* 299 [M+H]⁺, *t_R* = 0.87 min. HRMS (ESI⁺) [M+H]⁺ calcd. for C₁₅H₁₅N₄O₃: 299.1139; found: 299.1144, error = 1.92 ppm, purity 100%.

Ethyl 5-((quinoxaline-6-carboxamido)methyl)isoxazole-3-carboxylate (78)



The reaction was carried out with ethyl 5-(aminomethyl)isoxazole-3-carboxylate hydrochloride (59 mg, 0.43 mmol, 1 equiv) for 18 h according to general procedure A. The crude residue was purified by reverse phase silica chromatography eluting 5-80% MeCN in water (+0.1% formic acid), fractions containing product were collected and concentrated *in vacuo*. The residue was further purified by normal phase silica chromatography eluting 0-10% MeOH in CH₂Cl₂. The fractions containing product were collected and evaporated *in vacuo* to afford ethyl 5-((quinoxaline-6-carboxamido)methyl)isoxazole-3-carboxylate (**78**) (6 mg, 6%) as a white solid. ¹H NMR (600 MHz, DMSO-*d*₆) δ 9.6 (t, *J* = 5.6 Hz, 1H, -NH), 9.1 – 9.0 (m, 2H, 2'-CH and 3'-CH), 8.7 (d, *J* = 2.0 Hz, 1H, 5'-CH), 8.3 (dd, *J* = 8.7, 2.0 Hz, 1H, 7'-CH), 8.2 (d, *J* = 8.7 Hz, 1H, 8'-CH), 6.8 (d, *J* = 0.9 Hz, 1H, 4-CH), 4.8 – 4.7 (m, 2H, -CH₂), 4.4 (q, *J* = 7.1 Hz, 2H, -OCH₂), 1.3 (t, *J* = 7.1 Hz, 3H, -CH₃). ¹³C NMR (151 MHz, DMSO-*d*₆) δ 172.4 (5-qC), 165.6 (-C=O), 159.3 (-COOEt), 156.2 (3-qC), 147.2 (2'-CH or 3'-CH), 146.8 (2'-CH or 3'-CH), 143.5 (8'a-qC), 141.6 (4'a-qC), 134.6 (6'-qC), 129.5 (8'-CH), 128.6 (7'-CH or 5'-CH), 128.5 (7'-CH or 5'-CH), 102.6 (4-CH), 61.8 (-OCH₂), 35.4 (-CH₂), 13.9 (-CH₃). LCMS (ESI⁺) *m/z* 327 [M+H]⁺, *t*_R = 1.02 min. HRMS (ESI⁺) [M+H]⁺ calcd. for C₁₆H₁₅N₄O₄: 327.1087; found: 327.1096, error = 2.53 ppm, purity 96.4%.

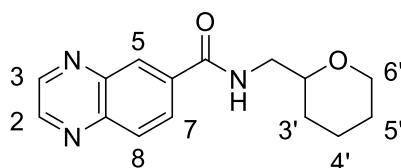
***N*-((Tetrahydrofuran-2-yl)methyl)quinoxaline-6-carboxamide (79)**



The reaction was carried out with (tetrahydrofuran-2-yl)methanamine (44 μL, 0.43 mmol, 1 equiv) for 22 h according to general procedure A. The crude residue was purified by reverse phase silica chromatography eluting 5-80% MeOH in water (+0.1% formic acid), and fractions containing product were collected and

evaporated *in vacuo* to afford *N*-((tetrahydrofuran-2-yl)methyl)quinoxaline-6-carboxamide (**79**) (78 mg, 70%) as a pale brown solid. ¹H NMR (600 MHz, DMSO-*d*₆) δ 9.05 – 8.99 (m, 2H, 2-CH and 3-CH), 8.97 (t, *J* = 5.8 Hz, 1H, -NH), 8.61 (d, *J* = 2.0 Hz, 1H, 5-CH), 8.27 (dd, *J* = 8.7, 2.0 Hz, 1H, 7-CH), 8.17 (d, *J* = 8.7 Hz, 1H, 8-CH), 4.06 – 4.00 (m, 1H, 2'-CH), 3.82 – 3.77 (m, 1H, 5'-CH), 3.68 – 3.61 (m, 1H, 5'-CH), 3.45 – 3.35 (m, 2H, -CH₂), 1.98 – 1.91 (m, 1H, 3'-CH), 1.90 – 1.77 (m, 2H, 4'-CH₂), 1.67 – 1.58 (m, 1H, 3'-CH). ¹³C NMR (151 MHz, DMSO-*d*₆) δ 165.4 (-C=O), 146.9 (2-CH or 3-CH), 146.7 (2-CH or 3-CH), 143.3 (8a-qC), 141.6 (4a-qC), 135.6 (6-qC), 129.3 (8-CH), 128.6 (7-CH), 128.3 (5-CH), 77.0 (2'-CH), 67.2 (5'-CH₂), 43.7 (-CH₂), 28.7 (3'-CH₂), 25.1 (4'-CH₂). LCMS (ESI⁺) *m/z* 258 [M+H]⁺, *t*_R = 0.88 min. HRMS (ESI⁺) [M+H]⁺ calcd. for C₁₄H₁₆N₃O₂: 258.1237; found: 258.1245, error = 2.91 ppm, purity 99.0%.

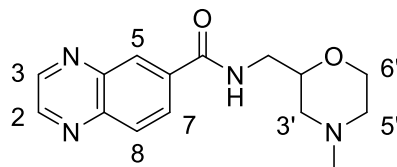
***N*-((Tetrahydro-2H-pyran-2-yl)methyl)quinoxaline-6-carboxamide (80)**



The reaction was carried out with (tetrahydro-2H-pyran-2-yl)methanamine (51 μL, 0.43 mmol, 1 equiv) for 22 h according to general procedure A. The crude residue was purified by reverse phase silica chromatography eluting 5-80% MeOH in water (+0.1% formic acid), and fractions containing product were collected and evaporated *in vacuo* to afford *N*-((tetrahydro-2H-pyran-2-yl)methyl)quinoxaline-6-carboxamide (**80**) (72 mg, 62%) as a pale brown solid. ¹H NMR (600 MHz, DMSO-*d*₆) δ 9.05 – 8.99 (m, 2H, 2-CH and 3-CH), 8.93 (t, *J* = 5.8 Hz, 1H, -NH), 8.61 (d, *J* = 1.9 Hz, 1H, 5-CH), 8.28 (dd, *J* = 8.7, 2.0 Hz, 1H, 7-CH), 8.17 (d, *J* = 8.7 Hz, 1H, 8-CH), 3.91 – 3.87 (m, 1H, 6'-CH), 3.49 (dtd, *J* = 11.2, 6.0, 2.1 Hz, 1H, 2'-CH), 3.39 – 3.29 (m, 3H, 6'-CH and -CH₂), 1.82 – 1.76 (m, 1H, 5'-CH), 1.69 – 1.63 (m, 1H, 4'-CH), 1.52 – 1.40 (m, 3H, 4'-CH₂ and 5'-CH), 1.26 – 1.16 (m, 1H, 3'-CH). ¹³C NMR (151 MHz, DMSO-*d*₆) δ 165.2 (-C=O), 146.9 (2-CH or 3-CH), 146.6 (2-CH or 3-CH), 143.3 (8a-qC), 141.6 (4a-qC), 135.5 (6-qC), 129.3 (8-CH), 128.6 (7-CH), 128.3 (5-CH), 75.7 (2'-CH), 67.3 (6'-CH₂), 44.7 (-CH₂), 29.3 (3'-

CH₂), 25.7 (4'-CH₂), 22.7 (5'-CH₂). LCMS (ESI⁺) *m/z* 272 [M+H]⁺, *t_R* = 1.01 min. HRMS (ESI⁺) [M+H]⁺ calcd. for C₁₅H₁₈N₃O₂: 272.1393; found: 272.1400, error = 2.43 ppm, purity 100%.

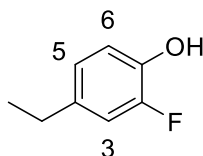
***N*-((4-Methylmorpholin-2-yl)methyl)quinoxaline-6-carboxamide (81)**



The reaction was carried out with (4-methylmorpholin-2-yl)methanamine (57 μ L, 0.43 mmol, 1 equiv) for 18 h according to general procedure A. The crude residue was dissolved in 1:1 MeOH/CH₂Cl₂ (5 mL) and purified by ion-exchange chromatography on acidic resin (2 g), eluting with MeOH (3 \times 10 mL) then 2 M NH₃ in MeOH (3 \times 10 mL). The basic fractions were concentrated *in vacuo* and the residue was further purified by reverse phase silica chromatography eluting 5-80% MeOH in water (+0.1% formic acid). The fractions containing product were concentrated *in vacuo* and dissolved in 1:1 MeOH/CH₂Cl₂ (2 mL) and further purified by ion-exchange chromatography on acidic resin (2 g), eluting with MeOH (3 \times 10 mL) then 2 M NH₃ in MeOH (3 \times 10 mL). The basic fractions were concentrated *in vacuo* to afford *N*-((4-methylmorpholin-2-yl)methyl)quinoxaline-6-carboxamide (**81**) (46 mg, 37%) as an orange oil. ¹H NMR (600 MHz, DMSO-*d*₆) δ 9.05 – 9.01 (m, 2H, 2-CH and 3-CH), 8.96 (t, *J* = 5.8 Hz, 1H, -NH), 8.62 (d, *J* = 1.9 Hz, 1H, 5-CH), 8.28 (dd, *J* = 8.7, 2.0 Hz, 1H, 7-CH), 8.18 (d, *J* = 8.7 Hz, 1H, 8-CH), 3.80 (ddd, *J* = 11.3, 3.3, 1.8 Hz, 1H, 6'-CH), 3.68 – 3.61 (m, 1H, 2'-CH), 3.53 – 3.47 (m, 1H, 6'-CH), 3.44 – 3.34 (m, 2H, -CH₂), 2.76 (dt, *J* = 11.3, 2.0 Hz, 1H, 3'-CH), 2.60 – 2.56 (m, 1H, 5'-CH), 2.17 (s, 3H, -NCH₃), 2.01 – 1.94 (m, 1H, 5'-CH), 1.76 (dd, *J* = 11.4, 9.8 Hz, 1H, 3'-CH). ¹³C NMR (151 MHz, DMSO-*d*₆) δ 165.3 (-C=O), 147.0 (2-CH or 3-CH), 146.7 (2-CH or 3-CH), 143.3 (8a-qC), 141.6 (4a-qC), 135.4 (6-qC), 129.3 (8-CH), 128.6 (7-CH), 128.3 (5-CH), 73.8 (2'-CH), 65.8 (6'-CH₂), 58.2 (3'-CH₂), 54.5 (5'-CH₂), 46.0 (-NCH₃), 42.3 (-CH₂). LCMS (ESI⁺) *m/z* 287 [M+H]⁺, *t_R* = 0.47 min. HRMS (ESI⁺) [M+H]⁺ calcd. for C₁₅H₁₉N₄O₂: 287.1502; found: 287.1506, error = 1.22 ppm, purity 98.4%.

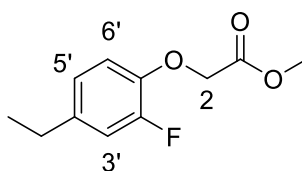
7.1.3 Chemical Syntheses from Chapter 3

4-Ethyl-2-fluoro-phenol (**83**)



SelectFluor (1171 mg, 3.30 mmol) was added to a solution of 4-ethylphenol (367 mg, 3.00 mmol) in MeOH (30 mL, 0.10 M) and the reaction was stirred at 65°C for 48 h. The reaction was concentrated *in vacuo*, CH₂Cl₂ (50 mL) was added, and the reaction was filtered under vacuum. The filtrate was washed with water (30 mL), dried with MgSO₄, filtered and concentrated *in vacuo*. The crude residue was purified by normal phase silica chromatography eluting 0-10% EtOAc in cyclohexane to afford 4-ethyl-2-fluoro-phenol (**83**) (67 mg, 16%) as a clear oil. ¹H NMR (600 MHz, DMSO-*d*₆) δ 9.50 (br s, 1H, -OH), 6.95 (dd, *J* = 12.5, 2.0 Hz, 1H, 3-CH), 6.86 – 6.77 (m, 2H, 5-CH and 6-CH), 2.51 – 2.45 (m, 2H, -CH₂), 1.12 (t, *J* = 7.6 Hz, 3H, -CH₃). ¹³C NMR (151 MHz, DMSO-*d*₆) δ 150.8 (d, *J* = 239.9 Hz, 2-CF), 142.5 (d, *J* = 12.0 Hz, 1-COH), 135.2 (d, *J* = 5.5 Hz, 4-qC), 123.5 (d, *J* = 3.0 Hz, 5-CH), 117.5 (d, *J* = 3.2 Hz, 6-CH), 115.2 (d, *J* = 17.9 Hz, 3-CH), 27.1 (-CH₂), 15.7 (-CH₃). ¹⁹F NMR (471 MHz, DMSO-*d*₆) δ -136.83. LCMS (ESI⁺) *m/z* mass ion not detected, *t*_R = 1.17 min.

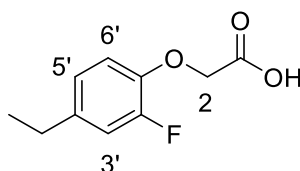
Methyl 2-(4-ethyl-2-fluoro-phenoxy)acetate (**85**)



Methyl bromoacetate (44 μL, 0.46 mmol) was added to a solution of 4-ethyl-2-fluoro-phenol (65 mg, 0.46 mmol) and K₂CO₃ in DMF (4.6 mL, 0.10 M). The reaction was stirred at rt for 22 h, then diluted with EtOAc (10 mL) and filtered under vacuum. The solid was washed with further EtOAc (25 mL), and filtrate was

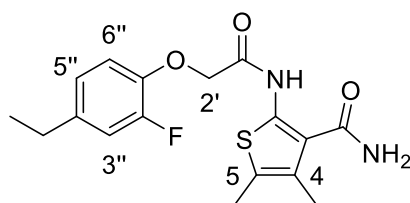
washed with brine (2 × 50 mL), dried with MgSO₄, filtered and concentrated *in vacuo* to afford methyl 2-(4-ethyl-2-fluoro-phenoxy)acetate (**85**) (74 mg, 75%) as a clear oil. ¹H NMR (600 MHz, MeOD-*d*₄) δ 6.96 (dd, *J* = 12.5, 2.0 Hz, 1H, 3'-CH), 6.94 – 6.88 (m, 2H, 5'-CH and 6'-CH), 4.73 (s, 2H, -OCH₂), 3.77 (s, 3H, -OCH₃), 2.58 (q, *J* = 7.6 Hz, 2H, -CH₂), 1.19 (t, *J* = 7.6 Hz, 3H, -CH₃). ¹³C NMR (151 MHz, MeOD-*d*₄) δ 171.1 (-C=O), 153.9 (d, *J* = 244.7 Hz, 2'-CF), 145.2 (d, *J* = 10.9 Hz, 1'-COH), 140.3 (d, *J* = 6.1 Hz, 4'-qC), 124.5 (d, *J* = 3.4 Hz, 5'-CH), 116.9 (d, *J* = 1.8 Hz, 6'-CH), 116.7 (d, *J* = 18.0 Hz, 3'-CH), 67.4 (-OCH₂), 52.6 (-OCH₂), 28.9 (-CH₂), 16.0 (-CH₃). ¹⁹F NMR (471 MHz, MeOD-*d*₄) δ -136.31. LCMS (ESI⁺) *m/z* 235 [M+Na]⁺, t_R = 1.27 min.

2-(4-Ethyl-2-fluoro-phenoxy)acetic acid (**86**)



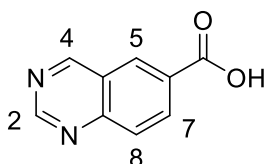
Lithium hydroxide monohydrate (69 mg, 1.60 mmol) was added to a solution of methyl 2-(4-ethyl-2-fluoro-phenoxy)acetate (68 mg, 0.32 mmol) in THF (0.80 mL, 0.20 M) and water (0.80 mL, 0.20 M). The reaction was stirred at rt for 3 h, then THF was removed *in vacuo* and water (40 mL) was added. The aqueous phase was washed with Et₂O (25 mL), acidified to pH 3 with aq. 2 M HCl solution and extracted with Et₂O (3 × 25 mL). The organic phases were combined, washed with brine (50 mL), dried with MgSO₄, filtered and concentrated *in vacuo* to afford 2-(4-ethyl-2-fluoro-phenoxy)acetic acid (**86**) (43 mg, 68%) as a white solid. ¹H NMR (600 MHz, DMSO-*d*₆) δ 13.07 (br s, 1H, -COOH), 7.07 (dd, *J* = 12.7, 2.0 Hz, 1H, 3'-CH), 6.98 – 6.92 (m, 1H, 6'-CH), 6.92 (dd, *J* = 8.5, 2.0 Hz, 1H, 5'-CH), 4.69 (s, 2H, -OCH₂), 2.57 – 2.51 (m, 2H, -CH₂), 1.14 (t, *J* = 7.6 Hz, 3H, -CH₃). ¹³C NMR (151 MHz, DMSO-*d*₆) δ 170.4 (-C=O), 151.8 (d, *J* = 243.5 Hz, 2'-CF), 137.9 (d, *J* = 5.9 Hz, 4'-qC), 123.9 (d, *J* = 3.3 Hz, 5'-CH), 115.9 (d, *J* = 17.6 Hz, 3'-CH), 115.2 (d, *J* = 2.0 Hz, 6'-CH), 65.7 (-OCH₂), 27.6 (-CH₂), 16.0 (-CH₃) (1 × qC missing). ¹⁹F NMR (471 MHz, DMSO-*d*₆) δ -135.01. LCMS (ESI⁺) *m/z* mass ion not detected, t_R = 0.22 min.

2-((2-(4-Ethyl-2-fluoro-phenoxy)acetyl)amino)-4,5-dimethyl-thiophene-3-carboxamide (30)



HATU (118 mg, 0.31 mmol) was added to a solution of 2-(4-ethyl-2-fluoro-phenoxy)acetic acid (41 mg, 0.21 mmol) and DIPEA (108 μ L, 0.62 mmol) in DMF (2.6 mL, 0.08 M). The reaction was stirred at rt for 1 h, then 2-amino-4,5-dimethylthiophene-3-carboxamide (35 mg, 0.21 mmol) was added. The reaction was stirred at rt for a further 23 h, then concentrated *in vacuo* using a Biotage V-10 evaporator. The crude residue was purified by trituration with MeOH (5 mL), solid was collected by filtration under vacuum and washed with MeOH (10 mL) to afford 2-((2-(4-ethyl-2-fluoro-phenoxy)acetyl)amino)-4,5-dimethyl-thiophene-3-carboxamide (**30**) (17 mg, 21%) as a white solid. ^1H NMR (600 MHz, DMSO- d_6) δ 12.03 (s, 1H, -NH), 7.65 (br s, 2H, -NH $_2$), 7.14 – 7.06 (m, 2H, 2 \times -ArCH), 6.96 (d, J = 8.0 Hz, 1H, -ArCH), 4.83 (s, 2H, -OCH $_2$), 2.55 (q, J = 7.6 Hz, 2H, -CH $_2$), 2.24 (s, 3H, -CH $_3$), 2.20 (s, 3H, -CH $_3$), 1.15 (t, J = 7.6 Hz, 3H, -CH $_3$). ^{19}F NMR (471 MHz, DMSO- d_6) δ -133.82. LCMS (ESI $^+$) m/z 334 [M-NH $_2$] $^+$, t_R = 1.41 min. HRMS (ESI $^+$) [M+H] $^+$ calcd. for C $_{17}$ H $_{20}$ N $_2$ O $_3$ SF: 373.0999; found: 373.0987, error = -3.2 ppm, purity (UV) = 98.4%, purity (^1H NMR) = 90%.

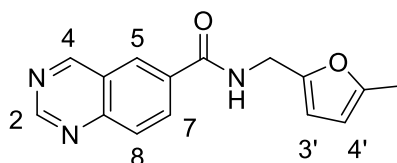
Quinazoline-6-carboxylic acid (89)



Palladium (II) acetate (17 mg, 0.073 mmol, 5 mol%) and XantPhos (42 mg, 0.073 mmol, 5 mol%) were added to a solution of 6-bromoquinazoline (304 mg, 1.45 mmol) in 1,4-dioxane (1.44 mL, 0.51 M) and water (1.44 mL, 0.51 M) in a dry vial. The vial was sealed, evacuated, and backfilled with nitrogen, evacuated once

more and fitted with a CO (g) balloon. Lastly, DIPEA (0.76 mL, 4.36 mmol) was added, and the reaction was stirred at 60 °C for 22 h, cooled to rt and slowly vented. The reaction was diluted with 1:1 CH₂Cl₂/MeCN (10 mL) and purified by ion-exchange chromatography on basic resin (5 g), eluting with CH₂Cl₂/MeCN (6 × 30 mL) and aq. 1 M HCl solution (3 × 20 mL). The acidic fractions were concentrated *in vacuo* to afford quinazoline-6-carboxylic acid (**89**) (303 mg, quantitative) as an orange solid. ¹H NMR (600 MHz, DMSO-*d*₆) δ 9.81 (s, 1H, 4-CH), 9.41 (s, 1H, 2-CH), 8.84 (d, *J* = 1.9 Hz, 1H, 5-CH), 8.46 (dd, *J* = 8.8, 2.0 Hz, 1H, 7-CH), 8.11 (d, *J* = 8.7 Hz, 1H, 8-CH) (1 × H missing, exchangeable). ¹³C NMR (151 MHz, DMSO-*d*₆) δ 166.3 (-C=O), 162.3 (4-CH), 156.7 (2-CH), 151.0 (8a-qC), 133.7 (7-CH), 130.6 (5-CH), 130.0 (6-qC), 128.3 (8-CH), 124.1 (4a-qC). LCMS (ESI⁺) *m/z* 175 [M+H]⁺, *t*_R = 0.53 min. HRMS (ESI⁺) [M+H]⁺ calcd. for C₉H₆N₂O₂: 175.0507; found: 175.0510, error = 1.7 ppm.

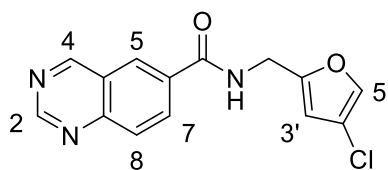
***N*-((5-Methylfuran-2-yl)methyl)quinazoline-6-carboxamide (91)**



HATU (81 mg, 0.34 mmol) was added to a solution of quinazoline-6-carboxylic acid (40 mg, 0.23 mmol), 5-methylfuran-2-yl)methanamine (25 μL, 0.23 mmol) and DIPEA (0.12 mL, 0.69 mmol) in DMF (2.3 mL, 0.10 M) and the reaction was stirred at rt for 5 h. The reaction was concentrated *in vacuo* using a Biotage V-10 instrument and the crude residue was purified by reverse phase silica chromatography eluting 5-80% MeOH in water (+0.1% formic acid). The fractions containing product were collected and evaporated *in vacuo* to afford *N*-((5-methylfuran-2-yl)methyl)quinazoline-6-carboxamide (**91**) (17 mg, 25%) as a yellow solid. ¹H NMR (600 MHz, DMSO-*d*₆) δ 9.71 (s, 1H, 4-CH), 9.38 (s, 1H, 2-CH), 9.29 (t, *J* = 5.6 Hz, 1H, -NH), 8.71 (d, *J* = 2.0 Hz, 1H, 5-CH), 8.44 (dd, *J* = 8.8, 2.0 Hz, 1H, 7-CH), 8.09 (d, *J* = 8.8 Hz, 1H, 8-CH), 6.20 (d, *J* = 3.0 Hz, 1H, 3'-CH), 6.01 (dd, *J* = 3.0, 1.2 Hz, 1H, 4'-CH), 4.48 (d, *J* = 5.5 Hz, 2H, -CH₂), 2.24 (d, *J* = 1.1 Hz, 3H, -CH₃). ¹³C NMR (151 MHz, DMSO-*d*₆) δ 164.9 (-C=O), 161.8

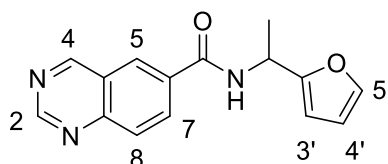
(4-CH), 156.2 (2-CH), 150.7 (5'-qC), 150.3 (8a-qC), 150.2 (2'-qC), 133.4 (6-qC), 132.7 (7-CH), 127.9 (8-CH), 127.8 (5-CH), 124.0 (4a-qC), 108.0 (4'-CH), 106.4 (3'-CH), 36.3 (-CH₂), 13.3 (-CH₃). LCMS (ESI⁺) *m/z* 300 [M+Na]⁺, *t_R* = 1.03 min. HRMS (ESI⁺) [M+H]⁺ calcd. for C₁₅H₁₄N₃O₂: 268.1086; found: 268.1086, error = 0.0 ppm, purity 89.8%.

***N*-(4-Chlorofuran-2-yl)methylquinazoline-6-carboxamide (92)**



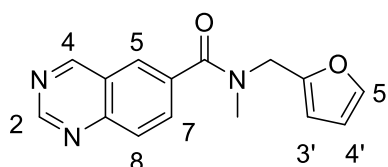
HATU (102 mg, 0.43 mmol) was added to a solution of quinazoline-6-carboxylic acid (51 mg, 0.29 mmol), (4-chlorofuran-2-yl)methanamine hydrochloride (49 mg, 0.29 mmol) and DIPEA (0.15 mL, 0.87 mmol) in DMF (2.9 mL, 0.10 M) and the reaction was stirred at rt for 18 h. The reaction was concentrated *in vacuo* using a Biotage V-10 instrument and the crude residue was purified by reverse phase silica chromatography eluting 5-80% MeOH in water (+0.1% formic acid). The fractions containing product were collected and evaporated *in vacuo* to afford *N*-((4-chlorofuran-2-yl)methyl)quinazoline-6-carboxamide (**92**) (38 mg, 45%) as a brown oil. ¹H NMR (600 MHz, DMSO-*d*₆) δ 9.73 (s, 1H, 4-CH), 9.40 – 9.35 (m, 2H, 2-CH and -NH), 8.71 (s, 1H, 5-CH), 8.46 – 8.41 (m, 1H, 7-CH), 8.10 (d, *J* = 8.8 Hz, 1H, 8-CH), 7.87 (s, 1H, 5'-CH), 6.54 (s, 1H, 3'-CH), 4.51 (d, *J* = 5.5 Hz, 2H, -CH₂). ¹³C NMR (151 MHz, DMSO-*d*₆) δ 165.2 (-C=O), 161.8 (4-CH), 156.3 (2-CH), 153.2 (2'-qC), 150.3 (8a-qC), 138.6 (5'-CH), 133.2 (6-qC), 132.6 (7-CH), 128.0 (8-CH), 127.8 (5-CH), 124.0 (4a-qC), 114.9 (4'-qC), 108.6 (3'-CH), 36.4 (-CH₂). LCMS (ESI⁺) *m/z* 288 [M+H]⁺, *t_R* = 1.02 min. HRMS (ESI⁺) [M+H]⁺ calcd. for C₁₄H₁₁N₃O₂Cl: 288.0540; found: 288.0541, error = 0.3 ppm, purity 98.0%.

***N*-(1-(Furan-2-yl)ethyl)quinazoline-6-carboxamide (93)**



HATU (73 mg, 0.31 mmol) was added to a solution of quinazoline-6-carboxylic acid (36 mg, 0.21 mmol), 1-(furan-2-yl)ethan-1-amine (23 μ L, 0.21 mmol) and DIPEA (0.11 mL, 0.62 mmol) in DMF (2.1 mL, 0.10 M) and the reaction was stirred at rt for 5 h. The reaction was concentrated *in vacuo* using a Biotage V-10 instrument and the crude residue was purified by reverse phase silica chromatography eluting 5-80% MeOH in water (+0.1% formic acid). The fractions containing product were collected and evaporated *in vacuo* to afford *N*-(1-(furan-2-yl)ethyl)quinazoline-6-carboxamide (**93**) (26 mg, 42%) as a brown oil. ^1H NMR (600 MHz, DMSO- d_6) δ 9.72 (s, 1H, 4-CH), 9.38 (s, 1H, 2-CH), 9.16 (d, J = 8.2 Hz, 1H, -NH), 8.71 (d, J = 2.0 Hz, 1H, 5-CH), 8.45 (dd, J = 8.8, 2.0 Hz, 1H, 7-CH), 8.09 (d, J = 8.8 Hz, 1H, 8-CH), 7.60 (d, J = 1.8 Hz, 1H, 5'-CH), 6.42 (dd, J = 3.3, 1.8 Hz, 1H, 4'-CH), 6.34 (d, J = 3.2 Hz, 1H, 3'-CH), 5.33 (*app* p, J = 7.2 Hz, 1H, -CH), 1.54 (d, J = 7.0 Hz, 3H, -CH $_3$). ^{13}C NMR (151 MHz, DMSO- d_6) δ 164.5 (-C=O), 161.8 (4-CH), 156.2 (2-CH), 155.9 (2'-qC), 150.3 (8a-qC), 142.0 (5'-CH), 133.5 (6-qC), 132.9 (7-CH), 127.8 (8-CH), 127.8 (5-CH), 123.9 (4a-qC), 110.3 (4'-CH), 105.6 (3'-CH), 42.7 (-CH), 19.0 (-CH $_3$). LCMS (ESI $^+$) m/z 300 [M+Na] $^+$, t_R = 0.98 min. HRMS (ESI $^+$) [M+H] $^+$ calcd. for C $_{15}$ H $_{14}$ N $_3$ O $_2$: 268.1086; found: 268.1078, error = -3.0 ppm, purity 89.5%.

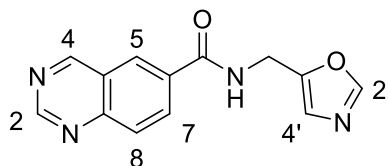
***N*-(Furan-2-ylmethyl)-*N*-methylquinazoline-6-carboxamide (94)**



HATU (100 mg, 0.43 mmol) was added to a solution of quinazoline-6-carboxylic acid (50 mg, 0.28 mmol), 1-(furan-2-yl)-*N*-methylmethanamine (23 μ L, 0.28 mmol) and DIPEA (0.15 mL, 0.85 mmol) in DMF (2.8 mL, 0.10 M) and the reaction was stirred at rt for 18 h. The reaction was concentrated *in vacuo* using a Biotage

V-10 instrument and the crude residue was purified by reverse phase silica chromatography eluting 5-80% MeOH in water (+0.1% formic acid). The fractions containing product were collected and evaporated *in vacuo* to afford *N*-(furan-2-ylmethyl)-*N*-methylquinazoline-6-carboxamide (**94**) (20 mg, 26%) as a brown oil. ¹H NMR (600 MHz, DMSO-*d*₆) δ 9.69 (s, 1H, 4-CH), 9.37 (s, 1H, 2-CH), 8.29 (s, 1H, 5-CH), 8.11 – 8.03 (m, 2H, 7-CH and 8-CH), 7.69 – 7.63 (m, 1H, 5'-CH), 6.51 – 6.32 (m, 2H, 3'-CH and 4'-CH), 4.80 – 4.39 (m, 2H, -CH₂), 3.03 – 2.88 (m, 3H, -NCH₃). ¹³C NMR (151 MHz, DMSO-*d*₆) δ 161.2 (4-CH), 155.8 (2-CH), 149.2 (8a-qC), 143.2 – 142.7 (m, 5'-CH), 132.9 (7-CH), 128.1 (8-CH), 126.4 (5-CH), 110.5 (4'-CH), 108.8 – 108.4 (m, 3'-CH), 47.7 – 42.9 (m, -CH₂), 37.0 – 32.3 (m, -CH₃) (4 × qC missing, rotational isomers observed). LCMS (ESI⁺) *m/z* 268 [M+H]⁺, t_R = 0.87 min. HRMS (ESI⁺) [M+H]⁺ calcd. for C₁₅H₁₃N₃O₂: 268.1086; found: 268.1088, error = 0.7 ppm, purity 100%.

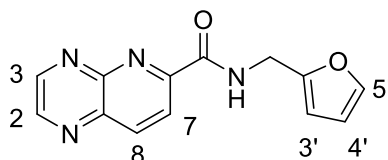
***N*-(Oxazol-5-ylmethyl)quinazoline-6-carboxamide (95)**



HATU (101 mg, 0.43 mmol) was added to a solution of quinazoline-6-carboxylic acid (50 mg, 0.29 mmol), oxazol-5-ylmethanamine hydrochloride (39 mg, 0.29 mmol) and DIPEA (0.20 mL, 1.15 mmol) in DMF (2.9 mL, 0.10 M) and the reaction was stirred at rt for 18 h. The reaction was concentrated *in vacuo* using a Biotage V-10 instrument and the crude residue was dissolved in MeOH (2 mL) and DMF (1 mL) and purified by ion-exchange chromatography on acidic resin (2 g), eluting with MeOH (3 × 10 mL) then 2 M NH₃ in MeOH (3 × 10 mL). The basic fractions were concentrated *in vacuo* and purified by reverse phase silica chromatography eluting 5-80% MeOH in water (+0.1% formic acid). The fractions containing product were concentrated *in vacuo* and dissolved in MeOH (1 mL) and DMF (0.1 mL) and further purified by ion-exchange chromatography on acidic resin (2 g), eluting with MeOH (3 × 10 mL) then 2 M NH₃ in MeOH (3 × 10 mL). The basic fractions were concentrated *in vacuo* to afford *N*-(oxazol-5-ylmethyl)quinazoline-

6-carboxamide (**95**) (18 mg, 21%) as a yellow solid. ^1H NMR (600 MHz, $\text{DMSO-}d_6$) δ 9.72 (d, $J = 0.8$ Hz, 1H, 4-CH), 9.41 – 9.36 (m, 2H, 2-CH and -NH), 8.70 (d, $J = 2.0$ Hz, 1H, 5-CH), 8.43 (dd, $J = 8.8, 2.0$ Hz, 1H, 7-CH), 8.32 (s, 1H, 2'-CH), 8.10 (d, $J = 8.8$ Hz, 1H, 8-CH), 7.12 (s, 1H, 4'-CH), 4.62 (dd, $J = 5.6, 1.0$ Hz, 2H, -CH₂). ^{13}C NMR (151 MHz, $\text{DMSO-}d_6$) δ 165.2 (-C=O), 161.9 (4-CH), 156.3 (2-CH), 151.7 (2'-CH), 150.4 (8a-qC), 149.2 (5'-qC), 133.1 (6-qC), 132.6 (7-CH), 128.0 (8-CH), 127.8 (5-CH), 124.0 (4a-qC), 123.6 (4'-CH), 34.0 (-CH₂). LCMS (ESI⁺) m/z 255 [M+H]⁺, $t_R = 0.56$ min. HRMS (ESI⁺) [M+H]⁺ calcd. for C₁₃H₁₁N₄O₂: 255.0876; found: 255.0884, error = 3.07 ppm, purity 97.4%.

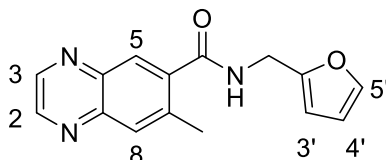
***N*-(Furan-2-ylmethyl)pyrido[2,3-*b*]pyrazine-6-carboxamide (**96**)**



HATU (152 mg, 0.65 mmol) was added to a solution of pyrido[2,3-*b*]pyrazine-6-carboxylic acid (75 mg, 0.40 mmol), furan-2-ylmethanamine (38 μL , 0.43 mmol) and DIPEA (0.23 mL, 1.29 mmol) in DMF (4.3 mL, 0.10 M) and the reaction was stirred at rt for 17 h. The reaction was concentrated *in vacuo* using a Biotage V-10 instrument and the crude residue was purified by reverse phase silica chromatography eluting 5-80% MeOH in water (+0.1% formic acid), and fractions containing product were collected and concentrated *in vacuo*. The residue was further purified by reverse phase silica chromatography eluting 5-80% MeOH in water (+0.1% formic acid). The fractions containing product were collected and evaporated *in vacuo* to afford *N*-(furan-2-ylmethyl)pyrido[2,3-*b*]pyrazine-6-carboxamide (**96**) (45 mg, 41%) as an orange-brown solid. ^1H NMR (600 MHz, $\text{DMSO-}d_6$) δ 9.52 (t, $J = 6.2$ Hz, 1H, -NH), 9.25 (d, $J = 1.7$ Hz, 1H, 3-CH), 9.16 (d, $J = 1.7$ Hz, 1H, 2-CH), 8.76 (d, $J = 8.5$ Hz, 1H, 8-CH), 8.49 (d, $J = 8.5$ Hz, 1H, 7-CH), 7.58 (dd, $J = 1.9, 0.9$ Hz, 1H, 5'-CH), 6.40 (dd, $J = 3.2, 1.8$ Hz, 1H, 4'-CH), 6.31 (dd, $J = 3.2, 0.9$ Hz, 1H, 3'-CH), 4.57 (d, $J = 6.1$ Hz, 2H, -CH₂). ^{13}C NMR (151 MHz, $\text{DMSO-}d_6$) δ 163.2 (-C=O), 153.0 (6-qC), 152.1 (2'-qC), 149.7 (3-CH), 149.3 (4a-qC), 148.1 (2-CH), 142.1 (5'-CH), 140.4 (8-CH), 138.6 (8a-qC), 123.3

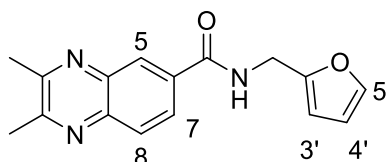
(7-CH), 110.5 (4'-CH), 107.1 (3'-CH), 36.1 (-CH₂). LCMS (ESI⁺) *m/z* 277 [M+Na]⁺, *t_R* = 0.99 min. HRMS (ESI⁺) [M+H]⁺ calcd. for C₁₃H₁₁N₄O₂: 255.0882; found: 255.0886, error = 1.2 ppm, purity 99.7%.

***N*-(Furan-2-ylmethyl)-7-methylquinoxaline-6-carboxamide (97)**



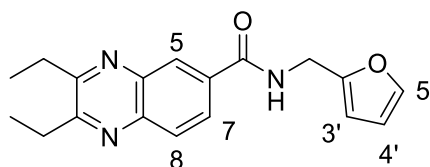
HATU (149 mg, 0.39 mmol) was added to a solution of 7-methylquinoxaline-6-carboxylic acid (49 mg, 0.26 mmol), furan-2-ylmethanamine (23 μ L, 0.26 mmol) and DIPEA (0.14 mL, 0.78 mmol) in DMF (2.6 mL, 0.10 M) and the reaction was stirred at rt for 17 h. The reaction was concentrated *in vacuo* using a Biotage V-10 instrument and the crude residue was purified by reverse phase silica chromatography eluting 5-95% MeOH in water (+0.1% formic acid). The fractions containing product were collected and evaporated *in vacuo* to afford *N*-(furan-2-ylmethyl)-7-methylquinoxaline-6-carboxamide (**97**) (41 mg, 58%) as a pale orange solid. ¹H NMR (600 MHz, DMSO-*d*₆) δ 9.10 (t, *J* = 5.8 Hz, 1H, -NH), 8.98 – 8.91 (m, 2H, 2-CH and 3-CH), 8.01 (s, 1H, 5-CH), 7.98 – 7.96 (m, 1H, 8-CH), 7.63 (dd, *J* = 1.9, 0.9 Hz, 1H, 5'-CH), 6.44 (dd, *J* = 3.2, 1.9 Hz, 1H, 4'-CH), 6.35 (dd, *J* = 3.2, 0.9 Hz, 1H, 3'-CH), 4.51 (d, *J* = 5.7 Hz, 2H, -CH₂), 2.55 (d, *J* = 1.0 Hz, 3H, -CH₃). ¹³C NMR (151 MHz, DMSO-*d*₆) δ 167.7 (-C=O), 152.1 (2'-qC), 146.5 (2-CH or 3-CH), 145.7 (2-CH or 3-CH), 142.3 (8a-qC), 142.2 (5'-CH), 140.3 (4a-qC), 139.3 (6-qC), 138.0 (7-qC), 129.6 (8-CH), 127.2 (5-CH), 110.5 (4'-CH), 106.9 (3'-CH), 35.9 (-CH₂), 19.6 (-CH₃). LCMS (ESI⁺) *m/z* 268 [M+H]⁺, *t_R* = 1.00 min. HRMS (ESI⁺) [M+H]⁺ calcd. for C₁₅H₁₄N₃O₂: 268.1086; found: 268.1082, error = -1.5 ppm, purity 97.7%.

***N*-(Furan-2-ylmethyl)-2,3-dimethylquinoxaline-6-carboxamide (98)**



HATU (151 mg, 0.64 mmol) was added to a solution of 2,3-dimethylquinoxaline-6-carboxylic acid (75 mg, 0.37 mmol), furan-2-ylmethanamine (38 μ L, 0.43 mmol) and DIPEA (0.22 mL, 1.28 mmol) in DMF (4.3 mL, 0.10 M) and the reaction was stirred at rt for 17 h. The reaction was concentrated *in vacuo* using a Biotage V-10 instrument and the crude residue was purified by reverse phase silica chromatography eluting 5-90% MeOH in water (+0.1% formic acid). The fractions containing product were collected and evaporated *in vacuo* to afford *N*-(furan-2-ylmethyl)-2,3-dimethylquinoxaline-6-carboxamide (**98**) (51 mg, 42%) as an off-white solid. ^1H NMR (600 MHz, DMSO- d_6) δ 9.27 (t, J = 5.7 Hz, 1H, -NH), 8.50 (d, J = 2.0 Hz, 1H, 5-CH), 8.15 (dd, J = 8.7, 2.0 Hz, 1H, 7-CH), 8.01 (d, J = 8.6 Hz, 1H, 8-CH), 7.59 (dd, J = 1.9, 0.9 Hz, 1H, 5'-CH), 6.41 (dd, J = 3.2, 1.8 Hz, 1H, 4'-CH), 6.32 (dd, J = 3.2, 0.9 Hz, 1H, 3'-CH), 4.53 (d, J = 5.6 Hz, 2H, -CH $_2$), 2.70 (s, 6H, 2 \times -CH $_3$). ^{13}C NMR (151 MHz, DMSO- d_6) δ 165.3 (-C=O), 155.7 (2-qC or 3-qC), 155.1 (2-qC or 3-qC), 152.2 (2'-qC), 142.1 (5'-CH), 141.7 (8a-qC), 139.7 (4a-qC), 133.9 (6-qC), 128.1 (8-CH), 127.4 (7-CH), 127.2 (5-CH), 110.5 (4'-CH), 107.0 (3'-CH), 36.2 (-CH $_2$), 22.9 (-CH $_3$), 22.9 (-CH $_3$). LCMS (ESI $^+$) m/z 282 [M+H] $^+$, t_R = 1.13 min. HRMS (ESI $^+$) [M+H] $^+$ calcd. for C $_{16}$ H $_{16}$ N $_3$ O $_2$: 282.1242; found: 282.1239, error = -1.1 ppm, purity 100%.

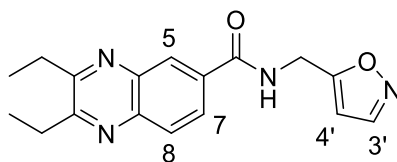
2,3-Diethyl-*N*-(furan-2-ylmethyl)quinoxaline-6-carboxamide (**99**)



HATU (186 mg, 0.49 mmol) was added to a solution of 2,3-diethylquinoxaline-6-carboxylic acid (75 mg, 0.33 mmol), furan-2-ylmethanamine (29 μ L, 0.33 mmol) and DIPEA (0.17 mL, 0.98 mmol) in DMF (3.3 mL, 0.10 M) and the reaction was stirred at rt for 17 h. The reaction was concentrated *in vacuo* using a Biotage V-

10 instrument and the crude residue was purified by reverse phase silica chromatography eluting 5-95% MeOH in water (+0.1% formic acid). The fractions containing product were collected and evaporated *in vacuo* to afford 2,3-diethyl-*N*-(furan-2-ylmethyl)quinoxaline-6-carboxamide (**99**) (66 mg, 65%) as a pale orange solid. ¹H NMR (600 MHz, DMSO-*d*₆) δ 9.30 (t, *J* = 5.7 Hz, 1H, -NH), 8.55 (d, *J* = 1.9 Hz, 1H, 5-CH), 8.17 (dd, *J* = 8.7, 2.0 Hz, 1H, 7-CH), 8.04 (d, *J* = 8.6 Hz, 1H, 8-CH), 7.59 (dd, *J* = 1.9, 0.9 Hz, 1H, 5'-CH), 6.41 (dd, *J* = 3.2, 1.9 Hz, 1H, 4'-CH), 6.32 (dd, *J* = 3.2, 0.9 Hz, 1H, 3'-CH), 4.52 (d, *J* = 5.6 Hz, 2H, -CH₂), 3.09 – 3.02 (m, 4H, -2CCH₂ and -3CCH₂), 1.41 – 1.31 (m, 6H, 2 × -CH₃). ¹³C NMR (151 MHz, DMSO-*d*₆) δ 165.3 (-C=O), 158.8 (2-qC or 3-qC), 158.1 (2-qC or 3-qC), 152.2 (2'-qC), 142.1 (5'-CH), 141.5 (8a-qC), 139.5 (4a-qC), 133.9 (6-qC), 128.3 (8-CH), 127.5 (7-CH), 127.3 (5-CH), 110.5 (4'-CH), 107.0 (3'-CH), 36.2 (-CH₂), 27.4 (-2CCH₂ or -3CCH₂), 27.2 (-2CCH₂ or -3CCH₂), 11.3 (-CH₃), 11.2 (-CH₃). LCMS (ESI⁺) *m/z* 310 [M+H]⁺, *t*_R = 1.29 min. HRMS (ESI⁺) [M+H]⁺ calcd. for C₁₈H₂₀N₃O₂: 310.1550; found: 310.1557, error = 2.13 ppm, purity 99.4%.

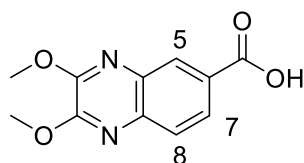
2,3-Diethyl-*N*-(isoxazol-5-ylmethyl)quinoxaline-6-carboxamide (**100**)



HATU (186 mg, 0.49 mmol) was added to a solution of 2,3-diethylquinoxaline-6-carboxylic acid (75 mg, 0.33 mmol), isoxazol-5-ylmethanamine hydrochloride (44 mg, 0.33 mmol) and DIPEA (0.23 mL, 1.29 mmol) in DMF (3.3 mL, 0.10 M) and the reaction was stirred at rt for 18 h. The reaction was concentrated *in vacuo* using a Biotage V-10 instrument and the crude residue was purified by reverse phase silica chromatography eluting 5-95% MeOH in water (+0.1% formic acid). The fractions containing product were collected and evaporated *in vacuo* to afford 2,3-diethyl-*N*-(isoxazol-5-ylmethyl)quinoxaline-6-carboxamide (**100**) (60 mg, 59%) as a pale yellow solid. ¹H NMR (600 MHz, DMSO-*d*₆) δ 9.50 (t, *J* = 5.8 Hz, 1H, -NH), 8.57 (d, *J* = 2.0 Hz, 1H, 5-CH), 8.51 (d, *J* = 1.8 Hz, 1H, 3'-CH), 8.17 (dd, *J* = 8.6, 2.0 Hz, 1H, 7-CH), 8.07 (d, *J* = 8.6 Hz, 1H, 8-CH), 6.43 (d, *J* = 1.8

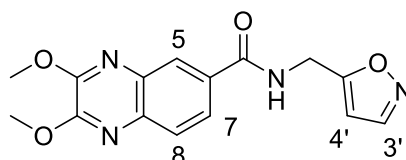
Hz, 1H, 4'-CH), 4.69 (d, $J = 5.7$ Hz, 2H, -CH₂), 3.10 – 3.03 (m, 4H, -2CCH₂ and -3CCH₂), 1.39 – 1.33 (m, 6H, 2 × -CH₃). ¹³C NMR (151 MHz, DMSO-*d*₆) δ 169.3 (5'-qC), 165.7 (-C=O), 158.9 (2-qC or 3-qC), 158.2 (2-qC or 3-qC), 150.9 (3'-CH), 141.6 (8a-qC), 139.5 (4a-qC), 133.5 (6-qC), 128.5 (8-CH), 127.6 (7-CH), 127.3 (5-CH), 101.5 (4'-CH), 35.2 (-CH₂), 27.4 (-2CCH₂ or -3CCH₂), 27.2 (-2CCH₂ or -3CCH₂), 11.3 (-CH₃), 11.2 (-CH₃). LCMS (ESI⁺) m/z 311 [M+H]⁺, $t_R = 1.17$ min. HRMS (ESI⁺) [M+H]⁺ calcd. for C₁₇H₁₉N₄O₂: 311.1502; found: 311.1506, error = 1.27 ppm, purity 100%.

2,3-Dimethoxyquinoxaline-6-carboxylic acid (105)



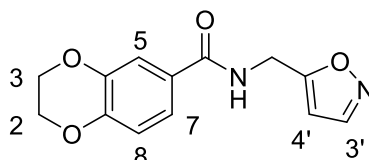
2,3-Dichloroquinoxaline-6-carboxylic acid (49 mg, 0.20 mmol) was dissolved in MeOH (1.15 mL, 0.175 M) and 0.5 M NaOMe in MeOH solution (1.52 mL, 0.76 mmol) was added. The reaction was stirred at 65 °C for 6 h, cooled to rt and concentrated *in vacuo*. The crude residue was taken up in aq. 1 M HCl solution (25 mL) and the aqueous phase was extracted with EtOAc (3 × 25 mL), then organic phases were combined and evaporated *in vacuo* to afford 2,3-dimethoxyquinoxaline-6-carboxylic acid (**105**) (34 mg, 72%) as a white solid. ¹H NMR (600 MHz, DMSO-*d*₆) δ 13.14 (br s, 1H, -COOH), 8.27 (d, $J = 1.9$ Hz, 1H, 5-CH), 8.03 (dd, $J = 8.5, 1.9$ Hz, 1H, 7-CH), 7.81 (d, $J = 8.5$ Hz, 1H, 8-CH), 4.08 (s, 3H, -OCH₃), 4.07 (s, 3H, -OCH₃). ¹³C NMR (151 MHz, DMSO-*d*₆) δ 166.9 (-C=O), 151.1 (2-qC or 3-qC), 150.5 (2-qC or 3-qC), 139.5 (8a-qC), 136.0 (4a-qC), 127.6 (5-CH), 126.8 (7-CH), 126.3 (8-CH), 54.3 (-OCH₃), 54.1 (-OCH₃) (1 × qC missing). LCMS (ESI⁺) $m/z = 235$ [M+H]⁺, $t_R = 1.25$ min. HRMS (ESI⁺) [M+H]⁺ calcd. for C₁₁H₁₁N₂O₄: 235.0719; found: 235.0717, error = -0.9.

N-(Isoxazol-5-ylmethyl)-2,3-dimethoxyquinoxaline-6-carboxamide (101)



HATU (80 mg, 0.21 mmol) was added to a solution of 2,3-dimethoxyquinoxaline-6-carboxylic acid (33 mg, 0.14 mmol), isoxazol-5-ylmethanamine hydrochloride (19 mg, 0.14 mmol) and DIPEA (98 μ L, 0.56 mmol) in DMF (1.4 mL, 0.10 M) and the reaction was stirred at rt for 26 h. The reaction was concentrated *in vacuo* using a Biotage V-10 instrument and the crude residue was purified by reverse phase silica chromatography eluting 5-90% MeOH in water (+0.1% formic acid). The fractions containing product were collected and evaporated *in vacuo* to afford *N*-(isoxazol-5-ylmethyl)-2,3-dimethoxyquinoxaline-6-carboxamide (**101**) (28 mg, 63%) as an off-white solid. ^1H NMR (600 MHz, DMSO- d_6) δ 9.38 (t, J = 5.8 Hz, 1H, -NH), 8.50 (d, J = 1.8 Hz, 1H, 3'-CH), 8.34 (d, J = 2.0 Hz, 1H, 5-CH), 8.01 (dd, J = 8.5, 2.0 Hz, 1H, 7-CH), 7.82 (d, J = 8.5 Hz, 1H, 8-CH), 6.40 (dd, J = 1.8, 0.9 Hz, 1H, 4'-CH), 4.67 (d, J = 5.7 Hz, 2H, -CH $_2$), 4.07 (s, 3H, -OCH $_3$), 4.06 (s, 3H, -OCH $_3$). ^{13}C NMR (151 MHz, DMSO- d_6) δ 169.4 (5'-qC), 165.7 (-C=O), 150.9 (3'-CH), 150.9 (2-qC or 3-qC), 150.5 (2-qC or 3-qC), 138.6 (8a-qC), 136.0 (4a-qC), 131.7 (6-qC), 126.1 (8-CH), 125.6 (7-CH), 125.3 (5-CH), 101.4 (4'-CH), 54.2 (-OCH $_3$), 54.1 (-OCH $_3$), 35.2 (-CH $_2$). LCMS (ESI $^+$) m/z 315 [M+H] $^+$, t_R = 1.11 min. HRMS (ESI $^+$) [M+H] $^+$ calcd. for C $_{15}$ H $_{15}$ N $_4$ O $_2$: 315.1087; found: 315.1093, error = 1.73 ppm, purity 99.1%.

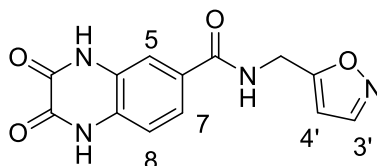
***N*-(Isoxazol-5-ylmethyl)-2,3-dihydrobenzo[*b*][1,4]dioxine-6-carboxamide (102)**



HATU (237 mg, 0.62 mmol) was added to a solution of 2,3-dihydrobenzo[*b*][1,4]dioxine-6-carboxylic acid (75 mg, 0.42 mmol), isoxazol-5-ylmethanamine hydrochloride (56 mg, 0.42 mmol) and DIPEA (0.29 mL, 1.67

mmol) in DMF (4.2 mL, 0.10 M) and the reaction was stirred at rt for 21 h. The reaction was concentrated *in vacuo* using a Biotage V-10 instrument and the crude residue was purified by reverse phase silica chromatography eluting 5-80% MeOH in water (+0.1% formic acid). The fractions containing product were collected and evaporated *in vacuo* to afford *N*-(isoxazol-5-ylmethyl)-2,3-dihydrobenzo[*b*][1,4]dioxine-6-carboxamide (**102**) (30 mg, 28%) as a yellow solid. ¹H NMR (600 MHz, DMSO) δ 8.98 (t, *J* = 5.8 Hz, 1H, -NH), 8.47 (d, *J* = 1.8 Hz, 1H, 3'-CH), 7.44 – 7.38 (m, 2H, 5-CH and 7-CH), 6.93 (d, *J* = 8.3 Hz, 1H, 8-CH), 6.32 (d, *J* = 1.8 Hz, 1H, 4'-CH), 4.58 (d, *J* = 5.7 Hz, 2H, -CH₂), 4.32 – 4.24 (m, 4H, 2-CH₂ and 3-CH₂). ¹³C NMR (151 MHz, DMSO) δ 169.6 (5'-qC), 165.5 (-C=O), 150.9 (3'-CH), 146.3 (Ar-qC), 143.0 (Ar-qC), 126.7 (6-qC), 120.8 (5-CH or 7-CH), 116.8 (8-CH), 116.4 (5-CH or 7-CH), 101.2 (4'-CH), 64.3 (2-CH₂ or 3-CH₂), 64.0 (2-CH₂ or 3-CH₂), 35.0 (-CH₂). LCMS (ESI⁺) *m/z* 283 [M+Na]⁺, t_R = 0.98 min. HRMS (ESI⁺) [M+H]⁺ calcd. for C₁₃H₁₃N₂O₄: 261.0869; found: 261.0875, error = 1.9 ppm, purity 100%.

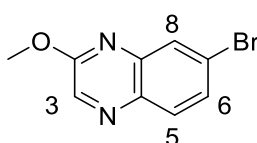
***N*-(Isoxazol-5-ylmethyl)-2,3-dioxo-1,2,3,4-tetrahydroquinoxaline-6-carboxamide (103)**



HATU (205 mg, 0.54 mmol) was added to a solution of 2,3-dioxo-1,2,3,4-tetrahydroquinoxaline-6-carboxylic acid (74 mg, 0.36 mmol), isoxazol-5-ylmethanamine hydrochloride (48 mg, 0.36 mmol) and DIPEA (0.25 mL, 1.44 mmol) in DMF (3.6 mL, 0.10 M) and the reaction was stirred at rt for 46 h. The reaction was concentrated *in vacuo* using a Biotage V-10 instrument and the crude residue was rinsed with MeOH (5 × 10 mL) and precipitate was collected by filtration to afford *N*-(isoxazol-5-ylmethyl)-2,3-dioxo-1,2,3,4-tetrahydroquinoxaline-6-carboxamide (**103**) (54 mg, 49%) as an orange solid. ¹H NMR (600 MHz, DMSO-*d*₆) δ 12.10 (s, 1H, -NH), 12.04 (s, 1H, -NH), 9.13 (t, *J* = 5.8 Hz, 1H, -NH), 8.49 (d, *J* = 1.8 Hz, 1H, 3'-CH), 7.65 (d, *J* = 1.8 Hz, 1H, 5-CH),

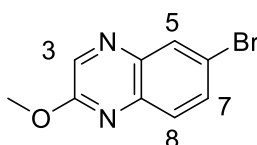
7.60 (dd, $J = 8.4, 1.9$ Hz, 1H, 7-CH), 7.15 (d, $J = 8.4$ Hz, 1H, 8-CH), 6.34 (dd, $J = 1.8, 0.9$ Hz, 1H, 4'-CH), 4.61 (d, $J = 5.7$ Hz, 2H, -CH₂). ¹³C NMR (151 MHz, DMSO-*d*₆) δ 169.5 (5'-CH), 165.7 (-C=O), 155.2 (-C=O), 155.1 (-C=O), 150.9 (3'-CH), 128.4, 128.3, 125.6, 121.7 (7-CH), 115.0 (5-CH), 114.7 (8-CH), 101.3 (4'-CH), 35.1 (-CH₂). LCMS (ESI⁺) m/z 287 [M+H]⁺, $t_R = 0.64$ min. HRMS (ESI⁺) [M+H]⁺ calcd. for C₁₃H₁₁N₄O₄: 287.0780; found: 287.0776, error = -1.4 ppm, purity 92.3%.

7-Bromo-2-methoxyquinoxaline (108)



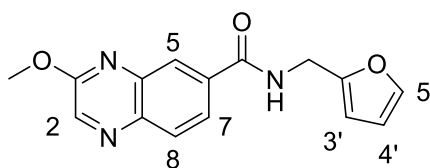
7-Bromo-2-chloroquinoxaline (250 mg, 1.03 mmol) and K₂CO₃ (288 mg, 2.05 mmol) were dissolved in MeOH (5.0 mL, 0.21 M) and the reaction was stirred at 65 °C for 4 h, then the reaction was cooled to rt and concentrated *in vacuo*. The crude residue was dissolved in THF (5 mL) and Et₂O (20 mL), then filtered under vacuum and the filtrate was evaporated *in vacuo* to afford 7-bromo-2-methoxyquinoxaline (**108**) (214 mg, 87%) as a white solid. ¹H NMR (600 MHz, DMSO-*d*₆) δ 8.63 (s, 1H, 3-CH), 8.05 (d, $J = 2.2$ Hz, 1H, 8-CH), 7.95 (d, $J = 8.7$ Hz, 1H, 5-CH), 7.78 (dd, $J = 8.8, 2.2$ Hz, 1H, 6-CH), 4.04 (s, 3H, -OCH₃). ¹³C NMR (151 MHz, DMSO-*d*₆) δ 157.9 (2-qC), 140.7 (8a-qC), 140.6 (3-CH), 137.2 (4a-qC), 130.5 (5-CH), 129.9 (6-CH), 129.0 (8-CH), 123.4 (7-CBr), 53.9 (-OCH₃). LCMS (ESI⁺) $m/z = 238/240$, $t_R = 1.45$ min. HRMS (ESI⁺) [M+H]⁺ calcd. for C₉H₈BrN₂O: 238.9820; found: 238.9817, error = -1.3 ppm.

6-bromo-2-methoxyquinoxaline (109)



6-Bromo-2-chloroquinoxaline (250 mg, 1.03 mmol) and K_2CO_3 (288 mg, 2.05 mmol) were dissolved in MeOH (5.0 mL, 0.21 M) and the reaction was stirred at 65 °C for 4 h, then the reaction was cooled to rt and concentrated *in vacuo*. The crude residue was dissolved in THF (5 mL) and Et₂O (20 mL), then filtered under vacuum and the filtrate was evaporated *in vacuo* to afford 6-bromo-2-methoxyquinoxaline (**109**) (169 mg, 69%) as a white solid. ¹H NMR (600 MHz, DMSO-*d*₆) δ 8.64 (s, 1H, 3-CH), 8.23 (d, *J* = 2.3 Hz, 1H, 5-CH), 7.89 (dd, *J* = 8.9, 2.3 Hz, 1H, 7-CH), 7.80 (d, *J* = 8.8 Hz, 1H, 8-CH), 4.04 (s, 3H, -OCH₃). ¹³C NMR (151 MHz, DMSO-*d*₆) δ 157.7 (2-qC), 141.1 (3-CH), 139.0 (4a-qC), 138.7 (8a-qC), 133.4 (7-CH), 130.7 (5-CH), 128.8 (8-CH), 119.0 (6-CBr), 53.9 (-OCH₃). LCMS (ESI⁺) *m/z* = 238/240, *t*_R = 1.44 min. HRMS (ESI⁺) [M+H]⁺ calcd. for C₉H₈BrN₂O: 238.9820; found: 238.9819, error = -0.4 ppm.

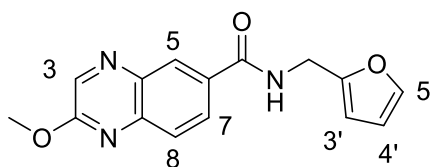
***N*-(Furan-2-ylmethyl)-3-methoxyquinoxaline-6-carboxamide (110)**



7-bromo-2-methoxyquinoxaline (**108**) (60 mg, 0.25 mmol), furfurylamine (22 μL, 0.25 mmol) and Xantphos Palladacycle Gen.4 (12 mg, 0.0125 mmol, 5 mol%) were dissolved in 1,4-dioxane (0.50 mL, 0.50 M) in a dry vial. The vial was sealed, evacuated, and backfilled with nitrogen, evacuated once more and fitted with a CO (g) balloon. Lastly, DIPEA (0.13 mL, 0.75 mmol) was added, and the reaction was stirred at 80 °C for 3 h, cooled to rt and slowly vented. The reaction mixture was diluted with CH₂Cl₂ (10 mL), filtered through a pre-packed celite column, and the filtrate was concentrated *in vacuo*. The crude residue was purified by reverse phase silica chromatography eluting 5-95% MeOH in water (+0.1% formic acid), and fractions containing product were collected and concentrated *in vacuo*. The residue was further purified by normal phase silica chromatography eluting 0-10% MeOH in CH₂Cl₂. The fractions containing product were collected and evaporated *in vacuo* to afford *N*-(furan-2-ylmethyl)-3-methoxyquinoxaline-6-carboxamide (**110**) (37 mg, 52%) as a pale yellow solid. ¹H NMR (600 MHz,

DMSO-*d*₆) δ 9.30 (t, J = 5.7 Hz, 1H, -NH), 8.68 (s, 1H, 2-CH), 8.40 (*app* t, J = 1.3 Hz, 1H, 7-CH), 8.09 – 8.07 (m, 2H, 5-CH and 8-CH), 7.59 (dd, J = 1.9, 0.9 Hz, 1H, 5'-CH), 6.41 (dd, J = 3.2, 1.8 Hz, 1H, 4'-CH), 6.32 (dd, J = 3.2, 0.9 Hz, 1H, 3'-CH), 4.52 (d, J = 5.6 Hz, 2H, -CH₂), 4.06 (s, 3H, -OCH₃). ¹³C NMR (151 MHz, DMSO-*d*₆) δ 165.2 (-C=O), 157.9 (3-qC), 152.2 (2'-qC), 142.1 (5'-CH), 141.4 (2-CH), 139.6 (8a-qC), 139.2 (4a-qC or 6-qC), 135.4 (4a-qC or 6-qC), 128.8 (5-CH or 8-CH), 126.0 (7-CH), 125.4 (5-CH or 8-CH), 110.5 (4'-CH), 107.0 (3'-CH), 53.8 (-OCH₃), 36.3 (-CH₂). LCMS (ESI⁺) m/z 306 [M+Na]⁺, t_R = 1.16 min. HRMS (ESI⁺) [M+H]⁺ calcd. for C₁₅H₁₄N₃O₃: 284.1035; found: 284.1028, error = -2.5 ppm, purity 100%.

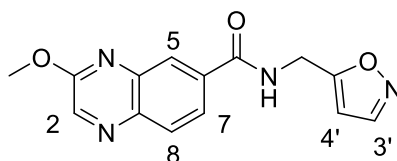
***N*-(Furan-2-ylmethyl)-2-methoxyquinoxaline-6-carboxamide (111)**



6-bromo-2-methoxyquinoxaline (**109**) (60 mg, 0.25 mmol), furfurylamine (22 μ L, 0.25 mmol) and Xantphos Palladacycle Gen.4 (12 mg, 0.0125 mmol, 5 mol%) were dissolved in 1,4-dioxane (0.50 mL, 0.50 M) in a dry vial. The vial was sealed, evacuated, and backfilled with nitrogen, evacuated once more and fitted with a CO (g) balloon. Lastly, DIPEA (0.13 mL, 0.75 mmol) was added, and the reaction was stirred at 80 °C for 2 h, cooled to rt and slowly vented. The reaction mixture was diluted with CH₂Cl₂ (10 mL), filtered through a pre-packed celite column, and the filtrate was concentrated *in vacuo*. The crude residue was purified by reverse phase silica chromatography eluting 5-95% MeOH in water (+0.1% formic acid), and fractions containing product were collected and evaporated *in vacuo* to afford *N*-(Furan-2-ylmethyl)-2-methoxyquinoxaline-6-carboxamide (**111**) (38 mg, 51%) as an off-white solid. ¹H NMR (600 MHz, DMSO-*d*₆) δ 9.27 (t, J = 5.7 Hz, 1H, -NH), 8.68 (s, 1H, 3-CH), 8.56 (d, J = 2.0 Hz, 1H, 5-CH), 8.21 (dd, J = 8.6, 2.1 Hz, 1H, 7-CH), 7.91 (d, J = 8.6 Hz, 1H, 8-CH), 7.59 (d, J = 1.8 Hz, 1H, 5'-CH), 6.41 (dd, J = 3.2, 1.8 Hz, 1H, 4'-CH), 6.32 (d, J = 3.2 Hz, 1H, 3'-CH), 4.53 (d, J = 5.6 Hz, 2H, -CH₂), 4.07 (s, 3H, -OCH₃). ¹³C NMR (151 MHz, DMSO-*d*₆) δ 165.2 (-

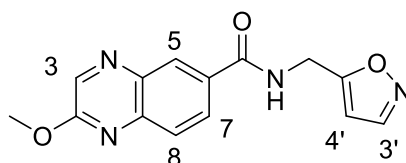
C=O), 158.2 (2-qC), 152.3 (2'-qC), 142.1 (5'-CH), 141.4 (8a-qC), 141.1 (3-CH), 137.6 (4a-qC), 132.1 (6-qC), 129.0 (7-CH), 127.9 (5-CH), 126.9 (8-CH), 110.5 (4'-CH), 107.0 (3'-CH), 53.9 (-OCH₃), 36.2 (-CH₂). LCMS (ESI⁺) *m/z* 306 [M+Na]⁺, *t_R* = 1.18 min. HRMS (ESI⁺) [M+H]⁺ calcd. for C₁₅H₁₄N₃O₃: 284.1035; found: 284.1021, error = -4.9 ppm, purity 95.0%.

***N*-(isoxazol-5-ylmethyl)-3-methoxyquinoxaline-6-carboxamide (112)**



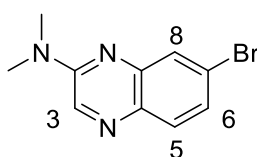
7-bromo-2-methoxyquinoxaline (**108**) (60 mg, 0.25 mmol), isoxazol-5-ylmethylamine hydrochloride (34 mg, 0.25 mmol) and Xantphos Palladacycle Gen.4 (12 mg, 0.0125 mmol, 5 mol%) were dissolved in 1,4-dioxane (0.50 mL, 0.50 M) in a dry vial. The vial was sealed, evacuated and backfilled with nitrogen, evacuated once more and fitted with a CO (g) balloon. Lastly, DIPEA (0.18 mL, 1.00 mmol) was added and the reaction was stirred at 80 °C for 3 h, cooled to rt and slowly vented. The reaction mixture was diluted with CH₂Cl₂ (10 mL), filtered through a pre-packed celite column, and the filtrate was concentrated *in vacuo*. The crude residue was purified by reverse phase silica chromatography eluting 5-95% MeOH in water (+0.1% formic acid), and fractions containing product were collected and evaporated *in vacuo* to afford *N*-(isoxazol-5-ylmethyl)-3-methoxyquinoxaline-6-carboxamide (**112**) (35 mg, 49%) as a pale yellow solid. ¹H NMR (600 MHz, DMSO-*d*₆) δ 9.50 (t, *J* = 5.8 Hz, 1H, -NH), 8.69 (s, 1H, 2-CH), 8.51 (d, *J* = 1.8 Hz, 1H, 3'-CH), 8.42 (dd, *J* = 1.8, 0.8 Hz, 1H, 7-CH), 8.10 (d, *J* = 0.7 Hz, 1H, 8-CH), 8.09 (d, *J* = 1.7 Hz, 1H, 5-CH), 6.42 (dd, *J* = 1.9, 0.9 Hz, 1H, 4'-CH), 4.69 (d, *J* = 5.7 Hz, 2H, -CH₂), 4.07 (s, 3H, -OCH₃). ¹³C NMR (151 MHz, DMSO-*d*₆) δ 169.2 (5'-qC), 165.6 (-C=O), 157.9 (3-qC), 150.9 (3'-CH), 141.6 (2-CH), 139.7 (8a-qC), 139.2 (4a-qC), 135.0 (6-qC), 128.9 (8-CH), 126.1 (7-CH), 125.3 (5-CH), 101.5 (4'-CH), 53.8 (-OCH₃), 35.2 (-CH₂). LCMS (ESI⁺) *m/z* 285 [M+H]⁺, *t_R* = 1.02 min. HRMS (ESI⁺) [M+H]⁺ calcd. for C₁₄H₁₃N₄O₃: 285.0988; found: 285.0968, error = -7.0 ppm, purity 99%.

***N*-(Isoxazol-5-ylmethyl)-2-methoxyquinoxaline-6-carboxamide (113)**



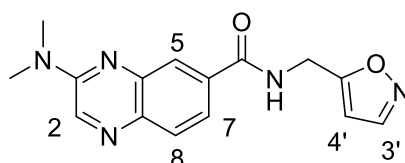
6-bromo-2-methoxyquinoxaline (**109**) (60 mg, 0.25 mmol), isoxazol-5-ylmethylamine hydrochloride (34 mg, 0.25 mmol) and Xantphos Palladacycle Gen.4 (12 mg, 0.0125 mmol, 5 mol%) were dissolved in 1,4-dioxane (0.50 mL, 0.50 M) in a dry vial. The vial was sealed, evacuated, and backfilled with nitrogen, evacuated once more and fitted with a CO (g) balloon. Lastly, DIPEA (0.18 mL, 1.00 mmol) was added, and the reaction was stirred at 80 °C for 2 h, cooled to rt and slowly vented. The reaction mixture was diluted with CH₂Cl₂ (10 mL), filtered through a pre-packed celite column, and the filtrate was concentrated *in vacuo*. The crude residue was purified by reverse phase silica chromatography eluting 5-95% MeOH in water (+0.1% formic acid), and fractions containing product were collected and evaporated *in vacuo* to afford *N*-(isoxazol-5-ylmethyl)-2-methoxyquinoxaline-6-carboxamide (**113**) (33 mg, 44%) as an orange solid. ¹H NMR (600 MHz, DMSO-*d*₆) δ 9.46 (t, *J* = 5.8 Hz, 1H, -NH), 8.69 (s, 1H, 3-CH), 8.58 (d, *J* = 2.0 Hz, 1H, 5-CH), 8.50 (d, *J* = 1.8 Hz, 1H, 3'-CH), 8.22 (dd, *J* = 8.6, 2.1 Hz, 1H, 7-CH), 7.93 (d, *J* = 8.6 Hz, 1H, 8-CH), 6.42 (d, *J* = 2.0 Hz, 1H, 4'-CH), 4.69 (d, *J* = 5.7 Hz, 2H, -CH₂), 4.07 (s, 3H, -OCH₃). ¹³C NMR (151 MHz, DMSO-*d*₆) δ 169.3 (5'-qC), 165.5 (-C=O), 158.2 (2-qC), 150.9 (3'-CH), 141.5 (8a-qC), 141.2 (3-CH), 137.6 (4a-qC), 131.7 (6-qC), 128.9 (7-CH), 128.0 (5-CH), 127.0 (8-CH), 101.5 (4'-CH), 53.9 (-OCH₃), 35.2 (-CH₂). LCMS (ESI⁺) *m/z* 285 [M+H]⁺, *t*_R = 1.04 min. HRMS (ESI⁺) [M+H]⁺ calcd. for C₁₄H₁₃N₄O₃: 285.0988; found: 285.0976, error = -4.2 ppm, purity 95.2%.

7-Bromo-*N,N*-dimethylquinoxalin-2-amine (114)



Dimethylamine (2 M in THF) (2.5 mL, 4.96 mmol) was added to a solution of 7-bromo-2-chloroquinoxaline (300 mg, 1.24 mmol) in DMF (2.5 mL, 0.50 M). The reaction was stirred at 80°C for 4 h, then cooled to rt and concentrated *in vacuo*. The crude residue was dissolved in 1:1 CH₂Cl₂/MeOH (10 mL) and purified by ion-exchange chromatography on acidic resin (10 g), eluting with MeOH (3 × 25 mL) then 2 M NH₃ in MeOH (3 × 25 mL). The basic fractions were concentrated *in vacuo* to afford 7-bromo-*N,N*-dimethylquinoxalin-2-amine (**114**) (288 mg, 91%) as a pale yellow solid. ¹H NMR (500 MHz, DMSO-*d*₆) δ 8.70 (s, 1H, 3-CH), 7.78 – 7.69 (m, 2H, 5-CH and 8-CH), 7.45 (dd, *J* = 8.7, 2.2 Hz, 1H, 6-CH), 3.22 (s, 6H, 2 × -NCH₃). ¹³C NMR (126 MHz, DMSO-*d*₆) δ 152.3 (2-qC), 142.5 (8a-qC), 136.9 (3-CH), 134.4 (4a-qC), 130.2 (5-CH), 127.6 (8-CH), 126.4 (6-CH), 122.8 (7-qCBr), 37.3 (2 × -NCH₃). LCMS (ESI⁺) *m/z* 252/254 [M+H]⁺, *t*_R = 1.39 min. HRMS (ESI⁺) [M+H]⁺ calcd. for C₁₀H₁₁BrN₃: 252.0136; found: 252.0142, error = 2.4 ppm.

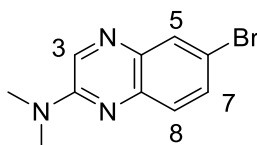
3-(Dimethylamino)-*N*-(isoxazol-5-ylmethyl)quinoxaline-6-carboxamide (115)



Isoxazol-5-ylmethanamine hydrochloride (35 mg, 0.26 mmol), 7-bromo-*N,N*-dimethylquinoxalin-2-amine (**114**) (66 mg, 0.26 mmol), and [Xantphos Pd(allyl)]Cl (10 mg, 0.013 mmol, 5 mol%) were added to a dry vial. The vial was sealed, evacuated and backfilled with nitrogen, evacuated once more, then 1,4-dioxane (0.52 mL, 0.50 M) and DIPEA (0.18 mL, 1.04 mmol) were added. Lastly, the vial was fitted with a CO (g) balloon and the reaction was stirred at 80 °C for 2.5 h, cooled to rt and slowly vented. The reaction mixture was flushed with nitrogen, diluted with CH₂Cl₂ (10 mL), filtered through a pre-packed celite column, and the filtrate was concentrated *in vacuo*. The crude residue was purified by reverse phase silica chromatography eluting 5-95% MeOH in water (+0.1% formic acid), and fractions containing product were collected and evaporated *in vacuo* to afford 3-(dimethylamino)-*N*-(isoxazol-5-ylmethyl)quinoxaline-6-carboxamide (**115**) (22

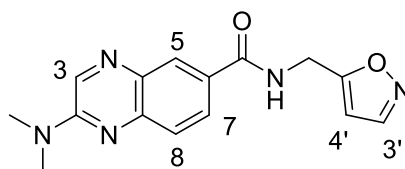
mg, 28%) as a pale yellow solid. ^1H NMR (600 MHz, $\text{DMSO-}d_6$) δ 9.38 (t, $J = 5.8$ Hz, 1H, -NH), 8.76 (s, 1H, 2-CH), 8.50 (d, $J = 1.8$ Hz, 1H, 3'-CH), 8.16 (d, $J = 1.9$ Hz, 1H, 5-CH), 7.88 (d, $J = 8.5$ Hz, 1H, 8-CH), 7.80 (dd, $J = 8.5, 2.0$ Hz, 1H, 7-CH), 6.40 (dd, $J = 1.9, 0.9$ Hz, 1H, 4'-CH), 4.66 (d, $J = 5.7$ Hz, 2H, -CH₂), 3.24 (s, 6H, 2 \times -NCH₃). ^{13}C NMR (151 MHz, $\text{DMSO-}d_6$) δ 169.4 (5'-qC), 166.0 (-C=O), 152.5 (3-qC), 150.9 (3'-CH), 140.9 (4a-qC), 137.9 (2-CH), 137.0 (8a-qC), 134.6 (6-qC), 128.5 (8-CH), 125.0 (5-CH), 122.1 (7-CH), 101.4 (4'-CH), 37.4 (2 \times -NCH₃), 35.2 (-CH₂). LCMS (ESI⁺) m/z 298 [M+H]⁺, $t_R = 1.10$ min. HRMS (ESI⁺) [M+H]⁺ calcd. for C₁₅H₁₆N₅O₂: 298.1304; found: 298.1299, error = -1.7 ppm, purity = 98.3%.

6-Bromo-*N,N*-dimethylquinoxalin-2-amine (116)



Dimethylamine (2 M in THF) (2.5 mL, 4.96 mmol) was added to a solution of 7-bromo-2-chloroquinoxaline (300 mg, 1.24 mmol) in DMF (2.5 mL, 0.50 M). The reaction was stirred at 80°C for 4 h, then cooled to rt and concentrated *in vacuo*. The crude residue was dissolved in 1:1 CH₂Cl₂/MeOH (10 mL) and purified by ion-exchange chromatography on acidic resin (10 g), eluting with MeOH (3 \times 25 mL) then 2 M NH₃ in MeOH (3 \times 25 mL). The basic fractions were concentrated *in vacuo* to afford 6-bromo-*N,N*-dimethylquinoxalin-2-amine (**116**) (296 mg, 95%) as a pale yellow solid. ^1H NMR (500 MHz, $\text{DMSO-}d_6$) δ 8.70 (s, 1H, 3-CH), 7.99 (d, $J = 2.3$ Hz, 1H, 5-CH), 7.68 (dd, $J = 8.9, 2.3$ Hz, 1H, 7-CH), 7.52 (d, $J = 8.9$ Hz, 1H, 8-CH), 3.22 (s, 6H, 2 \times -NCH₃). ^{13}C NMR (126 MHz, $\text{DMSO-}d_6$) δ 152.3 (2-qC), 140.4 (8a-qC), 137.4 (3-CH), 136.3 (4a-qC), 132.7 (7-CH), 130.2 (5-CH), 127.7 (8-CH), 115.1 (6-qCBr), 37.3 (2 \times -NCH₃). LCMS (ESI⁺) m/z 252/254 [M+H]⁺, $t_R = 1.37$ min. HRMS (ESI⁺) [M+H]⁺ calcd. for C₁₀H₁₁BrN₃: 252.0136; found: 252.0138, error = 0.8 ppm.

2-(Dimethylamino)-*N*-(isoxazol-5-ylmethyl)quinoxaline-6-carboxamide (117)



Isloxazol-5-ylmethanamine hydrochloride (35 mg, 0.26 mmol), 6-bromo-*N,N*-dimethylquinoxalin-2-amine (**116**) (66 mg, 0.26 mmol), and Xantphos Palladacycle Gen.4 (13 mg, 0.013 mmol, 5 mol%) were added to a dry vial. The vial was sealed, evacuated and backfilled with nitrogen, evacuated once more, then 1,4-dioxane (0.52 mL, 0.50 M) and DIPEA (0.18 mL, 1.04 mmol) were added. Lastly, the vial was fitted with a CO (g) balloon and the reaction was stirred at 80 °C for 4 h, cooled to rt and slowly vented. The reaction mixture was flushed with nitrogen, diluted with CH₂Cl₂ (10 mL), filtered through a pre-packed celite column, and the filtrate was concentrated *in vacuo*. The crude residue was dissolved in 1:1 CH₂Cl₂/MeOH (4 mL) and purified by ion-exchange chromatography on acidic resin (2 g), eluting with MeOH (3 × 10 mL) then 2 M NH₃ in MeOH (3 × 10 mL). The basic fractions were concentrated *in vacuo* and further purified by reverse phase silica chromatography eluting 5-90% MeOH in water (+0.1% formic acid), and fractions containing product were collected and evaporated *in vacuo*. The residue was further purified by normal phase silica chromatography eluting 0-20% MeOH in CH₂Cl₂, and fractions containing product were collected and evaporated *in vacuo* to afford 2-(dimethylamino)-*N*-(isoxazol-5-ylmethyl)quinoxaline-6-carboxamide (**117**) (8 mg, 10%) as a pale yellow solid. ¹H NMR (600 MHz, DMSO-*d*₆) δ 9.28 (t, *J* = 5.8 Hz, 1H, -NH), 8.77 (s, 1H, 3-CH), 8.49 (d, *J* = 1.8 Hz, 1H, 3'-CH), 8.39 (d, *J* = 2.1 Hz, 1H, 5-CH), 8.05 (dd, *J* = 8.7, 2.1 Hz, 1H, 7-CH), 7.62 (d, *J* = 8.7 Hz, 1H, 8-CH), 6.39 (d, *J* = 1.8 Hz, 1H, 4'-CH), 4.66 (d, *J* = 5.7 Hz, 2H, -CH₂), 3.26 (s, 6H, 2 × -NCH₃). ¹³C NMR (151 MHz, DMSO) δ 169.6 (5'-qC), 165.8 (-C=O), 152.7 (2-qC), 150.9 (3'-CH), 143.5 (8a-qC), 137.5 (3-CH), 134.6 (4a-qC), 128.5 (7-CH), 128.3 (6-qC), 127.9 (5-CH), 125.6 (8-CH), 101.4 (4'-CH), 37.4 (2 × -NCH₃), 35.1 (-CH₂). LCMS (ESI⁺) *m/z* 298 [M+H]⁺, t_R = 0.96 min. HRMS (ESI⁺) [M+H]⁺ calcd. for C₁₅H₁₆N₅O₂: 298.1304; found: 298.1307, error = 1.0 ppm, purity = 97.7%.

7.1.4 Chemical Syntheses from Chapter 4

General Procedure B: K₂CO₃ (173 mg, 1.23 mmol) was added to a solution of 7-bromo-2-chloroquinoxaline (150 mg, 0.62 mmol) in alcohol (3.1 mL, 0.20 M). The reaction was stirred at 80°C and white solids precipitated during this time. The reaction was then cooled to rt and CH₂Cl₂ (15 mL) was added, then the mixture was concentrated *in vacuo* and water (25 mL) was added. The aqueous phase was extracted with CH₂Cl₂ (3 × 25 mL), then organic phases were combined and washed with brine (25 mL), dried with MgSO₄, filtered and concentrated *in vacuo* to afford desired product with no further purification required.

General Procedure C: K₂CO₃ (173 mg, 1.23 mmol) was added to a solution of 7-bromo-2-chloroquinoxaline (150 mg, 0.62 mmol) and alcohol (1.23 mmol, 2 equiv) in DMF (3.1 mL, 0.2 M). The reaction was stirred at 80°C, then cooled to rt, diluted with CH₂Cl₂ (15 mL) and water (25 mL) was added. The aqueous phase was extracted with CH₂Cl₂ (3 × 25 mL), then organic phases were combined and washed with 5% w/v LiCl solution (50 mL) then brine (50 mL), dried with MgSO₄, filtered and concentrated *in vacuo* to afford crude residue, which was purified by flash column chromatography to afford desired product.

General Procedure D: Isoxazol-5-ylmethanamine hydrochloride (40 mg, 0.30 mmol), 7-bromo-2-alkoxyquinoxaline (0.30 mmol, 1 equiv), and [Xantphos Pd(allyl)]Cl (11 mg, 0.015 mmol, 5 mol%) were added to a dry vial. The vial was sealed, evacuated and backfilled with nitrogen, evacuated once more, then 1,4-dioxane (0.59 mL, 0.50 M) and DIPEA (0.21 mL, 1.19 mmol) were added. Lastly, the vial was fitted with a CO (g) balloon and the reaction was stirred at 80 °C, cooled to rt and slowly vented. The reaction mixture was flushed with nitrogen, diluted with CH₂Cl₂ (10 mL), filtered through a pre-packed celite column, and the filtrate was concentrated *in vacuo* to afford crude residue which was purified by flash column chromatography to afford desired product.

General Procedure E: Isoxazol-5-ylmethanamine hydrochloride (35 mg, 0.26 mmol), 7-bromo-2-alkoxyquinoxaline (0.26 mmol, 1 equiv), and [Xantphos

Pd(allyl)]Cl (10 mg, 0.013 mmol, 5 mol%) were added to a dry vial. The vial was sealed, evacuated and backfilled with nitrogen, evacuated once more, then 1,4-dioxane (0.52 mL, 0.50 M) and DIPEA (0.18 mL, 1.04 mmol) were added. Lastly, the vial was fitted with a CO (g) balloon and the reaction was stirred at 80 °C, cooled to rt and slowly vented. The reaction mixture was flushed with nitrogen, diluted with CH₂Cl₂ (10 mL), filtered through a pre-packed celite column, and the filtrate was concentrated *in vacuo* to afford crude residue which was purified by flash column chromatography to afford desired product.

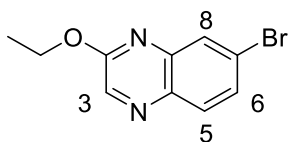
General Procedure F: Amine (neat or hydrochloride salt) (1.85 mmol, 3 equiv) was added to a solution of 7-bromo-2-chloroquinoxaline (150 mg, 0.62 mmol) in DMF (1.2 mL, 0.5 M). The reaction was stirred at 80°C, then cooled to rt and concentrated *in vacuo* to afford crude residue which was purified by ion-exchange chromatography on acidic resin (5 g) to afford desired product.

General Procedure G: Isoxazol-5-ylmethanamine hydrochloride (35 mg, 0.26 mmol), 7-bromo-*N*-alkylquinoxalin-2-amine (0.26 mmol, 1 equiv), and Xantphos Palladacycle Gen.4 (13 mg, 0.013 mmol, 5 mol%) were added to a dry vial. The vial was sealed, evacuated and backfilled with nitrogen, evacuated once more, then 1,4-dioxane (0.52 mL, 0.50 M) and DIPEA (0.18 mL, 1.04 mmol) were added. Lastly, the vial was fitted with a CO (g) balloon and the reaction was stirred at 80 °C, cooled to rt and slowly vented. The reaction mixture was flushed with nitrogen, diluted with CH₂Cl₂ (10 mL), filtered through a pre-packed celite column, and the filtrate was concentrated *in vacuo* to afford crude residue which was purified by flash column chromatography to afford desired product.

General Procedure H: 7-Bromo-*N,N*-dimethylquinoxalin-2-amine (**114**) (75 mg, 0.30 mmol), amine (neat or hydrochloride salt) (0.30 mmol, 1 equiv) and Xantphos Palladacycle Gen.4 (14 mg, 0.015 mmol, 5 mol%) were added to a dry vial. The vial was sealed, evacuated and backfilled with nitrogen, evacuated once more, then 1,4-dioxane (0.60 mL, 0.50 M) and DIPEA (0.16 mL, 0.89 mmol) were added. Lastly, the vial was fitted with a CO (g) balloon and the reaction was stirred at 80 °C, cooled to rt and slowly vented. The reaction mixture was flushed with nitrogen, diluted with CH₂Cl₂ (10 mL), filtered through a pre-packed celite column,

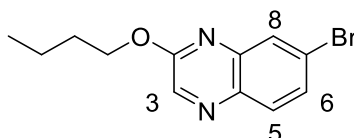
and the filtrate was concentrated *in vacuo* to afford crude residue which was purified by flash column chromatography to afford desired product.

7-Bromo-2-ethoxyquinoxaline (119)



The reaction was carried out in EtOH (3.1 mL, 0.20 M) for 4 h according to general procedure B to afford 7-bromo-2-ethoxyquinoxaline (**119**) (139 mg, 89%) as a white solid. ^1H NMR (500 MHz, DMSO) δ 8.59 (s, 1H, 3-CH), 8.01 (d, $J = 2.2$ Hz, 1H, 8-CH), 7.93 (d, $J = 8.7$ Hz, 1H, 5-CH), 7.76 (dd, $J = 8.8, 2.2$ Hz, 1H, 6-CH), 4.48 (q, $J = 7.0$ Hz, 2H, -OCH₂), 1.41 (t, $J = 7.0$ Hz, 3H, -CH₃). ^{13}C NMR (126 MHz, DMSO) δ 157.5 (2-qC), 140.7 (8a-qC), 140.6 (3-CH), 137.1 (4a-qC), 130.5 (5-CH), 129.8 (6-CH), 128.9 (8-CH), 123.3 (7-qCBr), 62.5 (-OCH₂), 14.1 (-CH₃). LCMS (ESI⁺) m/z 252/254 [M+H]⁺, $t_{\text{R}} = 1.52$ min. HRMS (ESI⁺) [M+H]⁺ calcd. for C₁₀H₁₀BrN₂O: 252.9976; found: 252.9978, error = 0.8 ppm.

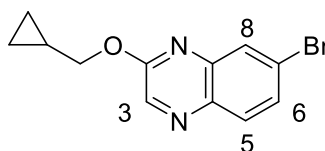
7-Bromo-2-butoxyquinoxaline (120)



The reaction was carried out in *n*-BuOH (3.1 mL, 0.20 M) for 4 h according to general procedure B to afford 7-bromo-2-butoxyquinoxaline (**120**) (108 mg, 62%) as a white solid. ^1H NMR (500 MHz, DMSO) δ 8.60 (s, 1H, 3-CH), 8.02 (d, $J = 2.1$ Hz, 1H, 8-CH), 7.93 (d, $J = 8.7$ Hz, 1H, 5-CH), 7.76 (dd, $J = 8.7, 2.2$ Hz, 1H, 6-CH), 4.43 (t, $J = 6.6$ Hz, 2H, -OCH₂), 1.83 – 1.74 (m, 2H, -CH₂), 1.52 – 1.41 (m, 2H, -CH₂), 0.95 (t, $J = 7.4$ Hz, 3H, -CH₃). ^{13}C NMR (126 MHz, DMSO) δ 157.6 (2-qC), 140.7 (8a-qC), 140.6 (3-CH), 137.1 (4a-qC), 130.5 (5-CH), 129.8 (6-CH), 128.9 (8-CH), 123.3 (7-qCBr), 66.2 (-OCH₂), 30.1 (-CH₂), 18.7 (-CH₂), 13.6 (-

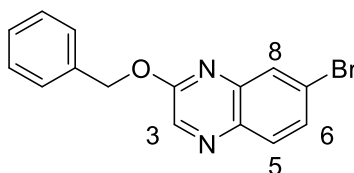
CH₃). LCMS (ESI⁺) *m/z* 281/283 [M+H]⁺, *t_R* = 1.68 min. HRMS (ESI⁺) [M+H]⁺ calcd. for C₁₀H₁₀BrN₂O: 281.0289; found: 281.0288, error = 0.4 ppm.

7-Bromo-2-(cyclopropylmethoxy)quinoxaline (121)



The reaction was carried out with cyclopropylmethanol (100 μ L, 1.23 mmol, 2 equiv) for 76 h according to general procedure C. The crude residue was purified by normal phase silica chromatography eluting 0-15% EtOAc in cyclohexane, and fractions containing product were collected and evaporated *in vacuo* to afford 7-bromo-2-(cyclopropylmethoxy)quinoxaline (**121**) (131 mg, 76%) as a white solid. ¹H NMR (500 MHz, DMSO-*d*₆) δ 8.64 (s, 1H, 3-CH), 8.01 (d, *J* = 2.2 Hz, 1H, 8-CH), 7.94 (d, *J* = 8.7 Hz, 1H, 5-CH), 7.77 (dd, *J* = 8.7, 2.2 Hz, 1H, 6-CH), 4.28 (d, *J* = 7.2 Hz, 2H, -OCH₂), 1.39 – 1.27 (m, 1H, -CH), 0.66 – 0.54 (m, 2H, -CH₂), 0.42 (dt, *J* = 6.2, 4.3 Hz, 2H, -CH₂). ¹³C NMR (126 MHz, DMSO-*d*₆) δ 157.6 (2-qC), 140.7 (3-CH), 137.1 (4a-qC), 132.4 (8a-qC), 130.5 (5-CH), 129.8 (6-CH), 128.9 (8-CH), 123.4 (7-qCBr), 71.2 (-OCH₂), 9.6 (-CH), 3.3 (2 \times -CH₂). LCMS (ESI⁺) *m/z* 279/281 [M+H]⁺, *t_R* = 1.60 min. HRMS (ESI⁺) [M+H]⁺ calcd. for C₁₂H₁₂BrN₂O: 279.0133; found: 279.0135, error = 0.7 ppm.

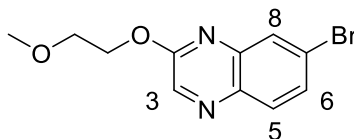
2-(Benzyloxy)-7-bromoquinoxaline (122)



The reaction was carried out with phenylmethanol (130 μ L, 1.23 mmol, 2 equiv) for 76 h according to general procedure C. The crude residue was purified by normal phase silica chromatography eluting 0-15% EtOAc in cyclohexane, and fractions containing product were collected and evaporated *in vacuo* to afford 2-

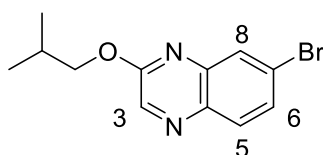
(benzyloxy)-7-bromoquinoxaline (**122**) (155 mg, 78%) as a white solid. ^1H NMR (500 MHz, DMSO) δ 8.68 (s, 1H, 3-CH), 8.07 (d, $J = 2.2$ Hz, 1H, 8-CH), 7.96 (d, $J = 8.8$ Hz, 1H, 5-CH), 7.79 (dd, $J = 8.8, 2.2$ Hz, 1H, 6-CH), 7.59 – 7.53 (m, 2H, 2 \times Ar-CH), 7.45 – 7.39 (m, 2H, 2 \times Ar-CH), 7.39 – 7.33 (m, 1H, Ar-CH), 5.52 (s, 2H, -OCH₂). ^{13}C NMR (126 MHz, DMSO) δ 157.3 (2-qC), 140.6 (3-CH), 140.5 (8a-qC), 137.3 (4a-qC), 135.9 (Ar-qC), 130.5 (5-CH), 130.0 (6-CH), 129.0 (8-CH), 128.5 (2 \times Ar-CH), 128.5 (2 \times Ar-CH), 128.2 (Ar-CH), 123.5 (7-qCBr), 68.0 (-OCH₂). LCMS (ESI⁺) m/z 315/317 [M+H]⁺, $t_{\text{R}} = 1.65$ min. HRMS (ESI⁺) [M+H]⁺ calcd. for C₁₅H₁₂BrN₂O: 315.0133; found: 315.0139, error = 1.9 ppm.

7-Bromo-2-(2-methoxyethoxy)quinoxaline (**123**)



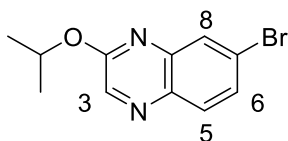
The reaction was carried out with 2-methoxyethan-1-ol (97 μL , 1.23 mmol, 2 equiv) for 21 h according to general procedure C. The crude residue was purified by normal phase silica chromatography eluting 0-15% EtOAc in cyclohexane, and fractions containing product were collected and evaporated *in vacuo* to afford 7-bromo-2-(2-methoxyethoxy)quinoxaline (**123**) (121 mg, 69%) as a yellow solid. ^1H NMR (600 MHz, DMSO) δ 8.65 (s, 1H, 3-CH), 8.03 (d, $J = 2.2$ Hz, 1H, 8-CH), 7.95 (d, $J = 8.8$ Hz, 1H, 5-CH), 7.78 (dd, $J = 8.8, 2.2$ Hz, 1H, 6-CH), 4.59 – 4.54 (m, 2H, -OCH₂), 3.77 – 3.73 (m, 2H, -OCH₂), 3.32 (s, 3H, -OCH₃). ^{13}C NMR (151 MHz, DMSO) δ 157.4 (2-qC), 140.6 (3-CH), 140.5 (8a-qC), 137.2 (4a-qC), 130.5 (5-CH), 130.0 (6-CH), 129.0 (8-CH), 123.4 (7-qCBr), 69.7 (-OCH₂), 65.6 (-OCH₂), 58.1 (-OCH₃). LCMS (ESI⁺) m/z 283/285 [M+H]⁺, $t_{\text{R}} = 1.47$ min. HRMS (ESI⁺) [M+H]⁺ calcd. for C₁₁H₁₂BrN₂O₂: 283.0082; found: 283.0084, error = 0.7 ppm.

7-Bromo-2-isobutoxyquinoxaline (**124**)



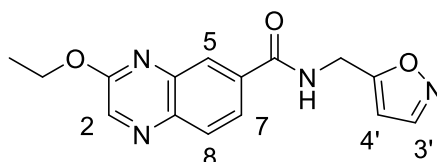
The reaction was carried out with 2-methylpropan-1-ol (114 μ L, 1.23 mmol, 2 equiv) for 21 h according to general procedure C. The crude residue was purified by normal phase silica chromatography eluting 0-10% EtOAc in cyclohexane, and fractions containing product were collected and evaporated *in vacuo* to afford 7-bromo-2-isobutoxyquinoxaline (**124**) (123 mg, 71%) as a yellow solid. ^1H NMR (600 MHz, DMSO) δ 8.62 (s, 1H, 3-CH), 8.01 (d, J = 2.2 Hz, 1H, 8-CH), 7.93 (d, J = 8.7 Hz, 1H, 5-CH), 7.76 (dd, J = 8.7, 2.2 Hz, 1H, 6-CH), 4.21 (d, J = 6.7 Hz, 2H, -OCH₂), 2.18 – 2.08 (m, 1H, -CH), 1.02 (d, J = 6.8 Hz, 6H, 2 \times -CH₃). ^{13}C NMR (151 MHz, DMSO) δ 157.7 (2-qC), 140.6 (8a-qC), 140.6 (3-CH), 137.1 (4a-qC), 130.5 (5-CH), 129.8 (6-CH), 128.9 (8-CH), 123.3 (7-qCBr), 72.4 (-OCH₂), 27.2 (-CH), 19.0 (2 \times -CH₃). LCMS (ESI⁺) m/z 281/283 [M+H]⁺, t_{R} = 1.83 min. HRMS (ESI⁺) [M+H]⁺ calcd. for C₁₂H₁₄BrN₂O: 281.0289; found: 281.0294, error = 1.8 ppm.

7-Bromo-2-isopropoxyquinoxaline (**125**)



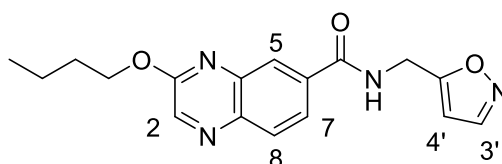
The reaction was carried out in *i*-PrOH (3.1 mL, 0.20 M) for 4 h according to general procedure B to afford 7-bromo-2-isopropoxyquinoxaline (**125**) (138 mg, 84%) as a yellow oil. ^1H NMR (600 MHz, DMSO) δ 8.54 (s, 1H, 3-CH), 8.01 (d, J = 2.2 Hz, 1H, 8-CH), 7.92 (d, J = 8.7 Hz, 1H, 5-CH), 7.75 (dd, J = 8.7, 2.2 Hz, 1H, 6-CH), 5.42 (hept, J = 6.2 Hz, 1H, -OCH), 1.39 (d, J = 6.3 Hz, 6H, 2 \times -CH₃). ^{13}C NMR (151 MHz, DMSO) δ 157.0 (2-qC), 141.0 (3-CH), 140.7 (8a-qC), 137.0 (4a-qC), 130.5 (5-CH), 129.7 (6-CH), 128.9 (8-CH), 123.3 (7-qCBr), 69.5 (-OCH), 21.5 (2 \times -CH₃). LCMS (ESI⁺) m/z 267/269 [M+H]⁺, t_{R} = 1.62 min. HRMS (ESI⁺) [M+H]⁺ calcd. for C₁₁H₁₂BrN₂: 267.0127; found: 267.0133, error = 2.0 ppm.

3-Ethoxy-*N*-(isoxazol-5-ylmethyl)quinoxaline-6-carboxamide (**126**)



The reaction was carried out with 7-bromo-2-ethoxyquinoxaline (**119**) (75 mg, 0.30 mmol) for 3 h according to general procedure D. The crude residue was purified by reverse phase silica chromatography eluting 5-95% MeOH in water (+0.1% formic acid), and fractions containing product were collected and evaporated *in vacuo* to afford 3-ethoxy-*N*-(isoxazol-5-ylmethyl)quinoxaline-6-carboxamide (**126**) (45 mg, 50%) as a yellow solid. ^1H NMR (500 MHz, $\text{DMSO-}d_6$) δ 9.50 (t, $J = 5.8$ Hz, 1H, -NH), 8.65 (s, 1H, 2-CH), 8.50 (d, $J = 1.8$ Hz, 1H, 3'-CH), 8.39 (*app* t, $J = 1.3$ Hz, 1H, 7-CH), 8.08 – 8.07 (m, 2H, 5-CH and 8-CH), 6.42 (dd, $J = 1.9, 0.9$ Hz, 1H, 4'-CH), 4.68 (d, $J = 5.7$ Hz, 2H, -CH₂), 4.52 (q, $J = 7.0$ Hz, 2H, -OCH₂), 1.43 (t, $J = 7.0$ Hz, 3H, -CH₃). ^{13}C NMR (126 MHz, $\text{DMSO-}d_6$) δ 169.2 (5'-qC), 165.6 (-C=O), 157.5 (3-qC), 150.9 (3'-CH), 141.7 (2-CH), 139.6 (8a-qC), 139.2 (4a-qC), 134.9 (6-qC), 128.9 (8-CH), 126.1 (7-CH), 125.2 (5-CH), 101.5 (4'-CH), 62.4 (-OCH₂), 35.2 (-CH₂), 14.1 (-CH₃). LCMS (ESI⁺) m/z 299 [M+H]⁺, $t_R = 1.11$ min. HRMS (ESI⁺) [M+H]⁺ calcd. for C₁₅H₁₅N₄O₃: 299.1144; found: 299.1136, error = -2.7 ppm, purity 99.2%.

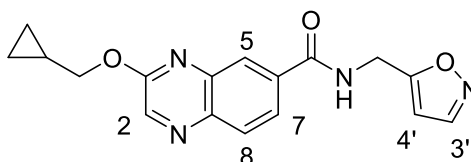
3-Butoxy-*N*-(isoxazol-5-ylmethyl)quinoxaline-6-carboxamide (**127**)



The reaction was carried out with 7-bromo-2-butoxyquinoxaline (**120**) (84 mg, 0.30 mmol) for 3 h according to general procedure D. The crude residue was purified by reverse phase silica chromatography eluting 5-95% MeOH in water (+0.1% formic acid), and fractions containing product were collected and evaporated *in vacuo* to afford 3-butoxy-*N*-(isoxazol-5-ylmethyl)quinoxaline-6-carboxamide (**127**) (38 mg, 39%) as a yellow solid. ^1H NMR (500 MHz, $\text{DMSO-}d_6$) δ 9.49 (t, $J = 5.8$ Hz, 1H, -NH), 8.66 (s, 1H, 2-CH), 8.51 (d, $J = 1.8$ Hz, 1H, 3'-

CH), 8.39 (*app* t, $J = 1.3$ Hz, 1H, 7-CH), 8.11 – 8.03 (m, 2H, 5-CH and 8-CH), 6.42 (dd, $J = 1.8, 0.9$ Hz, 1H, 4'-CH), 4.68 (d, $J = 5.8$ Hz, 2H, -CH₂), 4.46 (t, $J = 6.6$ Hz, 2H, -OCH₂), 1.85 – 1.76 (m, 2H, -OCH₂CH₂), 1.54 – 1.43 (m, 2H, -OCH₂CH₂CH₂), 0.96 (t, $J = 7.4$ Hz, 3H, -CH₃). ¹³C NMR (126 MHz, DMSO-*d*₆) δ 169.2 (5'-qC), 165.6 (-C=O), 157.6 (3-qC), 150.9 (3'-CH), 141.6 (2-CH), 139.6 (8a-qC), 139.2 (4a-qC), 134.9 (6-qC), 128.8 (8-CH), 126.1 (7-CH), 125.2 (5-CH), 101.5 (4'-CH), 66.2 (-OCH₂), 35.2 (-CH₂), 30.2 (-OCH₂CH₂), 18.7 (-OCH₂CH₂CH₂), 13.6 (-CH₃). LCMS (ESI⁺) m/z 349 [M+Na]⁺, $t_R = 1.31$ min. HRMS (ESI⁺) [M+H]⁺ calcd. for C₁₇H₁₉N₄O₃: 327.1457; found: 327.1448, error = -3.4 ppm, purity 98.3%.

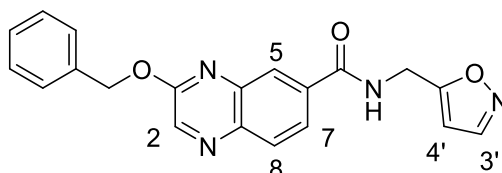
3-(Cyclopropylmethoxy)-*N*-(isoxazol-5-ylmethyl)quinoxaline-6-carboxamide (**128**)



The reaction was carried out with 7-bromo-2-(cyclopropylmethoxy)quinoxaline (**121**) (83 mg, 0.30 mmol) for 3 h according to general procedure D. The crude residue was purified by reverse phase silica chromatography eluting 5-95% MeOH in water (+0.1% formic acid), and fractions containing product were collected and evaporated *in vacuo* to afford 3-(cyclopropylmethoxy)-*N*-(isoxazol-5-ylmethyl)quinoxaline-6-carboxamide (**128**) (49 mg, 48%) as a yellow solid. ¹H NMR (600 MHz, DMSO) δ 9.48 (t, $J = 5.8$ Hz, 1H, -NH), 8.70 (s, 1H, 2-CH), 8.50 (d, $J = 1.8$ Hz, 1H, 3'-CH), 8.38 (dd, $J = 1.7, 0.8$ Hz, 1H, 7-CH), 8.11 – 8.02 (m, 2H, 5-CH and 8-CH), 6.42 (dd, $J = 1.8, 0.9$ Hz, 1H, 4'-CH), 4.68 (d, $J = 5.7$ Hz, 2H, -CH₂), 4.31 (d, $J = 7.3$ Hz, 2H, -OCH₂), 1.41 – 1.31 (m, 1H, -OCH₂CH), 0.66 – 0.58 (m, 2H, -OCH₂CHCH₂), 0.46 – 0.40 (m, 2H, -OCH₂CHCH₂). ¹³C NMR (151 MHz, DMSO) δ 169.2 (5'-qC), 165.5 (-C=O), 157.6 (3-qC), 150.9 (3'-CH), 141.7 (2-CH), 139.6 (8a-qC), 139.2 (4a-qC), 134.9 (6-qC), 128.9 (8-CH), 126.1 (7-CH), 125.2 (5-CH), 101.5 (4'-CH), 71.2 (-OCH₂), 35.2 (-CH₂), 9.7 (-OCH₂CH), 3.3 (2 × -OCH₂CHCH₂). LCMS (ESI⁺) m/z 347 [M+Na]⁺, $t_R = 1.34$ min. HRMS (ESI⁺)

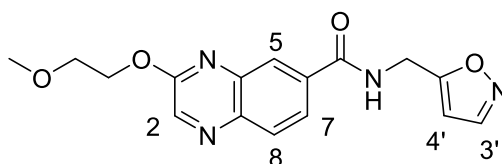
[M+H]⁺ calcd. for C₁₇H₁₇N₄O₃: 325.1301; found: 325.1301, error = 0.00 ppm, purity 94.2%.

3-(Benzyloxy)-*N*-(isoxazol-5-ylmethyl)quinoxaline-6-carboxamide (**129**)



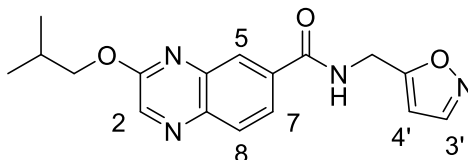
The reaction was carried out with 2-(benzyloxy)-7-bromoquinoxaline (**122**) (94 mg, 0.30 mmol) for 3 h according to general procedure D. The crude residue was purified by reverse phase silica chromatography eluting 5-95% MeOH in water (+0.1% formic acid), and fractions containing product were collected and evaporated *in vacuo* to afford 3-(benzyloxy)-*N*-(isoxazol-5-ylmethyl)quinoxaline-6-carboxamide (**129**) (62 mg, 55%) as a yellow solid. ¹H NMR (600 MHz, DMSO-*d*₆) δ 9.51 (t, *J* = 5.8 Hz, 1H, -NH), 8.74 (s, 1H, 2-CH), 8.51 (d, *J* = 1.8 Hz, 1H, 3'-CH), 8.42 (*app* t, *J* = 1.2 Hz, 1H, 7-CH), 8.14 – 8.05 (m, 2H, 5-CH and 8-CH), 7.59 – 7.54 (m, 2H, 2 × Ar-CH), 7.45 – 7.40 (m, 2H, 2 × Ar-CH), 7.40 – 7.34 (m, 1H, Ar-CH), 6.44 – 6.41 (m, 1H, 4'-CH), 5.55 (s, 2H, -OCH₂), 4.69 (d, *J* = 5.7 Hz, 2H, -CH₂). ¹³C NMR (151 MHz, DMSO) δ 169.2 (5'-qC), 165.5 (-C=O), 157.3 (3-qC), 150.9 (3'-CH), 141.6 (2-CH), 139.8 (8a-qC), 139.0 (4a-qC), 136.0 (Ar-qC), 135.1 (6-qC), 128.9 (8-CH), 128.5 (2 × Ar-CH), 128.4 (2 × Ar-CH), 128.2 (Ar-CH), 126.1 (7-CH), 125.4 (5-CH), 101.5 (4'-CH), 67.9 (-OCH₂), 35.2 (-CH₂). LCMS (ESI⁺) *m/z* 383 [M+Na]⁺, *t*_R = 1.43 min. HRMS (ESI⁺) [M+H]⁺ calcd. for C₂₀H₁₇N₄O₃: 361.1301; found: 361.1298, error = -0.8 ppm, purity 95.0%.

N-(Isoxazol-5-ylmethyl)-3-(2-methoxyethoxy)quinoxaline-6-carboxamide (**130**)



The reaction was carried out with 7-bromo-2-(2-methoxyethoxy)quinoxaline (**123**) (74 mg, 0.26 mmol) for 2 h according to general procedure E. The crude residue was purified by reverse phase silica chromatography eluting 5-95% MeOH in water (+0.1% formic acid), and fractions containing product were collected and evaporated *in vacuo* to afford *N*-(isoxazol-5-ylmethyl)-3-(2-methoxyethoxy)quinoxaline-6-carboxamide (**130**) (42 mg, 47%) as a yellow solid. ¹H NMR (600 MHz, DMSO-*d*₆) δ 9.50 (t, *J* = 5.8 Hz, 1H, -NH), 8.70 (s, 1H, 2-CH), 8.51 (d, *J* = 1.8 Hz, 1H, 3'-CH), 8.39 (dd, *J* = 1.7, 0.9 Hz, 1H, 7-CH), 8.12 – 8.06 (m, 2H, 5-CH and 8-CH), 6.44 – 6.40 (m, 1H, 4'-CH), 4.69 (d, *J* = 5.7 Hz, 2H, -CH₂), 4.61 – 4.57 (m, 2H, -OCH₂), 3.79 – 3.75 (m, 2H, -OCH₂), 3.33 (s, 3H, -OCH₃). ¹³C NMR (151 MHz, DMSO-*d*₆) δ 169.2 (5'-qC), 165.5 (-C=O), 157.4 (3-qC), 150.9 (3'-CH), 141.6 (2-CH), 139.7 (8a-qC), 139.0 (4a-qC), 135.0 (6-qC), 128.9 (8-CH), 126.1 (7-CH), 125.4 (5-CH), 101.5 (4'-CH), 69.7 (-OCH₂), 65.6 (-OCH₂), 58.1 (-OCH₃), 35.2 (-CH₂). LCMS (ESI⁺) *m/z* 351 [M+Na]⁺, *t*_R = 1.24 min. HRMS (ESI⁺) [M+H]⁺ calcd. for C₁₆H₁₇N₄O₄: 329.1250; found: 329.1246, error = -1.2 ppm, purity = 95.2%.

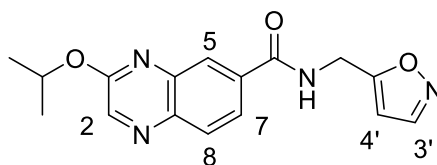
3-Isobutoxy-*N*-(isoxazol-5-ylmethyl)quinoxaline-6-carboxamide (**131**)



The reaction was carried out with 7-bromo-2-isobutoxyquinoxaline (**124**) (73 mg, 0.26 mmol) for 5 h according to general procedure E. The crude residue was purified by reverse phase silica chromatography eluting 5-95% MeOH in water (+0.1% formic acid), and fractions containing product were collected and evaporated *in vacuo*. The residue was further purified by normal phase silica chromatography eluting 0-100% EtOAc in cyclohexane. The fractions containing product were collected and evaporated *in vacuo* to afford 3-isobutoxy-*N*-(isoxazol-5-ylmethyl)quinoxaline-6-carboxamide (**131**) (24 mg, 28%) as an orange solid. ¹H NMR (600 MHz, DMSO-*d*₆) δ 9.48 (t, *J* = 5.8 Hz, 1H, -NH), 8.69 (s, 1H, 2-CH), 8.51 (d, *J* = 1.8 Hz, 1H, 3'-CH), 8.39 (dd, *J* = 1.7, 0.8 Hz, 1H, 7-

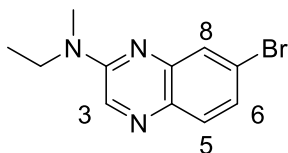
CH), 8.11 – 8.05 (m, 2H, 5-CH and 8-CH), 6.42 (dd, $J = 1.8, 0.9$ Hz, 1H, 4'-CH), 4.68 (d, $J = 5.7$ Hz, 2H, -CH₂), 4.25 (d, $J = 6.7$ Hz, 2H, -OCH₂), 2.16 (hept, $J = 6.7$ Hz, 1H, -CH), 1.03 (d, $J = 6.7$ Hz, 6H, 2 × -CH₃). ¹³C NMR (151 MHz, DMSO-*d*₆) δ 169.2 (5'-qC), 165.5 (-C=O), 157.7 (3-qC), 150.9 (3'-CH), 141.6 (2-CH), 139.6 (8a-qC), 139.2 (4a-qC), 135.0 (6-qC), 128.8 (8-CH), 126.1 (7-CH), 125.3 (5-CH), 101.5 (4'-CH), 72.4 (-OCH₂), 35.2 (-CH₂), 27.2 (-CH), 19.0 (2 × -CH₃). LCMS (ESI⁺) m/z 349 [M+Na]⁺, $t_R = 1.63$ min. HRMS (ESI⁺) [M+Na]⁺ calcd. for C₁₇H₁₈N₄O₃Na: 349.1277; found: 349.1270, error = -2.0 ppm, purity = 99.4%.

3-Isopropoxy-*N*-(isoxazol-5-ylmethyl)quinoxaline-6-carboxamide (132)



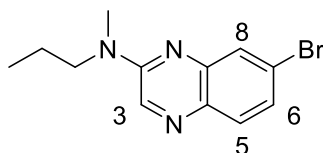
The reaction was carried out with 7-bromo-2-isopropoxyquinoxaline (**125**) (69 mg, 0.26 mmol) for 4 h according to general procedure E. The crude residue was purified by reverse phase silica chromatography eluting 5-95% MeOH in water (+0.1% formic acid), and fractions containing product were collected and evaporated *in vacuo* to afford 3-isopropoxy-*N*-(isoxazol-5-ylmethyl)quinoxaline-6-carboxamide (**132**) (28 mg, 33%) as an orange glass. ¹H NMR (600 MHz, DMSO-*d*₆) δ 9.49 (t, $J = 5.8$ Hz, 1H, -NH), 8.60 (s, 1H, 2-CH), 8.51 (d, $J = 1.8$ Hz, 1H, 3'-CH), 8.38 (*app* t, $J = 1.3$ Hz, 1H, 7-CH), 8.10 – 8.04 (m, 2H, 5-CH and 8-CH), 6.44 – 6.40 (m, 1H, 4'-CH), 5.44 (hept, $J = 6.2$ Hz, 1H, -OCH), 4.68 (d, $J = 5.7$ Hz, 2H, -CH₂), 1.42 (d, $J = 6.2$ Hz, 6H, 2 × -CH₃). ¹³C NMR (151 MHz, DMSO-*d*₆) δ 169.2 (5'-qC), 165.6 (-C=O), 157.0 (3-qC), 150.9 (3'-CH), 142.0 (2-CH), 139.5 (8a-qC), 139.2 (4a-qC), 134.9 (6-qC), 128.8 (8-CH), 126.1 (7-CH), 125.2 (5-CH), 101.5 (4'-CH), 69.5 (-OCH), 35.2 (-CH₂), 21.5 (2 × -CH₃). LCMS (ESI⁺) m/z 335 [M+Na]⁺, $t_R = 1.56$ min. HRMS (ESI⁺) [M+Na]⁺ calcd. for C₁₆H₁₆N₄O₃Na: 335.1121; found: 335.1115, error = -1.8 ppm, purity 94.6%.

7-Bromo-*N*-ethyl-*N*-methylquinoxalin-2-amine (133)



The reaction was carried out with *N*-methylethanamine (neat) (0.16 mL, 1.85 mmol) for 4 h according to general procedure F. The crude residue was dissolved in 1:1 CH₂Cl₂/MeOH (5 mL) and purified by ion-exchange chromatography on acidic resin (5 g), eluting with MeOH (3 × 15 mL) then 2 M NH₃ in MeOH (3 × 15 mL). The basic fractions were concentrated *in vacuo* to afford 7-bromo-*N*-ethyl-*N*-methylquinoxalin-2-amine (**133**) (159 mg, 96%) as a pale yellow solid. ¹H NMR (600 MHz, DMSO-*d*₆) δ 8.68 (s, 1H, 3-*CH*), 7.75 – 7.70 (m, 2H, 5-*CH* and 8-*CH*), 7.44 (dd, *J* = 8.6, 2.2 Hz, 1H, 6-*CH*), 3.72 (q, *J* = 7.1 Hz, 2H, -NCH₂), 3.18 (s, 3H, -NCH₃), 1.16 (t, *J* = 7.1 Hz, 3H, -NCH₂CH₃). ¹³C NMR (151 MHz, DMSO-*d*₆) δ 151.6 (2-*qC*), 142.7 (8a-*qC*), 136.9 (3-*CH*), 134.4 (4a-*qC*), 130.2 (5-*CH*), 127.6 (8-*CH*), 126.4 (6-*CH*), 122.8 (7-*qCBr*), 43.8 (-NCH₂), 34.9 (-NCH₃), 12.0 (-NCH₂CH₃). LCMS (ESI⁺) *m/z* 266/268 [M+H]⁺, *t_R* = 1.47 min. HRMS (ESI⁺) [M+H]⁺ calcd. for C₁₁H₁₃BrN₃: 266.0293; found: 266.0290, error = -1.1 ppm.

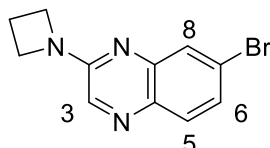
7-Bromo-*N*-methyl-*N*-propylquinoxalin-2-amine (**134**)



The reaction was carried out with *N*-methylpropan-1-amine (neat) (0.19 mL, 1.85 mmol) for 4 h according to general procedure F. The crude residue was dissolved in 1:1 CH₂Cl₂/MeOH (5 mL) and purified by ion-exchange chromatography on acidic resin (5 g), eluting with MeOH (3 × 15 mL) then 2 M NH₃ in MeOH (3 × 15 mL). The basic fractions were concentrated *in vacuo* to afford 7-bromo-*N*-methyl-*N*-propylquinoxalin-2-amine (**134**) (167 mg, 95%) as a pale yellow solid. ¹H NMR (600 MHz, DMSO-*d*₆) δ 8.69 (s, 1H, 3-*CH*), 7.74 – 7.70 (m, 2H, 5-*CH* and 8-*CH*), 7.44 (dd, *J* = 8.6, 2.2 Hz, 1H, 7-*CH*), 3.67 – 3.62 (m, 2H, -NCH₂), 3.19 (s, 3H, -NCH₃), 1.67 – 1.58 (m, 2H, -NCH₂CH₂), 0.90 (t, *J* = 7.4 Hz, 3H, -NCH₂CH₂CH₃). ¹³C NMR (151 MHz, DMSO-*d*₆) δ 151.9 (2-*qC*), 142.6 (8a-*qC*), 136.9 (3-*CH*),

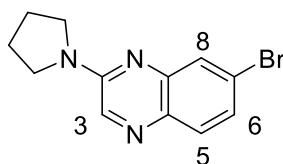
134.4 (4a-qC), 130.2 (5-CH), 127.6 (8-CH), 126.3 (6-CH), 122.8 (7-qCBr), 50.6 (-NCH₂), 35.7 (-NCH₃), 20.2 (-NCH₂CH₂), 11.1 (-NCH₂CH₂CH₃). LCMS (ESI⁺) *m/z* 280/282 [M+H]⁺, *t_R* = 1.54 min. HRMS (ESI⁺) [M+H]⁺ calcd. for C₁₂H₁₅BrN₃: 280.0449; found: 280.0449, error = 0.0 ppm.

2-(Azetidin-1-yl)-7-bromoquinoxaline (135)



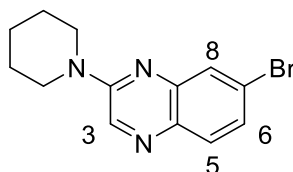
The reaction was carried out with azetidine (neat) (0.12 mL, 1.85 mmol) for 22 h according to general procedure F. The crude residue was dissolved in 1:1 CH₂Cl₂/MeOH (5 mL) and purified by ion-exchange chromatography on acidic resin (5 g), eluting with MeOH (3 × 15 mL) then 2 M NH₃ in MeOH (3 × 15 mL). The basic fractions were concentrated *in vacuo* and the residue was further purified by normal phase silica chromatography eluting 0-50% EtOAc in cyclohexane. The fractions containing product were collected and evaporated *in vacuo* to afford 2-(azetidin-1-yl)-7-bromoquinoxaline (**135**) (127 mg, 78%) as a pale yellow solid. ¹H NMR (600 MHz, DMSO-*d*₆) δ 8.30 (s, 1H, 3-CH), 7.77 – 7.71 (m, 2H, 5-CH and 8-CH), 7.47 (dd, *J* = 8.7, 2.2 Hz, 1H, 6-CH), 4.25 – 4.19 (m, 4H, 2 × -NCH₂), 2.46 – 2.38 (m, 2H, -CH₂). ¹³C NMR (151 MHz, DMSO-*d*₆) δ 152.8 (2-qC), 142.7 (8a-qC), 136.7 (3-CH), 135.0 (4a-qC), 130.5 (5-CH), 127.6 (8-CH), 126.6 (6-CH), 122.9 (7-qCBr), 50.4 (2 × -NCH₂), 16.4 (-CH₂). LCMS (ESI⁺) *m/z* 264/266 [M+H]⁺, *t_R* = 1.29 min. HRMS (ESI⁺) [M+H]⁺ calcd. for C₁₁H₁₁BrN₃: 264.0136; found: 264.0133, error = -1.1 ppm.

7-Bromo-2-(pyrrolidin-1-yl)quinoxaline (136)



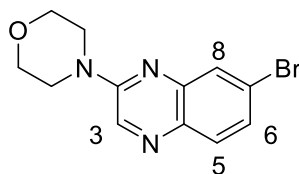
The reaction was carried out with pyrrolidine (neat) (0.15 mL, 1.85 mmol) for 22 h according to general procedure F. The crude residue was dissolved in 1:1 CH₂Cl₂/MeOH (5 mL) and purified by ion-exchange chromatography on acidic resin (5 g), eluting with MeOH (3 × 15 mL) then 2 M NH₃ in MeOH (3 × 15 mL). The basic fractions were concentrated *in vacuo* to afford 7-bromo-2-(pyrrolidin-1-yl)quinoxaline (**136**) (146 mg, 85%) as a pale yellow solid. ¹H NMR (600 MHz, DMSO-*d*₆) δ 8.49 (s, 1H, 3-CH), 7.75 – 7.70 (m, 2H, 5-CH and 8-CH), 7.43 (dd, *J* = 8.7, 2.2 Hz, 1H, 6-CH), 3.63 – 3.58 (m, 4H, 2 × -NCH₂), 2.01 – 1.96 (m, 4H, 2 × -NCH₂CH₂). ¹³C NMR (151 MHz, DMSO-*d*₆) δ 150.4 (2-qC), 143.1 (8a-qC), 138.0 (3-CH), 134.7 (4a-qC), 130.4 (5-CH), 127.5 (8-CH), 126.1 (6-CH), 122.8 (7-qCBr), 46.4 (2 × -NCH₂), 25.0 (2 × -NCH₂CH₂, observed in HSQC only). LCMS (ESI⁺) *m/z* 278/280 [M+H]⁺, *t*_R = 1.43 min. HRMS (ESI⁺) [M+H]⁺ calcd. for C₁₂H₁₃BrN₃: 278.0293; found: 278.0291, error = -0.7 ppm.

7-Bromo-2-(piperidin-1-yl)quinoxaline (**137**)



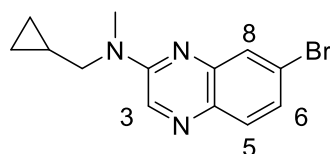
The reaction was carried out with piperidine (neat) (0.18 mL, 1.85 mmol) for 22 h according to general procedure F. The crude residue was dissolved in 1:1 CH₂Cl₂/MeOH (5 mL) and purified by ion-exchange chromatography on acidic resin (5 g), eluting with MeOH (3 × 15 mL) then 2 M NH₃ in MeOH (3 × 15 mL). The basic fractions were concentrated *in vacuo* to afford 7-bromo-2-(piperidin-1-yl)quinoxaline (**137**) (165 mg, 92%) as a pale yellow solid. ¹H NMR (600 MHz, DMSO-*d*₆) δ 8.83 (s, 1H, 3-CH), 7.75 – 7.69 (m, 2H, 5-CH and 8-CH), 7.46 (dd, *J* = 8.7, 2.2 Hz, 1H, 6-CH), 3.81 – 3.76 (m, 4H, 2 × -NCH₂), 1.70 – 1.63 (m, 2H, -CH₂), 1.63 – 1.56 (m, 4H, 2 × -NCH₂CH₂). ¹³C NMR (151 MHz, DMSO-*d*₆) δ 152.0 (2-qC), 142.4 (8a-qC), 137.4 (3-CH), 134.5 (4a-qC), 130.1 (5-CH), 127.6 (8-CH), 126.7 (6-CH), 122.8 (7-qCBr), 45.0 (2 × -NCH₂), 25.3 (2 × -NCH₂CH₂), 24.1 (-CH₂). LCMS (ESI⁺) *m/z* 292/294 [M+H]⁺, *t*_R = 1.59 min. HRMS (ESI⁺) [M+H]⁺ calcd. for C₁₃H₁₅BrN₃: 292.0449; found: 292.0444, error = -1.7 ppm.

4-(7-Bromoquinoxalin-2-yl)morpholine (138)



The reaction was carried out with morpholine (neat) (0.16 mL, 1.85 mmol) for 4 h according to general procedure F. The crude residue was dissolved in 1:1 CH₂Cl₂/MeOH (5 mL) and purified by ion-exchange chromatography on acidic resin (5 g), eluting with MeOH (3 × 15 mL) then 2 M NH₃ in MeOH (3 × 15 mL). The basic fractions were concentrated *in vacuo* to afford 4-(7-bromoquinoxalin-2-yl)morpholine (**138**) (172 mg, 95%) as a pale yellow solid. ¹H NMR (600 MHz, DMSO-*d*₆) δ 8.84 (s, 1H, 3-CH), 7.79 – 7.74 (m, 2H, 5-CH and 8-CH), 7.52 (dd, *J* = 8.7, 2.2 Hz, 1H, 6-CH), 3.79 – 3.71 (m, 8H, 2 × -NCH₂ and 2 × -OCH₂). ¹³C NMR (151 MHz, DMSO-*d*₆) δ 152.2 (2-qC), 142.0 (8a-qC), 137.4 (3-CH), 135.0 (4a-qC), 130.2 (5-CH), 127.9 (8-CH), 127.3 (6-CH), 123.0 (7-qCBr), 65.8 (2 × -OCH₂), 44.3 (2 × -NCH₂). LCMS (ESI⁺) *m/z* 294/296 [M+H]⁺, *t*_R = 1.40 min. HRMS (ESI⁺) [M+H]⁺ calcd. for C₁₂H₁₃BrN₃O: 294.0242; found: 294.0251, error = 3.1 ppm.

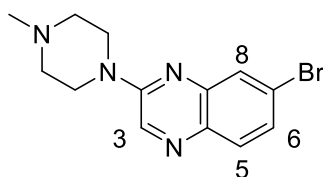
7-Bromo-*N*-(cyclopropylmethyl)-*N*-methylquinoxalin-2-amine (139)



The reaction was carried out with 1-cyclopropyl-*N*-methylmethanamine hydrochloride (157 mg, 1.85 mmol) and an additional equivalent of DIPEA (0.32 mL, 1.85 mmol) for 4 h according to general procedure F. The crude residue was dissolved in 1:1 CH₂Cl₂/MeOH (5 mL) and purified by ion-exchange chromatography on acidic resin (5 g), eluting with MeOH (3 × 15 mL) then 2 M NH₃ in MeOH (3 × 15 mL). The basic fractions were concentrated *in vacuo* and the residue was further purified by normal phase silica chromatography eluting 0-

30% EtOAc in cyclohexane. The fractions containing product were collected and evaporated *in vacuo* to afford 7-bromo-*N*-(cyclopropylmethyl)-*N*-methylquinoxalin-2-amine (**139**) (121 mg, 67%) as a pale yellow solid. ¹H NMR (600 MHz, Methanol-*d*₄) δ 8.58 (s, 1H, 3-CH), 7.77 (d, *J* = 2.2 Hz, 1H, 8-CH), 7.67 (d, *J* = 8.7 Hz, 1H, 5-CH), 7.42 (dd, *J* = 8.7, 2.2 Hz, 1H, 6-CH), 3.62 (d, *J* = 6.8 Hz, 2H, -NCH₂), 3.30 (s, 3H, -NCH₃), 1.19 – 1.10 (m, 1H, -NCH₂CH), 0.60 – 0.52 (m, 2H, -NCH₂CHCH₂), 0.39 – 0.33 (m, 2H, -NCH₂CHCH₂). ¹³C NMR (151 MHz, Methanol-*d*₄) δ 153.8 (2-qC), 144.4 (8a-qC), 137.3 (3-CH), 135.7 (4a-qC), 130.6 (5-CH), 129.4 (8-CH), 128.1 (6-CH), 124.8 (7-qCBr), 54.9 (-NCH₂), 36.5 (-NCH₃), 10.3 (-NCH₂CH), 3.8 (2 × -NCH₂CHCH₂). LCMS (ESI⁺) *m/z* 292/294 [M+H]⁺, *t*_R = 1.56 min. HRMS (ESI⁺) [M+H]⁺ calcd. for C₁₃H₁₅BrN₃: 292.0444; found: 292.0450, error = 1.94 ppm.

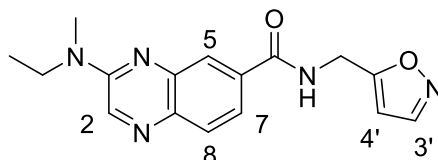
7-Bromo-2-(4-methylpiperazin-1-yl)quinoxaline (**140**)



The reaction was carried out with 1-methylpiperazine (neat) (0.20 mL, 1.85 mmol) for 4 h according to general procedure F. The crude residue was dissolved in 1:1 CH₂Cl₂/MeOH (5 mL) and purified by ion-exchange chromatography on acidic resin (5 g), eluting with MeOH (3 × 15 mL) then 2 M NH₃ in MeOH (3 × 15 mL). The basic fractions were concentrated *in vacuo* and the residue was further purified by normal phase silica chromatography eluting 0-10% MeOH in CH₂Cl₂. The fractions containing product were collected and evaporated *in vacuo* to afford 7-bromo-2-(4-methylpiperazin-1-yl)quinoxaline (**140**) (150 mg, 79%) as a pale yellow solid. ¹H NMR (600 MHz, DMSO) δ 8.85 (s, 1H, 3-CH), 7.78 – 7.72 (m, 2H, 5-CH and 8-CH), 7.50 (dd, *J* = 8.7, 2.2 Hz, 1H, 6-CH), 3.80 – 3.75 (m, 4H, 2 × -NCH₂), 2.44 (m, 4H, 2 × -CH₂NCH₃), 2.23 (s, 3H, -NCH₃). ¹³C NMR (151 MHz, DMSO) δ 152.1 (2-qC), 142.2 (8a-qC), 137.4 (3-CH), 134.8 (4a-qC), 130.2 (5-CH), 127.8 (8-CH), 127.1 (6-CH), 122.9 (7-qCBr), 54.2 (2 × -NCH₂), 45.7 (-NCH₃),

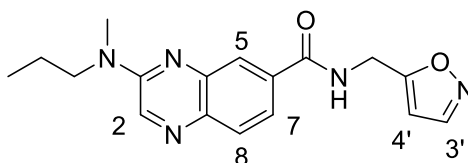
43.9 (2 × -CH₂NCH₃). LCMS (ESI⁺) *m/z* 307/309 [M+H]⁺, *t_R* = 0.85 min. HRMS (ESI⁺) [M+H]⁺ calcd. for C₁₃H₁₆BrN₄: 307.0558; found: 307.0559, error = 0.3 ppm.

3-(Ethyl(methyl)amino)-*N*-(isoxazol-5-ylmethyl)quinoxaline-6-carboxamide (141)



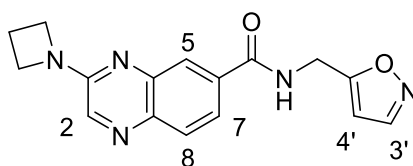
The reaction was carried out with 7-bromo-*N*-ethyl-*N*-methylquinoxalin-2-amine (**133**) (69 mg, 0.26 mmol) for 4 h according to general procedure G. The crude residue was dissolved in 1:1 CH₂Cl₂/MeOH (4 mL) and purified by ion-exchange chromatography on acidic resin (2 g), eluting with MeOH (3 × 10 mL) then 2 M NH₃ in MeOH (3 × 10 mL). The basic fractions were concentrated *in vacuo* and further purified by reverse phase silica chromatography eluting 5-90% MeOH in water (+0.1% formic acid), and fractions containing product were collected and evaporated *in vacuo*. The residue was further purified by normal phase silica chromatography eluting 20-100% EtOAc in cyclohexane, and fractions containing product were collected and evaporated *in vacuo* to afford 3-(ethyl(methyl)amino)-*N*-(isoxazol-5-ylmethyl)quinoxaline-6-carboxamide (**141**) (13 mg, 16%) as a pale yellow solid. ¹H NMR (600 MHz, DMSO-*d*₆) δ 9.37 (t, *J* = 5.8 Hz, 1H, -NH), 8.74 (s, 1H, 2-CH), 8.50 (d, *J* = 1.8 Hz, 1H, 3'-CH), 8.14 (d, *J* = 1.9 Hz, 1H, 5-CH), 7.87 (d, *J* = 8.5 Hz, 1H, 8-CH), 7.79 (dd, *J* = 8.5, 2.0 Hz, 1H, 7-CH), 6.39 (dd, *J* = 1.8, 0.9 Hz, 1H, 4'-CH), 4.65 (d, *J* = 5.7 Hz, 2H, -CH₂), 3.75 (q, *J* = 7.1 Hz, 2H, -NCH₂CH₃), 3.20 (s, 3H, -NCH₃), 1.18 (t, *J* = 7.1 Hz, 3H, -NCH₂CH₃). ¹³C NMR (151 MHz, DMSO) δ 169.4 (5'-qC), 166.0 (-C=O), 151.8 (3-qC), 150.9 (3'-CH), 141.0 (4a-qC), 137.8 (2-CH), 137.0 (8a-qC), 134.5 (6-qC), 128.5 (8-CH), 125.0 (5-CH), 122.1 (7-CH), 101.4 (4'-CH), 43.8 (-NCH₂CH₃), 35.2 (-CH₂), 35.0 (-NCH₃), 12.0 (-NCH₂CH₃). LCMS (ESI⁺) *m/z* 312 [M+H]⁺, *t_R* = 1.02 min. HRMS (ESI⁺) [M+H]⁺ calcd. for C₁₆H₁₈N₅O₂: 312.1460; found: 312.1467, error = 2.2 ppm, purity = 96.9%.

***N*-(Isoxazol-5-ylmethyl)-3-(methyl(propyl)amino)quinoxaline-6-carboxamide (142)**



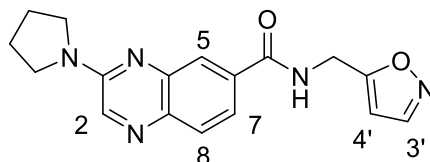
The reaction was carried out with 7-bromo-*N*-methyl-*N*-propylquinoxalin-2-amine (**134**) (73 mg, 0.26 mmol) for 3.5 h according to general procedure G. The crude residue was purified by normal phase silica chromatography eluting 0-100% EtOAc in cyclohexane, and fractions containing product were collected and evaporated *in vacuo* to afford *N*-(isoxazol-5-ylmethyl)-3-(methyl(propyl)amino)quinoxaline-6-carboxamide (**142**) (39 mg, 45%) as an orange gum. ¹H NMR (600 MHz, DMSO-*d*₆) δ 9.37 (t, *J* = 5.8 Hz, 1H, -NH), 8.75 (s, 1H, 2-CH), 8.50 (d, *J* = 1.8 Hz, 1H, 3'-CH), 8.13 (d, *J* = 1.9 Hz, 1H, 5-CH), 7.86 (d, *J* = 8.5 Hz, 1H, 8-CH), 7.79 (dd, *J* = 8.5, 2.0 Hz, 1H, 7-CH), 6.39 (dd, *J* = 1.8, 0.9 Hz, 1H, 4'-CH), 4.65 (d, *J* = 5.7 Hz, 2H, -CH₂), 3.69 – 3.63 (m, 2H, -NCH₂CH₂CH₃), 3.21 (s, 3H, -NCH₃), 1.69 – 1.60 (m, 2H, -NCH₂CH₂CH₃), 0.91 (t, *J* = 7.4 Hz, 3H, -NCH₂CH₂CH₃). ¹³C NMR (151 MHz, DMSO-*d*₆) δ 169.9 (5'-qC), 166.5 (-C=O), 152.5 (3-qC), 151.4 (3'-CH), 141.5 (4a-qC), 138.3 (2-CH), 137.5 (8a-qC), 135.0 (6-qC), 128.9 (8-CH), 125.4 (5-CH), 122.5 (7-CH), 101.9 (4'-CH), 51.2 (-NCH₂CH₂CH₃), 36.2 (-NCH₃), 35.7 (-CH₂), 20.6 (-NCH₂CH₂CH₃), 11.6 (-NCH₂CH₂CH₃). LCMS (ESI⁺) *m/z* 326 [M+H]⁺, *t*_R = 1.13 min. HRMS (ESI⁺) [M+H]⁺ calcd. for C₁₇H₂₀N₅O₂: 326.1617; found: 326.1602, error = -4.6 ppm, purity = 96.8%.

3-(Azetidin-1-yl)-*N*-(isoxazol-5-ylmethyl)quinoxaline-6-carboxamide (143)



The reaction was carried out with 2-(azetidin-1-yl)-7-bromoquinoxaline (**135**) (69 mg, 0.26 mmol) for 3.5 h according to general procedure G. The crude residue was purified by normal phase silica chromatography eluting 0-10% MeOH in CH₂Cl₂, and fractions containing product were collected and evaporated *in vacuo* to afford 3-(azetidin-1-yl)-*N*-(isoxazol-5-ylmethyl)quinoxaline-6-carboxamide (**143**) (33 mg, 40%) as an orange solid. ¹H NMR (600 MHz, DMSO-*d*₆) δ 9.35 (t, *J* = 5.8 Hz, 1H, -NH), 8.50 (d, *J* = 1.8 Hz, 1H, 3'-CH), 8.37 (s, 1H, 2-CH), 8.17 (d, *J* = 1.9 Hz, 1H, 5-CH), 7.88 (d, *J* = 8.5 Hz, 1H, 8-CH), 7.81 (dd, *J* = 8.5, 2.0 Hz, 1H, 7-CH), 6.39 (dd, *J* = 1.8, 0.9 Hz, 1H, 4'-CH), 4.65 (d, *J* = 5.7 Hz, 2H, -CH₂), 4.27 – 4.21 (m, 4H, 2 × -NCH₂), 2.48 – 2.40 (m, 2H, -NCH₂CH₂). ¹³C NMR (151 MHz, DMSO-*d*₆) δ 169.4 (5'-qC), 165.9 (-C=O), 153.1 (3-qC), 150.9 (3'-CH), 141.0 (4a-qC), 137.7 (2-CH), 137.6 (8a-qC), 134.6 (6-qC), 128.7 (8-CH), 124.9 (5-CH), 122.3 (7-CH), 101.4 (4'-CH), 50.4 (2 × -NCH₂), 35.2 (-CH₂), 16.4 (-NCH₂CH₂). LCMS (ESI⁺) *m/z* 310 [M+H]⁺, *t*_R = 0.89 min. HRMS (ESI⁺) [M+H]⁺ calcd. for C₁₆H₁₆N₅O₂: 310.1304; found: 310.1291, error = -4.2 ppm, purity = 96.9%.

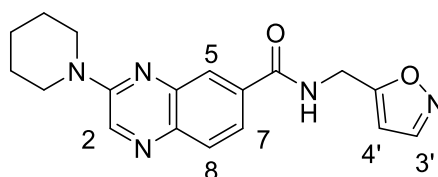
***N*-(Isoxazol-5-ylmethyl)-3-(pyrrolidin-1-yl)quinoxaline-6-carboxamide (144)**



The reaction was carried out with 7-bromo-2-(pyrrolidin-1-yl)quinoxaline (**136**) (72 mg, 0.26 mmol) for 3.5 h according to general procedure G. The crude residue was purified by normal phase silica chromatography eluting 20-100% EtOAc in cyclohexane, and fractions containing product were collected and evaporated *in vacuo* to afford *N*-(isoxazol-5-ylmethyl)-3-(pyrrolidin-1-yl)quinoxaline-6-carboxamide (**144**) (34 mg, 39%) as a yellow solid. ¹H NMR (600 MHz, DMSO-*d*₆) δ 9.37 (t, *J* = 5.8 Hz, 1H, -NH), 8.56 (s, 1H, 2-CH), 8.50 (d, *J* = 1.8 Hz, 1H, 3'-CH), 8.16 (d, *J* = 1.9 Hz, 1H, 5-CH), 7.87 (d, *J* = 8.5 Hz, 1H, 8-CH), 7.78 (dd, *J* = 8.5, 2.0 Hz, 1H, 7-CH), 6.39 (d, *J* = 1.8 Hz, 1H, 4'-CH), 4.65 (d, *J* = 5.7 Hz, 2H, -CH₂), 3.65 – 3.60 (m, 4H, 2 × -NCH₂), 2.04 – 1.97 (m, 4H, 2 × -NCH₂CH₂). ¹³C

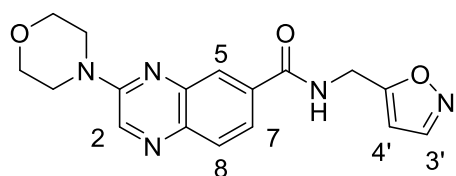
NMR (151 MHz, DMSO) δ 169.4 (5'-qC), 166.0 (-C=O), 150.9 (3'-CH), 150.6 (3-qC), 141.4 (4a-qC), 138.9 (2-CH), 137.3 (8a-qC), 134.5 (6-qC), 128.6 (8-CH), 124.9 (5-CH), 121.8 (7-CH), 101.4 (4'-CH), 46.4 (2 \times -NCH₂), 35.2 (-CH₂), 25.0 (2 \times -NCH₂CH₂, observed in HSQC only). LCMS (ESI⁺) m/z 324 [M+H]⁺, t_R = 0.97 min. HRMS (ESI⁺) [M+H]⁺ calcd. for C₁₇H₁₈N₅O₂: 324.1460; found: 324.1447, error = -4.0 ppm, purity = 97.4%.

***N*-(isoxazol-5-ylmethyl)-3-(piperidin-1-yl)quinoxaline-6-carboxamide (145)**



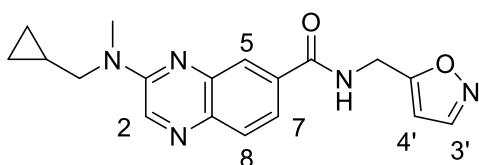
The reaction was carried out with 7-bromo-2-(piperidin-1-yl)quinoxaline (**137**) (76 mg, 0.26 mmol) for 2.5 h according to general procedure G. The crude residue was purified by normal phase silica chromatography eluting 20-100% EtOAc in cyclohexane, and fractions containing product were collected and evaporated *in vacuo* to afford *N*-(isoxazol-5-ylmethyl)-3-(piperidin-1-yl)quinoxaline-6-carboxamide (**145**) (26 mg, 29%) as a yellow solid. ¹H NMR (600 MHz, DMSO) δ 9.37 (t, J = 5.8 Hz, 1H, -NH), 8.89 (s, 1H, 2-CH), 8.50 (d, J = 1.8 Hz, 1H, 3'-CH), 8.13 (d, J = 1.9 Hz, 1H, 5-CH), 7.86 (d, J = 8.5 Hz, 1H, 8-CH), 7.80 (dd, J = 8.5, 1.9 Hz, 1H, 7-CH), 6.40 (dd, J = 1.9, 0.9 Hz, 1H, 4'-CH), 4.65 (d, J = 5.7 Hz, 2H, -CH₂), 3.82 – 3.78 (m, 4H, 2 \times -NCH₂), 1.71 – 1.64 (m, 2H, -NCH₂CH₂CH₂), 1.64 – 1.58 (m, 4H, 2 \times -NCH₂CH₂). ¹³C NMR (151 MHz, DMSO) δ 169.4 (5'-qC), 166.0 (-C=O), 152.2 (3-qC), 150.9 (3'-CH), 140.8 (4a-qC), 138.5 (2-CH), 137.2 (8a-qC), 134.6 (6-qC), 128.4 (8-CH), 125.0 (5-CH), 122.4 (7-CH), 101.4 (4'-CH), 45.1 (2 \times -NCH₂), 35.2 (-CH₂), 25.2 (2 \times -NCH₂CH₂), 24.1 (-NCH₂CH₂CH₂). LCMS (ESI⁺) m/z 338 [M+H]⁺, t_R = 1.17 min. HRMS (ESI⁺) [M+H]⁺ calcd. for C₁₈H₂₀N₅O₂: 338.1617; found: 338.1603, error = -4.14 ppm, purity = 97.8%.

***N*-(isoxazol-5-ylmethyl)-3-morpholinoquinoxaline-6-carboxamide (146)**



The reaction was carried out with 4-(7-bromoquinoxalin-2-yl)morpholine (**138**) (77 mg, 0.26 mmol) for 2 h according to general procedure G. The crude residue was purified by normal phase silica chromatography eluting 20-100% EtOAc in cyclohexane, and fractions containing product were collected and evaporated *in vacuo* to afford *N*-(isoxazol-5-ylmethyl)-3-morpholinoquinoxaline-6-carboxamide (**146**) (41 mg, 46%) as a yellow solid. ^1H NMR (600 MHz, DMSO- d_6) δ 9.39 (t, $J = 5.8$ Hz, 1H, -NH), 8.90 (s, 1H, 2-CH), 8.50 (d, $J = 1.8$ Hz, 1H, 3'-CH), 8.17 (d, $J = 1.9$ Hz, 1H, 5-CH), 7.91 (d, $J = 8.5$ Hz, 1H, 8-CH), 7.86 (dd, $J = 8.5, 2.0$ Hz, 1H, 7-CH), 6.40 (dd, $J = 1.8, 0.9$ Hz, 1H, 4'-CH), 4.66 (d, $J = 5.7$ Hz, 2H, -CH $_2$), 3.80 – 3.73 (m, 8H, 2 \times -NCH $_2$ and 2 \times -OCH $_2$). ^{13}C NMR (151 MHz, DMSO- d_6) δ 169.3 (5'-qC), 165.9 (-C=O), 152.5 (3-qC), 150.9 (3'-CH), 140.4 (4a-qC), 138.4 (2-CH), 137.6 (8a-qC), 134.7 (6-qC), 128.5 (8-CH), 125.3 (5-CH), 123.0 (7-CH), 101.4 (4'-CH), 65.9 (2 \times -OCH $_2$), 44.4 (2 \times -NCH $_2$), 35.2 (-CH $_2$). LCMS (ESI $^+$) m/z 340 [M+H] $^+$, $t_R = 0.97$ min. HRMS (ESI $^+$) [M+H] $^+$ calcd. for C $_{17}$ H $_{18}$ N $_5$ O $_3$: 340.1410; found: 340.1401, error = -2.6 ppm, purity = 99.1%.

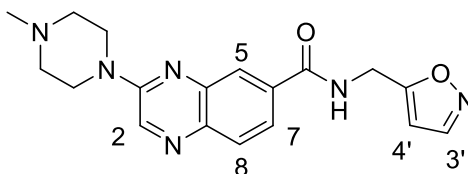
3-((Cyclopropylmethyl)(methyl)amino)-*N*-(isoxazol-5-ylmethyl)quinoxaline-6-carboxamide (**147**)



The reaction was carried out with 7-bromo-*N*-(cyclopropylmethyl)-*N*-methylquinoxalin-2-amine (**139**) (76 mg, 0.26 mmol) for 2 h according to general procedure G. The crude residue was purified by normal phase silica chromatography eluting 0-10% MeOH in CH $_2$ Cl $_2$, and fractions containing product were collected and evaporated *in vacuo*. The residue was further purified by reverse phase silica chromatography eluting 5-80% MeOH in water (+0.1%

formic acid), and fractions containing product were collected and evaporated *in vacuo* to afford 3-((cyclopropylmethyl)(methyl)amino)-*N*-(isoxazol-5-ylmethyl)quinoxaline-6-carboxamide (**147**) (36 mg, 40%) as a pearly yellow solid. ¹H NMR (600 MHz, DMSO-*d*₆) δ 9.38 (t, *J* = 5.8 Hz, 1H, -NH), 8.78 (s, 1H, 2-CH), 8.50 (d, *J* = 1.8 Hz, 1H, 3'-CH), 8.15 (d, *J* = 1.9 Hz, 1H, 5-CH), 7.87 (d, *J* = 8.5 Hz, 1H, 8-CH), 7.80 (dd, *J* = 8.5, 2.0 Hz, 1H, 7-CH), 6.39 (dd, *J* = 1.8, 0.9 Hz, 1H, 4'-CH), 4.66 (d, *J* = 5.7 Hz, 2H, -CH₂), 3.62 (d, *J* = 6.8 Hz, 2H, -NCH₂), 3.27 (s, 3H, -NCH₃), 1.18 – 1.08 (m, 1H, -NCH₂CH), 0.52 – 0.45 (m, 2H, -NCH₂CHCH₂), 0.38 – 0.32 (m, 2H, -NCH₂CHCH₂). ¹³C NMR (151 MHz, DMSO-*d*₆) δ 169.4 (5'-qC), 166.0 (-C=O), 152.1 (3-qC), 150.9 (3'-CH), 140.9 (4a-qC), 137.9 (2-CH), 137.1 (8a-qC), 134.6 (6-qC), 128.4 (8-CH), 125.0 (5-CH), 122.1 (7-CH), 101.4 (4'-CH), 53.0 (-NCH₂), 35.9 (-NCH₃), 35.2 (-CH₂), 9.3 (-NCH₂CH), 3.1 (2 × -NCH₂CHCH₂). LCMS (ESI⁺) *m/z* 338 [M+H]⁺, *t*_R = 1.32 min. HRMS (ESI⁺) [M+H]⁺ calcd. for C₁₈H₂₀N₅O₂: 338.1611; found: 338.1616, error = 1.43 ppm, purity = 98.4%.

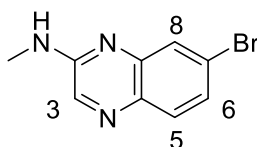
***N*-(isoxazol-5-ylmethyl)-3-(4-methylpiperazin-1-yl)quinoxaline-6-carboxamide (148)**



The reaction was carried out with 7-bromo-2-(4-methylpiperazin-1-yl)quinoxaline (**140**) (80 mg, 0.26 mmol) for 2 h according to general procedure G. The crude residue was purified by normal phase silica chromatography eluting 0-20% MeOH in CH₂Cl₂, and fractions containing product were collected and evaporated *in vacuo*. The residue was further purified by reverse phase silica chromatography eluting 5-80% MeOH in water (+0.1% formic acid), and fractions containing product were collected and evaporated *in vacuo* to afford *N*-(isoxazol-5-ylmethyl)-3-(4-methylpiperazin-1-yl)quinoxaline-6-carboxamide (**148**) (8 mg, 9%) (formic acid salt) as a pale yellow solid. ¹H NMR (600 MHz, DMSO-*d*₆) δ 9.38 (t, *J* = 5.8 Hz, 1H, -NH), 8.91 (s, 1H, 2-CH), 8.50 (d, *J* = 1.8 Hz, 1H, 3'-CH), 8.19

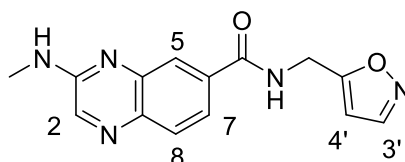
(s, 1H, -CHO, formic acid), 8.15 (d, $J = 1.9$ Hz, 1H, 5-CH), 7.89 (d, $J = 8.5$ Hz, 1H, 8-CH), 7.83 (dd, $J = 8.5, 1.9$ Hz, 1H, 7-CH), 6.40 (d, $J = 1.8$ Hz, 1H, 4'-CH), 4.66 (d, $J = 5.7$ Hz, 2H, -CH₂), 3.81 – 3.78 (m, 4H, 2 × -NCH₂), 2.48 – 2.43 (m, 4H, 2 × -CH₂NCH₃), 2.24 (s, 3H, -NCH₃). ¹³C NMR (151 MHz, DMSO) δ 169.4 (5'-qC), 166.0 (-C=O), 163.5 (-CHO, formic acid), 152.4 (3-qC), 150.9 (3'-CH), 140.5 (4a-qC), 138.5 (2-CH), 137.4 (8a-qC), 134.7 (6-qC), 128.5 (8-CH), 125.2 (5-CH), 122.8 (7-CH), 101.4 (4'-CH), 54.3 (2 × -CH₂NCH₃), 45.7 (-NCH₃), 44.0 (2 × -NCH₂), 35.2 (-CH₂). LCMS (ESI⁺) m/z 353 [M+H]⁺, $t_R = 0.60$ min. HRMS (ESI⁺) [M+H]⁺ calcd. for C₁₈H₂₁N₆O₂: 353.1726; found: 353.1726, error = -3.7 ppm, purity = 98.3%.

7-Bromo-*N*-methylquinoxalin-2-amine (149)



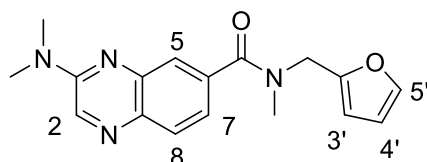
Methylamine (2 M in THF) (2.5 mL, 4.98 mmol) was added to a solution of 7-bromo-2-chloroquinoxaline (300 mg, 1.24 mmol) in DMF (2.5 mL, 0.50 M). The reaction was stirred at 80°C for 5 h, then cooled to rt and concentrated *in vacuo*. The crude residue was purified by normal phase silica chromatography eluting 0–35% EtOAc in cyclohexane. The fractions containing product were collected and evaporated *in vacuo* to afford 7-bromo-*N*-methylquinoxalin-2-amine (**149**) (231 mg, 78%) as a pale yellow solid. ¹H NMR (600 MHz, DMSO-*d*₆) δ 8.28 (s, 1H, 3-CH), 7.82 (q, $J = 5.1$ Hz, 1H, -NH), 7.72 (d, $J = 2.2$ Hz, 1H, 8-CH), 7.68 (d, $J = 8.6$ Hz, 1H, 5-CH), 7.42 (dd, $J = 8.6, 2.2$ Hz, 1H, 6-CH), 2.90 (d, $J = 4.8$ Hz, 3H, -NCH₃). ¹³C NMR (151 MHz, DMSO-*d*₆) δ 153.2 (2-qC), 143.1 (8a-qC), 140.6 (3-CH), 135.0 (4a-qC), 130.3 (5-CH), 127.6 (8-CH), 126.1 (6-CH), 122.5 (7-qCBr), 27.1 (-NCH₃). LCMS (ESI⁺) m/z 238/240 [M+H]⁺, $t_R = 1.23$ min. HRMS (ESI⁺) [M+H]⁺ calcd. for C₉H₉BrN₃: 237.9980; found: 237.9978, error = -0.8 ppm.

N-(Isoxazol-5-ylmethyl)-3-(methylamino)quinoxaline-6-carboxamide (150)



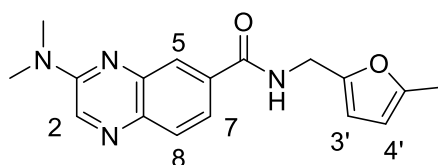
Isloxazol-5-ylmethanamine hydrochloride (25 mg, 0.19 mmol), 7-bromo-*N*-methylquinoxalin-2-amine (**149**) (44 mg, 0.19 mmol), Xantphos Palladacycle Gen.4 (9 mg, 0.009 mmol, 5 mol%) and K₂CO₃ (104 mg, 0.74 mmol) were added to a dry vial. The vial was sealed, evacuated and backfilled with nitrogen, evacuated once more, then 1,4-dioxane (0.37 mL, 0.50 M) was added. Lastly, the vial was fitted with a CO (g) balloon and the reaction was stirred at 80 °C for 3 h, cooled to rt and slowly vented. The reaction mixture was flushed with nitrogen, diluted with CH₂Cl₂ (10 mL), filtered through a pre-packed celite column, and the filtrate was concentrated *in vacuo*. The crude residue was purified by normal phase silica chromatography eluting 0-15% MeOH in CH₂Cl₂, and fractions containing product were collected and evaporated *in vacuo*. The residue was further purified by reverse phase silica chromatography eluting 5-80% MeOH in water (+0.1% formic acid), and fractions containing product were collected and evaporated *in vacuo* to afford *N*-(isoxazol-5-ylmethyl)-3-(methylamino)quinoxaline-6-carboxamide (**150**) (8 mg, 15%) as a yellow solid. ¹H NMR (600 MHz, DMSO) δ 9.35 (t, *J* = 5.8 Hz, 1H, -CONH), 8.49 (d, *J* = 1.8 Hz, 1H, 3'-CH), 8.34 (s, 1H, 2-CH), 8.14 (d, *J* = 1.9 Hz, 1H, 5-CH), 7.82 (d, *J* = 8.4 Hz, 1H, 8-CH), 7.78 (d, *J* = 4.9 Hz, 1H, -NH), 7.76 (dd, *J* = 8.4, 1.9 Hz, 1H, 7-CH), 6.41 – 6.37 (m, 1H, 4'-CH), 4.65 (d, *J* = 5.7 Hz, 2H, -CH₂), 2.92 (d, *J* = 4.8 Hz, 3H, -NCH₃). ¹³C NMR (151 MHz, DMSO) δ 169.4 (5'-qC), 166.0 (-C=O), 153.3 (3-qC), 150.9 (3'-CH), 141.4 (2-CH and 4a-qC), 137.6 (8a-qC), 134. (6-qC), 128.5 (8-CH), 124.8 (5-CH), 121.8 (7-CH), 101.4 (4'-CH), 35.2 (-CH₂), 27.2 (-NCH₃). LCMS (ESI⁺) *m/z* 284 [M+H]⁺, t_R = 0.79 min. HRMS (ESI⁺) [M+H]⁺ calcd. for C₁₄H₁₄N₅O₂: 284.1147; found: 284.1159, error = 4.2 ppm, purity = 99.5%

3-(Dimethylamino)-*N*-(furan-2-ylmethyl)-*N*-methylquinoxaline-6-carboxamide (151**)**



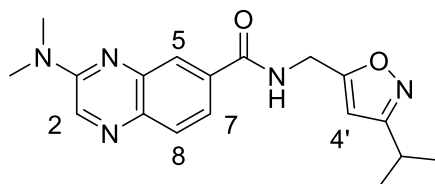
The reaction was carried out with 1-(furan-2-yl)-*N*-methylmethanamine (35 μ L, 0.30 mmol) for 8 h according to general procedure H. The crude residue was purified by normal phase silica chromatography eluting 20-100% EtOAc in cyclohexane, and fractions containing product were collected and evaporated *in vacuo*. The residue was further purified by reverse phase silica chromatography eluting 5-90% MeOH in water (+0.1% formic acid), and fractions containing product were collected and evaporated *in vacuo* to afford 3-(dimethylamino)-*N*-(furan-2-ylmethyl)-*N*-methylquinoxaline-6-carboxamide (**151**) (32 mg, 31%) as a pale yellow solid. ^1H NMR (600 MHz, $\text{DMSO-}d_6$) δ 8.73 (s, 1H, 2-CH), 7.86 (d, J = 8.3 Hz, 1H, 8-CH), 7.66 (d, J = 1.9 Hz, 1H, 5'-CH), 7.62 – 7.50 (m, 1H, 5-CH), 7.40 – 7.30 (m, 1H, 7-CH), 6.50 – 6.30 (m, 2H, 3'-CH and 4'-CH), 4.75 – 4.43 (m, 2H, -CH₂), 3.23 (s, 6H, 2 \times -NCH₃), 2.94 – 2.88 (m, 3H, -NCH₃). ^{13}C NMR (151 MHz, $\text{DMSO-}d_6$) δ 152.6 (3-qC), 150.4 (observed in HMBC, 2'-qC), 142.9 (observed in HSQC, 5'-CH), 140.9 (4a-qC), 137.4 (2-CH and 6-qC), 135.7 (8a-qC), 128.7 (8-CH), 123.8 (5-CH), 121.9 (7-CH), 110.6 (4'-CH), 108.4 (observed in HSQC, 3'-CH), 47.4+42.7 (observed in HSQC, -CH₂), 37.4 (2 \times -NCH₃), 36.6+32.2 (observed in HSQC, -CONCH₃) (1 \times qC missing, rotational isomers observed). LCMS (ESI⁺) m/z 311 [M+H]⁺, t_R = 1.14 min. HRMS (ESI⁺) [M+H]⁺ calcd. for C₁₇H₁₉N₄O₂: 311.1508; found: 311.1505, error = -1.0 ppm, purity = 95.8%.

3-(Dimethylamino)-*N*-((5-methylfuran-2-yl)methyl)quinoxaline-6-carboxamide (**152**)



The reaction was carried out with (5-methylfuran-2-yl)methanamine (32 μ L, 0.30 mmol) for 2 h according to general procedure H. The crude residue was purified by normal phase silica chromatography eluting 20-100% EtOAc in cyclohexane, and fractions containing product were collected and evaporated *in vacuo* to afford 3-(dimethylamino)-*N*-((5-methylfuran-2-yl)methyl)quinoxaline-6-carboxamide (**152**) (78 mg, 84%) as a pale yellow solid. ^1H NMR (600 MHz, DMSO) δ 9.14 (t, $J = 5.7$ Hz, 1H, -NH), 8.75 (s, 1H, 2-CH), 8.14 (d, $J = 1.9$ Hz, 1H, 5-CH), 7.85 (d, $J = 8.5$ Hz, 1H, 8-CH), 7.79 (dd, $J = 8.5, 1.9$ Hz, 1H, 7-CH), 6.15 (d, $J = 3.0$ Hz, 1H, 3'-CH), 5.99 (dd, $J = 3.0, 1.3$ Hz, 1H, 4'-CH), 4.43 (d, $J = 5.6$ Hz, 2H, -CH₂), 3.24 (s, 6H, 2 \times -NCH₃), 2.23 (d, $J = 1.1$ Hz, 3H, -CH₃). ^{13}C NMR (151 MHz, DMSO) δ 165.6 (-C=O), 152.5 (3-qC), 150.5 (2'-qC and 5'-qC), 140.9 (4a-qC), 137.8 (2-CH), 136.9 (8a-qC), 135.0 (6-qC), 128.4 (8-CH), 124.9 (5-CH), 122.2 (7-CH), 107.7 (3'-CH), 106.4 (4'-CH), 37.4 (2 \times -NCH₃), 36.2 (-CH₂), 13.3 (-CH₃). LCMS (ESI⁺) m/z 311 [M+H]⁺, $t_{\text{R}} = 1.17$ min. HRMS (ESI⁺) [M+H]⁺ calcd. for C₁₇H₁₉N₄O₂: 311.1508; found: 311.1505, error = -1.0 ppm, purity = 100%.

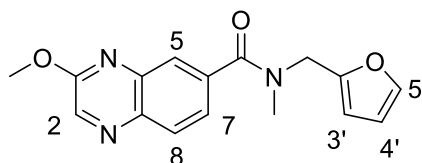
3-(Dimethylamino)-*N*-((3-isopropylisoxazol-5-yl)methyl)quinoxaline-6-carboxamide (**153**)



The reaction was carried out with (3-isopropylisoxazol-5-yl)methanamine (24 mg, 0.30 mmol) for 4 h according to general procedure H. The crude residue was purified by normal phase silica chromatography eluting 20-100% EtOAc in cyclohexane, and fractions containing product were collected and evaporated *in vacuo* to afford 3-(dimethylamino)-*N*-((3-isopropylisoxazol-5-yl)methyl)quinoxaline-6-carboxamide (**153**) (47 mg, 44%) as a yellow solid. ^1H NMR (600 MHz, DMSO) δ 9.35 (t, $J = 5.8$ Hz, 1H, -NH), 8.76 (s, 1H, 2-CH), 8.16 (d, $J = 1.9$ Hz, 1H, 5-CH), 7.88 (d, $J = 8.5$ Hz, 1H, 8-CH), 7.80 (dd, $J = 8.5, 2.0$ Hz, 1H, 7-CH), 6.34 (s, 1H, 4'-CH), 4.61 – 4.57 (m, 2H, -CH₂), 3.24 (s, 6H, 2 \times -NCH₃), 2.96 (*app* p, $J = 6.9$ Hz, 1H, -CH), 1.20 (d, $J = 6.9$ Hz, 6H, 2 \times -CH₃). ^{13}C

NMR (151 MHz, DMSO) δ 169.7 (5'-qC), 168.9 (3'-qC), 166.0 (-C=O), 152.5 (3-qC), 140.9 (4a-qC), 137.9 (2-CH), 137.0 (8a-qC), 134.6 (6-qC), 128.5 (8-CH), 125.0 (5-CH), 122.2 (7-CH), 100.1 (4'-CH), 37.4 (2 \times -NCH₃), 35.4 (-CH₂), 25.9 (-CH), 21.5 (2 \times -CH₃). LCMS (ESI⁺) m/z 340 [M+H]⁺, t_R = 1.16 min. HRMS (ESI⁺) [M+H]⁺ calcd. for C₁₈H₂₂N₅O₂: 340.1773; found: 340.1772, error = -0.3 ppm, purity = 95.2%.

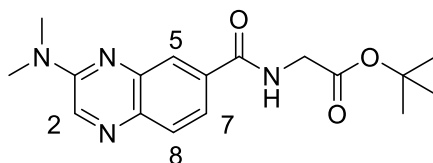
***N*-(Furan-2-ylmethyl)-3-methoxy-*N*-methylquinoxaline-6-carboxamide (154)**



7-bromo-2-methoxyquinoxaline (**108**) (75 mg, 0.31 mmol), 1-(furan-2-yl)-*N*-methylmethanamine (36 μ L, 0.31 mmol) and Xantphos Palladacycle Gen.4 (15 mg, 0.016 mmol, 5 mol%) were added to a dry vial. The vial was sealed, evacuated and backfilled with nitrogen, evacuated once more, then 1,4-dioxane (0.63 mL, 0.50 M) and DIPEA (0.16 mL, 0.94 mmol) were added. Lastly, the vial was fitted with a CO (g) balloon and the reaction was stirred at 80 °C for 8 h, cooled to rt and slowly vented. The reaction mixture was flushed with nitrogen, diluted with CH₂Cl₂ (10 mL), filtered through a pre-packed celite column, and the filtrate was concentrated *in vacuo*. The crude residue was purified by normal phase silica chromatography eluting 20-100% EtOAc in cyclohexane, and fractions containing product were collected and evaporated *in vacuo*. The residue was further purified by reverse phase silica chromatography eluting 5-90% MeOH in water (+0.1% formic acid), and fractions containing product were collected and evaporated *in vacuo* to afford *N*-(furan-2-ylmethyl)-3-methoxy-*N*-methylquinoxaline-6-carboxamide (**154**) (28 mg, 30%) as a yellow solid. ¹H NMR (600 MHz, DMSO-*d*₆) δ 8.65 (s, 1H, -NH), 8.07 (d, J = 8.4 Hz, 1H, 8-CH), 7.90 – 7.80 (m, 1H, 7-CH), 7.68 – 7.61 (m, 2H, 5-CH and 5'-CH), 6.48 – 6.35 (m, 2H, 3'-CH and 4'-CH), 4.76 – 4.40 (m, 2H, -CH₂), 4.05 (s, 3H, -OCH₃), 2.97 – 2.88 (m, 3H, -NCH₃). ¹³C NMR (151 MHz, DMSO) δ 169.8 – 169.0 (m, -C=O), 157.9 (3-qC), 150.5 – 149.9 (m, 2'-qC), 143.3 – 142.8 (m, 5'-CH), 141.0 (2-CH), 139.2 (4a-

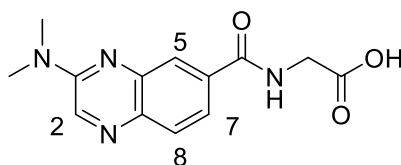
qC), 138.4 (8a-qC), 137.9 (6-qC), 129.2 (8-CH), 125.3 (5-CH), 125.0 (7-CH), 110.6 (4'-CH), 108.7 – 108.4 (m, 3'-CH), 53.8 (-OCH₃), 47.6 – 43.0 (m, -CH₂), 36.9 – 32.2 (m, -NCH₃) (rotational isomers observed). LCMS (ESI⁺) *m/z* 298 [M+H]⁺, *t_R* = 1.19 min. HRMS (ESI⁺) [M+H]⁺ calcd. for C₁₆H₁₆N₃O₃: 298.1191; found: 298.1198, error = 2.3 ppm, purity = 98.8%.

***tert*-Butyl (3-(dimethylamino)quinoxaline-6-carbonyl)glycinate (161)**



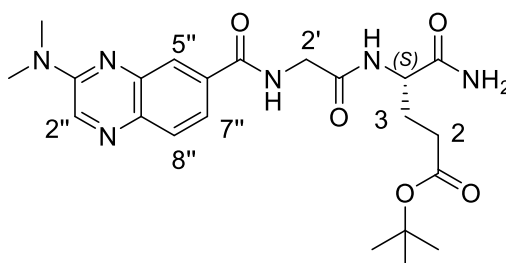
7-Bromo-*N,N*-dimethylquinoxalin-2-amine (**114**) (116 mg, 0.46 mmol), *tert*-butyl glycinate hydrochloride (77 mg, 0.46 mmol) and Xantphos Palladacycle Gen.4 (22 mg, 0.023 mmol, 5 mol%) were added to a dry vial. The vial was sealed, evacuated and backfilled with nitrogen, evacuated once more, then 1,4-dioxane (0.92 mL, 0.50 M) and DIPEA (0.32 mL, 1.84 mmol) were added. Lastly, the vial was fitted with a CO (g) balloon and the reaction was stirred at 80 °C for 12 h, cooled to rt and slowly vented. The reaction mixture was flushed with nitrogen, diluted with CH₂Cl₂ (20 mL), filtered through a pre-packed celite column, and the filtrate was concentrated *in vacuo*. The crude residue was purified by normal phase silica chromatography eluting 20-100% EtOAc in cyclohexane, and fractions containing product were collected and evaporated *in vacuo* to afford *tert*-butyl (3-(dimethylamino)quinoxaline-6-carbonyl)glycinate (**161**) (91 mg, 60%) as a yellow solid. ¹H NMR (600 MHz, DMSO) δ 9.05 (t, *J* = 5.9 Hz, 1H, -NH), 8.76 (s, 1H, 2-CH), 8.13 (d, *J* = 1.9 Hz, 1H, 5-CH), 7.87 (d, *J* = 8.5 Hz, 1H, 8-CH), 7.78 (dd, *J* = 8.5, 2.0 Hz, 1H, 7-CH), 3.92 (d, *J* = 5.9 Hz, 2H, -CH₂), 3.25 (s, 6H, 2 × -NCH₃), 1.43 (s, 9H, 3 × -CH₃). ¹³C NMR (151 MHz, DMSO) δ 169.0 (-C=O), 166.2 (-NHC=O), 152.6 (3-qC), 140.9 (4a-qC), 137.9 (2-CH), 137.0 (8a-qC), 134.7 (6-qC), 128.5 (8-CH), 124.9 (5-CH), 122.0 (7-CH), 80.7 (-qCCH₃), 42.0 (-CH₂), 37.4 (2 × -NCH₃), 27.8 (3 × -CH₃). LCMS (ESI⁺) *m/z* 331 [M+H]⁺, *t_R* = 1.32 min. HRMS (ESI⁺) [M+H]⁺ calcd. for C₁₇H₂₃N₄O₃: 331.1770; found: 331.1763, error = -2.1 ppm, purity = 100%.

(3-(Dimethylamino)quinoxaline-6-carbonyl)glycine (**162**)



Formic acid (0.94 mL, 25 mmol) was added to a solution of *tert*-butyl (3-(dimethylamino)quinoxaline-6-carbonyl)glycinate (**161**) (82 mg, 0.25 mmol) in CH₂Cl₂ (1.2 mL, 0.2 M). The reaction was stirred at 40 °C for 43 h, then concentrated *in vacuo* and the crude residue was purified by reverse phase silica chromatography eluting 5-80% MeOH in water (+0.1% formic acid). The fractions containing product were collected and evaporated *in vacuo* to afford (3-(dimethylamino)quinoxaline-6-carbonyl)glycine (**162**) (59 mg, 87%) as a yellow solid. ¹H NMR (600 MHz, DMSO) δ 12.58 (s, 1H, -COOH), 9.05 (t, *J* = 5.9 Hz, 1H, -NH), 8.76 (s, 1H, 2-CH), 8.14 (d, *J* = 1.9 Hz, 1H, 5-CH), 7.88 (d, *J* = 8.5 Hz, 1H, 8-CH), 7.78 (dd, *J* = 8.5, 1.9 Hz, 1H, 7-CH), 3.95 (d, *J* = 5.8 Hz, 2H, -CH₂), 3.25 (s, 6H, 2 × -NCH₃). ¹³C NMR (151 MHz, DMSO) δ 171.3 (-C=O), 166.1 (-NHC=O), 152.6 (3-qC), 140.9 (4a-qC), 137.9 (2-CH), 137.0 (8a-qC), 134.8 (6-qC), 128.5 (8-CH), 125.0 (5-CH), 122.1 (7-CH), 41.3 (-CH₂), 37.4 (2 × -NCH₃). LCMS (ESI⁺) *m/z* 275 [M+H]⁺, *t_R* = 0.78 min. HRMS (ESI⁺) [M+H]⁺ calcd. for C₁₃H₁₅N₄O₃: 275.1144; found: 275.1139, error = -1.8 ppm.

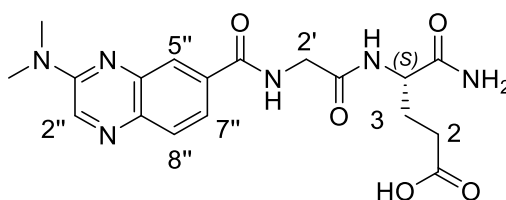
tert-Butyl (S)-5-amino-4-(2-(3-(dimethylamino)quinoxaline-6-carboxamido)acetamido)-5-oxopentanoate (**164**)



HATU (193 mg, 0.51 mmol) was added to a solution of (3-(dimethylamino)quinoxaline-6-carbonyl)glycine (**162**) (93 mg, 0.34 mmol), *tert*-

butyl (*S*)-4,5-diamino-5-oxopentanoate hydrochloride (81 mg, 0.34 mmol) and DIPEA (0.24 mL, 1.36 mmol) in DMF (3.4 mL, 0.10 M). The reaction was stirred at rt for 3 h and then concentrated *in vacuo* using a Biotage V-10 evaporator. The crude residue was purified by reverse phase silica chromatography eluting 5-90% MeOH in water (+0.1% formic acid), and fractions containing product were collected and evaporated *in vacuo* to afford *tert*-butyl (*S*)-5-amino-4-(2-(3-(dimethylamino)quinoxaline-6-carboxamido)acetamido)-5-oxopentanoate (**164**) (109 mg, 70%) as a yellow solid. ¹H NMR (600 MHz, DMSO) δ 8.99 (t, *J* = 5.8 Hz, 1H, 2'-CH₂NH), 8.76 (s, 1H, 2''-CH), 8.16 (d, *J* = 1.9 Hz, 1H, 5''-CH), 8.05 (d, *J* = 8.2 Hz, 1H, 4-CHNH), 7.87 (d, *J* = 8.5 Hz, 1H, 8''-CH), 7.78 (dd, *J* = 8.5, 2.0 Hz, 1H, 7''-CH), 7.35 – 7.32 (m, 1H, 5-CONH), 7.14 – 7.11 (m, 1H, 5-CONH), 4.22 (app td, *J* = 8.5, 4.9 Hz, 1H, 4-CH), 3.98 – 3.88 (m, 2H, 2'-CH₂), 3.25 (s, 6H, 2 × -NCH₃), 2.28 – 2.16 (m, 2H, 2-CH₂), 1.95 (dddd, *J* = 14.2, 9.5, 6.8, 4.9 Hz, 1H, 3-CH), 1.73 (app dtd, *J* = 13.6, 9.1, 6.4 Hz, 1H, 3-CH), 1.38 (s, 9H, 3 × -CH₃). ¹³C NMR (151 MHz, DMSO-*d*₆) δ 173.0 (5-CONH₂), 171.7 (-COO), 168.9 (4-NHC=O), 166.3 (6''-C=O), 152.5 (3''-qC), 140.9 (4''a-qC), 137.8 (2''-CH), 137.0 (8''a-qC), 134.9 (6''-qC), 128.4 (8''-CH), 125.1 (5''-CH), 122.2 (7''-CH), 79.7 (-qCCH₃), 51.6 (4-CH), 43.0 (2'-CH₂), 37.4 (2 × -NCH₃), 31.3 (2-CH₂), 27.7 (3 × -CH₃), 27.2 (3-CH₂). LCMS (ESI⁺) *m/z* 459 [M+H]⁺, *t*_R = 1.09 min. HRMS (ESI⁺) [M+H]⁺ calcd. for C₂₂H₃₁N₆O₅: 459.2356; found: 459.2348, error = -1.7 ppm, purity = 95.7%.

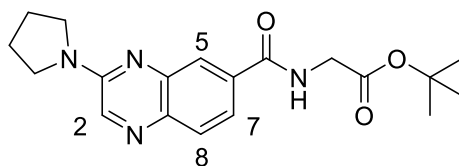
(*S*)-5-Amino-4-(2-(3-(dimethylamino)quinoxaline-6-carboxamido)acetamido)-5-oxopentanoic acid (118)



Trifluoroacetic acid (10 mL, 0.01 M) was added dropwise to a solution of *tert*-butyl (*S*)-5-amino-4-(2-(3-(dimethylamino)quinoxaline-6-carboxamido)acetamido)-5-oxopentanoate (**164**) (104 mg, 0.23 mmol) in CH₂Cl₂ (10 mL, 0.01 M) at 0 °C. The reaction was stirred at 0 °C for 2 h, then concentrated *in vacuo* and the crude

residue was purified by reverse phase silica chromatography eluting 5-80% MeOH in water (+0.1% formic acid). The fractions containing product were collected and evaporated *in vacuo*, then 20% MeCN in water (10 mL) was added and the product was lyophilised to afford (*S*)-5-amino-4-(2-(3-(dimethylamino)quinoxaline-6-carboxamido)acetamido)-5-oxopentanoic acid (**118**) (55 mg, 60%) as a yellow solid. ¹H NMR (600 MHz, DMSO-*d*₆) δ 12.09 (s, 1H, -COOH), 8.98 (t, *J* = 5.8 Hz, 1H, 2'-CH₂NH), 8.76 (s, 1H, 2''-CH), 8.16 (d, *J* = 1.9 Hz, 1H, 5''-CH), 8.06 (d, *J* = 8.2 Hz, 1H, 4-CHNH), 7.87 (d, *J* = 8.5 Hz, 1H, 8''-CH), 7.79 (dd, *J* = 8.5, 1.9 Hz, 1H, 7''-CH), 7.34 (d, *J* = 2.2 Hz, 1H, 5-CONH), 7.12 (d, *J* = 2.1 Hz, 1H, 5-CONH), 4.23 (app td, *J* = 8.5, 4.9 Hz, 1H, 4-CH), 3.99 – 3.88 (m, 2H, 2'-CH₂), 3.25 (s, 6H, 2 × -NCH₃), 2.24 (ddd, *J* = 9.3, 6.5, 3.1 Hz, 2H, 2-CH₂), 1.97 (dddd, *J* = 14.0, 9.2, 6.9, 5.0 Hz, 1H, 3-CH), 1.74 (app dtd, *J* = 13.6, 8.9, 6.5 Hz, 1H, 3-CH). ¹³C NMR (151 MHz, DMSO) δ 174.0 (-COOH), 173.1 (5-CONH₂), 168.9 (4-NHC=O), 166.3 (6''-C=O), 152.5 (3''-qC), 140.8 (4''a-qC), 137.8 (2''-CH), 136.9 (8''a-qC), 134.9 (6''-qC), 128.4 (8''-CH), 125.1 (5''-CH), 122.2 (7''-CH), 51.7 (4-CH), 42.9 (2'-CH₂), 37.4 (2 × -NCH₃), 30.2 (2-CH₂), 27.2 (3-CH₂). LCMS (ESI⁺) *m/z* 403 [M+H]⁺, *t*_R = 0.72 min. HRMS (ESI⁺) [M+H]⁺ calcd. for C₁₈H₂₃N₆O₅: 403.1730; found: 403.1723, error = -1.7 ppm, purity = 99.1%.

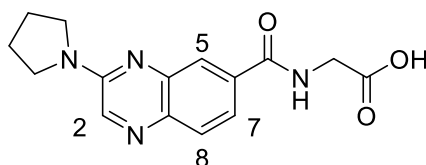
***tert*-Butyl (3-(pyrrolidin-1-yl)quinoxaline-6-carbonyl)glycinate (165)**



7-bromo-2-(pyrrolidin-1-yl)quinoxaline (**136**) (80 mg, 0.29 mmol), *tert*-butyl glycinate hydrochloride (48 mg, 0.29 mmol) and Xantphos Palladacycle Gen.4 (14 mg, 0.014 mmol, 5 mol%) were added to a dry vial. The vial was sealed, evacuated and backfilled with nitrogen, evacuated once more, then 1,4-dioxane (0.58 mL, 0.50 M) and DIPEA (0.20 mL, 1.15 mmol) were added. Lastly, the vial was fitted with a CO (g) balloon and the reaction was stirred at 80 °C for 3.5 h, cooled to rt and slowly vented. The reaction mixture was flushed with nitrogen, diluted with CH₂Cl₂ (20 mL), filtered through a pre-packed celite column, and the

filtrate was concentrated *in vacuo*. The crude residue was purified by normal phase silica chromatography eluting 20-100% EtOAc in cyclohexane, and fractions containing product were collected and evaporated *in vacuo* to afford *tert*-butyl (3-(pyrrolidin-1-yl)quinoxaline-6-carbonyl)glycinate (**165**) (83 mg, 78%) as a yellow solid. ¹H NMR (600 MHz, DMSO) δ 9.05 (t, *J* = 5.9 Hz, 1H, -NH), 8.55 (s, 1H, 2-CH), 8.14 (d, *J* = 1.9 Hz, 1H, 5-CH), 7.87 (d, *J* = 8.4 Hz, 1H, 8-CH), 7.76 (dd, *J* = 8.5, 2.0 Hz, 1H, 7-CH), 3.92 (d, *J* = 5.9 Hz, 2H, -CH₂), 3.66 – 3.61 (m, 4H, 2 × -NCH₂), 2.03 – 1.97 (m, 4H, 2 × -NCH₂CH₂), 1.43 (s, 9H, 3 × -CH₃). ¹³C NMR (151 MHz, DMSO) δ 169.0 (-C=O), 166.2 (-NHC=O), 150.6 (3-qC), 141.4 (4a-qC), 138.9 (2-CH), 137.3 (8a-qC), 134.7 (6-qC), 128.6 (8-CH), 124.8 (5-CH), 121.7 (7-CH), 80.7 (-qCCH₃), 46.4 (2 × -NCH₂), 42.0 (-CH₂), 27.8 (3 × -CH₃), 24.6 (2 × -NCH₂CH₂, observed in HSQC only). LCMS (ESI⁺) *m/z* 357 [M+H]⁺, *t_R* = 1.18 min. HRMS (ESI⁺) [M+H]⁺ calcd. for C₁₉H₂₅N₄O₃: 357.1927; found: 357.1909, error = -5.0 ppm, purity = 95.8%.

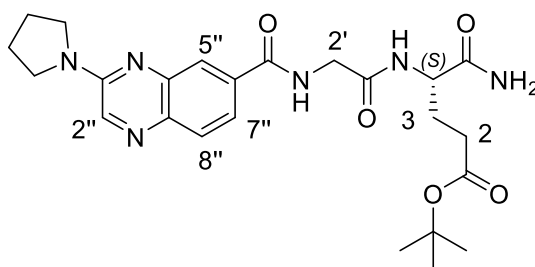
(3-(Pyrrolidin-1-yl)quinoxaline-6-carbonyl)glycine (**166**)



Formic acid (0.76 mL, 20 mmol) was added to a solution of *tert*-butyl (3-(pyrrolidin-1-yl)quinoxaline-6-carbonyl)glycinate (**165**) (72 mg, 0.20 mmol) in CH₂Cl₂ (1.0 mL, 0.2 M). The reaction was stirred at 40 °C for 96 h, then concentrated *in vacuo* and the crude residue was purified by reverse phase silica chromatography eluting 5-80% MeOH in water (+0.1% formic acid). The fractions containing product were collected and evaporated *in vacuo* to afford (3-(pyrrolidin-1-yl)quinoxaline-6-carbonyl)glycine (**166**) (51 mg, 81%) as a yellow solid. ¹H NMR (600 MHz, DMSO) δ 12.62 (s, 1H, -COOH), 9.01 (t, *J* = 5.9 Hz, 1H, -NH), 8.55 (s, 1H, 2-CH), 8.14 (d, *J* = 1.9 Hz, 1H, 5-CH), 7.87 (d, *J* = 8.4 Hz, 1H, 8-CH), 7.76 (dd, *J* = 8.5, 2.0 Hz, 1H, 7-CH), 3.93 (d, *J* = 5.8 Hz, 2H, -CH₂), 3.66 – 3.61 (m, 4H, 2 × -NCH₂), 2.03 – 1.99 (m, 4H, 2 × -NCH₂CH₂). ¹³C NMR (151 MHz, DMSO) δ 171.2 (-C=O), 166.1 (-NHC=O), 150.6 (3-qC), 141.4 (4a-

qC), 138.9 (2-CH), 137.2 (8a-qC), 134.7 (6-qC), 128.6 (8-CH), 124.8 (5-CH), 121.7 (7-CH), 46.4 (2 × -NCH₂), 41.4 (-CH₂), 24.7 (2 × -NCH₂CH₂, observed in HSQC only). LCMS (ESI⁺) *m/z* 301 [M+H]⁺, *t_R* = 0.80 min. HRMS (ESI⁺) [M+H]⁺ calcd. for C₁₅H₁₇N₄O₃: 301.1301; found: 301.1306, error = 1.7 ppm, purity = 96.2%.

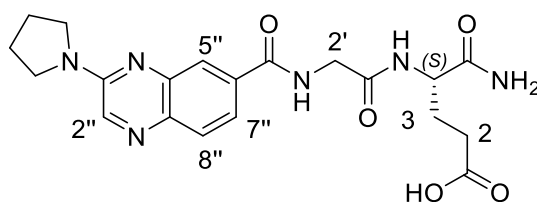
***tert*-Butyl (S)-5-amino-5-oxo-4-(2-(3-(pyrrolidin-1-yl)quinoxaline-6-carboxamido)acetamido)pentanoate (167)**



HATU (112 mg, 0.29 mmol) was added to a solution of (3-(pyrrolidin-1-yl)quinoxaline-6-carbonyl)glycine (**166**) (59 mg, 0.20 mmol), *tert*-butyl (S)-4,5-diamino-5-oxopentanoate hydrochloride (47 mg, 0.20 mmol) and DIPEA (0.14 mL, 1.02 mmol) in DMF (2.0 mL, 0.10 M). The reaction was stirred at rt for 22 h and then concentrated *in vacuo* using a Biotage V-10 evaporator. The crude residue was purified by reverse phase silica chromatography eluting 5-90% MeOH in water (+0.1% formic acid), and fractions containing product were collected and evaporated *in vacuo* to afford *tert*-butyl (S)-5-amino-5-oxo-4-(2-(3-(pyrrolidin-1-yl)quinoxaline-6-carboxamido)acetamido)pentanoate (**167**) (64 mg, 66%) as a yellow solid. ¹H NMR (600 MHz, DMSO) δ 8.98 (t, *J* = 5.8 Hz, 1H, 2'-CH₂NH), 8.55 (s, 1H, 2''-CH), 8.16 (d, *J* = 1.9 Hz, 1H, 5''-CH), 8.05 (d, *J* = 8.2 Hz, 1H, 4-CHNH), 7.86 (d, *J* = 8.5 Hz, 1H, 8''-CH), 7.76 (dd, *J* = 8.5, 1.9 Hz, 1H, 7''-CH), 7.33 (d, *J* = 2.1 Hz, 1H, 5-CONH), 7.13 (d, *J* = 2.0 Hz, 1H, 5-CONH), 4.22 (app td, *J* = 8.5, 4.9 Hz, 1H, 4-CH), 3.98 – 3.88 (m, 2H, 2'-CH₂), 3.63 (d, *J* = 6.5 Hz, 4H, 2 × -NCH₂), 2.26 – 2.16 (m, 2H, 2-CH₂), 2.00 (d, *J* = 6.4 Hz, 4H, 2 × -NCH₂CH₂), 1.98 – 1.90 (m, 1H, 3-CH), 1.73 (app dtd, *J* = 13.7, 9.0, 6.3 Hz, 1H, 3-CH), 1.38 (s, 9H, 3 × -CH₃). ¹³C NMR (151 MHz, DMSO-*d*₆) δ 173.1 (5-CONH₂), 171.7 (-COO), 168.9 (4-NHC=O), 166.4 (6''-C=O), 150.6 (3''-qC), 141.4 (4''a-qC), 138.8 (2''-CH), 137.2 (8''a-qC), 134.8 (6''-qC), 128.5 (8''-CH), 125.0 (5''-CH),

121.8 (7''-CH), 79.7 (-qCCH₃), 51.6 (4-CH), 46.4 (2 × -NCH₂), 43.0 (2'-CH₂), 31.3 (2-CH₂), 27.7 (3 × -CH₃), 27.2 (3-CH₂), 24.7 (2 × -NCH₂CH₂, observed in HSQC only). LCMS (ESI⁺) *m/z* 485 [M+H]⁺, *t_R* = 1.14 min. HRMS (ESI⁺) [M+H]⁺ calcd. for C₂₄H₃₃N₆O₅: 485.2512; found: 485.2495, error = -3.5 ppm, purity = 97.8%.

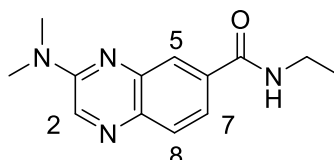
(S)-5-Amino-5-oxo-4-(2-(3-(pyrrolidin-1-yl)quinoxaline-6-carboxamido)acetamido)pentanoic acid (159)



Trifluoroacetic acid (10 mL, 0.006 M) was added dropwise to a solution of *tert*-butyl (S)-5-amino-5-oxo-4-(2-(3-(pyrrolidin-1-yl)quinoxaline-6-carboxamido)acetamido)pentanoate (**167**) (56 mg, 0.12 mmol) in CH₂Cl₂ (10 mL, 0.006 M) at 0 °C. The reaction was stirred at 0 °C for 1 h, then concentrated *in vacuo* and the crude residue was purified by reverse phase silica chromatography eluting 5-80% MeOH in water (+0.1% formic acid). The fractions containing product were collected and evaporated *in vacuo*, then 20% MeCN in water (10 mL) was added and the product was lyophilised to afford (S)-5-amino-5-oxo-4-(2-(3-(pyrrolidin-1-yl)quinoxaline-6-carboxamido)acetamido)pentanoic acid (**159**) (16 mg, 32%) as a yellow solid. ¹H NMR (600 MHz, DMSO-*d*₆) δ 12.10 (s, 1H, -COOH), 8.98 (t, *J* = 5.8 Hz, 1H, 2'-CH₂NH), 8.55 (s, 1H, 2''-CH), 8.16 (d, *J* = 1.9 Hz, 1H, 5''-CH), 8.08 (d, *J* = 8.2 Hz, 1H, 4-CHNH), 7.86 (d, *J* = 8.5 Hz, 1H, 8''-CH), 7.77 (dd, *J* = 8.5, 2.0 Hz, 1H, 7''-CH), 7.35 – 7.32 (m, 1H, 5-CONH), 7.13 – 7.10 (m, 1H, 5-CONH), 4.23 (app td, *J* = 8.5, 4.9 Hz, 1H, 4-CH), 3.99 – 3.88 (m, 2H, 2'-CH₂), 3.66 – 3.61 (m, 4H, 2 × -NCH₂), 2.24 (ddd, *J* = 9.2, 6.6, 3.0 Hz, 2H, 2-CH₂), 2.03 – 1.99 (m, 4H, 2 × -NCH₂CH₂), 1.99 – 1.93 (m, 1H, 3-CH), 1.74 (app dtd, *J* = 13.6, 8.9, 6.5 Hz, 1H, 3-CH). ¹³C NMR (151 MHz, DMSO-*d*₆) δ 174.0 (-COOH), 173.1 (5-CONH₂), 168.9 (4-NHC=O), 166.4 (6''-C=O), 150.6 (3''-qC), 141.4 (4''a-qC), 138.8 (2''-CH), 137.2 (8''a-qC), 134.8 (6''-qC), 128.5 (8''-CH), 124.9 (5''-CH), 121.9 (7''-CH), 51.7 (4-CH), 46.4 (2 × -NCH₂), 42.9 (2'-CH₂), 30.2 (2-CH₂), 27.2 (3-CH₂), 24.8 (2 × -NCH₂CH₂, observed in HSQC only). LCMS

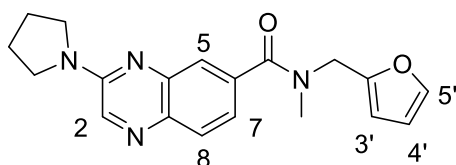
(ESI⁺) *m/z* 429 [M+H]⁺, *t_R* = 0.76 min. HRMS (ESI⁺) [M+H]⁺ calcd. for C₂₀H₂₅N₆O₅: 429.1886; found: 429.1873, error = -3.0 ppm, purity = 99.4%.

3-(Dimethylamino)-*N*-ethylquinoxaline-6-carboxamide (**168**)



The reaction was carried out with ethanamine hydrochloride (24 mg, 0.30 mmol) and an additional equivalent of DIPEA (0.21 mL, 1.19 mmol) for 3.5 h according to general procedure H. The crude residue was purified by normal phase silica chromatography eluting 20-100% EtOAc in cyclohexane, and fractions containing product were collected and evaporated *in vacuo* to afford 3-(dimethylamino)-*N*-ethylquinoxaline-6-carboxamide (**168**) (49 mg, 67%) as a yellow solid. ¹H NMR (600 MHz, DMSO) δ 8.74 (s, 1H, 2-CH), 8.67 (t, *J* = 5.6 Hz, 1H, -NH), 8.10 (d, *J* = 1.9 Hz, 1H, 5-CH), 7.85 (d, *J* = 8.5 Hz, 1H, 8-CH), 7.77 (dd, *J* = 8.5, 1.9 Hz, 1H, 7-CH), 3.35 – 3.28 (m, 2H, -NCH₂), 3.24 (s, 6H, 2 × -NCH₃), 1.15 (t, *J* = 7.2 Hz, 3H, -NCH₂CH₃). ¹³C NMR (151 MHz, DMSO) δ 165.5 (-C=O), 152.5 (3-qC), 140.8 (4a-qC), 137.6 (2-CH), 136.8 (8a-qC), 135.6 (6-qC), 128.3 (8-CH), 124.6 (5-CH), 122.2 (7-CH), 37.4 (2 × -NCH₃), 34.2 (-NCH₂), 14.7 (-NCH₂CH₃). LCMS (ESI⁺) *m/z* 245 [M+H]⁺, *t_R* = 0.91 min. HRMS (ESI⁺) [M+H]⁺ calcd. for C₁₃H₁₇N₄O: 245.1402; found: 245.1400, error = -0.8 ppm, purity = 99.8%.

N-(Furan-2-ylmethyl)-*N*-methyl-3-(pyrrolidin-1-yl)quinoxaline-6-carboxamide (**169**)



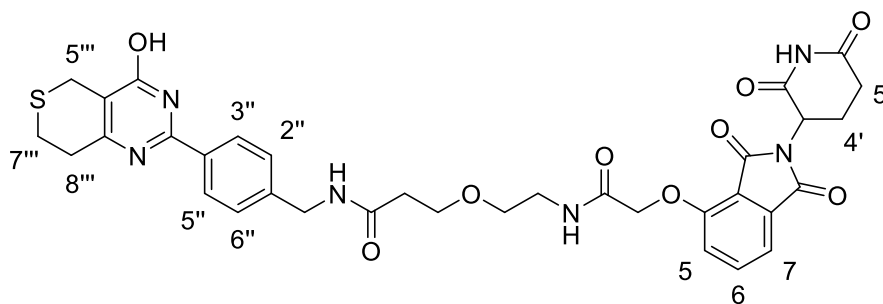
7-bromo-2-(pyrrolidin-1-yl)quinoxaline (**136**) (88 mg, 0.31 mmol), 1-(furan-2-yl)-*N*-methylethanamine (36 μL, 0.31 mmol) and Xantphos Palladacycle Gen.4 (15

mg, 0.016 mmol, 5 mol%) were added to a dry vial. The vial was sealed, evacuated and backfilled with nitrogen, evacuated once more, then 1,4-dioxane (0.63 mL, 0.50 M) and DIPEA (0.16 mL, 0.94 mmol) were added. Lastly, the vial was fitted with a CO (g) balloon and the reaction was stirred at 80 °C for 8 h, cooled to rt and slowly vented. The reaction mixture was flushed with nitrogen, diluted with CH₂Cl₂ (10 mL), filtered through a pre-packed celite column, and the filtrate was concentrated *in vacuo*. The crude residue was purified by normal phase silica chromatography eluting 20-100% EtOAc in cyclohexane, and fractions containing product were collected and evaporated *in vacuo*. The residue was further purified by reverse phase silica chromatography eluting 5-90% MeOH in water (+0.1% formic acid), and fractions containing product were collected and evaporated *in vacuo* to afford *N*-(furan-2-ylmethyl)-*N*-methyl-3-(pyrrolidin-1-yl)quinoxaline-6-carboxamide (**169**) (29 mg, 27%) as a yellow solid. ¹H NMR (600 MHz, DMSO-*d*₆) δ 8.52 (s, 1H, 2-CH), 7.85 (d, *J* = 8.3 Hz, 1H, 8-CH), 7.66 (s, 1H, 5'-CH), 7.62 – 7.49 (m, 1H, 5-CH), 7.35 – 7.30 (m, 1H, 7-CH), 6.48 – 6.32 (m, 2H, 3'-CH and 4'-CH), 4.74 – 4.40 (m, 2H, -CH₂), 3.66 – 3.58 (m, 4H, 2 × -NCH₂), 2.96 – 2.87 (m, 3H, -NCH₃), 2.03 – 1.97 (m, 4H, 2 × -NCH₂CH₂). ¹³C NMR (151 MHz, DMSO) δ 170.3 (-C=O), 150.6 (3-qC), 150.0 (2'-qC), 143.2 – 142.7 (m, 5'-CH), 141.5 (4a-qC), 138.4 (2-CH), 137.3 (6-qC), 136.0 (8a-qC), 128.9 (8-CH), 123.7 (5-CH), 121.6 (7-CH), 110.6 (4'-CH), 108.7 – 108.3 (m, 3'-CH), 46.4 (2 × -NCH₂), 48.0 – 42.6 (m, -CH₂), 36.9 – 32.0 (m, -CONCH₃), 24.9 (2 × -NCH₂CH₂) (rotational isomers observed). LCMS (ESI⁺) *m/z* 337 [M+H]⁺, *t*_R = 1.18 min. HRMS (ESI⁺) [M+H]⁺ calcd. for C₁₉H₂₁N₄O₂: 337.1664; found: 337.1658, error = -1.8 ppm, purity = 97.0%.

7.1.5 Chemical Syntheses from Chapter 5

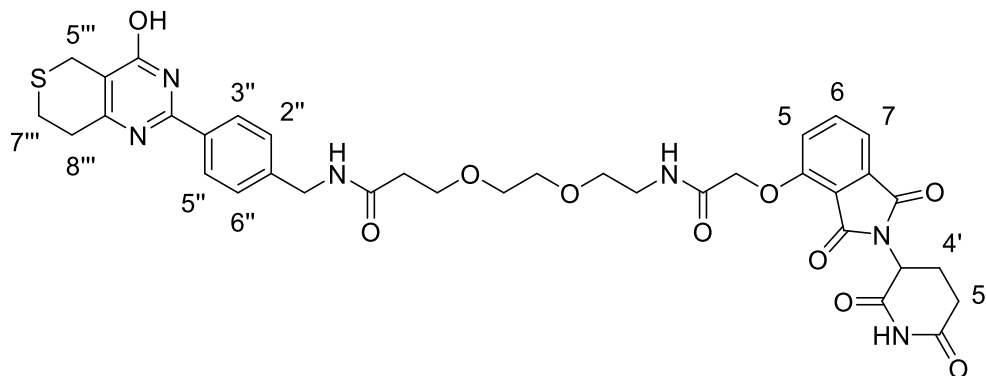
7.1.5.1 Synthesis of XAV939-based amide-linked PROTACs

3-(2-(2-((2-(2,6-Dioxopiperidin-3-yl)-1,3-dioxoisindolin-4-yl)oxy)acetamido)ethoxy)-*N*-(4-(4-hydroxy-7,8-dihydro-5*H*-thiopyrano[4,3-*d*]pyrimidin-2-yl)benzyl)propanamide (186-01)



HATU (24 mg, 0.10 mmol) was added to a solution of 3-(2-(2-((2-(2,6-dioxopiperidin-3-yl)-1,3-dioxoisindolin-4-yl)oxy)acetamido)ethoxy)propanoic acid (31 mg, 0.069 mmol), 2-(4-(aminomethyl)phenyl)-7,8-dihydro-5H-thiopyrano[4,3-d]pyrimidin-4-ol (19 mg, 0.069 mmol) and DIPEA (36 μ L, 0.21 mmol) in DMF (0.69 mL, 0.10 M) and the reaction was stirred at rt for 18 h. The reaction was concentrated *in vacuo* and the crude residue was purified by normal phase silica chromatography eluting 0-10% MeOH in CH₂Cl₂. The fractions containing product were collected and evaporated *in vacuo* to afford 3-(2-(2-((2-(2,6-dioxopiperidin-3-yl)-1,3-dioxoisindolin-4-yl)oxy)acetamido)ethoxy)-N-(4-(4-hydroxy-7,8-dihydro-5H-thiopyrano[4,3-d]pyrimidin-2-yl)benzyl)propenamide (**186-01**) (6 mg, 13%) as a white solid. ¹H NMR (600 MHz, DMSO-*d*₆) δ 12.69 (s, 1H, -OH), 11.11 (s, 1H, -NH), 8.41 (t, *J* = 6.0 Hz, 1H, -CONH), 8.04 – 7.98 (m, 3H, -CONH, 3''-CH and 5''-CH), 7.79 (dd, *J* = 8.5, 7.3 Hz, 1H, 6-CH), 7.48 (d, *J* = 7.3 Hz, 1H, 7-CH), 7.39 – 7.34 (m, 3H, 5-CH, 2''-CH and 6''-CH), 5.11 (dd, *J* = 12.9, 5.5 Hz, 1H, 3'-CH), 4.77 (s, 2H, 4-COCH₂), 4.33 (d, *J* = 6.0 Hz, 2H, 1''-CH₂), 3.66 (t, *J* = 6.4 Hz, 2H, -OCH₂), 3.52 (s, 2H, 5'''-CH₂), 3.46 (t, *J* = 5.8 Hz, 2H, -OCH₂), 3.33 – 3.31 (m, 2H, -NCH₂, observed in COSY and HSQC) 2.92 – 2.85 (m, 5H, 5'-CH, 7'''-CH₂ and 8'''-CH₂), 2.63 – 2.58 (m, 1H, 5'-CH), 2.59 – 2.54 (m, 1H, 4'-CH), 2.42 (t, *J* = 6.4 Hz, 2H, -COCH₂), 2.06 – 1.99 (m, 1H, 4'-CH). ¹³C NMR (151 MHz, DMSO-*d*₆) δ 173.2 (6'-C=O), 170.8 (-CH₂NHCO), 170.4 (2'-C=O), 167.4 (-OCH₂CONH), 167.2 (1-C=O), 165.9 (3-C=O), 155.5 (4-qC), 137.4 (6-CH), 133.5 (7a-qC), 128.0 (3''-CH and 5''-CH), 127.6 (2''-CH and 6''-CH), 120.8 (5-CH), 117.2 (3a-qC), 116.5 (7-CH), 69.0 (-OCH₂), 68.0 (4-COCH₂), 67.1 (-OCH₂), 49.3 (3'-CH), 42.2 (1''-CH₂), 38.8 (-NCH₂), 36.5 (-COCH₂), 33.3 (8'''-CH₂), 31.4 (5'-CH₂), 25.0 (7'''-CH₂), 23.2 (5'''-CH₂), 22.5 (4'-CH₂) (6 \times qC missing). LCMS (ESI⁺) *m/z* 703 [M+H]⁺, *t*_R = 2.50 min. HRMS (ESI⁺) [M+H]⁺ calcd. for C₃₄H₃₅N₆O₉S: 703.2181; found: 703.2154, error = -3.8 ppm, purity = 98.0%.

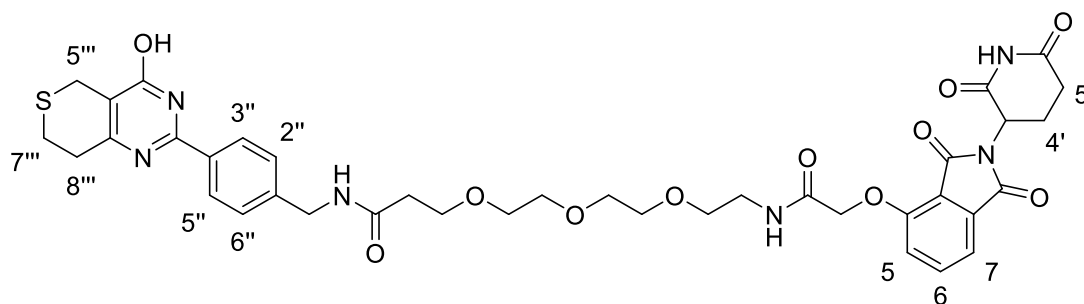
3-(2-(2-(2-((2-(2,6-Dioxopiperidin-3-yl)-1,3-dioxoisindolin-4-yl)oxy)acetamido)ethoxy)ethoxy)-N-(4-(4-hydroxy-7,8-dihydro-5H-thiopyrano[4,3-d]pyrimidin-2-yl)benzyl)propanamide (187)



HATU (14 mg, 0.059 mmol) was added to a solution of 3-(2-(2-(2-((2-(2,6-dioxopiperidin-3-yl)-1,3-dioxoisindolin-4-yl)oxy)acetamido)ethoxy)ethoxy)propanoic acid (19 mg, 0.039 mmol), 2-(4-(aminomethyl)phenyl)-7,8-dihydro-5H-thiopyrano[4,3-d]pyrimidin-4-ol (11 mg, 0.039 mmol) and DIPEA (20 μ L, 0.12 mmol) in DMF (0.39 mL, 0.10 M) and the reaction was stirred at rt for 18 h. The reaction was concentrated *in vacuo* and the crude residue was purified by normal phase silica chromatography eluting 0–10% MeOH in CH_2Cl_2 . The fractions containing product were collected and evaporated *in vacuo* to afford 3-(2-(2-(2-((2-(2,6-dioxopiperidin-3-yl)-1,3-dioxoisindolin-4-yl)oxy)acetamido)ethoxy)ethoxy)-N-(4-(4-hydroxy-7,8-dihydro-5H-thiopyrano[4,3-d]pyrimidin-2-yl)benzyl)propanamide (**187**) (11 mg, 36%) as a yellow glass. ^1H NMR (600 MHz, $\text{DMSO}-d_6$) δ 12.70 (s, 1H, -OH), 11.11 (s, 1H, -NH), 8.43 (t, $J = 6.0$ Hz, 1H, -CONH), 8.05 – 7.97 (m, 3H, -CONH, 3''-CH and 5''-CH), 7.79 (dd, $J = 8.5, 7.3$ Hz, 1H, 6-CH), 7.49 (d, $J = 7.2$ Hz, 1H, 7-CH), 7.42 – 7.34 (m, 3H, 5-CH, 2''-CH and 6''-CH), 5.11 (dd, $J = 12.9, 5.4$ Hz, 1H, 3'-CH), 4.78 (s, 2H, 4-COCH₂), 4.33 (d, $J = 5.9$ Hz, 2H, 1''-CH₂), 3.64 (t, $J = 6.3$ Hz, 2H, -OCH₂), 3.56 – 3.50 (m, 6H, 5'''-CH₂ and 2 \times -OCH₂), 3.47 (t, $J = 5.7$ Hz, 2H, -OCH₂), 3.35 – 3.30 (m, 2H, -NCH₂, observed in COSY and HSQC), 2.94 – 2.84 (m, 5H, 5'-CH, 7'''-CH₂ and 8'''-CH₂), 2.63 – 2.59 (m, 1H, 5'-CH), 2.60 – 2.54 (m, 1H, 4'-CH), 2.40 (t, $J = 6.3$ Hz, 2H, -COCH₂), 2.07 – 1.99 (m, 1H, 4'-CH). ^{13}C NMR (151 MHz, $\text{DMSO}-d_6$) δ 172.8 (6'-C=O), 170.4 (-CH₂NHCO), 169.9 (2'-C=O), 166.9 (-OCH₂CONH), 166.7 (1-C=O), 165.4 (3-C=O), 155.0 (4-qC), 136.9

(6-CH), 133.0 (7a-qC), 127.5 (3''-CH and 5''-CH), 127.2 (2''-CH and 6''-CH), 120.3 (5-CH), 116.7 (3a-qC), 116.0 (7-CH), 69.6 (-OCH₂), 69.5 (-OCH₂), 68.8 (-OCH₂), 67.5 (4-COCH₂), 66.9 (-OCH₂), 48.8 (3'-CH), 41.7 (1''-CH₂), 38.4 (-NCH₂), 36.2 (-COCH₂), 32.8 (8'''-CH₂), 30.9 (5'-CH₂), 24.5 (7'''-CH₂), 22.7 (5'''-CH₂), 22.0 (4'-CH₂) (6 × qC missing). LCMS (ESI⁺) *m/z* 747 [M+H]⁺, *t_R* = 2.54 min. HRMS (ESI⁺) [M+H]⁺ calcd. for C₃₆H₃₉N₆O₁₀S: 747.2443; found: 747.2467, error = 3.2 ppm, purity = 86.1%.

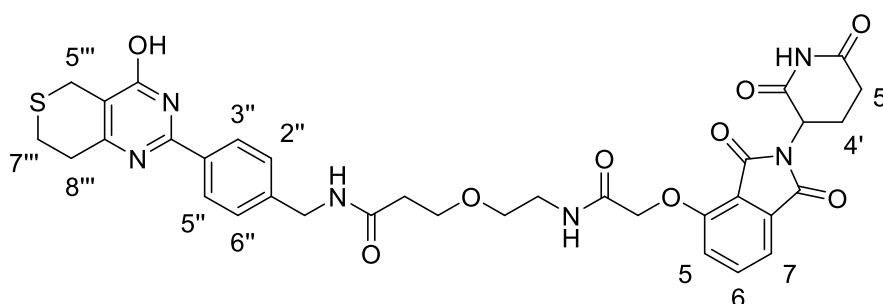
3-(2-(2-(2-(2-((2-(2,6-Dioxopiperidin-3-yl)-1,3-dioxoisindolin-4-yl)oxy)acetamido)ethoxy)ethoxy)ethoxy)-*N*-(4-(4-hydroxy-7,8-dihydro-5*H*-thiopyrano[4,3-*d*]pyrimidin-2-yl)benzyl)propanamide (188)



HATU (13 mg, 0.055 mmol) was added to a solution of 3-(2-(2-(2-((2-(2-(2,6-dioxo-3-piperidyl)-1,3-dioxo-isindolin-4-yl)oxy)acetyl)amino)ethoxy)ethoxy)ethoxy)propanoic acid (20 mg, 0.037 mmol), 2-(4-(aminomethyl)phenyl)-7,8-dihydro-5*H*-thiopyrano[4,3-*d*]pyrimidin-4-ol (10 mg, 0.037 mmol) and DIPEA (19 μ L, 0.11 mmol) in DMF (0.37 mL, 0.10 M) and the reaction was stirred at rt for 18 h. The reaction was concentrated *in vacuo* and the crude residue was purified by normal phase silica chromatography eluting 0-10% MeOH in CH₂Cl₂. The fractions containing product were collected and evaporated *in vacuo* to afford 3-(2-(2-(2-(2-((2-(2,6-dioxopiperidin-3-yl)-1,3-dioxoisindolin-4-yl)oxy)acetamido)ethoxy)ethoxy)ethoxy)-*N*-(4-(4-hydroxy-7,8-dihydro-5*H*-thiopyrano[4,3-*d*]pyrimidin-2-yl)benzyl)propanamide (**188**) (7 mg, 23%) as a yellow glass. ¹H NMR (600 MHz, DMSO-*d*₆) δ 12.70 (s, 1H, -OH), 11.11 (s, 1H, -NH), 8.43 (t, *J* = 5.9 Hz, 1H, -CONH), 8.07 – 7.96 (m, 3H, -CONH, 3''-CH and 5''-CH), 7.80 (dd, *J* = 8.5, 7.3 Hz, 1H, 6-CH), 7.49 (d, *J* = 7.2 Hz, 1H, 7-CH), 7.37 (dd, *J* = 13.4, 8.4 Hz, 3H, 5-CH, 2''-CH and 6''-CH), 5.11 (dd, *J* =

12.9, 5.4 Hz, 1H, 3'-CH), 4.78 (s, 2H, 4-COCH₂), 4.33 (d, *J* = 5.9 Hz, 2H, 1''-CH₂), 3.63 (t, *J* = 6.3 Hz, 2H, -OCH₂), 3.52 – 3.49 (m, 10H, 5'''-CH₂ and 4 × -OCH₂), 3.45 (t, *J* = 5.7 Hz, 2H, -OCH₂), 3.34 – 3.30 (m, 2H, -NCH₂, observed in COSY and HSQC), 2.93 – 2.84 (m, 5H, 5'-CH, 7'''-CH₂ and 8'''-CH₂), 2.63 – 2.59 (m, 1H, 5'-CH), 2.59 – 2.55 (m, 1H, 4'-CH), 2.40 (t, *J* = 6.3 Hz, 2H, -COCH₂), 2.07 – 2.00 (m, 1H, 4'-CH). ¹³C NMR (151 MHz, DMSO-*d*₆) δ 173.2 (6'-C=O), 170.8 (-CH₂NHCO), 170.3 (2'-C=O), 167.4 (-OCH₂CONH), 167.2 (1-C=O), 165.9 (3-C=O), 155.4 (4-qC), 137.4 (6-CH), 133.5 (7a-qC), 128.0 (3''-CH and 5''-CH), 127.6 (2''-CH and 6''-CH), 120.8 (5-CH), 117.2 (3a-qC), 116.5 (7-CH), 70.2 (-OCH₂), 70.2 (-OCH₂), 70.1 (-OCH₂), 70.0 (-OCH₂), 69.3 (-OCH₂), 68.0 (4-COCH₂), 67.3 (-OCH₂), 49.3 (3'-CH), 42.2 (1''-CH₂), 38.9 (-NCH₂), 36.6 (-COCH₂), 33.3 (8'''-CH₂), 31.4 (5'-CH₂), 25.0 (7'''-CH₂), 23.2 (5'''-CH₂), 22.5 (4'-CH₂) (6 × qC missing). LCMS (ESI⁺) *m/z* 791 [M+H]⁺, *t_R* = 2.57 min. HRMS (ESI⁺) [M+H]⁺ calcd. for C₃₈H₄₃N₆O₁₁S: 791.2705; found: 791.2685, error = -2.5 ppm, purity = 87.4%.

3-(2-(2-((2-(2,6-Dioxopiperidin-3-yl)-1,3-dioxoisindolin-4-yl)oxy)acetamido)ethoxy)-*N*-(4-(4-hydroxy-7,8-dihydro-5*H*-thiopyrano[4,3-*d*]pyrimidin-2-yl)benzyl)propanamide (186-02)

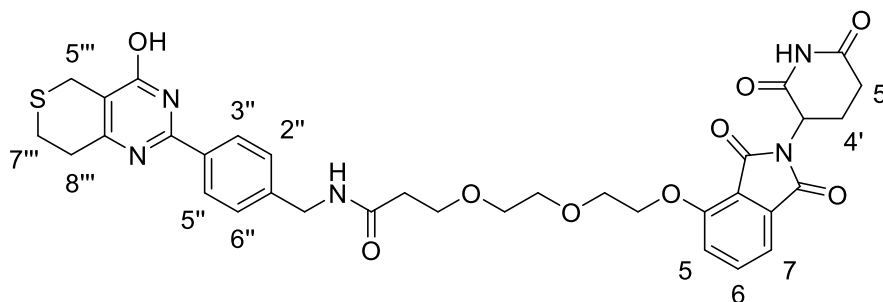


HATU (38 mg, 0.10 mmol) was added to a solution of 3-(2-(2-((2-(2,6-dioxopiperidin-3-yl)-1,3-dioxoisindolin-4-yl)oxy)acetamido)ethoxy)propanoic acid (30 mg, 0.067 mmol), 2-(4-(aminomethyl)phenyl)-7,8-dihydro-5*H*-thiopyrano[4,3-*d*]pyrimidin-4-ol (18 mg, 0.067 mmol) and DIPEA (35 μL, 0.20 mmol) in DMF (0.67 mL, 0.10 M) and the reaction was stirred at rt for 22 h. The reaction was concentrated *in vacuo* and the crude residue was purified by preparative HPLC (C18 250×10 mm column) eluting 10-90% MeOH in water

(+0.1% formic acid). The fractions containing product were collected and evaporated *in vacuo* to afford 3-(2-(2-((2-(2,6-dioxopiperidin-3-yl)-1,3-dioxoisindolin-4-yl)oxy)acetamido)ethoxy)-*N*-(4-(4-hydroxy-7,8-dihydro-5*H*-thiopyrano[4,3-*d*]pyrimidin-2-yl)benzyl)propenamide (**186-02**) (14 mg, 28%) as a white solid. ¹H NMR (600 MHz, DMSO-*d*₆) δ 12.66 (s, 1H, -OH), 11.11 (s, 1H, -NH), 8.42 (t, *J* = 6.1 Hz, 1H, -CONH), 8.05 – 7.99 (m, 3H, -CONH, 3''-CH and 5''-CH), 7.79 (dd, *J* = 8.5, 7.3 Hz, 1H, 6-CH), 7.48 (d, *J* = 7.3 Hz, 1H, 7-CH), 7.37 (d, *J* = 8.5 Hz, 1H, 5-CH), 7.35 (d, *J* = 8.1 Hz, 2H, 2''-CH and 6''-CH), 5.11 (dd, *J* = 12.9, 5.5 Hz, 1H, 3'-CH), 4.78 (s, 2H, 4-COCH₂), 4.33 (d, *J* = 6.0 Hz, 2H, 1''-CH₂), 3.66 (t, *J* = 6.4 Hz, 2H, -OCH₂), 3.51 (s, 2H, 5'''-CH₂), 3.46 (t, *J* = 5.8 Hz, 2H, -OCH₂), 3.35 – 3.29 (m, 2H, -NCH₂, observed in COSY and HSQC), 2.93 – 2.82 (m, 5H, 5'-CH, 7'''-CH₂ and 8'''-CH₂), 2.62 – 2.50 (m, 2H, 5'-CH and 4'-CH), 2.42 (t, *J* = 6.4 Hz, 2H, -COCH₂), 2.06 – 1.99 (m, 1H, 4'-CH). ¹³C NMR (151 MHz, DMSO-*d*₆) δ 172.8 (6'-C=O), 170.4 (-CH₂NHCO), 169.9 (2'-C=O), 167.0 (-OCH₂CONH), 166.8 (1-C=O), 165.5 (3-C=O), 155.0 (4-qC), 136.9 (6-CH), 133.0 (7a-qC), 127.5 (3''-CH and 5''-CH), 127.2 (2''-CH and 6''-CH), 120.4 (5-CH), 116.8 (3a-qC), 116.1 (7-CH), 68.6 (-OCH₂), 67.5 (4-COCH₂), 66.7 (-OCH₂), 48.8 (3'-CH), 41.7 (1''-CH₂), 38.4 (-NCH₂), 36.1 (-COCH₂), 33.1 (8'''-CH₂, observed in HSQC only), 31.0 (5'-CH₂), 24.5 (7'''-CH₂), 22.7 (5'''-CH₂), 22.0 (4'-CH₂) (6 × qC missing). LCMS (ESI⁺) *m/z* 703 [M+H]⁺, *t*_R = 1.08 min. HRMS (ESI⁺) [M+H]⁺ calcd. for C₃₄H₃₅N₆O₉S: 703.2186; found: 703.2209, error = 3.3 ppm, purity = 95.0%.

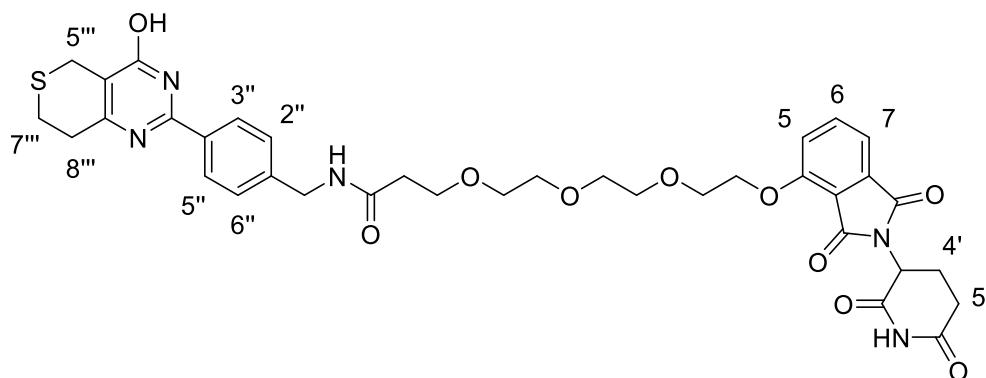
7.1.5.2 Synthesis of XAV939-based ether-linked PROTACs

3-(2-(2-((2-(2,6-Dioxopiperidin-3-yl)-1,3-dioxoisindolin-4-yl)oxy)ethoxy)ethoxy)-*N*-(4-(4-hydroxy-7,8-dihydro-5*H*-thiopyrano[4,3-*d*]pyrimidin-2-yl)benzyl)propenamide (190)



HATU (33 mg, 0.086 mmol) was added to a solution of 3-(2-(2-(2-(2,6-dioxo-3-piperidyl)-1,3-dioxo-isoindolin-4-yl)oxyethoxy)ethoxy)propanoic acid (25 mg, 0.058 mmol), 2-(4-(aminomethyl)phenyl)-7,8-dihydro-5*H*-thiopyrano[4,3-*d*]pyrimidin-4-ol (16 mg, 0.058 mmol) and DIPEA (30 μ L, 0.17 mmol) in DMF (0.58 mL, 0.10 M) and the reaction was stirred at rt for 21 h. The reaction was concentrated *in vacuo* and the crude residue was purified by preparative HPLC (C18 250 \times 10 mm column) eluting 50-60% MeOH in water. The fractions containing product were collected and evaporated *in vacuo* to afford 3-(2-(2-((2-(2,6-dioxopiperidin-3-yl)-1,3-dioxoisindolin-4-yl)oxy)ethoxy)ethoxy)-*N*-(4-(4-hydroxy-7,8-dihydro-5*H*-thiopyrano[4,3-*d*]pyrimidin-2-yl)benzyl)propenamide (**190**) (6.0 mg, 14%) as a white solid. ¹H NMR (600 MHz, DMSO-*d*₆) δ 12.63 (s, 1H, -OH), 11.10 (s, 1H, -NH), 8.42 (t, *J* = 6.0 Hz, 1H, -CONH), 8.02 (d, *J* = 8.3 Hz, 2H, 3''-CH and 5''-CH), 7.78 (dd, *J* = 8.5, 7.3 Hz, 1H, 6-CH), 7.49 (d, *J* = 8.5 Hz, 1H, 7-CH), 7.44 (d, *J* = 7.2 Hz, 1H, 5-CH), 7.34 (d, *J* = 8.1 Hz, 2H, 2''-CH and 6''-CH), 5.07 (dd, *J* = 12.9, 5.4 Hz, 1H, 3'-CH), 4.34 – 4.29 (m, 4H, 1''-CH₂ and -OCH₂), 3.82 – 3.78 (m, 2H, -OCH₂), 3.68 – 3.63 (m, 4H, 2 \times -OCH₂), 3.56 – 3.52 (m, 2H, -OCH₂), 3.49 (s, 2H, 5'''-CH₂), 2.89 – 2.80 (m, 5H, 5'-CH, 7'''-CH₂ and 8'''-CH₂), 2.63 – 2.50 (m, 2H, 5'-CH and 4'-CH), 2.40 (t, *J* = 6.3 Hz, 2H, -COCH₂), 2.05 – 1.98 (m, 1H, 4'-CH). ¹³C NMR (151 MHz, DMSO-*d*₆) δ 172.9 (6'-C=O), 170.5 (-CH₂NHCO), 170.0 (2'-C=O), 166.9 (1-C=O), 165.3 (3-C=O), 155.8 (4-qC), 143.2 (1''-qC), 137.0 (6-CH), 133.3 (7a-qC), 129.7 (4''-qC), 127.5 (3''-CH and 5''-CH), 127.2 (2''-CH and 6''-CH), 120.0 (5-CH), 116.3 (3a-qC), 115.4 (7-CH), 70.1 (-OCH₂), 69.7 (-OCH₂), 68.9 (-OCH₂), 68.7 (-OCH₂), 66.9 (-OCH₂), 48.8 (3'-CH), 41.8 (1''-CH₂), 36.2 (-COCH₂), 32.5 (8'''-CH₂, observed in HSQC only), 31.0 (5'-CH₂), 24.5 (7'''-CH₂), 22.8 (5'''-CH₂), 22.0 (4'-CH₂) (6 \times qC missing). LCMS (ESI⁺) *m/z* 690 [M+H]⁺, *t*_R = 1.11 min. HRMS (ESI⁺) [M+H]⁺ calcd. for C₃₄H₃₆N₅O₉S: 690.2234; found: 690.2254, error = 2.9 ppm, purity = 92.3%.

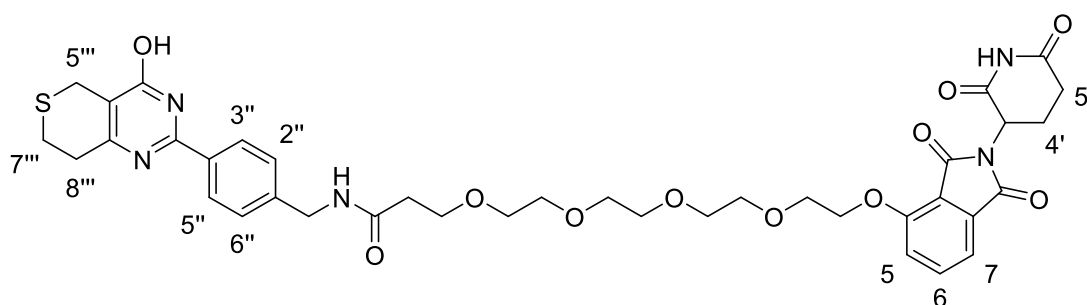
3-(2-(2-(2-((2-(2,6-Dioxopiperidin-3-yl)-1,3-dioxoisindolin-4-yl)oxy)ethoxy)ethoxy)ethoxy)-*N*-(4-(4-hydroxy-7,8-dihydro-5*H*-thiopyrano[4,3-*d*]pyrimidin-2-yl)benzyl)propenamide (191)



HATU (30 mg, 0.078 mmol) was added to a solution of 3-(2-(2-(2-(2-(2,6-dioxo-3-piperidyl)-1,3-dioxo-isoindolin-4-yl)oxyethoxy)ethoxy)ethoxy)propanoic acid (25 mg, 0.052 mmol), 2-(4-(aminomethyl)phenyl)-7,8-dihydro-5*H*-thiopyrano[4,3-*d*]pyrimidin-4-ol (14 mg, 0.052 mmol) and DIPEA (27 μ L, 0.16 mmol) in DMF (0.52 mL, 0.10 M) and the reaction was stirred at rt for 21 h. The reaction was concentrated *in vacuo* and the crude residue was purified by preparative HPLC (C18 250 \times 10 mm column) eluting 50-60% MeOH in water. The fractions containing product were collected and evaporated *in vacuo* to afford 3-(2-(2-(2-((2-(2,6-dioxopiperidin-3-yl)-1,3-dioxoisoindolin-4-yl)oxy)ethoxy)ethoxy)ethoxy)-*N*-(4-(4-hydroxy-7,8-dihydro-5*H*-thiopyrano[4,3-*d*]pyrimidin-2-yl)benzyl)propenamide (**191**) (7.7 mg, 19%) as a white solid. ^1H NMR (600 MHz, DMSO- d_6) δ 12.65 (s, 1H, -OH), 11.10 (s, 1H, -NH), 8.42 (t, J = 6.1 Hz, 1H, -CONH), 8.02 (d, J = 8.3 Hz, 2H, 3''-CH and 5''-CH), 7.79 (dd, J = 8.5, 7.3 Hz, 1H, 6-CH), 7.51 (d, J = 8.6 Hz, 1H, 7-CH), 7.45 (d, J = 7.2 Hz, 1H, 5-CH), 7.35 (d, J = 8.3 Hz, 2H, 2''-CH and 6''-CH), 5.08 (dd, J = 12.9, 5.4 Hz, 1H, 3'-CH), 4.37 – 4.30 (m, 4H, 1''-CH₂ and -OCH₂), 3.82 – 3.76 (m, 2H, -OCH₂), 3.66 – 3.59 (m, 4H, 2 \times -OCH₂), 3.55 – 3.48 (m, 8H, 3 \times -OCH₂ and 5'''-CH₂), 2.92 – 2.82 (m, 5H, 5'-CH, 7'''-CH₂ and 8'''-CH₂), 2.62 – 2.50 (m, 2H, 5'-CH and 4'-CH), 2.39 (t, J = 6.3 Hz, 2H, -COCH₂), 2.05 – 1.96 (m, 1H, 4'-CH). ^{13}C NMR (151 MHz, DMSO- d_6) δ 172.8 (6'-C=O), 170.4 (-CH₂NHCO), 170.0 (2'-C=O), 166.9 (1-C=O), 165.3 (3-C=O), 155.8 (4-qC), 143.3 (1''-qC), 137.0 (6-CH), 133.3 (7a-qC), 129.7 (4''-qC), 127.5 (3''-CH and 5''-CH), 127.2 (2''-CH and 6''-CH), 120.0 (5-CH), 116.3 (3a-qC), 115.4 (7-CH), 70.2 (-OCH₂), 69.9 (-OCH₂), 69.6 (-OCH₂), 69.6 (-OCH₂), 68.9 (-OCH₂), 68.7 (-OCH₂), 66.9 (-OCH₂), 48.8 (3'-CH), 41.7 (1''-CH₂), 36.2 (-COCH₂), 32.4 (8'''-CH₂, observed in HSQC), 31.0 (5'-CH₂), 24.5 (7'''-CH₂), 22.7

(5'''-CH₂), 22.0 (4'-CH₂) (6 × qC missing). LCMS (ESI⁺) *m/z* 734 [M+H]⁺, *t_R* = 1.12 min. HRMS (ESI⁺) [M+H]⁺ calcd. for C₃₆H₃₉N₅O₁₀S: 734.2496; found: 734.2521, error = 3.4 ppm, purity = 91.8%.

1-((2-(2,6-Dioxopiperidin-3-yl)-1,3-dioxoisindolin-4-yl)oxy)-*N*-(4-(4-hydroxy-7,8-dihydro-5*H*-thiopyrano[4,3-*d*]pyrimidin-2-yl)benzyl)-3,6,9,12-tetraoxapentadecan-15-amide (192)



HATU (27 mg, 0.072 mmol) was added to a solution of 3-(2-(2-(2-(2-(2,6-dioxo-3-piperidyl)-1,3-dioxo-isoindolin-4-yl)oxyethoxy)ethoxy)ethoxy)ethoxy)propanoic acid (25 mg, 0.048 mmol), 2-(4-(aminomethyl)phenyl)-7,8-dihydro-5*H*-thiopyrano[4,3-*d*]pyrimidin-4-ol (13 mg, 0.048 mmol) and DIPEA (25 μL, 0.14 mmol) in DMF (0.48 mL, 0.10 M) and the reaction was stirred at rt for 23 h. The reaction was concentrated *in vacuo* and the crude residue was purified by reverse phase silica chromatography eluting 5-95% MeOH in water (+0.1% formic acid). The fractions containing product were collected and evaporated *in vacuo* to afford 1-((2-(2,6-dioxopiperidin-3-yl)-1,3-dioxoisindolin-4-yl)oxy)-*N*-(4-(4-hydroxy-7,8-dihydro-5*H*-thiopyrano[4,3-*d*]pyrimidin-2-yl)benzyl)-3,6,9,12-tetraoxapentadecan-15-amide (**192**) (7.3 mg, 19%) as a white solid. ¹H NMR (600 MHz, DMSO-*d*₆) δ 12.70 (s, 1H, -OH), 11.10 (s, 1H, -NH), 8.43 (t, *J* = 6.0 Hz, 1H, -CONH), 8.02 (d, *J* = 8.3 Hz, 2H, 3''-CH and 5''-CH), 7.80 (dd, *J* = 8.5, 7.3 Hz, 1H, 6-CH), 7.52 (d, *J* = 8.5 Hz, 1H, 7-CH), 7.45 (d, *J* = 7.2 Hz, 1H, 5-CH), 7.38 – 7.34 (m, 2H, 2''-CH and 6''-CH), 5.08 (dd, *J* = 12.9, 5.5 Hz, 1H, 3'-CH), 4.35 – 4.31 (m, 4H, 1''-CH₂ and -OCH₂), 3.81 – 3.76 (m, 2H, -OCH₂), 3.66 – 3.60 (m, 4H, 2 × -OCH₂), 3.53 – 3.46 (m, 12H, 5 × -OCH₂ and 5'''-CH₂), 2.92 – 2.83 (m, 5H, 5'-CH, 7'''-CH₂ and 8'''-CH₂), 2.62 – 2.50 (m, 2H, 5'-CH and 4'-CH), 2.40 (t, *J* = 6.3 Hz, 2H, -COCH₂), 2.05 – 1.97 (m, 1H, 4'-CH). ¹³C NMR (151 MHz, DMSO-

d_6) δ 172.9 (6'-C=O), 170.5 (-CH₂NHCO), 170.0 (2'-C=O), 166.9 (1-C=O), 165.4 (3-C=O), 155.9 (4-qC), 143.4 (1''-qC), 137.1 (6-CH), 133.3 (7a-qC), 129.7 (4''-qC), 127.6 (3''-CH and 5''-CH), 127.2 (2''-CH and 6''-CH), 120.1 (5-CH), 116.4 (3a-qC), 115.5 (7-CH), 70.2 (-OCH₂), 69.9 (-OCH₂), 69.8 (2 × -OCH₂), 69.8 (-OCH₂), 69.6 (-OCH₂), 68.9 (-OCH₂), 68.7 (-OCH₂), 66.9 (-OCH₂), 48.8 (3'-CH), 41.8 (1''-CH₂), 36.2 (-COCH₂), 32.9 (8'''-CH₂), 31.0 (5'-CH₂), 24.6 (7'''-CH₂), 22.8 (5'''-CH₂), 22.1 (4'-CH₂) (4 × qC missing). LCMS (ESI⁺) m/z 778 [M+H]⁺, t_R = 1.16 min. HRMS (ESI⁺) [M+H]⁺ calcd. for C₃₈H₄₃N₅O₁₁S: 778.2758; found: 778.2766, error = 1.0 ppm, purity = 97.4%.

7.2 Protein Production

Human tankyrase ARC4 constructs were expressed and purified according to a literature reported procedure (Pollock *et al*, 2017).¹⁹⁶ TNKS2 ARC4 (488-649) was produced for all ligand-observed NMR experiments. TNKS1 ARC4 (646-807) was produced for X-ray crystallography studies and competitive FP experiments. Uniformly ¹⁵N-labelled TNKS2 ARC4 (488-649) was produced for all protein-observed NMR experiments in M9 minimal media containing ¹⁵N NH₄Cl, according to a literature reported protocol (Pollock *et al*, 2019)¹³⁵, and purified as for unlabelled TNKS2 ARC4 (488-649).¹⁹⁶

Table 7.1 Summary table of all ARC4 constructs produced for ligand-observed and protein-observed NMR, X-ray crystallography studies and competitive FP assays.

ARC4 construct	Molecular weight (kDa)	Expression media (L)	Purification date	Yield (mg)
TNKS2 ARC4 (488-649)	17.9	TB media (4 L)	01/04/2019	10.9 mg
TNKS2 ARC4 (488-649)	17.9	TB media (4 L)	24/01/2020	25.2 mg
TNKS1 ARC4 (646-807)	18.2	TB media (8 L)	06/07/2020	16.5 mg
TNKS1 ARC4 (646-807)	18.2	TB media (8 L)	23/01/2021	26.3 mg
¹⁵N TNKS2 ARC4 (488-649)	18.1	M9 minimal media (4 L)	17/01/2021	18.4 mg

7.2.1 Expression of Tankyrase ARC4s

The expression of unlabelled TNKS2 ARC4 (488-649) and TNKS1 ARC4 (646-807) were performed according to a literature reported procedure (see Pollock *et al*, 2017 for detailed protocol).¹⁹⁶ A single colony of BL21-CodonPlus (DE3)-RIL *E. coli* cells, transformed with expression vector pETM-30-2 encoding the gene for His₆-GST affinity tagged tankyrase ARC constructs, was selected. LB media (100 mL) supplemented with antibiotics (50 µg/mL kanamycin and 34 µg/mL chloramphenicol) was inoculated. The LB media pre-culture was incubated overnight at 37 °C with shaking at 220 rpm, then 5 mL was added to each litre of

TB media supplemented with antibiotics (50 µg/mL kanamycin and 34 µg/mL chloramphenicol). The expression culture was incubated at 37 °C with shaking at 180 rpm until an optical density at 600 nm (OD₆₀₀) of 2.0 was reached. The culture was then cooled at 4 °C for 30 min and protein expression was induced by the addition of isopropyl β-D-1-thiogalactopyranoside (IPTG, 0.5 mM). The culture was incubated overnight at 18 °C with shaking at 180 rpm for overnight protein expression. Cells were collected by centrifugation (4000 × *g*, 30 min, 4 °C), and either subjected to immediate cell lysis and purification (TNKS2 ARC4 (4 L) expressions) or flash-frozen and stored at -80 °C until required (TNKS1 ARC4 (8 L) expressions).

The expression of ¹⁵N-labelled TNKS2 ARC4 (488-649) was performed in M9 minimal media containing ¹⁵N-labelled NH₄Cl (Table 7.2) according to a literature reported procedure (see Pollock *et al*, 2019 for detailed protocol).¹³⁵ Glycerol stock (100 µL) of BL21-CodonPlus (DE3)-RIL *E. coli* cells, transformed with expression vector pETM-30-2 encoding the gene for His₆-GST affinity tagged TNKS2 ARC4 (488-649) construct, was added to M9 minimal media (200 mL) supplemented with supplemented with antibiotics (50 µg/mL kanamycin and 34 µg/mL chloramphenicol). The M9 minimal media pre-culture was incubated overnight at 37 °C with shaking at 220 rpm, then 25 mL was added to each litre of M9 minimal media, supplemented with antibiotics (50 µg/mL kanamycin and 34 µg/mL chloramphenicol). The expression culture was incubated at 37 °C with shaking at 180 rpm until an optical density at 600 nm (OD₆₀₀) of 0.85 was reached. The culture was then cooled at 4 °C for 30 min and protein expression was induced by the addition of isopropyl β-D-1-thiogalactopyranoside (IPTG, 0.5 mM). The culture was incubated overnight at 18 °C with shaking at 180 rpm for overnight protein expression. Cells were collected by centrifugation (4000 × *g*, 30 min, 4 °C), and subjected to immediate cell lysis and purification.

Table 7.2. Preparation of M9 minimal media used in expression of ¹⁵N-labelled TNKS2 ARC4. Stock solutions and minimal media were prepared using deionised and UV treated water, and stock solutions were filtered through 0.22 µm filter units.

Solution	Reagents
M9 medium (10 × stock)	Na ₂ HPO ₄ (60 g/L), KH ₂ PO ₄ (30 g/L), NaCl (5 g/L), ¹⁵ N-labelled NH ₄ Cl (25 g/L)
Trace elements (100 × stock)	EDTA (5 g/L), FeCl ₃ (anhydrous, 0.83 g/L), ZnCl ₂ (84 mg/L), CuCl ₂ (anhydrous, 10 mg/L), CoCl ₂ (monohydrate 5.9 mg/L), MnCl ₂ (anhydrous, 0.86 mg/L), boric acid (10 mg/L)
M9 minimal media	M9 medium (10 × stock, 100 mL/L), trace elements (100 × stock, 10 mL/L), glucose (20% w/v solution, 20 mL/L), MgSO ₄ (1 M solution, 1 mL/L), CaCl ₂ (1M solution, 0.3 mL/L), biotin (1 mg/mL solution, 1 mL/L), thiamin (1 mg/mL solution, 1 mL/L)

7.2.2 Purification of Tankyrase ARC4s

The purification of unlabelled TNKS2 ARC4 (488-649), TNKS1 ARC4 (646-807), and ¹⁵N-labelled TNKS2 ARC4 (488-649) were performed according to a literature reported procedure (see Pollock *et al*, 2017 for detailed protocol).¹⁹⁶ All buffers used in purifications were prepared using deionised and UV treated water, and were filtered through 0.22 µm filter units and degassed (Table 7.3).

Table 7.3. Buffers used in tankyrase ARC4 purifications.

Buffer	Reagents
Lysis buffer	50 mM Tris-HCl pH 7.5, 500 mM NaCl, 5 mM β-mercaptoethanol, Pierce protease inhibitor tablets EDTA-free (1 large tablet per 50 mL lysis buffer)
Buffer A	50 mM Tris-HCl pH 7.5, 500 mM NaCl, 5 mM β-mercaptoethanol, 10 mM imidazole
Buffer B	50 mM Tris-HCl pH 7.5, 500 mM NaCl, 5 mM β-mercaptoethanol, 250 mM imidazole
Dialysis buffer	50 mM Tris-HCl pH 7.5, 100 mM NaCl, 5 mM β-mercaptoethanol
Final buffer	25 mM HEPES pH 7.5, 100 mM NaCl, 1 mM TCEP (tris(2-carboxyethyl)phosphine)

Cells were suspended in lysis buffer (50 mL lysis buffer per litre of expression culture) and broken by large-tip sonication at 4 °C (40% amplitude, 5 s on, 5 s off, 5 min total sonication). Cell debris and insoluble material was removed by centrifugation (30000 × *g*, 30 min, 4 °C), then the soluble lysate supernatant was subject sonication at 4 °C (20 s total sonication) to break genomic DNA and filtered through 5.0 µm syringe filter units.

HisTrap Ni²⁺ FF affinity columns (5 mL) were equilibrated for purification by washing with 10 column volumes (CV) of water and 10 CV of buffer A using a low-pressure peristaltic pump or using an AKTA Pure FPLC (fast protein liquid chromatography) system. A single HisTrap column (5 mL total CV) was used for purification of TNKS2 ARC4 (488-649) and ¹⁵N TNKS2 ARC4 (488-649) (4 L expression culture) whilst two HisTrap columns connected in series (10 mL total CV) were used for purification of TNKS1 ARC4 (646-807) (8 L expression culture). The cleared lysate was loaded to the equilibrated HisTrap Ni²⁺ affinity column and unbound contaminants were removed by washing the column with 20 CV of buffer A. The His₆-GST tagged tankyrase ARC4 was eluted from the HisTrap Ni²⁺ affinity column with a gradient of 0-100% buffer B over 20 CV using an AKTA Pure FPLC purification system. Fractions containing protein were combined and His₆-tagged tobacco etch virus (TEV) protease was added (100 µL of 1 mg/mL stock per 5 mL protein solution), then protein was transferred to dialysis tubing and dialysed overnight at 4 °C in dialysis buffer. Protein was filtered through 0.22 µm syringe filter units and loaded on to an equilibrated HisTrap Ni²⁺ affinity column using a low-pressure peristaltic pump or using an AKTA Pure FPLC system. For purification of TNKS2 ARC4 (488-649) and ¹⁵N TNKS2 ARC4 (488-649), untagged ARC4 protein eluted in the flow-through. For purification of TNKS1 ARC4 (646-807), untagged ARC4 protein was eluted from the HisTrap Ni²⁺ affinity column with a gradient of 0-20% buffer B over 10 CV then 20-100% buffer B over 20 CV using an AKTA Pure FPLC purification system. Untagged ARC4 protein was concentrated in 3000 Da molecular weight cut-off (MWCO) spin concentrators in a swinging bucket rotor at 3500 × *g* for 30 min intervals until a volume of 5 mL was reached. A HiLoad 16/600 Superdex 75 size exclusion column (120 mL total CV) was connected to an AKTA Pure FPLC purification system and equilibrated with water (1 CV) and final buffer (2 CV). The

protein was centrifuged ($18000 \times g$, 10 min, 4 °C) to remove aggregates, then loaded to the equilibrated size exclusion column and eluted isocratically with final buffer (1.2 V) as 1 mL fractions. Fractions containing pure untagged ARC4 protein, as confirmed by SDS-PAGE analysis, were combined and concentrated in 3000 Da MWCO spin concentrators in a swinging bucket rotor at $3500 \times g$ for 30 min intervals until a concentration > 10 mg/mL was achieved. The UV absorbance of the protein was measured at 280 nm and the final tankyrase ARC4 concentration was calculated according to the Beer-Lambert law (equation 7.1),²⁸⁵ using molar extinction coefficients (ϵ) and molecular weight calculated by ProtParam (Table 7.4).²⁸⁶ The protein was flash-frozen in liquid nitrogen as small volume aliquots (25 μ L, 50 μ L or 100 μ L) and stored at -80 °C until used. When required, tankyrase ARC4 aliquots were thawed from -80 °C and centrifuged ($10000 \times g$, 5 min, 4 °C) prior to use in biophysical or biochemical assays.

Equation 7.1:
$$A = \epsilon cl$$

Where ϵ = molar extinction coefficient ($M^{-1} cm^{-1}$), c = concentration ($mol L^{-1}$) and l = absorption path length (cm).

Table 7.4. Molecular weights and molar extinction coefficients of tankyrase ARC4 constructs.

ARC4 construct	Molecular weight (Da)	Molar extinction coefficients (ϵ , $M^{-1} cm^{-1}$)
TNKS2 ARC4 (488-649)	17911	12950
TNKS2 ARC4 (488-649)	17911	12950
TNKS1 ARC4 (646-807)	18182	14440
TNKS1 ARC4 (646-807)	18182	14440
¹⁵ N TNKS2 ARC4 (488-649)	18136	12950

7.3 Biophysical and Biochemical Assays

7.3.1 Ligand-observed NMR Experiments

A Bruker 600 MHz AV-NEO instrument fitted with a 5 mm TCI-CryoProbe was used for ligand-observed NMR experiments, with 3 mm NMR tubes (Bruker). The ^1H NMR spectra were acquired at 298 K and were referenced to the internal deuterated solvent (10% D_2O) in NMR buffer (25 mM HEPES pH 7.5, 100 mM NaCl, 1 mM TCEP, 10% D_2O). The spectra were acquired according to in-house experimental parameters and processed using Bruker Topspin 4.0.

7.3.1.1 Quantitative NMR Assay

Stock solution concentration of fragments was measured using quantitative ^1H NMR. Fragment stock solutions were prepared to a calculated concentration of 70 mM in DMSO-d_6 , then the concentration was measured using quantitative ^1H NMR, and the stock solutions were diluted to a final concentration of 50 mM in DMSO-d_6 .

For each synthetic compound, solid fragment was weighed into a glass vial using an accurate balance (weight accurate to 2 d.p.) and the volume of DMSO-d_6 required for the preparation of a 70 mM stock solution was calculated, according to equation 7.2 and equation 7.3. The calculated volume of DMSO-d_6 was added to the solid fragment in a glass vial and the solution was well mixed using a Vortex mixer.

$$\text{Equation 7.2: } \textit{Number of moles (mol)} = \frac{\textit{Mass (g)}}{\textit{Molecular weight (g mol}^{-1}\text{)}}$$

$$\text{Equation 7.3: } \textit{Concentration (mol L}^{-1}\text{)} = \frac{\textit{Number of moles (mol)}}{\textit{Volume (L)}}$$

Quantitative NMR samples were prepared: fragments were manually dispensed into microcentrifuge tubes (10 μL \times 70 mM DMSO-d_6 stock) followed by DMSO-d_6 (170 μL), and the solutions were well mixed using a Vortex mixer. The solutions were manually transferred from microcentrifuge tubes to 3 mm NMR tubes. The

quantitative ^1H NMR spectra were acquired using an in-house 1D pulse sequence, processed using Bruker TopSpin and analysed using MestReNova Quantitation software for data processing. The ^1H NMR spectra were processed (Auto Phase correction, Auto Baseline correction, then Multiplet analysis) prior to using the Quantitation tool. Caffeine was used as an external standard to quantify ligand ^1H signals.

The concentration of fragment in the quantitative NMR samples, calculated using MestReNova quantitation software, was multiplied by the dilution factor according to equation 7.4, to obtain the measured concentration of fragment stock solutions. The fragment stock solutions were then diluted with the appropriate volume of DMSO- d_6 to obtain final fragment stock solution concentrations of 50 mM in DMSO- d_6 .

$$\text{Equation 7.4: } [\textit{Stock solution}] (\textit{mol L}^{-1}) = \frac{[\textit{Quantitative NMR solution}] (\textit{mol L}^{-1}) \times 180}{10}$$

7.3.1.2 Kinetic Solubility NMR Assay

Kinetic solubility of fragments was measured using quantitative ^1H NMR. The kinetic solubility of fragments was analysed at a final concentration of 1000 μM with a final DMSO- d_6 concentration of 2% v/v in NMR buffer. Fragments were manually dispensed into a 384 deep well plate (3.6 μL \times 50 mM DMSO- d_6 stock) followed by NMR buffer (176.4 μL) using a multichannel pipette with mixing three times. The kinetic solubility of caffeine was analysed at a final concentration of 200 μM with a final DMSO- d_6 concentration of 2% v/v in NMR buffer as a control for this experiment. Caffeine was manually dispensed into a 384 deep well plate (3.6 μL \times 10 mM DMSO- d_6 stock) followed by NMR buffer (176.4 μL) using a multichannel pipette with mixing three times. The plate was centrifuged (1 min, 1000 rpm, Eppendorf 5810R) and incubated for 20 h at rt. The plate was centrifuged again (1 min, 1000 rpm, Eppendorf 5810R), then the solutions (165 μL) were transferred from the 384 deep well plate to 3 mm NMR tubes using a Bruker SamplePro Tube liquid handling system. The quantitative ^1H NMR spectra

were acquired using an in-house 1D pulse sequence, processed using Bruker TopSpin and analysed using MestReNova Quantitation software for automated data processing. Caffeine was used as an external standard to quantify ligand ^1H signals.

7.3.1.3 Competitive Ligand-Observed NMR Assay

Fragments measured at 500 μM (1.8 μL \times 50 mM DMSO- d_6 stock), fragments measured at 200 μM (0.72 μL \times 50 mM DMSO- d_6 stock), and fragments measured at 50 μM (0.18 μL \times 50 mM DMSO- d_6 stock) were manually dispensed into Greiner 96 deep well plates in duplicate. NMR buffer only was added (180 μL) to 'blank' samples containing compound only using a multichannel pipette with mixing three times. TNKS2 ARC4 (20 μM) in NMR buffer was added (180 μL) to 'protein' samples containing compound and TNKS2 ARC4 using a multichannel pipette with mixing three times. The solutions were transferred to 3 mm NMR tubes using a Bruker SamplePro Tube liquid handling system. ^1H reference spectra were acquired for 'compound only' samples. T_2 relaxation-edited CPMG NMR spectra were acquired with a relaxation spin filter applied at 600 ms. The relative peak intensity difference (I) between 'blank' and 'protein' spectra for each ^1H signal between 5.5 – 9.5 ppm was calculated by MestReNova Screen software, according to equation 7.5. The average of the peak intensity percentage difference (%) for each ^1H signal was taken to determine the average peak intensity reduction (%) in the presence of TNKS2 ARC4 protein.

Equation 7.5:
$$I = \frac{(I_{\text{blank}} - I_{\text{protein}})}{I_{\text{blank}}}$$

WaterLOGSY NMR spectra were also acquired, the bulk water signal at 4.7 ppm was inverted, and the spectra were processed using MestReNova Screen software. The 'compound only' and 'protein' spectra between 5.5 – 9.5 ppm were compared qualitatively to determine binding.

For competitive experiments, fragments measured at 500 μM (1.8 μL \times 50 mM DMSO- d_6 stock), fragments measured at 200 μM (0.72 μL \times 50 mM DMSO- d_6 stock), and fragments measured at 50 μM (0.18 μL \times 50 mM DMSO- d_6 stock)

were manually dispensed into Greiner 96 deep well plate in triplicate. TNKS2 ARC4 protein and 3BP2 16mer peptide in NMR buffer (20 μM protein + 200 μM peptide) was added (180 μL) to ‘competitor’ samples containing compound, TNKS2 ARC4 and 3BP2 16mer peptide using a multichannel pipette with mixing three times. ‘Blank’ and ‘protein’ samples were prepared as discussed and ^1H reference, T_2 relaxation-edited CPMG and waterLOGSY NMR spectra were acquired and processed as previously. For T_2 relaxation-edited CPMG spectra, the relative peak intensity difference (I) between ‘blank’ and ‘competitor’ spectra was calculated by MestReNova Screen software according to equation 7.6. The average of the peak intensity percentage difference (%) for each ^1H signal was taken to determine the average peak intensity reduction (%) in the presence of TNKS2 ARC4 protein and 3BP2 16mer peptide competitor.

Equation 7.6:
$$I = \frac{(I_{blank} - I_{competitor})}{I_{blank}}$$

For waterLOGSY spectra, ‘blank’, ‘protein’ and ‘competitor’ spectra between 5.5 – 9.5 ppm were compared qualitatively to determine competitive binding.

7.3.2 ^1H - ^{15}N HSQC Protein-Observed NMR Experiments

A Bruker 500 MHz instrument fitted with a 5 mm probe was used for protein-observed NMR experiments, with 5 mm NMR tubes (Wilmad). 1D ^1H and 2D ^1H - ^{15}N HSQC spectra were acquired at 295 K and were referenced to the internal deuterated solvent (10% D₂O) in NMR buffer (25 mM HEPES pH 7.5, 100 mM NaCl, 1 mM TCEP, 10% D₂O). The ^1H NMR spectrum was acquired using an in-house 1D pulse sequence with 256 scans. The ^1H - ^{15}N HSQC spectra were acquired over 3 h, with 64 scans and a spectrum width of 16.00 ppm for ^1H and 29.00 ppm for ^{15}N , according to in-house experimental parameters.

1.3.3.1 Titration Sample Preparation

Separate fragment titration samples were prepared for each concentration point to a final total volume of 500 μL , according to Table 7.5. NMR buffer (461.5 μL) was added to the required volume of fragment stock solution (5 mM or 50 mM

DMSO-d₆ stock). The required volume of DMSO-d₆ was added to maintain a constant final concentration (25 μ L, 5% v/v) per sample, and DSS (100 μ M final concentration; 5 μ L \times 10 mM stock in D₂O) was added as an internal reference standard to each sample. Lastly, ¹⁵N-labelled TNKS2 ARC4 (488-649) (50 μ M final concentration; 8.5 μ L \times 3 mM stock in NMR buffer) was added to the fragment titration samples. The solutions were mixed three times using a pipette and transferred to 5 mm NMR tubes. ¹⁵N-labelled TNKS2 ARC4 (488-649) with DMSO-d₆ (5% v/v) and DSS (100 μ M) was used as the baseline spectra to exclude the effect of peak shifting due to the presence of DMSO-d₆.

Table 7.5. Fragment titration sample preparation for protein-observed NMR experiments.

Titration samples were prepared with a ¹⁵N-labelled TNKS2 ARC4 concentration of 50 μ M. ^a Volume of 5 mM DMSO-d₆ fragment stock solution added. ^b Volume of 50 mM DMSO-d₆ fragment stock solution added.

[Fragment] (μ M)	0	12.5	25	50	100	200	400	800	1600
<i>Volume Fragment (μL)</i>	0	1.25 ^a	2.5 ^a	5 ^a	10 ^a	2 ^b	4 ^b	8 ^b	16 ^b
<i>Volume DMSO-d₆ (μL)</i>	25	23.75	22.5	20	15	23	21	17	9
<i>Ratio Fragment:Protein</i>	-	1:4	1:2	1:1	2:1	4:1	8:1	16:1	32:1

1.3.3.2 Data Analysis

1D ¹H and 2D ¹H-¹⁵N HSQC spectra were referenced in Bruker Topspin software (v 4.0.7). The 1D proton spectrum calibration frequency was corrected by aligning DSS signal to 0.0000 ppm. The 2D calibration frequency for centre of spectrum was corrected in the F2 (proton) dimension by aligning internal reference standard DSS peak to 0.0000 ppm, and calculating the correction in the F1 (¹⁵N) dimension according to a ¹H-¹⁵N IUPAC-IUB recommended chemical shift referencing ratio of 0.101329118 for indirect chemical shift referencing.²⁸⁷

For each fragment titration, 2D spectra were analysed using the CcpNmr AnalysisAssign software (v 3.0.1).²⁸⁸ The NMR assignment of TNKS2 ARC4 (488-649) (Biological Magnetic Resonance Data Bank, BMRB accession code

27747) was propagated to picked peaks for each individual ^1H - ^{15}N HSQC spectra in the titration series.¹⁴⁷ The chemical shift perturbation ($\Delta\delta$), or average Euclidean distance shifted (Δd), in ppm from the baseline spectra for each backbone amide peak was calculated in CcpNmr from proton and nitrogen shifts, weighting the different nuclei, according to equation 7.7.^{182, 201}

$$\text{Equation 7.7: } \Delta\delta = d = \sqrt{\frac{1}{2}[\delta_H^2 + (\alpha \cdot \delta_N^2)]} \text{ where } \alpha = 0.14$$

Values of the average Euclidean distance shifted (d) against ligand concentration (μM) were plotted in GraphPad Prism (v 8.0) for backbone amide peaks which had shifted significantly compared with the mean CSP ($\Delta d > \text{average} + 1\sigma$). Dissociation constants (K_d) for individual shifted residues were calculated by non-linear regression analysis of chemical shift perturbation (Δd) against ligand concentration (μM), fitting the curve using the Levenberg-Marquardt method to equation 7.9 and the curve fit was analysed.¹⁸²

$$\text{Equation 7.8: } \Delta\delta_{obs} = \Delta\delta_{max} \frac{\{([P]_t + [L]_t + K_d) - \sqrt{([P]_t + [L]_t + K_d)^2 - 4([P]_t[L]_t)}\}}{2[P]_t}$$

$$\text{Equation 7.9: } Y = \Delta\delta_{max} \frac{\{([L]_t + K_d) - \sqrt{([L]_t + K_d)^2 - 4[L]_t}\}}{2}$$

The mean of individual dissociation constants for all shifted peaks with completely calculated 95% profile likelihood confidence intervals (95% CI) and goodness of fit (R^2) greater than 0.90 ($R^2 > 0.90$) was taken to give the reported average K_d by NMR values. Shifted peaks with incompletely calculated 95% CI or $R^2 < 0.90$ were excluded in average dissociation constant calculations. The reported error (\pm) was calculated as the standard deviation (SD) of the dissociation constants from residues included in the average dissociation constant calculation.

7.3.3 Fluorescence Polarisation Assay

A BMG LABTECH PHERAstar FSX microplate reader fitted with a Cy5 optic module was used for all fluorescence polarisation experiments.

7.3.3.1 Cy5 probe titration

The Cy5-labelled fluorescent probe (Cys-(Cy5)-RSPPDGQS), purchased from JPT peptide technologies, was dissolved in FP buffer (25 mM HEPES pH 7.5, 100 mM NaCl, 1 mM TCEP). The concentration was measured at 650 nm with a molar extinction coefficient of $250,000 \text{ M}^{-1} \text{ cm}^{-1}$, and the Cy5 probe solution was diluted to 4 μM in FP buffer. Aliquots of Cy5 probe stock solution (4 μM) were stored at $-80 \text{ }^\circ\text{C}$ and thawed as required.

Cy5 probe was dispensed in a 2-fold 10-point titration series (0 – 25 nM final concentrations) using an Echo acoustic liquid handler from a Cy5 probe stock solution (4 μM) in FP buffer into Plus F ProxiPlates (384 wells, black). The wells were backfilled to 1 μL with FP assay buffer (25 mM HEPES pH 7.5, 100 mM NaCl, 1 mM TCEP, + 0.01% CHAPS). TNKS1 ARC4 protein stock solution (500 μM) was diluted to 10 μM in FP assay buffer (+ 0.01% CHAPS). To the Cy5 probe titration wells was added either TNKS1 ARC4 in FP assay buffer (9 μL , 10 μM protein) or FP assay buffer only (9 μL , 10 μM protein) in triplicate using a Tempest microfluidic liquid dispenser. The plate was sealed, centrifuged for 1 min at $1000 \times g$ and incubated in the dark for 2 h before plate reading. Readings were taken with 50 flashes per well and fluorescence polarisation was calculated in millipolarisation (mP) units. Raw data was exported to excel and analysed in GraphPad Prism (v 9.3).

7.3.3.2 Direct binding FP assay with TNKS1 ARC4

TNKS1 ARC4 was dispensed in triplicate in a 2-fold 11-point titration series (0 – 25 μM final concentrations) using an Echo acoustic liquid handler from a TNKS1 ARC4 stock solution (100 μM) in FP buffer into Plus F ProxiPlates (384 wells, black). The wells were backfilled to 2.6 μL with FP assay buffer (+ 0.01% CHAPS). Cy5 probe stock solution (4 μM) was diluted to 5 nM in FP assay buffer (+ 0.01% CHAPS) and added to the TNKS1 ARC4 titration wells (7.4 μL , 5 nM Cy5 probe) using a Tempest microfluidic liquid dispenser. The plate was sealed, centrifuged for 1 min at $1000 \times g$ and incubated in the dark before plate reading at 2 h, 3 h, 4 h, 5 h, and 24 h. Readings were taken with 50 flashes per well and

fluorescence polarisation was calculated in millipolarisation (mP) units. Raw data was exported to excel, and the mean of the technical triplicate values was calculated at each TNKS1 ARC4 concentration. The mean FP values were baseline corrected using the mean FP for no protein wells (5 nM Cy5 probe only) to give baseline corrected mean FP (Δ FP) values. Data was analysed in GraphPad Prism (v 9.3). Baseline corrected mean FP values (Δ FP) were plotted against protein concentration and a non-linear regression analysis was performed using a total one-site binding model to calculate K_d values.

7.3.3.3 Competitive FP assay with control peptides

3BP2 16mer positive and negative (G6R) control peptides were dispensed in duplicate in a 3-fold 11-point titration series (0 – 935 μ M final concentrations) using an Echo acoustic liquid handler from peptide stock solutions (10 mM) in FP buffer into Plus F ProxiPlates (384 wells, black). The wells were backfilled to 1 μ L with FP assay buffer (+ 0.01% CHAPS). High control and low control rows were filled with 1 μ L FP assay buffer only (+ 0.01% CHAPS). A solution of Cy5 probe and TNKS1 ARC4 in FP assay buffer (+ 0.01% CHAPS) was prepared and added to the peptide titration wells and high control wells (9 μ L, 5 nM Cy5 probe and 7.25 μ M TNKS1 ARC4 final concentrations) using a Tempest microfluidic liquid dispenser. A solution of Cy5 probe in FP assay buffer (+ 0.01% CHAPS) was prepared and added to the low control wells (9 μ L, 5 nM Cy5 probe final concentration) using a Tempest microfluidic liquid dispenser. The plate was sealed, centrifuged for 1 min at 1000 $\times g$ and incubated in the dark before plate reading at 2 h. Readings were taken with 50 flashes per well and fluorescence polarisation was calculated in millipolarisation (mP) units. Raw data was exported to excel and analysed in GraphPad Prism (v 9.3). Concentrations were transformed to log values and FP values were normalised using the maximum and minimum FP values determined from the mean FP values of high and low control rows respectively. The mean normalised FP values from technical duplicates were plotted against log(concentration) and curves were fitted using a non-linear regression, log(inhibitor) vs. response – variable slope (four parameters) model.

7.3.3.4 Competitive FP assay with fragment compounds and control peptides

3BP2 16mer positive and negative (G6R) control peptides were dispensed in duplicate in a 3-fold 11-point titration series (0 – 935 μ M final concentrations) using an Echo acoustic liquid handler from peptide stock solutions (10 mM) in FP buffer into Plus F ProxiPlates (384 wells, black). The wells were backfilled to 0.8 μ L with FP assay buffer (+ 0.01% CHAPS). Compounds were dispensed in a 3-fold 11-point titration series (0 – 1000 μ M final concentrations) using an Echo acoustic liquid handler from compound stock solutions (50 mM) in DMSO-d₆ into Plus F ProxiPlates (384 wells, black). The wells were backfilled to 0.2 μ L with DMSO. High control and low control rows were filled with 0.2 μ L DMSO only.

A solution of Cy5 probe and TNKS1 ARC4 in FP assay buffer (+ 0.01% CHAPS) was prepared and added to the peptide titration wells and high control wells (9 μ L, 5 nM Cy5 probe and 7.25 μ M TNKS1 ARC4 final concentrations) using a Tempest microfluidic liquid dispenser. A solution of Cy5 probe in FP assay buffer (+ 0.01% CHAPS) was prepared and added to the low control wells (9 μ L, 5 nM Cy5 probe final concentration) using a Tempest microfluidic liquid dispenser. Finally, peptide titrations were backfilled with 0.2 μ L DMSO, and compound titrations along with high and low control wells were backfilled with 0.8 μ L FP assay buffer (+ 0.01% CHAPS).

The plate was sealed, centrifuged for 1 min at 1000 \times *g* and incubated in the dark before plate reading at 2 h. Readings were taken with 50 flashes per well and fluorescence polarisation was calculated in millipolarisation (mP) units. Raw data was exported to excel and analysed in GraphPad Prism (v 9.3). Concentrations were transformed to log values and FP values were normalised using the maximum and minimum FP values determined from the mean FP values of high and low control rows respectively. The mean normalised FP values were plotted against log(concentration) and curves were fitted using a non-linear regression, log(inhibitor) vs. response – variable slope (four parameters) model. Control peptides and compound CCT393128 (**115**) were tested in two independent experiments. All other compounds were tested in one independent experiment.

7.4 Computational Chemistry

7.4.1 MoKa Calculations

In silico physicochemical property predictions for compounds were calculated using MoKa software in Vortex from Dotmatics: calculated logP and calculated logD for fragments, and topological polar surface area for PROTACs. Compound structures were uploaded as a structure-data file (SDF) and calculations were run according to an in-house MoKa property prediction script.

7.4.2 Minimum Energy Conformations of Fragments

Minimum energy conformations of fragments were calculated using MOE software (2018.01) available from CCG.¹⁹⁸ Fragment structures were imported into MOE using an SDF file and energy minimisation was performed in the Energy Minimize tool using the Amber10:EHT forcefield, R-field solvation model and other default parameters.

7.4.3 Minimum Energy Conformations of Fragments based on CCT170746 (**28**) bound to TNKS2 ARC4

A crystal structure of human TNKS2 ARC4 in complex with the 3BP2 TBM peptide (PDB: 3TWR, chain D)⁶¹ was accessed using MOE software (2018.01) available from CCG.¹⁹⁸ The protein was prepared using the QuickPrep panel in MOE with default settings, including the Protonate3D function for addition of hydrogens. The binding modes of fragment hit CCT170746 (**28**) from *in silico* docking performed using GOLD software¹³⁵ were opened in MOE. The Builder tool was then used to add various substituents and fragment modifications to the structure of **28** in each of the five binding modes (binding modes 1, 2, 3, 4 and 5). The conformation of each fragment analogue in each binding mode was then minimised using the Minimize function in the Builder panel in the presence of TNKS2 ARC4 with all atoms of the protein fixed.

7.4.4 Fragment Docking into TNKS2 ARC4

In silico fragment docking was performed against a crystal structure of human TNKS2 ARC4 in complex with the 3BP2 TBM peptide (PDB: 3TWR, chain D)⁶¹ using MOE software (2018.01) available from CCG.¹⁹⁸ The protein was prepared and hydrogens were added using the QuickPrep panel and Protonate 3D function in MOE with default settings. Fragment structures were imported into MOE using an SDF file and saved as a MOE database (MDB) file. The fragment structures were processed and corrected for docking using the Wash panel within the MOE Database Viewer Wash panel with protonation at pH 7.0. With the protein and fragment structures prepared, fragment-protein docking was then performed using the General function of the Dock panel in MOE (Figure 7.1). In the Dock panel, the crystal structure of TNKS2 ARC4 was selected as the receptor and the docking site was chosen as 'selected residues'. The residues selected as the docking site were those which showed significant CSPs ($\Delta d > \text{average} + 1\sigma$) upon ligand titration. The ligand was imported as the prepared and washed MDB file. The docking was performed using the default methods and scoring functions for Placement and Refinement phases in MOE's Dock algorithm. The docking was performed using default methods: the Placement method was selected as Triangle Matcher scored using London dG scoring which retained 30 poses, then the Refinement method was selected as Rigid Receptor scored using GBVI/WSA dG which retained the top five ligand-protein docking poses for visual inspection.

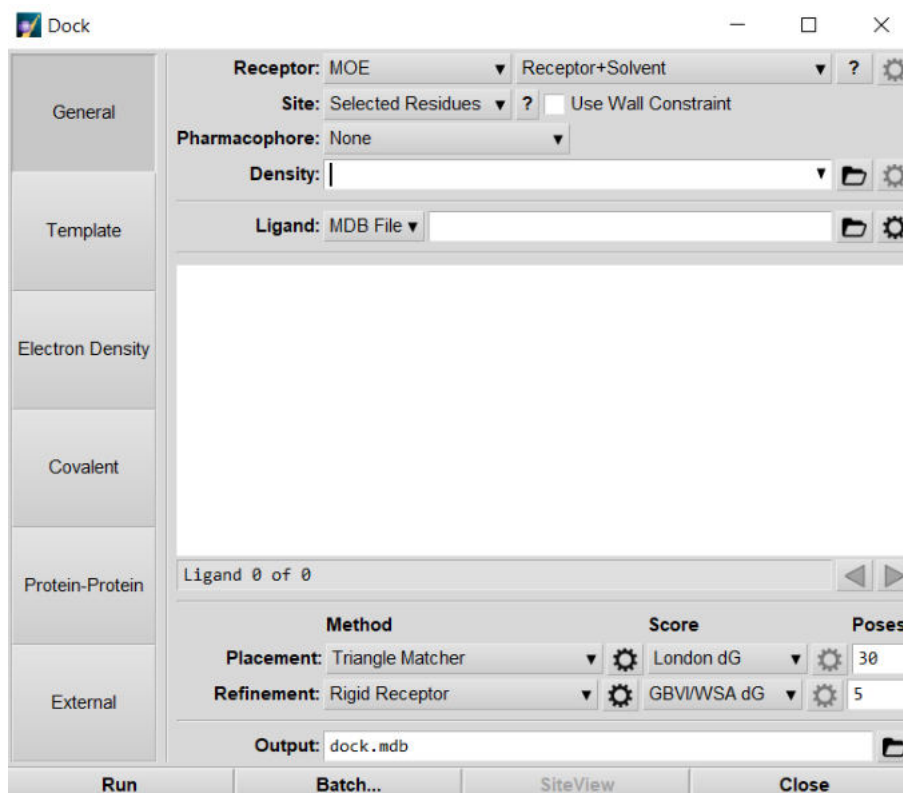


Figure 7.1. The Dock panel in MOE used for ligand-protein docking.

7.4.5 Minimum Energy Conformations of Hybrid Fragment-Peptidomimetics based on CCT393128 (**115**) and CCT394001 (**144**) bound to TNKS2 ARC4

A crystal structure of human TNKS2 ARC4 in complex with the 3BP2 TBM peptide (PDB: 3TWR, chain D)⁶¹ was accessed using MOE software (2018.01) available from CCG.¹⁹⁸ The protein was prepared using the QuickPrep panel in MOE with default settings, including the Protonate3D function for addition of hydrogen atoms. The binding mode of lead fragment CCT393128 (**115**) from *in silico* docking against TNKS2 ARC4:3BP2 crystal structure performed using MOE software was opened in MOE. The Builder tool was then used to delete the 3-dimethylamino quinoxaline substituent of **115** and generate the structure of CCT394001 (**144**) by addition of the 3-pyrrolidinyl substituent. The minimum energy conformation of **144** was obtained using the Minimize function with default parameters in the Builder panel in the presence of TNKS2 ARC4 with all atoms of the protein fixed.

Next, a crystal structure of human TNKS2 ARC4 in complex with the MCL1 TBM peptide (PDB: 3TWU, chain A)⁶¹ was accessed using MOE software (2018.01) available from CCG.¹⁹⁸ The protein was prepared using the QuickPrep panel in MOE with default settings, including the Protonate3D function for addition of hydrogen atoms. The binding mode of lead fragment **115** from *in silico* docking against TNKS2 ARC4:3BP2 crystal structure performed using MOE, and the binding mode of **144** from energy minimisation against TNKS2 ARC4:3BP2 crystal structure were opened in MOE. The Builder tool was then used to delete the isoxazole motif of **115** and **144**, and generate the chemical structures of CCT395505 (**118**) and CCT395504 (**159**) by addition of glycine and glutamate residues. The minimised conformations of **118** and **159** were then generated using the Minimize function in the Builder panel in the presence of TNKS2 ARC4 with all atoms of the protein fixed.

7.4.6 Minimum Energy Conformations of XAV939-based ether-linked PROTACs

Protein-protein docking of a crystal structure of the TNKS2 catalytic domain in complex with XAV939 (PDB: 3KR8)⁵² and an in-house structure of CRBN in complex with pomalidomide was performed in MOE. Docking pose 4 (p44) was used for *in silico* modelling of XAV939-based ether-linked PROTACs with 3-PEG, 4-PEG, and 5-PEG linker lengths. The Builder panel was used to modify the structures of XAV939 and pomalidomide and connect them with PEG linkers to generate the structures of CCT400031 (**190**), CCT400030 (**191**) and CCT400029 (**192**). The minimum energy conformations of the three compounds were obtained using the Minimize function in the Builder panel in the presence of TNKS2 catalytic domain and CRBN with all atoms of the protein fixed.

Chapter 8 References

1. Hahn, W. C.; Weinberg, R. A., Modelling the molecular circuitry of cancer. *Nat. Rev. Cancer* **2002**, *2* (5), 331-341.
2. Croce, C. M., Oncogenes and Cancer. *New Engl. J. Med.* **2008**, *358* (5), 502-511.
3. Hanahan, D.; Weinberg, R. A., The Hallmarks of Cancer. *Cell* **2000**, *100* (1), 57-70.
4. Hanahan, D.; Weinberg, Robert A., Hallmarks of Cancer: The Next Generation. *Cell* **2011**, *144* (5), 646-674.
5. Hanahan, D., Hallmarks of Cancer: New Dimensions. *Cancer Discov.* **2022**, *12* (1), 31-46.
6. Sung, H.; Ferlay, J.; Siegel, R. L.; Laversanne, M.; Soerjomataram, I.; Jemal, A.; Bray, F., Global Cancer Statistics 2020: GLOBOCAN Estimates of Incidence and Mortality Worldwide for 36 Cancers in 185 Countries. *CA: Cancer J. Clin.* **2021**, *71* (3), 209-249.
7. Esposito, M.; Ganesan, S.; Kang, Y., Emerging strategies for treating metastasis. *Nat. Cancer* **2021**, *2* (3), 258-270.
8. Zhong, L.; Li, Y.; Xiong, L.; Wang, W.; Wu, M.; Yuan, T.; Yang, W.; Tian, C.; Miao, Z.; Wang, T.; Yang, S., Small molecules in targeted cancer therapy: advances, challenges, and future perspectives. *Sig. Transduct. Target. Ther.* **2021**, *6* (1), 201.
9. Chaffer, C. L.; Weinberg, R. A., A Perspective on Cancer Cell Metastasis. *Science* **2011**, *331* (6024), 1559-1564.
10. Weber, G. F., DNA Damaging Drugs. In *Molecular Therapies of Cancer*, Weber, G. F., Ed. Springer International Publishing: Cham, 2015; pp 9-112.
11. Advancing Cancer Therapy. *Nat. Cancer* **2021**, *2* (3), 245-246.
12. Druker, B. J.; Sawyers, C. L.; Kantarjian, H.; Resta, D. J.; Reese, S. F.; Ford, J. M.; Capdeville, R.; Talpaz, M., Activity of a Specific Inhibitor of the BCR-ABL Tyrosine Kinase in the Blast Crisis of Chronic Myeloid Leukemia and Acute Lymphoblastic Leukemia with the Philadelphia Chromosome. *N. Engl. J. Med.* **2001**, *344* (14), 1038-1042.
13. Bedard, P. L.; Hyman, D. M.; Davids, M. S.; Siu, L. L., Small molecules, big impact: 20 years of targeted therapy in oncology. *Lancet* **2020**, *395* (10229), 1078-1088.
14. Yang, A.; Cho, K.; Park, H.-S., Chemical biology approaches for studying posttranslational modifications. *RNA Biol.* **2017**, *15* (4-5), 427-440.
15. Deribe, Y. L.; Pawson, T.; Dikic, I., Post-translational modifications in signal integration. *Nat. Struct. Mol. Biol.* **2010**, *17*, 666-672.
16. Chuh, K. N.; Batt, A. R.; Pratt, M. R., Chemical Methods for Encoding and Decoding of Posttranslational Modifications. *Cell Chem. Biol.* **2016**, *23* (1), 86-107.
17. Singh, V.; Ram, M.; Kumar, R.; Prasad, R.; Roy, B. K.; Singh, K. K., Phosphorylation: Implications in Cancer. *Protein J.* **2017**, *36* (1), 1-6.
18. Cohen, P., The Origins of Protein Phosphorylation. *Nat. Cell Biol.* **2002**, *4*, E127-E130.
19. Cohen, P., Protein kinases — the major drug targets of the twenty-first century? *Nat. Rev. Drug Discov.* **2002**, *1*, 309-315.

20. Kaniskan, H. Ü.; Martini, M. L.; Jin, J., Inhibitors of Protein Methyltransferases and Demethylases. *Chem. Rev.* **2018**, *118* (3), 989-1068.
21. Arrowsmith, C. H.; Bountra, C.; Fish, P. V.; Lee, K.; Schapira, M., Epigenetic protein families: a new frontier for drug discovery. *Nat. Rev. Drug Discov.* **2012**, *11*, 384.
22. Zheng, N.; Shabek, N., Ubiquitin Ligases: Structure, Function, and Regulation. *Ann. Rev. Biochem.* **2017**, *86* (1), 129-157.
23. Chopra, R.; Sadok, A.; Collins, I., A critical evaluation of the approaches to targeted protein degradation for drug discovery. *Drug Discov. Today Technol.* **2019**, *31*, 5-13.
24. Collins, I.; Wang, H.; Caldwell, J. J.; Chopra, R., Chemical approaches to targeted protein degradation through modulation of the ubiquitin–proteasome pathway. *Biochem. J.* **2017**, *474* (7), 1127-1147.
25. Shi, D.; Grossman, S. R., Ubiquitin becomes ubiquitous in cancer. *Cancer Biol. Ther.* **2010**, *10* (8), 737-747.
26. Lüscher, B.; Bütepage, M.; Ecker, L.; Krieg, S.; Verheugd, P.; Shilton, B. H., ADP-Ribosylation, a Multifaceted Posttranslational Modification Involved in the Control of Cell Physiology in Health and Disease. *Chem. Rev.* **2018**, *118* (3), 1092-1136.
27. Bhullar, K. S.; Lagarón, N. O.; McGowan, E. M.; Parmar, I.; Jha, A.; Hubbard, B. P.; Rupasinghe, H. P. V., Kinase-targeted cancer therapies: progress, challenges and future directions. *Mol. Cancer* **2018**, *17* (1), 48-48.
28. Baylin, S. B.; Jones, P. A., Epigenetic Determinants of Cancer. *Cold Spring Harb Perspect Biol* *8* (9), a019505.
29. Eckschlager, T.; Plch, J.; Stiborova, M.; Hrabeta, J., Histone Deacetylase Inhibitors as Anticancer Drugs. *Int. J. Mol. Sci.* **2017**, *18* (7).
30. Békés, M.; Langley, D. R.; Crews, C. M., PROTAC targeted protein degraders: the past is prologue. *Nat. Rev. Drug Discov.* **2022**, *21* (3), 181-200.
31. Jan, M.; Sperling, A. S.; Ebert, B. L., Cancer therapies based on targeted protein degradation — lessons learned with lenalidomide. *Nat. Rev. Clin. Oncol.* **2021**, *18* (7), 401-417.
32. Poltronieri, P.; Miwa, M.; Masutani, M., ADP-Ribosylation as Post-Translational Modification of Proteins: Use of Inhibitors in Cancer Control. *Int. J. Mol. Sci.* **2021**, *22* (19).
33. Robson, M.; Im, S.-A.; Senkus, E.; Xu, B.; Domchek, S. M.; Masuda, N.; Delaloge, S.; Li, W.; Tung, N.; Armstrong, A.; Wu, W.; Goessl, C.; Runswick, S.; Conte, P., Olaparib for Metastatic Breast Cancer in Patients with a Germline BRCA Mutation. *New Engl. J. Med.* **2017**, *377* (6), 523-533.
34. Kim, D.; Nam, H. J. PARP Inhibitors: Clinical Limitations and Recent Attempts to Overcome Them *Int. J. Mol. Sci.* [Online], 2022.
35. Barkauskaite, E.; Jankevicius, G.; Ahel, I., Structures and Mechanisms of Enzymes Employed in the Synthesis and Degradation of PARP-Dependent Protein ADP-Ribosylation. *Mol. Cell* **2015**, *58* (6), 935-946.
36. Hottiger, M. O.; Hassa, P. O.; Lüscher, B.; Schüler, H.; Koch-Nolte, F., Toward a unified nomenclature for mammalian ADP-ribosyltransferases. *Trends Biochem. Sci.* **2010**, *35* (4), 208-219.
37. Sung, V. M. H., Mechanistic overview of ADP-ribosylation reactions. *Biochimie* **2015**, *113*, 35-46.

38. Gibson, B. A.; Kraus, W. L., New insights into the molecular and cellular functions of poly(ADP-ribose) and PARPs. *Nat. Rev. Mol. Cell Biol.* **2012**, *13*, 411-424.
39. Hottiger, M. O., SnapShot: ADP-Ribosylation Signaling. *Mol. Cell* **2015**, *58* (6), 1134-1134.e1.
40. Vyas, S.; Matic, I.; Uchima, L.; Rood, J.; Zaja, R.; Hay, R. T.; Ahel, I.; Chang, P., Family-wide analysis of poly(ADP-ribose) polymerase activity. *Nat. Commun.* **2014**, *5*, 4426.
41. Bell, C. E.; Eisenberg, D., Crystal Structure of Diphtheria Toxin Bound to Nicotinamide Adenine Dinucleotide. *Biochemistry* **1996**, *35* (4), 1137-1149.
42. Steffen, J.; Brody, J.; Armen, R.; Pascal, J., Structural Implications for Selective Targeting of PARPs. *Front. Oncol.* **2013**, *3*, 301.
43. Karlberg, T.; Langelier, M.-F.; Pascal, J. M.; Schüler, H., Structural biology of the writers, readers, and erasers in mono- and poly(ADP-ribose) mediated signaling. *Mol. Asp. Med.* **2013**, *34* (6), 1088-1108.
44. Nizi, M. G.; Maksimainen, M. M.; Lehtiö, L.; Tabarrini, O., Medicinal Chemistry Perspective on Targeting Mono-ADP-Ribosylating PARPs with Small Molecules. *J. Med. Chem.* **2022**, *65* (11), 7532-7560.
45. Mariotti, L.; Pollock, K.; Guettler, S., Regulation of Wnt/ β -catenin signalling by tankyrase-dependent poly(ADP-ribosylation) and scaffolding. *Br. J. Pharmacol.* **2017**, *174* (24), 4611-4636.
46. Eisemann, T.; McCauley, M.; Langelier, M.-F.; Gupta, K.; Roy, S.; Van Duyne, G. D.; Pascal, John M., Tankyrase-1 Ankyrin Repeats Form an Adaptable Binding Platform for Targets of ADP-Ribose Modification. *Structure* **2016**, *24* (10), 1679-1692.
47. Narwal, M.; Venkannagari, H.; Lehtiö, L., Structural Basis of Selective Inhibition of Human Tankyrases. *J. Med. Chem.* **2012**, *55* (3), 1360-1367.
48. Chiang, Y. J.; Hsiao, S. J.; Yver, D.; Cushman, S. W.; Tessarollo, L.; Smith, S.; Hodes, R. J., Tankyrase 1 and Tankyrase 2 Are Essential but Redundant for Mouse Embryonic Development. *PLoS One* **2008**, *3* (7), e2639.
49. Smith, S.; Gariat, I.; Schmitt, A.; de Lange, T., Tankyrase, a Poly(ADP-Ribose) Polymerase at Human Telomeres. *Science* **1998**, *282* (5393), 1484-1487.
50. Lehtiö, L.; Chi, N.-W.; Krauss, S., Tankyrases as drug targets. *FEBS J.* **2013**, *280* (15), 3576-3593.
51. Lehtiö, L.; Collins, R.; van den Berg, S.; Johansson, A.; Dahlgren, L.-G.; Hammarström, M.; Helleday, T.; Holmberg-Schiavone, L.; Karlberg, T.; Weigelt, J., Zinc Binding Catalytic Domain of Human Tankyrase 1. *J. Mol. Biol.* **2008**, *379* (1), 136-145.
52. Karlberg, T.; Markova, N.; Johansson, I.; Hammarström, M.; Schütz, P.; Weigelt, J.; Schüler, H., Structural Basis for the Interaction between Tankyrase-2 and a Potent Wnt-Signaling Inhibitor. *J. Med. Chem.* **2010**, *53* (14), 5352-5355.
53. Teemu, H.; Stefan Krauss and Lari, L., Tankyrases: Structure, Function and Therapeutic Implications in Cancer. *Curr. Pharm. Des.* **2014**, *20* (41), 6472-6488.
54. Haikarainen, T.; Narwal, M.; Joensuu, P.; Lehtiö, L., Evaluation and Structural Basis for the Inhibition of Tankyrases by PARP Inhibitors. *ACS Med. Chem. Lett.* **2014**, *5* (1), 18-22.

55. Sowa, S. T.; Lehtiö, L., The zinc-binding motif in tankyrases is required for the structural integrity of the catalytic ADP-ribosyltransferase domain. *Open Biol* **2022**, *12* (3), 210365-210365.
56. De Rycker, M.; Price, C. M., Tankyrase Polymerization Is Controlled by Its Sterile Alpha Motif and Poly(ADP-Ribose) Polymerase Domains. *Mol. Cell. Biol.* **2004**, *24* (22), 9802-9812.
57. Mariotti, L.; Templeton, Catherine M.; Raney, M.; Paracuellos, P.; Cronin, N.; Beuron, F.; Morris, E.; Guettler, S., Tankyrase Requires SAM Domain-Dependent Polymerization to Support Wnt-B-Catenin Signaling. *Mol. Cell* **2016**, *63* (3), 498-513.
58. Riccio, Amanda A.; McCauley, M.; Langelier, M.-F.; Pascal, John M., Tankyrase Sterile α Motif Domain Polymerization Is Required for Its Role in Wnt Signaling. *Structure* **2016**, *24* (9), 1573-1581.
59. DaRosa, P. A.; Ovchinnikov, S.; Xu, W.; Klevit, R. E., Structural insights into SAM domain-mediated tankyrase oligomerization. *Protein Sci.* **2016**, *25* (9), 1744-1752.
60. Pillay, N.; Mariotti, L.; Zaleska, M.; Inian, O.; Jessop, M.; Hibbs, S.; Desfosses, A.; Hopkins, P. C. R.; Templeton, C. M.; Beuron, F.; Morris, E. P.; Guettler, S., Structural basis of tankyrase activation by polymerization. *Nature* **2022**.
61. Guettler, S.; LaRose, J.; Petsalaki, E.; Gish, G.; Scotter, A.; Pawson, T.; Rottapel, R.; Sicheri, F., Structural Basis and Sequence Rules for Substrate Recognition by Tankyrase Explain the Basis for Cherubism Disease. *Cell* **2011**, *147* (6), 1340-1354.
62. Li, J.; Mahajan, A.; Tsai, M.-D., Ankyrin Repeat: A Unique Motif Mediating Protein-Protein Interactions. *Biochemistry* **2006**, *45* (51), 15168-15178.
63. Seimiya, H.; Smith, S., The Telomeric Poly(ADP-ribose) Polymerase, Tankyrase 1, Contains Multiple Binding Sites for Telomeric Repeat Binding Factor 1 (TRF1) and a Novel Acceptor, 182-kDa Tankyrase-binding Protein (TAB182). *J. Biol. Chem.* **2002**, *277* (16), 14116-14126.
64. Seimiya, H.; Muramatsu, Y.; Smith, S.; Tsuruo, T., Functional Subdomain in the Ankyrin Domain of Tankyrase 1 Required for Poly(ADP-Ribosylation) of TRF1 and Telomere Elongation. *Mol. Cell. Biol.* **2004**, *24* (5), 1944.
65. Guettler, S., AXIN Shapes Tankyrase ARChitecture. *Structure* **2016**, *24* (10), 1625-1627.
66. Morrone, S.; Cheng, Z.; Moon, R. T.; Cong, F.; Xu, W., Crystal structure of a Tankyrase-Axin complex and its implications for Axin turnover and Tankyrase substrate recruitment. *Proc. Natl. Acad. Sci.* **2012**, *109* (5), 1500.
67. Sbodio, J. I.; Chi, N.-W., Identification of a Tankyrase-binding Motif Shared by IRAP, TAB182, and Human TRF1 but Not Mouse TRF1: NuMA CONTAINS THIS RXXPDG MOTIF AND IS A NOVEL TANKYRASE PARTNER. *J. Biol. Chem.* **2002**, *277* (35), 31887-31892.
68. Bhardwaj, A.; Yang, Y.; Ueberheide, B.; Smith, S., Whole proteome analysis of human tankyrase knockout cells reveals targets of tankyrase-mediated degradation. *Nat. Commun.* **2017**, *8* (1), 2214.
69. Huang, S.-M. A.; Mishina, Y. M.; Liu, S.; Cheung, A.; Stegmeier, F.; Michaud, G. A.; Charlat, O.; Wiellette, E.; Zhang, Y.; Wiessner, S.; Hild, M.; Shi, X.; Wilson, C. J.; Mickanin, C.; Myer, V.; Fazal, A.; Tomlinson, R.; Serluca, F.; Shao, W.; Cheng, H.; Shultz, M.; Rau, C.; Schirle, M.; Schlegl, J.; Ghidelli, S.; Fawell, S.; Lu, C.; Curtis, D.; Kirschner, M. W.; Lengauer, C.; Finan, P. M.;

- Tallarico, J. A.; Bouwmeester, T.; Porter, J. A.; Bauer, A.; Cong, F., Tankyrase inhibition stabilizes axin and antagonizes Wnt signalling. *Nature* **2009**, *461*, 614-620.
70. Bae, J.; Donigian, J. R.; Hsueh, A. J. W., Tankyrase 1 Interacts with Mcl-1 Proteins and Inhibits Their Regulation of Apoptosis*. *J. Biol. Chem.* **2003**, *278* (7), 5195-5204.
71. Bisht Kamlesh, K.; Dudognon, C.; Chang William, G.; Sokol Ethan, S.; Ramirez, A.; Smith, S., GDP-Mannose-4,6-Dehydratase Is a Cytosolic Partner of Tankyrase 1 That Inhibits Its Poly(ADP-Ribose) Polymerase Activity. *Mol. Cell. Biol.* **2012**, *32* (15), 3044-3053.
72. Smith, S.; de Lange, T., Tankyrase promotes telomere elongation in human cells. *Curr. Biol.* **2000**, *10* (20), 1299-1302.
73. Hsiao, S. J.; Smith, S., Tankyrase function at telomeres, spindle poles, and beyond. *Biochimie* **2008**, *90* (1), 83-92.
74. Chang, P.; Coughlin, M.; Mitchison, T. J., Tankyrase-1 polymerization of poly(ADP-ribose) is required for spindle structure and function. *Nat. Cell Biol.* **2005**, *7*, 1133.
75. Chang, P.; Coughlin, M.; Mitchison, T. J., Interaction between Poly(ADP-ribose) and NuMA Contributes to Mitotic Spindle Pole Assembly. *Mol. Biol. Cell* **2009**, *20* (21), 4575-4585.
76. Nagy, Z.; Kalousi, A.; Furst, A.; Koch, M.; Fischer, B.; Soutoglou, E., Tankyrases Promote Homologous Recombination and Check Point Activation in Response to DSBs. *PLoS Genet.* **2016**, *12* (2), e1005791.
77. Okamoto, K.; Ohishi, T.; Kuroiwa, M.; Iemura, S.-i.; Natsume, T.; Seimiya, H., MERIT40-dependent recruitment of tankyrase to damaged DNA and its implication for cell sensitivity to DNA-damaging anticancer drugs. *Oncotarget* **2018**, *9* (88).
78. Chi, N.-W.; Lodish, H. F., Tankyrase Is a Golgi-associated Mitogen-activated Protein Kinase Substrate That Interacts with IRAP in GLUT4 Vesicles*. *J. Biol. Chem.* **2000**, *275* (49), 38437-38444.
79. Zhong, L.; Ding, Y.; Bandyopadhyay, G.; Waaler, J.; Börgeson, E.; Smith, S.; Zhang, M.; Phillips, S. A.; Mahooti, S.; Mahata, S. K.; Shao, J.; Krauss, S.; Chi, N.-W., The PARsylation activity of tankyrase in adipose tissue modulates systemic glucose metabolism in mice. *Diabetologia* **2016**, *59* (3), 582-591.
80. Wang, W.; Li, N.; Li, X.; Tran, My K.; Han, X.; Chen, J., Tankyrase Inhibitors Target YAP by Stabilizing Angiomin Family Proteins. *Cell Rep.* **2015**, *13* (3), 524-532.
81. Troilo, A.; Benson, E. K.; Esposito, D.; Garibsingh, R.-A. A.; Reddy, E. P.; Mungamuri, S. K.; Aaronson, S. A., Angiomin stabilization by tankyrase inhibitors antagonizes constitutive TEAD-dependent transcription and proliferation of human tumor cells with Hippo pathway core component mutations. *Oncotarget* **2016**, *7* (20), 28765-28782.
82. Jia, J.; Qiao, Y.; Pilo, M. G.; Cigliano, A.; Liu, X.; Shao, Z.; Calvisi, D. F.; Chen, X., Tankyrase inhibitors suppress hepatocellular carcinoma cell growth via modulating the Hippo cascade. *PLoS One* **2017**, *12* (9), e0184068.
83. Riffell, J. L.; Lord, C. J.; Ashworth, A., Tankyrase-targeted therapeutics: expanding opportunities in the PARP family. *Nat. Rev. Drug Discov.* **2012**, *11*, 923.
84. Stamos, J. L.; Weis, W. I., The β -catenin destruction complex. *Cold Spring Harb Perspect Biol* *5* (1), a007898-a007898.

85. Salic, A.; Lee, E.; Mayer, L.; Kirschner, M. W., Control of β -Catenin Stability: Reconstitution of the Cytoplasmic Steps of the Wnt Pathway in Xenopus Egg Extracts. *Mol. Cell* **2000**, *5* (3), 523-532.
86. Yang, E.; Tacchelly-Benites, O.; Wang, Z.; Randall, M. P.; Tian, A.; Benchabane, H.; Freemantle, S.; Pikielny, C.; Tolwinski, N. S.; Lee, E.; Ahmed, Y., Wnt pathway activation by ADP-ribosylation. *Nat. Commun.* **2016**, *7*, 11430.
87. Callow, M. G.; Tran, H.; Phu, L.; Lau, T.; Lee, J.; Sandoval, W. N.; Liu, P. S.; Bheddah, S.; Tao, J.; Lill, J. R.; Hongo, J.-A.; Davis, D.; Kirkpatrick, D. S.; Polakis, P.; Costa, M., Ubiquitin Ligase RNF146 Regulates Tankyrase and Axin to Promote Wnt Signaling. *PLoS One* **2011**, *6* (7), e22595.
88. Chen, B.; Dodge, M. E.; Tang, W.; Lu, J.; Ma, Z.; Fan, C.-W.; Wei, S.; Hao, W.; Kilgore, J.; Williams, N. S.; Roth, M. G.; Amatruda, J. F.; Chen, C.; Lum, L., Small molecule-mediated disruption of Wnt-dependent signaling in tissue regeneration and cancer. *Nat. Chem. Biol.* **2009**, *5* (2), 100-107.
89. Pedersen, N. M.; Thorvaldsen, T. E.; Schultz, S. W.; Wenzel, E. M.; Stenmark, H., Formation of Tankyrase Inhibitor-Induced Degradasomes Requires Proteasome Activity. *PLoS One* **2016**, *11* (8), e0160507-e0160507.
90. de Lange, T., Shelterin: the protein complex that shapes and safeguards human telomeres. *Genes Dev.* **2005**, *19* (18), 2100-2110.
91. Diotti, R.; Loayza, D., Shelterin complex and associated factors at human telomeres. *Nucleus-Austin* **2011**, *2* (2), 119-135.
92. Smith, S.; de Lange, T., Cell cycle dependent localization of the telomeric PARP, tankyrase, to nuclear pore complexes and centrosomes. *J. Cell Sci.* **1999**, *112* (21), 3649-3656.
93. Yu, M.; Yang, Y.; Sykes, M.; Wang, S., Small-Molecule Inhibitors of Tankyrases as Prospective Therapeutics for Cancer. *J. Med. Chem.* **2022**, *65* (7), 5244-5273.
94. Dregalla, R. C.; Zhou, J.; Idate, R. R.; Battaglia, C. L. R.; Liber, H. L.; Bailey, S. M., Regulatory roles of tankyrase 1 at telomeres and in DNA repair: suppression of T-SCE and stabilization of DNA-PKcs. *Aging* **2010**, *2* (10), 691-708.
95. Nicolas, E.; Bertucci, F.; Sabatier, R.; Gonçalves, A. Targeting BRCA Deficiency in Breast Cancer: What are the Clinical Evidences and the Next Perspectives? *Cancers* [Online], 2018.
96. McCabe, N.; Cerone, M. A.; Ohishi, T.; Seimiya, H.; Lord, C. J.; Ashworth, A., Targeting Tankyrase 1 as a therapeutic strategy for BRCA-associated cancer. *Oncogene* **2009**, *28*, 1465-1470.
97. Ferri, M.; Liscio, P.; Carotti, A.; Ascitti, S.; Sardella, R.; Macchiarulo, A.; Camaioni, E., Targeting Wnt-driven cancers: Discovery of novel tankyrase inhibitors. *Eur. J. Med. Chem.* **2017**, *142*, 506-522.
98. Mehta, C. C.; Bhatt, H. G., Tankyrase inhibitors as antitumor agents: a patent update (2013 – 2020). *Expert Opin. Ther. Pat.* **2021**, *31* (7), 645-661.
99. Bregman, H.; Chakka, N.; Guzman-Perez, A.; Gunaydin, H.; Gu, Y.; Huang, X.; Berry, V.; Liu, J.; Teffera, Y.; Huang, L.; Egge, B.; Mullady, E. L.; Schneider, S.; Andrews, P. S.; Mishra, A.; Newcomb, J.; Serafino, R.; Strathdee, C. A.; Turci, S. M.; Wilson, C.; DiMauro, E. F., Discovery of Novel, Induced-Pocket Binding Oxazolidinones as Potent, Selective, and Orally Bioavailable Tankyrase Inhibitors. *J. Med. Chem.* **2013**, *56* (11), 4320-4342.
100. Bregman, H.; Gunaydin, H.; Gu, Y.; Schneider, S.; Wilson, C.; DiMauro, E. F.; Huang, X., Discovery of a Class of Novel Tankyrase Inhibitors that Bind to

Both the Nicotinamide Pocket and the Induced Pocket. *J. Med. Chem.* **2013**, *56* (3), 1341-1345.

101. Thorsell, A.-G.; Ekblad, T.; Karlberg, T.; Löw, M.; Pinto, A. F.; Trésaugues, L.; Moche, M.; Cohen, M. S.; Schüler, H., Structural Basis for Potency and Promiscuity in Poly(ADP-ribose) Polymerase (PARP) and Tankyrase Inhibitors. *J. Med. Chem.* **2017**, *60* (4), 1262-1271.

102. Kirby, C. A.; Cheung, A.; Fazal, A.; Shultz, M. D.; Stams, T., Structure of human tankyrase 1 in complex with small-molecule inhibitors PJ34 and XAV939. *Acta Crystallogr. Sect. F Struct. Biol. Cryst. Commun.* **2012**, *68* (2), 115-118.

103. Haikarainen, T.; Koivunen, J.; Narwal, M.; Venkannagari, H.; Obaji, E.; Joensuu, P.; Pihlajaniemi, T.; Lehtiö, L., para-Substituted 2-Phenyl-3,4-dihydroquinazolin-4-ones As Potent and Selective Tankyrase Inhibitors. *ChemMedChem* **2013**, *8* (12), 1978-1985.

104. Nathubhai, A.; Haikarainen, T.; Hayward, P. C.; Muñoz-Descalzo, S.; Thompson, A. S.; Lloyd, M. D.; Lehtiö, L.; Threadgill, M. D., Structure-activity relationships of 2-arylquinazolin-4-ones as highly selective and potent inhibitors of the tankyrases. *Eur. J. Med. Chem.* **2016**, *118*, 316-327.

105. Nathubhai, A.; Wood, P. J.; Lloyd, M. D.; Thompson, A. S.; Threadgill, M. D., Design and Discovery of 2-Arylquinazolin-4-ones as Potent and Selective Inhibitors of Tankyrases. *ACS Med. Chem. Lett.* **2013**, *4* (12), 1173-1177.

106. Narwal, M.; Koivunen, J.; Haikarainen, T.; Obaji, E.; Legala, O. E.; Venkannagari, H.; Joensuu, P.; Pihlajaniemi, T.; Lehtiö, L., Discovery of Tankyrase Inhibiting Flavones with Increased Potency and Isoenzyme Selectivity. *J. Med. Chem.* **2013**, *56* (20), 7880-7889.

107. Larsson, E. A.; Jansson, A.; Ng, F. M.; Then, S. W.; Panicker, R.; Liu, B.; Sangthongpitag, K.; Pendharkar, V.; Tai, S. J.; Hill, J.; Dan, C.; Ho, S. Y.; Cheong, W. W.; Poulsen, A.; Blanchard, S.; Lin, G. R.; Alam, J.; Keller, T. H.; Nordlund, P., Fragment-Based Ligand Design of Novel Potent Inhibitors of Tankyrases. *J. Med. Chem.* **2013**, *56* (11), 4497-4508.

108. Liscio, P.; Carotti, A.; Ascitti, S.; Karlberg, T.; Bellocchi, D.; Llacuna, L.; Macchiarulo, A.; Aaronson, S. A.; Schüler, H.; Pellicciari, R.; Camaioni, E., Design, Synthesis, Crystallographic Studies, and Preliminary Biological Appraisal of New Substituted Triazolo[4,3-b]pyridazin-8-amine Derivatives as Tankyrase Inhibitors. *J. Med. Chem.* **2014**, *57* (6), 2807-2812.

109. Johannes, J. W.; Almeida, L.; Barlaam, B.; Boriack-Sjodin, P. A.; Casella, R.; Croft, R. A.; Dishington, A. P.; Gingipalli, L.; Gu, C.; Hawkins, J. L.; Holmes, J. L.; Howard, T.; Huang, J.; Ioannidis, S.; Kazmirski, S.; Lamb, M. L.; McGuire, T. M.; Moore, J. E.; Ogg, D.; Patel, A.; Pike, K. G.; Pontz, T.; Robb, G. R.; Su, N.; Wang, H.; Wu, X.; Zhang, H.-J.; Zhang, Y.; Zheng, X.; Wang, T., Pyrimidinone Nicotinamide Mimetics as Selective Tankyrase and Wnt Pathway Inhibitors Suitable for in Vivo Pharmacology. *ACS Med. Chem. Lett.* **2015**, *6* (3), 254-259.

110. Quackenbush, K. S.; Bagby, S.; Tai, W. M.; Messersmith, W. A.; Schreiber, A.; Greene, J.; Kim, J.; Wang, G.; Purkey, A.; Pitts, T. M.; Nguyen, A.; Gao, D.; Blatchford, P.; Capasso, A.; Schuller, A. G.; Eckhardt, S. G.; Arcaroli, J. J., The novel tankyrase inhibitor (AZ1366) enhances irinotecan activity in tumors that exhibit elevated tankyrase and irinotecan resistance. *Oncotarget* **2016**, *7* (19), 28273-28285.

111. Shirai, F.; Tsumura, T.; Yashiroda, Y.; Yuki, H.; Niwa, H.; Sato, S.; Chikada, T.; Koda, Y.; Washizuka, K.; Yoshimoto, N.; Abe, M.; Onuki, T.; Mazaki, Y.; Hiramata, C.; Fukami, T.; Watanabe, H.; Honma, T.; Umehara, T.; Shirouzu, M.;

- Okue, M.; Kano, Y.; Watanabe, T.; Kitamura, K.; Shitara, E.; Muramatsu, Y.; Yoshida, H.; Mizutani, A.; Seimiya, H.; Yoshida, M.; Koyama, H., Discovery of Novel Spiroindoline Derivatives as Selective Tankyrase Inhibitors. *J. Med. Chem.* **2019**, *62* (7), 3407-3427.
112. Mizutani, A.; Yashiroda, Y.; Muramatsu, Y.; Yoshida, H.; Chikada, T.; Tsumura, T.; Okue, M.; Shirai, F.; Fukami, T.; Yoshida, M.; Seimiya, H., RK-287107, a potent and specific tankyrase inhibitor, blocks colorectal cancer cell growth in a preclinical model. *Cancer Sci.* **2018**, *109* (12), 4003-4014.
113. Shirai, F.; Mizutani, A.; Yashiroda, Y.; Tsumura, T.; Kano, Y.; Muramatsu, Y.; Chikada, T.; Yuki, H.; Niwa, H.; Sato, S.; Washizuka, K.; Koda, Y.; Mazaki, Y.; Jang, M.-K.; Yoshida, H.; Nagamori, A.; Okue, M.; Watanabe, T.; Kitamura, K.; Shitara, E.; Honma, T.; Umehara, T.; Shirouzu, M.; Fukami, T.; Seimiya, H.; Yoshida, M.; Koyama, H., Design and Discovery of an Orally Efficacious Spiroindolinone-Based Tankyrase Inhibitor for the Treatment of Colon Cancer. *J. Med. Chem.* **2020**.
114. Buchstaller, H.-P.; Anlauf, U.; Dorsch, D.; Kögler, S.; Kuhn, D.; Lehmann, M.; Leuthner, B.; Lodholz, S.; Musil, D.; Radtke, D.; Rettig, C.; Ritzert, C.; Rohdich, F.; Schneider, R.; Wegener, A.; Weigt, S.; Wilkinson, K.; Esdar, C., Optimization of a Screening Hit toward M2912, an Oral Tankyrase Inhibitor with Antitumor Activity in Colorectal Cancer Models. *J. Med. Chem.* **2021**, *64* (14), 10371-10392.
115. Menon, M.; Elliott, R.; Bowers, L.; Balan, N.; Rafiq, R.; Costa-Cabral, S.; Munkonge, F.; Trindade, I.; Porter, R.; Campbell, A. D.; Johnson, E. R.; Esdar, C.; Buchstaller, H.-P.; Leuthner, B.; Rohdich, F.; Schneider, R.; Sansom, O.; Wienke, D.; Ashworth, A.; Lord, C. J., A novel tankyrase inhibitor, MSC2504877, enhances the effects of clinical CDK4/6 inhibitors. *Sci Rep* **2019**, *9* (1), 201.
116. Waaler, J.; Machon, O.; von Kries, J. P.; Wilson, S. R.; Lundenes, E.; Wedlich, D.; Gradl, D.; Paulsen, J. E.; Machonova, O.; Dembinski, J. L.; Dinh, H.; Krauss, S., Novel Synthetic Antagonists of Canonical Wnt Signaling Inhibit Colorectal Cancer Cell Growth. *Cancer Res.* **2011**, *71* (1), 197.
117. Shultz, M. D.; Kirby, C. A.; Stams, T.; Chin, D. N.; Blank, J.; Charlat, O.; Cheng, H.; Cheung, A.; Cong, F.; Feng, Y.; Fortin, P. D.; Hood, T.; Tyagi, V.; Xu, M.; Zhang, B.; Shao, W., [1,2,4]Triazol-3-ylsulfanylmethyl-3-phenyl-[1,2,4]oxadiazoles: Antagonists of the Wnt Pathway That Inhibit Tankyrases 1 and 2 via Novel Adenosine Pocket Binding. *J. Med. Chem.* **2012**, *55* (3), 1127-1136.
118. Voronkov, A.; Holsworth, D. D.; Waaler, J.; Wilson, S. R.; Ekblad, B.; Perdreau-Dahl, H.; Dinh, H.; Drewes, G.; Hopf, C.; Morth, J. P.; Krauss, S., Structural Basis and SAR for G007-LK, a Lead Stage 1,2,4-Triazole Based Specific Tankyrase 1/2 Inhibitor. *J. Med. Chem.* **2013**, *56* (7), 3012-3023.
119. Haikarainen, T.; Venkannagari, H.; Narwal, M.; Obaji, E.; Lee, H.-W.; Nkizinkiko, Y.; Lehtiö, L., Structural basis and selectivity of tankyrase inhibition by a Wnt signaling inhibitor WIKI4. *PLoS one* **2013**, *8* (6), e65404-e65404.
120. James, R. G.; Davidson, K. C.; Bosch, K. A.; Biechele, T. L.; Robin, N. C.; Taylor, R. J.; Major, M. B.; Camp, N. D.; Fowler, K.; Martins, T. J.; Moon, R. T., WIKI4, a novel inhibitor of tankyrase and Wnt/ β -catenin signaling. *PLoS one* **2012**, *7* (12), e50457-e50457.
121. Okada-Iwasaki, R.; Takahashi, Y.; Watanabe, Y.; Ishida, H.; Saito, J.-i.; Nakai, R.; Asai, A., The Discovery and Characterization of K-756, a Novel Wnt/ β -Catenin Pathway Inhibitor Targeting Tankyrase. *Mol. Cancer Ther.* **2016**, *15* (7), 1525.

122. Haikarainen, T.; Waaler, J.; Ignatev, A.; Nkizinkiko, Y.; Venkannagari, H.; Obaji, E.; Krauss, S.; Lehtiö, L., Development and structural analysis of adenosine site binding tankyrase inhibitors. *Bioorg. Med. Chem. Lett.* **2016**, *26* (2), 328-333.
123. Waaler, J.; Machon, O.; Tumova, L.; Dinh, H.; Korinek, V.; Wilson, S. R.; Paulsen, J. E.; Pedersen, N. M.; Eide, T. J.; Machonova, O.; Gradl, D.; Voronkov, A.; von Kries, J. P.; Krauss, S., A Novel Tankyrase Inhibitor Decreases Canonical Wnt Signaling in Colon Carcinoma Cells and Reduces Tumor Growth in Conditional APC Mutant Mice. *Cancer Res.* **2012**, *72* (11), 2822.
124. Shultz, M. D.; Cheung, A. K.; Kirby, C. A.; Firestone, B.; Fan, J.; Chen, C. H.-T.; Chen, Z.; Chin, D. N.; DiPietro, L.; Fazal, A.; Feng, Y.; Fortin, P. D.; Gould, T.; Lagu, B.; Lei, H.; Lenoir, F.; Majumdar, D.; Ochala, E.; Palermo, M. G.; Pham, L.; Pu, M.; Smith, T.; Stams, T.; Tomlinson, R. C.; Touré, B. B.; Visser, M.; Wang, R. M.; Waters, N. J.; Shao, W., Identification of NVP-TNKS656: The Use of Structure–Efficiency Relationships To Generate a Highly Potent, Selective, and Orally Active Tankyrase Inhibitor. *J. Med. Chem.* **2013**, *56* (16), 6495-6511.
125. Elliott, R. J. R.; Jarvis, A.; Rajasekaran, M. B.; Menon, M.; Bowers, L.; Boffey, R.; Bayford, M.; Firth-Clark, S.; Key, R.; Aqil, R.; Kirton, S. B.; Niculescu-Duvaz, D.; Fish, L.; Lopes, F.; McLeary, R.; Trindade, I.; Vendrell, E.; Munkonge, F.; Porter, R.; Perrior, T.; Springer, C.; Oliver, A. W.; Pearl, L. H.; Ashworth, A.; Lord, C. J., Design and discovery of 3-aryl-5-substituted-isoquinolin-1-ones as potent tankyrase inhibitors. *MedChemComm* **2015**, *6* (9), 1687-1692.
126. McGonigle, S.; Chen, Z.; Wu, J.; Chang, P.; Kolber-Simonds, D.; Ackermann, K.; Twine, N. C.; Shie, J.-L.; Miu, J. T.; Huang, K.-C.; Moniz, G. A.; Nomoto, K., E7449: A dual inhibitor of PARP1/2 and tankyrase1/2 inhibits growth of DNA repair deficient tumors and antagonizes Wnt signaling. *Oncotarget* **2015**, *6* (38), 41307-41323.
127. Lee, H. C., K.; Joe, B.-Y.; Kim, E. S.; Jang, E. S.; Oh, H.; Kim, J.-M.; Park, J.; Lee, H. Tricyclic compound as PARP inhibitor and methods for the preparation thereof. WO2016200101, 2016.
128. Plummer, R.; Dua, D.; Cresti, N.; Drew, Y.; Stephens, P.; Foegh, M.; Knudsen, S.; Sachdev, P.; Mistry, B. M.; Dixit, V.; McGonigle, S.; Hall, N.; Matijevic, M.; McGrath, S.; Sarker, D., First-in-human study of the PARP/tankyrase inhibitor E7449 in patients with advanced solid tumours and evaluation of a novel drug-response predictor. *Br. J. Cancer* **2020**, *123* (4), 525-533.
129. Im, S.-A.; Lee, S.; Lee, K. W.; Lee, Y.; Sohn, J.; Kim, J. H.; Im, Y.-H.; Park, K. H.; Oh, D.-Y.; Kim, M. H.; Park, Y. H.; Kim, T. M.; Choi, Y. J.; Lee, C.-S.; Park, J.; Baek, N. S.; Choi, M.; Kim, J.; Yu, E.; Bang, Y.-J., A phase I dose-escalation and expansion study of JPI-547, a dual inhibitor of PARP/tankyrase in patients with advanced solid tumors. *J. Clin. Oncol.* **2021**, *39* (15_suppl), 3113-3113.
130. Lau, T.; Chan, E.; Callow, M.; Waaler, J.; Boggs, J.; Blake, R. A.; Magnuson, S.; Sambrone, A.; Schutten, M.; Firestein, R.; Machon, O.; Korinek, V.; Choo, E.; Diaz, D.; Merchant, M.; Polakis, P.; Holsworth, D. D.; Krauss, S.; Costa, M., A Novel Tankyrase Small-Molecule Inhibitor Suppresses APC Mutation–Driven Colorectal Tumor Growth. *Cancer Res.* **2013**, *73* (10), 3132-3144.
131. Zhong, Y.; Katavolos, P.; Nguyen, T.; Lau, T.; Boggs, J.; Sambrone, A.; Kan, D.; Merchant, M.; Harstad, E.; Diaz, D.; Costa, M.; Schutten, M., Tankyrase

Inhibition Causes Reversible Intestinal Toxicity in Mice with a Therapeutic Index < 1. *Toxicol. Pathol.* **2015**, *44* (2), 267-278.

132. Kahn, M., Can we safely target the WNT pathway? *Nat. Rev. Drug Discov.* **2014**, *13* (7), 513-532.

133. Scott, D. E.; Bayly, A. R.; Abell, C.; Skidmore, J., Small molecules, big targets: drug discovery faces the protein–protein interaction challenge. *Nat. Rev. Drug Discov.* **2016**, *15* (8), 533-550.

134. Xu, W.; Lau, Y. H.; Fischer, G.; Tan, Y. S.; Chattopadhyay, A.; de la Roche, M.; Hyvönen, M.; Verma, C.; Spring, D. R.; Itzhaki, L. S., Macrocyclized Extended Peptides: Inhibiting the Substrate-Recognition Domain of Tankyrase. *J. Am. Chem. Soc.* **2017**, *139* (6), 2245-2256.

135. Pollock, K.; Liu, M.; Zaleska, M.; Meniconi, M.; Pfuhl, M.; Collins, I.; Guettler, S., Fragment-based screening identifies molecules targeting the substrate-binding ankyrin repeat domains of tankyrase. *Sci Rep* **2019**, *9* (1), 19130-19130.

136. Cheng, H.; Li, X.; Wang, C.; Chen, Y.; Li, S.; Tan, J.; Tan, B.; He, Y., Inhibition of tankyrase by a novel small molecule significantly attenuates prostate cancer cell proliferation. *Cancer Lett.* **2019**, *443*, 80-90.

137. Sowa, S. T.; Vela-Rodríguez, C.; Galera-Prat, A.; Cázares-Olivera, M.; Prunskaitė-Hyyryläinen, R.; Ignatov, A.; Lehtiö, L., A FRET-based high-throughput screening platform for the discovery of chemical probes targeting the scaffolding functions of human tankyrases. *Sci Rep* **2020**, *10* (1), 12357.

138. Keskin, O.; Gursoy, A.; Ma, B.; Nussinov, R., Principles of Protein–Protein Interactions: What are the Preferred Ways For Proteins To Interact? *Chem. Rev.* **2008**, *108* (4), 1225-1244.

139. Blundell, T. L.; Sibanda, B. L.; Montalvão, R. W.; Brewerton, S.; Chelliah, V.; Worth, C. L.; Harmer, N. J.; Davies, O.; Burke, D., Structural biology and bioinformatics in drug design: opportunities and challenges for target identification and lead discovery. *Philos. Trans. R. Soc. B: Biol. Sci.* **2006**, *361* (1467), 413-423.

140. Li Petri, G.; Di Martino, S.; De Rosa, M., Peptidomimetics: An Overview of Recent Medicinal Chemistry Efforts toward the Discovery of Novel Small Molecule Inhibitors. *J. Med. Chem.* **2022**, *65* (11), 7438-7475.

141. Hughes, J. P.; Rees, S.; Kalindjian, S. B.; Philpott, K. L., Principles of early drug discovery. *Br. J. Pharmacol.* **2011**, *162* (6), 1239-1249.

142. Meyer, B.; Peters, T., NMR Spectroscopy Techniques for Screening and Identifying Ligand Binding to Protein Receptors. *Angew. Chem. Int. Ed.* **2003**, *42* (8), 864-890.

143. Stockman, B. J.; Dalvit, C., NMR screening techniques in drug discovery and drug design. *Prog. Nucl. Magn. Reson. Spectrosc.* **2002**, *41* (3), 187-231.

144. Gossert, A. D.; Jahnke, W., NMR in drug discovery: A practical guide to identification and validation of ligands interacting with biological macromolecules. *Prog. Nucl. Magn. Reson. Spectrosc.* **2016**, *97*, 82-125.

145. Ma, R.; Wang, P.; Wu, J.; Ruan, K., Process of Fragment-Based Lead Discovery—A Perspective from NMR. *Molecules* **2016**, *21* (7).

146. Erlanson, D. A.; Fesik, S. W.; Hubbard, R. E.; Jahnke, W.; Jhoti, H., Twenty years on: the impact of fragments on drug discovery. *Nat. Rev. Drug Discov.* **2016**, *15* (9), 605-619.

147. Zaleska, M.; Pollock, K.; Collins, I.; Guettler, S.; Pfuhl, M., Solution NMR assignment of the ARC4 domain of human tankyrase 2. *Biomol. NMR Assign.* **2019**, *13* (1), 255-260.
148. Lavecchia, A.; Giovanni, D. C., Virtual Screening Strategies in Drug Discovery: A Critical Review. *Curr. Med. Chem.* **2013**, *20* (23), 2839-2860.
149. Xu, D.; Liu, J.; Fu, T.; Shan, B.; Qian, L.; Pan, L.; Yuan, J., USP25 regulates Wnt signaling by controlling the stability of tankyrases. *Genes Dev.* **2017**, *31* (10), 1024-1035.
150. McNamara, D.; Smith, E. C. R.; Calligaro, D. O.; O'Malley, P. J.; McQuaid, L. A.; Dingledine, R., 5,7-Dichlorokynurenic acid, a potent and selective competitive antagonist of the glycine site on NMDA receptors. *Neurosci. Lett.* **1990**, *120* (1), 17-20.
151. Turski, L.; Huth, A.; Sheardown, M.; McDonald, F.; Neuhaus, R.; Schneider, H. H.; Dirnagl, U.; Wiegand, F.; Jacobsen, P.; Ottow, E., ZK200775: a phosphonate quinoxalinedione AMPA antagonist for neuroprotection in stroke and trauma. *Proc. Natl. Acad. Sci. USA* **1998**, *95* (18), 10960-10965.
152. Pollock, K. Identifying Inhibitors of the Tankyrase : Substrate Protein-Protein Interaction. University of London, 2017.
153. Ciulli, A.; Abell, C., Fragment-based approaches to enzyme inhibition. *Curr. Opin. Biotechnol.* **2007**, *18* (6), 489-496.
154. Lipinski, C. A.; Lombardo, F.; Dominy, B. W.; Feeney, P. J., Experimental and computational approaches to estimate solubility and permeability in drug discovery and development settings1PII of original article: S0169-409X(96)00423-1. The article was originally published in *Advanced Drug Delivery Reviews* 23 (1997) 3–25.1. *Adv. Drug Deliv. Rev.* **2001**, *46* (1), 3-26.
155. Erlanson, D. A.; McDowell, R. S.; O'Brien, T., Fragment-Based Drug Discovery. *J. Med. Chem.* **2004**, *47* (14), 3463-3482.
156. Congreve, M.; Carr, R.; Murray, C.; Jhoti, H., A 'Rule of Three' for fragment-based lead discovery? *Drug Discov. Today* **2003**, *8* (19), 876-877.
157. Jhoti, H.; Williams, G.; Rees, D. C.; Murray, C. W., The 'rule of three' for fragment-based drug discovery: where are we now? *Nat. Rev. Drug Discov.* **2013**, *12* (8), 644-644.
158. Hajduk, P. J.; Greer, J., A decade of fragment-based drug design: strategic advances and lessons learned. *Nat. Rev. Drug Discov.* **2007**, *6* (3), 211-219.
159. Giordanetto, F.; Jin, C.; Willmore, L.; Feher, M.; Shaw, D. E., Fragment Hits: What do They Look Like and How do They Bind? *J. Med. Chem.* **2019**, *62* (7), 3381-3394.
160. Ruddigkeit, L.; van Deursen, R.; Blum, L. C.; Reymond, J.-L., Enumeration of 166 Billion Organic Small Molecules in the Chemical Universe Database GDB-17. *J. Chem. Inf. Model.* **2012**, *52* (11), 2864-2875.
161. Bohacek, R. S.; McMartin, C.; Guida, W. C., The art and practice of structure-based drug design: A molecular modeling perspective. *Med. Res. Rev.* **1996**, *16* (1), 3-50.
162. Osborne, J.; Panova, S.; Rapti, M.; Urushima, T.; Jhoti, H., Fragments: where are we now? *Biochem. Soc. Trans.* **2020**, *48* (1), 271-280.
163. Renaud, J.-P.; Chung, C.-w.; Danielson, U. H.; Egner, U.; Hennig, M.; Hubbard, R. E.; Nar, H., Biophysics in drug discovery: impact, challenges and opportunities. *Nat. Rev. Drug Discov.* **2016**, *15* (10), 679-698.

164. Ciulli, A., Biophysical Screening for the Discovery of Small-Molecule Ligands. In *Protein-Ligand Interactions: Methods and Applications*, Williams, M. A.; Daviter, T., Eds. Humana Press: Totowa, NJ, 2013; pp 357-388.
165. Mashalidis, E. H.; Śledź, P.; Lang, S.; Abell, C., A three-stage biophysical screening cascade for fragment-based drug discovery. *Nat. Protoc.* **2013**, *8* (11), 2309-2324.
166. Bai, N.; Roder, H.; Dickson, A.; Karanicolas, J., Isothermal Analysis of ThermoFluor Data can readily provide Quantitative Binding Affinities. *Sci Rep* **2019**, *9* (1), 2650.
167. Giannetti, A. M., Chapter Eight - From Experimental Design to Validated Hits: A Comprehensive Walk-Through of Fragment Lead Identification Using Surface Plasmon Resonance. In *Methods Enzymol*, Kuo, L. C., Ed. Academic Press: 2011; Vol. 493, pp 169-218.
168. Li, Q., Application of Fragment-Based Drug Discovery to Versatile Targets. *Front. Mol. Biosci.* **2020**, *7*.
169. Erlanson, D. A.; Davis, B. J.; Jahnke, W., Fragment-Based Drug Discovery: Advancing Fragments in the Absence of Crystal Structures. *Cell Chem. Biol.* **2019**, *26* (1), 9-15.
170. Mureddu, L. G.; Vuister, G. W., Fragment-Based Drug Discovery by NMR. Where Are the Successes and Where can It Be Improved? *Front. Mol. Biosci.* **2022**, *9*.
171. Shuker, S. B.; Hajduk, P. J.; Meadows, R. P.; Fesik, S. W., Discovering High-Affinity Ligands for Proteins: SAR by NMR. *Science* **1996**, *274* (5292), 1531.
172. Harner, M. J.; Frank, A. O.; Fesik, S. W., Fragment-based drug discovery using NMR spectroscopy. *J. Biomol. NMR.* **2013**, *56* (2), 65-75.
173. Carr, R. A. E.; Congreve, M.; Murray, C. W.; Rees, D. C., Fragment-based lead discovery: leads by design. *Drug Discovery Today* **2005**, *10* (14), 987-992.
174. Rees, D. C.; Congreve, M.; Murray, C. W.; Carr, R., Fragment-based lead discovery. *Nat. Rev. Drug Discov.* **2004**, *3* (8), 660-672.
175. Tsai, J.; Lee, J. T.; Wang, W.; Zhang, J.; Cho, H.; Mamo, S.; Bremer, R.; Gillette, S.; Kong, J.; Haass, N. K.; Sproesser, K.; Li, L.; Smalley, K. S. M.; Fong, D.; Zhu, Y.-L.; Marimuthu, A.; Nguyen, H.; Lam, B.; Liu, J.; Cheung, I.; Rice, J.; Suzuki, Y.; Luu, C.; Settachatgul, C.; Shellooe, R.; Cantwell, J.; Kim, S.-H.; Schlessinger, J.; Zhang, K. Y. J.; West, B. L.; Powell, B.; Habets, G.; Zhang, C.; Ibrahim, P. N.; Hirth, P.; Artis, D. R.; Herlyn, M.; Bollag, G., Discovery of a selective inhibitor of oncogenic B-Raf kinase with potent antimelanoma activity. *Proc. Natl. Acad. Sci.* **2008**, *105* (8), 3041-3046.
176. Bollag, G.; Tsai, J.; Zhang, J.; Zhang, C.; Ibrahim, P.; Nolop, K.; Hirth, P., Vemurafenib: the first drug approved for BRAF-mutant cancer. *Nat. Rev. Drug Discov.* **2012**, *11* (11), 873-886.
177. Petros, A. M.; Dinges, J.; Augeri, D. J.; Baumeister, S. A.; Betebenner, D. A.; Bures, M. G.; Elmore, S. W.; Hajduk, P. J.; Joseph, M. K.; Landis, S. K.; Nettesheim, D. G.; Rosenberg, S. H.; Shen, W.; Thomas, S.; Wang, X.; Zanze, I.; Zhang, H.; Fesik, S. W., Discovery of a Potent Inhibitor of the Antiapoptotic Protein Bcl-xL from NMR and Parallel Synthesis. *J. Med. Chem.* **2006**, *49* (2), 656-663.
178. Souers, A. J.; Levenson, J. D.; Boghaert, E. R.; Ackler, S. L.; Catron, N. D.; Chen, J.; Dayton, B. D.; Ding, H.; Enschede, S. H.; Fairbrother, W. J.; Huang, D. C. S.; Hymowitz, S. G.; Jin, S.; Khaw, S. L.; Kovar, P. J.; Lam, L. T.; Lee, J.; Maecker, H. L.; Marsh, K. C.; Mason, K. D.; Mitten, M. J.; Nimmer, P. M.;

- Oleksijew, A.; Park, C. H.; Park, C.-M.; Phillips, D. C.; Roberts, A. W.; Sampath, D.; Seymour, J. F.; Smith, M. L.; Sullivan, G. M.; Tahir, S. K.; Tse, C.; Wendt, M. D.; Xiao, Y.; Xue, J. C.; Zhang, H.; Humerickhouse, R. A.; Rosenberg, S. H.; Elmore, S. W., ABT-199, a potent and selective BCL-2 inhibitor, achieves antitumor activity while sparing platelets. *Nat. Med.* **2013**, *19* (2), 202-208.
179. van Montfort, Rob L. M.; Workman, P., Structure-based drug design: aiming for a perfect fit. *Essays Biochem.* **2017**, *61* (5), 431-437.
180. Horst, R.; Farley, K. A.; Kormos, B. L.; Withka, J. M., NMR spectroscopy: the swiss army knife of drug discovery. *J. Biomol. NMR.* **2020**, *74* (10), 509-519.
181. Carneiro, Marta G.; Ab, E.; Theisgen, S.; Siegal, G., NMR in structure-based drug design. *Essays Biochem.* **2017**, *61* (5), 485-493.
182. Williamson, M. P., Using chemical shift perturbation to characterise ligand binding. *Prog. Nucl. Magn. Reson. Spectrosc.* **2013**, *73*, 1-16.
183. Turnbull, A. P.; Boyd, S. M.; Walse, B., Fragment-based drug discovery and protein-protein interactions. *Res. Rep. Biochem* **2014**, *4* (13.10), 2147.
184. Hajduk, P. J.; Sheppard, G.; Nettlesheim, D. G.; Olejniczak, E. T.; Shuker, S. B.; Meadows, R. P.; Steinman, D. H.; Carrera, G. M.; Marcotte, P. A.; Severin, J.; Walter, K.; Smith, H.; Gubbins, E.; Simmer, R.; Holzman, T. F.; Morgan, D. W.; Davidsen, S. K.; Summers, J. B.; Fesik, S. W., Discovery of Potent Nonpeptide Inhibitors of Stromelysin Using SAR by NMR. *J. Am. Chem. Soc.* **1997**, *119* (25), 5818-5827.
185. Fedorov, D. G.; Kitaura, K., Extending the Power of Quantum Chemistry to Large Systems with the Fragment Molecular Orbital Method. *J. Phys. Chem. A* **2007**, *111* (30), 6904-6914.
186. Fedorov, D. G.; Nagata, T.; Kitaura, K., Exploring chemistry with the fragment molecular orbital method. *Phys. Chem. Chem. Phys.* **2012**, *14* (21), 7562-7577.
187. Fedorov, D. G.; Kitaura, K., The importance of three-body terms in the fragment molecular orbital method. *J. Chem. Phys.* **2004**, *120* (15), 6832-6840.
188. Schmidt, M. W.; Baldrige, K. K.; Boatz, J. A.; Elbert, S. T.; Gordon, M. S.; Jensen, J. H.; Koseki, S.; Matsunaga, N.; Nguyen, K. A.; Su, S.; Windus, T. L.; Dupuis, M.; Montgomery Jr, J. A., General atomic and molecular electronic structure system. *J. Comput. Chem.* **1993**, *14* (11), 1347-1363.
189. Kumari, S.; Carmona, A. V.; Tiwari, A. K.; Trippier, P. C., Amide Bond Bioisosteres: Strategies, Synthesis, and Successes. *J. Med. Chem.* **2020**, *63* (21), 12290-12358.
190. Boström, J.; Brown, D. G.; Young, R. J.; Keserü, G. M., Expanding the medicinal chemistry synthetic toolbox. *Nat. Rev. Drug Discov.* **2018**, *17* (10), 709-727.
191. Valeur, E.; Bradley, M., Amide bond formation: beyond the myth of coupling reagents. *Chem. Soc. Rev.* **2009**, *38* (2), 606-631.
192. Hajduk, P. J.; Olejniczak, E. T.; Fesik, S. W., One-Dimensional Relaxation- and Diffusion-Edited NMR Methods for Screening Compounds That Bind to Macromolecules. *J. Am. Chem. Soc.* **1997**, *119* (50), 12257-12261.
193. Meiboom, S.; Gill, D., Modified Spin-Echo Method for Measuring Nuclear Relaxation Times. *Rev. Sci. Instrum.* **1958**, *29* (8), 688-691.
194. Dalvit, C.; Fogliatto, G.; Stewart, A.; Veronesi, M.; Stockman, B., WaterLOGSY as a method for primary NMR screening: Practical aspects and range of applicability. *J. Biomol. NMR.* **2001**, *21* (4), 349-359.

195. Raingeval, C.; Cala, O.; Brion, B.; Le Borgne, M.; Hubbard, R. E.; Krimm, I., 1D NMR WaterLOGSY as an efficient method for fragment-based lead discovery. *J. Enzyme Inhib. Med. Chem.* **2019**, *34* (1), 1218-1225.
196. Pollock, K.; Ranes, M.; Collins, I.; Guettler, S., Identifying and Validating Tankyrase Binders and Substrates: A Candidate Approach. In *Poly(ADP-Ribose) Polymerase: Methods and Protocols*, Tulin, A. V., Ed. Springer New York: New York, NY, 2017; pp 445-473.
197. Peng, C.; Frommlet, A.; Perez, M.; Cobas, C.; Blechschmidt, A.; Dominguez, S.; Lingel, A., Fast and Efficient Fragment-Based Lead Generation by Fully Automated Processing and Analysis of Ligand-Observed NMR Binding Data. *J. Med. Chem.* **2016**, *59* (7), 3303-3310.
198. *Molecular Operating Environment (MOE)*, 2018.01; Chemical Computing Group ULC. 1010 Sherbooke St. West, Suite #910, Montreal, QC, Canada, H3A 2R7, **2018**.
199. Fielding, L., NMR Methods for the Determination of Protein- Ligand Dissociation Constants. *Curr. Top. Med. Chem.* **2003**, *3* (1), 39-53.
200. Fielding, L., NMR methods for the determination of protein–ligand dissociation constants. *Prog. Nucl. Magn. Reson. Spectrosc.* **2007**, *51* (4), 219-242.
201. Mureddu, L.; Vuister, G. W., Simple high-resolution NMR spectroscopy as a tool in molecular biology. *FEBS J.* **2019**, *286* (11), 2035-2042.
202. Cavanagh, J.; Fairbrother, W. J.; Palmer, A. G.; Rance, M.; Skelton, N. J., Chapter 7 - Heteronuclear NMR Experiments. In *Protein NMR Spectroscopy (Second Edition)*, Cavanagh, J.; Fairbrother, W. J.; Palmer, A. G.; Rance, M.; Skelton, N. J., Eds. Academic Press: Burlington, 2007; pp 533-678.
203. Webb, G. A., NMR Spectroscopy, 14N and 15N. In *Encyclopedia of Spectroscopy and Spectrometry (Third Edition)*, Lindon, J. C.; Tranter, G. E.; Koppenaal, D. W., Eds. Academic Press: Oxford, 2017; pp 274-283.
204. Skinner, S. P.; Fogh, R. H.; Boucher, W.; Ragan, T. J.; Mureddu, L. G.; Vuister, G. W., CcpNmr AnalysisAssign: a flexible platform for integrated NMR analysis. *J. Biomol. NMR.* **2016**, *66* (2), 111-124.
205. Barrans, R. E.; Dougherty, D. A., An improved method for determining bimolecular association constants from NMR titration experiments. *Supramol. Chem.* **1994**, *4* (2), 121-130.
206. Hansen, S. V. F.; Ulven, T., Oxalyl Chloride as a Practical Carbon Monoxide Source for Carbonylation Reactions. *Org. Lett.* **2015**, *17* (11), 2832-2835.
207. Peng, J. W.; Moore, J.; Abdul-Manan, N., NMR experiments for lead generation in drug discovery. *Prog. Nucl. Magn. Reson. Spectrosc.* **2004**, *44* (3), 225-256.
208. DaRosa, P. A.; Klevit, R. E.; Xu, W., Structural basis for tankyrase-RNF146 interaction reveals noncanonical tankyrase-binding motifs. *Protein Sci.* **2018**, *27* (6), 1057-1067.
209. Jones, J., *Amino Acid and Peptide Synthesis*. Oxford University Press: 1992.
210. Lea, W. A.; Simeonov, A., Fluorescence polarization assays in small molecule screening. *Expert Opin. Drug Discov.* **2011**, *6* (1), 17-32.
211. Owicki, J. C., Fluorescence Polarization and Anisotropy in High Throughput Screening: Perspectives and Primer. *SLAS Discov.* **2000**, *5* (5), 297-306.

212. Uri, A.; Nonga, O. E., What is the current value of fluorescence polarization assays in small molecule screening? *Expert Opin. Drug Discov.* **2020**, *15* (2), 131-133.
213. Jameson, D. M.; Ross, J. A., Fluorescence Polarization/Anisotropy in Diagnostics and Imaging. *Chem. Rev.* **2010**, *110* (5), 2685-2708.
214. Huang, X., Fluorescence Polarization Competition Assay: The Range of Resolvable Inhibitor Potency Is Limited by the Affinity of the Fluorescent Ligand. *SLAS Discov.* **2003**, *8* (1), 34-38.
215. Perrin, F., Polarization of light of fluorescence, average life of molecules in the excited state. *J. Phys. Radium* **1926**, *7*, 390-401.
216. Fluorescence Anisotropy. In *Principles of Fluorescence Spectroscopy*, Lakowicz, J. R., Ed. Springer US: Boston, MA, 2006; pp 353-382.
217. Jablonski, A., On the notion of emission anisotropy. *Bull. Acad. Pol. Sci* **1960**, *8*, 259-264.
218. Rossi, A. M.; Taylor, C. W., Analysis of protein-ligand interactions by fluorescence polarization. *Nat. Protoc.* **2011**, *6* (3), 365-387.
219. Pollard, T. D., A Guide to Simple and Informative Binding Assays. *Mol. Biol. Cell* **2010**, *21* (23), 4061-4067.
220. Fluorescence Polarization. <https://www.bmglabtech.com/en/fluorescence-polarization/#:~:text=Fluorescence%20polarization%20immunoassay&text=It%20is%20a%20competitive%20biochemical,to%20bind%20a%20selected%20antibody>. (accessed September 2022).
221. Kleiger, G.; Mayor, T., Perilous journey: a tour of the ubiquitin–proteasome system. *Trends Cell Biol.* **2014**, *24* (6), 352-359.
222. Lucas, X.; Ciulli, A., Recognition of substrate degrons by E3 ubiquitin ligases and modulation by small-molecule mimicry strategies. *Curr. Opin. Struct. Biol.* **2017**, *44*, 101-110.
223. Bondeson, D. P.; Smith, B. E.; Burslem, G. M.; Buhimschi, A. D.; Hines, J.; Jaime-Figueroa, S.; Wang, J.; Hamman, B. D.; Ishchenko, A.; Crews, C. M., Lessons in PROTAC Design from Selective Degradation with a Promiscuous Warhead. *Cell Chem. Biol.* **2018**, *25* (1), 78-87.e5.
224. Sakamoto, K. M.; Kim, K. B.; Kumagai, A.; Mercurio, F.; Crews, C. M.; Deshaies, R. J., Protacs: Chimeric molecules that target proteins to the Skp1–Cullin–F box complex for ubiquitination and degradation. *Proc. Natl. Acad. Sci.* **2001**, *98* (15), 8554.
225. Roy, M. J.; Winkler, S.; Hughes, S. J.; Whitworth, C.; Galant, M.; Farnaby, W.; Rumpel, K.; Ciulli, A., SPR-Measured Dissociation Kinetics of PROTAC Ternary Complexes Influence Target Degradation Rate. *ACS Chem. Biol.* **2019**, *14* (3), 361-368.
226. Bondeson, D. P.; Mares, A.; Smith, I. E. D.; Ko, E.; Campos, S.; Miah, A. H.; Mulholland, K. E.; Routly, N.; Buckley, D. L.; Gustafson, J. L.; Zinn, N.; Grandi, P.; Shimamura, S.; Bergamini, G.; Faeltz-Savitski, M.; Bantscheff, M.; Cox, C.; Gordon, D. A.; Willard, R. R.; Flanagan, J. J.; Casillas, L. N.; Votta, B. J.; den Besten, W.; Famm, K.; Kruidenier, L.; Carter, P. S.; Harling, J. D.; Churcher, I.; Crews, C. M., Catalytic in vivo protein knockdown by small-molecule PROTACs. *Nat. Chem. Biol.* **2015**, *11* (8), 611-617.
227. Paiva, S.-L.; Crews, C. M., Targeted protein degradation: elements of PROTAC design. *Curr. Opin. Chem. Biol.* **2019**, *50*, 111-119.
228. Komander, D., The emerging complexity of protein ubiquitination. *Biochem. Soc. Trans.* **2009**, *37* (5), 937-953.

229. Ishida, T.; Ciulli, A., E3 Ligase Ligands for PROTACs: How They Were Found and How to Discover New Ones. *SLAS Discov.* **2021**, *26* (4), 484-502.
230. Lai, A. C.; Crews, C. M., Induced protein degradation: an emerging drug discovery paradigm. *Nat. Rev. Drug Discov.* **2017**, *16* (2), 101-114.
231. Schapira, M.; Calabrese, M. F.; Bullock, A. N.; Crews, C. M., Targeted protein degradation: expanding the toolbox. *Nat. Rev. Drug Discov.* **2019**, *18* (12), 949-963.
232. Belcher, B. P.; Ward, C. C.; Nomura, D. K., Ligandability of E3 Ligases for Targeted Protein Degradation Applications. *Biochemistry* **2021**.
233. Kannt, A.; Đikić, I., Expanding the arsenal of E3 ubiquitin ligases for proximity-induced protein degradation. *Cell Chem. Biol.* **2021**, *28* (7), 1014-1031.
234. Kramer, L. T.; Zhang, X., Expanding the landscape of E3 ligases for targeted protein degradation. *Current Research in Chemical Biology* **2022**, *2*, 100020.
235. Bemis, T. A.; La Clair, J. J.; Burkart, M. D., Unraveling the Role of Linker Design in Proteolysis Targeting Chimeras. *J. Med. Chem.* **2021**, *64* (12), 8042-8052.
236. Troup, R. I.; Fallan, C.; Baud, M. G. J., Current strategies for the design of PROTAC linkers: a critical review. *Explor. Target Antitumor Ther.* **2020**, *1* (5), 273-312.
237. Cyrus, K.; Wehenkel, M.; Choi, E.-Y.; Han, H.-J.; Lee, H.; Swanson, H.; Kim, K.-B., Impact of linker length on the activity of PROTACs. *Mol. BioSyst.* **2011**, *7* (2), 359-364.
238. Zorba, A.; Nguyen, C.; Xu, Y.; Starr, J.; Borzilleri, K.; Smith, J.; Zhu, H.; Farley, K. A.; Ding, W.; Schiemer, J.; Feng, X.; Chang, J. S.; Uccello, D. P.; Young, J. A.; Garcia-Irrizary, C. N.; Czabaniuk, L.; Schuff, B.; Oliver, R.; Montgomery, J.; Hayward, M. M.; Coe, J.; Chen, J.; Niosi, M.; Luthra, S.; Shah, J. C.; El-Kattan, A.; Qiu, X.; West, G. M.; Noe, M. C.; Shanmugasundaram, V.; Gilbert, A. M.; Brown, M. F.; Calabrese, M. F., Delineating the role of cooperativity in the design of potent PROTACs for BTK. *Proc. Natl. Acad. Sci.* **2018**, *115* (31), E7285.
239. Chessum, N. E. A.; Sharp, S. Y.; Caldwell, J. J.; Pasqua, A. E.; Wilding, B.; Colombano, G.; Collins, I.; Ozer, B.; Richards, M.; Rowlands, M.; Stubbs, M.; Burke, R.; McAndrew, P. C.; Clarke, P. A.; Workman, P.; Cheeseman, M. D.; Jones, K., Demonstrating In-Cell Target Engagement Using a Pirin Protein Degradation Probe (CCT367766). *J. Med. Chem.* **2018**, *61* (3), 918-933.
240. Poongavanam, V.; Kihlberg, J., PROTAC cell permeability and oral bioavailability: a journey into uncharted territory. *Future Med. Chem.* **2021**.
241. Gadd, M. S.; Testa, A.; Lucas, X.; Chan, K.-H.; Chen, W.; Lamont, D. J.; Zengerle, M.; Ciulli, A., Structural basis of PROTAC cooperative recognition for selective protein degradation. *Nat. Chem. Biol.* **2017**, *13* (5), 514-521.
242. Smith, B. E.; Wang, S. L.; Jaime-Figueroa, S.; Harbin, A.; Wang, J.; Hamman, B. D.; Crews, C. M., Differential PROTAC substrate specificity dictated by orientation of recruited E3 ligase. *Nat. Commun.* **2019**, *10* (1), 131.
243. Sun, D.; Zhang, J.; Dong, G.; He, S.; Sheng, C., Blocking Non-enzymatic Functions by PROTAC-Mediated Targeted Protein Degradation. *J. Med. Chem.* **2022**, *65* (21), 14276-14288.
244. Kim, C.; Wang, X.-D.; Liu, Z.; Zha, S.; Yu, Y., Targeting Scaffolding Functions of Enzymes Using PROTAC Approaches. *Biochemistry* **2022**.

245. Zhao, Q.; Lan, T.; Su, S.; Rao, Y., Induction of apoptosis in MDA-MB-231 breast cancer cells by a PARP1-targeting PROTAC small molecule. *Chem. Commun.* **2019**, *55* (3), 369-372.
246. Wang, S.; Han, L.; Han, J.; Li, P.; Ding, Q.; Zhang, Q.-J.; Liu, Z.-P.; Chen, C.; Yu, Y., Uncoupling of PARP1 trapping and inhibition using selective PARP1 degradation. *Nat. Chem. Biol.* **2019**, *15* (12), 1223-1231.
247. Cao, C.; Yang, J.; Chen, Y.; Zhou, P.; Wang, Y.; Du, W.; Zhao, L.; Chen, Y., Discovery of SK-575 as a Highly Potent and Efficacious Proteolysis-Targeting Chimera Degradator of PARP1 for Treating Cancers. *J. Med. Chem.* **2020**, *63* (19), 11012-11033.
248. Zhang, Z.; Chang, X.; Zhang, C.; Zeng, S.; Liang, M.; Ma, Z.; Wang, Z.; Huang, W.; Shen, Z., Identification of probe-quality degraders for Poly(ADP-ribose) polymerase-1 (PARP-1). *J. Enzyme Inhib. Med. Chem.* **2020**, *35* (1), 1606-1615.
249. He, M.; Cao, C.; Ni, Z.; Liu, Y.; Song, P.; Hao, S.; He, Y.; Sun, X.; Rao, Y., PROTACs: great opportunities for academia and industry (an update from 2020 to 2021). *Sig. Transduct. Target. Ther.* **2022**, *7* (1), 181.
250. Lu, J.; Qian, Y.; Altieri, M.; Dong, H.; Wang, J.; Raina, K.; Hines, J.; Winkler, James D.; Crew, Andrew P.; Coleman, K.; Crews, Craig M., Hijacking the E3 Ubiquitin Ligase Cereblon to Efficiently Target BRD4. *Chem. Biol.* **2015**, *22* (6), 755-763.
251. Ito, T.; Ando, H.; Suzuki, T.; Ogura, T.; Hotta, K.; Imamura, Y.; Yamaguchi, Y.; Handa, H., Identification of a Primary Target of Thalidomide Teratogenicity. *Science* **2010**, *327* (5971), 1345.
252. Winter, G. E.; Buckley, D. L.; Paulk, J.; Roberts, J. M.; Souza, A.; Dhe-Paganon, S.; Bradner, J. E., Phthalimide conjugation as a strategy for in vivo target protein degradation. *Science* **2015**, *348* (6241), 1376-1381.
253. Bricelj, A.; Steinebach, C.; Kuchta, R.; Gütschow, M.; Sosič, I., E3 Ligase Ligands in Successful PROTACs: An Overview of Syntheses and Linker Attachment Points. *Front. Chem.* **2021**, *9*.
254. Roberts, M. J.; Bentley, M. D.; Harris, J. M., Chemistry for peptide and protein PEGylation. *Adv. Drug Deliv. Rev.* **2012**, *64*, 116-127.
255. Fischer, E. S.; Böhm, K.; Lydeard, J. R.; Yang, H.; Stadler, M. B.; Cavadini, S.; Nagel, J.; Serluca, F.; Acker, V.; Lingaraju, G. M.; Tichkule, R. B.; Schebesta, M.; Forrester, W. C.; Schirle, M.; Hassiepen, U.; Ottl, J.; Hild, M.; Beckwith, R. E. J.; Harper, J. W.; Jenkins, J. L.; Thomä, N. H., Structure of the DDB1-CRBN E3 ubiquitin ligase in complex with thalidomide. *Nature* **2014**, *512* (7512), 49-53.
256. Riching, K. M.; Mahan, S.; Corona, C. R.; McDougall, M.; Vasta, J. D.; Robers, M. B.; Urh, M.; Daniels, D. L., Quantitative Live-Cell Kinetic Degradation and Mechanistic Profiling of PROTAC Mode of Action. *ACS Chem. Biol.* **2018**, *13* (9), 2758-2770.
257. NanoBRET™ TE Intracellular E3 Ligase Assays. <https://www.promega.co.uk/products/protein-detection/protein-degradation-protacs/nanobret-te-intracellular-e3-ligase-assays/?catNum=N2910> (accessed November 2022).
258. Matyskiela, M. E.; Lu, G.; Ito, T.; Pagarigan, B.; Lu, C.-C.; Miller, K.; Fang, W.; Wang, N.-Y.; Nguyen, D.; Houston, J.; Carmel, G.; Tran, T.; Riley, M.; Nosaka, L. A.; Lander, G. C.; Gaidarova, S.; Xu, S.; Ruchelman, A. L.; Handa, H.; Carmichael, J.; Daniel, T. O.; Cathers, B. E.; Lopez-Girona, A.; Chamberlain,

- P. P., A novel cereblon modulator recruits GSPT1 to the CRL4CRBN ubiquitin ligase. *Nature* **2016**, *535* (7611), 252-257.
259. Winter, G. E.; Mayer, A.; Buckley, D. L.; Erb, M. A.; Roderick, J. E.; Vittori, S.; Reyes, J. M.; di Iulio, J.; Souza, A.; Ott, C. J.; Roberts, J. M.; Zeid, R.; Scott, T. G.; Paulk, J.; Lachance, K.; Olson, C. M.; Dastjerdi, S.; Bauer, S.; Lin, C. Y.; Gray, N. S.; Kelliher, M. A.; Churchman, L. S.; Bradner, J. E., BET Bromodomain Proteins Function as Master Transcription Elongation Factors Independent of CDK9 Recruitment. *Mol. Cell* **2017**, *67* (1), 5-18.e19.
260. Doak, Bradley C.; Over, B.; Giordanetto, F.; Kihlberg, J., Oral Druggable Space beyond the Rule of 5: Insights from Drugs and Clinical Candidates. *Chem. Biol.* **2014**, *21* (9), 1115-1142.
261. Mattsson, P.; Kihlberg, J., How Big Is Too Big for Cell Permeability? *J. Med. Chem.* **2017**, *60* (5), 1662-1664.
262. Veber, D. F.; Johnson, S. R.; Cheng, H.-Y.; Smith, B. R.; Ward, K. W.; Kopple, K. D., Molecular Properties That Influence the Oral Bioavailability of Drug Candidates. *J. Med. Chem.* **2002**, *45* (12), 2615-2623.
263. Prasanna, S.; Doerksen, J. R., Topological Polar Surface Area: A Useful Descriptor in 2D-QSAR. *Curr. Med. Chem.* **2009**, *16* (1), 21-41.
264. Hughes, Scott J.; Ciulli, A., Molecular recognition of ternary complexes: a new dimension in the structure-guided design of chemical degraders. *Essays Biochem.* **2017**, *61* (5), 505-516.
265. Nowak, R. P.; DeAngelo, S. L.; Buckley, D.; He, Z.; Donovan, K. A.; An, J.; Safaee, N.; Jedrychowski, M. P.; Ponthier, C. M.; Ishoey, M.; Zhang, T.; Mancias, J. D.; Gray, N. S.; Bradner, J. E.; Fischer, E. S., Plasticity in binding confers selectivity in ligand-induced protein degradation. *Nat. Chem. Biol.* **2018**, *14* (7), 706-714.
266. Farnaby, W.; Koegl, M.; Roy, M. J.; Whitworth, C.; Diers, E.; Trainor, N.; Zollman, D.; Steurer, S.; Karolyi-Oezguer, J.; Riedmueller, C.; Gmaschitz, T.; Wachter, J.; Dank, C.; Galant, M.; Sharps, B.; Rumpel, K.; Traxler, E.; Gerstberger, T.; Schnitzer, R.; Petermann, O.; Greb, P.; Weinstabl, H.; Bader, G.; Zoephel, A.; Weiss-Puxbaum, A.; Ehrenhöfer-Wölfer, K.; Wöhrle, S.; Boehmelt, G.; Rinnenthal, J.; Arnhof, H.; Wiechens, N.; Wu, M.-Y.; Owen-Hughes, T.; Ettmayer, P.; Pearson, M.; McConnell, D. B.; Ciulli, A., BAF complex vulnerabilities in cancer demonstrated via structure-based PROTAC design. *Nat. Chem. Biol.* **2019**, *15* (7), 672-680.
267. Testa, A.; Hughes, S. J.; Lucas, X.; Wright, J. E.; Ciulli, A., Structure-Based Design of a Macrocyclic PROTAC. *Angew. Chem. Int. Ed.* **2020**, *59* (4), 1727-1734.
268. Liao, J.; Nie, X.; Unarta, I. C.; Ericksen, S. S.; Tang, W., In Silico Modeling and Scoring of PROTAC-Mediated Ternary Complex Poses. *J. Med. Chem.* **2022**.
269. Drummond, M. L.; Williams, C. I., In Silico Modeling of PROTAC-Mediated Ternary Complexes: Validation and Application. *J. Chem. Inf. Model.* **2019**, *59* (4), 1634-1644.
270. Drummond, M. L.; Henry, A.; Li, H.; Williams, C. I., Improved Accuracy for Modeling PROTAC-Mediated Ternary Complex Formation and Targeted Protein Degradation via New In Silico Methodologies. *J. Chem. Inf. Model.* **2020**, *60* (10), 5234-5254.

271. Zaidman, D.; Prilusky, J.; London, N., PROsettaC: Rosetta Based Modeling of PROTAC Mediated Ternary Complexes. *J. Chem. Inf. Model.* **2020**, *60* (10), 4894-4903.
272. Bai, N.; Miller, S. A.; Andrianov, G. V.; Yates, M.; Kirubakaran, P.; Karanicolas, J., Rationalizing PROTAC-Mediated Ternary Complex Formation Using Rosetta. *J. Chem. Inf. Model.* **2021**, *61* (3), 1368-1382.
273. Churcher, I., Protac-Induced Protein Degradation in Drug Discovery: Breaking the Rules or Just Making New Ones? *J. Med. Chem.* **2018**, *61* (2), 444-452.
274. Orts, J.; Gossert, A. D., Structure determination of protein-ligand complexes by NMR in solution. *Methods* **2018**, *138-139*, 3-25.
275. Targeted Protein Degradation Assays and Reagents. <https://www.perkinelmer.com/uk/category/targeted-protein-degradation-assays-reagents> (accessed November 2022).
276. Targeted Protein Degradation. <https://www.promega.co.uk/applications/small-molecule-drug-discovery/protein-degradation-drug-discovery/> (accessed November 2022).
277. HTRF® technology Basics. <https://uk.cisbio.eu/content/htrf-technology-basics/> (accessed December 2022).
278. Steinebach, C.; Sosič, I.; Lindner, S.; Bricelj, A.; Kohl, F.; Ng, Y. L. D.; Monschke, M.; Wagner, K. G.; Krönke, J.; Gütschow, M., A MedChem toolbox for cereblon-directed PROTACs. *MedChemComm* **2019**, *10* (6), 1037-1041.
279. Hayhow, T. G.; Borrow, R. E. A.; Diène, C. R.; Fairley, G.; Fallan, C.; Fillery, S. M.; Scott, J. S.; Watson, D. W., A Buchwald–Hartwig Protocol to Enable Rapid Linker Exploration of Cereblon E3-Ligase PROTACs**. *Chem. Eur. J.* **2020**, *26* (70), 16818-16823.
280. Diehl, C. J.; Ciulli, A., Discovery of small molecule ligands for the von Hippel-Lindau (VHL) E3 ligase and their use as inhibitors and PROTAC degraders. *Chem. Soc. Rev.* **2022**, *51* (19), 8216-8257.
281. Liu, X.; Kalogeropoulou, A. F.; Domingos, S.; Makukhin, N.; Nirujogi, R. S.; Singh, F.; Shpiro, N.; Saalfrank, A.; Sammler, E.; Ganley, I. G.; Moreira, R.; Alessi, D. R.; Ciulli, A., Discovery of XL01126: A Potent, Fast, Cooperative, Selective, Orally Bioavailable, and Blood–Brain Barrier Penetrant PROTAC Degrader of Leucine-Rich Repeat Kinase 2. *J. Am. Chem. Soc.* **2022**, *144* (37), 16930-16952.
282. Han, X.; Zhao, L.; Xiang, W.; Qin, C.; Miao, B.; Xu, T.; Wang, M.; Yang, C.-Y.; Chinnaswamy, K.; Stuckey, J.; Wang, S., Discovery of Highly Potent and Efficient PROTAC Degraders of Androgen Receptor (AR) by Employing Weak Binding Affinity VHL E3 Ligase Ligands. *J. Med. Chem.* **2019**, *62* (24), 11218-11231.
283. Schatoff, E. M.; Goswami, S.; Zafra, M. P.; Foronda, M.; Shusterman, M.; Leach, B. I.; Katti, A.; Diaz, B. J.; Dow, L. E., Distinct Colorectal Cancer–Associated APC Mutations Dictate Response to Tankyrase Inhibition. *Cancer Discov.* **2019**, *9* (10), 1358-1371.
284. Tanaka, N.; Mashima, T.; Mizutani, A.; Sato, A.; Aoyama, A.; Gong, B.; Yoshida, H.; Muramatsu, Y.; Nakata, K.; Matsuura, M.; Katayama, R.; Nagayama, S.; Fujita, N.; Sugimoto, Y.; Seimiya, H., APC Mutations as a Potential Biomarker for Sensitivity to Tankyrase Inhibitors in Colorectal Cancer. *Mol. Cancer Ther.* **2017**, *16* (4), 752-762.

285. Verhoeven, J. W., Glossary of terms used in photochemistry (IUPAC Recommendations 1996). **1996**, *68* (12), 2223-2286.
286. Gasteiger, E.; Hoogland, C.; Gattiker, A.; Duvaud, S. e.; Wilkins, M. R.; Appel, R. D.; Bairoch, A., Protein Identification and Analysis Tools on the ExPASy Server. In *The Proteomics Protocols Handbook*, Walker, J. M., Ed. Humana Press: Totowa, NJ, 2005; pp 571-607.
287. Wishart, D. S.; Bigam, C. G.; Yao, J.; Abildgaard, F.; Dyson, H. J.; Oldfield, E.; Markley, J. L.; Sykes, B. D., ¹H, ¹³C and ¹⁵N chemical shift referencing in biomolecular NMR. *J. Biomol. NMR.* **1995**, *6* (2), 135-140.
288. Mureddu, L.; Vuister, G. W., Simple high-resolution NMR spectroscopy as a tool in molecular biology. *The FEBS Journal* **2019**, *286* (11), 2035-2042.